Safe spaces for South Asia's vultures *p. 1066*

Synthetic Notch receptors enhance T cell therapies *p. 1112*

Dietary fiber fights diabetes *p. 1151*

Science

$15
9 MARCH 2018
sciencemag.org
AAAS

HOW LIES SPREAD

On social media, false news beats the truth

pp. 1094 & 1146

CONTENTS

9 MARCH 2018 • VOLUME 359 • ISSUE 6380

1082

Sailing for science

NEWS

IN BRIEF

1076 News at a glance

IN DEPTH

1080 LITHIUM-SULFUR BATTERIES POISED FOR LEAP
Promising chemistry is starting to compete commercially with lithium-ion
By R. F. Service

1081 GERMANY'S NEW GOVERNMENT MAKES BIG PROMISES
Coalition says it will hike research spending to 3.5% of gross domestic product—but is that feasible?
By G. Vogel

1082 SAILDRONE FLEET COULD HELP REPLACE AGING BUOYS
Robotic test in Pacific Ocean heralds new way to monitor El Niño events
By P. Voosen

1083 STUDY UNDERCUTS CLAIMS OF NEW NEURONS IN ADULT BRAINS
Other groups still see evidence for lifelong neurogenesis *By E. Underwood*

1084 SLOW COOLANT PHASEOUT COULD WORSEN WARMING
As countries crank up the AC, emissions of potent greenhouse gases are likely to skyrocket *By A. Reese*

1085 CHINA HONES PLANS FOR AMBITIOUS X-RAY PROBE
Mission would firm up China's status as a leader in x-ray astronomy
By D. Normile

FEATURES

1086 LOOKING FOR LOVE
South Asia's "vulture safe zones" aim to preserve, and win respect for, a vital scavenger *By W. Cornwall*
▸ VIDEO

1090 FEVER DILEMMA
When malaria isn't the cause, clinics in the developing world often have little to offer *By G. Vogel*
▸ EDITORIAL P. 1075

INSIGHTS

POLICY FORUM

1094 THE SCIENCE OF FAKE NEWS
Addressing fake news requires a multidisciplinary effort *By D. M. J. Lazer* et al.
▸ REPORT P. 1146

PERSPECTIVES

1097 INTESTINAL BARRIERS PROTECT AGAINST DISEASE
Leaky cell-cell junctions contribute to inflammatory and autoimmune diseases
By S. Citi
▸ REPORTS PP. 1156 & 1161; C. A. THAISS *ET AL.* 10.1126/science.aar3318

1098 DIVERGING ROADS TO THE HEART
Cardiovascular lineage decisions in the mouse embryo are explored at single-cell resolution
By R. G. Kelly and S. R. Sperling
▸ REPORT P. 1177

1100 HARMFUL NETWORKS IN THE BRAIN AND BEYOND
Membrane tubes can connect cancer cells and drive tumor progression and resistance *By F. Winkler and W. Wick*

1102 HEMIMETHYLATION: DNA'S LASTING ODD COUPLE
Stably inherited DNA hemimethylation regulates chromatin interaction and transcription *By J. Sharif and H. Koseki*
▸ REPORT P. 1166

1103 WILL MARINE PRODUCTIVITY WANE?
A model study points to slow but extensive nutrient removal from the surface ocean under long-term climate change *By C. Laufkötter and N. Gruber*
▸ REPORT P. 1139

1105 CAPTURING DYNAMIC PROTEIN INTERACTIONS
A method based on heat denaturation reveals how proteins interact in different cells *By X.-H. Li* et al.
▸ REPORT P. 1170

1106 PROTEOFORMS AS THE NEXT PROTEOMICS CURRENCY
Identifying precise molecular forms of proteins can improve our understanding of function
By L. M. Smith and N. L. Kelleher

BOOKS *ET AL.*

1108 BEHIND THE SCENES OF THE BUILT ENVIRONMENT
An approachable introduction to structural engineering entertains and inspires *By D. Riley*

1109 WHO HOLDS THE POWER?
A careful history examines pivotal moments and the networks that made them possible *By S. P. Cornelius*

LETTERS

1110 THE SNOW LEOPARD'S QUESTIONABLE COMEBACK
By S. B. Ale and C. Mishra

PHOTO: A. B. M. SAROWAR ALAM/VULTURE CONSERVATION INITIATIVES; (GRAPHIC) A. CUADRA AND N. DESAI/*SCIENCE*

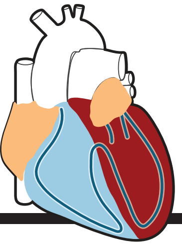

1098 & 1177
The developing heart

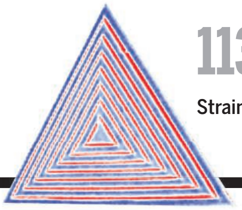

1131
Straining thin superlattices

1111 NIGERIA'S NEW GDP MEANS SCIENTISTS SUFFER
By W. G. Balogun and A. Seeni

1111 POSSIBLE BROODING OF PTEROSAUR PARENTS
By L. A. Somma

PRIZE ESSAY

1112 REFINING CELL THERAPY
Synthetic Notch receptors expand the therapeutic potential of engineered T cells *By K. T. Roybal*

RESEARCH

IN BRIEF

1114 From *Science* and other journals

REVIEW

1117 CHEMICAL BIOLOGY
Chemically induced proximity in biology and medicine *B. Z. Stanton* et al.
REVIEW SUMMARY; FOR FULL TEXT: dx.doi.org/10.1126/science.aao5902

RESEARCH ARTICLE

1118 STEM CELLS
Single-cell Wnt signaling niches maintain stemness of alveolar type 2 cells *A. N. Nabhan* et al.

REPORTS

1123 QUANTUM ELECTRONICS
Strong spin-photon coupling in silicon
N. Samkharadze et al.

1127 WATER STRUCTURE
A liquid-liquid transition in supercooled aqueous solution related to the HDA-LDA transition *S. Woutersen* et al.

1131 NANOMATERIALS
Coherent, atomically thin transition-metal dichalcogenide superlattices with engineered strain *S. Xie* et al.

1136 GEOCHEMISTRY
Ice-VII inclusions in diamonds: Evidence for aqueous fluid in Earth's deep mantle
O. Tschauner et al.

1139 CLIMATE CHANGE
Sustained climate warming drives declining marine biological productivity
J. K. Moore et al.
▸ PERSPECTIVE P. 1103

1143 NEUROSCIENCE
Local transformations of the hippocampal cognitive map *J. Krupic* et al.

1146 SOCIAL SCIENCE
The spread of true and false news online
S. Vosoughi et al.
▸ POLICY FORUM P. 1094; PODCAST

1151 MICROBIOTA
Gut bacteria selectively promoted by dietary fibers alleviate type 2 diabetes
L. Zhao et al.

1156 MICROBIOTA
Translocation of a gut pathobiont drives autoimmunity in mice and humans
S. Manfredo Vieira et al.
▸ PERSPECTIVE P. 1097; REPORT P. 1161;
C. A. THAISS *ET AL*. 10.1126/science.aar3318

1161 COLITIS
C1orf106 is a colitis risk gene that regulates stability of epithelial adherens junctions *V. Mohanan* et al.
▸ PERSPECTIVE P. 1097; REPORT P. 1156;
C. A. THAISS *ET AL*. 10.1126/science.aar3318

1166 MOLECULAR BIOLOGY
Nascent DNA methylome mapping reveals inheritance of hemimethylation at CTCF/cohesin sites
C. Xu and V. G. Corces
▸ PERSPECTIVE P. 1102

1170 PROTEIN FOLDING
Thermal proximity coaggregation for system-wide profiling of protein complex dynamics in cells
C. S. H. Tan et al.
▸ PERSPECTIVE P. 1105

1177 HEART DEVELOPMENT
Defining the earliest step of cardiovascular lineage segregation by single-cell RNA-seq
F. Lescroart et al.
▸ PERSPECTIVE P. 1098

DEPARTMENTS

1075 EDITORIAL
Health security's blind spot
By Seth Berkley
▸ NEWS STORY P. 1090

1186 WORKING LIFE
Why our ways parted
By Maria Ter-Mikaelian

ON THE COVER

Data visualization showing the spread of a false (orange) and true (teal) news story through Twitter. Longer lines represent longer retweet cascades, demonstrating the greater breadth and depth at which false news spreads. For further analysis on the dissemination of false news in the digital age, see pages 1094 and 1146. For more on the process behind the cover image, see http://scim.ag/2HYr5yE. *Image: Peter Beshai; Data: Soroush Vosoughi, Deb Roy, and Sinan Aral*

Science Staff 1074
New Products 1182
Science Careers 1183

CREDITS (CLOCKWISE FROM TOP LEFT): (GRAPHIC) N. DESAI/*SCIENCE*; (GRAPHIC) S. XIE *ET AL.*; (ILLUSTRATION) ROBERT NEUBECKER

SCIENCE (ISSN 0036-8075) is published weekly on Friday, except last week in December, by the American Association for the Advancement of Science, 1200 New York Avenue, NW, Washington, DC 20005. Periodicals mail postage (publication No. 484460) paid at Washington, DC, and additional mailing offices. Copyright © 2018 by the American Association for the Advancement of Science. The title SCIENCE is a registered trademark of the AAAS. Domestic individual membership, including subscription (12 months): $165 ($74 allocated to subscription). Domestic institutional subscription (51 issues): $1808; Foreign postage extra: Mexico, Caribbean (surface mail) $55; other countries (air assist delivery): $89. First class, airmail, student, and emeritus rates on request. Canadian rates with GST available upon request, GST #125488122. Publications Mail Agreement Number 1069624. **Printed in the U.S.A.**
Change of address: Allow 4 weeks, giving old and new addresses and 8-digit account number. **Postmaster:** Send change of address to AAAS, P.O. Box 96178, Washington, DC 20090–6178. **Single-copy sales:** $15 each plus shipping and handling; bulk rate on request. **Authorization to reproduce** material for internal or personal use under circumstances not falling within the fair use provisions of the Copyright Act is granted by AAAS to libraries and other users who use Copyright Clearance Center (CCC) Pay-Per-Use services provided that $35.00 per article is paid directly to CCC, 222 Rosewood Drive, Danvers, MA 01923. The identification code for *Science* is 0036-8075. *Science* is indexed in the *Reader's Guide to Periodical Literature* and in several specialized indexes.

Science

1200 New York Avenue, NW, Washington, DC 20005
Clarendon House, Clarendon Road, Cambridge, UK CB2 8FH

AAAS

Editor-in-Chief Jeremy Berg

Executive Editor Monica M. Bradford **News Editor** Tim Appenzeller

Deputy Editors Lisa D. Chong, Andrew M. Sugden(UK), Valda J. Vinson, Jake S. Yeston

Research and Insights

DEPUTY EDITOR, EMERITUS Barbara R. Jasny **SR. EDITORS** Gemma Alderton(UK), Caroline Ash(UK), Julia Fahrenkamp-Uppenbrink(UK), Pamela J. Hines, Stella M. Hurtley(UK), Paula A. Kiberstis, Marc S. Lavine(Canada), Steve Mao, Ian S. Osborne(UK), Beverly A. Purnell, L. Bryan Ray, H. Jesse Smith, Jelena Stajic, Peter Stern(UK), Phillip D. Szuromi, Sacha Vignieri, Brad Wible, Laura M. Zahn **ASSOCIATE EDITORS** Michael A. Funk, Brent Grocholski, Priscilla N. Kelly, Seth Thomas Scanlon(UK), Keith T. Smith(UK) **ASSOCIATE BOOK REVIEW EDITOR** Valerie B. Thompson **LETTERS EDITOR** Jennifer Sills **LEAD CONTENT PRODUCTION EDITORS** Harry Jach, Lauren Kmec **CONTENT PRODUCTION EDITORS** Amelia Beyna, Jeffrey E. Cook, Amber Esplin, Chris Filiatreau, Cynthia Howe, Catherine Wolner **SR. EDITORIAL COORDINATORS** Carolyn Kyle, Beverly Shields **EDITORIAL COORDINATORS** Aneera Dobbins, Joi S. Granger, Jeffrey Hearn, Lisa Johnson, Maryrose Madrid, Scott Miller, Jerry Richardson, Anita Wynn **PUBLICATIONS ASSISTANTS** Ope Martins, Nida Masiulis, Dona Mathieu, Hilary Stewart(UK), Alana Warnke, Alice Whaley(UK), Brian White **EXECUTIVE ASSISTANT** Jessica Slater **ADMINISTRATIVE SUPPORT** Janet Clements(UK), Lizanne Newton(UK)

News

NEWS MANAGING EDITOR John Travis **INTERNATIONAL EDITOR** Richard Stone **DEPUTY NEWS EDITORS** Elizabeth Culotta, Martin Enserink(Europe), David Grimm, Eric Hand, David Malakoff, Leslie Roberts **SR. CORRESPONDENTS** Daniel Clery(UK), Jeffrey Mervis, Elizabeth Pennisi **ASSOCIATE EDITORS** Jeffrey Brainard, Catherine Matacic **NEWS WRITERS** Adrian Cho, Jon Cohen, Jennifer Couzin-Frankel, Jocelyn Kaiser, Kelly Servick, Robert F. Service, Erik Stokstad(Cambridge, UK), Paul Voosen, Meredith Wadman **INTERNS** Roni Dengler, Katie Langin, Matt Warren **CONTRIBUTING CORRESPONDENTS** John Bohannon, Warren Cornwall, Ann Gibbons, Mara Hvistendahl, Sam Kean, Eli Kintisch, Kai Kupferschmidt(Berlin), Andrew Lawler, Mitch Leslie, Eliot Marshall, Virginia Morell, Dennis Normile(Shanghai), Charles Piller, Tania Rabesandratana(London), Emily Underwood, Gretchen Vogel(Berlin), Lizzie Wade(Mexico City) **CAREERS** Donisha Adams, Rachel Bernstein(Editor), Maggie Kuo **COPY EDITORS** Dorie Chevlen, Julia Cole (Senior Copy Editor), Cyra Master (Copy Chief) **ADMINISTRATIVE SUPPORT** Meagan Weiland

Executive Publisher Rush D. Holt

Publisher Bill Moran **Chief Digital Media Officer** Josh Freeman

DIRECTOR, BUSINESS STRATEGY AND PORTFOLIO MANAGEMENT Sarah Whalen **DIRECTOR, PRODUCT AND CUSTOM PUBLISHING** Will Schweitzer **MANAGER, PRODUCT DEVELOPMENT** Hannah Heckner **BUSINESS SYSTEMS AND FINANCIAL ANALYSIS DIRECTOR** Randy Yi **DIRECTOR, BUSINESS OPERATIONS & ANALYST** Eric Knott **SENIOR SYSTEMS ANALYST** Nicole Mehmedovich **SENIOR BUSINESS ANALYST** Cory Lipman **MANAGER, BUSINESS OPERATIONS** Jessica Tierney **BUSINESS ANALYSTS** Meron Kebede, Sandy Kim, Jourdan Stewart **FINANCIAL ANALYST** Julian Iriarte **ADVERTISING SYSTEM ADMINISTRATOR** Tina Burks **SALES COORDINATOR** Shirley Young **DIRECTOR, COPYRIGHT, LICENSING, SPECIAL PROJECTS** Emilie David **DIGITAL PRODUCT ASSOCIATE** Michael Hardesty **RIGHTS AND PERMISSIONS ASSOCIATE** Elizabeth Sandler **RIGHTS, CONTRACTS, AND LICENSING ASSOCIATE** Lili Catlett **RIGHTS & PERMISSIONS ASSISTANT** Alexander Lee

MARKETING MANAGER, PUBLISHING Shawana Arnold **MARKETING ASSOCIATE** Steven Goodman **SENIOR ART ASSOCIATES** Paula Fry **ART ASSOCIATE** Kim Huynh

INTERIM DIRECTOR, INSTITUTIONAL LICENSING Iquo Edim **ASSOCIATE DIRECTOR, RESEARCH & DEVELOPMENT** Elisabeth Leonard **SENIOR INSTITUTIONAL LICENSING MANAGER** Ryan Rexroth **INSTITUTIONAL LICENSING MANAGERS** Marco Castellan, Chris Murawski **SENIOR OPERATIONS ANALYST** Lana Guz **MANAGER, AGENT RELATIONS & CUSTOMER SUCCESS** Judy Lillibridge

WEB TECHNOLOGIES TECHINICAL DIRECTOR David Levy **TECHNICAL MANAGER** Chris Coleman **PORTFOLIO MANAGER** Trista Smith **PROJECT MANAGER** Tara Kelly, Dean Robbins **DEVELOPERS** Elissa Heller, Ryan Jensen, Brandon Morrison

DIGITAL MEDIA DIRECTOR OF ANALYTICS Enrique Gonzales **SR. MULTIMEDIA PRODUCER** Sarah Crespi **MANAGING DIGITAL PRODUCER** Kara Estelle-Powers **PRODUCER** Liana Birke **VIDEO PRODUCERS** Chris Burns, Nguyên Khôi Nguyễn **DIGITAL SOCIAL MEDIA PRODUCER** Brice Russ

DIGITAL/PRINT STRATEGY MANAGER Jason Hillman **QUALITY TECHNICAL MANAGER** Marcus Spiegler **DIGITAL PRODUCTION MANAGER** Lisa Stanford **ASSISTANT MANAGER DIGITAL/PRINT** Rebecca Doshi **SENIOR CONTENT SPECIALISTS** Steve Forrester, Antoinette Hodal, Lori Murphy, Anthony Rosen **CONTENT SPECIALISTS** Jacob Hedrick, Kimberley Oster

DESIGN DIRECTOR Beth Rakouskas **DESIGN MANAGING EDITOR** Marcy Atarod **SENIOR DESIGNER** Chrystal Smith **DESIGNER** Christina Aycock **GRAPHICS MANAGING EDITOR** Alberto Cuadra **GRAPHICS EDITOR** Nirja Desai **SENIOR SCIENTIFIC ILLUSTRATORS** Valerie Altounian, Chris Bickel, Katharine Sutliff **SCIENTIFIC ILLUSTRATOR** Alice Kitterman **INTERACTIVE GRAPHICS EDITOR** Jia You **SENIOR GRAPHICS SPECIALISTS** Holly Bishop, Nathalie Cary **PHOTOGRAPHY MANAGING EDITOR** William Douthitt **PHOTO EDITOR** Emily Petersen **IMAGE RIGHTS AND FINANCIAL MANAGER** Jessica Adams

SENIOR EDITOR, CUSTOM PUBLISHING Sean Sanders: 202-326-6430 **ASSISTANT EDITOR, CUSTOM PUBLISHING** Jackie Oberst: 202-326-6463 **ASSOCIATE DIRECTOR, BUSINESS DEVELOPMENT** Justin Sawyers: 202-326-7061 science_advertising@aaas.org **ADVERTISING PRODUCTION OPERATIONS MANAGER** Deborah Tompkins **SR. PRODUCTION SPECIALIST/GRAPHIC DESIGNER** Amy Hardcastle **SR. TRAFFIC ASSOCIATE** Christine Hall **DIRECTOR OF BUSINESS DEVELOPMENT AND ACADEMIC PUBLISHING RELATIONS, ASIA** Xiaoying Chu: +86-131 6136 3212, xchu@aaas.org **COLLABORATION/CUSTOM PUBLICATIONS/JAPAN** Adarsh Sandhu + 81532-81-5142 asandhu@aaas.org **EAST COAST/E. CANADA** Laurie Faraday: 508-747-9395, FAX 617-507-8189 **WEST COAST/W. CANADA** Lynne Stickrod: 415-931-9782, FAX 415-520-6940 **MIDWEST** Jeffrey Dembksi: 847-498-4520 x3005, Steven Loerch: 847-498-4520 x3006 **UK EUROPE/ASIA** Roger Goncalves: TEL/FAX +41 43 243 1358 **JAPAN** Kaoru Sasaki (Tokyo): + 81 (3) 6459 4174 ksasaki@aaas.org

GLOBAL SALES DIRECTOR ADVERTISING AND CUSTOM PUBLISHING Tracy Holmes: +44 (0) 1223 326525 **CLASSIFIED** advertise@sciencecareers.org **SALES MANAGER, US, CANADA AND LATIN AMERICA SCIENCE CAREERS** Claudia Paulsen-Young: 202-326-6577, **EUROPE/ROW SALES** Sarah Lelarge **SALES ADMIN ASSISTANT** Kelly Grace +44 (0)1223 326528 **JAPAN** Miyuki Tani(Osaka): +81 (6) 6202 6272 mtani@aaas.org **CHINA/TAIWAN** Xiaoying Chu: +86-131 6136 3212, xchu@aaas.org **GLOBAL MARKETING MANAGER** Allison Pritchard **DIGITAL MARKETING ASSOCIATE** Aimee Aponte

AAAS BOARD OF DIRECTORS, CHAIR Susan Hockfield **PRESIDENT** Margaret A. Hamburg **PRESIDENT-ELECT** Steven Chu **TREASURER** Carolyn N. Ainslie **CHIEF EXECUTIVE OFFICER** Rush D. Holt **BOARD** Cynthia M. Beall, May R. Berenbaum, Rosina M. Bierbaum, Kaye Husbands Fealing, Stephen P.A. Fodor, S. James Gates, Jr., Michael S. Gazzaniga, Laura H. Greene, Robert B. Millard, Mercedes Pascual, William D. Provine

SUBSCRIPTION SERVICES For change of address, missing issues, new orders and renewals, and payment questions: 866-434-AAAS (2227) or 202-326-6417, FAX 202-842-1065. Mailing addresses: AAAS, P.O. Box 96178, Washington, DC 20090-6178 or AAAS Member Services, 1200 New York Avenue, NW, Washington, DC 20005

INSTITUTIONAL SITE LICENSES 202-326-6730 **REPRINTS:** Author Inquiries 800-635-7181 **COMMERCIAL INQUIRIES** 803-359-4578 **PERMISSIONS** 202-326-6765, permissions@aaas.org **AAAS Member Central Support** 866-434-2227 www.aaas.org/membercentral.

Science serves as a forum for discussion of important issues related to the advancement of science by publishing material on which a consensus has been reached as well as including the presentation of minority or conflicting points of view. Accordingly, all articles published in *Science*—including editorials, news and comment, and book reviews—are signed and reflect the individual views of the authors and not official points of view adopted by AAAS or the institutions with which the authors are affiliated.

INFORMATION FOR AUTHORS See www.sciencemag.org/authors/science-information-authors

EDITORIAL

Health security's blind spot

The severity of this year's influenza virus is a reminder of the daunting task facing the global health community as it struggles to prevent infectious diseases from sparking deadly epidemics. Today, yellow fever and cholera continue to spread in Africa, while Brazil is in the midst of a major yellow fever outbreak. It was only recently that Zika virus and Ebola virus epidemics were in the headlines. The world needs to harness every resource and tool in the battle to catch outbreaks before they catch us. Prevention is always the first line of defense, and nations must maintain vigilant surveillance—and yet, effective and affordable, quick and definitive diagnostics are absent in the countries where they are most needed. This represents one of our most serious global health security blind spots.

"Early detection through…testing is essential to stopping outbreaks before they spread."

During the 2014 Ebola epidemic in West Africa, the first cases were initially misdiagnosed as cholera, and then later as Lassa fever on the basis of clinical symptoms. It took nearly 3 months before blood samples sent to Europe finally identified the disease as Ebola, during which time it was allowed to spread. Similarly, in Nigeria, a lack of rapid diagnostics is making it difficult to get ahead of the current yellow fever outbreak with targeted vaccination. Throughout 2016 and the first 8 months of 2017, Nigerian laboratories were unable to carry out tests on almost all suspected cases of yellow fever, owing to a shortage of chemicals needed for those diagnostics. When these reagents eventually became available last fall, yellow fever had spread to multiple states. As of last month, there were more than 350 suspected yellow fever cases over 16 states and 45 deaths. The world's poorest countries simply cannot equip and maintain their limited laboratory facilities.

But the problem is not just how well-stocked laboratories are, it's also about how quickly and reliably they can respond. For yellow fever, whenever lab tests are positive or inconclusive in Africa, samples are sent to a Regional Reference Laboratory for confirmation. For the whole of Africa there is just one such facility in Dakar, Senegal. Even under the best conditions, these lab tests are expensive and take at least a month. What's more, about 40% of samples found to be positive by Nigerian national laboratories have tested negative in Senegal, creating uncertainty about the reliability of the test. The United States Centers for Disease Control and Prevention (CDC) has historically played a major role in helping countries expand disease surveillance and modernize laboratories, particularly for new viruses and drug-resistant bacteria. But now it is feared that the CDC may scale back its global health security work in 39 developing countries. This prospect highlights the need for low-income countries to create a sustainable program for their disease surveillance.

Ultimately, to achieve sustainable global epidemic preparedness, we need to stimulate the development of cutting-edge diagnostic technologies—both for laboratories and for use in the field in remote locations—and make them available and affordable in low-income countries. One approach is to provide incentives to industry by creating markets that may have seemed impossible. At Gavi, the Vaccine Alliance, we have been doing this by working with industry to harness innovative refrigeration technologies to modernize vaccine cold chains in poor countries. The global health community could look at how partnerships with industry can be applied to innovative diagnostic technologies. Early detection through reliable, available, and efficient testing is essential to stopping outbreaks before they spread. With many diseases presenting similar first symptoms, it's all too easy to get a diagnosis wrong and potentially miss an outbreak. And given the ease and speed at which pathogens can now travel in the modern urban-dense global village, any delay in diagnosis will inevitably and increasingly be measured in lives lost.

–**Seth Berkley**

Seth Berkley is chief executive officer of Gavi, the Vaccine Alliance, Geneva, Switzerland.
sberkley@gavi.org

10.1126/science.aat4714

CREDITS: (INSET) REUTERS/ALBERT GONZALEZ FARRAN/UNAMID; (TOP RIGHT) GAVI, THE VACCINE ALLIANCE

> “Have the researchers considered the possible unintended side effects?”
> **Google engineer Blake Lemoine**, about a new algorithm that could identify gang crimes—but also might brand innocent people as gang members.

IN BRIEF

Edited by **Jeffrey Brainard**

ASTRONOMY

Space telescope faces cost overrun

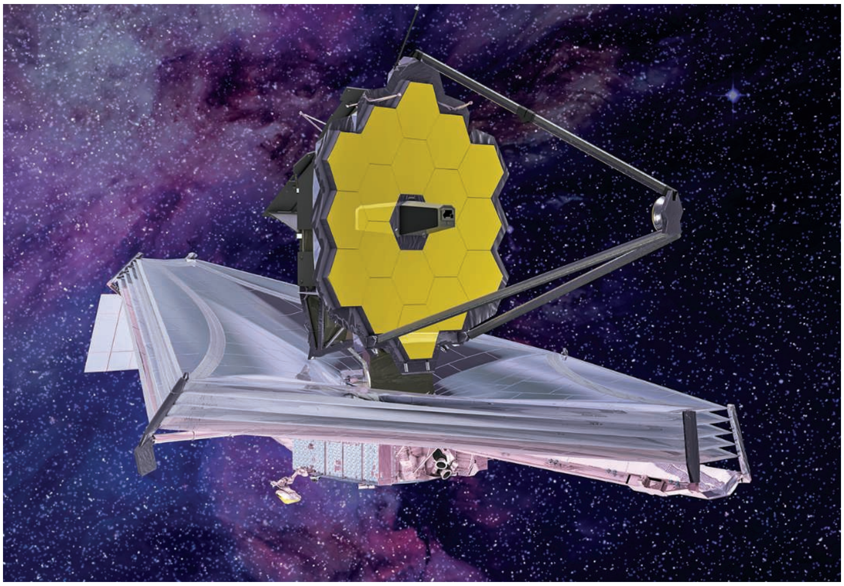

Tests of a sunscreen that will protect the James Webb Space Telescope caused a project delay.

Problems with assembly and testing of NASA's James Webb Space Telescope (JWST) are threatening to delay its scheduled launch in 2019 and bust its budget, the U.S. Government Accountability Office (GAO) said last week. The JWST is a bigger, better successor to the Hubble Space Telescope and could revolutionize our knowledge of the early universe, planets around other stars, and much else. Last year, vibration testing threw up some unexpected results that took time to resolve, reducing the project's schedule reserve, the GAO report says. Then, in October 2017, the first unfurling tests of the spacecraft's tennis court–size sunshield, made of five thin layers of metal-coated plastic, also fell behind schedule. “It took longer than predicted, but it's about getting it right,” says Scott Willoughby, Northrop Grumman's JWST program manager in Redondo Beach, California. Final assembly, now underway, will likely cause more challenges, and GAO says another launch delay is likely. With only 1.5 months of schedule reserve left, any further delays are expected to push the JWST's budget over the cap of $8 billion set by Congress, putting the project in uncharted territory.

Iranian leaders scrap over science

INTERNATIONAL AFFAIRS | A long-simmering dispute in Iran over how to put an Islamic “stamp” on science has flared up. In a speech last week, Iranian President Hassan Rouhani blasted what he called “wasteful” spending on efforts overseen by the country's hard-liners to define Islamic versions of various science disciplines, Iranian news agencies reported. “We have no Islamic car industry, no Islamic physics or chemistry,” Rouhani said. “Science is science; there is no difference.” Rouhani also sought to counter a paranoia among hard-liners that foreign researchers—environmental scientists in particular—are spying on Iran. “We will not make much progress if we limit our relations with the world,” he stated. Last month, Kavous Seyed-Emami, a Canadian-Iranian sociologist who co-founded the Persian Wildlife Heritage Foundation in Tehran and who had been accused of spying, allegedly committed suicide in an Iranian prison.

Appeal in harassment case fails

WORKPLACE | Boston University (BU) has denied geologist David Marchant's appeal of its decision to terminate him for sexual harassment, the Massachusetts institution announced 27 February. Last November, BU moved to fire Marchant after an investigation concluded that he harassed graduate student Jane Willenbring in Antarctica during the 1999–2000 field season. Now that his appeal has failed, Marchant has the right to have a faculty committee determine whether termination is the appropriate sanction. But J. Robb Dixon, who chairs BU's Faculty Council, says he has not been approached to constitute such a committee. Marchant remains on paid administrative leave, says BU spokesperson Colin Riley. Marchant and his lawyer did not reply to emails requesting comment.

Graduate students report anxiety

HIGHER EDUCATION | About 40% of graduate students say they suffer from moderate to severe anxiety or depression, which is six times the rate found in the general population, according to a new study of

IMAGE: NORTHROP GRUMMAN


Researchers discovered a supercolony of Adélie penguins in Antarctica, including these on Comb Island.

WILDLIFE CONSERVATION

Satellites reveal hidden refuge for 1.5 million penguins

The Adélie penguin, whose populations in western Antarctica are rapidly declining because sea ice is disappearing, may have a haven from climate change. Tipped off by evidence of guano in NASA Landsat images of the Danger Islands, just off of northeastern Antarctica, researchers have now confirmed that more than 750,000 breeding pairs live there. So far, the Danger Islands are less affected by warming temperatures, says Heather Lynch, a quantitative ecologist at the State University of New York in Stony Brook. Landing on the islands after their research ship managed to get through extensive summer sea ice, she and her colleagues used drones and other methods to estimate the Adélie population there. It's one of the largest colonies of these seabirds, they reported on 2 March in *Scientific Reports*. They argue that the waters around these islands should be designated a marine protected area, adding to reserves that would be created by treaties now being negotiated.

2279 master's and Ph.D. candidates across 26 countries. Of the students surveyed, 40% were pursuing degrees in the physical and biological sciences or engineering. About a third of male respondents reported experiencing each condition, compared with approximately 40% of female participants and more than half of transgender and gender-nonconforming respondents. Having supportive principal investigators and healthy work-life balance correlated with better mental health, concluded the survey, one of the largest of its kind, published in the March issue of *Nature Biotechnology*. To head off problems, the authors recommend that institutions increase awareness of mental health issues among students and their advisers and provide better support.

A dearth of gun research

PUBLIC HEALTH | An expansive study released last week points out how little is known about whether and how U.S. federal and state firearm laws affect gun violence. The nonprofit RAND Corporation, based in Santa Monica, California, reviewed many thousands of studies and found only 62 that demonstrated a causal relationship between gun policies and changes in outcomes, such as mass shootings and other homicides and suicides committed with firearms. Across 13 classes of policies, the evidence that laws preventing children's access to guns reduce suicides and accidental injuries and deaths in youths was the strongest, the researchers found. This chart (left) shows other selected findings from the report. Research on the causes of gun violence fell markedly after Congress enacted a policy in 1996 that complicated the awarding of federal funds for these studies.

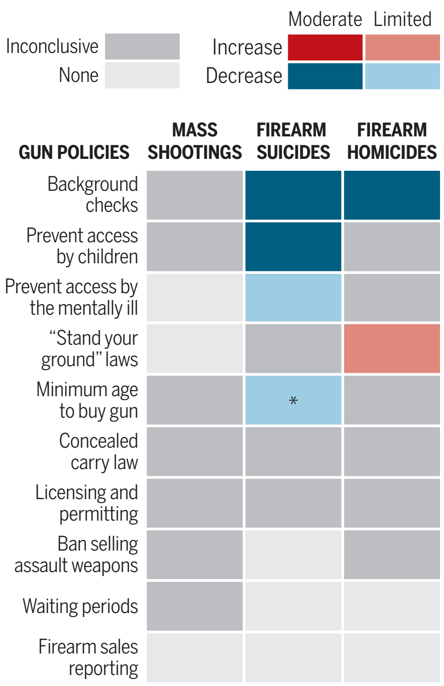
Strength of evidence that policies affect outcomes

GUN POLICIES	MASS SHOOTINGS	FIREARM SUICIDES	FIREARM HOMICIDES
Background checks	Inconclusive	Moderate decrease	Moderate decrease
Prevent access by children	Inconclusive	Moderate decrease	Inconclusive
Prevent access by the mentally ill	None	Limited decrease	Inconclusive
"Stand your ground" laws	None	Inconclusive	Limited increase
Minimum age to buy gun	Inconclusive	Limited decrease *	Inconclusive
Concealed carry law	Inconclusive	Inconclusive	Inconclusive
Licensing and permitting	Inconclusive	Inconclusive	Inconclusive
Ban selling assault weapons	Inconclusive	None	Inconclusive
Waiting periods	Inconclusive	None	None
Firearm sales reporting	None	None	None

* Firearm suicides among children only

Consumer test for cancer risk

GENETIC TESTING | The U.S. Food and Drug Administration (FDA) has approved the first genetic test for breast cancer risk marketed directly to consumers. The agency announced on 6 March that personal genomics company 23andMe can now analyze DNA from customers' saliva to tell them whether they carry any of three mutations in the *BRCA1* and *BRCA2*

CREDITS: (PHOTO) MICHAEL POLITO, LOUISIANA STATE UNIVERSITY; (GRAPHIC) J. YOU/*SCIENCE*; (DATA) RAND CORPORATION

RESEARCH FUNDING

Canadian science gets a boost

Canada's new 5-year budget plan includes a major increase for research spending. The plan, released 27 February, provides an increase of 25%, or CA$925 million, for the nation's three primary science grantmaking councils. In all, the plan calls for dedicating CA$3.8 billion to research through 2023, including CA$1.3 billion for new equipment and technology at academic science centers, as well as a CA$275 million increase for interdisciplinary, "high-risk" research. Many research advocates welcomed the increase, but noted it falls short of recommendations made last year by an expert panel convened by Prime Minister Justin Trudeau's Liberal government. And climate researchers were disappointed the plan doesn't commit to renewing funding for climate and atmospheric research in the Arctic, which is scheduled to expire this year.

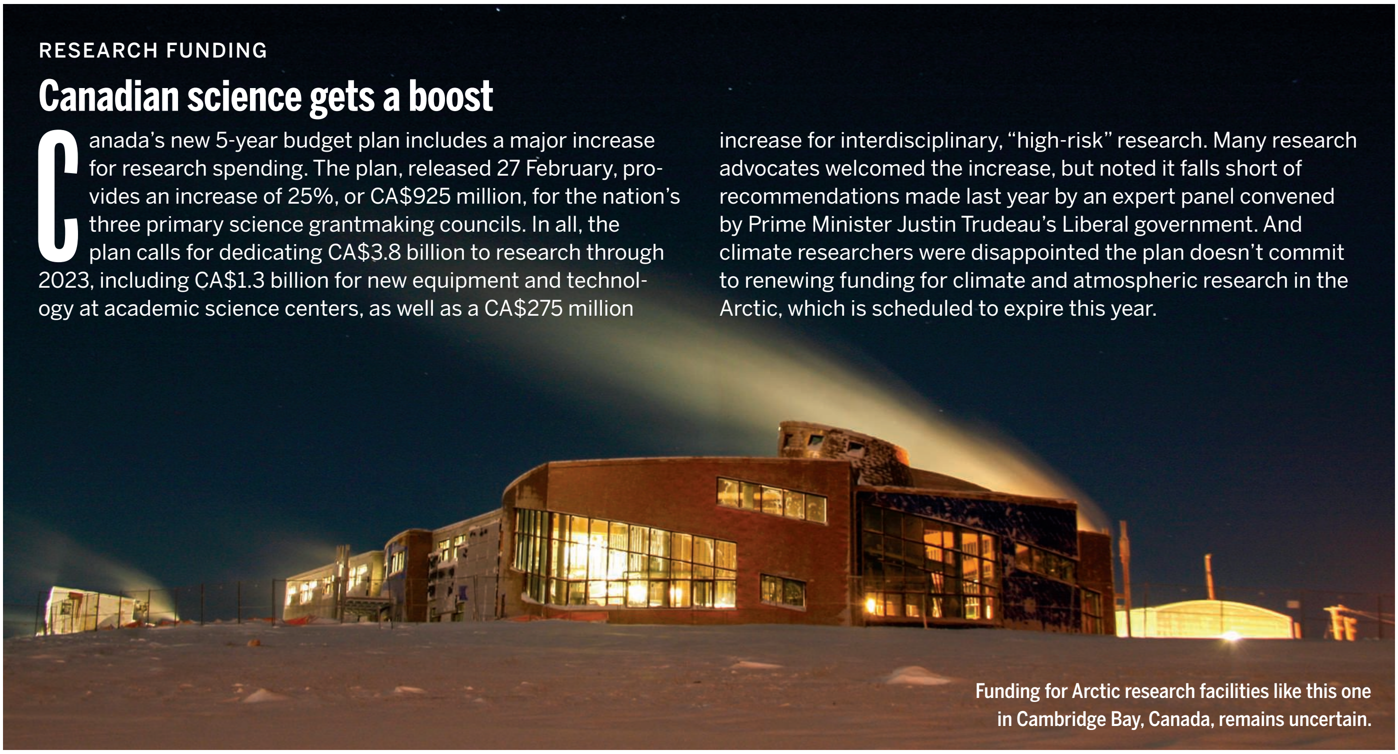

Funding for Arctic research facilities like this one in Cambridge Bay, Canada, remains uncertain.

PHOTO: GOVERNMENT OF CANADA

genes that increase the risk of breast and ovarian cancer. But these are just a few of more than 1000 known BRCA mutations, the agency noted, and although they're present in about 2% of women of Ashkenazi Jewish descent, they're exceedingly rare in the general population. In a 2013 warning letter that forced 23andMe to pull many of its health-related tests from the market, FDA specifically mentioned concerns that an unreliable BRCA test result could prompt women to opt for unnecessary prophylactic surgery. It's now urging customers and doctors not to rely on the new test alone to make treatment decisions.

A champion for EU open access

PUBLISHING | Dutchman Robert-Jan Smits, formerly one of the most powerful players in Brussels's science policy circles, has been tasked with spurring progress on the European Union's plans to promote open-access publication. Smits was named a special adviser for open access and innovation at the European Political Strategy Centre, the European Commission's in-house think tank, after almost 8 years as the commission's director general for research and innovation. In May 2016, ministers of all EU member states committed to making all scientific papers produced in the European Union freely accessible by 2020, but this optimistic, nonbinding pledge has failed to bring about radical changes. Smits says his new job, which he started on 1 March, is to "put open access high on the political agenda again, and motivate everyone to make the transition happen, and fast."

Italian election worries scientists

RESEARCH POLICY | Italian scientists worry the stunning victory of nationalist and populist parties in the 4 March parliamentary elections may bode ill for science in the country. Exactly where the two big winners—the populist Five Star Movement and the hard-right, anti-immigrant League—stand on research policy and other science-related topics can be hard to tell; their election platforms provide little information. But both parties have come under fire for endorsing antivaccine viewpoints and for opposing animal testing. How the election results will translate into science policy now depends on what are expected to be protracted coalition talks. But Italy's scientific community "will not allow an antiscience government," says Maria Chiara Carrozza, a professor in industrial bioengineering at the Sant'Anna School of Advanced Studies in Pisa, Italy, and a former education and research minister. "We will make our voices heard."

Ice blocks Antarctic mission

MARINE ECOLOGY | Sea ice last week forced researchers to delay plans to study newly exposed, unusual ocean-bottom life in an area along the eastern Antarctic Peninsula that had not seen daylight in 120,000 years. The opportunity arose last July when an iceberg the size of Delaware snapped off the Larsen C Ice Shelf and drifted seaward, opening a gap that a research ship could navigate. A team led by the British Antarctic Survey had hoped to find new species there and identify existing ones before opportunistic neighboring species moved in. But the *RRS James Clark Ross* had to turn back because of slow progress through the ice in the Weddell Sea. German scientists plan to try again next year.

Vaccine graphic wins award

The Society for News Design awarded a silver medal to *Science*'s Interactive Graphics Editor Jia You and News Writer Meredith Wadman for an infographic showing how rates of infectious diseases fell sharply after vaccines were developed to prevent them. The graphic was part of our Vaccine Wars package (*Science*, 28 April 2017, p. 364). "At a time when this topic is hotly debated," the judges wrote, "the visual team embraces a core journalistic mission: Show people the truth so they can make their own informed decisions."

S **SCIENCEMAG.ORG/NEWS**
Read more news from *Science* online.

In 2014, Airbus's Zephyr 7 drone relied on lithium-sulfur batteries for an 11-day nonstop flight.

IN DEPTH

ELECTROCHEMISTRY

Lithium-sulfur batteries poised for leap

Promising chemistry is starting to compete commercially with lithium-ion

By **Robert F. Service**

Take that, Tesla. Researchers at Oxis Energy, a startup company in Abingdon, U.K., are building batteries with a combination of lithium and sulfur that store nearly twice as much energy per kilogram as the lithium-ion batteries in electric cars today. The batteries don't last very long, conking out after 100 or so charging cycles. But the company hopes that for applications such as aerial drones, submersibles, and power packs that could be shouldered by soldiers, weight will matter more than price or longevity. Oxis's small pilot factory aims for an annual production of 10,000 to 20,000 batteries, which sit in thin pouches the size of cellphones.

The Gigafactory this is not—at least not yet. But Chief Technology Officer David Ainsworth says the company has its eye on a far bigger prize: the $100 billion electric vehicle market. "The next few years will be critical," Ainsworth says. He and others see lithium-sulfur as the heir apparent to lithium-ion as the dominant battery technology.

They are encouraged by a spate of recent reports suggesting that many of the technology's performance and durability challenges can be overcome. "You're seeing advances on a number of fronts," says Brett Helms, a chemist at Lawrence Berkeley National Laboratory in California. Others, like Linda Nazar, a chemist and lithium-sulfur pioneer at the University of Waterloo in Canada, remain cautious. "It's a really tall order" to create high-capacity lithium-sulfur batteries that are also cheap, lightweight, small, and safe, she says. Improving one factor, she adds, often comes at the expense of others. "You can't optimize all of them simultaneously."

Lithium-ion batteries contain two electrodes—an anode and a cathode—separated by a liquid electrolyte that allows lithium ions to move back and forth during charging cycles. At the anode, lithium atoms are wedged between layers of graphite, a highly conductive type of carbon. As the battery discharges, the lithium atoms give up electrons and generate a current. The resulting positively charged lithium ions move into the electrolyte. After powering anything from a cellphone to a Tesla, the electrons wind up back at the cathode, which is typically made from a mix of different metal oxides. Here, the positive lithium ions in the electrolyte snuggle up next to metal atoms that have taken up the traveling electrons. Charging reverses this molecular shuffle as an external voltage pushes the lithium ions to ditch their metallic hosts and return to the anode.

Powering up

Lithium-sulfur batteries have the potential to be both smaller and lighter than lithium-ion batteries.

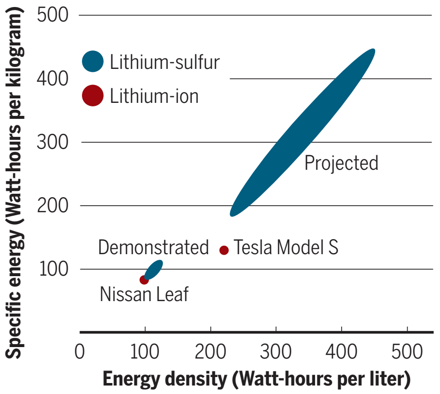

Metal oxide cathodes are reliable. But the metals—typically a combination of cobalt, nickel, and manganese—are expensive. And because it takes two metal atoms working together to hold a single electron, these cathodes are heavy, which limits the capacity of these cells to about 200 watt-hours per kilogram (Wh/kg). Sulfur is much cheaper, and each sulfur atom can hold two electrons. Theoretically, a battery with a sulfur cathode can store 500 Wh/kg or more.

But sulfur is anything but an ideal material for an electrode. For starters, it's insulating: It won't pass electrons to lithium ions crossing over from the anode. That was a deal breaker until 2009, when researchers led by Nazar showed that the sulfur could be embedded within a cathode that, like the anode, was made of conductive carbon. It worked, but it brought other problems. Forms of carbon like graphite are highly porous. That adds to the overall size of the battery without boosting its storage capacity, and it means that more of the expensive liquid electrolytes are needed to fill the pores. Even worse, when lithium ions bind to sulfur atoms at the cathode, they react to form soluble molecules called polysulfides that float away, degrading the cathode and limiting the number of charging cycles. Polysulfides can also migrate to the

CREDITS: (PHOTO) AIRBUS; (GRAPHIC) D. EROGLU *ET AL.*, *JOURNAL OF THE ELECTROCHEMICAL SOCIETY* 10.1149/2.0611506JES ADAPTED BY J. YOU/*SCIENCE*

anode, where they can wreak further havoc.

Now, advances are coming on all fronts. Three groups have made strides in solving problems at the cathode. Last year, for example, researchers led by Helms reported in *Nature Communications* that they added a polymer layer to a carbon-sulfur cathode, sealing in the polysulfides and enabling the battery to survive 100 charging cycles. Another group, led by Arumugam Manthiram at the University of Texas in Austin, replaced the graphite in a cathode with highly conductive graphene—graphite in sheets just a single atom thick. As they reported in the 12 January issue of *ACS Energy Letters*, the graphene cathodes held five times as much sulfur as traditional graphite ones, thereby boosting energy storage. And 2 weeks ago researchers led by Nanfeng Zheng, a chemist at Xiamen University in China, reported in *Joule* that they had created an ultrathin "separator" by topping a thin sheet of polypropylene with nitrogen-doped carbon particles. The separator sits atop the cathode, traps polysulfides, and converts them to harmless lithium-sulfide particles. That increased the energy output of the cells and helped them survive 500 charging cycles.

Others are working to fix the polysulfide problem by tweaking the electrolyte. In the 25 May 2017 issue of *ACS Central Science*, Nazar and her colleagues reported that they had made an electrolyte that permits the passage of lithium ions but inhibits the creation of soluble polysulfides.

Many teams are also targeting the anode, aiming to replace the lithium and graphite combination with pure lithium metal. That could boost the capacity of lithium-ion batteries to 500 Wh/kg—enough to drive a car nearly 500 kilometers between charges—and yield even bigger gains for lithium-sulfur batteries. To date, however, pure lithium anodes have been stymied by problems during charging, when lithium atoms migrate back from the cathode. They tend to pile up in one spot, creating spiky growths that can pierce the battery and cause shorts and even fires. Oxis Energy and another battery startup, Sion Power in Tucson, Arizona, say they have developed proprietary barriers around the anode that prevent the spiky growths. And this week in *Nature Energy*, researchers at Cornell University reported stabilizing their lithium anode with a tin alloy.

All of these advances will help push lithium-sulfur batteries forward, says George Crabtree, who directs the Joint Center for Energy Storage Research at Argonne National Laboratory in Lemont, Illinois. "It's hard to tell whether these are the final breakthroughs that are going to make it," he says. "But I'm optimistic." Electric car drivers everywhere hope he's right. ■

EUROPE

Germany's new government makes big promises

Coalition says it will hike research spending to 3.5% of gross domestic product—but is that feasible?

By **Gretchen Vogel**, *in Berlin*

Nearly 6 months after it held federal elections, Germany finally has a new government—and some welcome news for scientists. The new coalition, the fourth led by Chancellor Angela Merkel, has pledged to boost overall R&D spending from 2.9% to 3.5% of the country's gross domestic product (GDP) by 2025. That would make Germany a world leader in research spending, behind only South Korea and Israel. "The signs … are really quite promising," says Wilhelm Krull, secretary general of the Volkswagen Foundation in Hanover, Germany, a large private research funder.

But whether the government can deliver remains to be seen; it's not clear where the extra billions would come from. Meanwhile, researchers are wondering what to expect from the new research and education minister, Anja Karliczek, who trained as a banker and spent 2 decades running her family's hotel. And some chafe at the new government's positions on agricultural technology and climate.

The new German research and education minister, Anja Karliczek.

PHOTO: RAUβ FOTOGRAFIE

Germany's center-left Social Democratic Party voted to approve the coalition with Merkel's center-right Christian Democratic Union and its Bavarian sister party on 4 March. The three parties, which made up the previous government, all lost seats in the elections, leaving them reluctant to continue their collaboration. But after talks about a different coalition fell apart last November, the remaining options—a minority government or new elections—were even less appealing.

The three parties say a sharp rise in R&D budgets is necessary to keep Germany's edge in innovation, but don't detail how to get there. The agreement promises a yearly 3% increase in federal funding for research organizations such as the Max Planck Society and the Helmholtz Association of German Research Centres, but much more would be needed to reach the promised 3.5% of GDP. The government would also have to entice the private sector, which accounts for two-thirds of current research spending, to spend more freely, Krull says, for instance through tax breaks and matching funds. Still, says Jörg Hacker, president of the German national academy of sciences, the Leopoldina, in Halle, the target is welcome. "One has to have ambitious goals, or you don't get anywhere," he says.

In a stance that may be less popular among researchers, the new government favors a nationwide ban on planting genetically modified crops. No such crops are currently grown in Germany, but a complete ban would be very restrictive, Hacker says. He says research leaders will continue to lobby for gene technology regulations that focus on the benefits or drawbacks of the end product, rather than on the technique used to make it.

Meanwhile, climate activists say the coalition's goals aren't nearly ambitious enough. During the election campaign, Merkel said Germany would meet its target of reducing carbon emissions by 40% (from 1990 levels) by 2020, but the parties now admit that won't happen; current projections predict a 32% decrease. The government promises to redouble efforts to meet the 2030 goal of cutting emissions by 55%, but it has not named a deadline for phasing out coal. Environmental groups say the parties are too protective of Germany's auto and coal industries.

The biggest surprise was Merkel's choice of the little-known Karliczek, who has mostly worked on finance issues since her election to the German Bundestag in 2013. (Observers think the fact that she is young, female, and conservative played a role.) Karliczek told German media that research leaders should expect her to ask lots of questions. Her background in finance and management could be good preparation for many of her tasks as minister, Hacker says. "We look forward to meeting with her as soon as possible." ■

OCEANOGRAPHY

Saildrone fleet could help replace aging buoys

Robotic test in Pacific Ocean heralds new way to monitor El Niño events

By **Paul Voosen**

Two 7-meter-long sailboats are set to return next month to California, after nearly 8 months tacking across the Pacific Ocean. Puttering along at half-speed, they will be heavy with barnacles and other growth. No captains will be at their helms.

That is not because of a mutiny. These sailboats, outfitted with sensors to probe the ocean, are semiautonomous drones, developed by Saildrone, a marine tech startup based in Alameda, California, in close collaboration with the National Oceanic and Atmospheric Administration (NOAA) in Washington, D.C. The voyage is the longest test for the drones and also the first science test in the Pacific—an important step in showing that they could replace an aging and expensive array of buoys that are the main way scientists sniff out signs of climate-disrupting El Niño events.

After World War II, most sea surface data were collected from ships. Then came buoys and satellites. Now, NOAA scientists want to send in the drones. “We could be making the next epochal advancement in oceanography,” says Craig McLean, NOAA’s assistant administrator for oceanic and atmospheric research and acting chief scientist. Within the next decade, hundreds or even thousands of solar- and wind-powered drones could roam the world’s oceans, using satellites to relay information gathered from the sea surface and the air above.

The drones can’t come too soon for scientists who study the El Niño–Southern Oscillation, a set of shifting global temperature and rainfall patterns triggered by warm surface waters that slosh back and forth across the equatorial Pacific every few years. Since the 1980s, NOAA has supported a grid of buoys, moored to the Pacific sea floor, called the Tropical Atmosphere Ocean (TAO) array, to study and forecast these swings. Its success led to similar arrays in the Indian and Atlantic oceans.

But earlier this decade, the TAO array had a near-death experience. The marine growth on buoys and their moorings are fish magnets, which makes them a magnet for fishers as well, causing the distinctive TAO grid to appear on maps of global fish catches. As fishers dragged the buoys aside for easy pickings, they damaged them, and maintenance work began to pile up. Meanwhile, budget cuts and the soaring expense of operating research ships meant few new buoys were deployed. “That was a wake-up call for all of us,” says Christopher Sabine, an oceanographer at the University of Hawaii in Honolulu.

Winds of change

Two saildrones have carried a suite of 15 sensors into the tropical Pacific Ocean and back, powered only by the wind and sun. The data, relayed by satellites, are being compared to readings gathered by buoys and ships.

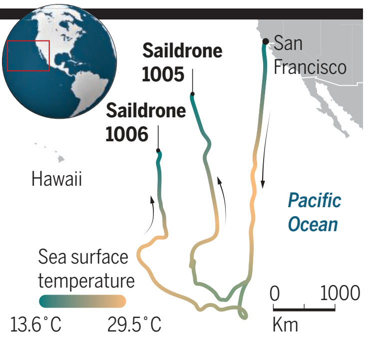

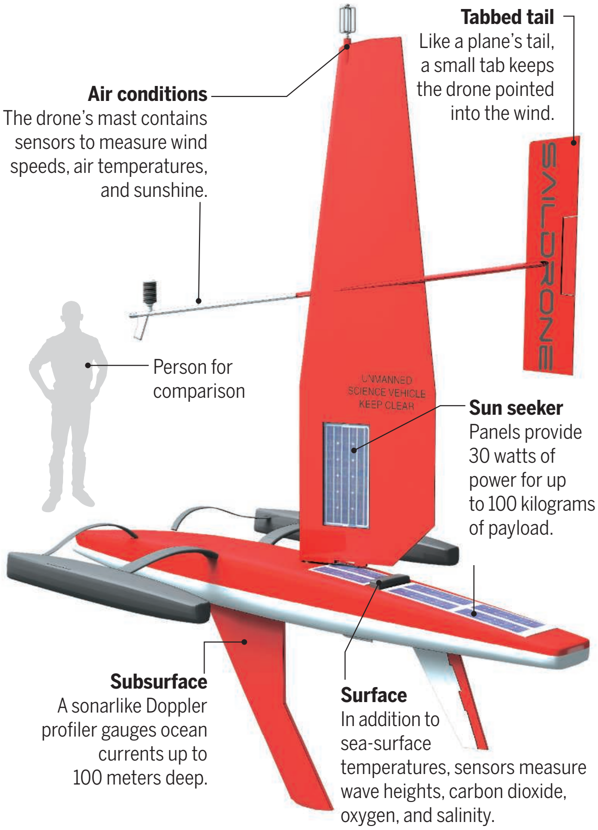

Tabbed tail Like a plane’s tail, a small tab keeps the drone pointed into the wind.

Air conditions The drone’s mast contains sensors to measure wind speeds, air temperatures, and sunshine.

Person for comparison

Sun seeker Panels provide 30 watts of power for up to 100 kilograms of payload.

Subsurface A sonarlike Doppler profiler gauges ocean currents up to 100 meters deep.

Surface In addition to sea-surface temperatures, sensors measure wave heights, carbon dioxide, oxygen, and salinity.

Ultimately, Congress restored funding for the TAO array, which costs about $10 million a year. But now Japan, which maintains a complementary array in the western Pacific called the Triangle Trans-Ocean Buoy Network, has pulled out almost all of its buoys because of limited funds and a lack of ship time to maintain them, degrading El Niño measurements once again. The crises prompted NOAA and others to look for a more sustainable system to deliver El Niño warnings, which help agencies plan for the heavy rains and droughts that follow in its wake. “It’s an opportunity to look at exactly what the array is and its requirements are,” says Meghan Cronin, an oceanographer at NOAA’s Pacific Marine Environmental Laboratory (PMEL) in Seattle, Washington.

Richard Jenkins, an engineer and Saildrone’s founder, smelled an opportunity. He had built a sailboat on wheels called *Greenbird* that in 2009 broke the land-speed record for a wind-powered vehicle, reaching 202 kilometers per hour on a dry lake bed in Nevada. Afterward, he helped two ocean-minded philanthropists, Eric and Wendy Schmidt, outfit their research vessel, the *R/V Falkor*, at a cost of $60 million. He marveled at the expense and wondered whether a smaller, seafaring version of *Greenbird* could gather ocean data more cheaply. In theory, an ocean-going saildrone would need no fuel for propulsion; solar panels could power instruments and communications. Simply set waypoints and the drone would ride the wind there. The Schmidts gave Jenkins $2.5 million to get started; by 2013, a test craft had completed its first voyage from California to Hawaii, propelled by a 4.6-meter-tall carbon fiber composite sail.

Since then, Saildrone has worked with PMEL scientists to rig the

CREDITS: (GRAPHIC) A. CUADRA AND N. DESAI/*SCIENCE*; (DATA) SAILDRONE

boats with sensors and test their limits. In 2015, they survived 40-knot winds during a 3-month foray into the Arctic to assess marine life. That success encouraged scientists to mull whether the drones could help anchor observations in the Pacific. Conceivably, the drones could sail in circles around a virtual mooring point, or run other preplanned patterns, before returning to port every year for cleaning—no ships necessary. The drones could be cheaper, too. Saildrone charges $2500 a day per drone to collect data, whereas ship time can cost $30,000 or more per day. Jenkins thinks his drones can profit off that difference in the Pacific. “We are anticipating a fleet to service that market exclusively,” he says.

The first Pacific test started on 5 September 2017, when two saildrones, 1005 and 1006, set out from San Francisco, California, for equatorial waters. Satellites had spotted cold tongues of surface water extending westward from the South American coast, an indicator of a strong La Niña, El Niño’s opposite number. It was not all smooth sailing. After arriving at the equator, the drones got stuck in the doldrums, a wind dead zone. “We knew the tropics were going to be a challenge,” Cronin says. (In July, another saildrone will depart for the tropics with a larger sail that Jenkins hopes will help it through the doldrums.)

Eventually, the saildrones caught the wind and escaped. And as Cronin looked back at the data from the cold tongues, she discovered a surprise: shifts in water temperature by 1° in less than a kilometer. “Some of these fronts are much sharper than you would ever imagine,” Cronin says. “That was shocking.” It is the type of detail a satellite’s lower resolution would smear out, and something a stationary buoy would have missed. Cronin says current climate models don’t account for these sharp gradients, which could churn the atmosphere above.

In addition to temperature, wind, and solar radiation data, the Pacific saildrones are measuring how the ocean and air exchange gases like carbon dioxide and oxygen, and they are using Doppler instruments to gauge currents coursing up to 100 meters below the surface. These sensors could reveal patterns that help explain why the tropical Pacific emits carbon dioxide, rather than absorbing it like most of the rest of ocean. Arrays like the TAO will continue to be important, Cronin says. But she foresees the emergence of a cheaper, more resilient oceanographic backbone. The new age of saildrones “is not going to solve all our problems,” Cronin says. “But it’s really interesting to think about doing oceanography without a ship.” ■

IMAGES: KEN PROBST

NEUROSCIENCE

Study undercuts claims of new neurons in adult brains

Other groups still see evidence for lifelong neurogenesis

By **Emily Underwood**

Over the past 20 years, evidence that adult humans can produce hundreds of new neurons per day has fueled hope that ramping up cell birth could be therapeutic. Boosting neurogenesis, researchers speculate, might prevent or treat depression, Alzheimer’s disease, and other brain disorders. But a controversial study in *Nature* this week threatens to dash such hopes by suggesting that the production of neurons declines sharply after early development and grinds to a halt by adulthood.

The results of the “exhaustive search” for new neurons in adult human and monkey brains “will disappoint many,” says neuroscientist Paul Frankland of the Hospital for Sick Children in Toronto, Canada. “It raises concern that levels of neurogenesis are too low to be functionally important” in humans, adds another observer, René Hen, a neuroscientist at Columbia University. But he and others suggest that the study left much room for error. The way the tissue was handled, the deceased patients’ psychiatric history, or whether they had brain inflammation could all explain why the researchers failed to confirm earlier, encouraging studies, Hen says.

The first evidence of neurogenesis in adult humans came in 1998 from the brains of deceased cancer patients who had received injections of a chemical called bromodeoxyuridine while they were still alive. The chemical labels newly divided cells, and in their brain tissue, it showed up in a sprinkling of neurons in the hippocampus—a seahorse-shaped structure involved in memory and learning. In 2013, Jonas Frisén’s lab at the Karolinska Institute in Stockholm buttressed the case by carbon dating individual neurons in brain tissue from 55 deceased people. From the cells’ ages, the group calculated that every day, humans replace 700 of their neurons in the dentate gyrus, a sliver of hippocampus thought to encode memories.

Arturo Alvarez-Buylla of the University of California, San Francisco, who has been studying the brain’s capacity to produce new cells since the 1980s, was skeptical. He is known for showing how niches of neural stem cells constantly regenerate parts of the rodent brain. But the carbon-dating evidence did not persuade him that people maintain similar stem cell reserves: The method involves “a lot of assumptions and steps in which there can be contamination or false positives,” he says.

For the new analysis, his team spent 5 years collecting brain tissue from 59 people who had died or had such tissue removed during surgery for epilepsy at different ages, ranging from before birth to 77 years of age. They used fluorescent antibodies to label proteins specific to cells at different states of maturity. With an electron microscope, they also looked for the characteristic long, slender, simple shapes of young neurons.

The team found that people have large numbers of neural stem cells and progenitors early in life—an average of 1618 young neurons per square millimeter of brain tissue at birth. But these cells did not go on to form a proliferating layer of neural stem cells, and production of new neurons dropped 23-fold between 1 and 7 years of age, the team reports. By adulthood the supply of young neurons had petered out entirely. “We just don’t see what other people are claiming” in adults, Alvarez-Buylla says.

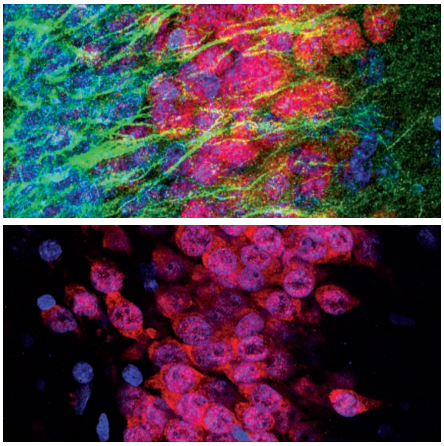

New neurons (green) were visible in a newborn’s brain (top), but not in brain tissue from a 35-year-old man (bottom.)

Frisén counters that the antibody markers used are far from reliable, because background fluorescence can muddy the results. He adds that other teams using the same techniques have seen adult neurogenesis. “I think this debate will rage on,” Frankland says. “A lot rests on this.” ■

CLIMATE CHANGE

Slow coolant phaseout could worsen warming

As countries crank up the AC, emissions of potent greenhouse gases are likely to skyrocket

By **April Reese**

In the summer of 2016, temperatures in Phalodi, an old caravan town on a dry plain in northwestern India, reached a blistering 51°C—a record high during a heat wave that claimed more than 1600 lives across the country. Wider access to air conditioning (AC) could have prevented many deaths—but only 8% of India's 249 million households have AC, Saurabh Diddi, director of India's Bureau of Energy Efficiency in New Delhi, noted at the World Sustainable Development Summit there last month. As the nation's economy booms, that figure could rise to 50% by 2050, he said. And that presents a dilemma: As India expands access to a lifesaving technology, it must comply with international mandates—the most recent imposed just last fall—to eliminate coolants that harm stratospheric ozone or warm the atmosphere.

Novel hydrocarbon-based coolants could enable India and other developing nations to embrace air conditioning while minimizing a climate threat.

PHOTO: KUNI TAKAHASHI/*THE NEW YORK TIMES*

"Growing populations and economic development are exponentially increasing the demand for refrigeration and air conditioning," says Helena Molin Valdés, head of the United Nations's (UN's) Climate & Clean Air Coalition Secretariat in Paris. "If we continue down this path," she says, "we will put great pressure on the climate system." But a slow start to ridding appliances of the most damaging compounds, hydrofluorocarbons (HFCs), suggests that the pressure will continue to build. HFCs are now "the fastest-growing [source of greenhouse gas] emissions in every country on Earth," Molin Valdés says.

HFCs, already widely used in the United States and other developed countries, are up-and-coming replacements for hydrochlorofluorocarbons (HCFCs) found today in most AC units and refrigerators in India and other developing nations. HCFCs are themselves replacements for chlorofluorocarbons (CFCs), ozone-destroying chemicals banned under the 1987 Montreal Protocol on Substances that Deplete the Ozone Layer. But HCFCs are potent greenhouse gases, as well as a threat to ozone, and they are now being phased out under a 2007 amendment to the protocol. Developed countries are to ditch them by 2020; developing countries have until 2030.

To meet those deadlines, manufacturers have turned to HFCs, which do not destroy ozone. But they are a serious climate threat. The global warming potency of HFC-134a, commonly used in vehicle AC units, is 1300 times that of carbon dioxide. Clamping down on HFCs, a 2014 analysis found, could avoid a full 0.5°C of future warming.

As with the HCFC phaseout, developed countries agreed to make the first move: They must begin abandoning the production and consumption of HFCs next year and achieve an 85% reduction by 2036. In the United States, the transition is off to a rough start. Last August, a U.S. federal appeals court rejected an Environmental Protection Agency rule that would have required manufacturers to replace HFCs with more climate-friendly substitutes, saying the agency lacks the regulatory authority to compel companies to make the switch. In January, the court declined to revisit its August 2017 decision.

In part because of rising demand for AC, developing countries negotiated a later deadline for ditching HFCs: They are to start phasing them down in 2029 and complete the process by 2047, about a decade after developed countries. In the meantime, the desire for cool air could drive up coolant emissions. An analysis done before the HFC phase-down agreement predicted that if no action were taken, HFC use in AC units would rise 2% a year in developed countries and 5.6% annually in the developing world through 2050. The agreement is unlikely to thwart that rise anytime soon: A recent UN report, which summarized studies of HFC use in Bangladesh, Chile, Colombia, Ghana, Indonesia, and Nigeria, found that use of HFCs will spike in all six countries in the coming years.

Some climate experts are more hopeful, pointing out that developing countries have an opportunity to bypass HFCs altogether. "The alternative when developed countries phased out HCFCs was HFCs. But developing countries are in a different position: They're at the beginning of phasing out HCFCs and can leap directly past HFCs" to benign alternatives, says Nathan Borgford-Parnell, regional assessment initiative coordinator for the UN's Climate & Clean Air Coalition.

India is crafting a National Cooling Action Plan that aims to do just that. It will include better city planning and building design, and it will embrace novel coolants, says Stephen Andersen of the Institute for Governance & Sustainable Development in Washington, D.C., who helped develop the plan.

Meanwhile, six AC manufacturers in India have already begun "leapfrogging" to hydrocarbon-based coolants such as R-290—refrigerant-grade propane—that have lower warming potential, says Anjali Jaiswal, the San Francisco, California–based director of the India Initiative at the Natural Resources Defense Council. Although R-290 is flammable and requires installers to be specially trained, it is one of the most promising alternatives, she adds.

"I'm hopeful," says A. R. Ravishankara, an atmospheric chemist at Colorado State University in Fort Collins. With many years to make the switch to alternatives, he says, "There's enough time for the free market to work and come up with various options." ■

April Reese is a freelance journalist in Santa Fe.

The enhanced X-Ray Timing and Polarimetry mission, planned for launch around 2025, would probe x-rays from violent, fast-changing cosmic events.

IMAGE: INSTITUTE OF HIGH ENERGY PHYSICS

SPACE SCIENCE

China hones plans for ambitious x-ray probe

Mission would firm up China's status as a leader in x-ray astronomy

By **Dennis Normile**, *in Shanghai, China*

China is raising the stakes in its bid to become a major player in space science. At a kick-off meeting in Beijing last week, China's National Space Science Center, part of the Chinese Academy of Sciences (CAS), began detailed design studies for a satellite that would round out an array of orbiting platforms for probing x-rays from the most violent corners of the cosmos.

The enhanced X-Ray Timing and Polarimetry (eXTP) mission would be China's most ambitious space science satellite yet—and its most expensive, with an estimated price tag of $473 million. To pull it off, China is assembling a collaboration involving more than 200 scientists so far from dozens of institutions in 20 countries. If the eXTP mission passes a final review next year, it would launch around 2025.

Chinese scientists "are becoming leaders in the field of x-ray astrophysics," says Andrea Santangelo, an astrophysicist at the University of Tübingen in Germany and eXTP's international coordinator. Last year, the National Space Science Center launched the Hard X-ray Modulation Telescope, which is observing high-energy objects such as black holes and neutron stars. As early as 2021 it will be joined by the Einstein Probe, a wide-field x-ray sentinel for transient phenomena such as gamma ray bursts and the titanic collisions of neutron stars or black holes that generate gravitational waves. "For years we have used data from U.S. and European missions," says eXTP Project Manager Lu Fangjun, an astrophysicist at the CAS Institute of High Energy Physics in Beijing. Now, he says, "We want to contribute [observational data] to the international community."

The eXTP mission would fill a unique niche in x-ray astronomy. Two pioneering x-ray telescopes launched in 1999, NASA's Chandra X-ray Observatory and Europe's XMM-Newton, capture x-rays from the distant universe, gleaning clues to the formation and evolution of stars and galaxies. eXTP will probe neutron stars and black holes closer to home. "The goal is to study fundamental physics in the most extreme conditions in terms of density of matter, magnetic fields and gravity that you cannot reproduce in labs," Santangelo says.

eXTP would be able to collect more photons at a wider range of energies than previous telescopes. Three of its instruments would simultaneously measure energy spectra and polarization of x-rays from cosmic sources, and track how emissions change over microseconds to milliseconds as objects pulsate or rotate. "This powerful payload is absolutely unique," Santangelo says.

Such data would provide clues to how matter behaves when compressed to the extreme densities thought to exist in the cores of neutron stars, and could reveal whether the stars really are made of neutrons or whether the particles have disintegrated into their constituent quarks or other exotic states. eXTP could also measure how matter behaves in the strong gravity close to black holes. Albert Einstein's general theory of relativity, which describes gravity, makes predictions, but these have never been tested under such extreme conditions. And eXTP's suite of instruments would look for evidence to support predictions about how light and matter interact in the powerful magnetic fields associated with certain neutron stars.

The eXTP Wide Field Monitor, in the meantime, would observe a large swath of sky for flashes of x-rays from transient events, for example from merging black holes and neutron stars. Other eXTP instruments, as well as visible light and gravitational wave observatories on the ground, could then train their sights on the object of interest.

Europe and China had each contemplated going it alone on a next-generation x-ray satellite before opting to team up. A European consortium has pledged to build two of the satellite's four scientific instruments. And European and Chinese scientists will provide electronics and detectors for each other's instruments. Europe could ante up further hardware or even funding if the European Space Agency (ESA) comes in on the project, which Santangelo calls "desirable and probable."

eXTP will be "a flagship mission for astrophysics" until other observatories come online, Santangelo says. These include ESA's Advanced Telescope for High-Energy Astrophysics, which, if given a final go-ahead, could be launched around 2028.

NASA is also studying a proposal called Strobe-X, which has goals similar to those of eXTP. "eXTP will get good estimates of the radii of a few neutron stars, but really mapping out the parameter space nature provides will require Strobe-X," says Strobe-X team member Thomas Maccarone of Texas Tech University in Lubbock. A handful of U.S.-based scientists are helping define eXTP's science objectives and will likely analyze data, which Lu expects to share openly. ■

With reporting by Daniel Clery.

LOOKING FOR LOVE

South Asia's "vulture safe zones" aim to preserve, and win respect for, a vital scavenger

By **Warren Cornwall**, *in Vulture Safe Zone 1 in Bangladesh*

PHOTO: JOEL SARTORE/NATIONAL GEOGRAPHIC CREATIVE

Conservation efforts have helped stabilize some populations of the endangered white-rumped vulture.

It was a grisly but irresistible spectacle. In a forest clearing here last December, a wake, or feeding flock, of white-rumped vultures pranced about a dead cow, jostling for a chance to grab a bite. One plucky bird repeatedly plunged its head deep into the carcass, tearing off bits of flesh. Others gave up and lifted off, unfurling 2-meter wingspans as they headed for a roost in a nearby tree.

Watching the feast through a hole in the wall of a nearby hut, Sarowar Alam, a conservation biologist with the International Union for Conservation of Nature (IUCN) in Dhaka, was delighted. The white-rumped vulture, he said admiringly, "is a majestic bird."

Once common, it is also gravely endangered. Just a few hundred white-rumped vultures (*Gyps bengalensis*) now soar above Bangladesh, researchers estimate, and about 10,000 remain in all of South Asia—less than 1% of the population a few decades ago. Two other South Asian species, the Indian vulture (*G. indicus*) and the less common slender-billed vulture (*G. tenuirostris*), have also suffered catastrophic declines. The cause: a drug that veterinarians use to keep cattle healthy, but that is deadly to vultures that eat the carcasses of treated livestock.

The vultures don't have to fear their food here in the Rema-Kalenga Wildlife Sanctuary, an 1800-hectare sliver of protected forest near Bangladesh's northeastern border with India. That's because the preserve is at the heart of Vulture Safe Zone 1, a 200-kilometer-wide circle where conservationists are working with local residents to provide uncontaminated carcasses for the vultures to eat, and with veterinarians to prevent the use of the drugs that kill the birds.

The zone—one of two in Bangladesh, which are modeled on a handful of similar zones elsewhere in South Asia (see map, p. 1088)—is just one part of a multifaceted effort to pull the three vulture species back from the brink of extinction. Over the past decade, several Asian governments have also banned one of the most problematic drugs, and captive breeding centers have begun hatching hundreds of chicks. There are hints that such moves are helping: Surveys suggest vulture declines have slowed, and some populations might even be increasing.

But a recent visit to Bangladesh's Vulture Safe Zone 1 highlighted the sobering difficulties that conservationists face in achieving their goal. Banned drugs deadly to vultures remain in ready supply. Then there's the image issue: Many Bangladeshis still view vultures as things to be avoided—not saved. In the past, people stayed clear of scavengers circling overhead, fearing the birds' shadows would bring sickness. Some have even beaten the birds with bamboo sticks and pelted them with stones. Changing those attitudes, conservationists say, will be key to building vital local support for the drug bans and other vulture protection measures, especially in nations where governments are short on money, manpower, and enforcement. "They don't love [vultures] like tigers or elephants," says Alam, who helped set up Bangladesh's vulture zones. "This is a problem."

THE PLUNGE of South Asia's vulture populations began in the 1990s and progressed with stunning rapidity. Millions of birds disappeared, seemingly overnight. It wasn't until 2004 that scientists in Pakistan found the culprit. Some vultures can't metabolize diclofenac, a painkiller that became widely used in the 1990s to treat fevers, udder inflammation, and other aches and pains in cattle. When the birds fed on tainted carcasses, uric acid crystallized in their kidneys. Kidney failure and death followed.

The disappearance of vultures meant the loss of one of nature's tidiest ways of disposing of a dead body. A wake of vultures can strip a dead cow to its bones in less than an hour. In India, where the Hindu proscription on eating beef means cows tend to die in the fields, officials have built rendering plants to dispose of carcasses previously consumed by the birds. In Mumbai, followers of the

Zoroastrian religion, who traditionally put their dead in open towers on remote hilltops so that vultures could pick the bones clean, erected solar ovens to burn off the flesh. A 2008 study warned that fewer scavenging vultures could even lead to a rise in rabies, if feral dogs took their place.

Eventually, governments in the region moved to save vultures by banning veterinary uses of diclofenac. In India, which has the largest vulture populations and the best tracking efforts, the restriction is credited with enabling the white-rumped vulture population to recover slightly, to about 6000, and slowing the decline of Indian vultures, now down to fewer than 15,000. (The population of slender-billed vultures in India, believed to be about 1500, is too small to reliably discern trends.)

Eradicating problematic drugs, however, has proved difficult. After India imposed a ban on veterinary forms of diclofenac, for example, drug companies there started selling an extra-large dose, ostensibly for human use, that was the same as the dose used on cattle. The government then issued a ban on the new formulation (which was upheld by an Indian court last year). But several of the most common alternatives to diclofenac—including ketoprofen, aceclofenac, and nimesulide—are also toxic to vultures. And in most places, veterinarians can still legally use those drugs.

The continuing contamination has slowed efforts to rear endangered vultures in captivity and release them into the wild. Breeding centers in Nepal and India have raised more than 300 chicks, but most are still being held in cages, because of fears they will wind up poisoned if released. A 2004 study estimated that diclofenac contamination of as few as one in 760 cow carcasses is enough to drive down vulture numbers.

Scavenger security

South Asian nations have established 11 safe zones as part of a wider effort to protect three highly endangered vulture species.

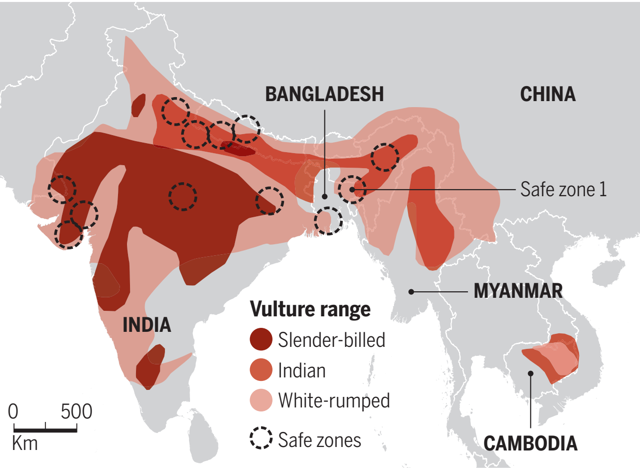

SUCH WORRYING STATISTICS have helped catalyze the creation of 11 safe zones across vulture territory in South Asia, centered on areas where relict populations are hanging on. The strategy, which is led by conservation groups, debuted in Nepal in 2012. It mixes practical measures for protecting vultures with public relations efforts aimed at transforming vultures from symbols of doom to icons of the environment.

In 2014, at the urging of Alam and others, the Bangladeshi government designated two "provisional" safety circles. Their 200-kilometer width matches the distance vultures typically travel to find food. Zone 2 covers part of the Sundarbans mangrove forest in the southwest. Zone 1 is centered on a vulture hot spot in the Rema-Kalenga sanctuary.

Inside the zones, conservationists ply veterinarians with materials warning of drug perils, as well as free stockpiles of meloxicam, a vulture-safe painkiller. They are also deploying undercover buyers to pharmacies, to see whether they are selling contraband drugs. (In 2017, Bangladesh became the first government to ban ketoprofen in addition to diclofenac, though only inside the safe zones.)

Such efforts appear to be having an effect. In Nepal, undercover pharmacy checks have shown a dramatic decline in the availability of diclofenac since the nation's only zone was created in 2012, with none found inside the zone since 2014. In Bangladesh, surveys have found that nearly all pharmacies within the safe zones have stopped selling diclofenac.

Then there are the measures to build good will. In Zone 1, a school near the preserve now sports a colorful mural depicting vultures. And several residents help run the vulture conservation program, serving as what amount to paid local ambassadors.

IUCN also moved to foster pro-vulture feelings by providing cows to 15 impoverished families living on a tea plantation adjacent to the Rema-Kalenga sanctuary. Later, the group bought them back for 25,000 taka each, equal to nearly a year's wages for a plantation worker. The hope is the extra income will dissuade the families from trying to earn money by foraging for wood in the reserve, where the vultures nest.

Those cows—and others bought from local farmers—also become a source of drug-free meals at a so-called vulture restaurant within the sanctuary. During breeding season from September to April, a steady supply of cattle—screened to make sure it isn't contaminated—is slaughtered and dropped in a secluded clearing 50 meters downhill from the small hut.

During one recent feeding, Alam and several guests watched through four small holes as a lone Himalayan griffon (*G. himalayensis*), distinguished by its brown back and hulking size, stood guard over the remains of a 2-day-old carcass. The griffon is also vulnerable to painkillers, but its numbers have declined more slowly because the birds spend much of their lives in mountainous regions where the drugs aren't widely used. This one was intent on protecting its meal from seven white-rumped vultures that also had designs on the carcass. As the griffon spread its wings and menaced the other birds, Alam, an enthusiastic birder, chortled from behind his binoculars. "You are lucky to see the vultures at this forest," he declares. "My dream is in 20 years our population definitely will be increased, and by 10 years our population remains stable."

ALAM IS WORRIED, however, by signs that the use of problematic alternatives to diclofenac, such as ketoprofen, is on the rise—even within safety zones. Just 100 white-rumped vultures live within Zone 1, he notes, and "If these 100 feed on only two or three cows with the harmful drugs, this will destroy the whole population."

A trip to the nearby town of Gazipur confirms that Alam has reason to be concerned. In a cramped one-room office, Muhammad Ali Babul, a local veterinarian, sets boxes of ketoprofen and meloxicam on his desk. He's heard that ketoprofen is banned in the area and bad for vultures, but he also finds it's the best drug for treating cows that are giving birth. So he strikes a balance by using the drug in just 30% of the cases he sees. "It's easy to get," he says, and officials haven't put much effort into enforcing the ban. "That's why we're using it."

A block down the potholed street, Nurul Alam, a veterinary technician with the government's Department of Livestock who advises locals on animal care, seems unaware that ketoprofen is banned in the zone. "I didn't get any kind of order. And many, many [people] use ketoprofen," he says. "I don't think the government bans it.

CREDITS: (MAP) J. YOU/*SCIENCE*; (DATA) SAVING ASIA'S VULTURES FROM EXTINCTION

At a feeding station in Cambodia, a slender-billed vulture eyes a carcass that is free of harmful contaminants, while a wake of white-rumped vultures waits to feed.

When the government bans it, then companies will not produce it."

So far, the drug problem is confined largely to South Asia. Vulture species in the Americas appear immune. Africa is having its own vulture crisis, but it is driven by other kinds of poisoning. Poachers, for instance, lace carcasses with poison to kill vultures and other birds, but only because scavenging flocks can alert antipoaching authorities to their presence. Farmers do the same to kill hyenas and other predators; vultures are unintended victims.

Still, conservationists worry that cattle drugs could become a wider problem. The conservation group BirdLife International, headquartered in Cambridge, U.K., has accused a Brazilian company of aggressively marketing diclofenac in Africa and exporting it to 15 countries there. And in 2013, Spain authorized the use of veterinary diclofenac, over the objections of bird conservationists. The country is home to three-quarters of Europe's griffon vultures (*G. fulvus*), and there are concerns that these birds could be sensitive to the drug.

The proliferation of problem drugs puts a premium on finding safer alternatives, says Toby Galligan, a conservation scientist at the United Kingdom's Royal Society for the Protection of Birds in Bedfordshire. Because governments sensitive to the wishes of the pharmaceutical industry appear unwilling to ban an array of drugs or force safety testing, his organization is now studying how vultures react to a variety of painkillers. Ultimately, he says, "We hope we can find two or three drugs that we can promote along with meloxicam, and flood the market with these safe drugs."

In the meantime, conservationists are working to strengthen existing vulture safe zones—and create new ones. "We hope to get initiatives like this all over the subcontinent, and they could all join together, and that would put pressure on the national governments to make the drug bans more effective," says Chris Bowden, the Bangaluru, India–based program manager for Saving Asia's Vultures from Extinction, a consortium of conservation groups and government agencies.

In Nepal, conservation groups recently launched a test to see whether their nation's safe zone lives up to its name. Last November, they released 17 white-rumped vultures, each carrying a satellite tracking tag, into the safe zone. If the birds, along with others released in the coming year, survive until April 2020 without a drug-related fatality, the region will be officially declared safe. To date, only one bird has died, and Galligan says the cause was a predator, not tainted meat. "So far," he says, "so good."

Here in Bangladesh's Vulture Safe Zone 1, some advocates think they are changing attitudes as well. Nirmal Chandra Dev, a manager of the tea plantation next to the Rema-Kalenga preserve, serves on a local conservation committee that he says is helping spawn a new appreciation for vultures. In the past, he recalls, people would chase the birds away from their houses. They "didn't know that vultures were becoming extinct," he says. "Nowadays, they don't believe vultures are bad luck. They become caring." ■

Banned drugs, as well as vulture-safe products, are still available from veterinarians within Bangladesh's vulture safe zones.

This project was supported with a grant from the Pulitzer Center on Crisis Reporting.

PHOTOS: (TOP TO BOTTOM) A. B. M. SAROWAR ALAM/VULTURE CONSERVATION INITIATIVES; WARREN CORNWALL

FEVER DILEMMA

When malaria isn't the cause, clinics in the developing world often have little to offer

By **Gretchen Vogel**

The toddler on her mother's lap is listless, her eyes dull. She has a fever, little appetite, and a cough. Her journey to the health clinic took an hour by bush taxi, and she had to wait two more hours to be examined. When it's finally her turn, the nurse practitioner pricks her finger and blots a drop of blood onto a rapid diagnostic test (RDT) for malaria. In 15 minutes the answer is clear: The child has malaria. She receives antimalarial drugs, which will most likely vanquish the parasites from her bloodstream within days, and she is sent home to recover.

If the test is negative, however, things get complicated. If malaria isn't making her sick, what is? Is it pneumonia, typhoid, or Lassa fever? Meningitis? Or more than one infection at the same time? If she has bacterial meningitis, the right antibiotic could save her life. If she has Lassa fever, antibiotics won't help.

Until recently, nearly every child with a temperature above 38.5°C was treated for malaria in regions where the disease is endemic. It was one of the most common and deadliest causes of fever, and there was no easy way to rule it out: A definitive diagnosis required a microscope and a skilled technician—unavailable in many places. To be safe, health workers were trained to treat most fevers with a dose of antimalarial medicine. Public health campaigns helped spread the word: If your child has a fever, get them treated for malaria!

In the past decade, malaria RDTs—which use antibodies to detect the parasite's proteins—have transformed the landscape. The tests help reduce unnecessary prescriptions for malaria medicines, but they have exposed a new problem: the previously hidden prevalence of "negative syndrome"—feverish kids who don't have malaria. Even in places with the highest rates of malaria, only about half of fevers are actually due to the disease. In many places, that figure is 10% or less. In 2014, the World Health Organization (WHO) estimated that 142 million suspected malaria cases tested negative worldwide.

Negative test results pose a dilemma for health care workers, who in remote areas may be community volunteers with minimal training. When their one diagnostic test comes up negative, they are left empty-handed, with nothing to offer except some advice: Return if the child gets sicker. But often the family lives hours from the nearest clinic and even farther from a hospital. And patients, or their parents, expect to receive some sort of treatment. So health workers "usually give all the medicine they have," says Didier Ménard, a malaria expert at the Pasteur Institute in Paris. That approach often means antibiotics.

Several research teams have documented dramatic increases in antibiotic prescriptions in places where malaria testing has

PHOTOS: (LEFT TO RIGHT) MAGALI ROCHAT; JACK KURTZ/ZUMA PRESS, INC./ALAMY STOCK PHOTO

A health worker examines a feverish child (left) using a diagnostic app. A blood test (right) can quickly diagnose malaria, but similar tests are lacking for other diseases that cause fever.

been introduced (*Science*, 11 August 2017, p. 536), with some clinics giving the drugs to almost all patients who test negative for malaria. At the same time, studies of the actual causes of fever in places such as Tanzania and Thailand suggest that only 5% to 10% of patients have a bacterial infection that antibiotics could help treat. Those unnecessary prescriptions can cause side effects in patients and increase the risk that antibiotic-resistant strains of bacteria will emerge and spread.

Meanwhile, because there are few reliable rapid tests for infections other than malaria, HIV/AIDS, and tuberculosis, most nonmalarial fevers go undiagnosed and untreated. Patients who have a fungal, parasitic, or viral infection and incorrectly receive antibiotics don't get the drugs or supportive treatments that might actually help them recover.

Public health advocates want to change that. "People are moving from malaria to fever diagnosis and management" as a primary challenge for public health in malaria risk areas, says Heidi Hopkins, an infectious disease researcher at the London School of Hygiene & Tropical Medicine (LSHTM).

To tackle the problem, researchers are starting to gather data on the myriad causes of fever—no small challenge in regions where diagnostic labs are scarce. Several teams are working on robust RDTs that can be used without refrigeration or electricity and can withstand many months of shipping and storage in tropical heat and humidity. Others are developing electronic tools—diagnostic apps—that can help identify the patients most in need of additional treatment.

Countless pathogens can trigger fever, one of the body's most basic immune reactions. "Based on symptoms alone, there is no way to determine what is causing a fever," Hopkins says. Common illnesses vary widely from place to place and from season to season. "What is a prominent cause of fever in Laos is not the same as in Tanzania," says Sabine Dittrich, who heads the program on malaria and fever at the Foundation for Innovative New Diagnostics (FIND), a nonprofit organization in Geneva, Switzerland. In one region, herpesvirus, typhoid fever, and leptospirosis might be the top culprits, whereas dengue, scrub typhus, and Japanese encephalitis might be more common in another.

"What we are really missing—desperately, desperately missing—is surveillance data" on the main pathogens in different regions that make people sick with fever, says Teri Roberts, a diagnostics expert at the Doctors Without Borders Access Campaign in Geneva. "If we were to ask a developer tomorrow to make a test for the top 20 pathogens you'd want to measure if someone has a febrile illness, we would not be able to tell them what to test for."

Without a clear diagnosis, simply knowing whether the patient's infection is bacte-

Published by AAAS

rial or viral can help. In wealthy countries, tests to distinguish between the two are fairly common. They detect biomarkers—proteins or other molecules that the body produces in response to various infections. For example, one key sign of inflammation or infection is an increased level of C-reactive protein (CRP) in the blood, and bacterial infections typically trigger higher levels of CRP than viral ones do.

However, such tests can be misleading in poorer regions. Malnutrition, for example, can suppress CRP levels, whereas parasitic infections can raise them. The tests "are promising in Europe, but we don't know enough about how they would work in areas where there are malaria and malnutrition," Dittrich says. To better understand the advantages and pitfalls, FIND and its partners are conducting clinical trials using CRP and other biomarker tests to help diagnose fever in Thailand, Myanmar, and Malawi.

Identifying the sickest patients also can aid treatment because they are the most likely to need either drugs or more complex care at a hospital. Valérie D'Acremont and her colleagues at the Swiss Tropical and Public Health Institute in Basel have found a way to help do that: They developed an app for a smartphone or tablet that builds on WHO guidelines for treating sick children, adding information from half a dozen simple diagnostic tests. A monitor that fits over a child's finger measures pulse and oxygen saturation in the blood, helping determine whether their breathing is seriously impaired and whether they are dehydrated. A glucose test can flag acute hypoglycemia, which is potentially deadly and easy to treat. A hemoglobin test diagnoses severe anemia, and an arm circumference test identifies malnourished patients. Both conditions can make infections more dangerous. If a child is severely ill, the algorithm recommends both immediate treatment and referral to a hospital or better-equipped clinic.

For children who are not severely ill, the algorithm uses the rate of breaths per minute to distinguish between an upper respiratory tract infection, which usually needs no further treatment, and a lower respiratory tract infection, which can lead to pneumonia. Patients at risk of pneumonia have their CRP levels tested to find out whether a bacterial cause is likely, in which case they receive antibiotics. If a virus is more likely, the child receives inhaled salbutamol, a common asthma medicine that widens the airways. Feverish children without cough, vomiting, or other symptoms also have their CRP levels tested. Kids with levels above the cutoff receive antibiotics; those below probably have a virus and don't need medicine.

In a trial involving 3600 children in Dar es Salaam, Tanzania, the algorithm cut in half the rate of "clinical failures"—children who got significantly sicker or were still seriously ill a week after their initial visit. At the same time, the app dramatically reduced the use of antibiotics: Only 11% of children treated according to the algorithm received antibiotics, compared with 95% of children treated according to standard guidelines. Dittrich calls the work extremely promising.

Other teams are developing tests that could search for multiple causes of fever in a single blood sample. Chembio Diagnostic Systems in Medford, New York, is working with FIND to develop a test that would detect some of the most common fever-causing pathogens in the Asia-Pacific region, based on antibodies or marker proteins. The test will cover four types of malaria, dengue virus, Zika virus, chikungunya virus, and the potentially deadly bacterial diseases leptospirosis, murine typhus, melioidosis, and scrub typhus—which are treatable but require the correct antibiotics.

When fever isn't malaria

Researchers have estimated the percentage of fevers that are—and are not—due to malaria in parts of Africa where the disease is endemic. But data are sparse, especially in west and central Africa.

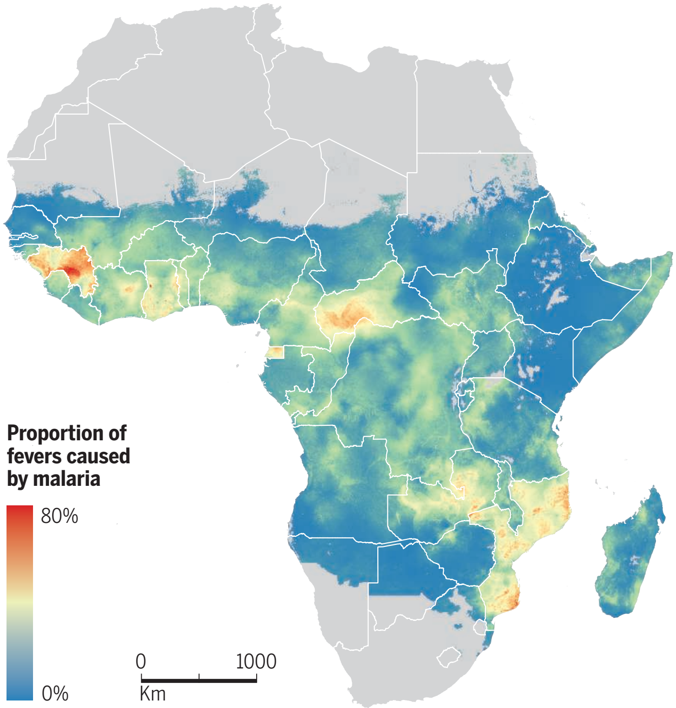

GRAPHIC: MALARIA ATLAS PROJECT ADAPTED BY J. YOU/SCIENCE

But even if such a test proves both reliable and durable enough to withstand tough field conditions, it would not be a quick fix for the problem of diagnosing fever. Often, says Clare Chandler, a medical anthropologist at LSHTM, tests that seem mobile and simple "aren't really simple at all." Even the rapid malaria tests, for example, have several unexpected pitfalls, she and her colleagues found: They take 15 minutes to get results, a strain for clinic workers who might have dozens of people waiting to see them. The lancets used to prick fingers pose another problem. After one use, they need to be disposed of. "You need a sharps bin, which has been a huge issue," she says. "We've seen people just throwing them on the floor, or trying to put them down latrines, not really knowing how to destroy them."

"We need to learn from our experience with malaria tests" and consider the potential downsides of new diagnostics, Hopkins agrees. Another problem: Because viruses are the most common cause of fever, the tests will often end up steering health workers away from giving improper treatment—rather than toward something that can help. "The tests are perceived as gatekeepers, to keep people from things we don't want them to have," Chandler says. That situation can frustrate both the patients and the people caring for them. In one study of RDTs, Chandler notes, patients avoided the clinic that offered the tests because they were less likely to receive medicine.

Chandler and others say the only lasting solution to the fever dilemma is to build stronger health systems with highly qualified health workers, a reliable supply of essential medicines, and well-equipped hospitals to treat severe disease. "In the end, it's not just the tool that's going to improve patient care and save lives. You need to reorganize the system," says Lee Schroeder, a pathologist and diagnostics expert at the University of Michigan in Ann Arbor. That's an effort that will take decades. But in the meantime, knowing what to offer a feverish child would make an immeasurable difference. ■

INSIGHTS

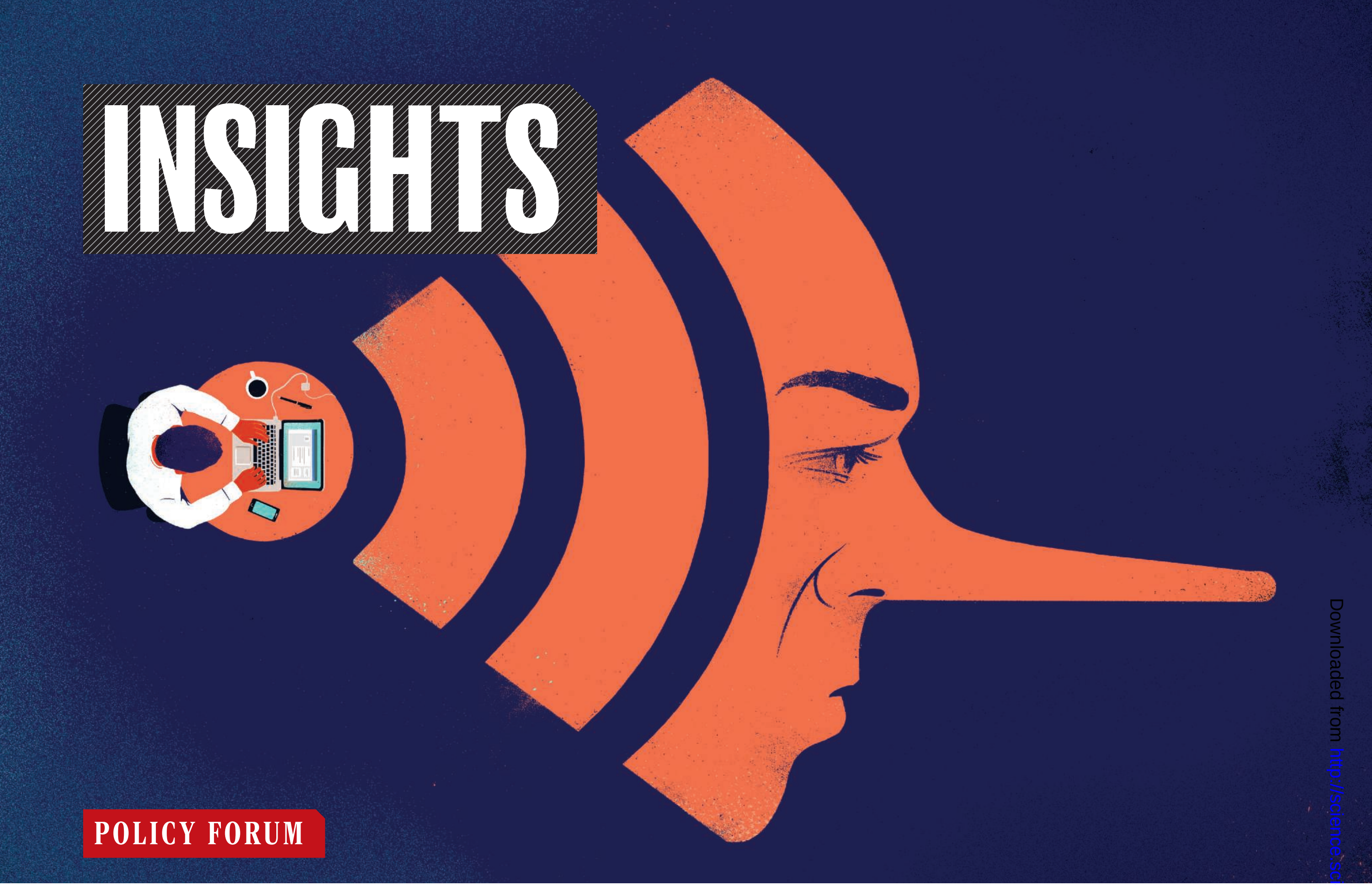

POLICY FORUM

SOCIAL SCIENCE

The science of fake news

Addressing fake news requires a multidisciplinary effort

By **David M. J. Lazer, Matthew A. Baum, Yochai Benkler, Adam J. Berinsky, Kelly M. Greenhill, Filippo Menczer, Miriam J. Metzger, Brendan Nyhan, Gordon Pennycook, David Rothschild, Michael Schudson, Steven A. Sloman, Cass R. Sunstein, Emily A. Thorson, Duncan J. Watts, Jonathan L. Zittrain**

The rise of fake news highlights the erosion of long-standing institutional bulwarks against misinformation in the internet age. Concern over the problem is global. However, much remains unknown regarding the vulnerabilities of individuals, institutions, and society to manipulations by malicious actors. A new system of safeguards is needed. Below, we discuss extant social and computer science research regarding belief in fake news and the mechanisms by which it spreads. Fake news has a long history, but we focus on unanswered scientific questions raised by the proliferation of its most recent, politically oriented incarnation. Beyond selected references in the text, suggested further reading can be found in the supplementary materials.

WHAT IS FAKE NEWS?

We define "fake news" to be fabricated information that mimics news media content in form but not in organizational process or intent. Fake-news outlets, in turn, lack the news media's editorial norms and processes for ensuring the accuracy and credibility of information. Fake news overlaps with other information disorders, such as misinformation (false or misleading information) and disinformation (false information that is purposely spread to deceive people).

Fake news has primarily drawn recent attention in a political context but it also has been documented in information promulgated about topics such as vaccination, nutrition, and stock values. It is particularly pernicious in that it is parasitic on standard news outlets, simultaneously benefiting from and undermining their credibility.

Some—notably First Draft and Facebook—favor the term "false news" because of the use of fake news as a political weapon (*1*). We have retained it because of its value as a scientific construct, and because its political salience draws attention to an important subject.

THE HISTORICAL SETTING

Journalistic norms of objectivity and balance arose as a backlash among journalists against the widespread use of propaganda in World War I (particularly their own role in propagating it) and the rise of corporate public relations in the 1920s. Local and national oligopolies created by the dominant 20th century technologies of information distribution (print and broadcast) sustained these norms. The internet has lowered the cost of entry to new competitors—many of which have rejected those norms—and undermined the business models of traditional news sources that had enjoyed high levels of public trust and credibility. General trust in the mass media collapsed to historic lows in 2016, especially on the political right, with

---

The list of author affiliations is provided in the supplementary materials. Email: d.lazer@northeastern.edu

ILLUSTRATION: SÉBASTIEN THIBAULT

Published by AAAS

51% of Democrats and 14% of Republicans expressing “a fair amount” or “a great deal” of trust in mass media as a news source (*2*).

The United States has undergone a parallel geo- and sociopolitical evolution. Geographic polarization of partisan preferences has dramatically increased over the past 40 years, reducing opportunities for cross-cutting political interaction. Homogeneous social networks, in turn, reduce tolerance for alternative views, amplify attitudinal polarization, boost the likelihood of accepting ideologically compatible news, and increase closure to new information. Dislike of the “other side” (affective polarization) has also risen. These trends have created a context in which fake news can attract a mass audience.

PREVALENCE AND IMPACT

How common is fake news, and what is its impact on individuals? There are surprisingly few scientific answers to these basic questions.

In evaluating the prevalence of fake news, we advocate focusing on the original sources—the publishers—rather than individual stories, because we view the defining element of fake news to be the intent and processes of the publisher. A focus on publishers also allows us to avoid the morass of trying to evaluate the accuracy of every single news story.

One study evaluating the dissemination of prominent fake news stories estimated that the average American encountered between one and three stories from known publishers of fake news during the month before the 2016 election (*3*). This likely is a conservative estimate because the study tracked only 156 fake news stories. Another study reported that false information on Twitter is typically retweeted by many more people, and far more rapidly, than true information, especially when the topic is politics (*4*). Facebook has estimated that manipulations by malicious actors accounted for less than one-tenth of 1% of civic content shared on the platform (*5*), although it has not presented details of its analysis.

By liking, sharing, and searching for information, social bots (automated accounts impersonating humans) can magnify the spread of fake news by orders of magnitude. By one recent estimate—that classified accounts based on observable features such as sharing behavior, number of ties, and linguistic features—between 9 and 15% of active Twitter accounts are bots (*6*). Facebook estimated that as many as 60 million bots (*7*) may be infesting its platform. They were responsible for a substantial portion of political content posted during the 2016 U.S. campaign, and some of the same bots were later used to attempt to influence the 2017 French election (*8*). Bots are also deployed to manipulate algorithms used to predict potential engagement with content by a wider population. Indeed, a Facebook white paper reports widespread efforts to carry out this sort of manipulation during the 2016 U.S. election (*5*).

However, in the absence of methods to derive representative samples of bots and humans on a given platform, any point estimates of bot prevalence must be interpreted cautiously. Bot detection will always be a cat-and-mouse game in which a large, but unknown, number of humanlike bots may go undetected. Any success at detection, in turn, will inspire future countermeasures by bot producers. Identification of bots will therefore be a major ongoing research challenge.

We do know that, as with legitimate news, fake news stories have gone viral on social media. However, knowing how many individuals encountered or shared a piece of fake news is not the same as knowing how many people read or were affected by it. Evaluations of the medium-to-long–run impact on political behavior of exposure to fake news (for example, whether and how to vote) are essentially nonexistent in the literature. The impact might be small—evidence suggests that efforts by political campaigns to persuade individuals may have limited effects (*9*). However, mediation of much fake news via social media might accentuate its effect because of the implicit endorsement that comes with sharing. Beyond electoral impacts, what we know about the effects of media more generally suggests many potential pathways of influence, from increasing cynicism and apathy to encouraging extremism. There exists little evaluation of the impacts of fake news in these regards.

POTENTIAL INTERVENTIONS

What interventions might be effective at stemming the flow and influence of fake news? We identify two categories of interventions: (i) those aimed at empowering individuals to evaluate the fake news they encounter, and (ii) structural changes aimed at preventing exposure of individuals to fake news in the first instance.

Empowering individuals

There are many forms of fact checking, from websites that evaluate factual claims of news reports, such as PolitiFact and Snopes, to evaluations of news reports by credible news media, such as the *Washington Post* and the *Wall Street Journal*, to contextual information regarding content inserted by intermediaries, such as those used by Facebook.

Despite the apparent elegance of fact checking, the science supporting its efficacy is, at best, mixed. This may reflect broader tendencies in collective cognition, as well as structural changes in our society. Individuals tend not to question the credibility of information unless it violates their preconceptions or they are incentivized to do so. Otherwise, they may accept information uncritically. People also tend to align their beliefs with the values of their community.

Research also further demonstrates that people prefer information that confirms their preexisting attitudes (selective exposure), view information consistent with their preexisting beliefs as more persuasive than dissonant information (confirmation bias), and are inclined to accept information that pleases them (desirability bias). Prior partisan and ideological beliefs might prevent acceptance of fact checking of a given fake news story.

Fact checking might even be counterproductive under certain circumstances. Research on fluency—the ease of information recall—and familiarity bias in politics shows that people tend to remember information, or how they feel about it, while forgetting the context within which they encountered it. Moreover, they are more likely to accept familiar information as true (*10*). There is thus a risk that repeating false information, even in a fact-checking context, may increase an individual’s likelihood of accepting it as true. The evidence on the effectiveness of claim repetition in fact checking is mixed (*11*).

Although experimental and survey research have confirmed that the perception of truth increases when misinformation is repeated, this may not occur if the misinformation is paired with a valid retraction. Some research suggests that repetition of the misinformation before its correction may even be beneficial. Further research is needed to reconcile these contradictions and determine the conditions under which fact-checking interventions are most effective.

Another, longer-run, approach seeks to improve individual evaluation of the quality of information sources through education. There has been a proliferation of efforts to inject training of critical-information skills into primary and secondary schools (*12*). However, it is uncertain whether such efforts improve assessments of information credibility or if any such effects will persist over time. An emphasis on fake news might also have the unintended consequence of reducing the perceived credibility of real-news outlets. There is a great need for rigorous program evaluation of different educational interventions.

Platform-based detection and intervention: Algorithms and bots

Internet platforms have become the most important enablers and primary conduits of fake news. It is inexpensive to create a website that has the trappings of a professional news organization. It has also been easy to monetize content through online ads and social media dissemination. The internet not only provides a medium for publishing fake news but offers tools to actively promote dissemination.

About 47% of Americans overall report getting news from social media often or sometimes, with Facebook as, by far, the dominant source (*13*). Social media are key conduits for fake news sites (*3*). Indeed, Russia successfully manipulated all of the major platforms during the 2016 U.S. election, according to recent congressional testimony (*7*).

How might the internet and social media platforms help reduce the spread and impact of fake news? Google, Facebook, and Twitter are often mediators not only of our relationship with the news media but also with our friends and relatives. Generally, their business model relies on monetizing attention through advertising. They use complex statistical models to predict and maximize engagement with content (*14*). It should be possible to adjust those models to increase emphasis on quality information.

The platforms could provide consumers with signals of source quality that could be incorporated into the algorithmic rankings of content. They could minimize the personalization of political information relative to other types of content (reducing the creation of "echo chambers"). Functions that emphasize currently trending content could seek to exclude bot activity from measures of what is trending. More generally, the platforms could curb the automated spread of news content by bots and cyborgs (users who automatically share news from a set of sources, with or without reading them), although for the foreseeable future, bot producers will likely be able to design effective countermeasures.

> ***"A new system of safeguards is needed."***

The platforms have attempted each of these steps and others (*5, 15*). Facebook announced an intent to shift its algorithm to account for "quality" in its content curation process. Twitter announced that it blocked certain accounts linked to Russian misinformation and informed users exposed to those accounts that they may have been duped. However, the platforms have not provided enough detail for evaluation by the research community or subjected their findings to peer review, making them problematic for use by policy-makers or the general public.

We urge the platforms to collaborate with independent academics on evaluating the scope of the fake news issue and the design and effectiveness of interventions. There is little research focused on fake news and no comprehensive data-collection system to provide a dynamic understanding of how pervasive systems of fake news provision are evolving. It is impossible to recreate the Google of 2010. Google itself could not do so even if it had the underlying code, because the patterns emerge from a complex interaction among code, content, and users. However, it is possible to record what the Google of 2018 is doing. More generally, researchers need to conduct a rigorous, ongoing audit of how the major platforms filter information.

There are challenges to scientific collaboration from the perspectives of industry and academia. Yet, there is an ethical and social responsibility, transcending market forces, for the platforms to contribute what data they uniquely can to a science of fake news.

The possible effectiveness of platform-based policies would point to either government regulation of the platforms or self-regulation. Direct government regulation of an area as sensitive as news carries its own risks, constitutional and otherwise. For instance, could regulators maintain (and, as important, be seen as maintaining) impartiality in defining, imposing, and enforcing any requirements? Generally, any direct intervention by government or the platforms that prevents users from seeing content raises concerns about either government or corporate censorship.

An alternative to direct government regulation would be to enable tort lawsuits alleging, for example, defamation by those directly and concretely harmed by the spread of fake news. To the extent that an online platform assisted in the spreading of a manifestly false (but still persuasive) story, there might be avenues for liability consistent with existing constitutional law, which, in turn, would pressure platforms to intervene more regularly. In the U.S. context, however, a provision of the 1996 Communications Decency Act offers near-comprehensive immunity to platforms for false or otherwise actionable statements penned by others. Any change to this legal regime would raise thorny issues about the extent to which platform content (and content-curation decisions) should be subject to second-guessing by people alleging injury. The European "right to be forgotten" in search engines is testing these issues.

Structural interventions generally raise legitimate concerns about respecting private enterprise and human agency. But just as the media companies of the 20th century shaped the information to which individuals were exposed, the far-more-vast internet oligopolies are already shaping human experience on a global scale. The questions before us are how those immense powers are being—and should be—exercised and how to hold these massive companies to account.

A FUTURE AGENDA

Our call is to promote interdisciplinary research to reduce the spread of fake news and to address the underlying pathologies it has revealed. Failures of the U.S. news media in the early 20th century led to the rise of journalistic norms and practices that, although imperfect, generally served us well by striving to provide objective, credible information. We must redesign our information ecosystem in the 21st century. This effort must be global in scope, as many countries, some of which have never developed a robust news ecosystem, face challenges around fake and real news that are more acute than in the United States. More broadly, we must answer a fundamental question: How can we create a news ecosystem and culture that values and promotes truth? ■

REFERENCES AND NOTES

1. C. Wardle, H. Derakhshan, "Information disorder: Toward an interdisciplinary framework for research and policy making" [Council of Europe policy report DGI(2017)09, Council of Europe, 2017]; https://firstdraftnews.com/wp-content/uploads/2017/11/PREMS-162317-GBR-2018-Report-de%CC%81sinformation-1.pdf?x29719.
2. A. Swift, Americans' trust in mass media sinks to new low (Gallup, 2016); www.gallup.com/poll/195542/americans-trust-mass-media-sinks-new-low.aspx.
3. H. Allcott, M. Gentzkow, *J. Econ. Perspect.* **31**, 211 (2017).
4. S. Vosoughi *et al.*, *Science* **359**, 1146 (2018).
5. J. Weedon *et al.*, Information operations and Facebook (Facebook, 2017); https://fbnewsroomus.files.wordpress.com/2017/04/facebook-and-information-operations-v1.pdf.
6. O. Varol *et al.*, in *Proceedings of the 11th AAAI Conference on Web and Social Media* (Association for the Advancement of Artificial Intelligence, Montreal, 2017), pp. 280–289.
7. Senate Judiciary Committee, Extremist content and Russian disinformation online: Working with tech to find solutions (Committee on the Judiciary, 2017); www.judiciary.senate.gov/meetings/extremist-content-and-russian-disinformation-online-working-with-tech-to-find-solutions.
8. E. Ferrara, *First Monday* **22**, 2017 (2017).
9. J. L. Kalla, D. E. Broockman, *Am. Polit. Sci. Rev.* **112**, 148 (2018).
10. B. Swire *et al.*, *J. Exp. Psychol. Learn. Mem. Cogn.* **43**, 1948 (2017).
11. U. K. H. Ecker *et al.*, *J. Appl. Res. Mem. Cogn.* **6**, 185 (2017).
12. C. Jones, Bill would help California schools teach about "fake news," media literacy (EdSource, 2017); https://edsource.org/2017/bill-would-help-california-schools-teach-about-fake-news-media-literacy/582363.
13. Gottfried, E. Shearer, News use across social media platforms 2017, Pew Research Center, 7 September 2017; www.journalism.org/2017/09/07/news-use-across-social-media-platforms-2017/.
14. E. Bakshy *et al.*, *Science* **348**, 1130 (2015).
15. C. Crowell, Our approach to bots & misinformation, Twitter, 14 June 2017; https://blog.twitter.com/official/en_us/topics/company/2017/Our-Approach-Bots-Misinformation.html.

ACKNOWLEDGMENTS

We acknowledge support from the Shorenstein Center at the Harvard Kennedy School and the NULab for Texts, Maps, and Networks at Northeastern University. D.M.J.L. acknowledges support by the Economic and Social Research Council ES/N012283/1. D.M.J.L. and M.A.B. contributed equally to this article. Y.B. is on the advisory board of the Open Science Foundation. C.R.S. has consulted for Facebook. K.M.G. acknowledges support by the National Endowment for the Humanities.

SUPPLEMENTARY MATERIALS

www.sciencemag.org/content/359/6380/1094/suppl/DC1

10.1126/science.aao2998

PERSPECTIVES

INFLAMMATION

Intestinal barriers protect against disease

Leaky cell-cell junctions contribute to inflammatory and autoimmune diseases

By **Sandra Citi**

All body surfaces and cavities are lined by layers of epithelial cells, which are connected by cell-cell junctions. These junctions serve three main purposes: adhesion, to maintain tissue integrity; creation of a barrier, to control the passage of ions, water, molecules, cells, and pathogens across epithelial layers; and signaling, to receive and transmit cues that affect cell behavior and tissue function. The barrier function is crucial to maintaining tissue homeostasis. Breaking or even slightly perturbing epithelial barriers can lead to serious pathological consequences, including infection and inflammation (*1*–*3*). The intestinal epithelial barrier is constantly being challenged by the gut microbiome, and is leaky in patients with inflammatory bowel disease (IBD) (*1, 3, 4*). Three studies now characterize how gut epithelial barrier dysfunction is involved in IBD, autoimmune disease, and systemic infection, respectively. On page 1161 of this issue, Mohanan *et al.* (*5*) describe how inactivation of the IBD susceptibility gene, *C1orf106* (chromosome 1 open reading frame 106), leads to decreased intestinal barrier function, thereby promoting intestinal inflammation and thus IBD. Also, on page 1156 of this issue, Manfredo Vieira *et al.* (*6*) show how pathogenic bacteria can induce intestinal barrier defects and translocate to lymph nodes and liver, triggering systemic autoimmune disease, such as systemic lupus erythematosus (SLE). Additionally, Thaiss *et al.* (*7*) report that hyperglycemia (high blood glucose concentration), which is common in people with obesity, diabetes, and other metabolic syndromes, disrupts the intestinal barrier, leading to intestinal inflammation and systemic infection complications.

Epithelial barriers are formed by two types of circumferential junctions, which together seal the apicolateral regions of neighboring cells, which have an apical pole facing a lumen, lateral sides in contact with other cells, and a basal face that contacts connective tissue. The tight junction (TJ), which contains claudins, occludin, and tricellulin as the main transmembrane proteins, is the most apical junction along the lateral surface, and is directly responsible for barrier function (*8, 9*). The *zonula adhaerens* (ZA), localized immediately below TJs between adjoining epithelial cells, is an adhesive junction composed of cadherin and nectin transmembrane adhesion molecules connected to the actin cytoskeleton. It regulates barrier function indirectly, because it is required for TJ formation, and because the contractility of the perijunctional actomyosin ring associated with its cytoplasmic surface modulates TJ function (*1*) (see the figure). The TJ barrier is made up of polymeric strands of proteins of the claudin family, which form tiny paracellular "pores" that either allow or block the passage of selected ions (*8, 10, 11*). Claudins are held in place by a cytoplasmic network of scaffolding molecules, linked to actin filaments (*12*). Thus, permeability of epithelial layers to ions and water depends on the specific expression of one or more of the 27 claudin isoforms, which varies within and between tissues, and is modulated by many different physiological and pathological cues, including inflammatory cytokines (*1*–*3, 8, 11*).

Larger solutes permeate across the barrier through the "leak" pathway, which is thought to result from temporary discontinuities within TJ polymeric claudin strands, mediated by occludin and tricellulin, and by the contraction of the actomyosin cytoskeleton (*1, 2, 12*). Another mechanism of barrier regulation is endocytic internalization of junctional protein components, which can drive constitutive physiological remodeling of cell-cell junctions, as well as pathological weakening of the barrier (*13*). Both TJs and ZAs are signaling hubs, recruiting and regulating proteins with different roles, including regulators of the actin cytoskeleton, gene expression, and response to growth factors and pathogens (*14*). Unrestricted passage of pathogens and cells across epithelial layers occurs when the integrity of cell-cell junctions is severely disrupted. Thus, diverse pathological states can ultimately affect barrier function, epithelial integrity, and tissue repair by acting on one or a combination of protein targets that are involved in the diverse functions of cell-cell junctions.

Cell-cell junctions create a barrier

Junctions between epithelial cells form a barrier that maintains tissue homeostasis. The intestinal epithelial barrier can become leaky as a result of genetic predisposition (such as *C1orf106* mutation), intestinal pathogens, and hyperglycemia resulting in IBD, autoimmunity, and systemic inflammation.

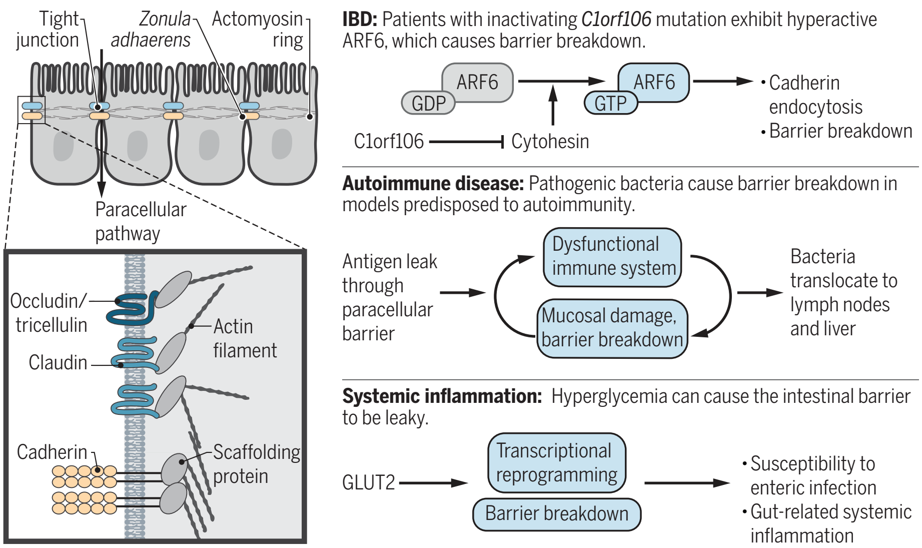

IBD: Patients with inactivating *C1orf106* mutation exhibit hyperactive ARF6, which causes barrier breakdown.

Autoimmune disease: Pathogenic bacteria cause barrier breakdown in models predisposed to autoimmunity.

Systemic inflammation: Hyperglycemia can cause the intestinal barrier to be leaky.

GRAPHIC: N. DESAI/*SCIENCE*

Department of Cell Biology, Faculty of Sciences, and Institute of Genetics and Genomics of Geneva (iGE3), University of Geneva, Switzerland 30, Quai Ernest Ansermet, 1205 Geneva, Switzerland. Email: sandra.citi@unige.ch

The pathogenesis of IBD involves both environmental factors (smoking, diet, exposure to pollution, and the commensal gut microbiome) and a genetic predisposition, which has been narrowed down to mutations in ~100 genes involved in pathways including epithelial cell and barrier function, and immunity (*4*). One of these genes is *C1orf106*. Mohanan *et al.* show that the role of the C1orf106 protein is to maintain appropriate amounts of cytohesin 1 protein in mature epithelia, by promoting its ubiquitination and subsequent proteolytic degradation. Cytohesins are activators of the Ras guanosine triphosphatase (GTPase) ARF6 (ADP ribosylation factor 6), which directs cytoskeletal remodeling and endocytic internalization of cadherins. When epithelial cells form mature monolayers, ARF6 activity must be down-regulated, to maintain TJ stability. Experimental depletion of C1orf106, which mimics the down-regulation of the mutant form that occurs in IBD patients, leads to abnormally high amounts of cytohesin, thus promoting excessive ARF6 activation (see the figure). This in turn causes increased cadherin endocytosis, which results in higher TJ permeability to small molecules, without detectable changes in TJ protein organization. The passage of some small molecules, notably of bacterial nanoparticles, debris, and other antigenic molecules, can induce an immune response and inflammation, potentially escalating barrier damage (*1*, *3*).

Manfredo Vieira *et al.* show that in organisms predisposed to autoimmune disease, exposure to pathogenic bacteria leads to a severe breakdown of the intestinal epithelial barrier, and eventually bacterial translocation to mesenteric lymph nodes and liver. This exacerbates autoimmune reactions (see the figure).

Thaiss *et al.* show that chronic hyperglycemia can affect barrier function through metabolic and transcriptional reprogramming in intestinal epithelial cells, which is mediated by the glucose transporter GLUT2. This results in enhanced dissemination of bacterial products and intestinal and systemic inflammation, which is common in patients with obesity, diabetes, and metabolic syndrome (see the figure). However, the mechanism by which the intestinal barrier becomes leaky is unclear and requires further investigation.

Because a defective intestinal barrier can lead to leakage of either bacterial antigens or bacteria into the underlying tissue as well as, potentially, into blood and lymph vessels, it can both initiate and maintain inflammation and spread of infection. Thus, therapeutic strategies should address the integrity of the TJ barrier. This can be done through small molecules that target proteins involved in the control of barrier function, when the underlying molecular mechanism is known. For example, in a mouse model of T cell–mediated acute diarrhea, pharmacological control of either actomyosin contractility or endocytosis reverses the symptoms (*15*). Thus, stabilizing C1orf106, as suggested by Mohanan *et al.*, could be a strategy in the subset of IBD patients that carry the mutation, provided that no off-target toxicity results from such stabilization. As additional information becomes available about the molecular mechanisms through which claudins, occludin, tricellulin, cytoplasmic adaptor proteins, and signaling proteins control the leak pathway, new potential direct TJ targets could be identified. For example, claudin isoform expression changes following the differentiation of intestinal cells along the crypt-surface axis, and dietary components, including fiber, favors differentiation and increased expression of TJ proteins. Therefore, promoting intestinal cell differentiation could help to strengthen the otherwise leakier barrier of intestinal crypts.

Another key strategy is to limit the inflammatory responses that occur once bacterial products and bacteria have crossed the epithelial barrier—for example, through immunosuppression and antibodies that target inflammatory cytokines (*3*). Conversely, because intestinal epithelial homeostasis results from a balance between shedding of damaged and old cells and their replacement by new cells, prevention and therapy of IBD must also include the stimulation of mechanisms that promote epithelial monolayer repair (*3*). Still, in the presence of massive bacterial invasion through defective epithelial barriers in hosts with a compromised immune system, antibiotic therapy and vaccination may be the most effective approach, as shown by Manfredo Vieira *et al.*, whereas Thaiss *et al.* suggest the control of glycemia as another important factor to consider. Future studies on the complex interplay between microbiome, intestinal epithelium, and immune response will help to refine rational strategies to maintain and repair intestinal barriers. ■

REFERENCES

1. A. Buckley, J. R. Turner, *Cold Spring Harb. Perspect. Biol.* **10**, a029314 (2018).
2. S. M. Krug *et al.*, *Semin. Cell Dev. Biol.* **36**, 166 (2014).
3. A.-C. Luissint *et al.*, *Gastroenterology* **151**, 616 (2016).
4. B. Khor *et al.*, *Nature* **474**, 307 (2011).
5. V. Mohanan *et al.*, *Science* **359**, 1161 (2018).
6. S. Manfredo Vieira *et al.*, *Science* **359**, 1156 (2018).
7. C. A. Thaiss *et al.*, *Science* 10.1126/science.aar3318 (2018).
8. C. M. Van Itallie, J. M. Anderson, *Annu. Rev. Physiol.* **68**, 403 (2006).
9. C. Zihni *et al.*, *Nat. Rev. Mol. Cell Biol.* **17**, 564 (2016).
10. S. Tsukita, M. Furuse, *J. Cell Biol.* **149**, 13 (2000).
11. D. Günzel, A. S. L. Yu, *Physiol. Rev.* **93**, 525 (2013).
12. A. S. Fanning, J. M. Anderson, *Ann. N. Y. Acad. Sci.* **1165**, 113 (2009).
13. A. I. Ivanov *et al.*, *Bioessays* **27**, 356 (2005).
14. S. Citi *et al.*, *Small GTPases* **5**, e973760 (2014).
15. D. R. Clayburgh *et al.*, *J. Clin. Invest.* **115**, 2702 (2005).

10.1126/science.aat0835

DEVELOPMENT

Diverging roads to the heart

Cardiovascular lineage decisions in the mouse embryo are explored at single-cell resolution

By **Robert G. Kelly**[1] *and* **Silke R. Sperling**[2,3,4]

Insight into early cardiac lineage diversification is essential to unravel the origins of congenital heart defects, which are among the most frequent birth anomalies. Congenital heart defects commonly affect specific regions of the heart or cardiac cell types (*1*). Moreover, directed differentiation of pluripotent stem cells into specific cardiac lineages is a pivotal step in modeling heart disease, drug testing, and regenerative therapies. On page 1177 of this issue, Lescroart *et al.* (*2*) used single-cell RNA sequencing to generate two high-resolution snapshots of gene expression in nascent cardiovascular mesoderm in the early mouse embryo. Their findings capture the transcriptional complexity of precardiac mesoderm and reveal how different lineages contributing to the heart first arise during embryogenesis.

Understanding the regulatory mechanisms that drive cell fate choices during lineage diversification is a central goal of developmental biology. Waddington's epigenetic landscape provides a powerful metaphor for such decisions, in which a cell is represented by a ball rolling across a contoured landscape signifying gene regulatory space (*3*). By defining the transcriptional content of many individual cells scattered across the landscape, single-cell transcriptomics heralds a revolution in our grasp of how cell fate decisions take place (see the figure). This technique is transforming our perception of biological complexity and has led to the discovery of new cell types and regulatory mechanisms in homeostasis

---

[1] *Aix-Marseille University, CNRS UMR 7288, Developmental Biology Institute of Marseille, Campus de Luminy Case 907, Marseille Cedex 9, France.* [2] *Department of Cardiovascular Genetics, Experimental and Clinical Research Center, Charité–Universitätsmedizin Berlin, Berlin, Germany.* [3] *Department of Biology, Chemistry, and Pharmacy, Freie Universität Berlin, Berlin, Germany.* [4] *Berlin Institute of Health, Berlin, Germany. Email: robert.kelly@univ-amu.fr*

and disease as well as during development (*4*–*7*). Furthermore, approaches coupling transcriptomics with epigenomic studies at single-cell resolution hold the promise of a holistic understanding of the gene regulatory networks underlying cell fate decisions.

During embryonic development, cardiac progenitor cells transiently express the transcription factor mesoderm posterior protein 1 (Mesp1) at gastrulation (*8*). Nascent cardiac mesoderm migrates to the anterior lateral region of the embryo, where progenitor cells of the first heart field give rise to the early heart tube. Subsequently, late differentiating multipotent progenitor cells of the second heart field contribute to growth of the heart from adjacent pharyngeal mesoderm. Second heart field cells give rise to the venous and arterial poles of the heart, which are hotspots of congenital heart defects (*1*). The first and second heart fields segregate before *Mesp1* is expressed (*9*, *10*).

Single-cell RNA sequencing has recently offered insights into the extent of transcriptional diversity in different regions and cell types of the developing heart, providing valuable resources for discovering new pathways and genes involved in cardiac disease (*6*, *7*). Lescroart *et al.* focused on *Mesp1*-expressing cells at the early time points when this gene is expressed in first and second heart field progenitor cells. The new data neatly fit a developmental continuum between single-cell transcriptomes from pregastrulation epiblast cells and later mesoderm, previously generated by this group (*11*). Using a clustering algorithm to visualize gene expression topology in these combined data sets, the authors identified distinct progenitor cell subpopulations indicative of early lineage diversification. These comprise cardiomyocyte and endothelial progenitor cells, presumably of first heart field origin, as well as cells with a pharyngeal mesoderm genetic signature, defined as posterior and anterior clusters of second heart field cells, the latter including head muscle progenitors. At later stages of development, posterior and anterior second heart field cells contribute to the venous and arterial poles of the heart, respectively. Of particular interest is the finding that the different progenitor cell clusters emerge at the edge of a core of molecularly heterogeneous cardiovascular progenitor cells.

Lescroart *et al.* computed pseudotime trajectories to track progress between pluripotent epiblast and distinct progenitor cell states based on transcriptional profiles. This analysis revealed that anterior and posterior second heart field clusters diverge from common progenitor cells expressing genes enriched in both lineages within the central core. Such multilineage priming has been observed in *Mesp1*-labeled cardiac and pharyngeal muscle progenitor cells in the basal chordate *Ciona intestinalis*, suggesting that this is a conserved feature of cell fate segregation in pharyngeal mesoderm (*12*). Cells within the core population may thus constitute a transition state between different trajectories, within which extrinsic signaling events influence lineage outcomes (*5*). Transcriptional heterogeneity in the core population would confer developmental plasticity and robustness in the face of genetic or environmental perturbation, potentially contributing to compensatory mechanisms and phenotypic variability in congenital heart defect patients. Mining the data set generated by Lescroart *et al.* will contribute to systematic approaches to defining the extrinsic and intrinsic regulators controlling sequential fate decisions in early mesoderm (*13*). As an example, the authors identified Notch signaling as a Mesp1-regulated pathway enriched early in the endothelial versus myocardial trajectory. Furthermore, transcriptome analysis of single cells from mutant embryos showed that Mesp1 itself controls the transition from pluripotency to progenitor cell specification.

Early road map to the heart

The transcriptional complexity of precardiac mesoderm reveals early segregation of lineages contributing to the heart.

The precardiac landscape

Cardiovascular progenitor cells distributed on Waddington's epigenetic landscape.

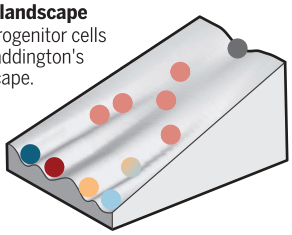

Gene expression topology

Distinct progenitor cell clusters emerge at the edge of a transcriptionally heterogeneous core of nascent cardiovascular mesoderm.

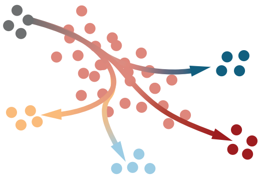

Contributions to heart development

Distinct progenitor cell populations give rise to different regions of the heart and cardiac cell types.

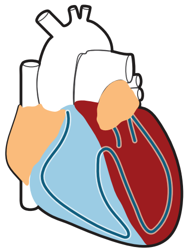

● Pluripotent epiblast cells

● Early myocardial progenitor cells

● Cardiovascular progenitor cells

● Anterior second heart field cells

● Endothelial progenitor cells

● Posterior second heart field cells

GRAPHIC: N. DESAI/SCIENCE

A major challenge of single-cell transcriptomic analysis is mapping cells to the tissue of origin. Using fluorescent in situ hybridization to track selected genes, the authors showed that myocardial and endocardial progenitor cells could be spatially distinguished in nascent mesoderm, as could anterior and posterior pharyngeal territories. Systematic methods have recently been developed to map single cells after RNA sequencing. These exploit high-resolution reference atlases generated from in situ hybridization of a series of landmark genes (*14*) or spatial transcriptomic approaches, such as single-embryo spatial RNA sequencing (*15*). The latter technique has been developed at a stage overlapping with the work of Lescroart *et al.* and should permit topological mapping of this new data set. This will allow identification of the niches harboring progenitor cells on divergent trajectories and clarify our understanding of how future regions of the heart and cardiac cell types are patterned in the progenitor population.

Another challenge of such high-throughput data sets concerns distinguishing biological from experimental noise; analysis of additional cells and time points is likely to refine our view of the progenitor population substructure. Integrating single-cell transcriptomic approaches at multiple time points with single-cell epigenomic data sets and lineage history will provide a fine-grained map of the dynamic cardiovascular progenitor cell landscape. This will guide systematic exploration of the mechanisms driving cardiac progenitor cell fate choices in development and disease. ■

REFERENCES

1. J. A. Epstein, *N. Engl. J. Med.* **363**, 1638 (2010).
2. F. Lescroart *et al.*, *Science* **359**, 1177 (2018).
3. C. H. Waddington, *The Strategy of the Genes: A Discussion of Some Aspects of Theoretical Biology* (Allen & Unwin, 1957).
4. C. Trapnell, *Genome Res.* **25**, 1491 (2015).
5. N. Moris *et al.*, *Nat. Rev. Genet.* **17**, 693 (2016).
6. D. M. DeLaughter *et al.*, *Dev. Cell* **39**, 480 (2016).
7. G. Li *et al.*, *Dev. Cell* **39**, 491 (2016).
8. Y. Saga *et al.*, *Trends Cardiovasc. Med.* **10**, 345 (2000).
9. F. Lescroart *et al.*, *Nat. Cell Biol.* **16**, 829 (2014).
10. W. P. Devine *et al.*, *eLife* **3**, e03848 (2014).
11. A. Scialdone *et al.*, *Nature* **535**, 289 (2016).
12. F. Razy-Krajka *et al.*, *Dev. Cell* **29**, 263 (2014).
13. K. M. Loh *et al.*, *Cell* **166**, 451 (2016).
14. R. Satija *et al.*, *Nat. Biotechnol.* **33**, 495 (2015).
15. G. Peng *et al.*, *Dev. Cell* **36**, 681 (2016).

10.1126/science.aat0230

CANCER

Harmful networks in the brain and beyond

Membrane tubes can connect cancer cells and drive tumor progression and resistance

By **Frank Winkler** *and* **Wolfgang Wick**

Communication in networks is the basis of many social and biological functions. Recent findings have added an uncomfortable twist to this view: Tumors can function as communicating networks, too. In several malignancies such as incurable brain tumors, long protrusions extend from cancer cells, connecting them to a functional syncytium and colonizing normal tissue. These invasive and network-building membrane tubes raise interesting questions about cancer biology.

During development and tissue repair, cell migration and pathfinding is closely associated with extension and retraction of long cellular protrusions (*1*). The discovery of a new class of long, thin membrane protrusions called tunneling nanotubes (TNTs) that connected cells of a pheochromocytoma (a benign tumor that affects adrenal glands), forming a complex multicellular network, paved the way for a new area of research (*2*). TNTs are long-range intercellular conduits that allow rapid communication, including exchange of organelles, vesicles, and molecules (*3*). These cytoplasmic bridges are open-ended, or they contain connexin gap junction proteins, which allow only the exchange of small molecules between cells, such as Ca^{2+}, second messengers, and RNAs (up to 23 ribonucleotides). TNTs seem to be a widespread phenomenon, not limited to particular cell types or tissues, and often increase in frequency with pathological states. TNTs have been involved in the spread of infections, the progression of neurodegenerative diseases, and cancer (*3*). Conceptually, tubular networks that connect cells might be of special importance in tissues where direct physical contact between cell bodies cannot be established, which is regularly the case in tumors where extracellular matrix and nonmalignant cell types occur, as well as tissue-invasive growth patterns, separating cancer cells from each other (*4*).

Until recently, the definitive function(s) of TNT connections in tumor biology remained an open question. TNT-based cellular networks appear more prominent in malignant cells, are induced in tumor cells under conditions of physiological and metabolic stress, and seem to be associated with invasiveness and resistance to chemotherapy in various cancers (*3*–*5*). One considerable limitation to understanding the function of TNTs was that TNTs had to be studied in cell culture because the delicacy of TNTs makes them difficult to preserve after fixation of tissues. This made skeptics question their relevance in vivo, even their existence. Only recently, new confocal intravital imaging technologies allow TNTs to be studied in live organisms (*6*).

Similarly, an in vivo microscopy method made it possible to follow individual cancer cells and their protrusions in a growing patient-derived brain tumor in mice (*7*). This led to the discovery of long cellular protrusions of glioblastoma cells at the invasive edge of growing tumors, extending and retracting, akin to scanning the surrounding brain tissue. These protrusions were also used for efficient brain colonization; after mitosis, daughter nuclei traveled in the mem-

Tubular networks connecting tumor cells

Tunneling nanotubes (TNTs) and tumor microtubes (TMs) have been found in multiple cancers, where they connect tumor cells to a multicellular syncytium. These tubular networks enable pathfinding, invasion, survival of stress, therapeutic resistance, and communication.

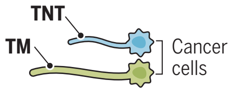

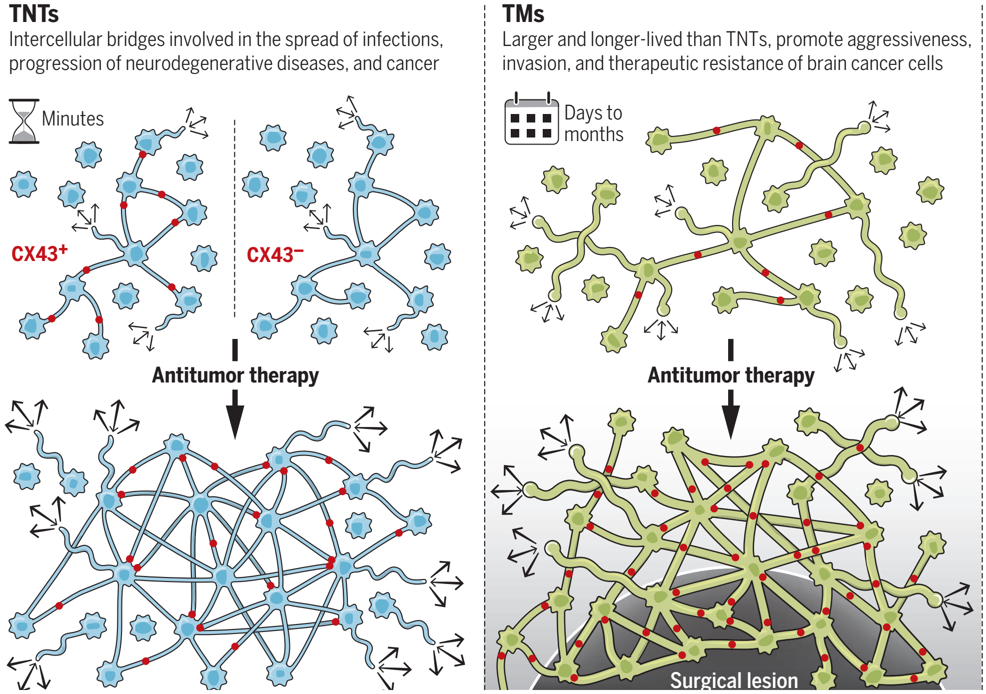

TNTs
Intercellular bridges involved in the spread of infections, progression of neurodegenerative diseases, and cancer

TMs
Larger and longer-lived than TNTs, promote aggressiveness, invasion, and therapeutic resistance of brain cancer cells

Roles in tumor biology

- 🔵🟢 Exchange of cytoplasmatic molecules and energy between tumor cells
- 🔵🟢 Ca^{2+} signaling (intercellular Ca^{2+} waves) in the presence of CX43
- 🔵🟢 Scanning and exploration of environment
- 🔵🟢 Rich in F-actin and myosins
- 🔵🟢 DNA and RNA exchange?
- 🔵🟢 If CX43 is interposed in tubes, transfer of molecules is limited to <760 MW and 23 ribonucleotides.
- 🔵 Exchange of organelles such as mitochondria and cell surface molecules
- 🟢 Nuclear translocation
- 🟢 Formed in a GAP43 and TTYH1-dependent manner

Mechanisms of resistance

- 🔵🟢 TNT and TM connections increase in response to therapy, which maintains cellular homeostasis and and contributes to therapeutic resistance.
- 🔵 Exchange of mitochondria
- 🟢 Detection of damage to members of the network and repair

GRAPHIC: K. SUTLIFF/SCIENCE

brane tubes rapidly to distant sites. As the tumor progressed, the membrane tubes formed a complex multicellular network, not unlike that described for TNTs, connecting about half the cancer cells to a functional syncytium that communicates with waves of Ca^{2+} impulses, like those from other cell types of the normal brain, such as astrocytes. Using this communication route, even single glioblastoma cells that invaded far into the normal brain parenchyma were in contact with other glioblastoma cells and the main tumor mass. Brain colonization by these cells was efficiently mastered by this previously unidentified mechanism of collective network migration, adding to the known mechanisms by which tumor cells can invade tissue (*8*).

Glioblastoma membrane tubes share many structural features with TNTs (*1*, *7*), including a high content of filamentous actin (F-actin), but formal differences exist. Membrane tubes are thicker (1 to 2 μm), longer (some are >1 mm), and longer-lived (hours to days, some >100 days) than the TNTs observed so far. It might be that these differences reflect improved structural stability in vivo compared with the in vitro systems used to study TNTs. Nonetheless, these TNT-like protrusions were called tumor microtubes (TMs).

Importantly, TM-connected glioblastoma cell networks showed a remarkable functionality: They were able to repair themselves when one cell in the network was ablated with a laser or when a larger surgical excision was performed (*7*, *9*). They also resisted the adverse effects of radiotherapy and chemotherapy, which mainly killed unconnected tumor cells. Mechanistically, an improved buffering of transient Ca^{2+} dysregulation within the tumor cell network seemed to play a role in this resistance (*7*). TM formation also correlated with increased tumor aggressiveness in glioblastoma patients. Remarkably, to extend TMs, glioblastoma cells reuse pathways from neurodevelopment that are critical for membrane tube extension, notably growth-associated protein 43 (GAP43) and tweety homolog 1 (TTYH1) (*7*, *10*) (see the figure). By contrast, oligodendroglioma, another type of glioma that has a better long-term prognosis, regularly lack TMs and the molecular machinery to build them. Oligodendrogliomas are characterized by loss of chromosomes 1p and 19q, where many genes relevant for the extension of these membrane processes are located (*7*, *10*). Because 1p and 19q loss is specific for oligodendrogliomas, other cancer types may be able to produce TMs, although this remains to be tested.

Do both TNTs and TMs represent the same fundamental biological process? Many structural and functional similarities exist between the two: Both TNTs and TMs can couple cells via Ca^{2+} signaling in the presence of connexin-43 (CX43)–containing gap junctions; have been associated with cancer cell invasion; increase in number when tumor cells experience stress; and are linked to better tumor cell resistance against cytotoxic agents, probably because of a better cellular homeostasis within the TNT- and TM-connected tumor cell networks (*3*, *4*, *7*, *9*–*11*). Nevertheless, it is likely that some functional differences remain. Most prominently, the extensive exchange of cellular organelles such as mitochondria via TNTs has not been described for TMs. This may not be possible because gap junctions do not allow the passage of such large items. Conversely, recent data increasingly argue for molecular and functional heterogeneity both of TNTs and of TMs (*10*, *12*), which underlines the importance to better study the subtypes of membrane tube cellular connections. Moreover, there is limited information about the molecular drivers involved. Interestingly, overexpression of GAP43 alone was sufficient for the outgrowth of TMs in non-neuronal nonmalignant cells (*13*), which could argue in favor of molecular similarities that are still to be discovered.

"...an uncomfortable twist... Tumors can function as communicating networks..."

TNTs can connect different cell types with each other in normal organismal function and disease (*3*). Interestingly, it has been shown that TNTs can also interconnect malignant cells with nonmalignant cells from the tumor stroma, which has been associated with cancer cell survival and therapeutic resistance (*11*). It will be important to learn whether this applies to TMs, too, and if so, which is the nonmalignant connection partner(s), and what are the consequences for tumor progression and resistance.

In normal development, long cellular protrusions that over time constitute a multicellular network have been recognized as a feature of the evolving mesenchyme. Interestingly, the transition from an epithelial to a mesenchymal state in tumor cells has been associated with extension of long cellular protrusions, including TNTs (*5*), and recently also treatment resistance. Thus, might TNT and TM formation reflect a mesenchymal cellular state? Notably, glioblastomas (which frequently express TMs) with a more mesenchymal gene expression profile have the worst prognosis of all.

A relevant question is whether TNTs or TMs in malignancies are associated with cellular stemness, as demonstrated for nanotubes of stem cells that guarantee maintenance of cellular hierarchy in the *Drosophila melanogaster* testis (*14*). The higher malignancy and resistance of cancer cell populations that produce TMs and TNTs (*4*, *7*, *9*) argue for this possibility. If verified, this would link TNT and TM formation to functionally relevant tumor cell heterogeneity. In this scenario, TNTs and TMs might be used by stem cell–like cancer cells to exert their tumor-driving effects: by conveying hierarchical communication and by constituting the resistant cellular backbone that gives rise to tumor relapse.

Challenges remain. The ability to study TNTs and TMs in clinical tumor samples requires reliable detection and 3D visualization methods. A specific staining method to identify TNTs and TMs would help to better understand their occurrence in different cancer entities, different organs, their correlation with tumor aggressiveness, and their potential role for primary and adaptive therapeutic resistance. To better understand the basic biology of TNTs and TMs in cancer, advanced intravital microscopy methods will most likely provide the greatest gain (*4*, *6*, *7*, *9*, *10*). Regardless, cancer research needs to stay open to thorough morphological analyses of cells.

It is increasingly clear that TNT and TM networks can play relevant functional roles for the malignant organ that constitutes a tumor. Because multicellular syncytia of primarily unicellular organisms have been shown to master remarkable tasks that can appear as primitive forms of intelligence (*15*), it remains to be explored what level of functionality such a tumor cell network can actually reach. The findings in primary brain tumors appear paradigmatic in this respect. New ideas of how to target tumor progression and treatment resistance through the development of anti-TNT or anti-TM therapies have already emerged (*1*, *3*, *4*) and should be explored in the future. ■

REFERENCES

1. M. Osswald *et al.*, *Neuro. Oncol.* **18**, 479 (2016).
2. A. Rustom *et al.*, *Science* **303**, 1007 (2004).
3. J. Ariazi *et al.*, *Front. Mol. Neurosci.* **10**, 333 (2017).
4. E. Lou *et al.*, *Trends Cancer* **3**, 678 (2017).
5. E. Lou *et al.*, *PLOS ONE* **7**, e33093 (2012).
6. M. Rehberg *et al.*, *Small* **12**, 1882 (2016).
7. M. Osswald *et al.*, *Nature* **528**, 93 (2015).
8. V. te Boekhorst *et al.*, *Ann. Rev. Cell. Dev. Biol.* **32**, 491 (2016).
9. S. Weil *et al.*, *Neuro. Oncol.* **19**, 1316 (2017).
10. E. Jung *et al.*, *J. Neurosci.* **37**, 6837 (2017).
11. R. Polak *et al.*, *Blood* **126**, 2404 (2015).
12. X. Wang, H. H. Gerdes, *Cell Death Differ.* **22**, 1181 (2015).
13. M. X. Zuber *et al.*, *Science* **244**, 1193 (1989).
14. M. Inaba *et al.*, *Nature* **523**, 329 (2015).
15. T. Nakagaki, H. Yamada, A. Toth, *Nature* **407**, 470 (2000).

10.1126/science.aar5555

Neurology Clinic, University Medical Center, and German Cancer Research Center (DKFZ), Heidelberg, Germany. Email: frank.winkler@med.uni-heidelberg.de

EPIGENETICS

Hemimethylation: DNA's lasting odd couple

Stably inherited DNA hemimethylation regulates chromatin interaction and transcription

By **Jafar Sharif** *and* **Haruhiko Koseki**

DNA methylation is an essential epigenetic modification that regulates gene transcription, embryonic development, and cell differentiation in both animals and plants. In mammals, DNA methylation generally occurs at CpG dinucleotides in a symmetric fashion (*1*), meaning that if a cytosine (C) residue on one CpG is methylated, the corresponding residue on the complementary strand will be too. This pattern temporarily breaks down during DNA replication, when the unmethylated daughter (nascent) strand and the methylated parent strand create an asymmetrically methylated CpG dyad termed hemimethylated DNA. It was thought that the destiny of hemimethylated DNA was to become fully methylated or unmethylated by replication-coupled dilution. However, about 10% of CpGs in embryonic stem cells (ESCs) (*1*) and trophoblast stem cells (*2*) remain hemimethylated. It is not known if this unusual hemimethylation signature occurs by chance or by design. On page 1166 of this issue, Xu and Corces (*3*) reveal that some CpGs in the genome can be hemimethylated by design. Intriguingly, they found that hemimethylated sites are inherited over several cell divisions. This challenges the prevailing view that hemimethylation is transient and suggests that this DNA modification could be maintained as a stable epigenetic state.

At the replication fork, hemimethylated DNA is bound by the reader protein UHRF1 (ubiquitin-like PHD and RING finger domains 1), which is followed by recruitment of DNMT1 [DNA (cytosine-5)-methyltransferase 1], reinstating the original symmetric methylation pattern (*4*) (see the figure). Generally, it is thought that DNMT1 preferentially acts on hemimethylated DNA (*5*), whereas other members of the family, DNMT3A and DNMT3B, methylate CpGs de novo (*6*). To investigate the link between DNMTs and their substrate CpGs in vivo, Xu and Corces labeled nascent replicating DNA or mature postreplication DNA in human ESCs and mapped the sequences bound by each DNMT to reveal the DNA methylation status of target genomic loci bound by each.

As expected, DNMT1-bound nascent DNA fragments were predominantly hemimethylated. In the mature DNA, the same loci were symmetrically methylated, showing efficient maintenance methylation by DNMT1 (*4*). DNMT3B-bound sites were also enriched in nascent hemimethylated DNA, representing DNMT3B-mediated de novo methylation. These sites became symmetrically methylated in the mature DNA, indicating that DNMT3B stays bound to chromatin long enough to carry out symmetrical methylation. Similar to DNMT3B, DNMT3A bound nascent DNA that was enriched in hemimethylated CpGs. Some of these DNMT3A-bound sites, however, remain hemimethylated even in postreplication DNA. Xu and Corces monitored DNA methylation levels over successive cell divisions to confirm persistent hemimethylation at these loci. This indicates that a DNMT3A-dependent mechanism may regulate locus-specific hemimethylation, which could then be inherited as a stable epigenetic modification.

This leads us to the question of how DNMT3A, and not DNMT3B, contributes to locus-specific hemimethylation, despite possessing similar domain structures and activities. Previous biochemical studies provide a hint. It was reported that DNMT3A shows high de novo activity to naked DNA, but not toward DNA that is wrapped around nucleosomes (*7*). DNA is packed in nucleosomes after replication, which could inhibit DNMT3A activity at specific CpGs, ensuring that these remain hemimethylated. Another important question that remains to be clarified is the mechanism by which DNMT3A is recruited to target DNA sites. We know that DNMT1 loading to DNA replication forks depends on UHRF1 (*4*) and that histone H3 lysine 36 methylation (H3K36me) could play a role in DNMT3B recruitment to target sites (*8*). It will be interesting to identify cofactors or histone modifications that recruit DNMT3A to mediate stable inheritance of hemimethylated CpGs.

Generally, methylated DNA is associated with transcriptional repression and unmethylated DNA with transcriptional activation. So, what about hemimethylated DNA? It has been shown that hemimethylated DNA gives rise to robust transcription from long terminal repeat–containing parasitic DNA elements called endogenous

The fate of hemimethylated DNA

After DNA replication, hemimethylated CpGs are converted to symmetrical methylation by DNMT1. De novo symmetric methylation by DNMT3B is possibly mediated by H3K36me binding. DNMT3A maintains hemimethylated DNA at specific loci, potentially marked by CTCF-cohesin and MBD proteins.

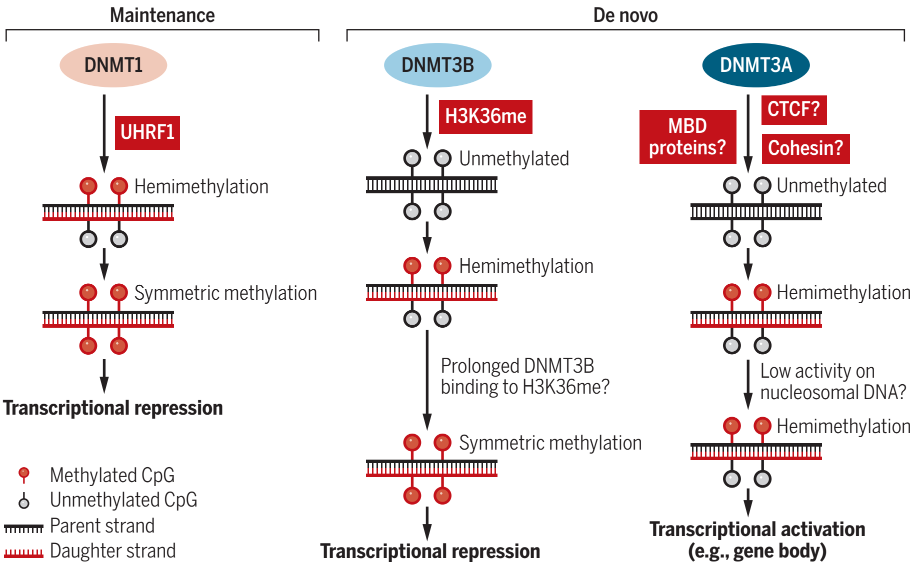

GRAPHIC: ADAPTED BY A. KITTERMAN/*SCIENCE* FROM J. SHARIF/IMS RIKEN

Developmental Genetics Group, Center for Integrative Medical Sciences (IMS), RIKEN, 1-7-22 Suehiro, Tsurumi, Yokohama, Kanagawa 230-0045, Japan. Email: jafarsharif@riken.jp; haruhiko.koseki@riken.jp

retroviruses (*2*). Indeed, Xu and Corces find that gene-body hemimethylation is associated with increased transcription. Notably, a link between gene-body methylation and transcription has been proposed (*9*). The findings of Xu and Corces raise the possibility that gene-body hemimethylation, rather that symmetrical methylation, could be an indicator of transcriptional activity.

What parts of the genome are targeted by DNMT3A for hemimethylation? The authors show that genomic regions bound by the transcriptional regulator CCCTC-binding factor (CTCF) and cohesin (which is involved in keeping replicated chromosomes together) are enriched in hemimethylation. Both CTCF and cohesin are required for long-range chromatin interactions (*10*) and therefore may influence gene expression. Consistent with this idea, Xu and Corces found that in the absence of hemimethylation, such chromatin interactions were disrupted.

How does hemimethylated DNA regulate chromatin interactions? The authors propose that the MBD (methyl-CpG-binding domain) proteins, such as MECP2 (methyl-CpG-binding protein 2), could play a role in this process. They took advantage of genome-wide binding data for MBD proteins and, by performing computational analyses, found that these proteins bound in the same orientation to hemimethylated DNA. In addition, in cells expressing a MECP2 loss-of-function mutant, chromatin interactions emanating from the hemimethylated regions were significantly reduced. These findings are curious, because MBD proteins were originally isolated by their biochemical affinity for symmetrically methylated DNA (*11*). Further studies are therefore required to elucidate how MBD proteins bind hemimethylated CpGs in vivo.

Intriguingly, Xu and Corces also reveal that hemimethylation in the genome dynamically changes during early development of the mammalian embryo. It will be interesting to see if such marks regulate mammalian embryogenesis by modulating expression of critical genes, by means of long-range chromatin interactions mediated by CTCF-cohesin and MBD proteins. ■

REFERENCES

1. L. Zhao *et al.*, *Genome Res.* **24**, 1296 (2014).
2. J. Sharif *et al.*, *Cell Stem Cell* **19**, 81 (2016).
3. C. Xu, V. G. Corces, *Science* **359**, 1166 (2018).
4. J. Sharif *et al.*, *Nature* **450**, 908 (2007).
5. E. Li *et al.*, *Cell* **69**, 915 (1992).
6. M. Okano *et al.*, *Cell* **99**, 247 (1999).
7. H. Takeshima *et al.*, *J. Biochem.* **139**, 503 (2006).
8. T. Baubec *et al.*, *Nature* **520**, 243 (2015).
9. X. Yang *et al.*, *Cancer Cell* **26**, 577 (2014).
10. J. E. Phillips-Cremins *et al.*, *Cell* **153**, 1281 (2013).
11. R. R. Meehan *et al.*, *Cell* **58**, 499 (1989).

10.1126/science.aat0789

PHOTO: NORMAN KURING/NASA'S OCEAN COLOR WEB

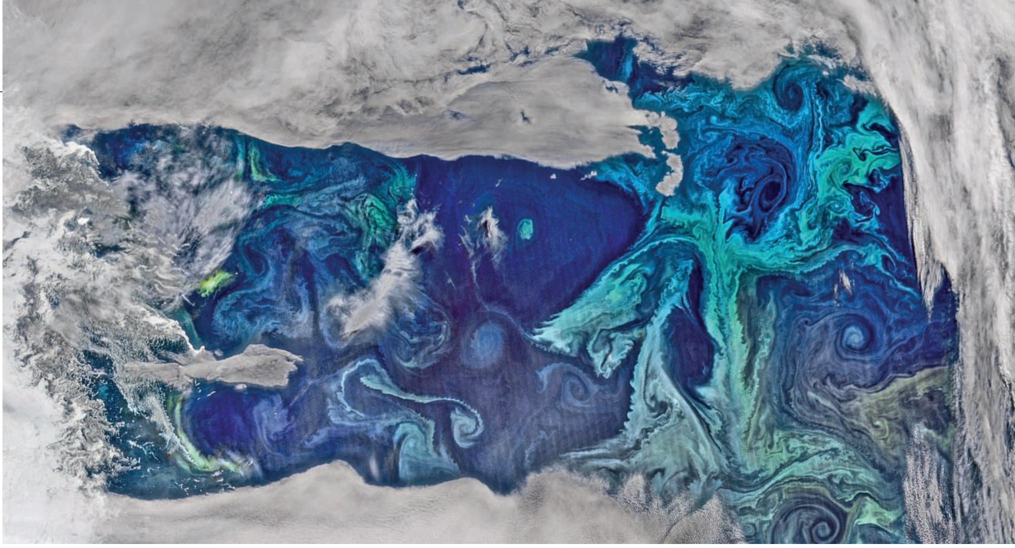

A phytoplankton bloom in the Southern Ocean, observed by the NOAA/NASA Suomi NPP satellite in January 2016.

OCEANS

Will marine productivity wane?

A model study points to slow but extensive nutrient removal from the surface ocean under long-term climate change

By **Charlotte Laufkötter**[1,2] *and* **Nicolas Gruber**[3]

If marine algae are impaired severely by global climate change, the resulting reduction in marine primary production would strongly affect marine life and the ocean's biological pump that sequesters substantial amounts of atmospheric carbon dioxide in the ocean's interior. Most studies, including the latest generation of Earth system models, project only moderate global decreases in biological production until 2100 (*1*, *2*), suggesting that these concerns are unwarranted. But on page 1139 of this issue, Moore *et al.* (*3*) show that this conclusion might be shortsighted and that there may be much larger long-term changes in ocean productivity than previously appreciated.

The authors show that past 2100, interactions between changes in primary production and ocean circulation may reorganize the global nutrient distribution, redirecting nutrients from the upper ocean to the deep ocean. From there, it would take many centuries for the nutrients to resurface and become available again to fuel growth. The consequences for marine life are grim; Moore *et al.* predict decreases in global primary production of up to 24% until 2300, leading to a 20% decrease in potential fishery yields and a 41% decrease in export production (the fraction of production that is exported to depth). This is an astonishingly long-term impact of organisms that live, on average, for a few days to weeks only.

The underlying mechanism is a self-aggravating interplay between warming-driven shifts in ocean circulation and primary production in the Southern Ocean (see the photo and figure). In the modern-day ocean, nutrient-rich water upwells from great depths at around 60°S and is partitioned into northward and southward flowing branches (the Antarctic divergence). Southern Ocean algae are strongly iron- and light-limited (*4*) and therefore cannot consume all nutrients before the water is submerged again. As a result, the northward flowing branch subducts with high nutrient concentrations at around 50°S, forming a nutrient-rich layer beneath the nutrient-depleted subtropical gyres. These nutrients fuel about 75% of the low-latitude productivity, making the Southern Ocean the gatekeeper of much of the global ocean productivity (*5*). The southward-flowing branch further cools and eventually forms the Antarctic bottom water, which does not come in contact with the upper ocean for centuries.

Using a global Earth system model, Moore *et al.* show that in a high-emission scenario, the Antarctic divergence moves southward after 2100, and growth conditions for algae improve substantially in the Southern Ocean because of warmer temperatures, improved light conditions resulting from sea-ice retreat and higher stratification, and higher iron availability. The increased growth leads to the consumption of a large part of the up-

---

[1] *Climate and Environmental Physics, Physics Institute, University of Bern, 3012 Bern, Switzerland.* [2] *Oeschger Centre for Climate Change Research, University of Bern, 3012 Bern, Switzerland.* [3] *Environmental Physics, Institute of Biogeochemistry and Pollutant Dynamics, ETH Zurich, 8092 Zurich, Switzerland. Email: laufkoetter@climate.unibe.ch*

Ocean circulation and primary productivity in the Southern Ocean

Today, the Southern Ocean plays a key role in the transport of nutrients to lower latitudes. A model study shows that this may change as a result of climate change. Under a high-emission scenario, nutrients will be trapped in the Southern Ocean, reducing nutrient export to low latitudes. Hatching indicates elevated nutrient concentrations.

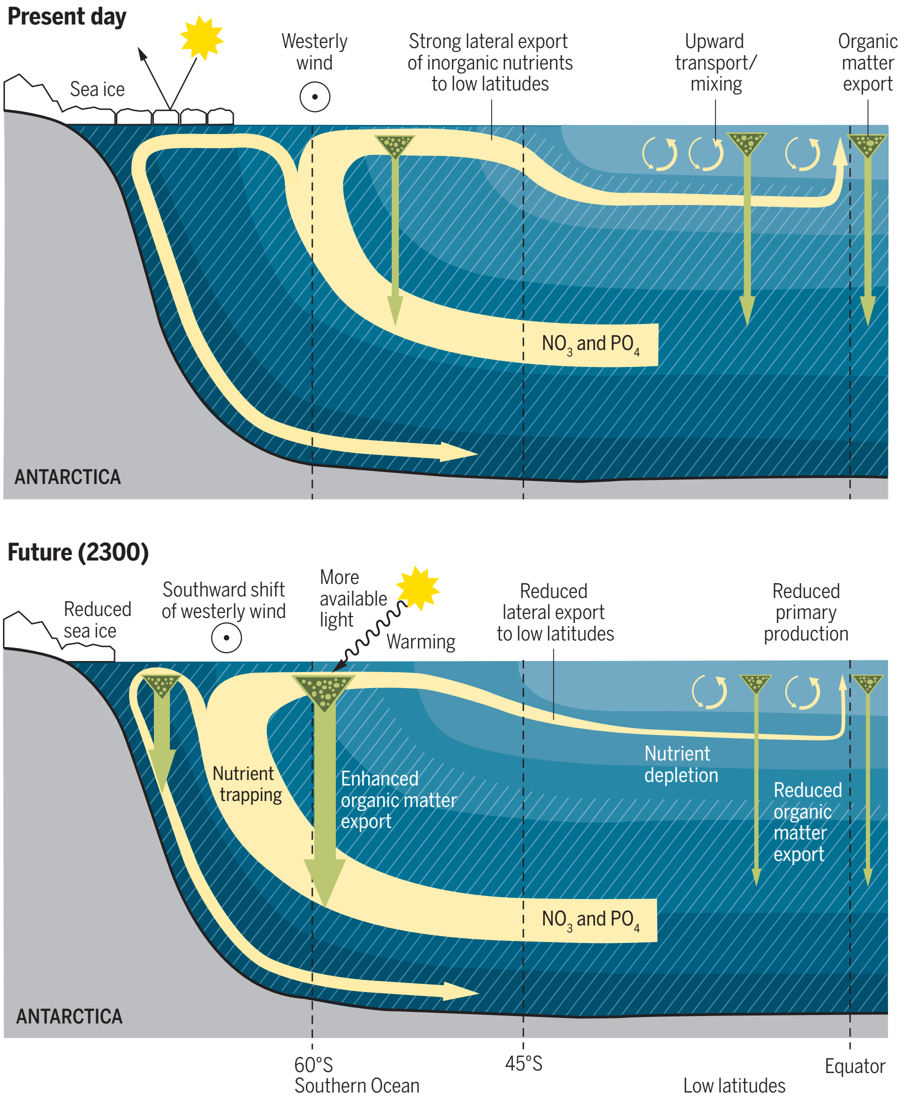

welled nutrients. As a result, nutrients are no longer transported northward but instead exported downward in the form of particulate organic matter. When this matter remineralizes in the water column, the associated nutrients are recycled into upwelling waters and thereby trapped in the Southern Ocean.

In this way, today's northward export of nutrients is transformed into an enclosed circuit. At the same time, southward flow continues to transport nutrients to the deep ocean. The net effect is a slow transfer of nutrients from the intermediate oceanic layers to the deep ocean, depriving the entire upper ocean north of 50°S of the nutrients that are critical to sustaining biological production.

The key role of the Southern Ocean as a global gatekeeper has been recognized before (*5*, *6*), although without realizing that this process could play such a critical role in a future warm ocean. But how robust are the results? Moore *et al.* make a compelling argument that Southern Ocean nutrient trapping is almost inevitable under strong global warming. Current Earth system models agree on a southward shift of the westerlies despite considerable differences in their atmospheric models. Likewise, a retreat of sea ice with global warming is likely, and many models project increasing Southern Ocean production by 2100 (*1*).

However, substantial uncertainties remain. The magnitude of the trapping is highly sensitive to how fast marine algae can consume the nutrients before the water is subducted again. But neither algae growth nor Southern Ocean circulation are well understood in the present ocean. It is thus not surprising that the current generation of ocean models struggle to correctly represent these processes, especially upper level stratification (*7*, *8*).

Iron supply, crucial for Southern Ocean nutrient trapping, is also highly uncertain. Model parameterization of sedimentary iron is based on only a few measurements, glacial iron sources are often not included in current Earth system models, and dust inputs differ widely between models (*9*). Furthermore, phytoplankton community composition and their specific stoichiometries may matter because they determine not only the magnitude but also the stoichiometric ratios of the exported nutrients (*10*, *5*). The interaction between these incompletely understood physical and biological processes could lead to rather different outcomes. This may be part of the reason why another recent study (*11*) found rather different results under a scenario of high emissions until 2100 but with climate mitigation after that; in this case, the authors found a rapid increase in net primary productivity above present-day levels beyond 2100.

Notwithstanding these uncertainties, the mere possibility of a future Southern Ocean nutrient–trapping scenario is highly concerning, warranting dedicated efforts to further our understanding of the unique role of the Southern Ocean in the global climate system. Emerging opportunities—such as the advent of biogeochemical measurements on profiling floats (*12*), coupled with dedicated field and modeling studies—could help to provide answers. Such an approach is even more needed when considering the potential cascade of changes in a range of biogeochemical processes set in motion by the Southern Ocean nutrient trapping, such as a large-scale depletion of oxygen in the deep waters. Regardless of future findings from such studies, one consequence is already obvious. In the political debate, long-term consequences beyond 2100 urgently need to be considered. ■

REFERENCES

1. C. Laufkötter *et al.*, *Biogeosciences* **12**, 6955 (2015).
2. L. Kwiatkowski *et al.*, *Nature Clim. Change* **7**, 355 (2017).
3. J. K. Moore *et al.*, *Science* **359**, 1139 (2018).
4. M. P. Gall, R. Strzepek, M. Maldonado, P. W. Boyd, *Deep Sea Res. Part II* **48**, 2571 (2001).
5. J. L. Sarmiento *et al.*, *Nature* **427**, 56 (2004).
6. I. Marinov *et al.*, *Nature* **441**, 964 (2006).
7. C. Heuzé, K. J. Heywood, D. P. Stevens, J. K. Ridley, *Geophys. Res. Lett.* **40**, 1409 (2013).
8. J.-B. Sallée *et al.*, *J. Geophys. Res.* **118**, 1845 (2013).
9. A. Tagliabue *et al.*, *Glob. Biogeochem. Cyc.* **30**, 149 (2016).
10. M. A. Brzezinski *et al.*, *Geophys. Res. Lett.* **29**, 5-1 (2002).
11. J. G. John, C. A. Stock, J. P. Dunne, *Geophys. Res. Lett.* **42**, 9836 (2015).
12. http://biogeochemical-argo.org

10.1126/science.aat0795

GRAPHIC: N. CARY/SCIENCE

Capturing dynamic protein interactions

A method based on heat denaturation reveals how proteins interact in different cells

By **Xiao-Han Li, Pavithra L. Chavali, M. Madan Babu**

Protein-protein interactions form the molecular basis for organismal development and function (*1*, *2*). In cells, protein interactions are dynamic and subject to spatiotemporal regulations that are specific to the cell type and cell cycle phase. Mutations that abolish or rewire protein-protein interaction networks (the interactome) are often detrimental and manifest in developmental anomalies and diseases (*3*, *4*). Recent advances in quantitative proteomics offer snapshots of cell type–specific proteomes, but scientific understanding of how protein-protein interactions vary between physiological and disease conditions is limited. On page 1170 of this issue, Tan *et al.* report a technique for inferring dynamics of protein interactions by characterizing protein thermal stability upon heat denaturation (*5*).

Thermal stability is a key molecular fingerprint of a protein and can be represented by the melting curve generated from its stepwise heat denaturation (*6*). Interactions between proteins and their ligands can influence protein conformation and, hence, thermal stability. The magnitude of change in thermal stability correlates with interaction affinity and can thus be used to quantify the interactions between proteins and other molecules. This principle forms the basis of the cellular thermal shift assay (CETSA), in which cells are treated with a compound of interest, the cell lysates are denatured by heating to different temperatures, aggregates are separated from the soluble fraction, and the proteins in the soluble fraction are quantified (*7*, *8*). The shifts in melting curves of proteins in the soluble fraction upon adding a drug represent the changes in thermal stability as a result of protein-drug interaction.

Coupling this technique with mass spectrometry enables high-throughput characterization of the melting curves for thousands of proteins (*9*, *10*). In this way, protein-drug interactions can be characterized on a systems level, revealing unknown targets stabilized by particular drugs and providing insights into drug efficacy in normal and diseased tissues.

Medical Research Council Laboratory of Molecular Biology, Francis Crick Avenue, Cambridge CB2 0QH, UK. Email: xli@mrc-lmb.cam.ac.uk; madanm@mrc-lmb.cam.ac.uk

Tan *et al.* adapt CETSA to observe the dynamic changes in the interactome. Their technique, called thermal proximity coaggregation (TPCA), is based on the assumption that proteins that interact with each other tend to coaggregate during denaturation and will exhibit similar solubility at a given temperature; they will hence display similar melting curves (TPCA signature; see the figure). TPCA can be performed on intact cells without specific treatment, allowing proteome-wide detection of interactions.

By obtaining melting curves for 7693 human proteins and investigating 111,776 published interactions between these proteins, the authors show that, as hypothesized, interacting protein pairs tend to have more similar melting curves than noninteracting proteins. The use of intact cells circumvents postlysis loss or gain of interactions and minimizes false discovery rates. For instance, the authors demonstrate the existence of two distinct subcomplexes of the kinetochore protein NDC80, which were not observed in cell lysates. These results highlight the importance of preserving the integrity of the cellular environment to reveal basic functional states of protein complexes, which dynamically change under different conditions.

How to monitor protein interactions

Interacting proteins tend to show similar melting profiles when compared to noninteracting proteins.

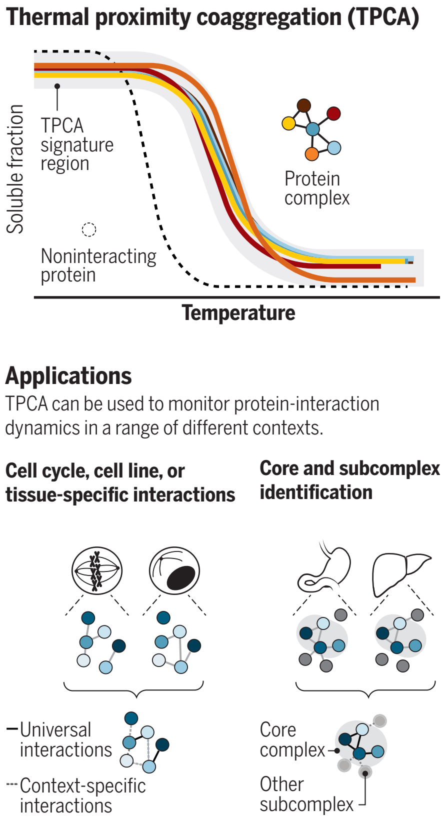

How can TPCA advance our understanding of the dynamic interactome? TPCA can be used to track the dynamics of protein complexes in different cell cycle phases and cell states to discover new core protein subcomplexes. By comparing differential TPCA signatures of K562 cells (human leukemia cell line) that were synchronized to the DNA replication phase (S phase) of the cell cycle to those of K562 cells that were not synchronized, the authors identified 18 protein complexes implicated in S phase; three of these had not been previously reported.

TPCA can also be used to monitor interactome differences across different cell lines and tissues. For example, Tan *et al.* show that across six different cell lines, there was only 70% overlap of TPCA signatures among the detected protein complexes, indicative of cell type–specific interactions. Notably, protein complex stoichiometry and composition vary even in fundamental and abundant complexes, such as the eukaryotic initiation factor 3 (eIF3) core complex. Furthermore, using these data, the authors generated a TPCA-weighted interaction network and elucidated dynamic interactions in different pathways. Thus, use of TPCA signatures could contribute to the discovery of cell-specific interactions and signaling pathways that have been rewired, thereby revealing new biology.

Finally, TPCA signatures can be used to infer the stoichiometry and/or abundance of subunits in a complex in a tissue-specific manner. With the convenience of using intact cells, the authors show that mouse liver cells could be used as a source for comparing TPCA signatures.

Although interacting proteins tend to show similar melting curves, similarity in melting curves cannot be interpreted directly as protein interactions. However, it should be possible to develop algorithms that use TPCA signatures to predict protein-protein interactions in different tissues or cell lines. It should also be possible to adapt TPCA to

GRAPHIC: ADAPTED BY V. ALTOUNIAN/*SCIENCE*

discover proteins that interact with DNA and RNA in different cellular contexts. This could provide an integrated description of how DNA-, RNA-, and protein-protein interactions govern cell physiology.

In a recent study, Leuenberger *et al.* used proteome-wide heat denaturation to measure protein stability from cell lysates using a different method called limited proteolysis–coupled mass spectrometry (*11*). They found that half of the detected proteins that were computationally predicted to lack stable tertiary structures (that is, intrinsically disordered) exhibited a two-state denaturation profile, which is indicative of a stable structure. This seeming contradiction may now be interpreted in light of Tan *et al.*'s findings. Because intrinsically disordered proteins (IDPs) interact with other structural partners, this may result in a melting curve similar to that seen for structured proteins.

Because of their lack of stable tertiary structure and their promiscuous interactions, IDPs are referred to as the dark proteome (*12*, *13*). Techniques such as TPCA could provide much-needed insights into protein-protein interactions involving IDPs in a cellular context, and on a proteome-wide scale. This would be especially useful considering the role of IDPs in modulating protein interaction networks. By offering the possibility to decipher and interpret the dynamic interactome, techniques such as TPCA may be the key to determining how cellular function emerges from dynamic changes in protein interaction networks. ■

> ***"TPCA [thermal proximity coaggregation] can be performed on intact cells… allowing proteome-wide detection of interactions."***

REFERENCES AND NOTES

1. E. L. Huttlin *et al.*, *Cell* **162**, 425 (2015).
2. T. Rolland *et al.*, *Cell* **159**, 1212 (2014).
3. N. Sahni *et al.*, *Cell* **161**, 647 (2015).
4. X. Wang *et al.*, *Nat. Biotechnol.* **30**, 159 (2012).
5. C. S. H. Tan *et al.*, *Science* **359**, 1170 (2018).
6. K. Ghosh, K. Dill, *Biophys. J.* **99**, 3996 (2010).
7. R. Jafari *et al.*, *Nat. Protoc.* **9**, 2100 (2014).
8. D. Martinez Molina *et al.*, *Science* **341**, 84 (2013).
9. M. M. Savitski *et al.*, *Science* **346**, 1255784 (2014).
10. K. V. Huber *et al.*, *Nat. Methods* **12**, 1055 (2015).
11. P. Leuenberger *et al.*, *Science* **355**, eaai7825 (2017).
12. A. Bhowmick *et al.*, *J. Am. Chem. Soc.* **138**, 9730 (2016).
13. https://darkproteome.wordpress.com/about/what-is-the-dark-proteome/

ACKNOWLEDGMENTS

We thank G. Slodkowicz and M. M. Solano for reading the manuscript and the Medical Research Council (MC_U105185859) and European Research Council (ERC-COG-2015-682414; IDR-Seq) for financial support.

10.1126/science.aat0576

PROTEOMICS

Proteoforms as the next proteomics currency

Identifying precise molecular forms of proteins can improve our understanding of function

By **Lloyd M. Smith**[1] *and* **Neil L. Kelleher**[2]

Proteoforms—the different forms of proteins produced from the genome with a variety of sequence variations, splice isoforms, and myriad posttranslational modifications (*1*)—are critical elements in all biological systems (see the figure, left). Yang *et al.* (*2*) recently showed that the functions of proteins produced from splice variants from a given gene—different proteoforms—can be as different as those for proteins encoded by entirely different genes. Li *et al.* (*3*) showed that splice variants play a central role in modulating complex traits. However, the standard paradigm of proteomic analysis, the "bottom-up" strategy pioneered by Eng and Yates some 20 years ago (*4*), does not directly identify proteoforms. We argue that proteomic analysis needs to provide the identities and abundances of the proteoforms themselves, rather than just their peptide surrogates. Developing new proteome-wide strategies to accomplish this goal presents a formidable but not insurmountable technological challenge that will benefit the biomedical community.

The function of proteins can be strongly modulated by posttranslational modifications (PTMs) such as phosphorylation (consider kinase cascades), acetylation, methylation (consider histones), and many more of the >400 known PTMs in biology. These sources of variation combine to create a complex and largely uncharted world of natural proteins. Knowledge of the identities and quantities of these proteoforms present in dynamic biological systems is indispensable to development of a complete picture of functional regulation at the protein level.

Conventional proteomics digests protein mixtures into peptides, some of which are identified by tandem mass spectrometry (MS). Each identified peptide acts as a surrogate for the presence of the protein molecule from which it is derived. This strategy provides invaluable information on protein expression in complex systems. However, as many different gene products, isoforms, and proteoforms can contain the same peptide, direct information about the proteoforms present is lost (see the figure, bottom). This issue is the proteomic analog of the problem of "phasing" in genomics (*5*)—determining whether multiple alleles are present on the same segment of DNA. The step of digestion into peptides is essential to the success and robustness of the bottom-up strategy, as well-behaved peptides are more amenable to liquid chromatographic separation and MS analysis than are intact proteins. However, only inferences can be made as to the actual proteoform or proteoforms from which the identified peptide was derived (*6*).

An alternative approach is "top-down" proteomics, in which whole proteins are analyzed directly using tandem MS methods (see the figure, top left). Although great strides have recently been made in the top-down analysis of high-mass proteins (*7*) and complex proteomic samples (*8*), limitations remain to be addressed in the degree of sequence coverage and the ability to analyze low-abundance species. A complementary approach reported the proteome-wide identification of proteoforms in yeast, based primarily upon a high-accuracy determination of their intact mass, aided by a corollary measurement of the number of lysine residues in the molecule (*9*). Comparison of the measured masses and lysine counts with a theoretical database of possible yeast proteoforms yielded proteoform identifications. Further comparisons of all experimental masses with one another revealed related proteoforms differing by common PTMs, yielding more identifications. These pairwise relations (experimental:theoretical and experimental:experimental) were assembled into "families" of related proteoforms (see the figure, top center).

Such "proteoform families" offer a new and more detailed way of viewing the proteome (see the figure, top right). To extend the strategy to mammalian genomes, RNA sequencing can be used to construct sample-specific proteoform databases that capture the genetic variation and extent of splicing

---

[1] *Department of Chemistry, University of Wisconsin, 1101 University Avenue, Madison, WI 53706-1396, USA.* [2] *Departments of Chemistry and Molecular Biosciences and Feinberg School of Medicine, Northwestern University, Evanston, IL 60208, USA. Email: smith@chem.wisc.edu*

patterns in the sample (*10*, *11*). Integrating such proteogenomic data with synergistic information obtained from bottom-up (for PTM identification and localization), top-down (for protein identification and PTM localization), and intact mass measurements (for proteoform identification) can provide the comprehensive analysis needed to broadly identify and quantify proteoforms in complex samples.

The question of how many proteoforms exist in nature quickly arises in this discussion (*12*). This question may prove impossible to answer fully, as errors in transcription and translation can produce numerous low-abundance proteoforms, perhaps as few as only a single molecule per cell, or even a single molecule in a large population of cells. We currently can only detect proteoforms present at concentrations above the instrumental detection limits of existing mass spectrometers, although the advent of single-molecule nanopore or other strategies for proteoform identification may change that landscape in the future.

However, the number and variety of proteoforms expressed in biological systems appear to be far below the calculated combinatorial possibilities (*12*). Garcia and coworkers have pioneered MS methods for histone proteoform analysis, finding much smaller numbers of histone proteoform variants than the maximal number of combinatorial possibilities would suggest (*13*). Similarly, in a deep study of histone H4 proteoforms by Coon and co-workers, only 74 were identified (*14*). This stands in striking contrast to the ~3 million possibilities that are theoretically possible from the combinatorial explosion of known site-specific modifications (*14*). This difference may simply indicate that many or most proteoforms are not detectable with current technology, and that we are only able to see at present the few of those that are most abundant. Alternatively, nature may only make and use a small subset of the proteoforms that are theoretically possible, as deduced from the combinatorial possibilities offered by considering all of the various possible PTM combinations. Understanding which of these explanations is correct, or perhaps a blend of both, will require improved technologies that can reveal proteoforms at ever lower abundance.

Proteoform analyses will become increasingly straightforward as information is accrued and archived on the proteoforms that actually exist in nature and can be observed. Establishing a comprehensive atlas of identified proteoforms for human and other species has begun, and over time this atlas will begin to yield transformative insights into the levels and roles of proteoform complexity present in biological systems. As proteoforms are tightly linked to the functioning of cells and tissues that underlie complex phenotypes, their identification and quantification will provide critical insights into the fundamental workings of biological systems (see the figure, top right). Proteoforms should also help identify key diagnostic markers and therapeutic targets and thereby provide greater statistical power for deciphering human disease phenotypes. ■

REFERENCES AND NOTES

1. L. M. Smith *et al.*, *Nat. Methods* **10**, 186 (2013).
2. X. Yang *et al.*, *Cell* **164**, 805 (2016).
3. Y. I. Li *et al.*, *Science* **352**, 600 (2016).
4. J. K. Eng, A. L. McCormack, J. R. Yates, *J. Am. Soc. Mass Spectrom.* **5**, 976 (1994).
5. S. R. Browning, B. L. Browning, *Nat. Rev. Genet.* **12**, 703 (2011).
6. A. I. Nesvizhskii, R. Aebersold, *Mol. Cell. Proteomics* **4**, 1419 (2005).
7. X. Han, M. Jin, K. Breuker, F. W. McLafferty, *Science* **314**, 109 (2006).
8. J. C. Tran *et al.*, *Nature* **480**, 254 (2011).
9. M. R. Shortreed *et al.*, *J. Proteome Res.* **15**, 1213 (2016).
10. X. Wang *et al.*, *J. Proteome Res.* **11**, 1009 (2012).
11. V. C. Evans *et al.*, *Nat. Methods.* **9**, 1207 (2012).
12. R. Aebersold *et al.*, *Nat. Chem. Biol.* **14**, 206 (2018).
13. Z.-F. Yuan, A. M. Arnaudo, B. A. Garcia, *Annu. Rev. Analyt. Chem.* **7**, 113 (2014).
14. D. Phanstiel *et al.*, *Proc. Natl. Acad. Sci. U.S.A.* **105**, 4093 (2008).

ACKNOWLEDGMENTS

We thank J. Loo, J. Chamot-Rooke, L. Pasa-Tolic, Y. Ge, and Y. Tsybin for their comments and suggestions and D. Walt for pointing out the potential effects of errors in transcription and translation. The Proteoform Atlas is supported by a grant from the Paul G. Allen Family Foundation (http://repository.topdown-proteomics.org; Award 11715). We thank the National Institute of General Medical Sciences for their support under grants 1R01GM114292 (L.M.S.) and P41 GM108569 (N.L.K.). The authors are members of the Consortium for Top Down Proteomics.

10.1126/science.aat1884

Identifying proteoforms within their families and protein networks

Proteoforms underlie complex traits and molecular mechanisms in biology. Top-down (whole protein) and bottom-up (peptide) proteomics methods are compared.

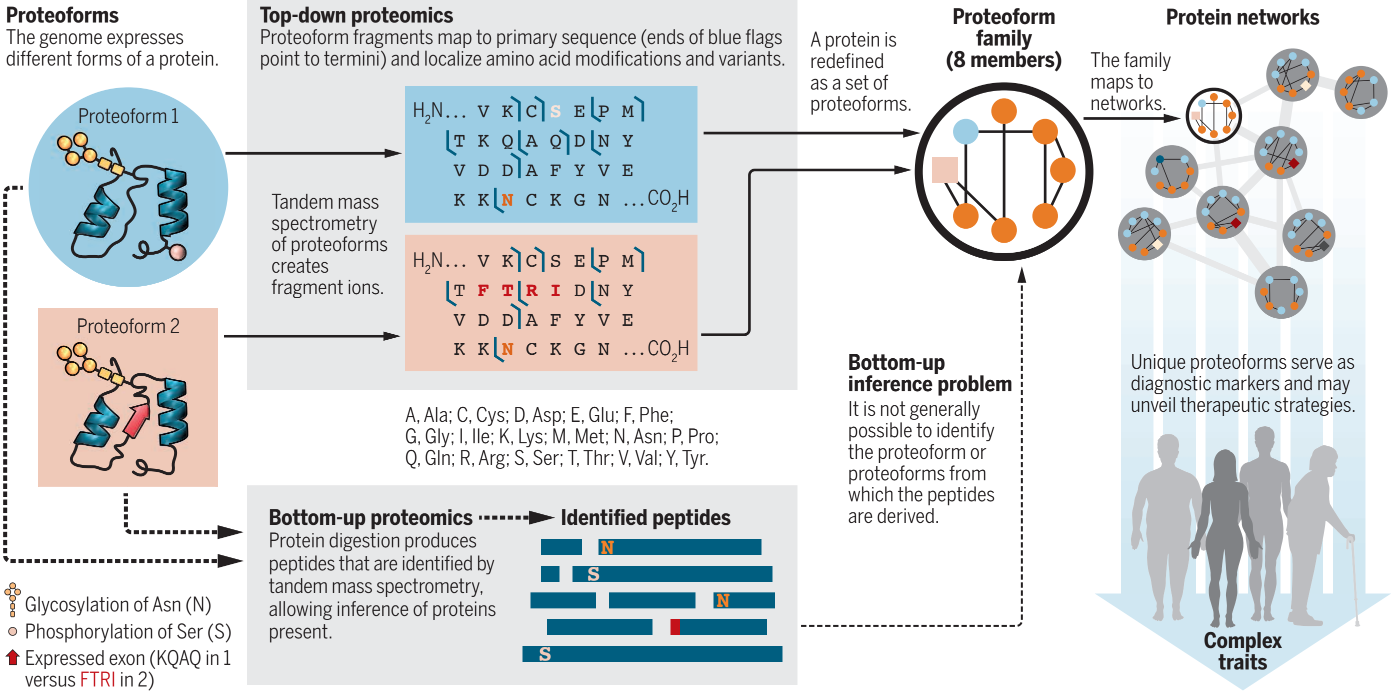

GRAPHIC: ADAPTED BY A. KITTERMAN/*SCIENCE* FROM M. MULLOWNEY AND S. PATRIE/NORTHWESTERN UNIVERSITY

Agrawal's structural engineering expertise is on display in her work on the iconic spire of The Shard.

ENGINEERING

Behind the scenes of the built environment

An approachable introduction to structural engineering entertains and inspires

By **Donna Riley**

Roma Agrawal's *Built* is a full-throated celebration of structural engineering, interspersed with clearly explained, hand-illustrated lessons on engineering fundamentals, including statics, fluids, and strength of materials. She is passionate about her profession, and with carefully curated and beautifully narrated historical and contemporary examples, she reveals the nuts and bolts of engineering ingenuity.

Seamlessly weaving together the technical and the social, Agrawal quietly illustrates the value of engineering skills related to cultural context, aesthetics, user experience, communication, teaming, sustainability, safety, leadership, and ethics. In doing so, she makes it clear that this is just what engineers do, part and parcel of professional practice.

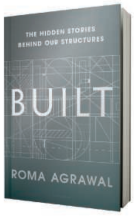

Built
The Hidden Stories Behind Our Structures
Roma Agrawal
Bloomsbury, 2018.
308 pp.

Agrawal uses her deep global knowledge of engineering contributions to create a geographically inclusive celebration of engineering feats. The book balances innovative new builds like The Shard in London with challenging restorative projects in urban underground infrastructure and tried-and-true designs such as the Middle Eastern water transport system known as the qanat. There is something here for seasoned engineers and novices alike; classic narratives of the Brooklyn Bridge and the Hancock Tower are interspersed with more obscure examples, including a lovely description of spider silk as bridge material.

The book is organized into chapters with one-word titles such as "Force," "Clay," and "Fire"; each is a stand-alone piece that can engage a busy professional or accompany engineering course material without overburdening students. In-text citations would have been preferable to a source list in order to readily locate further reading or to trace back historical accounts constructed from primary sources.

In her touching tribute to Emily Roebling, who oversaw the completion of the Brooklyn Bridge in the late 19th century, one feels deeply the importance of this role model. In the field of structural engineering, women remain grossly underrepresented. "That she, as a woman, could traverse every social circle, and was welcomed by politicians, engineers and workers, her opinions heeded and instructions followed, was in itself proof of her exceptional skills, in an age when a woman's presence on a construction site was unheard of," writes Agrawal.

With the force of her connection to Roebling, one wonders why Agrawal did not hold up a few more examples of women's contributions to structural engineering. Women are not so rare in the field: Elmina Wilson and the Met Life Tower, Aine Brazil and the Hudson Yards development, Julia Morgan and Hearst Castle, and Hi Sun Choi and We've the Zenith in South Korea, to name a few.

Agrawal makes passing reference to workplace gender discrimination: "It's hard to keep a straight face and conduct professional conversations about finite element modelling or soil strength profiles when I'm in a site office surrounded by pictures of naked women." Stark in their normalcy and minimized as anomalies, her vignettes nonetheless may elicit a #metoo from many readers, as they serve to remind us how far we have yet to go.

Agrawal is almost absolute in her technological optimism: "The possibilities are limited only by our imaginations—for whatever we can dream up, engineers can make real." She lauds Singapore's desalination effort as evidence that "engineering can solve critical, real-world problems," recognizing that "engineers and scientists across the planet will have to confront the escalating challenges of locating this precious liquid, creating new pathways to channel it, and enhancing the science to purify it."

As Cape Town counts down to Day Zero in April, when running water will cease for some 4 million people, engineers and governments need to do a much better job understanding access to clean water as a sociotechnical system. Whiz-bang technical feats alone cannot solve our water crises. This points to perhaps the biggest shortcoming of the book: a missing discussion of how public policy interfaces with large engineering projects and the processes by which such projects are planned, funded, administered, and maintained.

In all, *Built* is a welcome addition to the library of accessible reads on engineering. It is globally inclusive, provides personal insight into the life and achievements of a broadly accomplished female structural engineer, and teaches key engineering concepts in an approachable and engaging way. It does all this while making visible and palpable the passion and care engineers bring in shaping our built environment. ■

10.1126/science.aas8717

The reviewer is the Kamyar Haghighi Head of the School of Engineering Education, Purdue University, West Lafayette, IN 47907, USA. Email: riley@purdue.edu

PHOTO: ISTOCKPHOTO.COM/MBBIRDY

HISTORY OF SCIENCE

Who holds the power?

A careful history examines pivotal moments and the networks that made them possible

The Square and the Tower
Networks and Power, from the Freemasons to Facebook
Niall Ferguson
Penguin Press, 2018.
607 pp.

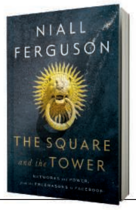

By **Sean P. Cornelius**

What was the cause of Donald Trump's stunning victory over Hillary Clinton in the 2016 U.S. presidential election? Was it the peculiarities of the electoral college? Voter resistance to three-term rule by a single party? Anxiety about illegal immigration?

As Niall Ferguson explains in *The Square and the Tower*, the answer lies largely in one word: networks. Specifically, without the cyber infrastructure that facilitated Russian interference, the "alt-right" networks that churned out memes and "fake news," and the social media that gave them wing, history may have turned out very differently.

Ferguson, a historian who has held posts at Harvard and Stanford, argues that historiography has traditionally been a top-heavy enterprise that focuses on hierarchies—the states, armies, and corporations that stand astride the world like colossi—while minimizing less overt or well-documented power structures like the Freemasons and the salons of the Enlightenment. *The Square and the Tower* is Ferguson's attempt to right this imbalance, taking a fresh look at some of history's most pivotal moments through the lens of networks.


A crowd celebrates the release of Bekele Gerba on 14 February 2018.

PHOTO: TIKSA NEGERI/REUTERS/NEWSCOM

The book's enigmatic title evokes the heart of the archetypical medieval town—the high tower of the state looming over the noisy public square below. It's an apt metaphor for Ferguson's central point: Networks have always been with us, and their interaction with hierarchies has catalyzed some of the most momentous events in history.

Effective networks can topple hierarchies, as shown in Luther's Reformation against the Catholic church. But under the right circumstances, the tower can cast its shadow over the square anew. Look no further than the age of empire and colonialism that lasted from Napoleon's defeat to the First World War.

The study of networks can be traced to the work of 18th-century mathematician Leonhard Euler. It was Euler who used the mathematical language of graphs to solve a puzzle that vexed the citizens of Königsberg: whether it was possible to walk through the town crossing each of its seven bridges exactly once. (No.)

In the intervening centuries, the work of many scholars augmented our understanding of the interconnected world, notably the social scientists Stanley Milgram and Mark Granovetter and the renowned mathematician Paul Erdős. Yet it was only in the late 1990s that network science emerged as a formal, interdisciplinary field in its own right.

The Square and the Tower sets the stage by summarizing some of the most important discoveries of network science in the past two decades. You may already be familiar with the idea that you are, at most, six friendships away from any other person on the planet, as immortalized in the game Six Degrees of Kevin Bacon. Did you also know that your next job opportunity will likely come from a cocktail party acquaintance instead of a close friend (the "strength of weak ties")? These are network leitmotifs with profound historical consequences, explaining among other things Paul Revere's singular success in rallying revolution and the intercontinental reach of the Black Death.

Ferguson weaves his narrative largely in microcosm. This is an effective narrative tool, but also one mandated by his thesis; if history is indeed a tale of networks, then it cannot be fully understood through a blinkered preoccupation with princes, presidents, and prime ministers. In this fashion, we learn about Stalin's ruthless subjugation of social networks from the vantage point of the ill-fated poet Anna Akhmatova.

Among this cast, we also find familiar faces from Ferguson's other books, including Henry Kissinger and the dynastic Rothschilds. Although hardly obscure, and indeed near the apex of power, these actors arrived and thrived at these lofty heights by virtue of their favorable positions in the relevant social, political, and economic networks.

At times, the book strains to unite too much under its thesis, abetted by the fact that if you squint hard enough, almost anything can be a hierarchy (or network). For example, should hierarchy and its putative apotheosis—the modern "administrative state" (Ferguson's pejorative)—really be scapegoated for its failure to anticipate the global financial crisis? One could equally well place the blame on networks and their Achilles' Heel—vulnerability to cascading failure. This quibble aside, Ferguson's overall thesis is too compelling to dismiss.

The Square and the Tower offers an enthralling "reboot" of history from a novel perspective, spanning antiquity to the present day. Ferguson, at once insightful and droll, builds his case meticulously. And, like the best historians, he always pauses to learn from the past and anticipate the future. If only for this reason, the book is well worth a read.

After all, we live in a time when networks appear ascendant. Smartphone usage has penetrated deep into the developing world, Twitter has galvanized revolutions in Tunisia and Egypt, and cryptocurrency has (at times) rivaled Fortune 500 companies in market capitalization. Surely this all signifies the dawn of a new era, the inexorable, final triumph of networks over the ossified hierarchies of the past? If history is any guide, don't count on it. ■

The reviewer is at the Network Science Institute, Northeastern University, Boston, MA 02115, USA. Email: s.cornelius@neu.edu

10.1126/science.aar8692

Snow leopards have been downgraded from endangered to vulnerable, but some data suggest that the change was premature.

Edited by **Jennifer Sills**

The snow leopard's questionable comeback

Elusive snow leopards were recently pronounced abundant enough to be removed from the IUCN's endangered species list, after 45 years, and categorized as vulnerable (*1*). Amid gloomy reports of habitat loss and poaching [over 450 cats killed annually since 2008 (*2*)], the news should be welcome. Instead, it split scientists, and all 12 range-country governments rejected the decision (*3*).

New estimates placed snow leopards at 4678 to 8745 in 44% of their range (*4*), implying a much higher figure than previous estimates. However, the new, higher figures come from small study areas, located in the best habitats, and those unrepresentative numbers have been extrapolated to a vast range half the size of Europe (*5*). For 63 of 69 study samples, opinions and sign surveys yielded new numbers, whereas studies using scientifically valid techniques such as camera traps and genetics barely covered 2% of the range (*5*). When the new estimate received scrutiny, another estimate (7463 to 7980 range-wide), based on similarly questionable methods, was submitted in justification of downlisting (*1*).

IUCN assessments use estimates of mature individuals: If there are fewer than 2500, the species is considered "endangered"; if there are more than 2500, the species is deemed "vulnerable." This figure depends on population size and the age at which animals first reproduce. Larger population and lower reproductive age yield higher numbers. Radio telemetry studies in the wild showed no leopard reproduction at age 2 (*6*), and snow leopards in zoos reproduce just under 5 years old (*7*). Records show just 3 of 344 captive leopards bred at 2 years old (*8*). Yet, the IUCN assessment (*1*) used ages 2 to 3 as the age of maturity, and presumed that 25% of 2-year-olds would breed. This classification inflated the number of "mature" individuals above the 2500 threshold (*1*).

Recent surveys also contradict the IUCN's findings. Bhutan camera-trap studies revealed fewer leopards (96) nationwide than earlier estimates (100 to 200) (*9*). Surveys from Pakistan were even more dire: Only 23 leopards were found in the country's best habitats, compared to 300 to 420 a decade ago (*10*). Snow leopards might have decreased rather than increased.

Downlisting affects protection. Snow leopard assessment deserves a precautionary approach. Desk-based announcements and celebrations of reduced extinction risks (*11*) should be rejected in favor of rigorous field-based scientific evidence.

S. B. Ale[1]* and C. Mishra[2]
[1]Department of Biological Sciences, University of Illinois at Chicago, Chicago, IL 60607, USA. [2]Snow Leopard Trust and Nature Conservation Foundation, Mysore, 570002, India.
*Corresponding author. Email: sale1@uic.edu

REFERENCES

1. T. McCarthy, D. Mallon, R. Jackson, P. Zahler, K. McCarthy, "*Panthera uncia*" (The IUCN Red List of Threatened Species, 2017).
2. K. Nowell, J. Li, M. Paltsyn, R. K. Sharma, "An Ounce of Prevention: Snow Leopard Crime Revisited" (TRAFFIC, UK, 2016).
3. Global Snow Leopard & Ecosystem Protection Program, "Statement of Concern Regarding the Status of the Snow Leopard on the IUCN Red List" (Bishkek, Kyrgyz Republic, 2017)
4. T. McCarthy, D. Mallon, E. W. Sanderson, P. Zahler, K. Fisher, *Snow Leopards* (Elsevier, New York, 2016), pp. 23–42.
5. Snow Leopard Network, "Snow Leopard Survival Strategy: Revised 2014 Version" (Snow Leopard Network, Seattle, WA, 2014).
6. Ö. Johansson, J. Malmsten, C. Mishra, P. Lkhagvajav, T. McCarthy, *J. Wildl. Dis*. **49**, 338 (2013).
7. C. Lynch, J. Tetzloff, L. Tupa, "Snow Leopard (*Uncia uncia*) AZA Species Survival Plan® Yellow Program: Population Analysis and Breeding & Transfer Plan" (AZA Population Management Center, Chicago, 2015).
8. L. Blomqvist, *International Pedigree Book for Snow leopards, Vol 9* (Helsinki Zoo, 2008).
9. DoFPS, "National Snow Leopard Survey of Bhutan 2014 – 2016 (Phase II): Camera Trap Survey for Population Estimation" (Department of Forests and Park Services, Ministry of Agriculture and Forests, Thimphu, Bhutan, 2016).
10. M. N. Ali, S. Hameed, "Research Update 2008-2014 Snow leopard program: Report prepared for Snow Leopard Red List Assessment Team" (Pakistan, 2015).
11. D. P. Mallon, R. M. Jackson, *Oryx* **51**, 605 (2017).

10.1126/science.aas9893

PHOTO: OSAMA MUHAMMAD

Nigeria's new GDP means scientists suffer

In 2014, Nigeria's government rebased Nigeria's gross domestic product (GDP), adjusting the number from US$270 billion to US$510 billion to account for emerging industries such as telecommunication and entertainment that were not captured in previous calculations (*1*). The new GDP propels Nigeria over South Africa as Africa's biggest economy (*1*) and makes the country the 26th biggest economy in the world (*1*). In response to the adjusted GDP, the World Bank recategorized Nigeria as a lower middle-income country (*2*), even though 62% of the population live in poverty (*3*). Changing the GDP to a more accurate number is a step in the right direction and seemed like an avenue for new opportunities for politicians and economists. However, the decision has unintended consequences, especially for Nigerian scientists.

Because of Nigeria's reclassification as a middle-income country, Nigerian scientists will no longer benefit from a variety of aid previously available to them. Nigeria has been removed from the list of countries eligible for fee waivers from publishing houses such as Hindawi and BioMed Central (*4*), which will affect the output of scientific papers. Young Nigerian scientists who look to international not-for-profit organizations for grants and fellowships will find that Nigeria's new status means that they are no longer eligible for such awards from organizations such as Organization for Women in Science for the Developing World (OWSD) and The World Academy of Science (TWAS) (*5*).

The Nigerian government must provide funding for its scientists to make up for the benefits they are losing and support them going forward. The government should also engage scientists and other stakeholders in the decision-making process before enacting new policies. By providing Nigerians the opportunity to convey concerns and propose solutions, the government can address the full cost of policy decisions and mitigate unintended consequences.

Wasiu Gbolahan Balogun* and Azman Seeni
Advanced Medical and Dental Institute, Universiti Sains Malaysia, 13200, Bertam, Penang, Malaysia.
*Corresponding author.
Email: wbalogun3@gmail.com

REFERENCES

1. O. N. Awojobi, J. Ayakpat, O. D. Adisa, *Int. J. Educ. Res.* **2**, 301 (2014).
2. World Bank, "Lower middle income" (https://data.worldbank.org/income-level/lower-middle-income).
3. N. Keteku, "Nigeria: How will the economic downturn affect outbound student mobility?" *World Education News and Reviews* (2017); http://wenr.wes.org/2017/03/nigeria-why-the-recent-recession-hasnt-dampened-outbound-student-mobility.
4. Hindawi, "Waiver Policy" (2017); www.hindawi.com/waiver/.
5. E. W. Lempinen, "A new list of TWAS target countries" (2017); https://twas.org/article/new-list-twas-target-countries.

10.1126/science.aar8549

Possible brooding of pterosaur parents

In his Perspective "How pterosaurs bred" (1 December 2017, p. 1124), D. C. Deeming discussed the remarkable fossils of eggs and developing embryos of the pterosaur reptile *Hamipterus tianshanensis*, discovered by X. Wang *et al.* ("Egg accumulation with 3D embryos provides insight into the life history of a pterosaur," Report, 1 December 2017, p. 1197). Deeming asserts that the thin and flexible-shelled ("parchment-shelled") ectohydric eggs of lizards (and presumably other reptiles with similar eggshell morphologies) must be buried and covered in a moist substrate to prevent desiccation and embryonic death. Moreover, he suggests that all such developing embryos must rely on ambient environmental sources, presumably the nest material, for heat. He concludes that these constraints preclude contact of the clutch with incubating pterosaur parents because their eggs share this flexible-shelled morphology.

Nesting behaviors of pterosaur parents may have included brooding their eggs.

These assertions ignore evidence of brooding reptilian parents in a wide variety of extant lineages of lizards and snakes in which mothers coil around or completely cover their ectohydric eggs, using their own bodies as nests or partial nests (*1*, *2*). Some relevant examples include various species of pythonid snakes—obligate brooders that coil around their unburied developing eggs, providing either maternal thermogenic heat, protection from ambient hydric extremes, or a combination of both brooding functions (*2*–*5*).

Although the discoveries of Wang *et al.* and others (*6*) provide some suggestive evidence of posthatching care of neonatal pterosaurs, the conditions of these fossilized nests do not allow determination of the presence of brooding parents covering or partially covering their eggs. If pterosaur parents had the ability to use a body posture or nest construction that prevented them from crushing their eggs with their own weight, they conceivably could have adjusted brooding postures to regulate the amount of water lost or gained by the embryo. More speculatively, if brooding pterosaurs were endothermic (warm-blooded), a physiology supported by equivocal fossil evidence (*7*), they could have regulated the incubation temperatures of their developing embryos, further controlling growth, mortality, and perhaps hatchling sex ratios. A more accurate understanding of the nesting behaviors of pterosaurs awaits further discoveries of more complete fossil nests under conditions that allow more detailed interpretation of the positions of eggs and attending parents. Current fossil evidence based on eggshell morphology does not exclude the possibility that pterosaur parents brooded their eggs.

Louis A. Somma
Division of Herpetology, Florida Museum of Natural History, University of Florida, Gainesville, FL 32611, USA. Email: somma@ufl.edu

REFERENCES

1. R. Shine, in *Biology of the Reptilia. Vol. 16: Ecology B: Defense and Life History*, C. Gans, R. B. Huey, Eds. (Alan R. Liss, 1988 [1987]), pp. 275–329.
2. L. A. Somma, *Parental Behavior in Lepidosaurian and Testudinian Reptiles: A Literature Survey* (Krieger Publishing Co., 2003).
3. O. Lourdais, T. C. M. Hoffman, D. F. DeNardo, *J. Comp. Physiol. B* **177**, 569 (2007).
4. Z. R. Stahlschmidt, D. F. DeNardo, *J. Exp. Biol.* **213**, 1691 (2010).
5. Z. R. Stahlschmidt, D. F. DeNardo, in *Reproductive Biology and Phylogeny. Vol. 9: Reproductive Biology and Phylogeny of Snakes*, R. D. Aldridge, D. M. Sever, Eds. (Science Publishers, Inc., 2011), pp. 673–702.
6. L. M. Chiappe, L. Codorniú, G. Grellet-Tinner, D. Rivarola, *Nature* **432**, 571 (2004).
7. A. Clarke, H.-O. Pörtner, *Biol. Rev.* **85**, 703 (2010).

10.1126/science.aas9153

ILLUSTRATION: CHUANG ZHOU

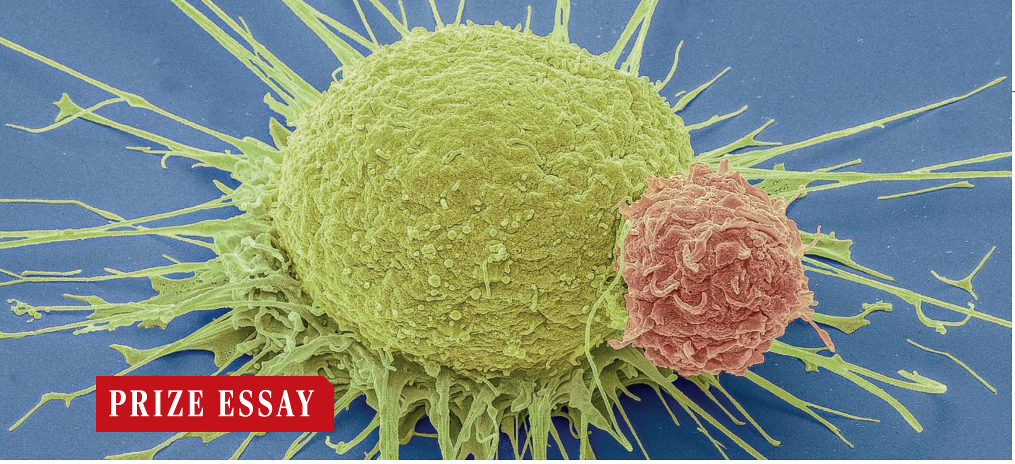

T lymphocyte cells (pink) attach to a prostate cancer cell in this electron micrograph.

PRIZE ESSAY

REGENERATIVE MEDICINE

Refining cell therapy

Synthetic Notch receptors expand the therapeutic potential of engineered T cells

By **Kole T. Roybal**

We are in the midst of a major shift in how we think about treating disease and the regeneration of damaged tissues. Although small-molecule and protein therapeutics are the dominant forms of treatment today, we are now at the point where we can engineer our own body's cells to detect and treat disease. Using the cutting-edge tools of synthetic biology, we may one day be able to build smart therapeutic cells that reside in the body for life, poised to respond to diseases that would otherwise thwart our natural immune system.

My colleagues and I envision cell therapies that act as microscopic "physicians," capable of detecting, diagnosing, and directly eradicating disease via a multifaceted mechanism that is difficult to resist and circumvent. This therapeutic vision contrasts with more traditional drug therapies, which often require chronic administration and generally target individual disease mechanisms that are easily bypassed, resulting in disease recurrence.

T CELL THERAPY: CURRENT CHALLENGES

The promise of engineered cell therapy is beginning to be realized with the remarkable success of T cell therapies for cancer. T cells engineered to express chimeric antigen receptors (CARs)—synthetic receptors consisting of a tumor-specific extracellular antibody fragment fused to the signaling chain from the native T cell receptor—can target and eliminate difficult-to-treat B cell malignancies that have few therapeutic alternatives.

While exciting, these therapies suffer from some challenges. The inability to control CAR T cells, off-target tissue damage, and uecked inflammation has led to severe adverse effects in some patients. Treatment of solid tumors with T cell therapies has been largely ineffective due to problems with infiltration and immunosuppressive tumor microenvironments. With these common pitfalls of T cell therapies in mind, I sought to develop a new class of synthetic receptors that would allow cells to initiate more customized, controlled, and localized therapeutic activity.

Although CARs can retarget T cells to tumors, in doing so, they elicit the full T cell response that includes elements that are both therapeutic and toxic. To develop a new class of receptors for more precise control over cellular behavior, I teamed up with a fellow postdoctoral researcher, Leonardo Morsut, and looked to the Notch receptor, a classic receptor involved in development and a myriad of other biological processes.

The Sartorius & *Science*
Prize for Regenerative
Medicine & Cell Therapy

CREATING SYNTHETIC NOTCH RECEPTORS

The Notch receptor is mechanistically direct, in that ligand binding leads to proteolytic cleavage of the cytoplasmic domain, which is then transported into the nucleus, where it acts as a transcriptional regulator. Notch receptors do not initiate the activation of complex kinase cascades like most other receptor families. Thus, we reasoned that Notch could be a perfect platform on which to build custom environmental sensors that detect disease- or tissue-specific cues and initiate a more streamlined custom therapy.

By engineering chimeric versions of the Notch receptor, we found that both the extracellular ligand-binding domain and the intracellular domain of Notch can be readily exchanged, such that synthetic versions of the receptor can be built with a user-defined ligand-binding module (e.g., a single-chain variable fragment or nanobody to a tissue- or disease-related antigen) and an orthogonal intracellular transcriptional regulator (to control a custom genetic program) (*1*).

Synthetic Notch (synNotch) receptors have proven to be a versatile platform for cellular environmental sensing coupled to precise gene regulation. The cellular machinery required for Notch activation is ubiquitously expressed, meaning that we can engineer a spectrum of cell types with therapeutic synNotch receptor circuits. For example, a stem cell could be engineered with a synNotch receptor circuit that senses damaged tissue and coordinates tissue repair by locally secreting growth factors.

A LA CARTE CELL THERAPY

Many of the therapeutics that aid in cancer clearance are genetically encodable (e.g., cytokines, antibodies, and toxins) and could benefit from more targeted delivery because they are ineffective or toxic when administered systemically. We have established that synNotch receptor circuits in T cells can drive a la carte secretion of cytokines, biased T cell differentiation, and local delivery of non-native therapeutic payloads, such as antibodies, in response to tumor antigens (*2*).

SynNotch receptors are also able to improve the specificity of engineered T cells for tumors when they are combined with CARs (*3*). T cells engineered with synNotch receptors and CARs require a combination of antigens to activate instead of a single tumor antigen. These dual-antigen-targeted synNotch/CAR T cells initially only express the synNotch receptor targeted to a primary tumor antigen. Upon recognition of that antigen, the receptor drives the expression of a CAR to a second tumor antigen. The control of CAR expression by a tumor-targeted synNotch receptor effectively confines T cell activity to the tumor.

Given that single, highly specific tumor antigens are rare, combinatorial antigen sensing by cells is a powerful approach to enhance the discrimination of tumors from off-target tissue. We have recently identified clinically relevant combinatorial tumor antigen signatures and have built synNotch/CAR

Department of Microbiology and Immunology, University of California, San Francisco, San Francisco, CA 94143, USA. Email: kole.roybal@ucsf.edu

PHOTO: STEVE GSCHMEISSNER/SCIENCE SOURCE

GRAND PRIZE WINNER

Kole Roybal

Kole Roybal is an assistant professor in the Department of Microbiology and Immunology at the University of California, San Francisco, a member of the Parker Institute for Cancer Immunotherapy, and a Chan Zuckerberg Biohub Investigator. His laboratory harnesses the tools of synthetic and chemical biology to engineer the immune cell therapies for cancer and autoimmunity of the future. He received his doctorate from the University of Texas Southwestern Medical Center at Dallas. There he studied the fundamental cellular and biochemical mechanisms required for immune cell activation and clearance of infections. While a Jane Coffin Childs Postdoctoral Fellow in Wendell Lim's laboratory at UCSF, he developed a new class of synthetic receptors, which provide unprecedented customization of therapeutic cells for treatment of a broad range of diseases. **www.sciencemag.org/content/359/6380/1112**

FINALIST

Shruti Naik

Shruti Naik received her B.S. in cell and molecular biology from the University of Maryland and her Ph.D. in immunology from the University of Pennsylvania–National Institutes of Health Graduate Partnership Program. During her graduate training, she discovered that normal bacteria living on our skin educate the immune system and help protect us from harmful pathogens, opening the door for microbiota-based therapies in the skin. She is currently at Rockefeller University, where she is studying the interactions between immune cells and stem cells in an effort to develop stem cell–based therapies for inflammatory disorders. She is also a strong advocate for women in science. **www.sciencemag.org/content/359/6380/1113.1**

FINALIST

Fotios Sampaziotis

Fotios Sampaziotis graduated from the University of Athens in Greece with a degree in medicine. He obtained a Ph.D. in stem cell biology from the University of Cambridge. During his doctoral research, he pioneered the use of bile duct organoids to model diseases of the biliary system, test multiple drugs, and identify new therapeutic agents. Currently, Fotios continues his research at the interface between basic science and clinical medicine as a clinical lecturer in hepatology at the University of Cambridge with clinical commitments in Addenbrooke's Hospital. His scientific work focuses on combining organoids, bioengineering, and animal studies to regenerate damaged bile ducts in the liver as an alternative therapy to liver transplantation. **www.sciencemag.org/content/359/6380/1113.2**

FINALIST

Will McLean

As an undergraduate, Will McLean studied biology at Tufts University before going on to attain a Ph.D. at the Massachusetts Institute of Technology within the Harvard-MIT Division of Health Sciences and Technology. While at MIT, his doctoral research elucidated the distinct progenitor cell types that exist within the inner ear and their capacity to form sensory cells and neural cell types. As a postdoctoral researcher at Harvard Medical School, he investigated manipulation of signaling pathways to enable otherwise senescent progenitor cells of the cochlea to divide and form new sensory cells. He is currently vice president of biology and regenerative medicine at Frequency Therapeutics. Frequency is currently using McLean's insights to develop a drug to treat hearing loss by regenerating lost sensory cells. **www.sciencemag.org/content/359/6380/1113.3**

PHOTOS: (TOP TO BOTTOM) SONYA YRUEL PHOTOGRAPHY © 2017; ROCKEFELLER UNIVERSITY; DEREK GEORGE; FREQUENCY THERAPEUTICS

circuits capable of recognizing them, with the hope of rapidly moving this new cell therapy to the clinic.

SynNotch receptors provide unprecedented control and customization of cell activity and have far-reaching implications for cancer, autoimmunity, and regenerative medicine. In the future, we hope to use synNotch T cells to remodel immunosuppressive tumor microenvironments and improve the efficacy of T cell therapies for solid tumors. We also hope to go beyond the treatment of cancer and develop synNotch engineered T cells that can detect and suppress autoinflammatory disease.

REFERENCES

1. L. Morsut *et al.*, *Cell* **164**, 780 (2016).
2. K. T. Roybal *et al.*, *Cell* **167**, 419 (2016).
3. K. T. Roybal *et al.*, *Cell* **164**, 770 (2016).

10.1126/science.aat0962

PRIZE ESSAY

FINALIST

Shruti Naik

Shruti Naik received her B.S. in cell and molecular biology from the University of Maryland and her Ph.D. in immunology from the University of Pennsylvania–National Institutes of Health Graduate Partnership Program. During her graduate training, she discovered that normal bacteria living on our skin educate the immune system and help protect us from harmful pathogens, opening the door for microbiota-based therapies in the skin. She is currently at Rockefeller University, where she is studying the interactions between immune cells and stem cells in an effort to develop stem cell–based therapies for inflammatory disorders. She is also a strong advocate for women in science. **www.sciencemag.org/content/359/6380/1113.1**

REGENERATIVE MEDICINE

The healing power of painful memories

Epidermal stem cells “remember” inflammation, accelerating subsequent wound repair

By **Shruti Naik**

Our body’s epithelia are barriers that interface with the terrestrial environment and routinely experience inflammation. Although a vast majority of these inflammatory reactions resolve, they imprint the tissue with a memory. Cells of the immune system are traditionally thought to be the bearers of this memory, allowing them to react faster to subsequent inflammatory pressures (*1*, *2*). Yet, barrier tissues are composites of epithelial, mesenchymal, nervous, vascular, and immunological networks working in unison to sustain optimal function in health and disease. The question of whether tissue-resident cells, distinct from the immune system, are entrained in response to a perturbation remains to be addressed.

TRACKING TISSUE STEM CELLS IN INFLAMMATION

Somatic stem cells are responsible for maintaining tissues throughout an organism’s lifetime (*3*). Thus, I teamed up with a group of tissue stem cell and chromatin biologists to understand the enduring consequences of inflammation on stem cells of the epidermis. Throughout the course of our research, we discovered that stem cells have a remarkable capacity to “remember” inflammation, which ultimately and consequently enhances their regenerative potential.

To induce an acute response, we employed a well-defined and self-resolving model of inflammation by applying a TLR7 agonist, imiquimod (IMQ), to mouse skin (*4*). Inducible-marker–based fate mapping (*5*) of skin epithelial stem cells and differentiated progeny revealed that basal skin epithelial stem cells (EpSCs) not only expanded during inflammation but also persisted for more than 180 days. At the peak of the response, EpSCs expressed all the hallmarks of IMQ inflammation, including hyperproliferation, activated STAT3, and increased cell death, but nevertheless returned to baseline upon resolution.

INFLAMMATION-EXPERIENCED SKIN HEALS FASTER

Tissue repair is a cardinal function of stem cells (*6*). Therefore, we sought to determine how a previous immune response would alter stem cells’ ability to cope with a secondary challenge and subjected post-inflamed skin to wounds.

The Sartorius & *Science* Prize for Regenerative Medicine & Cell Therapy

Remarkably, wounds in post-inflamed epidermis healed 2.5 times as fast as wounds in naïve controls (*7*). Accelerated wound repair was also observed 180 days after the initial challenge and in response to a variety of acute stimuli, including a primary wound, a fungal infection, a model of atopic dermatitis, and another model of hyperplasia, all of which underscore the generality of our findings and the long-lasting duration of the effect. Although EpSC proliferation was comparable between control and post-inflamed wounds, inflammation-experienced EpSCs exhibited a significant increase in their migratory capacity.

We next sought to determine the upstream regulators of the observed enhancement. To this end, we excluded a role for circulating factors in controlling wound repair post-inflammation, because wounds distal to the initial inflammatory site did not exhibit any boost in healing. Additionally, we established that enhanced wound repair after inflammation occurred independently of skin-resident macrophages and lingering Rorc^{+} immune cells. These results directed our focus to the possibility of a sustained change within the EpSC compartment that may occur as a result of inflammation.

CHROMATIN CHANGES ARE THE CRUX OF MEMORY

Sustained epigenetic changes in innate immune cells were recently shown to alter

---

Laboratory of Mammalian Cell Biology and Development, The Rockefeller University, New York, NY 10065, USA. Email: snaik@rockefeller.edu

PHOTO: ROCKEFELLER UNIVERSITY

their responsiveness to subsequent stimuli (*1*). To determine whether EpSCs similarly encoded a memory of previous inflammation, we evaluated alterations in chromatin accessibility of epidermal stem cells during and after inflammation.

Although the initial inflammatory response resulted in dramatic alterations to chromatin accessibility within EpSCs (>40,000 regions), a vast majority of inflammation-induced accessible regions reverted upon restoration of homeostasis (*7*). Remarkably, however, a small subset of open chromatin domains were retained (9561 peaks), ~2000 of which had been acquired during the primary response. Genes associated with these acquired peaks were enriched for apoptosis signaling, interleukin signaling, the oxidative stress response, Ras, and PI3 kinase pathways.

Intriguingly, transcription factor MOTIF analysis revealed that inflammation-instilled chromatin domains were enriched for EpSC homeostatic transcription factors such as p63, KLF5, and AP-1, as well as inflammatory transcription factors such as STAT1/3 and NF-κB. STAT3, a major mediator of IMQ response (*8*), was phosphorylated and activated specifically during both the primary (IMQ) and secondary (wounding) stimulus, but not in the interim (*7*).

Our data thus revealed a model in which memory chromatin domains serve as accessible platforms for accelerated reactivation after a secondary challenge. Indeed, using fluorescent reporters driven by memory chromatin domains, we found that these sustained open regions were functional in sensing inflammatory stress.

INFLAMMATION-TRAINED STEM CELLS EXPRESS TISSUE DAMAGE SENSORS

If these accessible chromatin elements were in fact conferring memory, we would expect that a secondary insult would result in augmented transcription of their associated genes. Strikingly, transcriptional profiles of inflammation-experienced EpSCs shortly after secondary wounding revealed that 140 genes were rapidly up-regulated. More than 50% of these genes were associated with sustained open chromatin domains post-inflammation (*7*).

Enriched among the transcriptional changes was the inflammasome signaling pathway, including the double-stranded DNA sensor, *Absence in Melanoma 2* (AIM2), which is known to detect tissue damage (*9*). Remarkably, *Aim2*-deficient stem cells lost the wound repair advantage endowed by inflammation, and elevating *Aim2* expression in EpSCs was sufficient to recapitulate the phenotype (*7*). Further probing revealed that a downstream effector of the AIM2 inflammasome, IL-1β, mediated this effect. In summary, inflammatory cues were able to tune EpSC function, enabling their adaptation to subsequent stressors.

MANIPULATING MEMORY

These findings reveal that inflammatory memory is not exclusive to the immune system but also exists in long-lived tissue stem cells. However, it remains to be determined whether memory occurs only in response to inflammation or whether a stem cell can remember all of its past stressors. Moreover, it is unclear whether these mechanisms of adaptation are always beneficial or if they may exert detrimental effects such as recurrent inflammatory disease, tumor formation, or premature aging.

Intriguingly, impaired wound responses in aging are associated with dysregulated skin immunity (*10*). Accumulating epigenetic alterations (*11*) resulting from recurrent stressors could contribute to the diminished regenerative capacity of aged stem cells. Thus, understanding how memory is established within an EpSC—whether it is passed on to differentiating progeny and whether it can be reversed—will be important for fine-tuning the remarkable ability of stem cells to regenerate tissues.

Our work indicates that inflammatory reprogramming can have a lasting impact on the tissue's healing capacity. Understanding the factors that rewire stem cells to remember inflammation may ultimately enable the development of therapies aimed at honing the stem cells' regenerative potential.

REFERENCES

1. M. G. Netea, J. Quintin, J. W. M. van der Meer, *Cell Host Microbe* **9**, 355 (2011).
2. S. N. Mueller, L. K. Mackay, *Nat. Rev. Immunol.* **16**, 79 (2016).
3. C. Blanpain, E. Fuchs, *Ann. Rev. Cell Dev. Biol.* **22**, 339 (2006).
4. L. van der Fits *et al.*, *J. Immunol.* **182**, 5836 (2009).
5. M. P. Alcolea, P. H. Jones, *Cold Spring Harbor Perspectives in Medicine* **4**, a015206 (2014).
6. C. Blanpain, E. Fuchs, *Science* **344**, 1242281 (2014).
7. S. Naik, et al. *Nature* **550**, 7677 (2017).
8. B. Flutter, F. O. Nestle, *Eur. J. Immunol.* **43**, 3138 (2013).
9. K. L. DeYoung *et al.*, *Oncogene* **15**, 453 (1997).
10. B. E. Keyes *et al.*, *Cell* **167**, 1323 (2016).
11. I. Beerman, D. J. Rossi, *Cell Stem Cell* **16,** 613 (2015).

10.1126/science.aat0963

PRIZE ESSAY

FINALIST

Fotios Sampaziotis

Fotios Sampaziotis graduated from the University of Athens in Greece with a degree in medicine. He obtained a Ph.D. in stem cell biology from the University of Cambridge. During his doctoral research, he pioneered the use of bile duct organoids to model diseases of the biliary system, test multiple drugs, and identify new therapeutic agents. Currently, Fotios continues his research at the interface between basic science and clinical medicine as a clinical lecturer in hepatology at the University of Cambridge with clinical commitments in Addenbrooke's Hospital. His scientific work focuses on combining organoids, bioengineering, and animal studies to regenerate damaged bile ducts in the liver as an alternative therapy to liver transplantation.

www.sciencemag.org/content/359/6380/1113.2

REGENERATIVE MEDICINE

Building better bile ducts

An organoid-based model promises to improve our understanding of bile duct disorders

By **Fotios Sampaziotis**

The bile ducts form a network of tubes within the liver and transfer bile produced in the liver to the bowel. In biliary disorders, this transport system fails, leading to the accumulation of toxic bile in the liver, damage, and permanent scarring (cirrhosis), which can ultimately be treated only through liver transplantation. Indeed, bile duct diseases (cholangiopathies) are the leading disorder treated (70%) by pediatric liver transplantation and account for a third of adult transplanted livers.

Despite the impact of these conditions, our insight into bile duct disease pathogenesis is very limited due to the lack of effective laboratory models and difficulties in growing bile duct cells (cholangiocytes) in vitro. Furthermore, treatment options remain limited, with few effective drugs and a lack of healthy cells and tissue suitable for surgical reconstruction or replacement of diseased segments of bile ducts. My research has focused on addressing these challenges.

More specifically, my aim has been to develop a system that will allow the growth of human cholangiocytes outside of the body; to use these cells to model cholangiopathies in vitro; and to use the in vitro models to screen, test, and identify new drugs for bile duct disorders. I have also sought to use healthy cells to generate a bioengineered bile duct and demonstrate its potential for surgical reconstruction or replacement of the biliary tree in an animal model.

CULTURING HUMAN CHOLANGIOCYTES

Two major limitations have hindered culture of human cholangiocytes: access to bile duct tissue without surgery and loss of function during primary cholangiocyte culture. To circumvent access issues, I developed a protocol for generating cholangiocytes from human induced pluripotent stem cells (hIPSCs), which can be easily derived from patient skin samples.

To preserve the function and characteristics of human cholangiocytes in vitro, I grew the cells as "organoids" in three-dimensional culture, demonstrating small cystic or tubular structures with a central lumen (*1*, *2*). The structure of the evolving organoid around a lumen resembled native bile ducts and was associated with both improved cholangiocyte function and faster growth of hIPSC-derived cholangiocytes. This approach also enabled the growth of human primary cholangiocytes isolated from excised bile ducts or gallbladders in abundance for the first time (*3*).

To confirm that the organoid platform provided a growth advantage, while retaining normal cholangiocyte function, I compared the physiological and functional characteristics of cholangiocytes derived from hIPSC or primary culture with human bile duct cells in vivo. These experiments allowed me to conclude that the organoid culture-generated cholangiocytes resembled their in vivo counterparts, providing the most accurate in vitro cholangiocyte platform to date.

The Sartorius & *Science* Prize for Regenerative Medicine & Cell Therapy

MODELING CHOLANGIOPATHIES IN VITRO

I then hypothesized that cholangiocytes from patients with bile duct disorders will reproduce key features of these disorders when cultured in vitro. I tested this hypothesis using cholangiocytes from patients with Alagille syndrome (AGS), polycystic liver disease (PLD), and cystic fibrosis (CF). In all cases, the disease phenotype was reproduced in the lab (AGS, a lack of lumen formation; PLD, cyst formation; CF, defective chloride transfer in the organoid lumen), providing the first in vitro bile duct models for these disorders (*1*).

DRUG SCREENING

I subsequently used my disease models to screen known (octreotide) and new therapeutic compounds and demonstrated that an experimental therapeutic compound (VX809) initially developed for CF lung disease could be repurposed for the prevention of CF liver disease (*1*). This finding is particularly important because VX809 is

---

Department of Medicine, University of Cambridge, Cambridge CB2 1TN, UK. Email: fs347@cam.ac.uk

PHOTO: DEREK GEORGE

already used in phase 2 clinical trials and could potentially be tested for the treatment of CF liver disease imminently. These results provide one of the first successful applications of in vitro drug screening for cholangiopathies.

GENERATING AND TRANSPLANTING BIOENGINEERED BILE DUCTS

In some cases, such as biliary atresia—which constitutes the leading cause for pediatric liver transplantation—the common outflow of the biliary tree (common bile duct) is obliterated, and the only possible treatment is surgery. In this context, the use of a bioengineered bile duct could provide an alternative to liver transplantation.

To achieve this goal, I developed a method for generating bioengineered biliary tissue and bioengineered bile ducts using healthy cholangiocytes (*3*). The bioengineered organ retained the architecture, structural properties, marker, and function (alkaline phosphatase and gamma glutamyl transferase activity) of a human bile duct.

The bioengineered ducts were transplanted into immunodeficient mice, successfully replacing the native bile duct. Furthermore, the mice receiving the artificial organ exhibited normal liver function and prolonged survival. To my knowledge, this is the first demonstration of organ engineering in the biliary system and the first report of the generation of a bioengineered organ using organoids.

CONCLUSION

My research has generated a series of tools with unique translational applications for the field of cholangiopathies. I have demonstrated that my cholangiocyte organoid system can be used to generate the first in vitro models for bile duct disorders. These models can increase our insight in disease pathogenesis and represent transferrable technology that can be used to benefit multiple groups working in the same field. Furthermore, this system can be used as the first drug screening platform for biliary disease, and I have demonstrated proof of principle for the potential of this system for drug discovery in a field where the only treatment option is liver transplantation.

Finally, through the generation of an engineered bile duct, I have provided proof of principle for regenerative medicine as a therapeutic approach for biliary disease and advanced the field of organ reconstruction by developing techniques that can be applied for the regeneration of a variety of different organs and tissues.

REFERENCES

1. F. Sampaziotis *et al.*, *Nat. Biotech* **33**, 845 (2015).
2. F. Sampaziotis *et al.*, *Nat. Protocols* **12**, 814 (2017).
3. F. Sampaziotis *et al.*, *Nat. Med.* **23**, **954** (2017).

10.1126/science.aat0964

PRIZE ESSAY

FINALIST

Will McLean

As an undergraduate, Will McLean studied biology at Tufts University before going on to attain a Ph.D. at the Massachusetts Institute of Technology within the Harvard-MIT Division of Health Sciences and Technology. While at MIT, his doctoral research elucidated the distinct progenitor cell types that exist within the inner ear and their capacity to form sensory cells and neural cell types. As a postdoctoral researcher at Harvard Medical School, he investigated maniuplation of signaling pathways to enable otherwise senescent progenitor cells of the cochlea to divide and form new sensory cells. He is currently vice president of biology and regenerative medicine at Frequency Therapeutics. Frequency is currently using McLean's insights to develop a drug to treat hearing loss by regenerating lost sensory cells. **www.sciencemag.org/content/359/6380/1113.3**

REGENERATIVE MEDICINE

Toward a true cure for hearing impairment

The regenerative power of progenitor cells holds promise for reversing hearing loss

By **Will McLean**

Five percent of the human population (360 million people) experience some form of hearing impairment. Patients with hearing loss often describe the experience as socially isolating, and recent research has shown a significant correlation with hearing loss and later onset of dementia.

Each of us is born with 15,000 sound-sensing cells per ear. Hearing loss occurs when these cells (called hair cells) die from noise exposure, certain medications, and other environmental factors. Unlike birds, fish, and amphibians, mammals lack the ability to regenerate these cells.

Currently, the only way to treat hearing loss is with palliative devices such as hearing aids. Although these technologies improve hearing performance for many patients, the benefit is limited because only the residual hair cells can be stimulated. Thus, a large unmet need exists for a therapeutic solution to restore hair cells.

Because other species regenerate hair cells, and other mammalian tissues regenerate, my colleagues and I reasoned that there must be a way to induce hair cell regeneration in mammals. We just needed to find the key to unlock this ability.

DEFINING THE LIMITATIONS OF INNER EAR PROGENITOR CELLS

The inner ear contains the hearing organ (cochlea) and balance organs (vestibular system), and both contain their own specialized hair cell types. Hearing and balance dysfunction can arise from hair cell loss or damage to the neurons that connect to these hair cells (or a combination of the two).

Although the hair cells of the inner ear cannot regenerate, it has been suggested that the inner ear contains stem cells that can form hair cells and neurons in cell culture (*1*). However, it was thought that this capability was all due to a single universal stem cell that was pluripotent. This was particularly surprising given the inner ear's limited ability to repair itself.

My research showed that instead of having a universal stem cell, the inner ear contains distinct populations of progenitor cells (*2*). One such population expresses the leucine-rich repeat–containing G protein–coupled receptor (Lgr5), a stem cell marker originally identified in the intestine (*3*). Later, it was found that Lgr5 cells also serve as hair cell precursors during cochlear development (*4*, *5*). We found that even after development, these cells could form new hair cells that had protein and gene expression profiles like native hair cells. When tested physiologically, these newly formed hair cells resembled those found in the mature organ.

The Sartorius & *Science* Prize for Regenerative Medicine & Cell Therapy

I also showed that the balance organs have progenitor cells that could form fully functioning hair cells. Interestingly, the cochlea and vestibular system could only form hair cells from their native organ, suggesting that these two populations of progenitor cells are distinct.

Whereas previous work showed that neurons could be obtained from inner ear stem cells (*1*), presumably from the universal stem cell, my research showed that neural cell types specifically arise from glial cells within the inner ear that express myelination proteolipid protein 1 (Plp1) (*2*).

In addition to identifying a new population of progenitors, we also showed that the Plp1 cells have greater plasticity than cochlear or vestibular progenitor cells because they could form cell types outside of their native environment. In fact, the Plp1 progenitors formed neurons and glial cells from both the peripheral and central nervous system.

Together, this work demonstrated that different progenitor types exist within the ear that have defined capacities to form

---

Cofounder and vice president, Biology and Regenerative Medicine, Frequency Therapeutics, Woburn, MA 01801, USA. Email: wmclean@frequencytx.com

PHOTO: FREQUENCY THERAPEUTICS

Published by AAAS

specific cell types. Thus, tailoring a treatment for hearing loss, balance ailments, or neural damage may require targeting mechanisms that are unique to each progenitor cell type.

UNLOCKING THE REGENERATIVE POTENTIAL OF PROGENITORS

Although it was shown that progenitor cells are present in the inner ear after organ development is complete, it was evident that such cells fail to divide and differentiate to repair the surrounding tissue. In addition to preventing hearing repair, this has also impeded drug discovery because it is difficult to obtain adequate numbers of primary cochlear cells for therapeutic screening.

To overcome this lack of regenerative behavior in the ear, studies of how intestinal Lgr5 cells regenerate served as inspiration (*6*). This particular stem cell is responsible for completely renewing your gut epithelium every 5 to 7 days. Using insights from pathways and signals that drive this process, a drug combination was identified that stimulates inner ear Lgr5 progenitor cells to divide by reprogramming them to a more plastic state (*7*). These drugs produced over 2000-fold more Lgr5 cells compared with methods used before, and the cells could be subsequently converted into nearly pure populations of hair cells. Further, these drugs proved to be effective with cells from adult mouse, nonhuman primate, and human. This breakthrough effectively relieved a bottleneck in the field and created the first large-scale drug-discovery platform for hearing loss.

From this initial discovery with single cells, it was further shown that treating damaged mouse cochleae with molecules that proliferate Lgr5 cells in cell culture could effectively induce progenitor cells to divide and regenerate lost hair cells in situ. This technology, referred to as Progenitor Cell Activation (PCA), was the catalyst for forming Frequency Therapeutics, a startup that I cofounded with Bob Langer and Jeff Karp, that seeks to treat hearing loss and other ailments by using drugs to activate the body's progenitor cells to initiate repair. To date, PCA has been successfully used to identify drug combinations that elicit similar effects in multiple tissues throughout the body.

TRANSLATING DISCOVERIES INTO POTENTIAL TREATMENTS

Since publishing proof-of-concept results to regenerate hair cells in damaged tissue (*7*), recent experiments have shown that local treatment to the ear can elicit a functional hearing improvement in animals with hearing loss. Based on these results, Frequency Therapeutics has expanded development for therapeutic application in humans and recently completed a first-in-human phase I safety study that met all end points. Therefore, this work could one day provide patients with a regenerative therapy to restore their hearing.

REFERENCES

1. K. Oshima *et al.*, *J. Assoc. Res. Otolaryngol.* **8**, 18 (2007).
2. W. J. McLean, D. T. McLean, R. A. Eatock, A. S. Edge, *Development* **143**, 4381 (2016).
3. N. Barker *et al.*, *Nature* **449**, 1003 (2007).
4. R. Chai *et al.*, *Proc. Natl. Acad. Sci. U.S.A.* **109**, 8167 (2012).
5. F. Shi, J. S. Kempfle, A. S. Edge, *J. Neurosci.* **32**, 9639 (2012).
6. X. Yin *et al.*, *Nat. Meth.* **11**, 106 (2014).
7. W. J. McLean *et al.*, *Cell Rep.* **18**, 1917 (2017).

10.1126/science.aat0966

RESEARCH

Systematic analysis of chemically induced proximity

Stanton et al., *p. 1117*

IN *SCIENCE* JOURNALS

Edited by **Stella Hurtley**

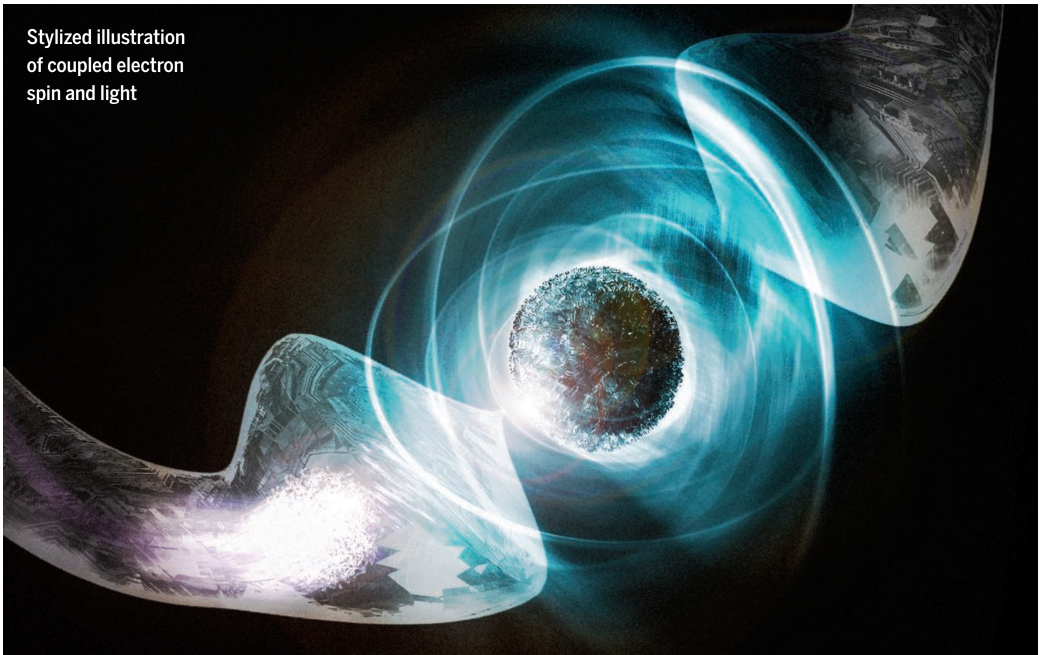

Stylized illustration of coupled electron spin and light

QUANTUM ELECTRONICS

Coupling light to single spins

To help develop quantum circuits, much effort has been directed toward achieving the strong-coupling regime by using gate-defined semiconductor quantum dots. Potentially, the magnetic dipole, or spin, of a single electron for use as a qubit has advantages over charge-photon coupling owing to its longer lifetime. Samkharadze *et al*. hybridized the electron spin with the electron charge in a double silicon quantum dot. This approach yielded strong coupling between the single electron spin and a single microwave photon, providing a route to scalable quantum circuits with spin qubits. —ISO

Science, this issue p. 1123

CLIMATE CHANGE

Starving ocean productivity

Projected increases in greenhouse gas emissions could suppress marine biological productivity for a thousand years or more. As the climate warms, westerly winds in the Southern Hemisphere will strengthen and shift poleward, surface waters will warm, and sea ice will disappear. Moore *et al.* suggest that one effect of these changes will be a dramatic decrease in marine biological productivity (see the Perspective by Laufkötter and Gruber). This decrease will result from a global-scale redistribution of nutrients, with a net transfer to the deep ocean. By 2300, this could drive declines in fisheries yields by more than 20% globally and by nearly 60% in the North Atlantic. —HJS

Science, this issue p. 1139; see also p. 1103

MICROBIOTA

Microbial modulation of diabetes

Short-chain fatty acids (SCFAs) are produced by various human gut microbes. SCFAs act as an energy source to the colonic epithelium and are also sensed by host signaling pathways that modulate appetite and inflammation. Deficiency of gut SCFAs is associated with type 2 diabetes. Zhao *et al*. found that adopting a high-fiber diet promoted the growth of SCFA-producing organisms in diabetic humans. The high-fiber diet induced changes in the entire gut microbe community and correlated with elevated levels of glucagon-like peptide-1, a decline in acetylated hemoglobin levels, and improved blood-glucose regulation. —CA

Science, this issue p. 1151

APPLIED ECOLOGY

Unscientific hunt management plans

Governments often claim, and society often believes, that science guides policy for natural resource management, including hunting policies across the United States and Canada. But no standard exists for what science-based management entails. Artelle *et al*. identified four fundamental hallmarks of science for natural resource management. Fewer than half were present in most hunt management plans surveyed across U.S. states and Canadian provinces and territories. Broader application of a science-based framework could improve policies and mitigate risks. —AC

Sci. Adv. 10.1126/sciadv.aao0167 (2018).

MOLECULAR BIOLOGY

Hemimethylation drives chromatin assembly

Cytosine DNA methylation is a heritable and essential epigenetic mark. During DNA replication, cytosines on mother strands remain methylated, but those on daughter strands are initially unmethylated. These

CREDITS: (TOP TO BOTTOM) B. Z. STANTON *ET AL.*; N. SAMKHARADZE *ET AL.*

hemimethylated sites are rapidly methylated to maintain faithful methylation patterns. Xu and Corces mapped genome-wide strand-specific DNA methylation sites on nascent chromatin, confirming such maintenance in the vast majority of the DNA methylome (see the Perspective by Sharif and Koseki). However, they also identified a small fraction of sites that were stably hemimethylated and showed their inheritance at CTCF (CCCTC-binding factor)/cohesin binding sites. These inherited hemimethylation sites were required for CTCF and cohesin to establish proper chromatin interactions. —SYM

Science, this issue p. 1166;
see also p. 1102

MALARIA

Malaria relief, one amino acid at a time

Malaria infection during pregnancy can disrupt placental vasculature and cause complications. Nitric oxide plays a key role in placental vascular function, and its synthesis requires L-arginine. L-arginine and nitric oxide are both depleted during malaria-induced hemolysis, and many people in malaria-endemic areas lack sufficient L-arginine in their diets. McDonald *et al.* examined the effects of dietary L-arginine supplementation. In a cohort of pregnant women in Malawi, the blood of patients with malaria had less L-arginine, and this was associated with worse pregnancy outcomes. Conversely, L-arginine supplementation in a mouse model of malaria in pregnancy improved fetal weight and viability. —YN

Sci. Transl. Med. **10**, eaan6007 (2018).

Malaria-infected pregnant women in Malawi lack L-arginine.

CREDITS: (LEFT TO RIGHT) PAUL JEFFREY/ALAMY STOCK PHOTO; Q. GUO *ET AL.*, *CELL* **172**, 696 (2018)

GEOCHEMISTRY

Encapsulating Earth's deep water filter

Small inclusions in diamonds brought up from the mantle provide valuable clues to the mineralogy and chemistry of parts of Earth that we cannot otherwise sample. Tschauner *et al*. found inclusions of the high-pressure form of water called ice-VII in diamonds sourced from between 410 and 660 km depth, the part of the mantle known as the transition zone. The transition zone is a region where the stable minerals have high water storage capacity. The inclusions suggest that local aqueous pockets form at the transition zone boundary owing to the release of chemically bound water as rock cycles in and out of this region. —BG

Science, this issue p. 1136

SOCIAL SCIENCE

Lies spread faster than the truth

There is worldwide concern over false news and the possibility that it can influence political, economic, and social well-being. To understand how false news spreads, Vosoughi *et al.* used a data set of rumor cascades on Twitter from 2006 to 2017. About 126,000 rumors were spread by ~3 million people. False news reached more people than the truth; the top 1% of false news cascades diffused to between 1000 and 100,000 people, whereas the truth rarely diffused to more than 1000 people. Falsehood also diffused faster than the truth. The degree of novelty and the emotional reactions of recipients may be responsible for the differences observed. —BJ

Science, this issue p. 1146

IN OTHER JOURNALS

Edited by **Sacha Vignieri**
and **Jesse Smith**

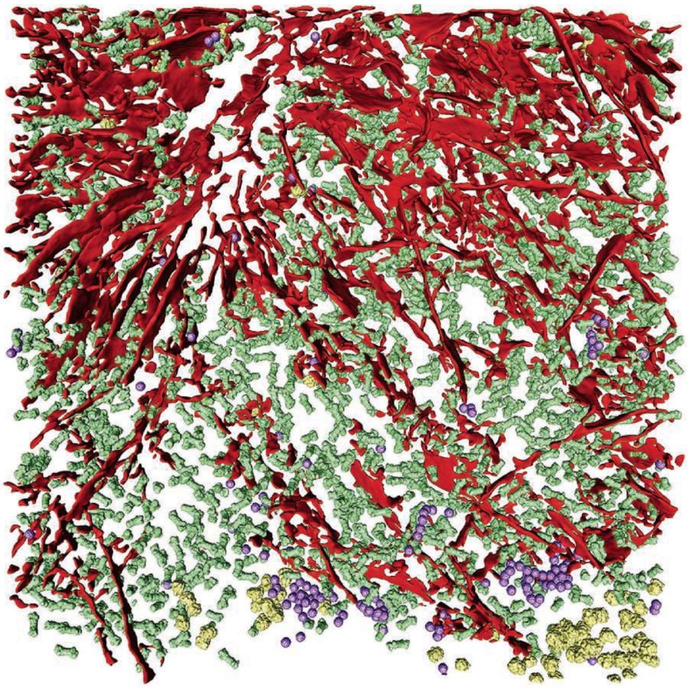

Poly-GA aggregate within a neuron

PROTEOSTASIS

Gumming up the works

Amyotrophic lateral sclerosis (ALS) is a neurodegenerative disorder that has been linked to toxic aggregates of poly-Gly-Ala (poly-GA) peptides generated by aberrant translation of an expanded nucleotide repeat sequence. Proteasomes are cytosolic molecular machines involved in the degradation of misfolded and aggregated proteins. Guo *et al.* used cryo–electron tomography to examine the molecular architecture of poly-GA aggregates in situ in intact neurons. The peptide aggregates formed twisted ribbons that clumped together and that were surrounded by proteasomes trapped in their normally transient substrate-processing conformation. The extent of proteasome accumulation was such that the ability of the remaining proteasomes within the neuron to perform their normal housekeeping functions was likely to be impaired, potentially explaining the neuronal pathologies observed in ALS. —SMH

Cell **172**, 696 (2018).

NEUROSCIENCE

Speed representation in the brain

Speed- and direction-responsive neurons in the medial entorhinal cortex and the hippocampus form a major component of the mammalian space representation system. There are long-range GABAergic projections between these two brain regions. Some of these inputs originate from parvalbumin-expressing inhibitory neurons. However, it has not been shown whether the parvalbumin cells projecting to the hippocampus are speed cells. Ye *et al*. used extracellular

ALSO IN *SCIENCE* JOURNALS

Edited by **Stella Hurtley**

CHEMICAL BIOLOGY

Regulating molecule proximity

The physical distance, or proximity, between molecules often directs biological events. The development of membrane-permeable small molecules that reversibly regulate proximity has enabled advances in fields such as synthetic biology, signal transduction, transcription, protein degradation, epigenetic memory, and chromatin dynamics. This "induced proximity" can also be applied to the development of new therapeutics. Stanton *et al*. review the wide range of advances and speculate on future applications of this fundamental approach. —BAP

Science, this issue p. 1117

STEM CELLS

Fibroblasts as lung stem cell niche

Each breath that we take provides oxygen to the bloodstream via tiny sacs in the lung called alveoli. AT1 cells line the alveoli and mediate gas exchange, whereas AT2 cells secrete lung surfactant. A subset of AT2s also serve as stem cells that slowly generate new alveolar cells throughout adult life. Nabhan *et al*. show that the rare AT2 stem cells have a special niche next to a fibroblast secreting Wnts. This Wnt activity is needed to select and maintain the stem cells. Injury expands the stem cell pool by transiently inducing autocrine Wnts in other surfactant-secreting alveolar cells. This simple but expandable niche sustains oxygen delivery, and it is co-opted in lung cancer. —BAP

Science, this issue p. 1118

NANOMATERIALS

Coherent strained superlattices

Two-dimensional superlattices represent the atomic-thickness limit of heterostructures that enable technologies such as strain-engineered multiferroics and quantum-cascade lasers. Xie *et al*. were able to produce monolayer superlattices of transition metal dichalcogenides (WS_2 and WSe_2) with full lattice coherence, despite a 4% lattice mismatch. They used a modulated metal-organic chemical vapor deposition process that precisely controlled each precursor. Furthermore, the authors could strain-engineer the optical properties of the superlattices to observe out-of-plane rippling. —PDS

Science, this issue p. 1131

WATER STRUCTURE

Unmasking supercooled water transitions

The unusual thermodynamic properties of water suggest that when supercooled, a second critical point should exist between two liquid phases that differ in density. Pure water crystallizes before such conditions can be reached. Woutersen *et al.* studied hydrazinium trifluoroacetate solutions that have similar hydrogen bonding to that of water. They observed a liquid-liquid transition near 190 K by using infrared spectroscopy and calorimetry. The liquid states were analogous to the predicted high- and low-density amorphous phases of water. —PDS

Science, this issue p. 1127

MICROBIOTA

Bacterial involvement in autoimmunity

The composition of the commensal microbiota is known to influence autoimmune disease development and persistence. Manfredo-Vieira *et al*. identified a gut microbe, *Enterococcus gallinarum*, that translocates from the gut into the organs of mice with a genetic predisposition to lupus-like autoimmunity (see the Perspective by Citi). Molecular signatures of gut barrier disintegration and pathogenic T helper cells were evident in the gut, liver, and lymphoid organs during colonization with the pathobiont. The ensuing pathology could be reversed by vancomycin treatment and by vaccination against *E. gallinarum*. The same bug was also found in liver biopsies of autoimmune patients, but not in healthy controls. —CA

Science, this issue p. 1156; see also p. 1097

NEUROSCIENCE

The mechanisms behind grid cell changes

When grid cells were first discovered in the brain, the grids were considered to have rigid coordinates beyond the borders of the testing environments. However, recent findings suggest that the grid cell pattern can be altered easily by changing the space of the enclosure. But how? Krupic *et al*. discovered that local changes in the geometry of the environment shifted individual neighboring grid fields, while more distant fields remained unchanged. Thus, changes to the grid structure are localized. Stable landmarks continue to exert an effect on most grid cells, whereas the ones close to changed borders are modified. —PRS

Science, this issue p. 1143

COLITIS

Overcoming a barrier to IBD

Inflammatory bowel disease (IBD) is a group of disorders linked to inflammation of the gastrointestinal tract. Colitis is a type of IBD that affects the inner lining of the colon and has been linked to a gene known as *C1orf106*. Mohanan *et al*. found that *C1orf106* encodes a protein that stabilizes the integrity of epithelial junctions and enhances barrier defense (see the Perspective by Citi). IBD-associated mutations in *C1orf106* lead to greater cytohesin-1 protein levels, changes in E-cadherin localization, and enhanced susceptibility to intestinal pathogens. Modulation of C1orf106 may thus hold promise for treating colitis and other IBDs. —PNK

Science, this issue p. 1161; see also p. 1097

HEART DEVELOPMENT

Committing the heart

The heart is a complex organ composed of multiple cell types such as cardiomyocytes and endothelial cells. Cardiovascular cells arise from *Mesp1*-expressing progenitor cells. Lescroart *et al*. performed single-cell RNA-sequencing analysis of mouse wild-type and *Mesp1*-deficient cardiovascular progenitor cells at early gastrulation (see the Perspective by Kelly and Sperling). When *Mesp1* was eliminated, embryonic cells remained pluripotent and could not differentiate into cardiovascular progenitors. During gastrulation, the different *Mesp1* progenitors rapidly became committed to a particular cell fate and heart region. *Notch1* expression marked the earliest step of cardiovascular lineage segregation. —BAP

Science, this issue p. 1177; see also p. 1098

PROTEIN FOLDING

Taking the heat together

Many of the processes in living cells are mediated by protein complexes that dynamically assemble and dissociate depending on cellular needs. Tan *et al*. developed a method called thermal proximity coaggregation (TPCA) to monitor the dynamics of native protein complexes inside cells (see the Perspective by Li *et al*.). The method is based on the idea that proteins within a complex will coaggregate upon heat denaturation. It uses a previously described cellular shift assay to determine melting curves for thousands of proteins and assigns a TPCA signature on the basis of similarity between the curves. The method was validated by detection of many known protein complexes. It identified cell-specific interactions in six cell lines, highlighting the potential for identifying protein complexes that are modulated by disease. —VV

Science, this issue p. 1170;
see also p. 1105

SKIN INFLAMMATION

Curbing ILC2 enthusiasm

Atopic dermatitis is an allergic disease driven by type 2 immune responses in the skin. Malhotra *et al*. studied mouse models of dermatitis. They identified the TNF (tumor necrosis factor) family cytokine TL1A (TNF ligand–related molecule 1) and its receptor DR3 (death receptor 3) as being critical in regulating cross-talk between skin-resident T regulatory cells (T_{regs}) and type 2 innate lymphoid cells (ILC2s) that drive skin inflammation. RORα (retinoid-related orphan receptor α) drove expression of DR3 in T_{regs}. Upon deletion of RORα, skin-resident T_{regs} were unable to sequester TL1A, which drives effector functions of ILC2s. Thus, targeting the TL1A-DR3 axis may provide a route to treating dermatitis and other skin allergies. —AB

Sci. Immunol. **3**, eaao6923 (2018).

RHEUMATOID ARTHRITIS

Kinase networks in inflammation

Although inflammation in rheumatoid arthritis is driven by the increased activity of p38, inhibitors of this kinase are ineffective in patients. Using synovial fibroblasts and fluid from rheumatoid arthritis patients, Jones *et al*. found that p38 mediated negative cross-talk to the related kinase JNK. Thus, inhibiting p38 facilitated JNK activity and the perpetuation of inflammatory cytokine production. Inhibitors of the upstream kinase TAK1 curbed the activity of both the p38 and JNK pathways in synovial fibroblasts cells. Such inhibitors might thus be effective in treating rheumatoid arthritis. —LKF

Sci. Signal. **11**, eaal1601 (2018).

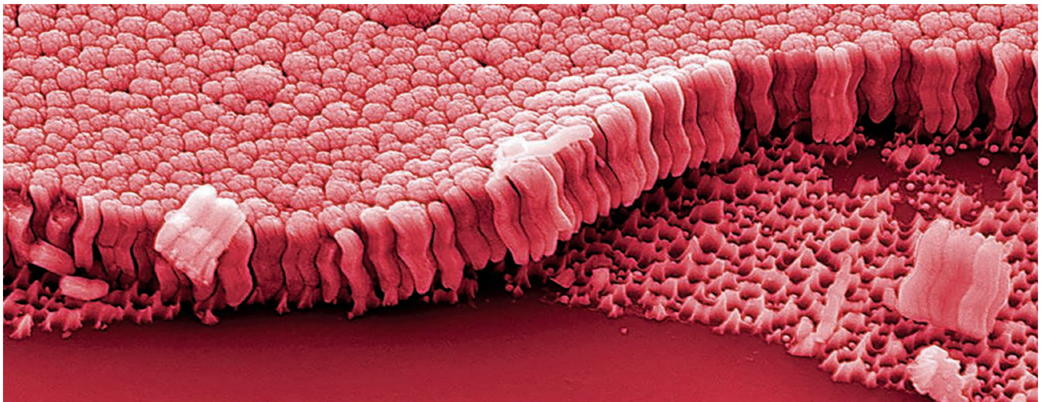

GLASS TRANSITION

A simple theory for simple glass

Glasses have many important industrial applications, yet understanding the changes that occur over the wide range of time and length scales of the glass transition remains a challenge. Hansen *et al.* performed simultaneous neutron scattering and dielectric spectroscopy measurements that allowed dynamic observations to be made over an impressive 14 orders of magnitude. Unexpectedly, for van der Waals fluids, they found identical dynamics across this massive time scale at different state points in the phase diagram. This finding dramatically simplifies the theory that describes these fluids, which include technologically important materials such as metallic glasses. —BG

Nat. Commun. 10.1038/s41467-017-02324-3 (2018).

A microscopic image of glass made from a metallic alloy

recording, optogenetic tagging, and immunohistochemistry to investigate whether, and how, speed-responsive cells in the entorhinal cortex and hippocampus are functionally connected. The majority of medial entorhinal speed cells were fast-spiking, the hippocampus received direct input from such cells, and GABAergic long-range projections to the hippocampus originated almost exclusively from parvalbumin-positive neurons. This indicates that hippocampus-projecting speed cells are part of this subpopulation. —PRS

Proc. Natl. Acad. Sci. U.S.A. 10.1073/pnas.1720855115 (2018).

SIGNAL TRANSDUCTION

Protein kinase signaling without phosphorylation

Protein kinases usually propagate signals by phosphorylating substrate molecules. Goncharov *et al.* find a different mechanism for the protein kinase RIP2 (receptor interacting protein 2) in inflammatory signaling. RIP2 acts in the innate immune system to signal the detection of bacterial infection. The authors found that inhibitors of RIP2's protein kinase activity prevented signaling not by reducing autophosphorylation (no other substrates for the kinase are known) but rather by inhibiting interaction of RIP2 with the ubiquitin ligase XIAP (x-linked inhibitor of apoptosis). Ubiquitination of RIP2 by XIAP was in turn required for proper signaling. This unusual mechanism, whereby dimerization of RIP2 appears to alter protein interactions rather than kinase activity to propagate a signal, could provide a therapeutic target for inflammatory diseases in which such signaling is inappropriately activated. —LBR

Mol. Cell 10.1016/j.molcel.2018.01.016 (2018).

BATTERIES

A solid electrolyte

In an electrochemical cell, the electrolyte has the role of separating and shuttling ions to produce a current. A good electrolyte thus should have high ionic conductivity and good thermal and electrochemical stability, although many in use do not have all these attributes. For example, solid electrolytes can show greater stability, but they are often poorer conductors. Joos *et al.* consider a deep eutectic solvent, in which the combination of two compounds radically lowers the melting temperature, immobilized within a silica matrix to form a gel. This material was easily processed, had decent ionic conductivity and thermal stability up to 130°C, and was successfully cycled in a Li/LiFePO_4 cell. —MSL

Chem. Mater. 10.1021/acs.chemmater.7b03736 (2018).

EDUCATION

Scientific reasoning on paper

Helping students develop skills in both critical thinking and scientific reasoning is fundamental to science education. However, the relationship between these two constructs remains largely unknown. Dowd *et al.* examined this issue by investigating how students' critical thinking skills related to scientific reasoning in the context of undergraduate thesis writing. The authors used the BioTAP rubric to assess scientific reasoning and the California Critical Thinking Skills Test to assess critical thinking. Results support the role of inference in scientific reasoning in writing, while also revealing other aspects of scientific reasoning (epistemological considerations and writing conventions) not related to critical thinking. In considering future implications for instruction, the authors suggest that further research into the impact of interventions focused on specific critical thinking skills (i.e., inference) for improved science reasoning in writing is needed. —MMc

CBE Life Sci. Educ. 10.1187/cbe.17-03-0052 (2018).

FRAMEWORK MORPHOLOGY

Mesocrystal morphogenesis

Control of the formation of mesoscale crystals of metal-organic framework (MOF) compounds can offer ways to control their reactivity and sorption properties and create more elaborate structures. Hwang *et al.* show that a copolymer with two hydrophilic blocks—polyethylene oxide and polymethylmethacrylate—modulates the crystal formation of a MOF in which zinc cations and bdc (benzene-1,4-dicarboxylic acid) linkers form two-dimensional sheets connected by a second ligand that act as pillars. The copolymer kinetically favors metastable hexagonal crystal polymorphs. After partial removal of the copolymer with methanol soaking, the crystals transform into more stable tetragonal crystals. —PDS

J. Am. Chem. Soc. 10.1021/jacs7b12633 (2018).

CREDIT: AN SCHROERS, YALE

REVIEW SUMMARY

CHEMICAL BIOLOGY

Chemically induced proximity in biology and medicine

Benjamin Z. Stanton,* Emma J. Chory,* Gerald R. Crabtree†

BACKGROUND: Nature has evolved elegant mechanisms to regulate the physical distance between molecules, or proximity, for a wide variety of purposes. Whether it is activation of cell-membrane receptors, neuronal transmission across the synapse, or quorum sensing in bacterial biofilms, proximity is a ubiquitous regulatory mechanism in biology. Over the past two decades, chemically induced proximity has revealed that many essential features and processes, including protein structure, chromosomal architecture, chromatin accessibility, transcription, and cellular signaling, are governed by the proximity of molecules. We review the critical advances in chemical inducers of proximity (CIPs), which have informed active areas of research in biology ranging from basic advances to the development of cellular and molecular therapeutics.

ADVANCES: Until the 1990s, it was unclear whether proximity was sufficient to initiate signaling events or drive their effect on transcription. Synthetic small molecule–induced dimerization of the T cell receptor provided the first evidence that proximity could be used to understand signal transduction. A distinguishing feature of small-molecule induced-proximity systems (compared to canonical knockdown or knockout methods) is the ability to initiate a process midway and discern the ensuing order of events with precise temporal control. The rapid reversibility of induced proximity has enabled precise analysis of cellular and epigenetic memory and enabled the construction of synthetic regulatory circuits. Integration of CRISPR-Cas technologies into CIP strategies has broadened the scope of these techniques to study gene regulation on time scales of minutes, at any locus, in any genetic context. Furthermore, CIPs have been used to dissect the mechanisms governing seemingly well-understood processes, ranging from transport of proteins between the Golgi and endoplasmic reticulum to synaptic vesicle transmission. Recent advances in proximity-induced apoptosis, inhibition of aggregation, and selective degradation of endogenous proteins will likely yield new classes of drugs in the near future.

ON OUR WEBSITE

Read the full article at http://dx.doi.org/10.1126/science.aao5902

OUTLOOK: We review fundamental conceptual advances enabled by synthetic proximity as well as emerging CIP-based therapeutic approaches. Gene therapy with precise regulation and fully humanized systems are now possible. Integration of proximity-based apoptosis through caspase activation with chimeric antigen receptor (CAR) T cell therapies provides a safety switch, enabling mitigation of complications from engineered immune cells, such as graft-versus-host disease and B cell aplasia. Furthermore, this integration facilitates the potential for repopulation of a patient's cells after successful transplantation. With the recent approval of CTL019, a CAR T cell therapeutic from Novartis, integrated strategies involving the use of CIP-based safety switches are emerging. Innovative exemplars include BPX-601 (NCT02744287) and BPX-701 (NCT02743611), which are now in phase 1 clinical trials. By using a similar proximity-based approach, conditional small-molecule protein degraders are also expected to have broad clinical utility. This approach uses bifunctional small molecules to degrade pathogenic proteins by dimerizing with E3 ubiquitin ligases. Degradation-by-dimerization strategies are particularly groundbreaking, because they afford the ability to repurpose any chemical probe that binds tightly with its pathogenic protein but which may not have previously provided a direct therapeutic effect. We anticipate that the translation of CIP methodology through both humanized gene therapies and degradation-by-dimerization approaches will have far-reaching clinical impact. ■

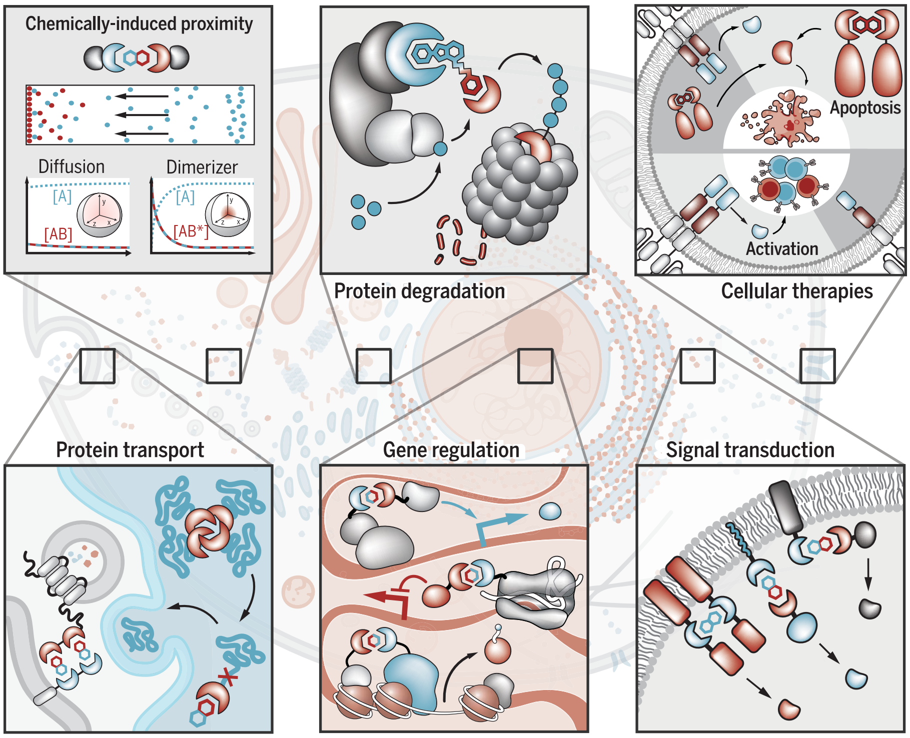

Chemically induced proximity. (Top) Left: Small molecules (hexagons) bind proteins of interest (crescents), dimerizing them to increase the effective molarity of reactions. [A] monomeric protein and [AB*] dimer concentrations; arrows, position coordinates. Middle: Synthetic dimerizers tag proteins (blue circles) for proteasomal degradation (red rods). Right: Homodimerizing molecules form kill switches for apoptosis. (Bottom) CIPs mimic cellular processes. Left: Protein transport mechanisms—nuclear import and export, membrane fusion, and protein folding. Middle: Regulation of gene activation by binding to DNA or chromatin (spheres with white strands), through recruitment of transcriptional activators or repressors (blue and red arrows). Right: Signal transduction pathways.

The list of author affiliations is available in the full article online.
*These authors contributed equally to this work.
†Corresponding author. Email: crabtree@stanford.edu

Cite this article as B. Z. Stanton *et al.*, *Science* 359, eaao5902 (2018). DOI: 10.1126/science.aao5902

Stanton *et al.*, *Science* **359**, 1117 (2018) 9 March 2018 **1 of 1**

CHEMICAL BIOLOGY

Chemically induced proximity in biology and medicine

Benjamin Z. Stanton,[1,2]* Emma J. Chory,[1,3]* Gerald R. Crabtree[1,4]†

Proximity, or the physical closeness of molecules, is a pervasive regulatory mechanism in biology. For example, most posttranslational modifications such as phosphorylation, methylation, and acetylation promote proximity of molecules to play deterministic roles in cellular processes. To understand the role of proximity in biologic mechanisms, chemical inducers of proximity (CIPs) were developed to synthetically model biologically regulated recruitment. Chemically induced proximity allows for precise temporal control of transcription, signaling cascades, chromatin regulation, protein folding, localization, and degradation, as well as a host of other biologic processes. A systematic analysis of CIPs in basic research, coupled with recent technological advances utilizing CRISPR, distinguishes roles of causality from coincidence and allows for mathematical modeling in synthetic biology. Recently, induced proximity has provided new avenues of gene therapy and emerging advances in cancer treatment.

Biochemical processes are often regulated by the physical distance, or proximity, between molecules to initiate an effect. Proximity plays both a ubiquitous and essential role in biology, whether it relates to individual cells, as in confining enzymes within densely packed organelles, or whole populations, as with quorum sensing in bacteria. The importance of utilizing small molecules to induce proximity of proteins was recognized upon the discovery that the Src homology 2 (SH2) domain of tyrosine kinases mediates signal transduction by binding phosphotyrosine in the absence of catalysis (*1*). Later research showed that acetylation, methylation, ubiquitination, and a host of other transient or stable protein modifications recruit proteins that influence many processes, such as gene regulation and protein degradation. The realization that these changes in localization could produce distinct cell-fate decisions led to a fundamental question, "How does a quantitative change in localization produce discrete biologic responses?" The answer appears to lie in the simple fact that the probability of an effective collision between two molecules is a third-order function of distance (*2*). This simple relation allows steep concentration gradients to produce qualitative changes, such as cell lineage commitment. Yet, mechanisms other than proximity, like allostery, might mediate these biologic responses. How does one separate the consequences of these processes?

The effects of proximity were first distinguished from allosteric or alternative effects by the synthesis of a bivalent molecule, FK1012, that bound its ligands with no detectable allosteric changes. The nontoxic molecule simultaneously binds two FK binding proteins (FKBPs), each of which is a 108–amino acid prolyl isomerase. FK1012 was first used to homodimerize the intracellular domain of the T cell receptor (TCR) zeta chain (Fig. 1), producing signaling events that reproduce transmembrane signaling by the TCR (*3*). This first demonstration that chemically induced proximity (also referred to as chemically induced dimerization) could activate signaling was followed by similar approaches with Ras signaling (*4*), death receptor signaling (*5*), and transcriptional activation (*6*), among others. Each case supported a causative role of simple proximity in qualitative cellular changes. Although the role of proximity in the absence of allostery is still debated (*7*), we will focus this review on the emerging use of induced proximity with small molecules in resolving complex biologic questions and designing new therapeutic strategies.

Tool kits to explore proximity in biology

The first chemical inducer of proximity (CIP), FK1012 (*3*), a homodimer of FK506, was followed by many others (Fig. 1). These molecules have the common feature of binding two peptide tags on either side of each molecule. Given that induced proximity is observed within minutes, one can study the immediate, primary effects of activating a specific molecule without concern for delayed toxic effects of the dimerizer on proliferation, transcription, or other much slower processes. Often these molecules are naturally occurring and illustrate how biology regulates proximity to its own benefit. For example, FK506 binds FKBP12 on one of its sides and calcineurin, a phosphatase essential for immunologic activation, on the other side (Fig. 1), illustrating how induced proximity and inhibition of calcineurin by FKBP12 functions in immunosuppression. Other examples of naturally induced proximity include cyclosporine A (Fig. 1), which also inhibits calcineurin by recruiting cyclophilin to its active site (*8*), thereby inhibiting phosphatase activity and nuclear localization of NFATc (nuclear factor of activated T cells) family members (*9*). Rapamycin, an immunosuppressant structurally related to FK506, also shares the primary target FKBP and acts through formation of a ternary complex (Fig. 1) with the FKBP12-rapamycin-binding (FRB) domain of target of rapamycin (TOR) kinases (*10*, *11*).

In plants, induced proximity with abscisic acid (Fig. 1) blocks germination and also induces leaves to abscise in the fall. It functions by inducing proximity of the monomeric receptor Pyl to the protein phosphatase ABI1 (*12*, *13*). This molecule is present at high concentrations in our diets and is not toxic in humans. Similarly, gibberellin (Fig. 1), which promotes germination and stem elongation in plants, functions by induced proximity of the receptor GID1 and hormone GA1 (*14*).

Dynamics of chemically induced proximity

Over the past 20 years, CIP technology has advanced from its origins to afford methods to understand signaling, transcription, and protein localization on rapid time scales. Much of the progress hinges on the ability to initiate biologic processes midpathway in vivo, such as downstream of a signal-activation event, and then discern the order of reactions after induced activation. The power of this approach arises from the fact that temporally ordering events places rigorous limits on causality.

Paradoxically, the responses from chemically induced proximity are often more robust than those from rigid protein fusions, especially in cases where a protein fusion can result in steric hindrances that prevent functionality. Furthermore, chemically induced proximity provides minute-by-minute kinetic analysis, allowing precise mathematical modeling. The fundamental concept of effective molarity—that a localized concentration within solution may differ from the bulk concentration—underlies the rationale and practicality of using chemically induced proximity to study complex biologic mechanisms. Proximity becomes a critical regulator of cellular processes by the fact that the probability of an effective interaction between two molecules is a function of the distance between them. This phenomenon can be observed by considering the scaling relationships between physical distance and reaction probability. In most relevant cases, reaction rate scales with concentration (the inverse cubed root of particle density), which scales with mean interparticle distance, i.e., the closeness of molecules (*2*).

The contributions of effective molarity are readily observed in natural processes such as protein compartmentalization within organelles, membrane localization, and protein scaffolds. Molecular

---

[1] Departments of Pathology and Developmental Biology, Stanford University School of Medicine, Stanford, CA 94305, USA. [2] Division of Preclinical Innovation, National Center for Advancing Translational Sciences, National Institutes of Health, Rockville, MD 20850, USA. [3] Department of Chemical Engineering, Stanford University, Stanford, CA 94305, USA. [4] Howard Hughes Medical Institute, Stanford University School of Medicine, Stanford, CA 94305, USA.
*These authors contributed equally to this work.
†Corresponding author. Email: crabtree@stanford.edu

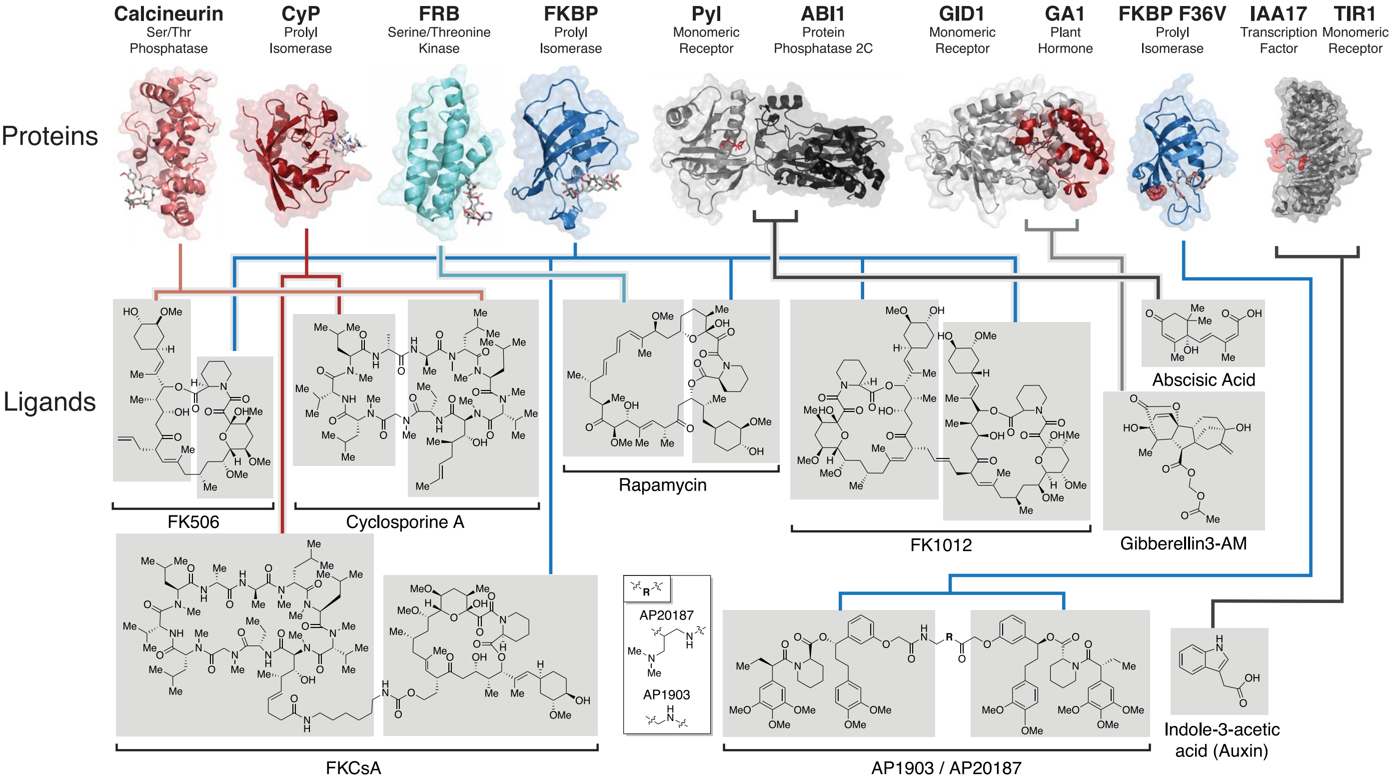

Fig. 1. The evolution of systems for CIPs. Protein targets and chemical ligands are shown for CIP systems. Proteins are represented as ribbon diagrams from available crystal structures, with endogenous monomeric functions indicated. Chemical ligands are represented in bound conformations docked with protein targets and also represented separately as individual structures. Gray shading of the chemical structures is divided to annotate specific structural moieties associated with molecular recognition of annotated protein targets. CIP systems are represented from left to right in approximate order of development. Me, methyl group; R, linker moiety.

scaffolds increase effective molarity in biochemical processes such as transcription, translation, and biosynthetic pathways. Protein scaffolds can enhance the speed of enzymatic reactions by several thousandfold (15, 16). Organelles sequester critical reaction components through compartmentalization to increase the effective molarity of relevant substrates.

Previously, mathematical models of reaction-diffusion systems have been used to describe dynamic biologic processes that correspond to a change in concentration with respect to space, time, and changing substances (reactions). Some examples of reaction-diffusion models in biology include those that explain the improved enzyme catalytic efficiency resulting from compartmentalization (17) and those that describe the improved kinetics of push-pull networks in which two enzymes control signal transduction pathways in an antagonistic manner (18). Similarly, the effective concentration increase at a CIP recruitment site can be understood by considering any dimerization event as a reaction occurring in a classic reaction-diffusion system (Fig. 2A) (because equilibrium models cannot describe steep concentration gradients). In a chemically induced–proximity event, one member of a ternary complex, [A], is freely diffusing, while the other, [B], is localized (at the cell membrane, on chromatin, etc.). The addition of a chemical dimerizer creates a concentration gradient of the complete complex, [AB*], with a maximum concentration at the recruitment site (Fig. 2A).

The reaction-diffusion equation is as follows:

$$\frac{\partial u(x,t)}{\partial t} = D\frac{\partial^2 u(x,t)}{\partial x^2} + ku(x,t)$$

From Fick's laws of diffusion, the flux of the substance at position (x) is proportional to the concentration gradient, and the change in concentration with respect to time ($\partial u/\partial t$) is related through the differential equation $\frac{\partial^2 u}{dx^2}$. The rate of concentration changes ($\partial u/\partial t$) is also impacted by the reaction rate, $ku(x, t)$. In the absence of a chemical dimerizer, dimerizing proteins [A] and [B] have little-to-no binding affinity for each other (Fig. 2B). Although they freely collide, their rate of diffusion dominates over the binding rate. By contrast, in the presence of a CIP (Fig. 2B), reaction is faster than diffusion. As a result, the concentration of bound [AB*] near the recruitment site is far greater than the freely diffusing condition, which creates a virtual cloud of molecules to amplify the effects of proximity while relieving steric constraints.

Although it is tempting to solely credit the superiority of chemical dimerization to pure kinetics, the thermodynamic contributions of the system should not be understated (Fig. 2C). By increasing the effective molarity of a substrate, the cell is relieving the cost of translational (x, y, z) entropy (Fig. 2C). The use of a CIP minimizes the relative configurational entropy of the system by reducing the possible collision angles relative to freely diffusing molecules. As a result, the CIP provides both kinetic and thermodynamic advantages by increasing the probability of interactions through effective concentration and by minimizing translational or rotational entropy.

Despite the early characterization of binary-complex equilibria in 1916 by Irving Langmuir (19), a mathematical description of a three-body system, for example, FKBP-rapamycin-FRB, in equilibria (Fig. 2D) has only recently been described (20). Spiegel and others developed a mathematical framework for ternary-complex formation that used measurable parameters (analogous to total concentration and dissociation constants) to define the maximum concentration of dimerized complexes, $[AB^*]_{max}$ (20). Their framework was extended to several biologic systems and cooperative ternary complexes, including the TCR. For systems such as FKBP-rapamycin-FRB, where the dissociation constant K_d values have been rigorously defined (21), more complete descriptions of the kinetics of ternary systems may prove useful when characterizing the fundamental processes governed by proximity.

Using induced proximity to explore biologic mechanisms: Biologic mimicry

Arguably the major contribution of chemically induced proximity is the ability to rapidly initiate

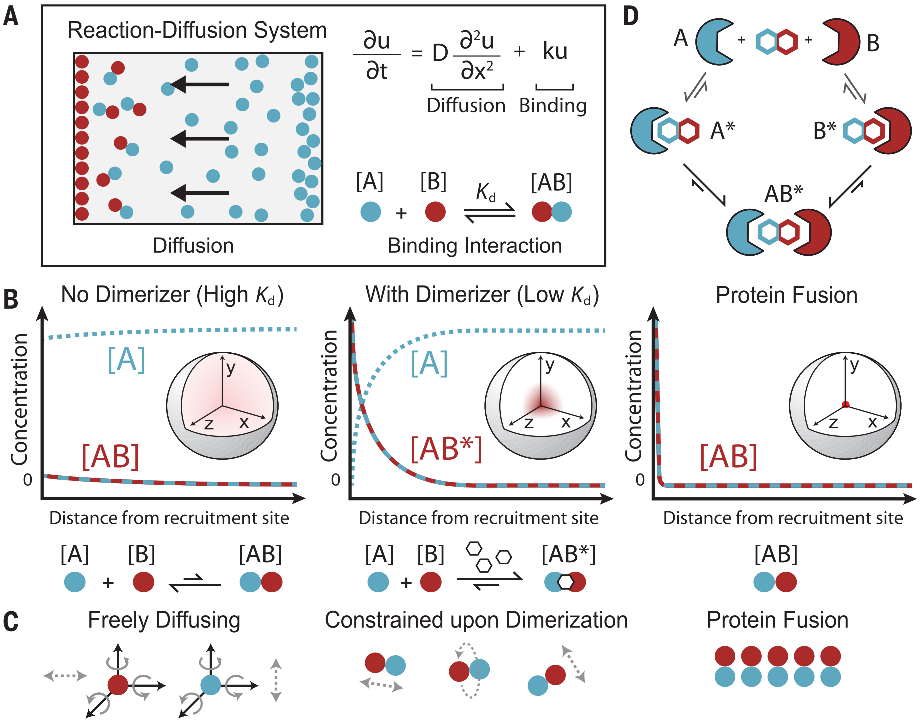

Fig. 2. Modeling reaction kinetics associated with systems of induced proximity. (**A**) The differential concentration with respect to time is explained by the changes in the rate of diffusion and the binding kinetics of the dimerizer system. (**B**) Changes in concentrations of monomeric and dimeric complexes are dependent on rate of reaction and rate of diffusion, defined by the distance to the site of recruitment. With no chemical induction or high K_d, formation of ternary complexes is determined by the rate of diffusion, as $ku(x, t)$ approaches zero. With chemical induction and low K_d, induced ternary-complex formation is strongly dependent on the rate of the reaction $ku(x,t)$, which dominates the rate of diffusion. Direct-fusion systems are exclusively localized at the site of recruitment as the reaction rate approaches infinity and dominates the rate of diffusion. In protein-dimerizer interactions, these complexes are designated by *. (**C**) Thermodynamic contributions to chemically induced dimerization include minimizing translational and rotational entropy. Multistate binding equilibria associated with initial binding of a bifunctional dimerizer molecule (hexagons) to respective targets by forming unstable binary complexes that form composite surfaces and rapidly assemble ternary complexes. Arrows show direction of movement or rotation. (**D**) Kinetics of ternary-complex assembly can be described by three-body binding equilibria.

and track the minute-by-minute consequences of a biochemical process in living cells. This allows precise kinetic studies, construction of synthetic regulatory circuits, and analysis of cellular memory and places stringent limitations on causality within genetic and biochemical networks.

Induced proximity in signal transduction and transcription

Chemically induced proximity fueled conceptual advances in understanding signaling, including the role of proximity, the ordering of biochemical events, and the intersection with transcription. By using molecules that did not show allosteric effects upon binding their ligands by crystallography, it was found that receptor signaling could be induced by chemically mediated proximity (Fig. 3A), initially at the TCR (*3*) and later for a host of different receptors. Dimerizing TCR-signaling components at the membrane with FK1012 revealed that dimerization was sufficient to initiate downstream TCR signaling events (*22*, *23*). In addition, recruiting the guanine nucleotide exchange factor Sos to the membrane revealed that Sos proximity could induce Ras signaling and that a major role of the linking molecule Grb-2 was to increase effective local concentration (*24*).

Temporal analysis of the biochemical consequences of proximity defined the order of complex signaling mechanisms using both linear and parallel steps in a pathway. Membrane-induced proximity of zeta chain–associated protein kinase (ZAP70) helped place its function in the TCR signaling cascade, as did similar approaches for signal components downstream of death and growth factor receptors (*25*). Activation of individual signaling molecules, not possible with ligands that induce several pathways, unveiled the "AND gate" function of several transcription factors, including NFAT, meaning that two signaling inputs are required for a robust transcriptional output. For example, isolated Ras activation could not activate NFAT nor could isolated Ca^{2+} signaling. Simultaneous Ras and Ca^{2+} signals were essential for NFAT-dependent transcription and provided a check on inappropriate gene activation (*24*).

The role of proximity in transcriptional regulation became clear with the early understanding of the spatial organization of promoters and the proteins bound by them. However, chemically induced dimerization allowed the examination of the in vivo kinetics in yeast, flies, and mammals. Chemical recruitment of transcriptional activators led to the finding that transcriptional activation can be accomplished through proximity on time scales of minutes, rather than hours or days (Fig. 3B) (*6*), helping investigators to temporally order events in the complex sequence leading to transcriptional activation.

An important feature of a CIP is its rapid reversibility (by small-molecule washout with competitive inhibitors), which enables the study of molecular memory in cells. To enhance reversibility, nontoxic FK506 analogs were developed to competitively wash out synthetic dimerizers. The first competitive inhibitor of dimerization (FK506M) (*3*) was used to demonstrate that dimerizer-mediated transcription was rapidly reversible and induced no stable memory (Fig. 3B). However, developing a system for carrying out order-of-addition and co-occupancy of activators and repressors lead to the discovery that transcription could persist in certain contexts in yeast even after the activator was released (*26*). This indicated that memory was hardwired into these systems, by virtue of repressor resistance. More-refined analysis of transcriptional memory emerged from later studies of epigenetic regulators (see section "Chromatin regulation" below and Fig. 3E).

Induced proximity has also been pivotal for understanding the kinetics of transcriptional regulation in individual cells. In both yeast and human cells, transcription at a single allele was induced in an all-or-none quantal manner (*6*, *27*).

CRISPR and CIP-regulated transcription

Recent advances with CRISPR-Cas9 (*28*) have ushered in a new era of CIP transcriptional regulation (*29*, *30*). Zhang and others developed a rapamycin-inducible assembly of enzymatically dead Cas9 (dCas9) and locus-specific guide RNAs (Fig. 3B) (*31*). Recently, other dCas9 fusions (Fig. 3B) were found to be highly compatible with a variety of CIP systems (*32*, *33*).

The dCas9-based dimerizer systems allow combinatorial recruitment as well as ordered recruitment of activators and repressors, which have enabled studies of synergy and antagonism. For example, proximity-induced formation of repressive transcriptional states by recruiting a KRAB repression domain had a deterministic silencing effect on transcription, even with co-recruitment of an activator (*32*).

Protein folding and localization

Regulated compartmentalization of molecules is a common biological process easily mimicked by CIPs. Schreiber and others used a synthetic heterodimer, FKCsA (Fig. 1) (*34*), which targeted

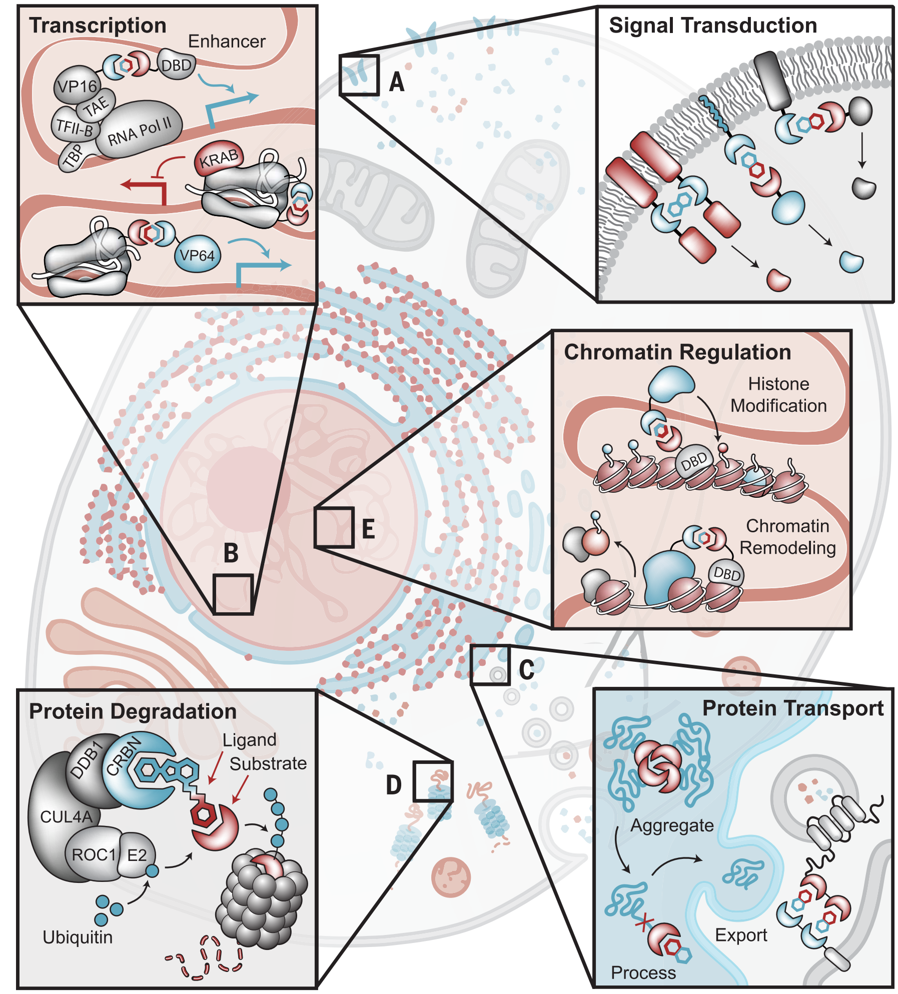

Fig. 3. Chemical induction of proximity is sufficient for the regulation of diverse cellular processes. Induced proximity has been shown to regulate initiation of transcription, signaling cascades, chromatin dynamics, proteasomal degradation, and subcellular localization. (**A**) Induced proximity has been systematically explored to bypass T cell antigen receptor activation and for synthetic induction of a variety of signaling cascades. (**B**) CIPs have been developed for rapid induction of transcriptional activation (VP16) and repression (KRAB or HP1) using DNA binding domains (DBDs) as well as CIP of split–CRISPR-Cas proteins or CIP recruitment of activators or repressors through CRISPR-Cas9 systems. (**C**) CIP has been used for rapid protein localization, including nuclear import and export, localization to components of the secretory pathway, synaptic vesicles, and mitochondria. (**D**) Rapid proximity-based protein degradation is achieved through bifunctional molecule–mediated recruitment of E3 ubiquitin ligase complexes (complex composed of E2, ROC1, CUL4A, DDB1, and CRBN). With a related approach, auxin can induce ubiquitin-mediated degradation through recruitment of the TIR1-Cul1 complex. (**E**) Induced proximity has been used for rapid induction of activated chromatin states through recruitment of ATP-dependent remodeling complexes and induction of repressive chromatin states through HP1-mediated heterochromatin formation.

FKBP and prolyl isomerase CyP without binding calcineurin, to rapidly induce nuclear translocation of CyP-tagged green fluorescent protein (GFP) with a nuclear-localized NLS-FKBP. A CIP was also used to rapidly export proteins from the nucleus, thereby reversibly inactivating them (*35*). Furthermore, this approach proved highly effective in yeast for inactivating nuclear proteins by shuttling them out of the nucleus using the "anchor-away" system (*36*–*39*). Anchor away is now frequently used to rapidly inactivate and reactivate nuclear proteins to understand their direct actions.

By expanding CIP localization beyond the nucleus to other organelles, Rivera and colleagues sought to activate specific secretory pathways in the endoplasmic reticulum (ER) for therapeutic purposes, building upon two critical advances (*40*). First, a multimer-forming, conditional aggregator of FKBP12(F36M) was found to be retained in the ER (Fig. 3C) in the absence of chemical ligands (AP22542, APAP21998). Second, a Golgi-specific protease (furin) was harnessed to target a cleavage site (FCS) engineered into fusion proteins with human growth hormone or insulin. By coupling these two advances, it was demonstrated that a CIP could both simultaneously cleave FKBP and, by resolving the aggregation, induce protein secretion (*40*). Furthermore, these ligands induced insulin secretion in hyperglycemic, FKBP(F36M)-FCS-insulin transgenic mice. This study showcased the clinical potential of CIPs for gene therapy applications, in addition to providing new insights into the secretory pathway.

Chemical dimerizers were further utilized to investigate how Golgi membranes associate with the ER during cell division (*41*). To investigate secretory mechanisms of Golgi-ER interaction during the cell cycle, the authors expressed fusions of FKBP-GFP with sialyltransferase (ST; Golgi specific), and FRAP-HA with the human invariant-chain protein (li; ER specific) (*41*). When coexpressed in COS-7 cells, the proteins remained associated within their respective cellular compartments as monomers, even upon the addition of chemical dimerizer. Notably, when treated with brefeldin A, a small molecule that induces Golgi-ER membrane fusion, the authors observed rapamycin-dependent colocalization of ST and li. This unexpected finding, that the Golgi and ER exhibit spatial independence during cell division, demonstrates how CIPs continue to reveal previously unknown aspects of seemingly well-characterized biologic mechanisms.

Svoboda and others developed an ingenious CIP approach to tether synaptic vesicle proteins. This allowed for inducible and reversible activation of synaptic transmission in neurons (Fig. 3C) (*42*). In motor neurons expressing vesicle-associated membrane protein (VAMP) or synaptobrevin-FKBP(F36V), the authors inhibited 50 to 100% of synaptic transmission in minutes using the synthetic dimerizer AP20187 (Fig. 1). This system was extended to both cultured neurons ex vivo and motor neurons in vivo. Furthermore, in Purkinje neurons of living mice, dimerization of VAMP–Syb-FKBP(F36V) with AP20187 induced functional ataxia during learned balancing tasks (*42*). This study highlights the potential for CIPs in understanding neuron function and complements invasive optogenetic systems.

The mechanism of Ca^{2+} entry was probed by Lewis and others through stromal interaction molecule 1 (STIM1) oligomerization (*43*). The authors demonstrated that the rapalogue AP21967 could rapidly oligomerize STIM1-FKBP and FRB-STIM1 and localize the complex to the cell periphery. This activated CRAC (Ca^{2+} release–activated Ca^{2+}) channel currents and revealed that induced oligomerization of STIM1 was sufficient for calcium entry via CRAC channels.

The expanded chemical repertoire (including new orthogonal rapalogs that were specifically tuned to FRB mutants) heavily influenced the multiplex ability of subcellular-localization studies (*44*). First, a triple-mutant FRB [residue Lys2095→Pro2095 (Lys2095Pro), Thr2098Leu, Trp2101Phe], denoted FRB*, was developed to selectively form a ternary complex with FKBP and C20-methallylrapamycin (C20-MaRap) (*45*). Through utilization of a CIP transcriptional-reporter screen, it was found that by introducing rapalogs and respective FRB mutants, precise

Fig. 4. Ubiquitin ligase complexes rapidly degrade oncogenic protein targets. (**A**) The CBRN-CUL4A ubiquitin ligase complex can be recruited to BCR-ABL and BRD4 with thalidomide conjugated to bosutinib and JQ1, respectively. Induced proximity rapidly degrades these targets, which are known to drive chronic myelogenous leukemia (BCR-ABL) and acute myeloid leukemia (BRD4). (**B**) The VHL ligand fused to desatinib or JQ1 can efficiently recruit the VHL-Cullin2 ubiquitin ligase complex to ABL and BRD4, respectively. In each case, rapid degradation of the oncogenic targets results in inhibition of cancer growth.

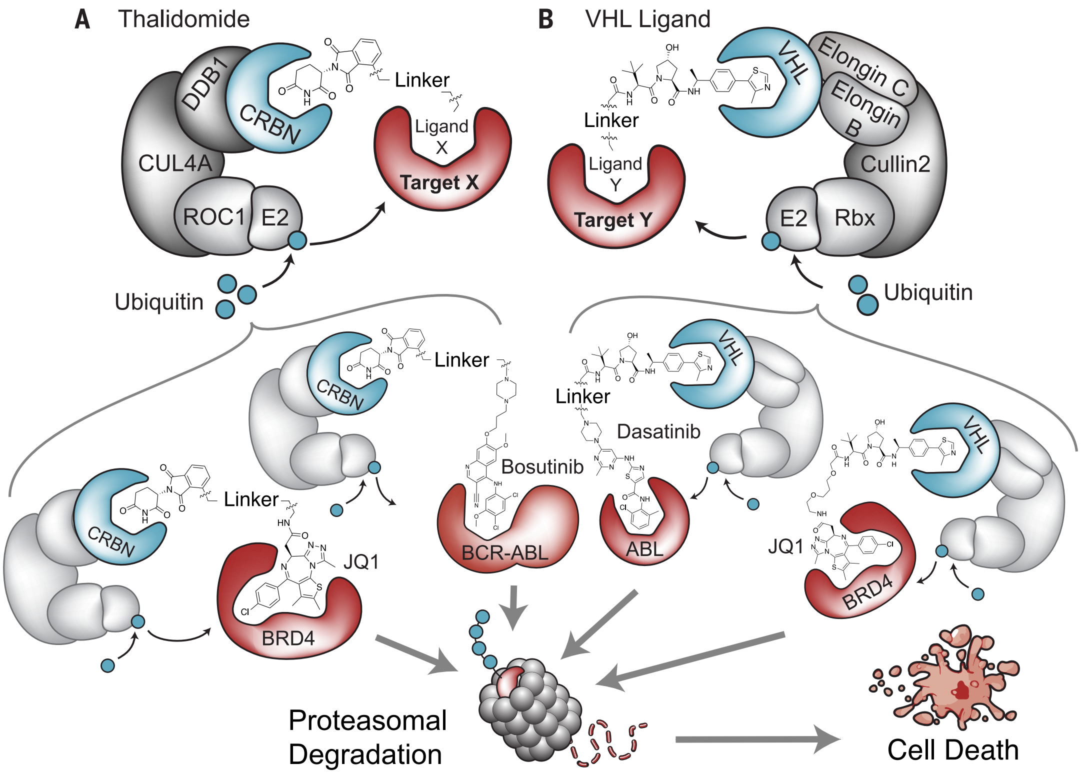

measurements could be made to define new patterns of specificity. By using these new orthogonal dimerizers, simultaneous expression of nuclear exporting FRB*(LT) and nuclear localizing FRB*(LW) provided a platform for push-pull control of FKBP–GSK3β (glycogen synthase kinase 3β), which was modulated by treatment with the appropriate orthogonal rapalog (*44*).

Modulating protein structure is another critical component of posttranslational modification that has been explored through proximity-based approaches. Muir and others developed a facile approach to conditional protein structural variation. Using rapamycin, they were able to mimic natural protein splicing with proximity-based intein cleavage (*46*).

Recently, Ballister and colleagues developed a clever light-induced proximity system—defining a photon as the smallest dimerizer (*47*). Modifying a previous bifunctional *bis*-methotrexate dimerization system (*48*), the authors labeled the dihydrofolate reductase (DHFR) ligand with a photocleavable moiety, which blocked the requisite DHFR-interacting surfaces in the absence of irradiation. Tagging the photocleavable moiety with a HaloTag linker formed an irreversible adduct with a Haloenzyme allowing for selective, light-inducible Halo-tagging and subcellular relocalization of DHFR upon irradiation. Furthermore, photoinduced DHFR relocalization was extended to the centromere, kinetochore, centrosome, and mitochondria with CENP-Halo, Nuf2-Halo, AKAP9-Halo, and ActA-Halo, respectively.

Protein degradation

Loss-of-function studies have been the mainstay of genetics but are plagued by the slow loss of protein, allowing the accumulation of compensatory and indirect responses clouding mechanistic interpretation. CIP-regulated protein stability was developed to circumvent these classic problems. By using C20-MaRap, it was determined that the stability of FRB* fusions (*44*, *45*) was dependent on formation of the FRB*–C20-MaRap–FKBP ternary complex. To investigate the function of GSK3β in developing mice, FRB* was knocked into the endogenous GSK3β gene. Because expressed GSK3β could only be stabilized in the presence of C20-MaRap and was otherwise degraded, dosing for short periods allowed the authors to define separate, discrete periods of development during which the gene executed its function in skeletogenesis and palate development (*49*).

Wandless and others found that double-mutant FKBP(Phe36Val, Leu106Pro) could also be used as a conditionally stabilizing allele, which allowed for rapid in vitro degradation of target proteins (*21*). The synthetic dimerizer (Shield-1) used in these studies was degraded in minutes in cell culture, allowing rapid reversal of the reaction.

To regulate proteasome-mediated degradation, CIP systems were developed to target chimeric E3 ligase complexes. The TIR1 receptor–auxin (Fig. 1) degradation pathway in *Arabidopsis*, which utilizes the dimerizer indole-3-acetic acid (IAA; auxin), induces dimerization of the TIR1-SCF E3 ubiquitin ligase complex with an auxin-inducible degron (AID) (*50*, *51*). In nonplant systems, TIR1 was successfully reconstituted into endogenous E3 ligase complexes to selectively recruit AID-fusion proteins to the Cul1 complex (*50*). This resulted in auxin-mediated ubiquitination of the AID fusion and rapid proteasomal degradation (Fig. 3D). Later, a short 44–amino acid tag referred to as IAA17 (AID*) was developed to expand the utility of the auxin system (*52*). The auxin-degron (AID*) system has been used to regulate kinases and essential genes that lack selective inhibitors. The essential Plk4 kinase, which is associated with tumor suppression (*53*, *54*), was degraded with AID-fusion transgenes (*55*) and homozygous knockins (*56*) to reveal that Plk4 positively regulates centriole duplication in a reversible and dosage-dependent manner. The auxin system has enabled rapid degradation of a wide variety of targets across many species (*55*, *57*–*59*). Recently, auxin-mediated degradation of the transcription factor CTCF (*60*) has differentiated its roles in local topologically associating domain (TAD) structure from chromosomal-compartment architecture.

Chromatin regulation

The immense complexity of chromatin, with its many developmentally specific histone modifications, topology, long-range interactions, variegated DNA methylation, and uncharacterized chromatin components, has proven to be a formidable target for investigation. The limitations encountered in formation of chromatin in vitro have become apparent (*61*). To circumvent these challenges, a CIP technique (CiA, chromatin in vivo assay) was developed to study chromatin in all its topological, biochemical, and developmental diversity (*62*). With CiA, one can "chemically pipette" a chromatin regulator of interest into essentially any locus in the genome of any cell type (Fig. 3E).

The CiA system was first used to study chromatin-based memory. Recruiting heterochromatin protein 1α (HP1α) to the active *Oct4* (transcription factor) locus in mouse embryonic stem cells (ESCs), resulted in an expanding domain of repression

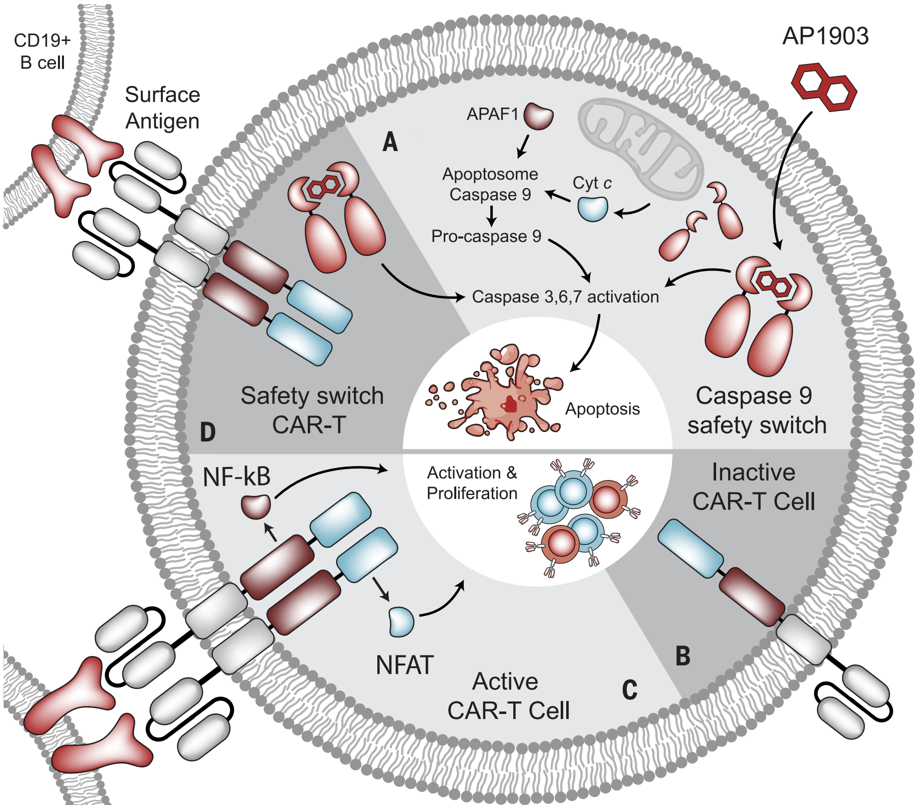

Fig. 5. CAR T cell therapeutic applications of CIPs. (**A**) Engineered safety switches using ATTAC systems with AP1903. (**B**) An inactive engineered CAR T cell receptor and (**C**) an active engineered CAR T cell receptor binding its cognate antigen. (**D**) AP1903-induced caspase dimerization and activation allows for rapid apoptosis of CAR T cells to prevent complications that may arise from transplant.

that silenced Oct4. By washing out the CIP, it was observed that H3K9me3 (trimethylated histone H3 on lysine 9) islands are stable for days after rapamycin washout but that the effect could be rapidly reversed by initiating transcription by plant hormone abscisic acid (ABA)–mediated recruitment of the transcriptional factor VP-16 (*62*). Furthermore, the ability to rapidly control H3K9me3-based heterochromatin permitted mathematical modeling, which put forth a "balanced intrinsic reaction rate" model for the propagation of H3K9me3 repression on the basis of kinetic parameters (*62*, *63*). In this model, rates of addition and removal determine the propagation rate of H3K9me3 and accurately predict 99% of the H3K9 domains over the murine ESC genome.

One of the most persistent problems in epigenetics has been understanding the placement and stability of polycomb repressive complexes (PRCs). In 1988, mutations in the *Brahma* gene, which encodes an adenosine triphosphate (ATP)–dependent chromatin remodeler, were found to repress mutations in the PRC1 complex, indicating that these two chromatin regulators opposed one another (*64*). The mechanism was elusive because of the inability to form PRC-repressed heterochromatin in vitro. To understand this problem, the SWI/SNF (switch-sucrose nonfermentable) or BAF (Brahma/Brg associated factor) complex was recruited to a polycomb-repressed promoter with the CiA system (*65*, *66*). PRC1 eviction occurred in minutes, followed by PRC2 eviction. The rapid action of BAF complexes led to the finding that they directly bind and release PRC1 by an ATP-dependent mechanism (*65*, *66*). Furthermore, heterozygous expression of cancer mutations of Brg, the regulatory adenosine triphosphatase (ATPase) of BAF, lead to polycomb accumulation, extending the CiA results to the genome. New CIP-dCas9 systems for manipulating chromatin architecture (*33*, *67*) will likely prove critical in uncovering chromatin regulatory mechanisms in a host of genomic contexts.

CIPs provided additional insights into the dissolution and formation of heterochromatin by the observation that recruitment of the BAF complex lead to accumulation of TopoIIα binding at the recruitment site, as suggested from an earlier study (*68*). Unexpectedly, TopoIIα function was found to be essential for both the dissolution of heterochromatin after recruiting BAF and the formation of heterochromatin after releasing BAF (*69*). Remarkably, the strand-cleaved reaction intermediate was found at the precise time and position of heterochromatin formation and dissolution. These studies, using rapid reversible corecruitment of TopoIIα and BAF, indicated that decatenation is essential for the regulation of heterochromatin.

Chromosomal dynamics

To assess the mechanisms of DNA association with the cohesin complex during cell division, Nasmyth and others used dimerizers to "lock" the Smc1-Smc3 complex in place during specific windows of the cell cycle in yeast (*70*). By releasing yeast from G_1 (prereplicative phase) arrest, with or without the conditional dimerization of Smc1 and Smc3, it was discovered that the Smc1-Smc3 complex must open during mitosis and that this was necessary for chromatid cohesion.

A similar CIP-based approach was used to understand the role of Scc1 in sister chromatin association. Relocalization and inhibition of Scc1-FRB by rapamycin with ribosomal protein anchor RPL13A-FKBP demonstrated that 30% of sister chromatid association was disrupted by anchoring away Scc1 in yeast (*36*).

Induced proximity in medicine

Degrading or inactivating pathogenic proteins

The above studies, directed primarily at dissecting biologic mechanisms, demonstrate how widely this methodology can be used. However, the application to the treatment of disease had been hampered by the requirement that proteins must be tagged with dimerizing peptides. Graef and others reasoned that induced proximity of endogenous, unmodified proteins would be widely useful. To make a potential therapeutic for Alzheimer's disease, they synthesized a molecule that bound both FKBP (SLF, synthetic ligand of FKBP) and the pathogenic β-amyloid (Aβ) peptide (CR, Congo red) (*71*). Their two-sided molecule (SLF-CR) showed activity in in vitro assays of Aβ aggregation but was too toxic to be used as a therapeutic. A similar approach also extended the half-life of an HIV protease inhibitor by causing it to remain intracellular and protected (*72*).

Although neither of these bifunctional molecules had good pharmacologic characteristics, this conceptual advance precipitated a wave of efforts to extend proximity-inducing molecules to many other medical problems. One of the first of these was designed to stabilize the pathogenic aggregation of proteins. Transthyretin (TTR) can produce aggregating amyloid fibrils and causes amyloidoses, including cardiomyopathies such as senile system amyloidoses, familial amyloid cardiomyopathy, and familial amyloid polyneuropathy. The development of bifunctional stabilizers of TTR, such as AG10 by Graef and others (*73*), provides a promising candidate in preventing the progression of diseases associated with amyloid aggregation.

In many diseases, pathogenic proteins arise from mutation, recombination, or stable allosteric modification. What if these culprits could be degraded by induced proximity? In 2010, CRBN, a component of the DDBI-CRBN E3 ubiquitin ligase complex (Fig. 3D), was found to be the primary molecular target of thalidomide and related molecules (IMiDs, immunomodulatory drugs) (74). Several years later, elegant structural studies for IKAROS family transcription factors (IKZF1, IKZF3) indicated that ubiquitin binding and targeting was IMiD dependent (75). These insights, coupled with the knowledge that thalidomide differed from analogs lenalidomide and pomalidomide through a single C-4 aniline substitution (75), provided a clear path to conjugate new ligands for the purposes of proximity-based protein degradation.

To investigate the potential applications of CRBN-IMiDs, the Bradner and Crews labs developed strategies to conjugate BRD4-targeting cell-permeable small molecule JQ1 (76) with thalidomide and investigated its potential as an inducible proximity-based ubiquitinase (Fig. 4) (77, 78). These studies were precipitated by the observation that IMiDs could bind directly to CRBN without inhibiting the associated ubiquitin ligase complex. In the first study, the phthalimide-JQ1 conjugate (dBET1) induced ubiquitin-mediated degradation of BRD4 on a time scale of hours, with a mechanism analogous to auxin-based degradation systems (without requiring genetic manipulations). The same C-4 phthalimide linkage was used to construct thalidomide-SLF conjugates (d-FKBP-1) for rapid and selective ubiquitin-mediated degradation of FKBP12. This demonstrated that these bifunctional conjugates were highly selective and had activity in human cells. By using a longer polyethylene glycol (PEG)–based linker attached to phthalimide, Crews and others simultaneously found that BRD4 could be degraded using both CRBN and von Hippel–Lindau tumor suppressor (VHL) ubiquitin ligase–targeting ligands with their strategy termed proteolysis targeting chimeras (PROTACs) (Fig. 4). Their bifunctional PROTACs were capable of rapidly recruiting the VHL-associated ubiquitin ligase complexes by using ligands specific to both estrogen-related receptor alpha (ERRα) and the serine-threonine protein kinase RIPK2 with notably high selectivity and activity in live mice (79).

In an important follow-up study, Bradner and others identified ENL, bearing a YEATS acetylated-lysine reader domain, as the product of an essential gene in a human acute myeloid leukemia (AML) model system with a mixed-lineage leukemia (MLL)–AF4 translocation (MV4;11) (80). To understand the function of ENL as a potential driver in AML, the authors expressed the ENL-FKBP12(F36V) protein in an ENL-deficient ($ENL^{-/-}$) MV4;11 cell line and used SLF (with no calcineurin or mTOR inhibition) conjugated to phthalimide (dTAG-13). Selective degradation of ENL with dTAG-13 resulted in decreased expression of AML drivers, including MYC, HOXA10, and MYB, and substantial reduction in elongation factors AFF9 and CDK9. This revealed that ENL may drive leukemogenesis through binding and elongation of canonical AML targets and demonstrated a creative use of degrading-CIPs with therapeutic potential.

Inhibition of BRD4, which results in repression of c-Myc activity, has been proposed as a therapeutic strategy in a host of diseases, including AML, acute lymphoblastic leukemia, NUT midline carcinoma, and HIV (76, 81, 82). Concomitantly, Crews and others, aware of the limitations of peptide-based degradation strategies, independently identified potent, small molecules targeting VHL E3 ubiquitin ligase (83). By utilizing this VHL-targeting strategy, dimeric ligands have selectively degraded ERRα RIPK2, which is involved in nuclear factor κB (NF-κB) and mitogen-activated protein kinase (MAPK) activation, and BRD4 (79, 84, 85). Furthermore, proximity-induced degradation provides a platform for rapid iteration through combination. Crews and others recently demonstrated that by varying the E3 ligase target and the functional protein-targeting warhead, the selectivity of known tyrosine kinase inhibitors (TKIs) could be improved (85). By modulating known TKIs—imatinib, dasatinib, or bosutinib—and the E3 ligase target, these small molecules degraded both c-ABL and the oncogenic BCR-ABL (Fig. 4), with varying degrees of specificity (85). Even though TKIs have proven to be immensely successful in the treatment of chronic myelogenous leukemia, it remains a lifelong condition. One hypothesis for persistent leukemic cells is that the pathogenesis is not entirely dependent on kinase activity and that BCR-ABL may play a scaffolding role in signaling (86). As such, proximity-induced degradation may not only provide a mechanism for inhibition of oncogenic proteins [with efficacy comparable to RNA interference (RNAi) or CRISPR, but without the immunogenicity of Cas9] but may also provide cures for diseases for which present catalytic inhibitors are inadequate. This strategy may revive the imperfect chemical probes that bound the protein of interest but failed to deliver cures for critical therapeutic targets.

Induced proximity in cellular therapies

Gene therapies require the delivery of precise amounts of therapeutic proteins at specific times as well as a humanized system to prevent immune rejection of the engineered cells. On the basis of earlier FK1012-mediated transcriptional activation studies (6), Clackson and others developed a completely humanized delivery system that provides long-term, regulated expression in primates (87–89). A major challenge for any method of regulated gene expression is the steep dose-response curve induced by rapamycin. The use of nontoxic dimerizers such as abscisic acid provide a more graded dose response (13) and could be useful for precise dosage control.

Certain therapeutic strategies require removal of pathogenic cell types. Early studies demonstrated that dimerizing the intracellular domain of the Fas receptor or other death-signaling molecules could accomplish this goal (90–93). By using a technique called apoptosis through targeted activation of caspase 8 (ATTAC) (Fig. 5A), an animal model was developed to study obesity and glucose-stimulated insulin secretion. This CIP "suicide-switch" strategy was extended to a senescent cell–clearing mouse to study age-related pathologies (94). Baker and colleagues observed that CIP-mediated clearance of senescent cells extended health and life span of normal tissues. Furthermore, with precise temporal control, the ATTAC system attenuated the progression of age-related diseases (94, 95).

Cellular therapies remain one of the most hopeful strategies; however, concerns remain around potential off-target damage or possible malignancy that may result from genomic integration of an introduced gene. Although allogenic transplantation of hematopoietic stem cells is an effective leukemia treatment, positive benefits of this therapy are often counteracted by graft-versus-host disease (GVHD). To circumvent this, a CIP "safety switch" was developed to selectively induce apoptosis in hematopoietic transplants in the case that severe GVHD arises in patients (96). In a small clinical trial, patients with GVHD were treated with AP1903 (Fig. 1), a bioinert analog of FK1012 (97). AP1903 selectively eliminated 90% of the modified T cells within 30 min and eliminated GVHD without recurrence (96). Subsequent studies further demonstrated the usefulness of this safety switch in long-term GVHD complications (98, 99).

CIP safety switches may also prove to be a promising strategy for mitigating side effects of cancer immunotherapy treatments. In a recent study in humanized mice, T cells were simultaneously modified with a chimeric antigen receptor (CAR) and the iCaspase9 safety switch (Fig. 5, B to D). Despite the effectiveness of CAR T cell therapies for treating B cell malignancies (including acute lymphoblastic leukemia and lymphomas) (100, 101), possible side effects can be severe. Treating mice with a CD19–FKBP-iCaspase9 T cell therapy provided two advantages. First, induced dimerization of the caspase 9 protein provides a built-in temporally controlled mechanism to ablate harsh side effects in patients, such as cytokine release syndrome or B cell aplasia. Second, selective apoptosis provides a mechanism to eliminate transplanted T cells in a controlled manner that allows for patient-specific responses in the clinic, along with the ability to repopulate a patient's own immunity (102).

Summary

The application of chemically induced proximity to elucidate biologic mechanisms continues to grow with recent advances in understanding epigenetic regulation, chromosomal dynamics, and topology. However, the use of this mechanism in treatment of disease is still in its embryonic form. Bifunctional molecules that use induced proximity for the elimination of pathogenic proteins and aggregated proteins and to control subcellular localization are likely to make a substantial impact on the treatment of disease in the near future. The development of totally humanized systems for gene and cellular therapy is now under clinical investigation and showing promise. Small molecules that capture the universal biologic regulatory mechanism of induced proximity will likely have many other unanticipated uses and provide a playground for our imaginations.

REFERENCES AND NOTES

1. Z. Songyang *et al.*, SH2 domains recognize specific phosphopeptide sequences. *Cell* **72**, 767–778 (1993). doi: 10.1103/RevModPhys.62.251; pmid: 7680959

2. P. Hänggi, P. Talkner, M. Borkovec, Reaction-rate theory: Fifty years after Kramers. *Rev. Mod. Phys.* **62**, 251–341 (1990). doi: 10.1103/RevModPhys.62.251
3. D. M. Spencer, T. J. Wandless, S. L. Schreiber, G. R. Crabtree, Controlling signal transduction with synthetic ligands. *Science* **262**, 1019–1024 (1993). doi: 10.1126/science.7694365; pmid: 7694365
4. Z. Luo *et al*., Oligomerization activates c-Raf-1 through a Ras-dependent mechanism. *Nature* **383**, 181–185 (1996). doi: 10.1038/383181a0; pmid: 8774885
5. P. J. Belshaw, D. M. Spencer, G. R. Crabtree, S. L. Schreiber, Controlling programmed cell death with a cyclophilin-cyclosporin-based chemical inducer of dimerization. *Chem. Biol.* **3**, 731–738 (1996). doi: 10.1016/S1074-5521(96)90249-5; pmid: 8939689
6. S. N. Ho, S. R. Biggar, D. M. Spencer, S. L. Schreiber, G. R. Crabtree, Dimeric ligands define a role for transcriptional activation domains in reinitiation. *Nature* **382**, 822–826 (1996). doi: 10.1038/382822a0; pmid: 8752278
7. M. J. Holliday, C. Camilloni, G. S. Armstrong, M. Vendruscolo, E. Z. Eisenmesser, Networks of dynamic allostery regulate enzyme function. *Structure* **25**, 276–286 (2017). doi: 10.1016/j.str.2016.12.003; pmid: 28089447
8. J. Kallen *et al*., Structure of human cyclophilin and its binding site for cyclosporin A determined by x-ray crystallography and NMR spectroscopy. *Nature* **353**, 276–279 (1991). doi: 10.1038/353276a0; pmid: 1896075
9. N. A. Clipstone, G. R. Crabtree, Identification of calcineurin as a key signalling enzyme in T-lymphocyte activation. *Nature* **357**, 695–697 (1992). doi: 10.1038/357695a0; pmid: 1377362
10. X. F. Zheng, D. Florentino, J. Chen, G. R. Crabtree, S. L. Schreiber, TOR kinase domains are required for two distinct functions, only one of which is inhibited by rapamycin. *Cell* **82**, 121–130 (1995). doi: 10.1016/0092-8674(95)90058-6; pmid: 7606777
11. S. W. Michnick, M. K. Rosen, T. J. Wandless, M. Karplus, S. L. Schreiber, Solution structure of FKBP, a rotamase enzyme and receptor for FK506 and rapamycin. *Science* **252**, 836–839 (1991). doi: 10.1126/science.1709301; pmid: 1709301
12. S. R. Cutler, P. L. Rodriguez, R. R. Finkelstein, S. R. Abrams, Abscisic acid: Emergence of a core signaling network. *Annu. Rev. Plant Biol.* **61**, 651–679 (2010). doi: 10.1146/annurev-arplant-042809-112122; pmid: 20192755
13. F. S. Liang, W. Q. Ho, G. R. Crabtree, Engineering the ABA plant stress pathway for regulation of induced proximity. *Sci. Signal.* **4**, rs2 (2011). doi: 10.1126/scisignal.2001449; pmid: 21406691
14. T. Miyamoto *et al*., Rapid and orthogonal logic gating with a gibberellin-induced dimerization system. *Nat. Chem. Biol.* **8**, 465–470 (2012). doi: 10.1038/nchembio.922; pmid: 22446836
15. S. An, R. Kumar, E. D. Sheets, S. J. Benkovic, Reversible compartmentalization of de novo purine biosynthetic complexes in living cells. *Science* **320**, 103–106 (2008). doi: 10.1126/science.1152241; pmid: 18388293
16. S. Y. Tsuji, D. E. Cane, C. Khosla, Selective protein-protein interactions direct channeling of intermediates between polyketide synthase modules. *Biochemistry* **40**, 2326–2331 (2001). doi: 10.1021/bi002463n; pmid: 11327852
17. R. J. Conrado, T. J. Mansell, J. D. Varner, M. P. DeLisa, Stochastic reaction-diffusion simulation of enzyme compartmentalization reveals improved catalytic efficiency for a synthetic metabolic pathway. *Metab. Eng.* **9**, 355–363 (2007). doi: 10.1016/j.ymben.2007.05.002; pmid: 17601761
18. S. B. van Albada, P. R. ten Wolde, Enzyme localization can drastically affect signal amplification in signal transduction pathways. *PLOS Comput. Biol.* **3**, e195 (2007). doi: 10.1371/journal.pcbi.0030195; pmid: 17937496
19. I. Langmuir, The constitution and fundamental properties of solids and liquids. Part I. Solids. *J. Am. Chem. Soc.* **38**, 2221–2295 (1916). doi: 10.1021/ja02268a002
20. E. F. Douglass Jr., C. J. Miller, G. Sparer, H. Shapiro, D. A. Spiegel, A comprehensive mathematical model for three-body binding equilibria. *J. Am. Chem. Soc.* **135**, 6092–6099 (2013). doi: 10.1021/ja311795d; pmid: 23544844
21. L. A. Banaszynski, L.-C. Chen, L. A. Maynard-Smith, A. G. L. Ooi, T. J. Wandless, A rapid, reversible, and tunable method to regulate protein function in living cells using synthetic small molecules. *Cell* **126**, 995–1004 (2006). doi: 10.1016/j.cell.2006.07.025; pmid: 16959577
22. M. N. Pruschy *et al*., Mechanistic studies of a signaling pathway activated by the organic dimerizer FK1012. *Chem. Biol.* **1**, 163–172 (1994). doi: 10.1016/1074-5521(94)90006-X; pmid: 9383386
23. D. M. Spencer, I. Graef, D. J. Austin, S. L. Schreiber, G. R. Crabtree, A general strategy for producing conditional alleles of Src-like tyrosine kinases. *Proc. Natl. Acad. Sci. U.S.A.* **92**, 9805–9809 (1995). doi: 10.1073/pnas.92.21.9805; pmid: 7568222
24. L. J. Holsinger, D. M. Spencer, D. J. Austin, S. L. Schreiber, G. R. Crabtree, Signal transduction in T lymphocytes using a conditional allele of Sos. *Proc. Natl. Acad. Sci. U.S.A.* **92**, 9810–9814 (1995). doi: 10.1073/pnas.92.21.9810; pmid: 7568223
25. I. A. Graef, L. J. Holsinger, S. Diver, S. L. Schreiber, G. R. Crabtree, Proximity and orientation underlie signaling by the non-receptor tyrosine kinase ZAP70. *EMBO J.* **16**, 5618–5628 (1997). doi: 10.1093/emboj/16.18.5618; pmid: 9312021
26. S. R. Biggar, G. R. Crabtree, Chemically regulated transcription factors reveal the persistence of repressor-resistant transcription after disrupting activator function. *J. Biol. Chem.* **275**, 25381–25390 (2000). doi: 10.1074/jbc.M002991200; pmid: 10801867
27. S. R. Biggar, G. R. Crabtree, Cell signaling can direct either binary or graded transcriptional responses. *EMBO J.* **20**, 3167–3176 (2001). doi: 10.1093/emboj/20.12.3167; pmid: 11406593
28. J. A. Doudna, E. Charpentier, The new frontier of genome engineering with CRISPR-Cas9. *Science* **346**, 1258096 (2014). doi: 10.1126/science.1258096; pmid: 25430774
29. D. M. Heery, E. Kalkhoven, S. Hoare, M. G. Parker, A signature motif in transcriptional co-activators mediates binding to nuclear receptors. *Nature* **387**, 733–736 (1997). doi: 10.1038/42750; pmid: 9192902
30. J. D. Chen, R. M. Evans, A transcriptional co-repressor that interacts with nuclear hormone receptors. *Nature* **377**, 454–457 (1995). doi: 10.1038/377454a0; pmid: 7566127
31. B. Zetsche, S. E. Volz, F. Zhang, A split-Cas9 architecture for inducible genome editing and transcription modulation. *Nat. Biotechnol.* **33**, 139–142 (2015). doi: 10.1038/nbt.3149; pmid: 25643054
32. Y. Gao *et al*., Complex transcriptional modulation with orthogonal and inducible dCas9 regulators. *Nat. Methods* **13**, 1043–1049 (2016). doi: 10.1038/nmeth.4042; pmid: 27776111
33. S. M. G. Braun *et al*., Rapid and reversible epigenome editing by endogenous chromatin regulators. *Nat. Commun.* **8**, 560 (2017). doi: 10.1038/s41467-017-00644-y; pmid: 28916764
34. P. J. Belshaw, S. N. Ho, G. R. Crabtree, S. L. Schreiber, Controlling protein association and subcellular localization with a synthetic ligand that induces heterodimerization of proteins. *Proc. Natl. Acad. Sci. U.S.A.* **93**, 4604–4607 (1996). doi: 10.1073/pnas.93.10.4604; pmid: 8643450
35. J. D. Klemm, C. R. Beals, G. R. Crabtree, Rapid targeting of nuclear proteins to the cytoplasm. *Curr. Biol.* **7**, 638–644 (1997). doi: 10.1016/S0960-9822(06)00290-9; pmid: 9285717
36. H. Haruki, J. Nishikawa, U. K. Laemmli, The anchor-away technique: Rapid, conditional establishment of yeast mutant phenotypes. *Mol. Cell* **31**, 925–932 (2008). doi: 10.1016/j.molcel.2008.07.020; pmid: 18922474
37. X. Fan *et al*., Nucleosome depletion at yeast terminators is not intrinsic and can occur by a transcriptional mechanism linked to 3′-end formation. *Proc. Natl. Acad. Sci. U.S.A.* **107**, 17945–17950 (2010). doi: 10.1073/pnas.1012674107; pmid: 20921369
38. K. H. Wong, K. Struhl, The Cyc8-Tup1 complex inhibits transcription primarily by masking the activation domain of the recruiting protein. *Genes Dev.* **25**, 2525–2539 (2011). doi: 10.1101/gad.179275.111; pmid: 22156212
39. A. Charbin, C. Bouchoux, F. Uhlmann, Condensin aids sister chromatid decatenation by topoisomerase II. *Nucleic Acids Res.* **42**, 340–348 (2014). doi: 10.1093/nar/gkt882; pmid: 24062159
40. V. M. Rivera *et al*., Regulation of protein secretion through controlled aggregation in the endoplasmic reticulum. *Science* **287**, 826–830 (2000). doi: 10.1126/science.287.5454.826; pmid: 10657290
41. M. Y. Pecot, V. Malhotra, Golgi membranes remain segregated from the endoplasmic reticulum during mitosis in mammalian cells. *Cell* **116**, 99–107 (2004). doi: 10.1016/S0092-8674(03)01068-7; pmid: 14718170
42. A. Y. Karpova, D. G. R. Tervo, N. W. Gray, K. Svoboda, Rapid and reversible chemical inactivation of synaptic transmission in genetically targeted neurons. *Neuron* **48**, 727–735 (2005). doi: 10.1016/j.neuron.2005.11.015; pmid: 16337911
43. R. M. Luik, B. Wang, M. Prakriya, M. M. Wu, R. S. Lewis, Oligomerization of STIM1 couples ER calcium depletion to CRAC channel activation. *Nature* **454**, 538–542 (2008). doi: 10.1038/nature07065; pmid: 18596693
44. J. H. Bayle *et al*., Rapamycin analogs with differential binding specificity permit orthogonal control of protein activity. *Chem. Biol.* **13**, 99–107 (2006). doi: 10.1016/j.chembiol.2005.10.017; pmid: 16426976
45. K. Stankunas *et al*., Conditional protein alleles using knockin mice and a chemical inducer of dimerization. *Mol. Cell* **12**, 1615–1624 (2003). doi: 10.1016/S1097-2765(03)00491-X; pmid: 14690613
46. H. D. Mootz, E. S. Blum, A. B. Tyszkiewicz, T. W. Muir, Conditional protein splicing: A new tool to control protein structure and function in vitro and in vivo. *J. Am. Chem. Soc.* **125**, 10561–10569 (2003). doi: 10.1021/ja0362813; pmid: 12940738
47. E. R. Ballister, C. Aonbangkhen, A. M. Mayo, M. A. Lampson, D. M. Chenoweth, Localized light-induced protein dimerization in living cells using a photocaged dimerizer. *Nat. Commun.* **5**, 5475 (2014). doi: 10.1038/ncomms6475; pmid: 25400104
48. S. J. Kopytek, R. F. Standaert, J. C. Dyer, J. C. Hu, Chemically induced dimerization of dihydrofolate reductase by a homobifunctional dimer of methotrexate. *Chem. Biol.* **7**, 313–321 (2000). doi: 10.1016/S1074-5521(00)00109-5; pmid: 10801470
49. K. J. Liu, J. R. Arron, K. Stankunas, G. R. Crabtree, M. T. Longaker, Chemical rescue of cleft palate and midline defects in conditional GSK-3β mice. *Nature* **446**, 79–82 (2007). doi: 10.1038/nature05557; pmid: 17293880
50. K. Nishimura, T. Fukagawa, H. Takisawa, T. Kakimoto, M. Kanemaki, An auxin-based degron system for the rapid depletion of proteins in nonplant cells. *Nat. Methods* **6**, 917–922 (2009). doi: 10.1038/nmeth.1401; pmid: 19915560
51. X. Tan *et al*., Mechanism of auxin perception by the TIR1 ubiquitin ligase. *Nature* **446**, 640–645 (2007). doi: 10.1038/nature05731; pmid: 17410169
52. M. Morawska, H. D. Ulrich, An expanded tool kit for the auxin-inducible degron system in budding yeast. *Yeast* **30**, 341–351 (2013). doi: 10.1002/yea.2967; pmid: 23836714
53. M. A. Ko *et al*., Plk4 haploinsufficiency causes mitotic infidelity and carcinogenesis. *Nat. Genet.* **37**, 883–888 (2005). doi: 10.1038/ng1605; pmid: 16025114
54. C. O. Rosario *et al*., A novel role for Plk4 in regulating cell spreading and motility. *Oncogene* **34**, 3441–3451 (2015). doi: 10.1038/onc.2014.275; pmid: 25174401
55. A. J. Holland, D. Fachinetti, J. S. Han, D. W. Cleveland, Inducible, reversible system for the rapid and complete degradation of proteins in mammalian cells. *Proc. Natl. Acad. Sci. U.S.A.* **109**, E3350–E3357 (2012). doi: 10.1073/pnas.1216880109; pmid: 23150568
56. B. G. Lambrus *et al*., p53 protects against genome instability following centriole duplication failure. *J. Cell Biol.* **210**, 63–77 (2015). doi: 10.1083/jcb.201502089; pmid: 26150389
57. M. Kanke *et al*., Auxin-inducible protein depletion system in fission yeast. *BMC Cell Biol.* **12**, 8 (2011). doi: 10.1186/1471-2121-12-8; pmid: 21314938
58. L. Zhang, J. D. Ward, Z. Cheng, A. F. Dernburg, The auxin-inducible degradation (AID) system enables versatile conditional protein depletion in *C. elegans*. *Development* **142**, 4374–4384 (2015). doi: 10.1242/dev.129635; pmid: 26552885
59. T. Natsume, T. Kiyomitsu, Y. Saga, M. T. Kanemaki, Rapid protein depletion in human cells by auxin-inducible degron tagging with short homology donors. *Cell Reports* **15**, 210–218 (2016). doi: 10.1016/j.celrep.2016.03.001; pmid: 27052166
60. E. P. Nora *et al*., Targeted degradation of CTCF decouples local insulation of chromosome domains from genomic compartmentalization. *Cell* **169**, 930–944.e22 (2017). doi: 10.1016/j.cell.2017.05.004; pmid: 28525758
61. H. D. Ou *et al*., ChromEMT: Visualizing 3D chromatin structure and compaction in interphase and mitotic cells. *Science* **357**, eaag0025 (2017). doi: 10.1126/science.aag0025; pmid: 28751582
62. N. A. Hathaway *et al*., Dynamics and memory of heterochromatin in living cells. *Cell* **149**, 1447–1460 (2012). doi: 10.1016/j.cell.2012.03.052; pmid: 22704655
63. C. Hodges, G. R. Crabtree, Dynamics of inherently bounded histone modification domains. *Proc. Natl. Acad. Sci. U.S.A.*

109, 13296–13301 (2012). doi: 10.1073/pnas.1211172109; pmid: 22847427

64. J. A. Kennison, J. W. Tamkun, Dosage-dependent modifiers of polycomb and antennapedia mutations in *Drosophila*. *Proc. Natl. Acad. Sci. U.S.A.* **85**, 8136–8140 (1988). doi: 10.1073/pnas.85.21.8136; pmid: 3141923
65. C. Kadoch *et al*., Dynamics of BAF-Polycomb complex opposition on heterochromatin in normal and oncogenic states. *Nat. Genet.* **49**, 213–222 (2017). doi: 10.1038/ng.3734; pmid: 27941796
66. B. Z. Stanton *et al*., *Smarca4* ATPase mutations disrupt direct eviction of PRC1 from chromatin. *Nat. Genet.* **49**, 282–288 (2017). doi: 10.1038/ng.3735; pmid: 27941795
67. S. L. Morgan *et al*., Manipulation of nuclear architecture through CRISPR-mediated chromosomal looping. *Nat. Commun.* **8**, 15993 (2017). doi: 10.1038/ncomms15993; pmid: 28703221
68. E. C. Dykhuizen *et al*., BAF complexes facilitate decatenation of DNA by topoisomerase IIα. *Nature* **497**, 624–627 (2013). doi: 10.1038/nature12146; pmid: 23698369
69. E. L. Miller *et al*., TOP2 synergizes with BAF chromatin remodeling for both resolution and formation of facultative heterochromatin. *Nat. Struct. Mol. Biol.* **24**, 344–352 (2017). doi: 10.1038/nsmb.3384; pmid: 28250416
70. S. Gruber *et al*., Evidence that loading of cohesin onto chromosomes involves opening of its SMC hinge. *Cell* **127**, 523–537 (2006). doi: 10.1016/j.cell.2006.08.048; pmid: 17081975
71. J. E. Gestwicki, G. R. Crabtree, I. A. Graef, Harnessing chaperones to generate small-molecule inhibitors of amyloid β aggregation. *Science* **306**, 865–869 (2004). doi: 10.1126/science.1101262; pmid: 15514157
72. P. S. Marinec *et al*., FK506-binding protein (FKBP) partitions a modified HIV protease inhibitor into blood cells and prolongs its lifetime in vivo. *Proc. Natl. Acad. Sci. U.S.A.* **106**, 1336–1341 (2009). doi: 10.1073/pnas.0805375106; pmid: 19164520
73. S. C. Penchala *et al*., AG10 inhibits amyloidogenesis and cellular toxicity of the familial amyloid cardiomyopathy-associated V122I transthyretin. *Proc. Natl. Acad. Sci. U.S.A.* **110**, 9992–9997 (2013). doi: 10.1073/pnas.1300761110; pmid: 23716704
74. T. Ito *et al*., Identification of a primary target of thalidomide teratogenicity. *Science* **327**, 1345–1350 (2010). doi: 10.1126/science.1177319; pmid: 20223979
75. E. S. Fischer *et al*., Structure of the DDB1-CRBN E3 ubiquitin ligase in complex with thalidomide. *Nature* **512**, 49–53 (2014). doi: 10.1038/nature13527; pmid: 25043012
76. P. Filippakopoulos *et al*., Selective inhibition of BET bromodomains. *Nature* **468**, 1067–1073 (2010). doi: 10.1038/nature09504; pmid: 20871596
77. G. E. Winter *et al*., Phthalimide conjugation as a strategy for in vivo target protein degradation. *Science* **348**, 1376–1381 (2015). doi: 10.1126/science.aab1433; pmid: 25999370
78. J. Lu *et al*., Hijacking the E3 ubiquitin ligase cereblon to efficiently target BRD4. *Chem. Biol.* **22**, 755–763 (2015). doi: 10.1016/j.chembiol.2015.05.009; pmid: 26051217
79. D. P. Bondeson *et al*., Catalytic in vivo protein knockdown by small-molecule PROTACs. *Nat. Chem. Biol.* **11**, 611–617 (2015). doi: 10.1038/nchembio.1858; pmid: 26075522
80. M. A. Erb *et al*., Transcription control by the ENL YEATS domain in acute leukaemia. *Nature* **543**, 270–274 (2017). doi: 10.1038/nature21688; pmid: 28241139
81. J. E. Delmore *et al*., BET bromodomain inhibition as a therapeutic strategy to target c-Myc. *Cell* **146**, 904–917 (2011). doi: 10.1016/j.cell.2011.08.017; pmid: 21889194
82. C. J. Ott *et al*., BET bromodomain inhibition targets both c-Myc and IL7R in high-risk acute lymphoblastic leukemia. *Blood* **120**, 2843–2852 (2012). doi: 10.1182/blood-2012-02-413021; pmid: 22904298
83. D. L. Buckley *et al*., Targeting the von Hippel–Lindau E3 ubiquitin ligase using small molecules to disrupt the VHL/HIF-1α interaction. *J. Am. Chem. Soc.* **134**, 4465–4468 (2012). doi: 10.1021/ja209924v; pmid: 22369643
84. D. L. Buckley *et al*., HaloPROTACS: Use of small molecule PROTACs to induce degradation of HaloTag fusion proteins. *ACS Chem. Biol.* **10**, 1831–1837 (2015). doi: 10.1021/acschembio.5b00442; pmid: 26070106
85. A. C. Lai *et al*., Modular PROTAC design for the degradation of oncogenic BCR-ABL. *Angew. Chem.* **55**, 807–810 (2016). doi: 10.1002/anie.201507634; pmid: 26593377
86. A. Hamilton *et al*., Chronic myeloid leukemia stem cells are not dependent on Bcr-Abl kinase activity for their survival. *Blood* **119**, 1501–1510 (2012). doi: 10.1182/blood-2010-12-326843; pmid: 22184410
87. V. M. Rivera *et al*., Long-term pharmacologically regulated expression of erythropoietin in primates following AAV-mediated gene transfer. *Blood* **105**, 1424–1430 (2005). doi: 10.1182/blood-2004-06-2501; pmid: 15507527
88. V. M. Rivera *et al*., A humanized system for pharmacologic control of gene expression. *Nat. Med.* **2**, 1028–1032 (1996). doi: 10.1038/nm0996-1028; pmid: 8782462
89. X. Ye *et al*., Regulated delivery of therapeutic proteins after in vivo somatic cell gene transfer. *Science* **283**, 88–91 (1999). doi: 10.1126/science.283.5398.88; pmid: 9872748
90. D. M. Spencer *et al*., Functional analysis of Fas signaling in vivo using synthetic inducers of dimerization. *Curr. Biol.* **6**, 839–847 (1996). doi: 10.1016/S0960-9822(02)00607-3; pmid: 8805308
91. R. A. MacCorkle, K. W. Freeman, D. M. Spencer, Synthetic activation of caspases: Artificial death switches. *Proc. Natl. Acad. Sci. U.S.A.* **95**, 3655–3660 (1998). doi: 10.1073/pnas.95.7.3655; pmid: 9520421
92. L. Fan, K. W. Freeman, T. Khan, E. Pham, D. M. Spencer, Improved artificial death switches based on caspases and FADD. *Hum. Gene Ther.* **10**, 2273–2285 (1999). doi: 10.1089/10430349950016924; pmid: 10515447
93. U. B. Pajvani *et al*., Fat apoptosis through targeted activation of caspase 8: A new mouse model of inducible and reversible lipoatrophy. *Nat. Med.* **11**, 797–803 (2005). doi: 10.1038/nm1262; pmid: 15965483
94. D. J. Baker *et al*., Clearance of p16Ink4a-positive senescent cells delays ageing-associated disorders. *Nature* **479**, 232–236 (2011). doi: 10.1038/nature10600; pmid: 22048312
95. D. J. Baker *et al*., Naturally occurring $p16^{Ink4a}$-positive cells shorten healthy lifespan. *Nature* **530**, 184–189 (2016). doi: 10.1038/nature16932; pmid: 26840489
96. A. Di Stasi *et al*., Inducible apoptosis as a safety switch for adoptive cell therapy. *N. Engl. J. Med.* **365**, 1673–1683 (2011). doi: 10.1056/NEJMoa1106152; pmid: 22047558
97. T. Clackson *et al*., Redesigning an FKBP-ligand interface to generate chemical dimerizers with novel specificity. *Proc. Natl. Acad. Sci. U.S.A.* **95**, 10437–10442 (1998). doi: 10.1073/pnas.95.18.10437; pmid: 9724721
98. X. Zhou *et al*., Inducible caspase-9 suicide gene controls adverse effects from alloreplete T cells after haploidentical stem cell transplantation. *Blood* **125**, 4103–4113 (2015). doi: 10.1182/blood-2015-02-628354; pmid: 25977584
99. X. Zhou *et al*., Long-term outcome after haploidentical stem cell transplant and infusion of T cells expressing the inducible caspase 9 safety transgene. *Blood* **123**, 3895–3905 (2014). doi: 10.1182/blood-2014-01-551671; pmid: 24753538
100. J. N. Kochenderfer, S. A. Rosenberg, Treating B-cell cancer with T cells expressing anti-CD19 chimeric antigen receptors. *Nat. Rev. Clin. Oncol.* **10**, 267–276 (2013). doi: 10.1038/nrclinonc.2013.46; pmid: 23546520
101. C. R. Cruz *et al*., Infusion of donor-derived CD19-redirected virus-specific T cells for B-cell malignancies relapsed after allogeneic stem cell transplant: A phase 1 study. *Blood* **122**, 2965–2973 (2013). doi: 10.1182/blood-2013-06-506741; pmid: 24030379
102. I. Diaconu *et al*., Inducible caspase-9 selectively modulates the toxicities of CD19-specific chimeric antigen receptor-modified T cells. *Mol. Ther.* **25**, 580–592 (2017). doi: 10.1016/j.ymthe.2017.01.011; pmid: 28187946

ACKNOWLEDGMENTS

We apologize to the many people who have made important contributions to this field whom we were unable to acknowledge because of space constraints. We wish to honor the lasting memory of Joseph P. Calarco, who was a great friend and incisive colleague. E.J.C. was supported by an NSF Graduate Research Fellowship and the Ruth L. Kirschstein National Research Service Award (F31 CA203228-02). G.R.C. active-research funding includes support from the Howard Hughes Medical Institute, NIH 5R01CA163915-04, the NIH Javits Neuroscience Investigator Award R37 NS046789-12, the Congressionally Directed Medical Research Program Breast Cancer Research Breakthrough Award, and the Simons Foundation Autism Research Initiative. The authors declare no competing interests. G.R.C. is an inventor on several patents and patent applications related to chemical inducers of proximity and the uses thereof, filed between 1997 and 2017. These include patent applications WO2017074943A1, WO2013188406A1, US20130158098A1, and WO2002024957A1 submitted by The Board of Trustees of Leland Stanford Junior University, applications US20110160246A1 and US20110003385A1 submitted by G.R.C., patent application US20020173474A1 submitted by the President and Fellows of Harvard College. Patents US8084596B2, US6984635B1, and US6063625A are held by The Board of Trustees of Leland Stanford Junior University and the President and Fellows of Harvard College.

10.1126/science.aao5902

RESEARCH ARTICLE

STEM CELLS

Single-cell Wnt signaling niches maintain stemness of alveolar type 2 cells

Ahmad N. Nabhan,[1,2] Douglas G. Brownfield,[1,2] Pehr B. Harbury,[1] Mark A. Krasnow,[1,2]* Tushar J. Desai[3]*

Alveoli, the lung's respiratory units, are tiny sacs where oxygen enters the bloodstream. They are lined by flat alveolar type 1 (AT1) cells, which mediate gas exchange, and AT2 cells, which secrete surfactant. Rare AT2s also function as alveolar stem cells. We show that AT2 lung stem cells display active Wnt signaling, and many of them are near single, Wnt-expressing fibroblasts. Blocking Wnt secretion depletes these stem cells. Daughter cells leaving the Wnt niche transdifferentiate into AT1s: Maintaining Wnt signaling prevents transdifferentiation, whereas abrogating Wnt signaling promotes it. Injury induces AT2 autocrine Wnts, recruiting "bulk" AT2s as progenitors. Thus, individual AT2 stem cells reside in single-cell fibroblast niches providing juxtacrine Wnts that maintain them, whereas injury induces autocrine Wnts that transiently expand the progenitor pool. This simple niche maintains the gas exchange surface and is coopted in cancer.

Although there has been great progress identifying tissue stem cells, much less is known about their niches and how niche signals control stem cell function and influence daughter cell fate (*1*, *2*). The best understood examples come from genetic systems (*3*) such as the *Drosophila* testis niche, where 10 to 15 cells ("the hub") provide three short-range signals to the 5 to 10 stem cells they contact (*4*). These signals promote stem cell adhesion to the niche and inhibit differentiation, but after polarized division, a daughter cell leaves the niche, escaping the inhibitory signals and initiating sperm differentiation. In mammalian systems, stem cells and their niches are typically more complex, with more cells and more complex cell dynamics. Even in the best-studied tissues (*5*–*8*), there is incomplete understanding of niche cells, signals, and the specific aspects of stem cell behavior each signal controls. Here, we describe an exquisitely simple stem cell niche and control program that maintains the lung's gas exchange surface.

Mouse genetic studies have identified a hierarchy of stem cells that replenish the alveolar surface (*9*), some of which are active only after massive injury (*10*, *11*). Normally, the epithelium is maintained by rare "bifunctional" alveolar type 2 (AT2) cells, cuboidal epithelial cells that retain the surfactant biosynthetic function of standard ("bulk") AT2 cells (*12*) but also serve as stem cells (*13*, *14*). Their intermittent activation gives rise to AT1 cells—exquisitely thin epithelial cells that mediate gas exchange—and generates slowly expanding clonal "renewal foci" that together create ~7% new alveoli per year (*13*). Dying cells are proposed to provide a mitogenic signal transduced by the epidermal growth factor receptor (EGFR)–KRAS pathway that triggers stem cell division (*13*). However, it is unclear how stem cells are selected from bulk AT2 cells, how they are maintained, and how the fate of daughter cells—stem cell renewal versus reprogramming to AT1 identity—is controlled.

Here, we molecularly identify alveolar stem cells as a rare subpopulation of AT2 cells with constitutive Wnt pathway activity and show that a single fibroblast near each stem cell comprises a Wnt signaling niche that maintains the stem cell and controls daughter cell fate. Severe injury recruits ancillary stem cells by transiently inducing autocrine Wnt signaling in "bulk" AT2 cells.

Results

Wnt pathway gene Axin2 *is expressed in a rare subpopulation of AT2 cells*

Canonical Wnt signaling activity marks stem cells in various tissues (*8*), and the Wnt pathway is active in developing alveolar progenitors (*15*–*17*). To determine whether AT2 cells in adult mice show Wnt activity, we examined expression of Wnt target *Axin2* (*18*) using an *Axin2-Cre-ERT2* knock-in allele crossed to Cre reporter *Rosa26mTmG*. After three daily tamoxifen injections to induce Cre-ERT2 at age 2 months, fluorescence-activated cell sorting (FACS) showed 1% of purified AT2 cells expressed the green fluorescent protein (GFP) reporter (Fig. 1D). Immunostaining for GFP and canonical AT2 marker SftpC showed labeled AT2 cells distributed sporadically throughout the alveolar region (Fig. 1, A to C). Multiplexed single-molecule fluorescence in situ hybridization [proximity ligation in situ hybridization (PLISH) (*19*)] confirmed a distributed population of *Axin2*-expressing AT2 cells (fig. S1). Axin2$^+$ AT2 cells represent a stable subpopulation because the percentage of labeled AT2 cells did not increase when tamoxifen injections were repeated 1 and 2 weeks after the initial induction, and the percentage was similar among animals induced at different ages (Fig. 1G). This subpopulation expressed all AT2 markers, including surfactant proteins and lipids (fig. S2), suggesting that the cells are physiologically functional. No AT1 or airway epithelial cells were marked under these "pulse-labeling" conditions (>1000 AT1 cells scored in each of three mice), although other (nonepithelial) alveolar cells were. Thus, Axin2$^+$ AT2 cells represent a rare, stable subpopulation of mature AT2 cells.

Axin2$^+$ AT2 cells have alveolar stem cell activity

The fate of the labeled AT2 cells was examined a half or 1 year later (half or full year "chase") (Fig. 1, E to I). Labeled cells exhibited three features of stem cells. First, unlike most AT2 cells, which are quiescent (*20*), 79% of Axin2$^+$ AT2 cells generated small clones of labeled cells (Fig. 1, H to J). Daughter cells remained local (Fig. 1I), with some found as doublets (fig. S3B), indicating recent division; on occasion, an Axin2$^+$ AT2 cell was seen dividing (fig. S3A), an intermediate that we never observed for bulk AT2 cells in normal lungs. Second, lineage-labeled AT2 cells expanded sixfold relative to unlabeled cells during a 1-year chase (Fig. 1G). Third, labeled cells gave rise to another alveolar cell type, shown by appearance of AT1 cells expressing the lineage label (Fig. 1F). Like AT2 daughter cells, daughter AT1 cells were typically found in close association with the presumed founder Axin2$^+$ AT2 cell. Thus, Axin2$^+$ cells constitute a rare AT2 subpopulation with stem cell activity, which slowly (about once every 4 months) self-renew and produce new AT2 and AT1 cells.

Fibroblasts provide short-range Wnt signals to neighboring AT2 stem cells

Wnts are local signals with a typical range of just one or two cells (*21*). Fibroblasts were an excellent candidate for the Wnt source because some contact AT2 cells (*22*), such as Pdgfrα-expressing fibroblasts that support surfactant production and formation of alveolospheres in culture (*14*, *23*, *24*). Transmembrane protein Porcupine, which acylates and promotes secretion of Wnts (*25*) and marks Wnt signaling centers (*26*), was expressed in rare alveolar stromal cells (fig. S4A), most of which were

---

[1]Department of Biochemistry, Stanford University School of Medicine, Stanford, CA 94305-5307, USA. [2]Howard Hughes Medical Institute, Stanford University School of Medicine, Stanford, CA 94305-5307, USA. [3]Department of Internal Medicine, Division of Pulmonary and Critical Care, and Institute for Stem Cell Biology and Regenerative Medicine, Stanford University School of Medicine, Stanford, CA 94305-5307, USA.
*Corresponding author. Email: tdesai@stanford.edu (T.J.D.); krasnow@stanford.edu (M.A.K.)

Pdgfrα-expressing fibroblasts (fig. S4C) and some were closely associated with AT2 cells (fig. S4B). Serial dosing of Porcupine Porcn inhibitor C59 reduced the pool of Axin2^{+} AT2 cells by 68% (Fig. 2A). Targeted deletion in lung mesenchyme (by using *Tbx4*^{LME}*-Cre*) or fibroblasts (*Pdgfrα-Cre-ER*) of *Wntless*, another transmembrane protein required for Wnt secretion (27), also reduced the pool (Fig. 2, B and C). The remaining Axin2^{+} AT2 cells could be due to incomplete deletion or perdurance of *Wntless* in PDGFRα^{+} fibroblasts or to another Wnt source.

Single-cell RNA sequencing (scRNA-seq) of alveolar fibroblasts revealed a subset expressing *Wnt5a*, most of which (74%) also expressed *Pdgfra* (Fig. 2D). Many *Wnt5a*$^{+}$ fibroblasts also expressed low levels of one or two other *Wnts*—including *Wnt2*, *Wnt2b*, *Wnt4*, and *Wnt9a*—as did other smaller subpopulations of fibroblasts (Fig. 2D). AT2 cells did not express *Porcupine* (fig. S4) or any *Wnt* genes (fig. S5) under normal conditions. *Wnt5a*-expressing fibroblasts (fig. S6) were scattered throughout the alveolar region, most near an Axin2^{+} AT2 cell (Fig. 2, E to H). Although Wnt5a is sufficient to induce *Axin2* in AT2 cells (Fig. 2H), it is not the only Wnt operative in vivo because others can also induce *Axin2* (Fig. 2I), and deletion of *Wnt5a* with *Tbx4*^{LME}*-Cre* reduced Axin2^{+} AT2 cells in vivo by 15%, and the effect did not reach significance ($P = 0.12$). We conclude that *Wnt5a* and other Wnts expressed by the fibroblasts activate the canonical Wnt pathway in neighboring AT2 cells. This signal is short range because AT1 cells derived from Axin2^{+} AT2 cells do not express *Axin2* ($n > 1000$ cells scored in three lungs at age 4 months), implying that they do not maintain *Axin2* expression once they move away from the Wnt source. Some *Wnt*-expressing fibroblasts themselves expressed *Axin2* (Fig. 2D and fig. S6), suggesting that they can also provide an autocrine signal.

Wnt signaling prevents reprogramming of alveolar stem cells into AT1 cells

To investigate the function of Wnt signaling, we deleted β-*catenin*, a transducer of canonical Wnt pathway activity, in mature AT2 cells by using *Lyz2-Cre* or *SftpC-CreERT2* while simultaneously marking recombined cells by using *Rosa26mTmG*. We reasoned that only cells with active Wnt signaling (Axin2^{+} AT2 cells) would be affected. The number of AT1 cells expressing the AT2 lineage mark tripled, while preserving the percentage of lineage-labeled AT2 cells (85 ± 3% of AT2 cells versus 82 ± 3% in wild-type β-*catenin* controls, $n = 500$ AT2 scored in three biological replicates) and alveolar structure (Fig. 3, A, B, and D; and fig. S7, A, B, and D). Of the AT2-lineage-marked AT1 cells in this experiment (48 of 172 scored cells in three animals), 27% were not physically associated with a marked founder AT2 cell (Fig. 3, E and F), implying that the stem cell had directly converted into an AT1 cell, which was rare in control lungs (4%; $n = 145$ scored cells in three biological replicates). Thus, abrogation of constitutive Wnt signaling promotes transdifferentiation of Axin2^{+} AT2 cells into AT1 cells.

We also prevented AT2 cells from downregulating Wnt signaling by expressing a stabilized

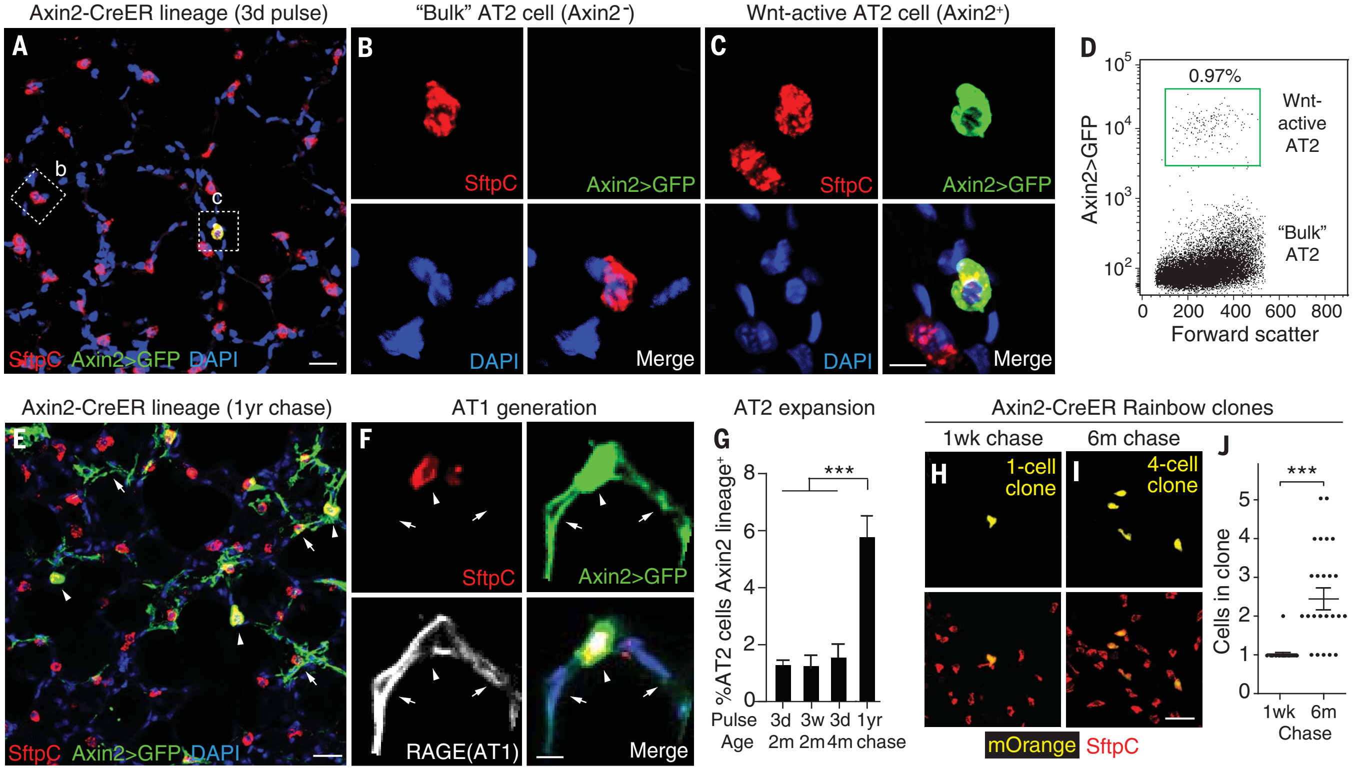

Fig. 1. *Axin2* marks rare AT2 cells with stem cell activity. (**A** to **C**) Alveoli of adult (2 months) *Axin2-CreERT2;Rosa26mTmG* mouse lung immunostained for Cre reporter mGFP (membrane-bound form of GFP), AT2 marker pro-surfactant protein C (SftpC), and 4′,6-diamidino-2-phenylindole (DAPI) 5 days after three daily injections of 3 mg tamoxifen (3-day pulse) to lineage-label *Axin2*-expressing (Axin2^{+}) cells (Axin2>GFP). Close-ups show (B) Axin2^{-} bulk AT2 cell and (C) rare Axin2^{+} AT2, indicating Wnt pathway activation. (**D**) FACS of AT2 cells in (A) to (C) shows 1.0 ± 0.5% ($n = 3$ biological replicates) express Axin2>GFP. (**E**) Alveoli labeled as in (A) to (C), harvested 1 year later (1-year chase). There are increased Axin2-lineage AT2 cells (arrowheads) and labeled AT1 cells and fibroblasts (arrows), the latter from another Axin2^{+} lineage. (**F**) Close-up of lung as in (E), showing Axin2^{+} lineage-labeled AT1 cells (arrows). RAGE, AT1 membrane marker; arrowhead, AT2 cell. (**G**) Quantification of Axin2-lineage labeled AT2 cells immediately after 3-day or 3-week pulse (3-day pulse each week) at age 2 months, 3-day pulse at 4 months, or after 3-day pulse at 2 months plus 1-year chase. Mean ± SD ($n = 3500$ AT2 cells scored in two to four biological replicates). (**H** and **I**) Alveoli of *Axin2-CreERT2;Rosa26Rainbow* mice given limiting dose of tamoxifen (2 mg) at 2 months to sparsely label Axin2^{+} cells (H) with different fluorescent clone markers [mOrange in (H) and (I)], and immunostained for SftpC 1 week (H) or 6 months (I) later to detect AT2 clones. (**J**) Quantification of AT2 clone sizes 1 week and 6 months after labeling. ***$P < 0.001$ (Student's *t* test). Scale bars, 25 μm (A) and (E); 5μm (C) and (F); and 20 μm (I).

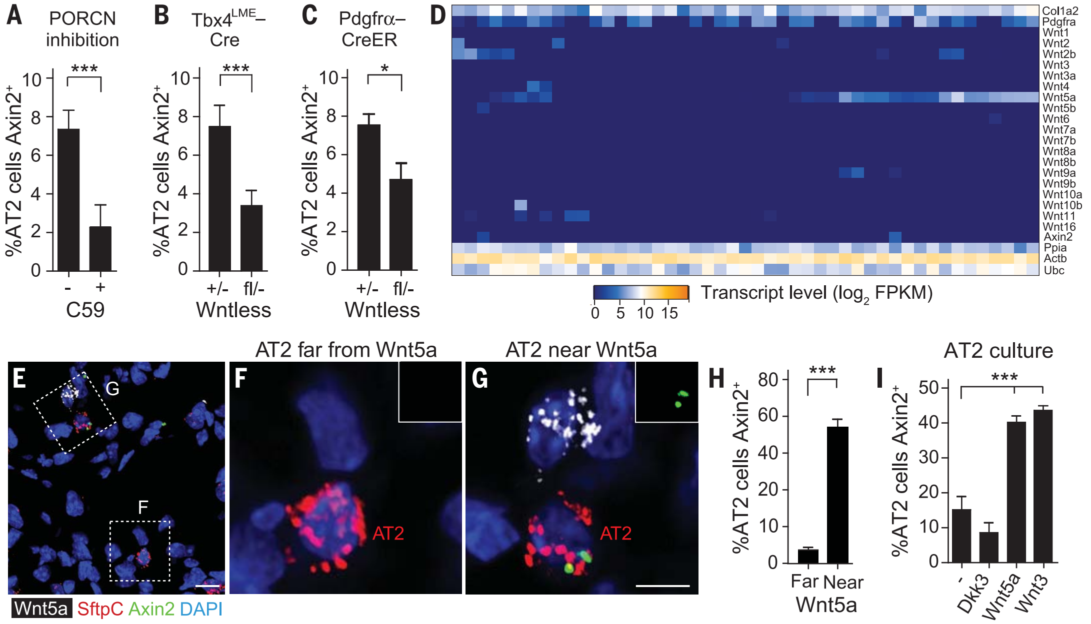

Fig. 2. Single, Wnt-secreting fibroblasts comprise the stem cell niche. (**A**) Effect of five daily doses of Wnt secretion [Porcupine (PORCN)] inhibitor C59 (+) or vehicle control (–) on *Axin2* expression in AT2 cells at age 2 months, measured with PLISH for *Axin2* and *Sftpc*. Mean ± SD (n = 900 AT2 cells scored in three biological replicates). ***P = 0.001 (Student's t test). (**B** and **C**) Effect on *Axin2*-expresssion in AT2 cells of inhibiting fibroblast Wnt secretion by deleting *Wntless* with (B) *Tbx4*^{LME}*-Cre* or (C) *Pdgfrα-CreERT2* induced with 3 mg tamoxifen 3 days before analysis. *P = 0.02; ***P = 0.003 (Student's t test). (**D**) Expression of Wnts, fibroblast markers (*Pdgfrα* and *Col1a2*), *Axin2*, and ubiquitous controls (*Ubc*, *Ppia*, and *Actb*) in 47 alveolar fibroblasts (columns) from B6 adult lungs analyzed by means of scRNA-seq. (**E**) *Wnt5a*, *Axin2*, and *SftpC* mRNA detected with PLISH of adult (2 months) alveoli. Blue, DAPI. Shown is a rare *Wnt5a*-expressing cell (dotted box "g"). (**F** and **G**) Close-ups showing AT2 cells (F) far from or (G) near a *Wnt5a*-expressing cell. (Insets) *Axin2* channel of AT2 cell. AT2 near *Wnt5a* source expresses *Axin2*. (**H**) Quantification showing percent (mean ± SD) of AT2 cells, located far (>15 μm, n = 132 cells from three biological replicates) or near (<15 μm, n = 150 cells) a *Wnt5a* source, that express *Axin2*. ***P < 0.0001 (Student's t test). (**I**) *Axin2* expression in AT2 cells isolated from adult *Axin2-lacZ* mice and cultured (5 days) with indicated Wnts at 0.1 μg/mL or antagonist Dickkopf 3 at 1 μg/mL, then assayed (Spider-gal) for LacZ. ***P < 0.0001 (Student's t test). Scale bars, 10 μm (E) and 5 μm (G).

β-catenin (*β-catenin*^{Ex3}). This did not induce proliferation (fig. S8) or other obvious effects on AT2 cells but reduced lineage-marked AT1 cells 63% (Fig. 3, C and D, and fig. S7, C and D).

Under culture conditions that maintain AT2 identity (*28*), Wnt antagonist Dickkopf 3 (*29*) increased the percentage of cells that reprogrammed to AT1 fate 3.8-fold (2.5 ± 1.5% versus 9.5 ± 0.1%) (Fig. 3, G and H). Conversely, under conditions that promote differentiation to AT1 fate (*28*), Wnt5a inhibited this transdifferentiation 2.6-fold (21 ± 1% versus 8 ± 1%) (Fig. 3I). CHIR99021, a pharmacological activator of canonical Wnt signaling, had a similar effect (Fig. 3I).

Thus, canonical Wnt signaling maintains the AT2 stem cell pool by preventing their reprogramming to AT1 identity, both in vivo and in vitro. Although Wnt signaling alone had little effect on AT2 proliferation (Fig. 3, J and K, and fig. S8), it enhanced EGF's mitogenic activity (Fig. 3, J and K).

Wnt signaling is induced in "ancillary" AT2 stem cells after epithelial injury

To investigate stem cell activity after injury, we established a genetic system (*30*) to ablate alveolar epithelial cells. Diphtheria toxin receptor was expressed throughout the lung epithelium of adult mice by using *Shh-Cre*. Diphtheria toxin (DT) (150 ng) triggered apoptosis in ~40% of alveolar epithelial cells (fig. S9, A and B) but spared enough for repair (fig. S9C) and survival. Nearly all remaining AT2 cells (85%) began proliferating after injury (Fig. 4, A and C), indicating that bulk AT2 cells are recruited as ancillary progenitors during repair; similar recruitment of bulk AT2 cells was observed after hyperoxic injury (see below) (*31*, *32*). Most AT2 cells (73%) expressed *Axin2* after DT-triggered injury, indicating that canonical Wnt signaling is broadly induced in ancillary stem cells (Fig. 4, B and C, and fig. S10C). Inhibition of Wnt signaling with C59 abrogated AT2 proliferation and blocked repair (Fig. 4C and fig. S9D). Thus, Wnt signaling recruits ancillary AT2 cells with progenitor capacity after severe injury.

Injury induces autocrine signaling in AT2 cells

There was no change in *Wnt5a* expression (fig. S10C) or stromal expression of Porcupine (fig. S11, A and B) after DT-triggered injury. By contrast, Porcupine was broadly induced in AT2 cells (figs. S10C and S11, A to C), suggesting that injury activates autocrine Wnt secretion. We found *Wnt7b*, expressed in alveolar progenitors during development (*16*) but not healthy adult AT2 cells (fig. S5), was broadly induced in AT2 cells after DT-triggered injury (Fig. 4, D and E). AT2 expression of *Wnt7b* and Porcupine and activation of canonical Wnt signaling were induced within 24 hours of injury (Fig. 4, D and E, and fig. S10C). AT2 proliferation initiated over the next 2 days, peaking at day 5 as epithelial integrity was restored, after which AT2 proliferation and gene expression returned toward baseline and new AT1 cells appeared (fig. S10, B and C).

To explore the generality of injury-induced autocrine Wnt signaling, we used hyperoxic injury (75% oxygen) to induce alveolar repair (fig. S12A) (*31*). This allowed us to mark and genetically manipulate alveolar cells through endotracheal delivery of an adeno-associated virus encoding Cre (AAV9-Cre) into lungs of mice carrying a Cre-dependent reporter and conditional Wnt pathway alleles. Quantitative polymerase chain reaction (PCR) analysis of FACS-purified, lineage-labeled AT2 cells (fig. S12, B and C) showed hyperoxic injury induced AT2 expression of *Wnt7b* and six other *Wnt* genes by 3- to 12-fold and similarly induced *Axin2* (fivefold) and *Lef1* (sevenfold), indicating autocrine activation of the canonical Wnt pathway (Fig. 5A). The suite of induced Wnts did not include most Wnts expressed by the fibroblast niche, including *Wnt5a* (Fig. 5A). AAV9-Cre–mediated mosaic deletion of *Wntless* in ~50% of alveolar epithelial cells (fig. S12, D to F) decreased AT2 proliferation after injury (Fig. 5, B and C). The effect was cell-autonomous because AT2 cells expressing Cre-GFP, but not neighboring AT2 cells, showed diminished proliferation (Fig. 5, B and C). This autocrine effect is mediated by multiple Wnts because deletion of just one induced Wnt (*Wnt7b*) did not diminish proliferation. Thus, epithelial injury induces AT2 expression of a suite of autocrine Wnts, which transiently endow bulk AT2 cells with progenitor function and proliferative capacity.

Discussion

We molecularly identified a rare subset of AT2 cells with stem cell function (AT2^{stem}) scattered

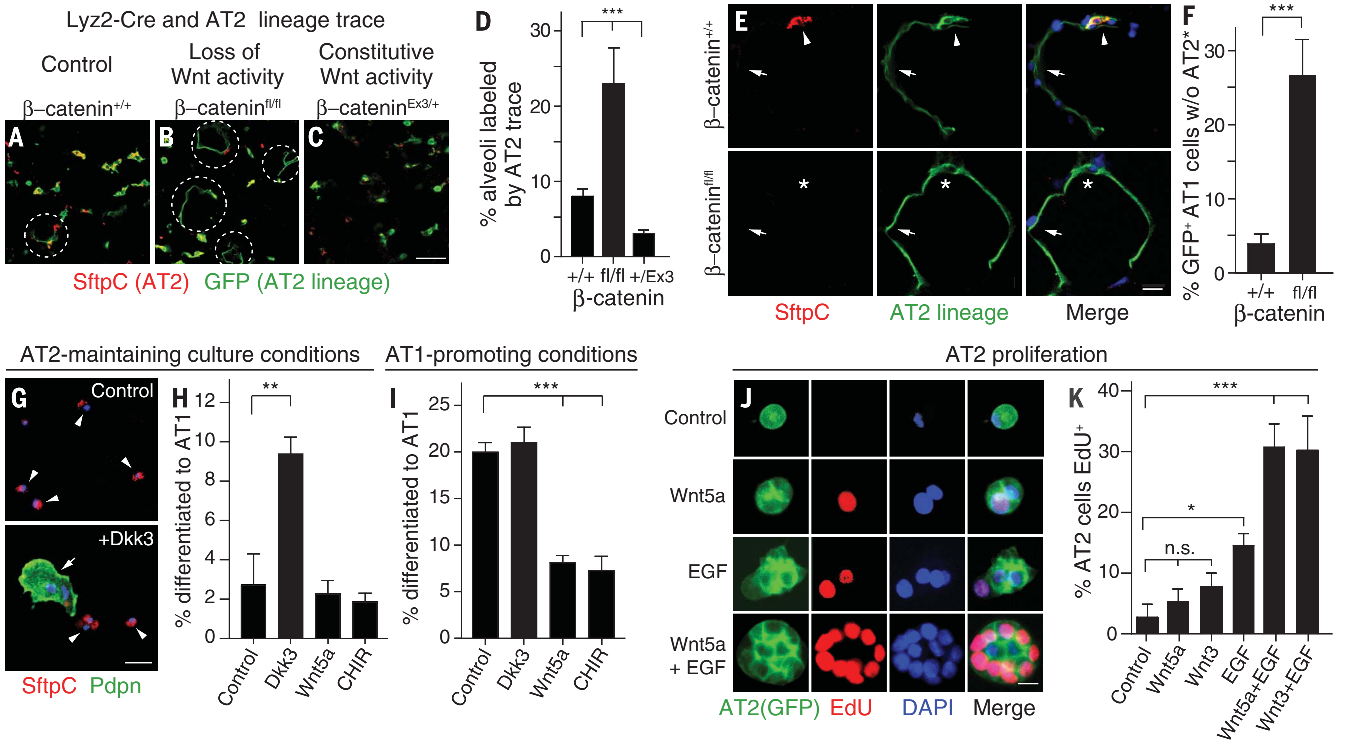

Fig. 3. Wnt signaling prevents reprogramming to AT1 fate. (**A** to **C**) Alveoli of adult (8 months) (A) *Lyz2-Cre;Rosa26mTmG*, (B) *Lyz2-Cre; Rosa26mTmG* β*-catenin*$^{fl/fl}$ and (C) *Lyz2-Cre;Rosa26mTmG;*β*-catenin*$^{Ex3/+}$ mice immunostained for SftpC and Lyz2-Cre (AT2) lineage trace (mGFP). Dashed circles indicate alveolar renewal foci identified through squamous AT1 expressing AT2 lineage trace. Scale bar, 50 μm. (**D**) Quantification showing percent (mean ± SD) alveoli with AT2 lineage-labeled AT1 cells (n = 25 100-μm z-stacks scored in two or three biological replicates). ***P = 0.002 (Kruskal-Wallis test). (**E**) Close up of renewal foci as above in control (*Lyz2-Cre;*β*-catenin*$^{+/+}$, top) or β*-catenin* conditional deletion (*Lyz2-Cre;*β*-catenin*$^{fl/fl}$, bottom). Shown are AT1 (arrows) and its AT2 parent (arrowheads) in control, but absence of AT2 parent (asterisk) in β*-catenin* deletion, implying loss of stem cell by reprogramming to AT1 fate. (**F**) Quantification shows percent (mean ± SD) AT1 cells from AT2 lineage (GFP$^+$) lacking AT2 parent. ***P = 0.0004 (Student's t test). (**G** to **I**) AT2 cells from B6 adult mouse lungs cultured in Matrigel [AT2-maintaining conditions, (G) and (H)] or on poly-lysine–coated glass [AT1-promoting conditions (I)] without (control) or with indicated Wnt pathway antagonist (1 μg/ml Dkk3) or agonists (100 ng/ml Wnt5a or 10nM CHIR99201). After 4 days, cells were immunostained for SftpC and Podoplanin (Pdpn) (G), and percent (mean ± SD) of AT2 (cuboidal SftpC$^+$; arrowheads) and AT1 cells (large, squamous, Podoplanin$^+$; arrow) were quantified (n = 500 cells from three biological replicates) [(H) and (I)] **P = 0.002; ***P < 0.001 (Student's t test). (**J**) AT2 cells isolated from adult (2 months) *Sftpc-CreER;Rosa26mTmG* mice were cultured in Matrigel as above without (control) or with indicated Wnts (100 ng/ml) and EGF (50 ng/ml), then proliferation was assayed by means of EdU incorporation. (**K**) Quantification (n = 400 cells scored, four biological replicates). *P = 0.007; ***P < 0.001 (Student's t test). n.s., not significant. Scale bars, 50 μm (C) and (G), 10 μm (E), and 5 μm (J).

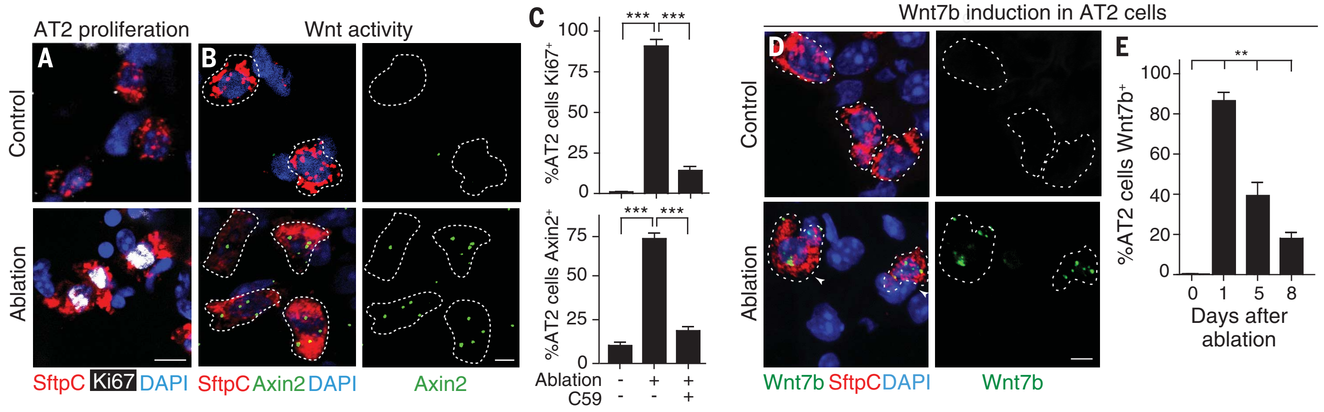

Fig. 4. Genetically targeted epithelial injury induces Wnt signaling and proliferation of bulk AT2 cells. (**A** and **B**) Alveoli of *Shh-Cre;Rosa26LSL-DTR* (Diphtheria toxin receptor) animals injected with vehicle (control, top) or limiting dose (150 ng) of Diphtheria toxin (DT) to induce sporadic epithelial cell ablation (bottom) then (A) immunostained 5 days later for SftpC and Ki67 or (B) probed with PLISH for *SftpC* and *Axin2* expression. (**C**) Quantification (n = 250 cells in four animals) of percent AT2 cells expressing Ki67 (mean ± SD) or *Axin2* (mean ± SD). Ablation induces proliferation and Wnt signaling in most AT2 cells, both abrogated by Wnt secretion inhibitor C59. ***P < 0.001 (Student's t test). (**D**) Alveoli as (A) and (B) probed with PLISH for *Wnt7b* and *SftpC* mRNA 1 day after vehicle (control) or DT injection (ablation). (**E**) Kinetics of *Wnt7b* induction after ablation (n = 300 AT2 cells scored per animal, four biological replicates per time point, mean ± SD). **P = 0.005 (Kruskal-Wallis). Scale bars, 10 μm (A), 5 μm (B) and (D).

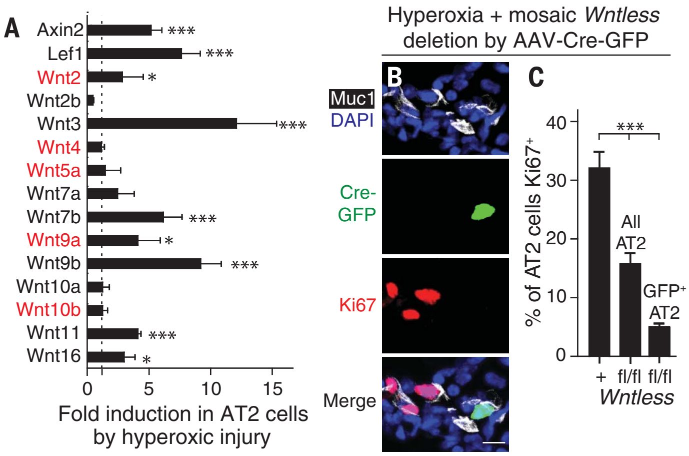

Fig. 5. Hyperoxic injury induces autocrine Wnt signaling in bulk AT2 cells. (**A**) Expression of Wnt genes and targets (*Axin2* and *Lef1*) measured with quantitative reverse transcription PCR of FACS-sorted, lineage-labeled bulk AT2 cells from mice 2 days after hyperoxic alveolar injury (5 days at 75% O_2) (fig. S12B), normalized to values before hyperoxic injury (mean ± SD, $n = 3$ mice per condition). Red, Wnts expressed by fibroblast niche (Fig. 2D). $^*P < 0.05$, $^{***}P < 0.001$ (Student's t test). (**B**) Alveoli immunostained as indicated from adult (age 2 months) *Wntless*$^{fl/fl}$ mouse with alveolar epithelium infected with *AAV9-GFP-Cre* virus (fig. S12, D to F) to mosaically delete *Wntless* 1 week before hyperoxic injury. Shown is injury-induced proliferation (Ki67 staining) of AT2 cells (Muc1 apical marker) (fig. S12A), except AT2 infected with AAV-Cre-GFP to delete *Wntless*. (**C**) Quantification showing percent AT2 cells Ki67$^+$ after hyperoxic injury of AAV9-Cre-GFP–infected control (*Wntless*$^{+/+}$) and *Wntless*$^{fl/fl}$ mice, scored for all or just GFP$^+$ (AAV9-Cre-GFP–infected) AT2 cells. Mean ± SD ($n = 500$ total AT2 cells scored per mouse, three mice per condition, including 52 GFP$^+$ cells). Scale bar, 10 μm.

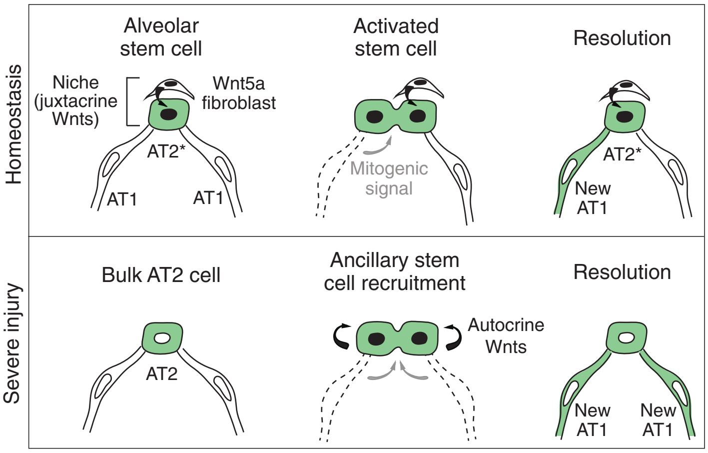

Fig. 6. Model of alveolar stem cells and their niches. (**Top**) (Left) During homeostasis, the niche is a single fibroblast constitutively expressing *Wnt5a* and/or other Wnts that provide "juxtacrine" signal (arrow) to the neighboring AT2 cell (green cytoplasm, lineage trace; black nucleus, Wnt pathway active), selecting/maintaining it as a stem cell. (Middle) Upon receiving a mitogenic signal from the dying AT1 cell, the activated stem cell proliferates. Daughter cells (green) compete for the niche. (Right) One remains in the niche as a stem cell; the other leaves the niche, losing Wnt signal and transdifferentiating into a new AT1 cell. (**Bottom**) After severe injury, bulk AT2 are recruited as "ancillary" stem cells through induction of autocrine Wnts, allowing unlimited proliferation in response to mitogens. Autocrine Wnts diminish as injury resolves.

throughout the mouse lung in specialized niches that renew the alveolar epithelium throughout adult life. AT2^{stem} cells express Wnt target *Axin2*, and many lie near single fibroblasts expressing *Wnt5a* and other *Wnt* genes that serve as a signaling niche (Fig. 6). AT2^{stem} cells divide intermittently, self-renewing and giving rise to daughter AT1 cells that lose Wnt activity when they exit the niche. Maintaining canonical Wnt signaling blocked transdifferentiation to AT1 identity, whereas loss of Wnt signaling promoted it.

Our results support a model in which each Wnt-expressing fibroblast defines a niche accommodating one AT2^{stem} cell, and this short-range ("juxtacrine") signal selects and maintains AT2^{stem} identity (Fig. 6). When an AT2^{stem} cell divides, daughter cells compete for the niche. The one that remains in the niche retains AT2^{stem} identity; the other leaves the Wnt niche, escaping the signal and reprogramming to AT1 fate. Cells leaving the niche can also become standard AT2 cells, presumably if they land near a signaling center that selects bulk AT2 fate. This streamlined niche, comprising just a single Wnt-expressing fibroblast and stem cell, minimizes niche impact on alveolar gas exchange. It also explains why each expanding focus of new alveoli is clonal, derived from a single AT2^{stem} that typically remains associated with the growing focus (*13*). Although our model posits that the niche cell selects the stem cell, it remains uncertain how the scattered niche cells are selected. Some niche cells themselves are Axin2$^+$ (Fig. 2D and fig. S6) (*24*), suggesting that autocrine Wnt signaling might maintain the niche as juxtacrine signaling maintains the stem cell within it.

Our results also reveal a transient expansion of the alveolar progenitor population after epithelial injury, when the rare AT2^{stem} are insufficient. Many normally quiescent bulk AT2 cells turn on *Axin2* and serve as ancillary progenitors that rapidly proliferate and regenerate lost alveolar cells (Fig. 6). This widespread recruitment of AT2 cells to AT2^{stem} function is not achieved through expansion of the fibroblast Wnt niche. Rather, injury induces Porcupine and another suite of Wnts, including *Wnt7b*, in AT2 cells. This switch to autocrine control of stem cell identity obviates dependence on the stromal niche. As the epithelium is restored, *Wnt* expression subsides in ancillary AT2^{stem}, and they cease proliferating and begin differentiating into AT1 cells or returning to bulk AT2 identity. The Wnt pathway is broadly active during alveolar development (*16*, *17*) and cancer, where most cells proliferate, so it may have a general role in maintaining alveolar stem or progenitor states.

Our data suggest that Wnt signaling, whether juxtacrine Wnts from a fibroblast or autocrine Wnts induced by injury, endows AT2 cells with two stem cell properties. One is AT2^{stem} gene expression and identity, preventing reprogramming to AT1 (and presumably bulk AT2) fate (Fig. 3). The other is an ability to proliferate extensively, as observed after injury when ancillary AT2^{stem} divide rapidly to restore the epithelium (Fig. 6). Thus, Wnt signaling confers stem cell identity ("stemness") on AT2 cells but does not itself activate the stem cells (Fig. 3, J and K, and fig. S8). Proliferation is controlled by EGFR/KRAS signaling (Fig. 3, J and K) (*13*), presumably activated by EGF ligand(s) from dying cells (*33*). We propose that Wnt and EGFR/KRAS pathways function in parallel to select and activate alveolar stem cells, respectively, explaining their synergy (Fig. 3, J and K).

The above findings have implications for lung adenocarcinoma, the leading cancer killer (*34*) initiated by oncogenic mutations that activate EGFR/KRAS signaling in AT2 cells (*13*, *35*, *36*). Although most AT2 cells show a limited proliferative response, a rare subset proliferates indefinitely, forming deadly tumors (*13*): The tumor-initiating cells could be AT2^{stem}. Indeed, a subpopulation of adenocarcinoma cells was recently found to have Wnt pathway activity and function as tumor stem cells, with associated cells serving as their Wnt signaling niche (*26*). As oncogenic EGFR/KRAS drives stem cell proliferation, Wnt signaling would maintain their identity; this explains why Wnt signaling has little proliferative effect on its own but potentiates KRAS^{G12D} and BRAF^{V600E} mouse models of lung carcinogenesis and why Wnt inhibition induces tumor senescence (*26*, *37*, *38*). Wnt antagonists might thus be powerful adjuvants in adenocarcinoma therapy, attacking stem cell identity, while EGFR antagonists target stem cell activity. One reason stem cell identity may have restricted during evolution to rare AT2 cells is that it minimizes cells susceptible to transformation.

There is growing appreciation that some mature cells in other tissues can also provide stem cell function (*8*, *9*, *39*). Like AT2^{stem}, their clinical utility has been overlooked as more classical "undifferentiated," and pluripotent stem cells have been sought. Our study shows that stem cells and their niche cells can each represent minor, solitary subsets of mature cell types. By molecularly identifying such rare subpopulations and niche signals, it should be possible to isolate and expand them for regenerative medicine.

REFERENCES AND NOTES

1. S. J. Morrison, A. C. Spradling, *Cell* **132**, 598–611 (2008).
2. D. T. Scadden, *Cell* **157**, 41–50 (2014).
3. V. P. Losick, L. X. Morris, D. T. Fox, A. Spradling, *Dev. Cell* **21**, 159–171 (2011).
4. M. de Cuevas, E. L. Matunis, *Development* **138**, 2861–2869 (2011).
5. P. Rompolas, V. Greco, *Semin. Cell Dev. Biol.* **25-26**, 34–42 (2014).
6. S. J. Morrison, D. T. Scadden, *Nature* **505**, 327–334 (2014).
7. Y. C. Hsu, L. Li, E. Fuchs, *Nat. Med.* **20**, 847–856 (2014).
8. H. Clevers, K. M. Loh, R. Nusse, *Science* **346**, 1248012 (2014).
9. C. Y. Logan, T. J. Desai, *BioEssays* **37**, 1028–1037 (2015).
10. H. A. Chapman *et al.*, *J. Clin. Invest.* **121**, 2855–2862 (2011).
11. P. A. Kumar *et al.*, *Cell* **147**, 525–538 (2011).
12. J. A. Whitsett, S. E. Wert, T. E. Weaver, *Annu. Rev. Med.* **61**, 105–119 (2010).
13. T. J. Desai, D. G. Brownfield, M. A. Krasnow, *Nature* **507**, 190–194 (2014).
14. C. E. Barkauskas *et al.*, *J. Clin. Invest.* **123**, 3025–3036 (2013).
15. M. L. Mucenski *et al.*, *J. Biol. Chem.* **278**, 40231–40238 (2003).
16. J. Rajagopal *et al.*, *Development* **135**, 1625–1634 (2008).
17. D. B. Frank *et al.*, *Cell Reports* **17**, 2312–2325 (2016).
18. E. H. Jho *et al.*, *Mol. Cell. Biol.* **22**, 1172–1183 (2002).
19. M. Nagendran, D. P. Riordan, P. B. Harbury, T. J. Desai, *eLife* **7**, e30510 (2018).
20. B. Messier, C. P. Leblond, *Am. J. Anat.* **106**, 247–285 (1960).
21. H. F. Farin *et al.*, *Nature* **530**, 340–343 (2016).
22. I. Y. Adamson, C. Hedgecock, D. H. Bowden, *Am. J. Pathol.* **137**, 385–392 (1990).
23. J. H. Lee *et al.*, *Cell* **170**, 1149–1163.e12 (2017).
24. J. A. Zepp *et al.*, *Cell* **170**, 1134–1148.e10 (2017).
25. M. D. Resh, *Prog. Lipid Res.* **63**, 120–131 (2016).
26. T. Tammela *et al.*, *Nature* **545**, 355–359 (2017).
27. C. Bänziger *et al.*, *Cell* **125**, 509–522 (2006).
28. R. F. Gonzalez, L. G. Dobbs, *Methods Mol. Biol.* **945**, 145–159 (2013).
29. A. Glinka *et al.*, *Nature* **391**, 357–362 (1998).
30. T. Buch *et al.*, *Nat. Methods* **2**, 419–426 (2005).
31. D. H. Bowden, I. Y. Adamson, J. P. Wyatt, *Arch. Pathol.* **86**, 671–675 (1968).
32. M. J. Evans, L. J. Cabral, R. J. Stephens, G. Freeman, *Exp. Mol. Pathol.* **22**, 142–150 (1975).
33. B. S. Ding *et al.*, *Cell* **147**, 539–553 (2011).
34. R. Siegel, D. Naishadham, A. Jemal, *CA Cancer J. Clin.* **63**, 11–30 (2013).
35. X. Xu *et al.*, *Proc. Natl. Acad. Sci. U.S.A.* **109**, 4910–4915 (2012).
36. C. Lin *et al.*, *PLOS ONE* **7**, e53817 (2012).
37. E. C. Pacheco-Pinedo *et al.*, *J. Clin. Invest.* **121**, 1935–1945 (2011).
38. J. Juan, T. Muraguchi, G. Iezza, R. C. Sears, M. McMahon, *Genes Dev.* **28**, 561–575 (2014).
39. A. Q. Sheikh, A. Misra, I. O. Rosas, R. H. Adams, D. M. Greif, *Sci. Transl. Med.* **7**, 308ra159 (2015).

ACKNOWLEDGMENTS

We thank A. Andalon for technical assistance; D. Riordan and M. Nagendran for advice on PLISH; B. Treutlein and S. Quake for help with scRNA-seq; R. Nusse and colleagues for generously sharing mouse lines and reagents; members of the Krasnow, Desai, and Nusse laboratories for discussion; and M. Peterson for help preparing the manuscript and figures. **Funding:** This work was supported by a National Heart, Lung, and Blood Institute (NHLBI) U01HL099995 Progenitor Cell Biology Consortium grant (M.A.K., T.J.D., and P.B.H.), NHLBI grant 1R56HL1274701 (T.J.D.), and Stanford BIO-X grant IIP-130 (T.J.D. and P.B.H.). A.N.N. was supported by NIH Comparative Medicine Branch training grant fellowship 2T32GM007276. M.A.K. is an investigator of the Howard Hughes Medical Institute. **Data and materials availability:** Expression-profiling data sets were deposited in Gene Expression Omnibus (www.ncbi.nlm.nih.gov/geo). GEO accession numbers are GSE109444 for the adult mesenchyme and GSE52583 for the adult AT2 cells. **Competing interests:** T.J.D. and P.B.H. are co-inventors of a patent application (#62475090) submitted by Stanford University that covers the technology used for the multiplexed in situ hybridization experiments. **Author contributions:** A.N.N., T.D., and M.A.K. conceived, designed, and analyzed experiments and wrote the manuscript. All experiments except fibroblast and AT2 scRNA-seq were performed by A.N.N. D.G.B. performed and analyzed RNA-seq of alveolar fibroblasts and AT2 cells. P.B.H. conceived and advised on PLISH (*19*).

SUPPLEMENTARY MATERIALS

www.sciencemag.org/content/359/6380/1118/suppl/DC1
Figs. S1 to S13
References (*40*–*52*)

22 December 2016; resubmitted 20 January 2017
Accepted 23 January 2018
Published online 1 February 2018
10.1126/science.aam6603

REPORT

QUANTUM ELECTRONICS

Strong spin-photon coupling in silicon

N. Samkharadze,[1*] G. Zheng,[1*] N. Kalhor,[1] D. Brousse,[2] A. Sammak,[2] U. C. Mendes,[3] A. Blais,[3,4] G. Scappucci,[1] L. M. K. Vandersypen[1†]

Long coherence times of single spins in silicon quantum dots make these systems highly attractive for quantum computation, but how to scale up spin qubit systems remains an open question. As a first step to address this issue, we demonstrate the strong coupling of a single electron spin and a single microwave photon. The electron spin is trapped in a silicon double quantum dot, and the microwave photon is stored in an on-chip high-impedance superconducting resonator. The electric field component of the cavity photon couples directly to the charge dipole of the electron in the double dot, and indirectly to the electron spin, through a strong local magnetic field gradient from a nearby micromagnet. Our results provide a route to realizing large networks of quantum dot–based spin qubit registers.

In cavity quantum electrodynamics, a photon is stored in a cavity so that its interaction with a resonant atom (or other two-level system) in the cavity is enhanced to the point where a single quantum of energy is exchanged coherently between the cavity photon mode and the atom (*1*). This regime of strong coupling has been achieved across a wide range of experimental platforms, from atoms to superconducting qubits and self-assembled quantum dots, using either optical or microwave photons (*2*–*7*). Given that cavities extend over macroscopic distances, the coherent cavity-atom interaction can be used to indirectly couple well-separated atoms coherently, offering a path to scalable quantum computing.

This prospect has motivated extensive theoretical and experimental work to achieve the strong-coupling regime with gate-defined semiconductor quantum dots, one of the leading platforms for the realization of quantum circuits (*8*–*11*). Recently, strong coupling has been reported between a microwave photon and a charge qubit formed in a double quantum dot (DQD), an impressive achievement given the small electric dipole of a double dot and the short-lived charge qubit coherence (*12*–*14*). Even more challenging, but also more desirable, is the strong coupling to a spin qubit (*15*, *16*). Compared with the electron charge, the electron spin has far superior coherence properties, but its direct interaction with the cavity magnetic field is exceedingly small (*17*). Therefore, one must resort to indirect interaction of the electron spin with the cavity electric field by hybridization of the spin with the electron charge degree of freedom, without compromising spin coherence too severely in the process (*18*–*23*). For a single spin, spin-charge hybridization can be achieved in a controlled way through a transverse magnetic field gradient (*23*–*28*).

We report the observation of vacuum Rabi splitting of a single electron spin resonant with an on-chip microwave cavity, the telltale sign of strong coupling. The spin-photon coupling strength is controlled by the charge qubit settings, and we can extract all the relevant coupling strengths and decay rates. At a spin-photon coupling strength of 10 MHz, we observe cavity decay and spin dephasing rates of 4.1 and 1.8 MHz, respectively.

The superconducting cavity consists of a NbTiN half-wavelength coplanar resonator with a narrow center conductor and remote ground planes (Fig. 1, A and B), capacitively coupled to a feed line. The cavity resonator is wrapped in a square shape,

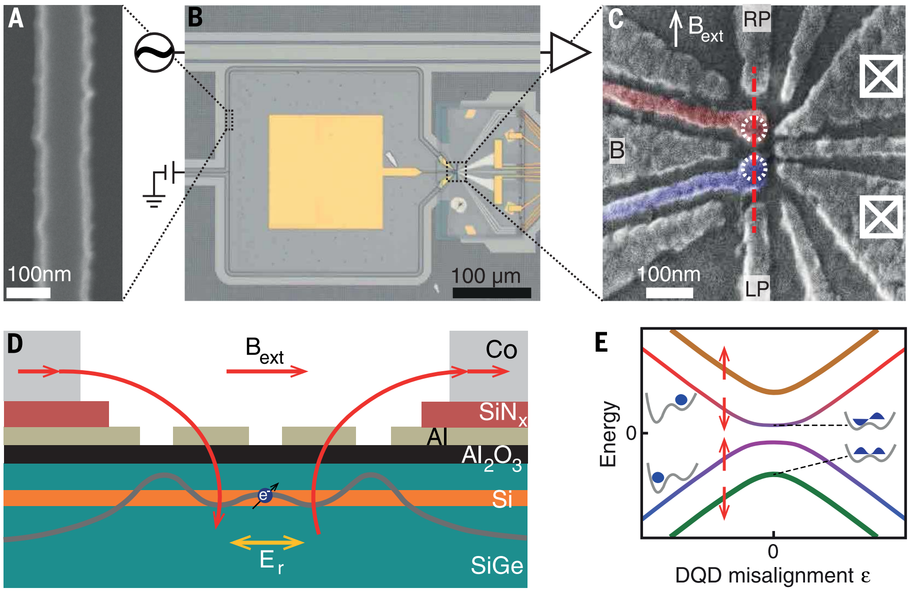

Fig. 1. Device images and schematic. (**A**) Scanning electron micrograph of a segment of the NbTiN resonator center conductor. (**B**) Optical micrograph of the resonator (square shape delineated by narrow black line) adjacent to the feed line (top) and double dot (right). The yellow square in the center is a bond pad to bias gate B. (**C**) Scanning electron micrograph showing the gates used to form the double quantum dot (DQD; white dotted circles indicate dot positions). The purple- and red-colored gates are connected to the resonator ends. White squares with X's, Fermi reservoirs connected to ohmic contacts; RP and LP, plunger gates used to control chemical potentials of the dots. (**D**) Schematic cross section of the DQD along the red dashed line in (C), showing the Si quantum well, with SiGe buffer and spacer layers, and the Al_2O_3 and SiN_x dielectrics separating the substrate from the Al gates and Co micromagnets. In the experiment, a single electron moves in the double dot potential landscape (gray line) in response to the resonator electric field E_r. A magnetic field is applied in the plane of the quantum well. The Co micromagnets create an additional magnetic field component (red curves with arrows), with a different orientation between the two dots. (**E**) The DQD energy levels as a function of DQD misalignment ε. Near ε = 0, the left and right dot levels hybridize, forming bonding and antibonding states that define a charge qubit (*34*). Each of the DQD levels is split by the Zeeman energy. The micromagnets cause spin and orbital levels to hybridize as well, as reflected in the color gradients near ε = 0 for the middle two energy levels.

---

[1] QuTech and Kavli Institute of Nanoscience, Delft University of Technology, Lorentzweg 1, 2628 CJ Delft, Netherlands. [2] QuTech and Netherlands Organization for Applied Scientific Research (TNO), Stieltjesweg 1, 2628 CK Delft, Netherlands. [3] Institut Quantique and Département de Physique, Université de Sherbrooke, Sherbrooke, Québec J1K 2R1, Canada. [4] Canadian Institute for Advanced Research, Toronto, Ontario, Canada.
*These authors contributed equally to this work.
†Corresponding author. Email: l.m.k.vandersypen@tudelft.nl

and its two ends are connected to two Al gates that extend over the quantum dot locations. The resonator's material and dimensions give it a high characteristic impedance of about 1 kilohm that enhances the coupling g_c to the double dot charge dipole (*13*, *29*) and make it resilient to in-plane magnetic fields of up to 6 T (*29*). The DQD is formed electrostatically in an undoped Si/SiGe quantum well (natural isotopic abundance), using a single layer of Al gates (*30*) (Fig. 1C). A positive bias on a gate accumulates electrons in the quantum well underneath, and a negative bias repels electrons (fig. S1D). An external in-plane magnetic field B_{ext} induces a Zeeman splitting on an electron in the DQD. Two cobalt micromagnets placed near the quantum dots (fig. S1, B and C) produce an additional local in-plane magnetic field, as well as a transverse magnetic field gradient. As a result, when an electron oscillates between the two dots, it experiences an oscillating transverse magnetic field, providing the necessary (indirect) spin-charge hybridization that allows an electric field to couple to the spin (*24*–*26*) (Fig. 1E).

We apply a probe tone to the feed line at frequency f_p and record the transmission through the feed line (unless indicated, all transmission plots show the normalized amplitude of the transmission through the feed line). With the DQD tuned to keep the electron fixed in one of the dots, the transmission shows a dip for f_p near 6.051 GHz, the bare resonance frequency f_r of the NbTiN resonator (Fig. 2B, square symbol). From the linewidth, we find the bare resonator decay rate $\kappa_r/2\pi = 2.7$ MHz, with an internal loss rate $\kappa_{int}/2\pi = 1.5$ MHz (fig. S5). We monitor the transmission through the feed line at low probe power (below −125 dBm, corresponding to <1 photon in the resonator) to tune up the DQD, characterize the charge-photon interaction, and study spin-photon coupling.

To characterize the charge-photon interaction, we tune the DQD to a regime where the electron can move back and forth between the two dots in response to the cavity electric field, setting B_{ext} = 110 mT, well above the spin-photon resonance condition. Such motion is possible whenever the electrochemical potentials of the two dots are aligned—i.e., where it costs equal energy for an electron to be in either dot. This occurs for specific combinations of gate voltages, seen as the short bright lines in Fig. 2A, where the charge-photon interaction modifies the transmission (*31*). We focus on the lower left line, which corresponds to the last electron in the DQD.

To place the charge-photon interaction in the dispersive regime, the gate voltages are adjusted to set $2t_c/h$ in the range of 8 to 15 GHz, so that the charge qubit splitting $hf_c = \sqrt{4t_c^2 + \varepsilon^2}$ is always well above hf_r (t_c, interdot tunnel coupling; h, Planck's constant). We measure f_c using two-tone spectroscopy. In the dispersive regime, the charge-photon interaction results in a frequency shift of the resonator (Fig. 2F). In Fig. 2B, the characteristic dependence of this dispersive shift on the DQD misalignment ε is apparent. At ε = 0, the electron can most easily move between the dots; hence, the electrical susceptibility is the highest, and the dispersive shift the largest (triangle). At ε = 0, the magnitude of the dispersive shift is approximated by $(g_c/2\pi)^2/(f_c - f_r)$, where the charge-photon coupling strength g_c is mostly fixed by design, and the detuning between f_c and f_r can be adjusted. From a fit based on input-output theory (*32*), a charge-photon coupling strength $g_c/2\pi$ of ~200 MHz is extracted.

To probe coherent spin-photon coupling, the charge sector parameters are kept constant so that the interaction with charge remains dispersive.

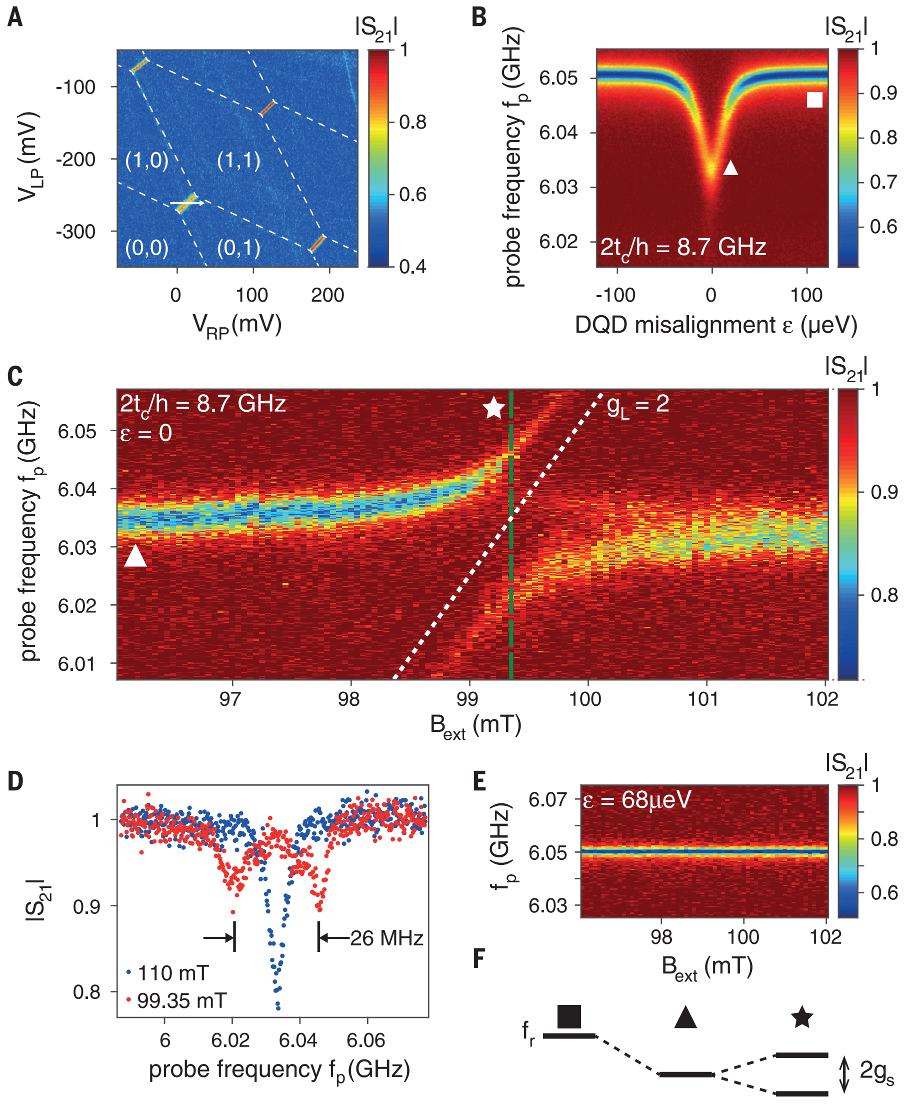

Fig. 2. Strong spin-photon coupling. (**A**) Normalized amplitude S_{21} of the transmission through the feed line, probed at f_p = 6.051 GHz. At the four short bright lines, the electron can move between the dots. The dashed lines connecting the short lines indicate alignment of a dot with a reservoir electrochemical potential. Labels indicate the electron number in the two dots. The DQD misalignment ε is varied along the direction of the white arrow, causing an inconsequential uniform shift in the DQD potential as well. (**B**) Transmission as a function of ε and f_p. At large |ε|, we measure the bare resonator transmission (square). Near ε = 0, the DQD charge qubit interacts dispersively with the cavity frequency, leading to a characteristic frequency shift (triangle). (**C**) Transmission as a function of B_{ext} and f_p. When B_{ext} makes the spin splitting resonant with the resonator frequency (star), a clear avoided crossing occurs, which we attribute to the strong coupling of a single spin and a single photon. The white dotted line shows the expected spin splitting for a spin in silicon. (**D**) Line cut through (C) at the position of the green dashed vertical line (red data points) and line cut at 110 mT (blue points). The red data show clear vacuum Rabi splitting. (**E**) Similar to (C), but with the DQD misaligned, so the electron cannot move between the two dots. The spin-photon coupling is no longer visible. (**F**) Schematic representation of the transmission resonance of the superconducting cavity. The bare transmission resonance (square) is shifted dispersively by its interaction with the charge qubit (triangle) and splits when it is resonant with the spin qubit (star).

By varying B_{ext}, the spin splitting is controlled so that the interaction with the spin goes from dispersive to resonant. On resonance, spin and photon hybridize (Fig. 2F, star). In Fig. 2C, the transmission through the feed line is shown as a function of the strength of B_{ext} (the total field is the vector sum of the external field and the micromagnet stray field) and the probe frequency f_p applied to the feed line. As expected, the cavity resonance seen in transmission is (nearly) independent of B_{ext} at large spin-resonator detuning. When the spin splitting approaches resonance with the resonator frequency, we observe a strong response in the form of an anticrossing (Fig. 2C, star). The slope f_p/B_{ext} of the slanted

Fig. 3. Two-tone spectroscopy of the charge and spin qubit. (**A**) Transmission at f_p = 6.041 GHz as a function of DQD misalignment ε and the frequency f_s of a second tone (pump frequency) that is applied to gate LP. When the second tone is in resonance with the charge qubit splitting (white dashed line), the steady-state occupation of the charge qubit is changed, and, owing to the charge-photon coupling, this is reflected in a modified dispersive shift of the resonator. (**B**) Line cut at ε = 0, from which we extract a charge qubit dephasing rate of 52 MHz. (**C**) Transmission (phase response) at f_p = 6.043 GHz as a function of B_{ext} and the pump frequency applied to gate LP. When the pump frequency is in resonance with the spin qubit splitting, the steady-state occupation of the spin qubit is changed, and, owing to the spin-photon coupling, this is reflected in a modified response of the resonator. The slope of the response corresponds to a spin with $g_L \approx 2$. (**D**) Line cut at B_{ext} = 100.1 mT, from which we extract a spin qubit dephasing rate of 1.4 MHz.

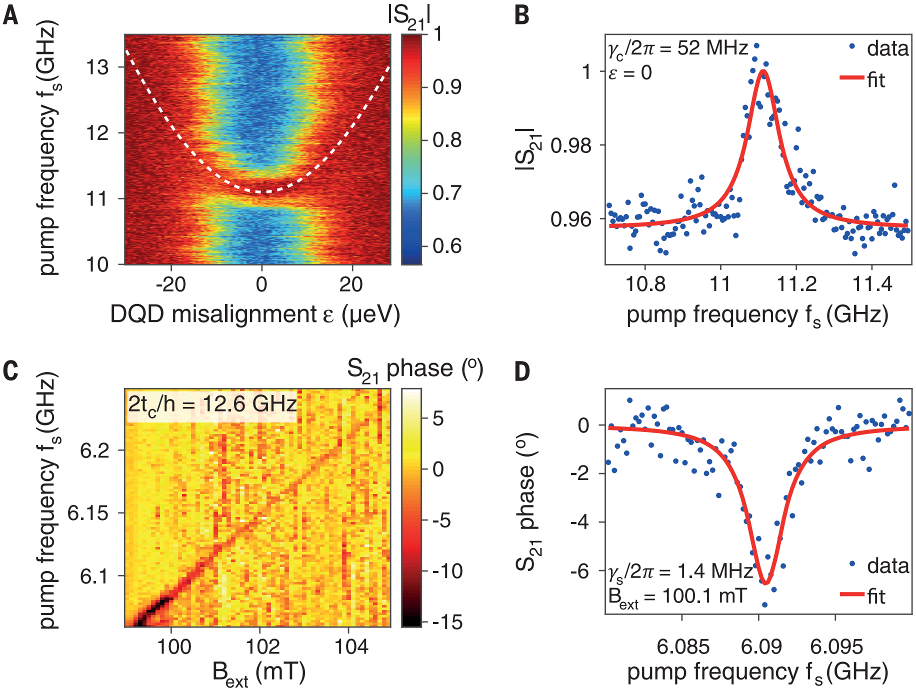

Fig. 4. Control of the spin-photon coupling. (**A**) The dependence on DQD tunnel coupling of g_s, κ, and γ_s (upper panel) and of the ratio of peak splitting to linewidth $2g_s/(\gamma_s + \kappa/2)$ (lower panel) for ε = 0. Although all three separate quantities increase with lower t_c, the ratio $2g_s/(\gamma_s + \kappa/2)$, which is the most relevant quantity, shows an optimum value around f_c = 9.5 GHz. The black dashed line shows g_s approximated as $\frac{1}{4}g_c g_L \mu_B \Delta B_x/(2t_c/h - f_r)$ (*28*), taking ΔB_x = 20 mT (which translates to an estimated interdot distance of 45 nm, given the 0.45 mT/nm simulated transverse gradient). (**B** to **D**) Similar data to Fig. 2C for three different values of DQD tunnel coupling, as indicated. The small differences in the resonant magnetic field are mostly due to different magnetic field sweep histories and hysteresis in the micromagnet. (**E**) Transmission as a function of B_{ext} and ε for $2t_c/h$ = 10.3 GHz and f_p = 6.040 GHz. Where the blue band is interrupted, the Zeeman splitting is resonant with the (dispersively shifted) resonator.

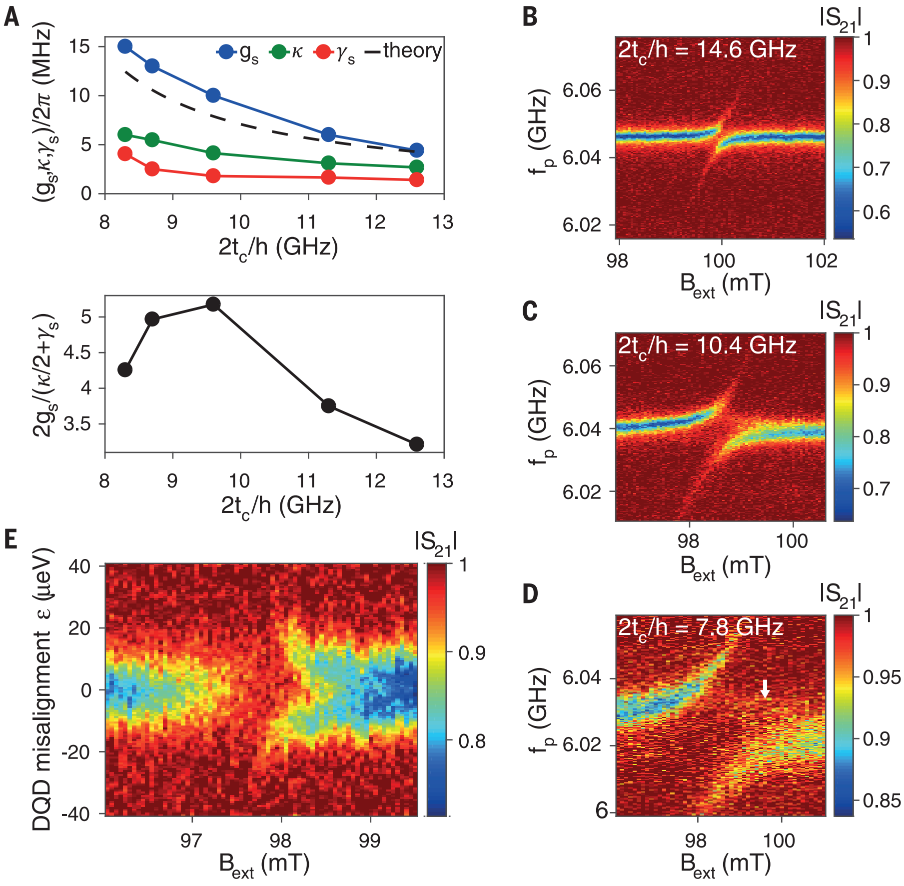

branch corresponds to $g_L\mu_B/h$ (μ_B, the Bohr magneton; $g_L \approx 2$, the Landé g-factor of an electron spin in Si). The observed avoided crossing is thus a clear signature of the coherent hybridization of the spin qubit with a single microwave photon.

The line cut indicated by the dashed green line in Fig. 2C and shown in Fig. 2D reveals two well-separated peaks. This feature is known as the vacuum Rabi splitting and is expected for strong coherent spin-photon coupling. The peak separation is about 26 MHz, corresponding to a spin-photon coupling strength $g_s/2\pi$ of 13 MHz. The cavity decay rate can be extracted independently from the linewidth away from spin-photon resonance, which here is $\kappa/2\pi$ = 5.4 MHz [the cavity dispersively interacts with the charge, so $\kappa > \kappa_r$ (*31*)]. The spin dephasing rate $\gamma_s/2\pi$ = 2.5 MHz is independently obtained from two-tone spectroscopy of the spin transition (discussed next). We observe that $g_s > \kappa, \gamma_s$, satisfying the condition for strong coupling of a single electron spin to a single microwave photon.

Two-tone spectroscopy of the charge and spin qubits allows us to independently extract the respective qubit splittings and dephasing rates. In Fig. 3, A and B, the second tone is resonant with the charge qubit splitting around 11.1 GHz, with a dependence on ε described by $hf_c = \sqrt{4t_c^2 + \varepsilon^2}$ [white dashed line (neglecting spin-charge hybridization)]. In this case, a charge qubit dephasing rate $\gamma_c/2\pi$ = 52 MHz is extracted from the linewidth. In Fig. 3, C and D, the second tone is swept through the spin resonance condition while keeping the spin-cavity system in the dispersive regime. A linear dependence of the spin splitting on B_{ext} is observed, with a slope corresponding to $g_L \approx 2$. At $2t_c/h$ = 12.6 GHz, we extract $\gamma_s/2\pi$ = 1.4 MHz from the linewidth. This is somewhat larger than the ~0.3-MHz single-spin dephasing rates observed in a single Si/SiGe quantum dot (*10*, *11*, *25*), as is expected given that an electron in a DQD at ε = 0 is more susceptible to charge noise, which affects spin coherence through the magnetic field gradient (*23*, *27*, *28*).

The spin-photon hybridization can be controlled with gate voltages. By moving away from ε = 0, the photon and charge no longer hybridize, and the spin-photon coupling vanishes (Fig. 2E). Furthermore, at ε = 0, the spin-photon coupling strength can be approximated as $g_s = \frac{1}{4} g_c g_L \mu_B \Delta B_x/(2t_c/h - f_r)$ (provided the magnetic field profile is symmetric relative to the DQD) (*23*, *27*, *28*). Here, ΔB_x is the difference in the transverse field between the two dots. Starting from large t_c, reducing t_c increases spin-charge admixing—and thus, indirectly, spin-photon coupling—as seen experimentally in Fig. 4, B to D. With increased spin-charge admixing, the asymmetry in the intensity of the two branches also increases, which is understood as a result of quantum interference in the one-excitation manifold of photon, charge, and spin (*28*). Furthermore, an additional feature (Fig. 4D, white arrow) appears close to the lower branch (discussed in the supplementary materials). The variation of g_s with t_c is summarized in Fig. 4A, along with the theoretical approximation for g_s versus t_c. However, as seen in the same figure, with lower t_c, the spin dephasing rate γ_s increases as well, as does the cavity decay rate κ (*28*). Ultimately, we wish to maximize the peak separation over linewidth, $2g_s/(\gamma_s + \kappa/2)$. In this respect, there is an optimal choice of tunnel coupling, as seen from Fig. 4A.

Last, we study how close together the charge and spin sweet spots occur, where the relevant frequency (charge or spin) is, to first order, insensitive to the DQD misalignment. The charge sweet spot is seen in Fig. 2B at ε = 0 and f_p = 6.032 GHz. If the micromagnets are placed symmetrically with respect to the DQD (as in Fig. 1D), the total magnetic field magnitude is symmetric around the center of the DQD. In this case, the spin splitting has no first-order dependence on ε at ε = 0, and the charge and spin sweet spots coincide. For asymmetrically placed magnets, the spin sweet spot occurs away from ε = 0. To find the spin sweet spot, we vary ε and B_{ext} at f_p = 6.040 GHz (Fig. 4E). Throughout the blue band, f_p is resonant with the cavity frequency (in the dispersive charge-photon coupling regime). Where the blue band is interrupted, the magnetic field brings the spin on resonance with the cavity photon, spin and photon hybridize, and the transmission is modified. This spin-photon resonance condition shifts down in magnetic field as a function of $|\varepsilon|$ (*26*). The value of ε where this shift has no first-order dependence on ε occurs close to ε = 0, i.e., the spin sweet spot lies close to the charge sweet spot.

The strong coupling of spin and photon not only opens a new range of physics experiments, but also is the crucial requirement for coupling spin qubits at a distance by means of a superconducting resonator. Given the large dimensions of resonators compared with those of double dots, multiple spin qubits can interact with and through the same resonator, enabling scalable networks of interconnected spin qubit registers (*33*). Importantly, the spin-photon coupling can be switched on or off on nanosecond time scales by using gate voltage pulses that control the double dot misalignment and tunnel coupling, facilitating on-demand coupling of one or more spins to a common resonator.

REFERENCES AND NOTES

1. S. Haroche, J.-M. Raimond, *Exploring the Quantum: Atoms, Cavities, and Photons* (Oxford Univ. Press, 2006).
2. R. J. Thompson, G. Rempe, H. J. Kimble, *Phys. Rev. Lett.* **68**, 1132–1135 (1992).
3. M. Brune *et al.*, *Phys. Rev. Lett.* **76**, 1800–1803 (1996).
4. A. Wallraff *et al.*, *Nature* **431**, 162–167 (2004).
5. I. Chiorescu *et al.*, *Nature* **431**, 159–162 (2004).
6. J. P. Reithmaier *et al.*, *Nature* **432**, 197–200 (2004).
7. T. Yoshie *et al.*, *Nature* **432**, 200–203 (2004).
8. M. D. Shulman *et al.*, *Science* **336**, 202–205 (2012).
9. M. Veldhorst *et al.*, *Nature* **526**, 410–414 (2015).
10. T. F. Watson, S. G. J. Philips, E. Kawakami, D. R. Ward, P. Scarlino, M. Veldhorst, D. E. Savage, M. G. Lagally, M. Friesen, S. N. Coppersmith, M. A. Eriksson, L. M. K. Vandersypen, arXiv:1708.04214 [cond-mat.mes-hall] (14 August 2017).
11. D. M. Zajac *et al.*, *Science* **359**, 439–442 (2018).
12. X. Mi, J. V. Cady, D. M. Zajac, P. W. Deelman, J. R. Petta, *Science* **355**, 156–158 (2017).
13. A. Stockklauser *et al.*, *Phys. Rev. X* **7**, 011030 (2017).
14. L. E. Bruhat, T. Cubaynes, J. J. Viennot, M. C. Dartiailh, M. M. Desjardins, A. Cottet, T. Kontos, arXiv:1612.05214 [cond-mat.mes-hall] (15 December 2016).
15. X. Mi, M. Benito, S. Putz, D. M. Zajac, J. M. Taylor, G. Burkard, J. R. Petta, arXiv:1710.03265 [cond-mat.mes-hall] (9 October 2017).
16. A. J. Landig, J. V. Koski, P. Scarlino, U. C. Mendes, A. Blais, C. Reichl, W. Wegscheider, A. Wallraff, K. Ensslin, T. Ihn, arXiv:1711.01932 [cond-mat.mes-hall] (6 November 2017).
17. P. Haikka, Y. Kubo, A. Bienfait, P. Bertet, K. Mølmer, *Phys. Rev. A* **95**, 022306 (2017).
18. L. Childress, A. S. Sørensen, M. D. Lukin, *Phys. Rev. A* **69**, 042302 (2004).
19. G. Burkard, A. Imamoglu, *Phys. Rev. B* **74**, 041307 (2006).
20. M. Trif, V. N. Golovach, D. Loss, *Phys. Rev. B* **77**, 045434 (2008).
21. A. Cottet, T. Kontos, *Phys. Rev. Lett.* **105**, 160502 (2010).
22. C. Kloeffel, M. Trif, P. Stano, D. Loss, *Phys. Rev. B* **88**, 241405 (2013).
23. F. Beaudoin, D. Lachance-Quirion, W. A. Coish, M. Pioro-Ladrière, *Nanotechnology* **27**, 464003 (2016).
24. M. Pioro-Ladrière, Y. Tokura, T. Obata, T. Kubo, S. Tarucha, *Appl. Phys. Lett.* **90**, 024105 (2007).
25. E. Kawakami *et al.*, *Nat. Nanotechnol.* **9**, 666–670 (2014).
26. J. J. Viennot, M. C. Dartiailh, A. Cottet, T. Kontos, *Science* **349**, 408–411 (2015).
27. X. Hu, Y.-X. Liu, F. Nori, *Phys. Rev. B* **86**, 035314 (2012).
28. M. Benito, X. Mi, J. M. Taylor, J. R. Petta, G. Burkard, *Phys. Rev. B* **96**, 235434 (2017).
29. N. Samkharadze *et al.*, *Phys. Rev. Appl.* **5**, 044004 (2016).
30. S. Rochette, M. Rudolph, A.-M. Roy, M. Curry, G. Ten Eyck, R. Manginell, J. Wendt, T. Pluym, S. M. Carr, D. Ward, M. P. Lilly, M. S. Carroll, M. Pioro-Ladriare, arXiv:1707.03895 [cond-mat.mes-hall] (12 July 2017).
31. T. Frey *et al.*, *Phys. Rev. Lett.* **108**, 046807 (2012).
32. K. D. Petersson *et al.*, *Nature* **490**, 380–383 (2012).
33. L. M. K. Vandersypen *et al.*, *npj Quantum Inf.* **3**, 34 (2017).
34. T. Hayashi, T. Fujisawa, H. D. Cheong, Y. H. Jeong, Y. Hirayama, *Phys. Rev. Lett.* **91**, 226804 (2003).

ACKNOWLEDGMENTS

We thank J. Taylor, P. Scarlino, A. Yacoby, J. Kroll, A. Bruno, and members of the spin qubit team at QuTech for useful discussions and L. Kouwenhoven and his team for access to NbTiN films. This research was undertaken thanks in part to funding from the European Research Council (ERC Synergy Quantum Computer Lab), the Netherlands Organisation for Scientific Research (NWO/OCW) as part of the Frontiers of Nanoscience (NanoFront) program, Intel Corporation, the Canada First Research Excellence Fund, and the Natural Sciences and Engineering Research Council of Canada. Data reported in this paper are archived at http://doi.org/10.4121/uuid:1483c28e-c1d5-45d5-971c-8e660f01f768.

SUPPLEMENTARY MATERIALS

www.sciencemag.org/content/359/6380/1123/suppl/DC1
Materials and Methods
Supplementary Text
Figs. S1 to S5

3 November 2017; accepted 15 January 2018
Published online 25 January 2018
10.1126/science.aar4054

WATER STRUCTURE

A liquid-liquid transition in supercooled aqueous solution related to the HDA-LDA transition

Sander Woutersen,[1*] **Bernd Ensing,**[1,2] **Michiel Hilbers,**[1]
Zuofeng Zhao,[3] **C. Austen Angell**[3*]

Simulations and theory suggest that the thermodynamic anomalies of water may be related to a phase transition between two supercooled liquid states, but so far this phase transition has not been observed experimentally because of preemptive ice crystallization. We used calorimetry, infrared spectroscopy, and molecular dynamics simulations to investigate a water-rich hydrazinium trifluoroacetate solution in which the local hydrogen bond structure surrounding a water molecule resembles that in neat water at elevated pressure, but which does not crystallize upon cooling. Instead, this solution underwent a sharp, reversible phase transition between two homogeneous liquid states. The hydrogen-bond structures of these two states are similar to those established for high- and low-density amorphous (HDA and LDA) water. Such structural similarity supports theories that predict a similar sharp transition in pure water under pressure if ice crystallization could be suppressed.

The divergent behavior of pure-water thermodynamic properties during deep supercooling was interpreted by Poole *et al.* (*1*) in terms of the existence of a nearby second critical point at which two liquid phases, differing in density, become identical. A thermodynamic model, a variant of the van der Waals equation of state, was devised by Poole *et al.* (*2*), to show how the two critical points could be related through the splitting of the familiar van der Waals coexistence domain into two segments. Poole *et al.* (*2*) argued that this splitting would result if a liquid structure of low coordination number could be stabilized, by directional bonding, at a density that is intermediate between gas and close-packed liquid, as occurs in ice and in random tetrahedral network models of water (*3*).

However, for studies of pure water in the laboratory, none of this latter scenario can be established by direct experimentation because of the preempting crystallization of ice I_h (ordinary ice) that forms by homogeneous nucleation and growth in a pattern that closely follows the pattern of divergences of the thermodynamic susceptibilities (*4*). The addition of second components (salts or other liquids) can depress crystallization rates (i.e., act as antifreeze) and permit formation of glassy phases. This approach can act as a proxy for pressure increases for mapping out the phase diagram. Theory (*5*–*7*) indicates the possibility of obtaining information on hidden critical phenomena in single-component systems by virtue of critical lines emanating from the pure solvent into the binary solution. Unfortunately, most ionic (*8*–*10*) and many molecular (*11*) second components destroy the water anomalies more rapidly than they block the nucleation of ice.

Recently, however, a class of ionic solutes has been discovered for which the latter discouraging scenario is reversed; that is, they permit supercooling to the point of vitrification without destruction of the liquid-state anomalies. Rather, they seem to displace the second critical point to lower pressures and temperatures, as described by Anisimov and colleagues (*6*, *7*), in such a way that the ambient-temperature cooling leads the system to cross a liquid-liquid coexistence line before any ice crystallization can occur (*12*). Thus, the "crystallization curtain" can be lifted.

The solutions in which these observations have been made obey the ideal-solution laws for depression of the ice melting point (*12*, *13*). Such behavior indicates that the solute ion–water molecule and water molecule–water molecule interactions are not distinguishable from the point of view of thermodynamics, so that thermodynamically the water molecules will continue to behave in waterlike ways, one of which is to undergo a phase transition in the absence of ice crystallization. Although we investigate ideal solutions here, we note that the arguments of Anisimov (*6*) and of Biddle *et al.* (*7*) for the displacement of the critical point to lower temperatures and pressures also hold in nonideal solutions and are consistent with computer simulation findings for NaCl-water solutions (*14*, *15*).

Figure 1 shows the thermodynamic behavior that is revealed when cooling an ideal aqueous solution. Instead of salt addition leading to a replacement of the pure water anomaly with a decreasing solution molar heat capacity (C_p) and finally a glass transition [as shown for the familiar case of an 11.4 mole percent (mol %) LiCl solution (*9*)], we saw an almost first-order–like spike in heat capacity in the case of solutions of ionic liquid hydrazinium trifluoroacetate (N_2H_5TFA), although the salt content was higher for the latter case. The "spike anomaly" was fully reversible upon reheating; it was followed, at higher temperature, by crystallization of ice I_h. In (*12*), it was noted that the onset of the heat capacity anomaly was preceded by a density anomaly—a flattening out of the density decrease with decreasing temperature. Against the background of linearly decreasing density with decreasing *T*, the flattening corresponds to an anomalous density decrease approaching the C_p maximum. Unfortunately, at the highest water content, 84.4 mol %, where the sharp transition of the present work occurs, the density anomaly could not be observed. The reasons are straightforwardly related to the sample size required for the density measurement (*16*).

A related phenomenon has been reported by Murata and Tanaka (*17*) using glycerol as the solute, but in that case, the formation of the second liquid phase was accompanied by ice formation and so was irreversible. The problem then becomes one of identifying the participating structures in the new, almost first-order transition.

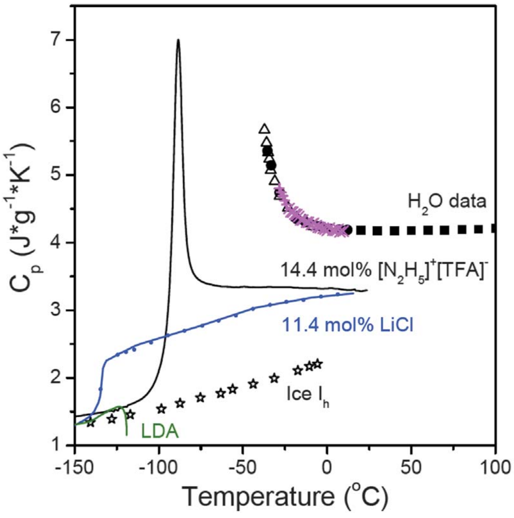

Fig. 1. Contrasting thermal behavior of ideal and nonideal aqueous solutions during supercooling. Compositions are identified on the plots. Apparent values of C_p were determined during cooling scans at 20 K min^{-1} in each case. Data for pure H_2O are a compendium of reported results [see (*12*)]. Data for the LiCl solution are from (*9*).

---

[1] Van 't Hoff Institute for Molecular Sciences, University of Amsterdam, Science Park 904, 1098 XH Amsterdam, Netherlands. [2] Catalan Institute of Nanoscience and Nanotechnology (ICN2), CSIC and Barcelona Institute of Science and Technology, Campus UAB, Bellaterra, 08193 Barcelona, Spain. [3] School of Molecular Sciences, Arizona State University, Tempe, AZ 85287, USA.
***Corresponding author. Email: s.woutersen@uva.nl (S.W.); austenangell@gmail.com (C.A.A.)**

As a probe, the decoupled vibration frequency of the OH oscillator is ideal because its frequency is very sensitive to the OH···O H-bond strength.

We prepared aqueous solutions of N_2H_5TFA with molar water fractions x_{water} ranging from 0.50 to 0.84 (*16*). The small sample volume (~1 μl, kept between two CaF_2 windows separated by ~25 μm; Fig. 2A) allowed for comparatively slow temperature scans without crystallization. Water volumes of this size (>10^{19} molecules) behave thermodynamically like bulk water (*16*). We used dilute H/D isotopic mixtures (H:D fraction ~0.03) to prevent coupling between the OH-stretch modes (*18*). This choice ensured that the center frequency and width of the OH-stretch absorption peak reflected the H-bond structure. The thermodynamics of H_2O and D_2O are essentially the same, once a correction for the zero-point motion is taken into account (*19*, *20*). Figure 2B shows the infrared (IR) absorption spectrum of an x_{water} = 0.84 solution at room temperature (red curve) and down to 140 K during cooling at 7 K min^{-1} (spectra are shown at 2.2 K temperature intervals).

At 25°C, the OH/NH-stretch region contained a broad intense band centered at 3420 cm^{-1} and a much weaker peak at 3300 cm^{-1}. The latter was absent from the spectrum of an NaTFA solution with the same x_{water} value (fig. S1) (*16*), which showed that the 3420 cm^{-1} peak arose from the OH-stretch mode of water (HDO), whereas the 3300 cm^{-1} peak arose from the NH-stretch mode of hydrazinium ($N_2HD_4^+$). This assignment was confirmed by the change in relative intensities of the two peaks upon changing the water fraction (Fig. 2E). The absorption spectrum of the fully deuterated solution showed negligible absorption in the investigated frequency region (fig. S4) (*16*). We attribute the striking jump in IR absorption observed in Fig. 2B in the lower temperature range (about 190 K) to the liquid-liquid transition, as discussed below.

The OH-stretch mode of the solution has a center frequency and width [245 cm^{-1} full width at half maximum (FWHM)] comparable to those of liquid HDO:D_2O (*21*), and in both cases the line shapes are approximately Gaussian. These similarities indicate that even at the high concentration of ions in the solution, the H-bond local structure surrounding a water molecule resembles that in neat water, as is reflected at the macroscopic level by the ideal-solution behavior already mentioned. Hydrazinium contains five H-bond–donating groups, and trifluoroacetate has five H-bond acceptor sites, so that N_2H_5TFA formed an H-bond network resembling that of water. This bonding motif has been shown previously for the similar ionic liquid ethyl ammonium nitrate (*22*). Thus, N_2H_5TFA fit remarkably well into the three-dimensional water H-bond network and left it essentially unperturbed, as was demonstrated by the OH-stretch spectrum consisting of a single absorption band at the same frequency as that of neat HDO:D_2O. The macroscopic ideal mixing behavior could thus be described as an ideal mixing of the structures.

This structural description was confirmed by molecular dynamics (MD) simulations of the

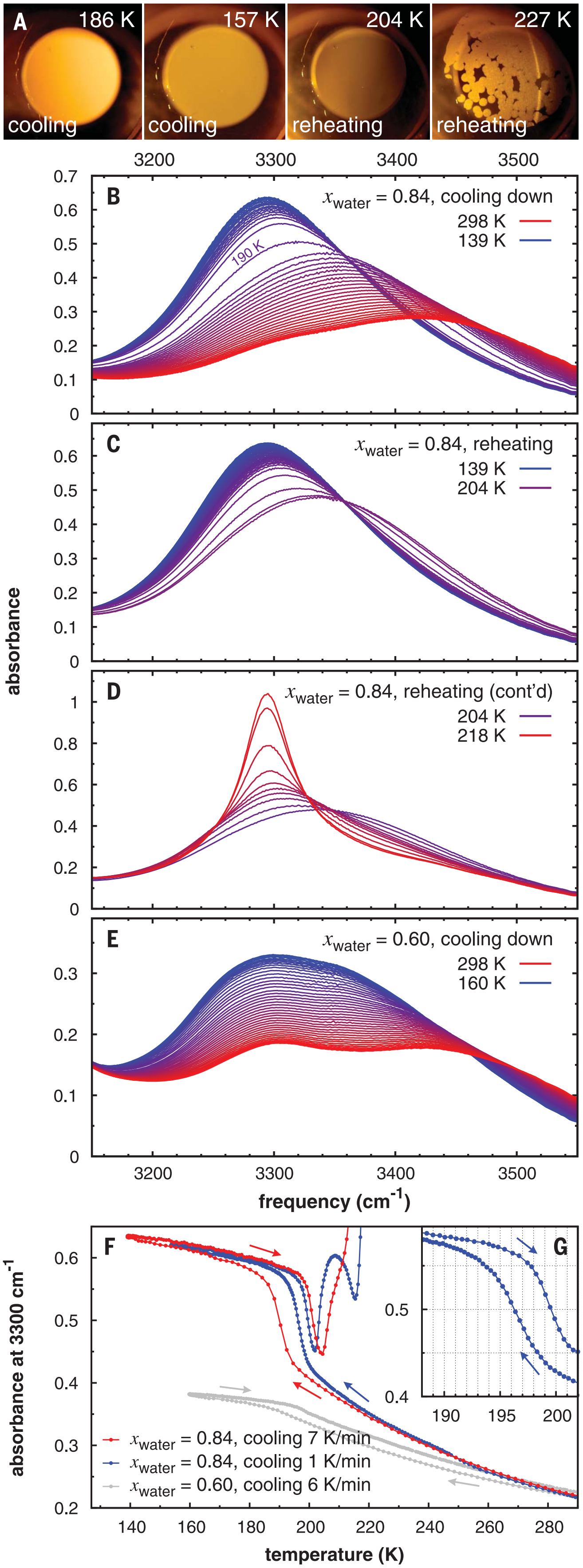

Fig. 2. Liquid-liquid transition in aqueous solution. (**A**) Droplet of (N_2HD_4/N_2D_5)TFA solution in HDO/D_2O (H/D fraction ~3%) with x_{water} = 0.84, between two CaF_2 windows, during cooling and subsequent reheating. All temperatures given in the figures and text are those of a thermocouple close to the liquid layer (*16*). The circle is the optical exit of the sample holder. The circumference of the droplet is visible as the sharp squiggly line. During reheating, crystallization occurs (rightmost panel), but only after the liquid-liquid transition. (**B**) IR spectra of the same solution. Upon decreasing the temperature (at 7 K min^{-1}), the OH-stretch peak showed a gradual redshift. At ~190 K, an intense, broad low-frequency OH-stretch mode appeared, indicating a discrete change in H-bond structure. (**C**) Upon reheating, this phenomenon was reversed and the low-frequency peak disappeared again. (**D**) Upon further reheating, the water crystallized, resulting in a narrow low-frequency OH-stretch peak (assigned to ice) superimposed on a broad OH/NH-stretch background caused by the surrounding liquid. (**E**) In a solution with a water fraction *x* = 0.60, no structural transition occurred, only a gradual lowering of the OH-stretch frequency with decreasing temperature. (**F**) IR absorbance at 3300 cm^{-1} versus temperature during cooling and reheating as indicated by the arrows. Each point indicates a measured IR spectrum. At a lower cooling and reheating rate, the hysteresis was much less. (**G**) Close-up showing the reduced hysteresis at a lower cooling rate.

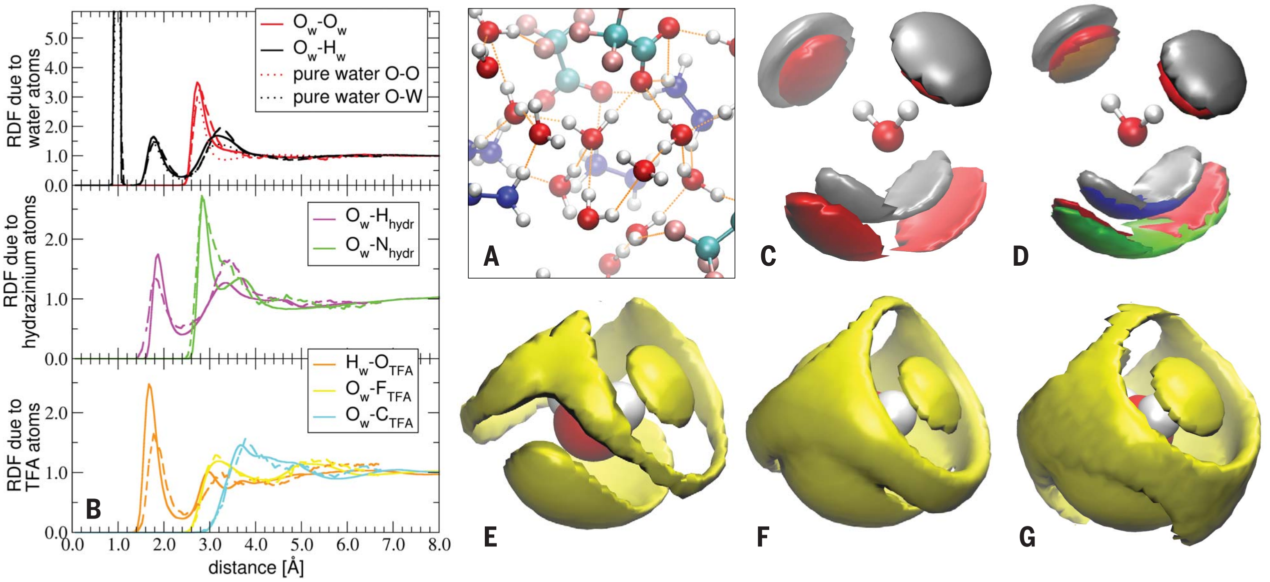

Fig. 3. MD simulations of the investigated solution. (**A**) Snapshot of the classical MD simulation. (**B**) Radial distribution functions (RDFs) of different H-bond donor and acceptor atoms in the solution around water atoms, obtained from the classical (solid lines) and DFT (dashed lines) MD simulations. In the top panel, radial distributions of the water O and H atoms are compared to these functions in bulk water (dotted lines). (**C** and **D**) Three-dimensional structural density plots of the first coordination shell of a water molecule, in neat water (C) and in N_2H_5TFA solution (D), showing the distribution of different H-bond donor and acceptor atoms. Color code for isosurfaces: red, water O atom; gray, water H atom; orange, TFA O atom; blue, hydrazinium H atom; green, hydrazinium N atom. (**E** to **G**) Three-dimensional structural density plots of the H-bond acceptor atoms (water O, TFA O, and hydrazinium N) in the first and second coordination shells of a water molecule (in the center) in neat water at 1 bar (E), in neat water at 6 kbar (F), and in N_2H_5TFA solution at 1 bar (G).

N_2H_5TFA solution (Fig. 3). We performed both classical and ab initio simulations and found that the latter confirmed the former very well. The simulations showed that the ions fit well into the H-bond network of water (Fig. 3). The radial distribution functions (Fig. 3B) showed that in the first coordination shell of the water molecules in the solution, the H and N/O atoms of the solute partly replaced the water H and O atoms as H-bond donor and acceptor atoms. The N/O···H and N/O···O distance distributions in the solution were very similar to the O···H and O···O distributions in neat water. This similarity can be quantified by comparing the average H-bond coordination number of a water molecule in our ionic solution and in neat water, for which we found values of 4.3 and 3.8, respectively (table S1) (*16*).

Because H-bond directionality is an important structural characteristic of water, we also calculated the orientational distribution of the H-bond donor and acceptor atoms around water. These orientational distributions are again very similar in the solution and in neat water (Fig. 3, C and D): The hydrazinium H atoms partly replaced water H atoms as H-bond donors, and the hydrazinium N and TFA O atoms partly replaced water O atoms as H-bond acceptors (the spatial distributions of the H atoms of hydrazinium and water overlap so closely that the intersection of their isosurfaces in Fig. 3D is determined mostly by the noise in the simulations). The same holds for the hydrazinium N and water O atoms, and for the TFA O and water O atoms.

Finally, we investigated the second coordination shell of the water molecules. The structure of the solution (Fig. 3G) differed somewhat from that of neat water at ambient pressure (Fig. 3E). However, the second solvation shell structure of our solution is virtually identical to that of neat water at high pressure, which was determined previously from combined neutron-diffraction experiments and simulations (*23*, *24*) and which we reproduced when performing a simulation of neat water at high pressure (6 kbar in Fig. 3F; intermediate pressures in fig. S8) (*16*). This similarity confirms the experiments by Leberman and Soper (*25*), demonstrating that adding salt modifies the water structure in the same way as increasing the pressure.

Upon cooling the solution (Fig. 2B), the frequency of the OH-stretch frequency initially decreased gradually, in a fashion similar to neat supercooled water (*26*). However, at a temperature close to that of the heat capacity spike (~190 K), a discontinuous change occurred: A new OH-stretch mode appeared at 3300 cm^{-1} and the initial OH-stretch mode vanished. Upon further cooling, this new OH-stretch mode also gradually decreased in frequency. The transition was reversible (Fig. 2C): Upon reheating the sample, the low-frequency OH-stretch mode disappeared and the original high-frequency OH-stretch mode reappeared.

The sample remained transparent during cooling, as well as during subsequent reheating to ~204 K. At that temperature, ice crystallites started to form (Fig. 2A, rightmost panel). The presence of ice appeared distinctly in the IR spectrum (Fig. 2D) as a narrow peak at 3295 cm^{-1} with a width of 50 cm^{-1}. These numbers agreed well with the center frequency and width of the OH-stretch mode of HDO:D_2O ice at this temperature (*21*). The complete absence of the ice peak in the earlier stages of the temperature scan demonstrated that no ice formed during the structural transition associated with the heat capacity spike, neither during cooling nor during reheating. Crystallization occurred at a temperature above that of the heat capacity spike, and only during reheating, not during cooling. This is because crystallization requires both nucleation and growth, and the rate of the latter is generally much smaller than that of the former, which also peaks at a much lower temperature (*27*). Consequently, some nuclei (but no crystals) can be formed at the very lowest temperatures accessed during our experiment, but these nuclei can turn into crystals only at high temperatures (well above that of the heat capacity spike) where the growth rate is sufficient.

The discontinuous nature of the observed structural transition was visible when monitoring the absorbance at 3300 cm^{-1} during cooling and reheating (Fig. 2F). When cooling at a rate of 7 K min^{-1} (red points), the appearance (during cooling) and disappearance (during reheating) of the 3300 cm^{-1} peak occurred at temperatures that differed by about 10 K. However, when cooling at a rate of 1 K min^{-1} (blue points in Fig. 2F), the difference was only 3 K (*28*).

The discontinuous change in the OH-stretch spectrum indicated that the heat capacity spike involves an abrupt change in the H-bond structure. Thus, this transition cannot be a glass transition, which is an arrest—not a change—of structure (caused by the structural equilibration time scale becoming longer than the experimental time scale). The difference is well illustrated by a measurement on a sample with a water fraction of 0.60, which exhibited a glass transition, visible in differential scanning calorimetry as a step decrease in the heat capacity (like that seen in Fig. 1 for the LiCl solution, but at higher temperature). In the IR spectrum, however, we observed only a gradual shift and no discontinuity of the OH-stretch mode (Fig. 2E and gray points in Fig. 2F; note that the x_{water} = 0.84 and x_{water} = 0.60 data were obtained with the same cooling rate).

On the basis of the IR spectra, we can exclude the possibility that the heat capacity spike was caused by ice formation or by a glass transition. Rather, the observed change in H-bond structure indicates that the heat capacity spike can be associated with a phase transition involving a change in the H-bond structure. The OH-stretch spectrum provided direct information on the differences in H-bond structures between the high-temperature and low-temperature liquid phases (Fig. 4): The lower center frequency implies stronger (shorter) H bonds in the low-temperature liquid (relative to the high-temperature liquid), whereas the smaller width (~180 cm^{-1} FWHM) indicates that the H-bond structure is more ordered.

The spectral changes (redshift, narrowing, asymmetry) during the transition from the high- to the low-temperature phase were similar to the changes when going from low-density amorphous (LDA) to high-density amorphous (HDA) water (*29*–*31*) (Fig. 4). The spectra of our solutions have somewhat larger widths, indicating more disorder, probably because of the presence of the ions. The similarity of these spectra strongly suggests that the liquid-liquid transition observed here is directly connected to the HDA-LDA transition in water. The equivalence of high ionic concentrations with the application of high pressure (*22*), as confirmed by our simulations, strongly suggests that a liquid-liquid transition also exists in neat water, as was predicted by Poole (*1*) and others (*32*) and indicated by recent evaporative cooling experiments (*33*, *34*). We hope that our studies will stimulate further work to confirm this implication—for instance, by studying the effect of pressure (by increasing the pressure in the low-temperature phase, it should be possible to recross the liquid-liquid phase line), ionic concentration, and isotope composition [to investigate the role of nuclear quantum effects (*34*)].

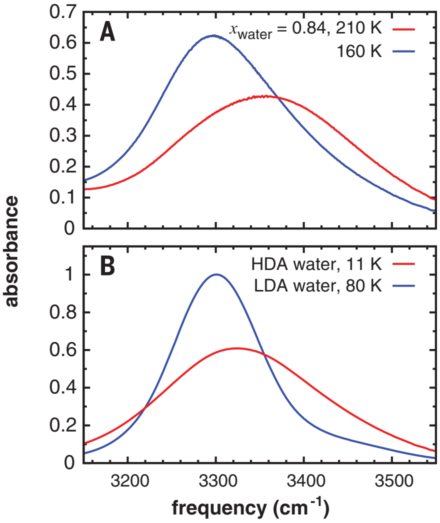

Fig. 4. IR absorption spectra of the two liquid phases and amorphous water. (**A**) High-temperature and low-temperature liquid phases observed in our experiment. (**B**) Low-density and (vapor-deposited) high-density amorphous water; data were measured as described in (*30*, *31*) and provided by the authors of those papers. In (B), the LDA spectrum was normalized to its maximum, and the HDA spectrum was normalized so as to have the same frequency-integrated absorption as the LDA spectrum.

A solid theoretical basis for this scenario has been provided by the groups of Anisimov (*7*) and Debenedetti (*5*), who have shown that a liquid-liquid transition in a binary mixture need not require the usual nonideal positive heat of mixing in the binary solution but can arise purely as a consequence of an anomalous tendency to liquid-liquid unmixing (i.e., polyamorphism) in the pure solvent. The liquid-liquid transition we observed in our crystallization-resistant aqueous solution has all of the features predicted for the latter source of first-order solution transition and would seem to provide direct evidence for the existence of a liquid-liquid transition behind the “crystallization curtain” in pure water. Our IR measurements and MD simulations both indicate that the structures of the two liquid phases are very similar to those of the liquid phases to be expected in neat water at high pressure; thus, they provide forceful arguments for the occurrence of a liquid-liquid transition (similar to the one observed here) in neat water at elevated pressure. In this case, our findings would provide a unifying explanation for the thermodynamic anomalies of liquid water.

REFERENCES AND NOTES

1. P. H. Poole, F. Sciortino, U. Essmann, H. E. Stanley, *Nature* **360**, 324–328 (1992).
2. P. H. Poole, F. Sciortino, T. Grande, H. E. Stanley, C. A. Angell, *Phys. Rev. Lett.* **73**, 1632–1635 (1994).
3. M. G. Sceats, S. A. Rice, in *Water: A Comprehensive Treatise*, F. Franks, Ed. (Plenum, 1982), vol. 7, pp. 83–211.
4. H. Kanno, C. A. Angell, *J. Chem. Phys.* **70**, 4008–4016 (1979).
5. S. Chatterjee, P. G. Debenedetti, *J. Chem. Phys.* **124**, 154503 (2006).
6. M. A. Anisimov, *Russ. J. Phys. Chem. B* **6**, 861–867 (2012).
7. J. W. Biddle, V. Holten, M. A. Anisimov, *J. Chem. Phys.* **141**, 074504 (2014).
8. D. G. Archer, R. W. Carter, *J. Phys. Chem. B* **104**, 8563–8584 (2000).
9. C. A. Angell, *Science* **319**, 582–587 (2008).
10. J. Riemenschneider, R. Ludwig, *J. Chem. Phys.* **135**, 117101 (2011).
11. M. Oguni, C. A. Angell, *J. Chem. Phys.* **73**, 1948–1954 (1980).
12. Z. Zhao, C. A. Angell, *Angew. Chem. Int. Ed.* **55**, 2474–2477 (2016).
13. W. J. Moore, *Physical Chemistry* (Prentice-Hall, ed. 4, 1972).
14. D. Corradini, M. Rovere, P. Gallo, *J. Chem. Phys.* **132**, 134508 (2010).
15. D. Corradini, M. Rovere, P. Gallo, *J. Phys. Chem. B* **115**, 1461–1468 (2011).
16. See supplementary materials.
17. K. Murata, H. Tanaka, *Nat. Mater.* **11**, 436–443 (2012).
18. M. Yang, J. L. Skinner, *Phys. Chem. Chem. Phys.* **12**, 982–991 (2010).
19. A. K. Wyczalkowska, K. S. Abdulkadirova, M. A. Anisimov, J. V. Sengers, *J. Chem. Phys.* **113**, 4985–5002 (2000).
20. C. A. Angell, E. J. Sare, J. Donnella, D. R. MacFarlane, *J. Phys. Chem.* **85**, 1461–1464 (1981).
21. T. A. Ford, M. Falk, *Can. J. Chem.* **46**, 3579–3586 (1968).
22. K. Fumino, A. Wulf, R. Ludwig, *Angew. Chem. Int. Ed.* **48**, 3184–3186 (2009).
23. P. G. Debenedetti, H. E. Stanley, *Phys. Today* **56**, 40–46 (2003).
24. A. K. Soper, M. A. Ricci, *Phys. Rev. Lett.* **84**, 2881–2884 (2000).
25. R. Leberman, A. K. Soper, *Nature* **378**, 364–366 (1995).
26. F. Perakis, P. Hamm, *J. Phys. Chem. B* **115**, 5289–5293 (2011).
27. H. Senapati, K. K. Kadiyala, C. A. Angell, *J. Phys. Chem.* **95**, 7050–7054 (1991).
28. This small difference probably originated mainly from the sample temperature lagging behind the temperature of the thermocouple (see fig. S3), which was not immersed in the liquid but attached to the brass holder keeping the CaF$_2$ windows together.
29. O. Mishima, Y. Suzuki, *Nature* **419**, 599–603 (2002).
30. A. Shalit, F. Perakis, P. Hamm, *J. Phys. Chem. B* **117**, 15512–15518 (2013).
31. A. Shalit, F. Perakis, P. Hamm, *J. Chem. Phys.* **140**, 151102 (2014).
32. P. Gallo *et al.*, *Chem. Rev.* **116**, 7463–7500 (2016).
33. P. Gallo, H. E. Stanley, *Science* **358**, 1543–1544 (2017).
34. K. H. Kim *et al.*, *Science* **358**, 1589–1593 (2017).

ACKNOWLEDGMENTS

We thank H. Sanders for preparing the samples and A. Shalit and P. Hamm for providing the data shown in Fig. 4B. **Funding:** Supported by the John van Geuns Foundation (S.W.) and NSF grant CHE 12-13265 (C.A.A.). **Author contributions:** C.A.A. and S.W. conceived the experiments; Z.Z. and C.A.A. performed and analyzed the calorimetric measurements; M.H. and S.W. performed and analyzed the cryogenic IR measurements; B.E. performed and analyzed the MD simulations; and C.A.A., S.W., and B.E. jointly wrote the manuscript. **Competing interests:** None declared. **Data and materials availability:** All data are reported in the main text and supplement and are also publicly available at the University of Amsterdam's Figshare (doi: 10.21942/uva.5808366).

SUPPLEMENTARY MATERIALS

www.sciencemag.org/content/359/6380/1127/suppl/DC1
Materials and Methods
Supplementary Text
Figs. S1 to S8
Table S1
References (*35*–*44*)

27 September 2017; accepted 24 January 2018
10.1126/science.aao7049

NANOMATERIALS

Coherent, atomically thin transition-metal dichalcogenide superlattices with engineered strain

Saien Xie,[1,2] Lijie Tu,[1]* Yimo Han,[1]* Lujie Huang,[3] Kibum Kang,[2] Ka Un Lao,[3] Preeti Poddar,[2] Chibeom Park,[2] David A. Muller,[1,4] Robert A. DiStasio Jr.,[3] Jiwoong Park[2,3]†

Epitaxy forms the basis of modern electronics and optoelectronics. We report coherent atomically thin superlattices in which different transition metal dichalcogenide monolayers—despite large lattice mismatches—are repeated and laterally integrated without dislocations within the monolayer plane. Grown by an omnidirectional epitaxy, these superlattices display fully matched lattice constants across heterointerfaces while maintaining an isotropic lattice structure and triangular symmetry. This strong epitaxial strain is precisely engineered via the nanoscale supercell dimensions, thereby enabling broad tuning of the optical properties and producing photoluminescence peak shifts as large as 250 millielectron volts. We present theoretical models to explain this coherent growth and the energetic interplay governing the ripple formation in these strained monolayers. Such coherent superlattices provide building blocks with targeted functionalities at the atomically thin limit.

Epitaxial structures with coherent heterointerfaces, in which lattices of dissimilar materials are matched without dislocations, enable advanced scientific and technological applications, including multiferroic oxides with engineered strain and symmetry (*1*, *2*), high-performance quantum cascade lasers (*3*), and high-efficiency light-emitting diodes (*4*). Two-dimensional (2D) coherent heterostructures and superlattices (Fig. 1, A and B) can serve as ultrathin building blocks for advanced stacking and heterointegration with other materials (*5*–*7*) and provide opportunities not available with their 3D analogs. Realizing this goal would require the integration of various 2D materials whose properties can be tuned by the strain required for coherent lattice matching, as well as a method for precisely controlling the superlattice dimensions while maintaining lattice coherence over the entire structure. Monolayer transition metal dichalcogenides (TMDs), many of which share similar crystal structures, provide an ideal material platform with diverse electrical, optical (*8*, *9*), piezoelectric (*10*, *11*), and valley properties (*12*). However, recent studies on TMD heterostructure synthesis have shown only limited capabilities toward realizing coherent 2D superlattices (*13*–*21*).

We report coherent monolayer TMD superlattices with precisely controlled supercell dimensions and lattice coherence maintained over the entire structure, which result in broad tuning of their optical properties. We used WS_2 and WSe_2 as the two main TMDs for our heterostructures and superlattices (Fig. 1A, inset), where the repeat direction of the superlattice is in the growth plane of a monolayer, rather than the out-of-plane direction of conventional thin-film superlattices. These TMDs have a substantial lattice mismatch (Δ) of ~4%, with WSe_2 having the larger lattice constant. In scanning electron microscope (SEM) images of three representative WS_2/WSe_2 heterostructures with controlled supercell dimensions (Fig. 1C), dark (bright) regions correspond to WS_2 (WSe_2) monolayers. Every triangular unit of WS_2 and WSe_2 shows a highly symmetric, equilateral triangular shape of uniform width, each defined by straight, parallel heterointerfaces, that could be directly controlled with nanoscale precision. These widths could be as narrow as 20 nm (Fig. 1C, center) and periodically modulated to form superlattices with different dimensions, represented by the two widths $\{d_{WS2}$ and $d_{WSe2}\}$. Two examples of superlattices are shown, one primarily composed of WS_2 ($d_{WS2} >> d_{WSe2}$) (Fig. 1C, left) and the other by WSe_2 ($d_{WS2} << d_{WSe2}$) (Fig. 1C, right). Heterostructures consisting of different metal and chalcogen elements could also be synthesized with a similar level of control (see fig. S1C for an example of a WSe_2/MoS_2/WS_2 heterostructure).

These crystalline TMD superlattices were synthesized by a modulated metal-organic chemical vapor deposition (MOCVD) (*22*) process (see Fig. 1, supplementary materials, and fig. S1), with two distinctive features compared with previous approaches (*13*–*21*). First, the concentration of each precursor was individually and precisely controlled, which allowed the direct tuning of the supercell dimensions. The composition of TMD could be switched, for example, from WS_2 to WSe_2 and vice versa, by simply changing the chalcogen precursors. The width of each component was determined by controlling the timing of the switch, according

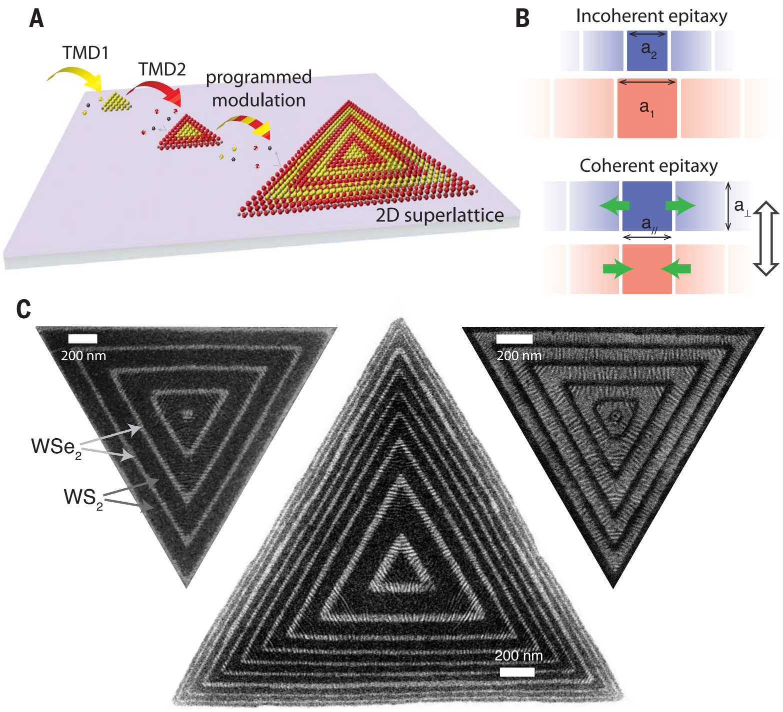

Fig. 1. 2D monolayer TMD superlattices. (**A**) Schematic of 2D superlattices based on monolayer TMDs. (**B**) Schematic of incoherent and coherent epitaxy, with the epitaxy direction represented by the outlined arrow. (**C**) SEM images of three monolayer WS_2/WSe_2 superlattices. Scale bars, 200 nm.

---

[1] School of Applied and Engineering Physics, Cornell University, Ithaca, NY 14853, USA. [2] Department of Chemistry, Institute for Molecular Engineering, and James Franck Institute, University of Chicago, Chicago, IL 60637, USA. [3] Department of Chemistry and Chemical Biology, Cornell University, Ithaca, NY 14853, USA. [4] Kavli Institute at Cornell for Nanoscale Science, Cornell University, Ithaca, NY 14853, USA.
*These authors contributed equally to this work.
†Corresponding author. Email: jwpark@uchicago.edu

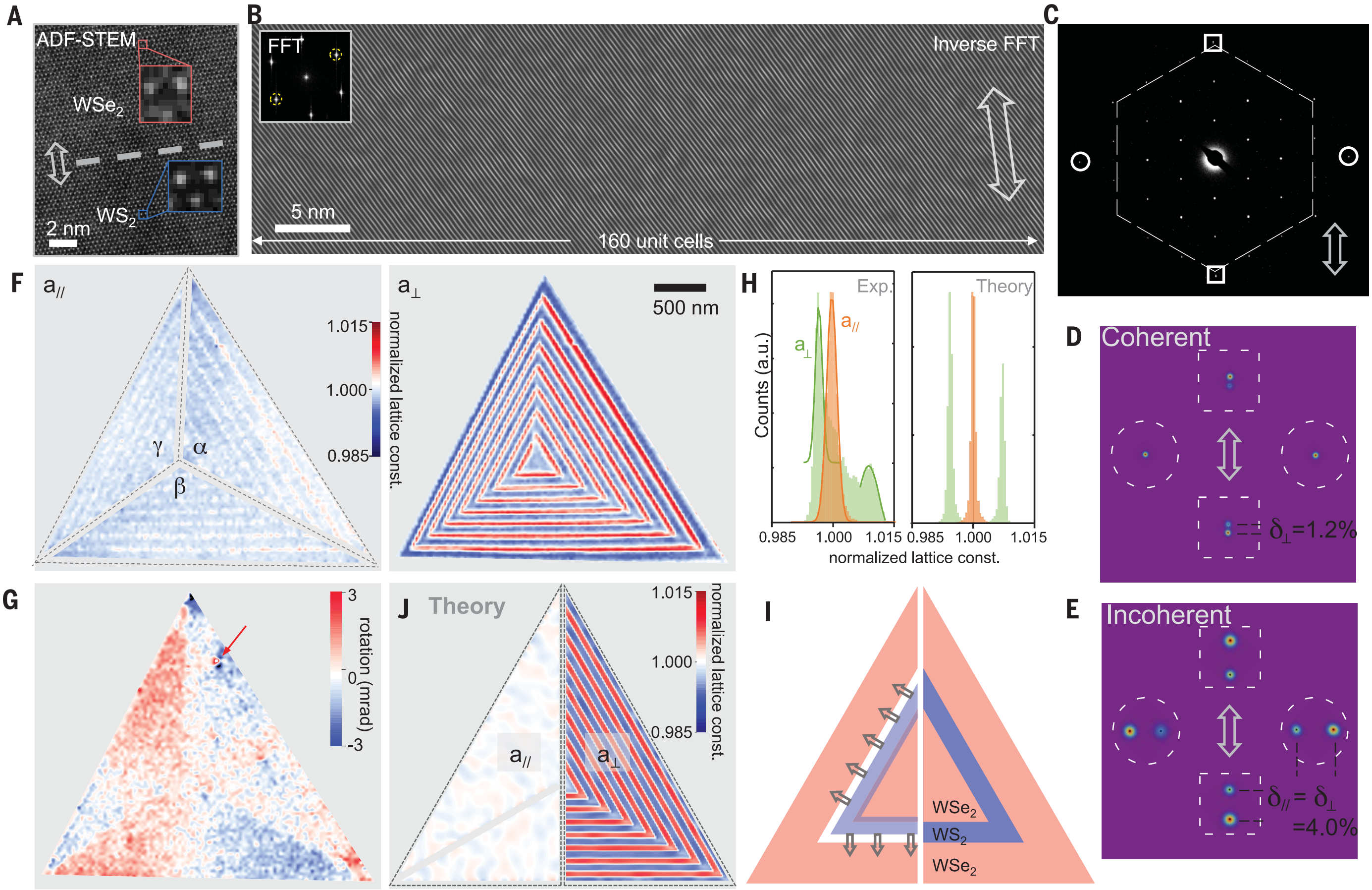

Fig. 2. Lattice coherence of WS_2/WSe_2 superlattices. (**A**) An ADF-STEM image at the heterointerface area between WS_2 and WSe_2 (epitaxy direction represented by the arrow; same for all). Scale bar, 2 nm. (**B**) Inverse FFT of an ADF-STEM image from a larger area near the heterointerface, based on the circled spots in its FFT (inset). Scale bar, 5 nm. (**C**) SAED pattern of superlattice {50 and 40 nm}, taken from an area with a diameter of 280 nm. (**D**) Enlarged diffraction spots as indicated in (C). (**E**) The same diffraction spots as in (D) from an incoherent WS_2/WSe_2 heterostructure. (**F** and **G**) Spatial maps of normalized lattice constants $a_{//}$, $a_\perp$, and lattice rotation map of superlattice {75 and 60 nm}. Scale bar, 500 nm. (**H**) Histograms of $a_{//}$ and $a_\perp$ from experiment [for region α in (F)] and theory [for the superlattice depicted in (J)]. (**I**) Schematic of the isotropic expansion of the WS_2 lattice in an omnidirectional coherent WS_2/WSe_2 heterostructure. (**J**) Composite maps of $a_{//}$ (left) and $a_\perp$ (right) of a superlattice with ratio $d_{WS2}/d_{WSe2} = 1.25$, computed from a coarse-grained theoretical simulation (see fig. S7 and supplementary materials).

to a simple linear dependence between the width and the growth time (see supplementary materials, table S1, and fig. S1).

Second, the growth environment was maintained constant throughout the synthesis regardless of the specific TMD composition, which was crucial for producing coherent heterointerfaces. For example, both WS_2 and WSe_2 were grown under constant temperature, pressure, and overall flow rate, with the only difference being the chalcogen precursors. In our experiment, different components of our superlattices were grown with a slow growth rate (ranging between 20 and 60 nm/min) near thermodynamic equilibrium and exhibited straight heterointerfaces with the most stable W-zigzag edges (fig. S2) (*23*, *24*).

Our WS_2/WSe_2 superlattices maintained lattice coherence over the entire crystal (Fig. 2). First, the superlattices were free of misfit dislocations. Figure 2A shows an annular dark-field scanning transmission electron microscope (ADF-STEM) image near a heterointerface (dashed line) between WS_2 (lower) and WSe_2 (upper). The ADF-STEM data taken from a larger area (Fig. 2B) shows continuous lines of atoms with no misfit dislocations near the heterointerface across ~160 unit cells [shown after the inverse fast Fourier transform (FFT)]. One dislocation is expected every 25 unit cells on average for incoherent heterointerfaces with Δ ≈ 4%, so these images are consistent with our superlattice forming coherent heterointerfaces.

Second, our superlattices displayed lattice constants that were uniform over the entire structure. Figure 2C shows selective-area electron diffraction (SAED) data measured from a representative superlattice {50 and 40 nm} within a region with a single epitaxy direction (denoted by the arrow). These data exhibited a single-crystal–like pattern with sharp and isotropic diffraction spots. We used their positions to measure the lattice constants along the directions parallel ($a_{//}$) or perpendicular ($a_\perp$) to the heterointerfaces (schematic, Fig. 1B), as well as the lattice mismatch along each direction [e.g., $\delta_{//} = 2|a_{//,1} - a_{//,2}|/(a_{//,1} + a_{//,2})$]. Diffraction data corresponding to $a_{//}$ (circles in Fig. 2C, enlarged in Fig. 2D) showed a single diffraction spot with no separation, confirming perfect lattice matching ($\delta_{//} = 0$). Diffraction data corresponding to $a_\perp$ (squares in Fig. 2C, enlarged in Fig. 2D) also showed similar lattice constants; although two spots were observed, each originating from the WS_2 and WSe_2 regions (see below), the mismatch $\delta_\perp = 1.2\%$ was much smaller than Δ. In contrast, the same diffraction spots measured from an incoherent WS_2/WSe_2 heterostructure displayed a 4% concentric separation, with $\delta_{//} = \delta_\perp = \Delta$ (Fig. 2E; see fig. S3 for original SAED patterns).

Lattice coherence was directly confirmed with nanoscale resolution over the entire WS_2/WSe_2 superlattice. We used our newly developed electron microscope pixel array detector (EMPAD), which measures local diffraction maps pixel by pixel, providing structural information for imaging with nanoscale resolution (see supplementary materials) (*25*). Figure 2, F and G, shows three maps generated based on EMPAD data taken

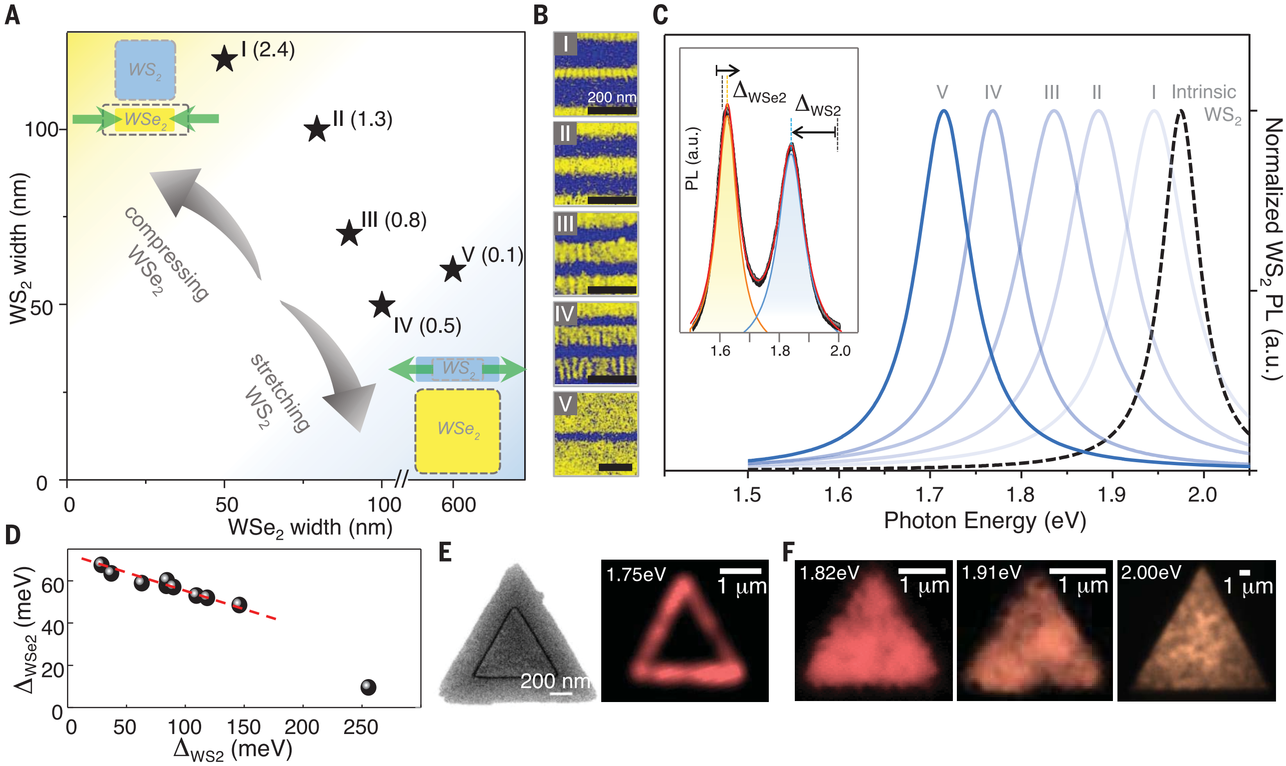

Fig. 3. Strain engineering of PL of WS_2/WSe_2 superlattices. (**A**) Plot of WS_2/WSe_2 superlattices I to V with different ratios $\rho = d_{WS2}/d_{WSe2}$ (values shown in parentheses). (Insets) Schematic of supercell dimension-dependent strain magnitude in the superlattice. (**B**) False-color SEM images of superlattices I to V. Scale bars, 200 nm. (**C**) Normalized PL spectra of WS_2 for intrinsic WS_2 (dashed line) and superlattices I to V. (Inset) A representative PL spectrum of a WS_2/WSe_2 superlattice showing the WS_2 peak red-shifted by Δ_{WS2} and the WSe_2 peak blue-shifted by Δ_{WSe2}. (**D**) Plot of Δ_{WSe2}-Δ_{WS2} for WS_2/WSe_2 superlattices with different supercell dimensions. (**E**) (Left) SEM image of a narrow WS_2 stripe embedded in WSe_2. (Right) PL image of a heterostructure similar to the left, taken at photon energy of 1.75 eV. (**F**) PL images of two WS_2/WSe_2 superlattices at photon energies near their WS_2 peak positions (left and middle, at 1.82 eV and 1.91 eV, respectively) and an intrinsic monolayer WS_2 (right, at 2.00 eV). Scale bars, 1 μm.

from another superlattice {75 and 60 nm}, each plotting $a_{//}$, $a_\perp$, and lattice rotation. The superlattice consists of three regions (α, β, and γ, as outlined in Fig. 2F), with heterointerface orientations rotated by 120° from each other. The orientations of $a_{//}$ and $a_\perp$ are different for α, β, and γ and are defined relative to the heterointerfaces in each region. The $a_{//}$ map (Fig. 2F, left) showed little contrast between WS_2 and WSe_2, generating a single histogram peak as shown in Fig. 2H, left (region α; see fig. S4 for β and γ histograms). The $a_\perp$ map showed a small contrast between the WS_2 and WSe_2 regions, generating two peaks (Fig. 2H, left) centered 0.4% below (corresponding to WS_2) and 0.8% above (corresponding to WSe_2) the $a_{//}$ peak, resulting in $\delta_\perp = 1.2\%$, as seen in Fig. 2D. Third, the lattice rotation map resolved only one dislocation clearly (arrow) within the entire superlattice (lateral size ~3.2 μm), suggesting the existence of a dislocation-free, coherent lattice everywhere, including the boundary regions between the α, β, and γ regions. In contrast, incoherent heterostructures showed arrays of dislocations at heterointerfaces (fig. S5).

Figure 2 shows that $\delta_{//} = 0$ everywhere, confirming coherent heterointerfaces in our superlattice. In addition, the lattice isotropy and rotational symmetry were maintained over the entire superlattice. Our TEM and EMPAD data confirm (i) nearly identical and isotropic unit cell dimensions for both the WS_2 and WSe_2 regions; (ii) that the lattice orientation in our EMPAD map (Fig. 2G) was highly uniform (standard deviation < 1 mrad), consistent with the observed sharp and isotropic TEM diffraction spots (Fig. 2, C and D); and (iii) that the superlattice is triangular with straight edges and heterointerfaces. This result is in sharp contrast to the lattice anisotropy expected from conventional unidirectional epitaxy, where $a_{//}$ is matched for the epilayers and $a_\perp$ is free from any constraints, causing the superlattice to have a different symmetry from that of the original crystal. Instead, our superlattice grew with coherent omnidirectional epitaxy (see supplementary text and fig. S6), where regions of different epitaxy directions (α, β, and γ) coherently connect with each other while maintaining the same symmetry of the original crystal.

The perfect symmetry in our coherent superlattices imposes an additional constraint that requires identical values of $a_\perp$ for both WS_2 and WSe_2. This feature is further illustrated in Fig. 2I: When a triangular WSe_2 unit was replaced by WS_2, the latter needed to expand by the same amount in all directions (i.e., larger $a_{//}$ and $a_\perp$) to coherently bridge the inner and outer triangular WSe_2 units. This ideal picture changes in real superlattices with finite bulk and shear moduli values, where the final structure will minimize the total elastic strain energy. In this case, the lattice would deviate from having identical $a_\perp$ values for WS_2 and WSe_2, resulting in $0 \lesssim \delta_\perp < \Delta$, as seen from our data.

These observations were quantitatively predicted by coarse-grained simulations of these superlattices that account for both bond and angle interactions on an appropriate footing (Fig. 2H, right, and 2J). In this regard, it is the inclusion of angular interactions, in particular, that accounts for the shear stiffness inside the TMD superlattice and thereby introduces local frustration (analogous to the antiferromagnetic triangular-lattice Ising model) that is key to predicting coherent omnidirectional epitaxy across the entire lattice, as well as a small but nonvanishing $\delta_\perp$ (see fig. S7 and supplementary materials). The lattice coherence further allows for high-performance p-n diodes showing high rectification ratios ($>10^6$) and electroluminescence, as well as double heterostructure transistors, which we successfully fabricated using our heterostructures (see figs. S8 and S9 and supplementary text).

This lattice coherence also resulted in a tensile (compressive) strain within the WS_2 (WSe_2) region in our superlattices, the magnitude of which varied depending on the supercell dimensions.

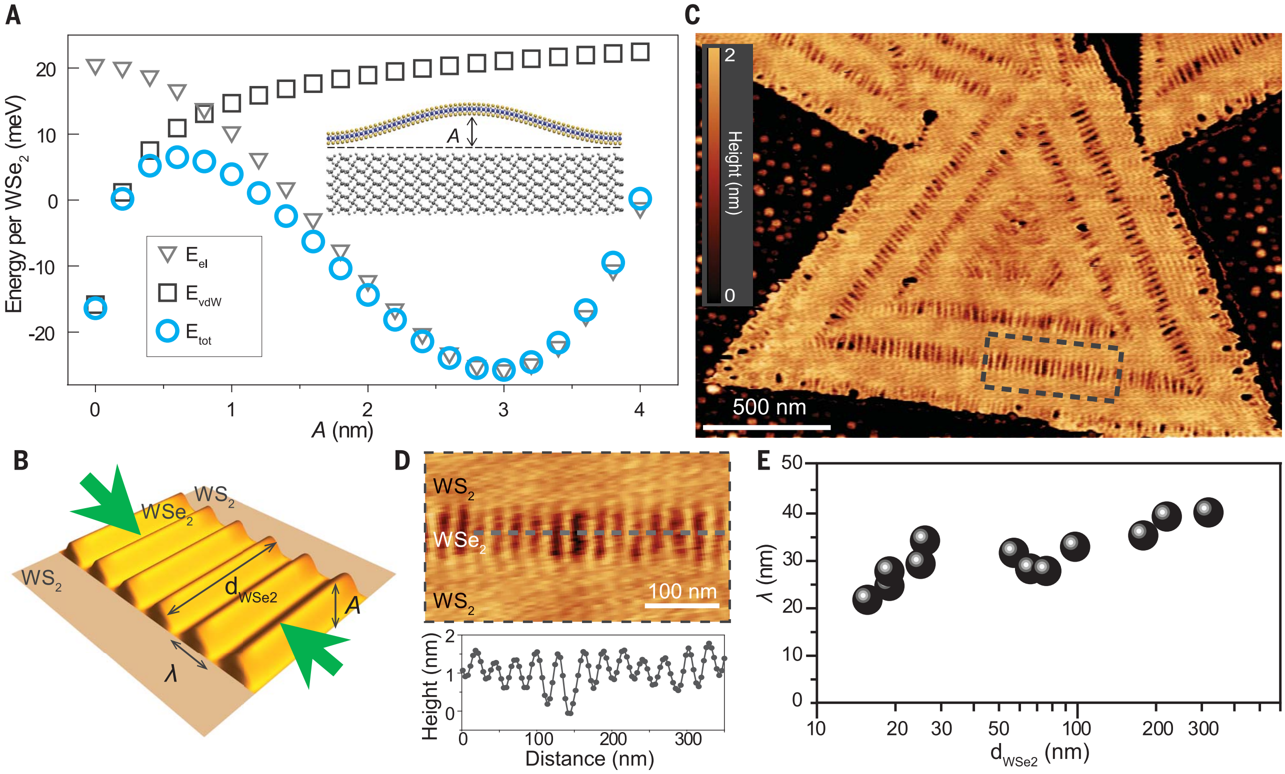

Fig. 4. Formation of out-of-plane ripples in WSe$_2$. (**A**) Theoretically calculated elastic strain energy (E_{el}), interlayer van der Waals binding energy (E_{vdW}), and total energy (E_{tot}) per WSe$_2$ as a function of WSe$_2$ ripple height (A) (E_{el} and E_{vdW} shifted by −32 meV and 53 meV, respectively, for clarity). (Inset) Schematic of the rippled WSe$_2$ on substrate. (**B**) Schematic of rippled WSe$_2$ and flat WS$_2$, where the ripple wavelength (λ), A, and d_{WSe2} are indicated. (**C**) AFM height image of a representative WS$_2$/WSe$_2$ superlattice. Scale bar, 500 nm. (**D**) Enlarged AFM image of the boxed area in (C) and height profile along the dashed line. Scale bar, 100 nm. (**E**) λ of superlattices with different d_{WSe2}.

Figure 3A illustrates such strain control. For example, a smaller d_{WS2} or larger d_{WSe2} (with a small ratio $\rho = d_{WS2}/d_{WSe2}$) increased the tensile strain in WS$_2$ and decreased the compressive strain in WSe$_2$ as it brought $a_{//}$ and $a_{\perp}$ closer to the intrinsic values for WSe$_2$. In addition, the band structure of both WS$_2$ and WSe$_2$ was sensitive to the applied strain; the size of the direct band gap decreased (increased) when subjected to tensile (compressive) strain (*26–29*).

This strain-dependent band structure allowed for broad tuning of the optical properties by superlattice design. Figure 3B shows the false-color SEM images of five representative WS$_2$ (blue)/WSe$_2$ (yellow) coherent superlattices I to V with different ρ (dimensions plotted in Fig. 3A). The resulting photoluminescence (PL) spectra showed two peaks, with one corresponding to WS$_2$ and the other to WSe$_2$ (Fig. 3C, inset). However, the WS$_2$ peak was red-shifted from the intrinsic peak energy of 1.97 eV by Δ_{WS2}, whereas the WSe$_2$ peak was blue-shifted from the intrinsic value of 1.61 eV by Δ_{WSe2}. Figure 3C compares the normalized WS$_2$ peaks measured from superlattices I to V (each extracted from the full PL spectra) to the intrinsic WS$_2$ peak (dashed curve). Superlattices with smaller ρ showed larger Δ_{WS2}, as large as 250 meV (see fig. S10 for representative original PL spectra). Figure 3D further plots Δ_{WS2} versus Δ_{WSe2} for additional superlattices with different supercell dimensions.

These PL characteristics were consistent with the strain engineered by the superlattice design. The positive values for both Δ_{WS2} and Δ_{WSe2} confirmed the tensile (compressive) strain in WS$_2$ (WSe$_2$). Their magnitudes showed a negative correlation, which is consistent with their expected negatively correlated strain magnitude (Fig. 3A). The largest Δ_{WS2} of 250 meV, corresponding to a 3.4% uniaxial strain or a 1.4% isotropic biaxial strain (*26*), was consistent with the large tensile strain expected from superlattice V with a small $\rho = 0.1$. Moreover, the PL image (Fig. 3E, right; taken at 1.75 eV) confirmed that the highly red-shifted WS$_2$ PL peak indeed originated from the strained WS$_2$ region (SEM image of a similarly grown sample shown in Fig. 3E, left). In general, superlattices with supercell dimensions below the diffraction limit (Fig. 3F, left and middle) showed uniform PL intensities at their respective peak energies over the entire structure, with a similar uniformity compared with intrinsic WS$_2$ (Fig. 3F, right).

Strained thin films relax through out-of-plane deformations such as wrinkles and ripples, which makes these films nonflat and their edges curved (*30–32*). However, our ultrathin superlattices maintained lattice coherence and symmetry, despite being highly strained and their edges being under alternating compressive and tensile stress during growth, because of strong van der Waals (vdW) interactions between the superlattice and the underlying growth substrate (*5*, *33*) (SiO$_2$ in our experiment), which keep the 2D superlattice flat. Figure 4A plots the theoretically calculated total energy (E_{tot}, circles) per WSe$_2$ of a strained WSe$_2$ monolayer on SiO$_2$ as a function of the out-of-plane ripple height (A, measured from peak to valley; see schematic in Fig. 4B). E_{tot} consists of the elastic strain energy (E_{el}, triangles), computed using a macroscopic elastic energy model (that accounts for both stretching and bending energy components in an ultrathin film), and the interlayer vdW binding energy between the WSe$_2$ and SiO$_2$ (E_{vdW}, squares), computed using an all-atom quantum-mechanical vdW energy model (see supplementary text and fig. S11). Although the rippled state ($A \approx 3$ nm) that relaxes the compressive strain is lowest in energy, the energetic profile shows another minimum at $A = 0$ nm, corresponding to the flat state. These two states have similar energies because the reduction in E_{el} roughly equals the increase in E_{vdW} for the rippled state.

The rippled and flat states are separated by an energetic barrier (with an activation energy of 10 to 20 meV per WSe$_2$), because the increase in A in the regime $0 < A < 1$ nm rapidly destabilizes E_{vdW} without substantially stabilizing E_{el}. Figure 4A thus predicts that the attractive vdW force from the substrate keeps WSe$_2$ flat and that the transition from the flat to rippled state can only occur in the presence of a substantial perturbation.

As a result, these theoretical findings suggest that the synthesis conditions in our experiment, which maintained a constant growth environment with no strong perturbations, allowed the superlattice to remain flat and the growth edge straight during growth.

The superlattices reported here were subjected to a cool-down process after growth, from a relatively high growth temperature (600°C) to room temperature. This process could perturb the samples (e.g., thermal expansion/contraction of the superlattice and SiO_2) and induce ripples in WSe_2, which is what we observed in our samples. The atomic force microscope (AFM) height image of a representative WS_2/WSe_2 superlattice (Fig. 4C) shows out-of-plane ripples in WSe_2 (schematically illustrated in Fig. 4B). These ripples ran continuously across the WSe_2 stripes only and were periodic along the heterointerfaces, as shown in the enlarged AFM image (Fig. 4D, top). The peak-to-valley height (A) was between 1 and 2 nm (measured from the AFM profile shown in Fig. 4D, bottom). This value is surprisingly near that of A for the lowest energy state in Fig. 4A, despite the use of a simple energetic model and an idealized superlattice geometry. We also observed that the ripple wavelengths (λ) for superlattices with different d_{WSe2} remained relatively constant (near 30 nm, as shown in Fig. 4E), with little dependence on d_{WSe2} over one order of magnitude (ranging from 20 to 320 nm). This result suggests that the presence of WS_2/WSe_2 interfaces had minimal effect on the energetics of the ripple formation in this regime and that the constant compressive strain in WSe_2 (even up to d_{WSe2} = 320 nm) was released through rippling. This finding also explains the smaller range of Δ_{WSe2} shown in Fig. 3D.

For superlattices with $d_{\mathrm{WSe2}} > 320$ nm, however, the periodic ripples were no longer continuous across the WSe_2 area (see fig. S12). This difference indicates the presence of an alternative strain relaxation mechanism, including the formation of misfit dislocations and a coherence length of ~320 nm for our WS_2/WSe_2 superlattices. This coherence length was substantially greater than the critical thickness of 2 nm for the Si/Ge system with a similar $\Delta \sim 4\%$ (*34*), as well as the critical thickness for the WS_2/WSe_2 system estimated using the People-Bean model (below 20 nm) (see supplementary materials and fig. S13) (*35*). A full explanation for such a long coherence length would require a general theory optimized for 2D, which is currently lacking. However, we expect that our stable superlattice growth conditions and a larger energetic barrier for dislocation formation in 2D systems may account for the long coherence length. For example, there are limited configurations of covalent bonding for dislocations in 2D systems and no screw dislocations. Our demonstration of omnidirectional coherent 2D superlattices not only presents a powerful framework for the epitaxial synthesis of nanomaterials and the engineering of their properties but also opens up the possibility of a new interdisciplinary research direction because our coherent superlattice is crystalline yet highly deformable. Generation of ordered arrays of coherent superlattices would further accelerate their electronic and optoelectronic applications, which may be achieved with improved spatial control of nucleation (*36*) and superlattice orientation (*37*, *38*).

REFERENCES AND NOTES

1. J. Wang *et al.*, *Science* **299**, 1719–1722 (2003).
2. D. G. Schlom *et al.*, *MRS Bull.* **39**, 118–130 (2014).
3. J. Faist *et al.*, *Science* **264**, 553–556 (1994).
4. S. Nakamura, *Science* **281**, 955–961 (1998).
5. A. K. Geim, I. V. Grigorieva, *Nature* **499**, 419–425 (2013).
6. D. Jariwala, T. J. Marks, M. C. Hersam, *Nat. Mater.* **16**, 170–181 (2017).
7. D. Sarkar *et al.*, *Nature* **526**, 91–95 (2015).
8. Q. H. Wang, K. Kalantar-Zadeh, A. Kis, J. N. Coleman, M. S. Strano, *Nat. Nanotechnol.* **7**, 699–712 (2012).
9. X. Xu, W. Yao, D. Xiao, T. F. Heinz, *Nat. Phys.* **10**, 343–350 (2014).
10. W. Wu *et al.*, *Nature* **514**, 470–474 (2014).
11. H. Zhu *et al.*, *Nat. Nanotechnol.* **10**, 151–155 (2015).
12. K. F. Mak, J. Shan, *Nat. Photonics* **10**, 216–226 (2016).
13. X. Duan *et al.*, *Nat. Nanotechnol.* **9**, 1024–1030 (2014).
14. Y. Gong *et al.*, *Nat. Mater.* **13**, 1135–1142 (2014).
15. C. Huang *et al.*, *Nat. Mater.* **13**, 1096–1101 (2014).
16. M.-Y. Li *et al.*, *Science* **349**, 524–528 (2015).
17. K. Chen *et al.*, *ACS Nano* **9**, 9868–9876 (2015).
18. Y. Gong *et al.*, *Nano Lett.* **15**, 6135–6141 (2015).
19. X. Q. Zhang, C. H. Lin, Y. W. Tseng, K. H. Huang, Y. H. Lee, *Nano Lett.* **15**, 410–415 (2015).
20. H. Heo *et al.*, *Adv. Mater.* **27**, 3803–3810 (2015).
21. K. Bogaert *et al.*, *Nano Lett.* **16**, 5129–5134 (2016).
22. K. Kang *et al.*, *Nature* **520**, 656–660 (2015).
23. S. Helveg *et al.*, *Phys. Rev. Lett.* **84**, 951–954 (2000).
24. J. V. Lauritsen *et al.*, *Nat. Nanotechnol.* **2**, 53–58 (2007).
25. M. W. Tate *et al.*, *Microsc. Microanal.* **22**, 237–249 (2016).
26. P. Johari, V. B. Shenoy, *ACS Nano* **6**, 5449–5456 (2012).
27. Y. Wang *et al.*, *Nano Res.* **8**, 2562–2572 (2015).
28. R. Schmidt *et al.*, *2D Mater.* **3**, 021011 (2016).
29. R. Frisenda *et al.*, *npj 2D Mater. Appl.* **1**, 10 (2017).
30. Y. Klein, E. Efrati, E. Sharon, *Science* **315**, 1116–1120 (2007).
31. B. Davidovitch, R. D. Schroll, D. Vella, M. Adda-Bedia, E. A. Cerda, *Proc. Natl. Acad. Sci. U.S.A.* **108**, 18227–18232 (2011).
32. D. Nandwana, E. Ertekin, *Nano Lett.* **15**, 1468–1475 (2015).
33. A. Ambrosetti, N. Ferri, R. A. DiStasio Jr., A. Tkatchenko, *Science* **351**, 1171–1176 (2016).
34. J. W. Matthews, A. E. Blakeslee, *J. Cryst. Growth* **27**, 118–125 (1974).
35. R. People, J. C. Bean, *Appl. Phys. Lett.* **47**, 322–324 (1985).
36. S. Najmaei *et al.*, *Nat. Mater.* **12**, 754–759 (2013).
37. D. Dumcenco *et al.*, *ACS Nano* **9**, 4611–4620 (2015).
38. D. Ruzmetov *et al.*, *ACS Nano* **10**, 3580–3588 (2016).

ACKNOWLEDGMENTS

We thank S. Nagel, T. Witten, and A. Tkatchenko for helpful discussions. We thank J.-U. Lee for help with EL measurements. **Funding:** This work was primarily supported by the Air Force Office of Scientific Research (FA9550-16-1-0031, FA9550-16-1-0347, and FA2386-13-1-4118) and the National Science Foundation (NSF) through the Cornell Center for Materials Research with funding from the NSF Materials Research Science and Engineering Centers (MRSEC) program (DMR-1719875), the University of Chicago MRSEC (NSF DMR-1420709), and the Platform for the Accelerated Realization, Analysis, and Discovery of Interface Materials (PARADIM; DMR-1539918). Additional funding was provided by the Samsung Advanced Institute of Technology. Material characterizations including electron microscopy were supported by the Cornell Center for Materials Research (NSF DMR-1719875) and the MRSEC Shared User Facilities at the University of Chicago (NSF DMR-1420709). L.T., K.U.L., and R.D. acknowledge partial support from Cornell University through start-up funding. This research used resources of the Argonne Leadership Computing Facility at Argonne National Laboratory, which is supported by the Office of Science of the U.S. Department of Energy under contract no. DE-AC02-06CH11357 and resources of the National Energy Research Scientific Computing Center, which is supported by the Office of Science of the U.S. Department of Energy under contract no. DE-AC02-05CH11231. **Author contributions:** S.X. and J.P. conceived the experiments. S.X. developed the superlattice synthesis and performed DF-TEM, electron diffraction, and optical measurements. Y.H. and D.A.M. conducted the atomic-resolution STEM imaging and EMPAD characterizations. L.T., K.U.L., and R.A.D. developed and conducted the coarse-grained simulations and vdW calculations. S.X., K.K., and C.P. carried out AFM and SEM characterizations, and S.X., L.H., and P.P. performed the device fabrication and measurements. S.X., R.A.D., and J.P. wrote the manuscript. All authors discussed and commented on the manuscript. **Competing interests:** The authors declare no competing financial interests. A provisional U.S. patent has been filed based on this work. **Data and materials availability:** All data are reported in the main text and supplementary materials.

SUPPLEMENTARY MATERIALS

www.sciencemag.org/content/359/6380/1131/suppl/DC1
Materials and Methods
Supplementary Text
Figs. S1 to S13
Table S1
References (*39*–*61*)

9 August 2017; accepted 22 January 2018
10.1126/science.aao5360

GEOCHEMISTRY

Ice-VII inclusions in diamonds: Evidence for aqueous fluid in Earth's deep mantle

O. Tschauner,[1]* S. Huang,[1] E. Greenberg,[2] V. B. Prakapenka,[2] C. Ma,[3] G. R. Rossman,[3] A. H. Shen,[4] D. Zhang,[2,5] M. Newville,[2] A. Lanzirotti,[2] K. Tait[6]

Water-rich regions in Earth's deeper mantle are suspected to play a key role in the global water budget and the mobility of heat-generating elements. We show that ice-VII occurs as inclusions in natural diamond and serves as an indicator for such water-rich regions. Ice-VII, the residue of aqueous fluid present during growth of diamond, crystallizes upon ascent of the host diamonds but remains at pressures as high as 24 gigapascals; it is now recognized as a mineral by the International Mineralogical Association. In particular, ice-VII in diamonds points toward fluid-rich locations in the upper transition zone and around the 660-kilometer boundary.

The water content of Earth's mantle is a key parameter of Earth's water budget (*1*). Global recycling of water in Earth drives important forms of volcanism such as island arcs (*2*, *3*), controls upper-mantle rheology (*4*), and plays a role in the evolution of mantle plumes (*5*). Subducted oceanic crust dehydrates at shallow depth (*2*, *3*), whereas faster and colder slabs can carry water much deeper (*6*). Average water abundance in the mantle changes markedly across the boundary between the upper mantle (UM) and the transition zone (TZ), as well as across the boundary between the TZ and the lower mantle (LM). These boundaries originate in the pressure-driven phase transformations of mantle rock minerals—in particular, the transformations of olivine to wadsleyite at 410 km and from ringwoodite to bridgmanite and periclase at 660 km depth. The UM contains only modest amounts of water on average (*7*), whereas the average water content in the TZ has been estimated at ~0.1 weight percent (*8*), or more than 10 times that of the UM. The abundance of water in the LM is unknown, but its constituent minerals appear to have much lower solubility of water than the minerals of the TZ (*9*, *10*). The average abundance of chemically bound water in these different regions of Earth, as well as possible occurrences of smaller layers or loci of water-rich rock or melt, are central to our understanding of Earth's water budget over extended geologic time. Furthermore, fluids and water-assisted partial melting mobilize mantle-incompatible elements, including heat-generating K, Th, and U. Previous models have proposed that upwelling mantle releases water while crossing the TZ-UM boundary and generates a buoyant layer of a comparatively water-rich melt that accounts for much of Earth's budget of heat-generating elements (*11*). Further, downward-moving material that crosses the TZ-LM boundary may lose its chemically bound water upon transformation into the LM minerals bridgmanite and periclase, thus triggering mantle metasomatism around the 660-km boundary (*10*, *11*).

The actual water content of different mantle regions depends not only on thermodynamic limits on water solubility but also on the mechanism in real Earth that carries water to beyond 410 km depth (*1*). The question of water abundance in the deeper mantle can therefore only be decided on the basis of actual samples from these regions whose mineralogical or petrographic record is placed in context with geochemical and geophysical observations, such as seismic wave attenuation and electrical conductivity (*1*, *4*, *8*), and by using experimentally obtained thermodynamic properties. Diamond is the main source of minerals from the deeper mantle: A mineralogical record from depths as great as 660 km or even beyond has been identified as inclusions in natural diamonds (*12*, *13*). Pearson *et al.* (*14*) reported an inclusion of hydrous ringwoodite in diamond from below 520 km depth whose formation implies a much more hydrous environment than the UM average. Generally, peridotitic diamonds mark regions of mantle metasomatism (*15*). Over long geologic time, metasomatism is almost pervasive, at least in Earth's UM. Diamonds conserve important information about these important processes (*16*).

Here, we provide evidence for the presence of aqueous fluid in regions of the TZ and around the TZ-LM boundary by showing the presence of ice-VII as inclusions in diamonds from these regions of the mantle. Ice-VII has recently been recognized as a mineral by the International Mineralogical Association [2017-029 (*17*)] (Table 1) on the basis of x-ray diffraction data that are presented here (Fig. 1). Ice-VII is a high-pressure form of water ice that is stable above 2.4 GPa (*18*). As we show, ice-VII (along with magnesian calcite, ilmenite, and halite) sensitively records high remnant pressures, which then also constrain the pressure and temperature where it has been encapsulated in the host diamond crystal, similar to other micrometer-scale inclusions of soft molecular materials such as CO_2, CO_2-H_2O, and N_2 in diamond (*19*–*23*).

By retaining high pressures, ice-VII inclusions monitor the former presence of H_2O-rich fluid at different depths in the diamond-bearing mantle. Remnants of former fluids and melts have been found as inclusions in many diamonds through infrared (IR) spectroscopy and microchemical analysis (*19*, *22*). On the basis of IR spectroscopy, a lower-pressure ice phase, VI, has been reported as an inclusion in diamond (*24*), but the fact that aqueous fluid has been trapped in the TZ or LM and crystallized as ice-VII was previously unknown.

Diamonds from southern Africa (Orapa, Namaqualand), China (Shandong), Zaire, and Sierra Leone were examined by diffraction with hard x-rays (0.3344 Å) and a beam focused to 2 μm × 3 μm at the undulator beamline 13-IDD (GSECARS, Advanced Photon Source, Argonne National Laboratory). A PILATUS 3X CdTe1M pixel array detector was used for collecting diffraction data. Diffraction from ice-VII was observed in diamonds from southern Africa and China as isolated arrays within the diamond matrix of dimensions ranging from 3 μm × 10 μm to less than 2 μm × 3 μm. Ice-VII was observed as isolated inclusions tens of micrometers afar from other inclusions, in proximity to small amounts of nickeliferous carbonaceous iron (Fig. 1), similar to metal inclusions reported in earlier studies on diamond (*24*), to ilmenite, and, in one case, to alkali halides. Many inclusions, such as silicates, carbonates, oxides, and halides, were observed through x-ray fluorescence mapping, some of which could be clearly identified through diffraction or microchemical analysis (Table 1). The observation of olivine with 94 to 97 mol % forsterite component (Fo 94-97) places the origin of the hosting diamonds in mantle peridotite rather than eclogite, whereas ilmenite is indicative of metasomatized mantle (*15*).

In all cases, the diffraction pattern of ice-VII is powderlike with no visible granularity (Fig. 1, inset). The patterns were unambiguously identified by Rietveld refinement as those of ice-VII (Table 1 and Fig. 1) (*26*) and correlate with IR absorption bands of O-H stretching vibrations (*26*). The high quality of some of the diffraction data resulted in noticeable proton contributions to the patterns (Fig. 1). Aqueous fluid in Earth's mantle is expected to be saline (*22*) and ice-VII can dissolve at least up to ~2 mole percent (mol %) of alkali halides (*27*, *28*). For structure analysis and for the assessment of pressure, dissolution of (Na,K)Cl has been taken into consideration. We provide details about the crystallography of natural ice-VII in (*26*); here, we focus on the

---

[1]Department of Geoscience, University of Nevada, Las Vegas, NV 89154, USA. [2]Center of Advanced Radiation Sources, University of Chicago, Chicago, IL 60637, USA. [3]Division of Geology and Planetary Science, California Institute of Technology, Pasadena, CA 91125, USA. [4]Gemological Institute, China University of Geosciences, Wuhan 430074, China. [5]School of Ocean and Earth Science and Technology, University of Hawai'i at Manoa, Honolulu, HI 96822, USA. [6]Royal Ontario Museum, Toronto, Ontario M5S 2C6, Canada.
*Corresponding author. Email: olivert@physics.unlv.edu

petrologic implications. We note that, with one exception (Table 1), the total salinity of the observed inclusions (ice-VII plus coexisting phases) is much lower than the alkali halide content of fluid inclusions commonly observed in diamonds. These inclusions also contain high amounts of silicate or carbonate (*22*). Many inclusions of silicates, carbonates, oxides, and halides are found within distances of several tens to 100 μm from the ice-VII inclusions. Plausibly, some of these phases that have been encapsulated at the same depth are precipitates from one complex fluid. We propose that a complex aqueous fluid was entrapped as separate inclusions that crystallized as ice-VII, carbonate, halide, and silicate rather than mimicking the bulk fluid composition in each inclusion (*26*).

Because of their confinement by the rigid diamond host crystal, the inclusions of ice-VII remain at high pressure, allowing us to use the equation of state of ice-VII to determine minimum pressures for formation of the surrounding diamond (Table 1). We found pressures of about 6 GPa and 9 ± 1.6 GPa for diamonds from Orapa, Botswana. We determined a pressure of 12 ± 2 GPa for a diamond from Shandong, China, and 24 to 25 (±3) GPa for a specimen from Namaqualand. In the fibrous rim of one diamond, we found a NaCl hydrate at a pressure of at least 1 GPa, rather than ice-VII (Table 1). We note that this sample was found at the same locality as three of the samples with inclusions around 6 and 9 GPa (Orapa, Botswana). Thus, ice-bearing diamonds from one location are not from the same source region or underwent additional growth at shallow depth. However, diamonds from geologically different locations such as China and southern Africa contain ice inclusions that reside at high pressures of 9 to 12 GPa (Table 1). Differences in nitrogen aggregation also indicate markedly different geologic ages or temperatures of the host diamonds and overall low nitrogen aggregation (*26*). Of 13 occurrences of ice-VII, eight fall into a narrow pressure

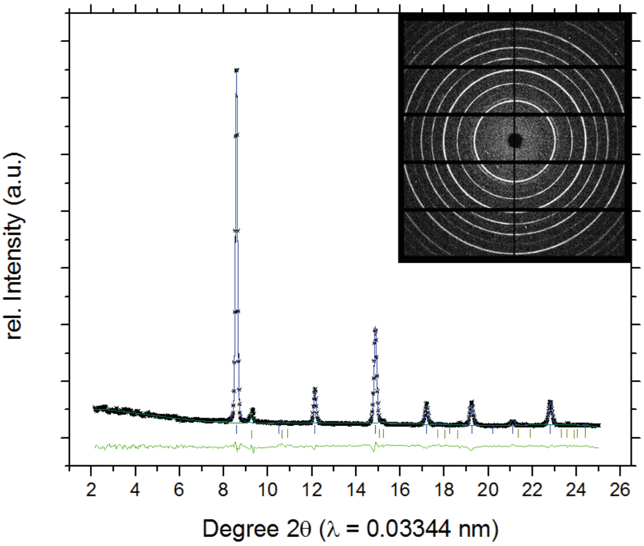

Fig. 1. Diffraction pattern of ice-VII in diamond M57666 from Orapa. Black crosses are data points; the Rietveld refinement based on this pattern of the type material (blue curve) converged to a weighted profile refinement parameter R_{wp} of 5.72% with a profile refinement parameter R_p of 4.57% and with $\chi^2 = 1.71$ for 1398 observations. The structure factor–based refinement parameter R_F was 4.0% (see table S3). The green line indicates the residual of fit. Blue tick marks denote symmetry-allowed reflections of ice-VII; olive tick marks denote allowed reflections of (Fe,Ni,C). (Fe,Ni,C) contributes 0.75 ± 0.05 volume percent to the pattern. The equation of state (*27*) allows estimation of the current pressure of this inclusion of ice-VII as 9.2 ± 1.6 GPa. The inset is a diffraction image of ice-VII. A diffraction image of ice-free diamond ~20 μm afar was used as a background image. Remaining single-crystal reflections are from the hosting diamond.

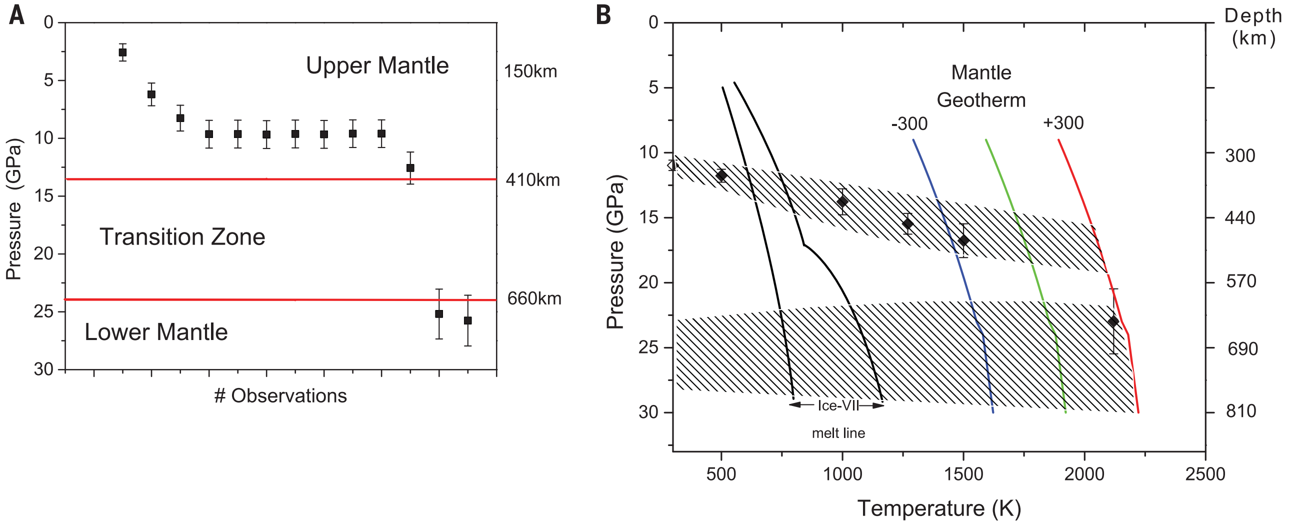

Fig. 2. Pressures of occurrences of ice-VII in natural diamonds. (**A**) Current residual pressures (black squares; error bars denote SD). These residual pressures also represent lower bounds of the pressures of entrapment. Thirteen inclusions have been identified with pressures ranging from >1 to 25 (±3) GPa. The majority of inclusions have residual pressures around 9 GPa. Red lines indicate the transitions between UM and TZ and between TZ and LM. (**B**) Reconstruction of entrapment conditions. We used the equations of state of diamond and fluid H_2O (*26*) to estimate plausible entrapment conditions. Current pressures were corrected for elastic relaxation of surrounding diamond (*33*). Within uncertainties, entrapment conditions can be estimated by the intersection of fluid H_2O isochores and mantle adiabats. We consider the current average mantle geotherm (*25*) and two adiabats that are 300 K hotter and cooler as a reference frame. The intersection of the isochores with these adiabats gives ranges of pressure of encapsulation of the aqueous fluid in growing diamond. We also show the entrapment path of ilmenite (black diamonds; error bars denote SD) with a residual pressure of 11 to 12 GPa that was found in ice-bearing diamond GRR1507 (Table 1). Simultaneous entrapment of ilmenite and fluid H_2O occurred at a pressure-temperature regime of 450 to 550 km depth and 1400 to 1900 K. The melting curve of ice-VII (*26*) is given for reference.

Table 1. Occurrences of ice-VII inclusions in diamond, number of occurrences, current pressure, and other observed inclusions. The assessment of pressure and its correction for elastic relaxation (P_{cor}) is described in (*26*). (Na,K)Cl·5H_2O has an ice-VII–like structure with Na + K + Cl residing on sites 2a and 4b (*26*). Volumes (μm^3) are approximate values based on integrated diffraction signal over the two-dimensional sampling grid; the depth was taken as an average of the two measured dimensions. A volume of 40 μm^3 corresponds to occurrences in single patterns. For weak single patterns, we assume a volume much smaller than 40 μm^3. Coexisting phases are defined as those observed in the same patterns as ice-VII; the phases may not be hosted by the same cavity. Errors in the last significant digit(s) are shown in parentheses.

Specimen	Ice-VII volume (Å^3)	(Na,K)Cl (mol %)	P (GPa)	P_{cor} (GPa)	O-H stretch and combination bands (cm^{-1})	Volume (μm^3)	Coexisting phases	Other phases
GRR1518	88.0(1)	16.8	≥1	—	3220(20)	<40	(Na,K)Cl, (Na,K)Cl·5H_2O	
GRR1507	33.689(8)	3(1)	6(1)	7(2)	3210(20)	<<40	Ilmenite† 85%	Olivine (Fo94-97),‡ calcite, sellaite
GRR1507	32.40(1)	<5	7.9(1.4)	9(2)	—	<40	Ilmenite† 81%	
GRR1521	31.647(5)	<0.1	9.2(1.6)	11(2)	3000 to 3100	<40	—	Garnet, olivine
M57666*	31.653(4)	4.4(6)	9.2(1.6)	11(2)	2950 to 3100	3000	(Fe,Ni,C) 0.75%	
GRR1521	31.632(5)	2.4(6)	9.3(1.6)	11(2)	—	500	(Fe,Ni,C) 59.7%	
GRR1521	31.658(8)	1.8(1)	9.2(1.6)	11(2)	—	500	(Fe,Ni,C) 0.7%	
GRR1521	31.641(5)	<0.1	9.3(1.6)	11(2)	—	<40	(Fe,Ni,C) 1.0%	
GRR1521	31.671(5)	3.6(4)	9.2(1.6)	11(2)	—	<40	(Fe,Ni,C) 1.3%	
GRR1521	31.6705(9)	<0.1	9.2(1.6)	11(2)	—	3000	—	
Balas-1	26.38(4)	3(1)	24(3)	28(5)	3140(20), 4500(50)	<40	—	Calcite, halite, sellaite,‡ chromite
Balas-3	26.25(9)	3(2)	25(3)	28(5)	—	<<40	—	
SM548	30.284(9)	2 to 5	12.0(2.0)	14(2)	3100(50)	<40	—	Calcite,§ halite,§ olivine

*Ice-VII type specimen. †(Ilm92-97 Geik3-8), $a = b = 5.0161(6)$ Å, $c = 13.686(4)$ Å. ‡Sellaite, MgF_2, olivine composition was measured by SEM-EDS from four different locations. §$(Ca_{0.75(2)}Mg_{0.25(2)})CO_3$, $a = b = 4.803(2)$, $c = 15.98(1)$ Å, which corresponds to 8 to 9 GPa (*26*); halite, $a = 5.231$ Å, which corresponds to 10(1) GPa (*26*).

interval around 8 to 12 GPa (Fig. 2A and Table 1). This pronounced clustering of sustained pressures and the observation of ice inclusions at 24 to 25 GPa have geologic implications: They point toward regions in the deep mantle where aqueous fluid was present during growth of diamond. We note that the sustained pressures of ice-VII inclusions match those of inclusions of ilmenite, magnesian calcite, and halite in the same host diamonds (Table 1) (*26*), indicating growth at similar depth.

We can attempt to go a step further and estimate the pressure under which the inclusions were trapped by correcting for the thermal contribution to pressure and volume caused by the high temperatures in the deeper mantle. This requires reconstruction of plausible paths that connect the current residual pressure of these inclusions with the pressures and temperatures of their possible host regions in the deep Earth. That temperature can be along the current average mantle geotherm, a possibly higher geothermal temperature in the geologic past, or a cooler regime in the vicinity of subducted slabs or within harzburgitic restites. Therefore, we encompass these different possible temperature-depth regimes by a reference frame defined through three adiabats whose temperatures include possible cool and hot regimes (*25*, *29*–*32*): the modern average mantle geotherm (*25*) plus two adiabats 300 K below and above this geotherm. This does not imply that the ice-bearing diamonds formed in a convecting mantle; rather, it defines a temperature-pressure range that includes different plausible source regions. We argue that within given uncertainties of thermoelastic properties, the pressure range of entrapment is constrained by the intersection of these adiabats, with pressure-temperature paths of the inclusions approximated as isochores (*19*, *20*) (Fig. 2B); see (*26*) for details. We note that our estimation of entrapment conditions for ice-VII and ilmenite overlap in the depth of the shallower TZ (Fig. 2B).

Two main conclusions can be drawn: (i) The aqueous inclusions were entrapped as fluid rather than solid ice (*32*). Crystallization into ice-VII has occurred at much shallower depth during ascent. (ii) Despite marked uncertainties in the equations of state, the entrapment pressures for the ice inclusions that are currently at ~8 to 12 GPa turn out to be sufficiently narrow to permit a statement of the depth of their source regions (Fig. 2B): They range from 400 to 550 km depth. For the inclusions at 24 to 25 GPa, the source region is less narrowly estimated at 610 to 800 km depth; 620 km is the depth of entrapment estimated for dense N_2 inclusions in diamond (*20*). Overall, the ice-VII inclusions show directly that water-rich fluid occurs in regions within the TZ and around the 660-km boundary, or possibly in the shallow LM (Fig. 2B). Taken together with the occurrence of magnesian calcite and halite at similar pressures, we can infer the presence of complex aqueous, saline, and carbonaceous fluid at those depths. At present, we cannot assess the extent of these fluid-rich regions, although it is plausible that they were constrained both in space and time before evolving into less hydrous partial melts.

The much lower compatibility of H_2O in the LM relative to the TZ (*9*, *10*) has been suggested to cause mantle metasomatism when slabs or surrounding mantle are sinking to below the 660-km boundary: H_2O that cannot be chemically bound by the bridgmanite-periclase phase assembly of the lower mantle is released and interacts with surrounding mantle (*10*, *11*). Our observation of ice and its plausible origin from a free aqueous fluid below 610 km depth (Fig. 2B) is consistent with this hypothesis and connects the experimental and geodynamic work with observations from nature. More generally, natural ice-VII, magnesian calcite, and halite provide new indicators for the presence of water-bearing and carbonaceous fluid in actual deep Earth samples, which can be linked to geochemical and geophysical information obtained from the same regions in Earth. Ice-VII and other micro-inclusions (Table 1) provide, through their residual density, an accurate minimal pressure of formation, although the reconstruction of the entrapment pressure at mantle temperatures is currently limited by the available thermoelastic data on aqueous (saline) fluid.

REFERENCES AND NOTES

1. S. Karato, in *Treatise on Geophysics*, G. Schubert, Ed. (Elsevier, 2015), pp. 105–144.
2. T. L. Grove, C. B. Till, E. Lev, N. Chatterjee, E. Médard, *Nature* **459**, 694–697 (2009).
3. S. G. Nielsen, H. R. Marschall, *Sci. Adv.* **3**, e1602402 (2017).
4. H. Jung, S. Karato, *Science* **293**, 1460–1463 (2001).
5. N. Métrich *et al.*, *J. Petrol.* **55**, 377–393 (2014).
6. L. H. Rupke, J. P. Morgan, M. Hort, J. A. D. Connolly, *Earth Planet. Sci. Lett.* **223**, 17–34 (2004).
7. D. R. Bell, G. R. Rossman, *Science* **255**, 1391–1397 (1992).

8. S. Karato, *Earth Planet. Sci. Lett.* **301**, 413–423 (2011).
9. T. Inoue, T. Wada, R. Sasaki, H. Yurimoto, *Phys. Eartheart Planet. Inter.* **183**, 245–251 (2010).
10. B. Schmandt, S. D. Jacobsen, T. W. Becker, Z. Liu, K. G. Dueker, *Science* **344**, 1265–1268 (2014).
11. D. Bercovici, S. Karato, *Nature* **425**, 39–44 (2003).
12. F. E. Brenker, T. Stachel, J. W. Harris, *Earth Planet. Sci. Lett.* **198**, 1–9 (2002).
13. T. Stachel, J. W. Harris, G. P. Brey, W. Joswig, *Contrib. Mineral. Petrol.* **140**, 16–27 (2000).
14. D. G. Pearson *et al.*, *Nature* **507**, 221–224 (2014).
15. N. V. Sobolev *et al.*, *Lithos* **39**, 135–157 (1997).
16. S. B. Shirey *et al.*, *Rev. Mineral. Geochem.* **75**, 355–421 (2013).
17. O. Tschauner, E. Greenberg, V. Prakapenka, C. Ma, K. Tait, *Mineral. Mag.* **81**, 1033–1038 (2017).
18. V. F. Petrenko, R. W. Whitworth, *Physics of Ice* (Oxford Univ. Press, 1999), p. 253.
19. O. Navon, *Nature* **353**, 746–748 (1991).
20. O. Navon *et al.*, *Earth Planet. Sci. Lett.* **464**, 237–247 (2017).
21. E. S. Izraeli, J. W. Harris, O. Navon, *Earth Planet. Sci. Lett.* **187**, 323–332 (2001).
22. Y. Weiss, I. Kiflawi, O. Navon, in *Proceedings of 10th International Kimberlite Conference* (Springer, 2013), pp. 271–280.
23. H. Kagi *et al.*, *Mineral. Mag.* **64**, 1089–1097 (2000).
24. E. M. Smith *et al.*, *Science* **354**, 1403–1405 (2016).
25. J. M. Brown, T. J. Shankland, *Geophys. J. R. Astron. Soc.* **66**, 579–596 (1981).
26. See supplementary materials.
27. M. R. Frank, E. Aarestad, H. P. Scott, V. B. Prakapenka, *Phys. Earth Planet. Inter.* **215**, 12–20 (2013).
28. L. E. Bové *et al.*, *Proc. Natl. Acad. Sci. U.S.A.* **112**, 8216–8220 (2015).
29. C. Herzberg, K. Condie, J. Korenaga, *Earth Planet. Sci. Lett.* **292**, 79–88 (2010).
30. C. T. A. Lee, P. Luffi, T. Plank, H. Dalton, W. P. Leeman, *Earth Planet. Sci. Lett.* **279**, 20–33 (2009).
31. C. A. Dalton, C. H. Langmuir, A. Gale, *Science* **344**, 80–83 (2014).
32. C. R. Bina, A. Navrotsky, *Nature* **408**, 844–847 (2000).
33. R. J. Angel, M. L. Mazzucchelli, M. Alvaro, P. Nimis, F. Nestola, *Am. Mineral.* **99**, 2146–2149 (2014).

ACKNOWLEDGMENTS

We thank four anonymous reviewers for their helpful comments, and H. A. Bechtel for support at the Advanced Light Source. **Funding:** This work was supported by U.S. Department of Energy (DOE) awards DESC0005278, DE-FG02-94ER14466, and DE-NA0001974, and by NSF grants EAR-1634415, EAR-1128799, EAR-1322082, EAR-0318518, and DMR-0080065. The Advanced Photon Source, a DOE Office of Science User Facility, is operated by Argonne National Laboratory under contract DE-AC02-06CH11357. The Advanced Light Source is supported through contract DE-AC02-05CH11231. **Author contributions:** O.T. participated in design, interpretation, data collection, and analysis of the reported results, and in drafting and revising the manuscript; S.H. participated in interpretation of the results and in drafting and revising the manuscript; E.G., V.B.P., C.M., G.R.R., A.H.S., D.Z., and K.T. participated in data collection and revising the manuscript; and M.N. and A.L. participated in data collection. **Competing interests:** The authors have no competing interests. **Availability of data and materials:** Additional chemical and crystallographic information about ice-VII is provided as supplementary material. Raw data are deposited at Dryad (doi:10.5061/dryad.7145v). Crystallographic and chemical information on type material ice-VII are deposited with the ICSD database.

SUPPLEMENTARY MATERIALS

www.sciencemag.org/content/359/6380/1136/suppl/DC1
Materials and Methods
Figs. S1 to S4
Tables S1 to S3
References (*34*–*59*)

5 July 2017; accepted 19 January 2018
10.1126/science.aao3030

CLIMATE CHANGE

Sustained climate warming drives declining marine biological productivity

J. Keith Moore,[1]* Weiwei Fu,[1]* Francois Primeau,[1] Gregory L. Britten,[1] Keith Lindsay,[2] Matthew Long,[2] Scott C. Doney,[3] Natalie Mahowald,[4] Forrest Hoffman,[5] James T. Randerson[1]

Climate change projections to the year 2100 may miss physical-biogeochemical feedbacks that emerge later from the cumulative effects of climate warming. In a coupled climate simulation to the year 2300, the westerly winds strengthen and shift poleward, surface waters warm, and sea ice disappears, leading to intense nutrient trapping in the Southern Ocean. The trapping drives a global-scale nutrient redistribution, with net transfer to the deep ocean. Ensuing surface nutrient reductions north of 30°S drive steady declines in primary production and carbon export (decreases of 24 and 41%, respectively, by 2300). Potential fishery yields, constrained by lower–trophic-level productivity, decrease by more than 20% globally and by nearly 60% in the North Atlantic. Continued high levels of greenhouse gas emissions could suppress marine biological productivity for a millennium.

The Southern Ocean strongly influences Earth's climate and biogeochemistry (*1*, *2*). Deep ocean waters upwell to the surface at the Antarctic Divergence. Subantarctic Mode and Antarctic Intermediate waters form as northward-drifting surface waters sink and continue northward at mid-depths, transporting nutrients into the low-latitude thermocline. The Southern Ocean increasingly dominates ocean uptake of heat and CO_2 with strong climate warming because of a poleward shift and intensification of the mid-latitude westerly winds (*3*–*5*). Earth system models (ESMs) in the fifth phase of the Coupled Model Intercomparison Project (CMIP5) show consistent declines in global marine net primary production (NPP) during the 21st century in scenarios with high fossil fuel emissions, often with increasing Southern Ocean NPP (*4*, *6*–*8*).

Biological export of organic matter transfers nutrients vertically as sinking particles decompose, releasing nutrients. Where surface currents diverge (and subsurface currents converge), nutrients are transported upward, but some of the nutrients subsequently rain down as a result of biological export, instead of being advected away laterally at the surface. If the time scale for downward transfer by sinking particles is fast relative to the flushing time, nutrients become trapped, increasing concentrations locally and reducing lateral transport of nutrients out of the area. Idealized model studies, with imposed increases in Southern Ocean productivity, can develop nutrient trapping that boosts Southern Ocean nutrient concentrations and decreases northward lateral nutrient transport, reducing subsurface nutrient concentrations and decreasing biological productivity at low latitudes (*9*–*16*). Southern Ocean nutrient trapping, modulated by circulation, can potentially transfer nutrients from the upper ocean to the deep ocean (*12*, *15*).

We found intense Southern Ocean nutrient trapping as a result of climate warming in a fully coupled simulation to the year 2300, with the Community Earth System Model forced with representative concentration pathway 8.5 (RCP8.5) and extended concentration pathway 8.5 scenarios. The prescribed atmospheric CO_2 concentrations increase to 1960 parts per million by 2250, before leveling off (*17*, *18*). We previously used this ESM to examine marine biogeochemistry to the year 2100 (*19*–*21*) and century-by-century changes in the climate-carbon feedback to 2300 (*22*). Southern Ocean nutrient trapping has not been simulated previously without imposed NPP increases (arbitrarily modifying biological or physical forcings). In our simulation, nutrient trapping develops naturally after centuries of climate warming. This nutrient trapping drives a global reorganization of nutrient distributions, with a net transfer to the deep ocean, leading to a steady decline in global-scale marine biological productivity. This climate-biogeochemistry interaction amplifies the declines in productivity due to increasing stratification projected previously for the 21st century, and its negative effects on productivity eventually exceed those of increasing stratification (*6*–*8*).

The Southern Hemisphere westerly winds strengthen and shift poleward with climate warming, approaching Antarctica by 2300 (Fig. 1 and fig. S1). The Antarctic Divergence upwelling zone also strengthens and shifts poleward (*1*), ultimately initiating coastal upwelling along Antarctica, in areas with downwelling today (Fig. 1 and figs. S1 and S2). Ocean heat content and stratification increase globally, and deep mixing in the North Atlantic collapses, reducing North Atlantic Deep Water (NADW) formation from 30 to 5 sverdrups by 2200 (1 sverdrup = 10^6 m^3 s^{-1}) (*21*, *22*). Global sea surface temperature and stratification (0 to 500 m) peak by 2200 (*22*). Deeper down, the ocean is still warming in 2300, increasing stratification between intermediate depths and the deep ocean. Density differences between 500 and 1500 m and between 1000 and 2000 m more than double preindustrial differences by 2300, with most (>80%) of the change occurring after 2100 (table S1). Vertical exchange with cold, deep waters contributes to a slower warming trend in the Southern Ocean at depth, though surface waters warm considerably (Fig. 1 and fig. S4).

Biological export in the Southern Ocean increases by 2100 but declines at lower latitudes and in the high-latitude North Atlantic (table S1). Both patterns intensify after 2100, leading to nutrient trapping, with subsurface nutrient concentrations near Antarctica increasing substantially by 2300 (Fig. 2, fig. S3, and table S2). Concentrations of macronutrients (phosphate, nitrate, and silicic acid) decrease in the northward-subducting waters, decreasing thermocline concentrations and depressing low-latitude NPP and export (Fig. 2, figs. S3 and S4, and tables S1 to S3). Low-latitude productivity steadily drops as stratification increases and both surface and subsurface nutrient concentrations decline (Fig. 2, fig. S3, and tables S1 and S3). The equatorial upwelling flux of phosphate declines sharply (41%), even though the mean equatorial upwelling rate declines modestly (3%). The sharp drop in nutrient flux is due to the decrease in subsurface nutrients after 2100, driven by reduced lateral transport from the Southern Ocean (Fig. 3, fig. S3, and tables S1 and S3).

The nutrients stripped out of surface waters by enhanced productivity in the Southern Ocean are redistributed through the deep ocean by large-scale circulation (Fig. 4). Nutrient concentrations steadily increase in the Southern Ocean and the global deep ocean after 2100, while declining everywhere to the north, from the surface down to the depth of Antarctic Intermediate Water (~1500 m) (Fig. 4). We found similar global redistribution patterns for nitrate and silicic acid but not for iron (figs. S5 to S7), because iron is removed on time scales too short to permit long-range transport (*23*, *24*) (supplementary materials).

Three distinct processes drive the transfer of nutrients to the deep ocean. First, Southern Ocean nutrient trapping lowers the nutrient flux from the deep ocean to the upper ocean within the northward-subducting Antarctic Intermediate and Subantarctic Mode waters. This is the primary pathway for nutrients to return to the upper ocean (*12*, *15*). Second, increasing stratification globally decreases vertical mixing and exchange between the upper and deep ocean (table S1). Third, reduced vertical mixing and reduced NADW formation (*21*, *22*) decrease the main

---

[1]Department of Earth System Science, University of California, Irvine, CA, USA. [2]Climate and Global Dynamics Division, Natural Center for Atmospheric Research, Boulder, CO, USA. [3]Department of Environmental Sciences, University of Virginia, Charlottesville, VA, USA. [4]Department of Earth and Atmospheric Sciences, Cornell University, Ithaca, NY, USA. [5]Oak Ridge National Laboratory, U.S. Department of Energy, Oak Ridge, TN, USA.
*Corresponding author. Email: jkmoore@uci.edu (J.K.M.); weiweif@uci.edu (W.F.)

source of lower-nutrient waters to the deep ocean (*12*), driving nutrient declines that are larger in the Atlantic basin and high northern latitudes than in other regions (Fig. 4, figs. S5 to S7, and supplementary materials).

Increasing NPP in the Southern Ocean (south of 60°S) is driven by the poleward shift of the westerlies, warming surface waters, and vanishing sea ice, all of which enhance phytoplankton growth. Initially, the rise in NPP is driven by the shifting westerlies, with upwelling rates increasing to the year 2150 before leveling off (Fig. 3A). Surface stratification intensifies to the year 2300, driven by strong surface warming and decreases in surface salinity (Fig. 3, fig. S3, and table S2). The 6°C warming of polar surface waters increases maximum phytoplankton growth rates by 52% (table S2 and supplementary materials). The mean surface mixed-layer depth shoals with increasing stratification, declining from 75 m in 1850 to 40 m by 2300 (table S2). Sea ice cover reduces radiation to the contemporary Southern Ocean, but this shielding is weakened considerably by 2300 because the ice-covered area declines by 96% (fig. S9 and tables S1 and S2). Mean light levels in the surface mixed layer increase 245% by 2300 as a consequence of near-complete sea ice loss and shoaling mixed-layer depths (table S2 and supplementary materials).

Iron availability modulates phytoplankton capacity to take advantage of improving light and temperature growth conditions. Subsurface iron concentrations increase by 34% south of 60°S by 2300, with particularly high subsurface concentrations near Antarctica (table S2 and figs. S7 and S10). Volumetric upwelling rates remain ~25% above preindustrial levels after 2150, and the upwelling phosphate flux follows this temporal pattern, boosted modestly by the nutrient trapping effect (table S2 and supplementary materials). In contrast, the iron upwelling flux continues to rise to the year 2300, increasing 276% relative to preindustrial levels (Fig. 3 and table S2). This large increase is due to the southward shift in the upwelling zone, which entrains more margin-influenced, high-iron waters, further boosting productivity (Fig. 2; figs. S2, S3, and S9 to S12; and supplementary materials).

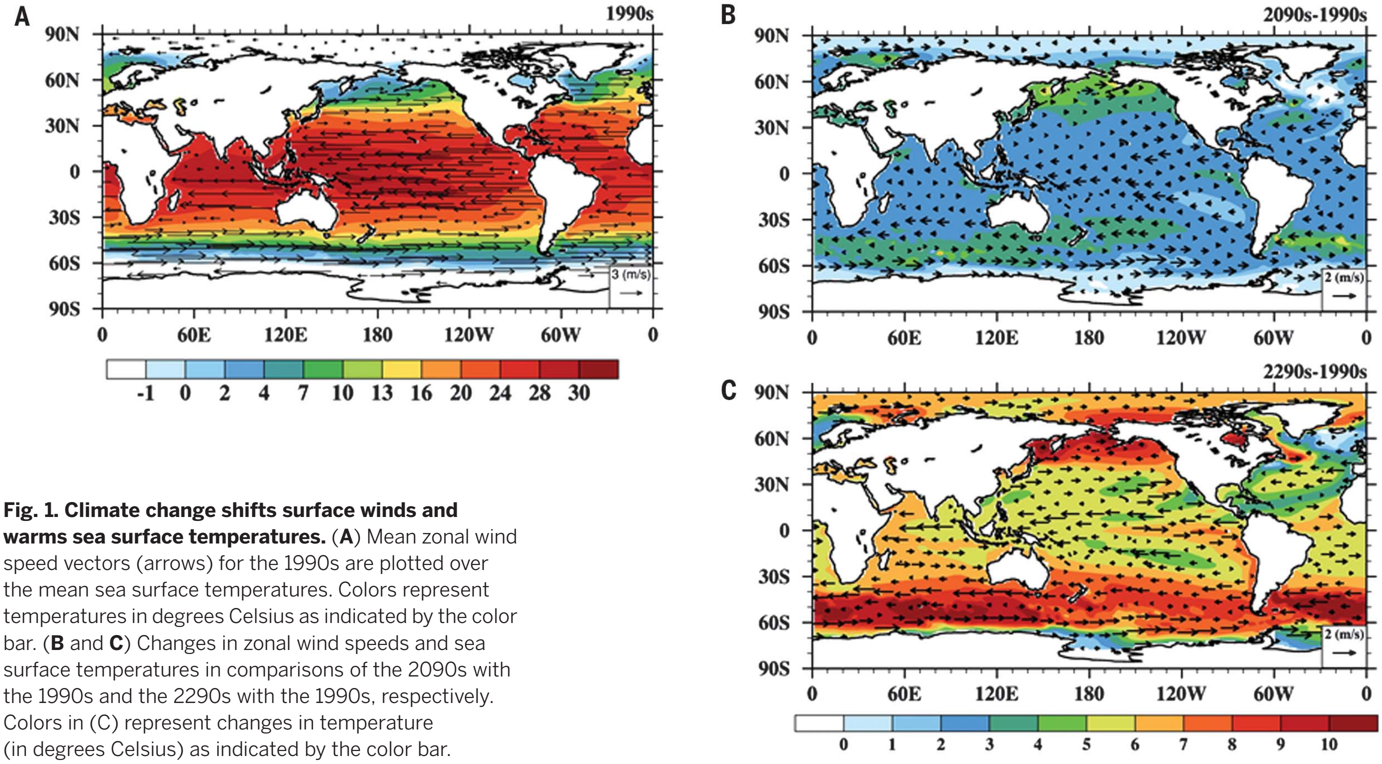

Fig. 1. Climate change shifts surface winds and warms sea surface temperatures. (**A**) Mean zonal wind speed vectors (arrows) for the 1990s are plotted over the mean sea surface temperatures. Colors represent temperatures in degrees Celsius as indicated by the color bar. (**B** and **C**) Changes in zonal wind speeds and sea surface temperatures in comparisons of the 2090s with the 1990s and the 2290s with the 1990s, respectively. Colors in (C) represent changes in temperature (in degrees Celsius) as indicated by the color bar.

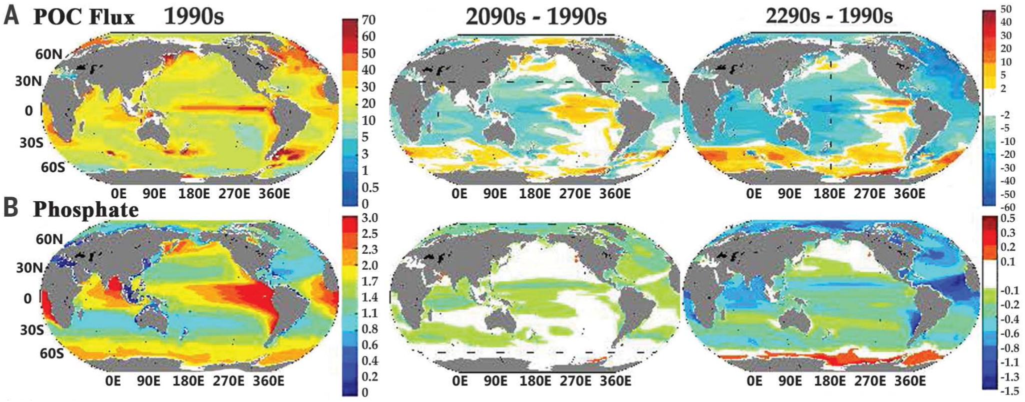

Fig. 2. Climate change effects on biological export and nutrient distributions. Global maps of (**A**) particulate organic carbon (POC) flux at a depth of 100 m (expressed in grams of carbon per square meter per year) and (**B**) mean phosphate concentrations at depths of 200 to 1000 m (expressed as micromolar concentrations). The left column shows 1990s means, the middle column shows the difference between the 2090s and the 1990s, and the right column shows the difference between the 2290s and the 1990s. Phosphate concentrations increase around the Antarctic by 2300 because of nutrient trapping.

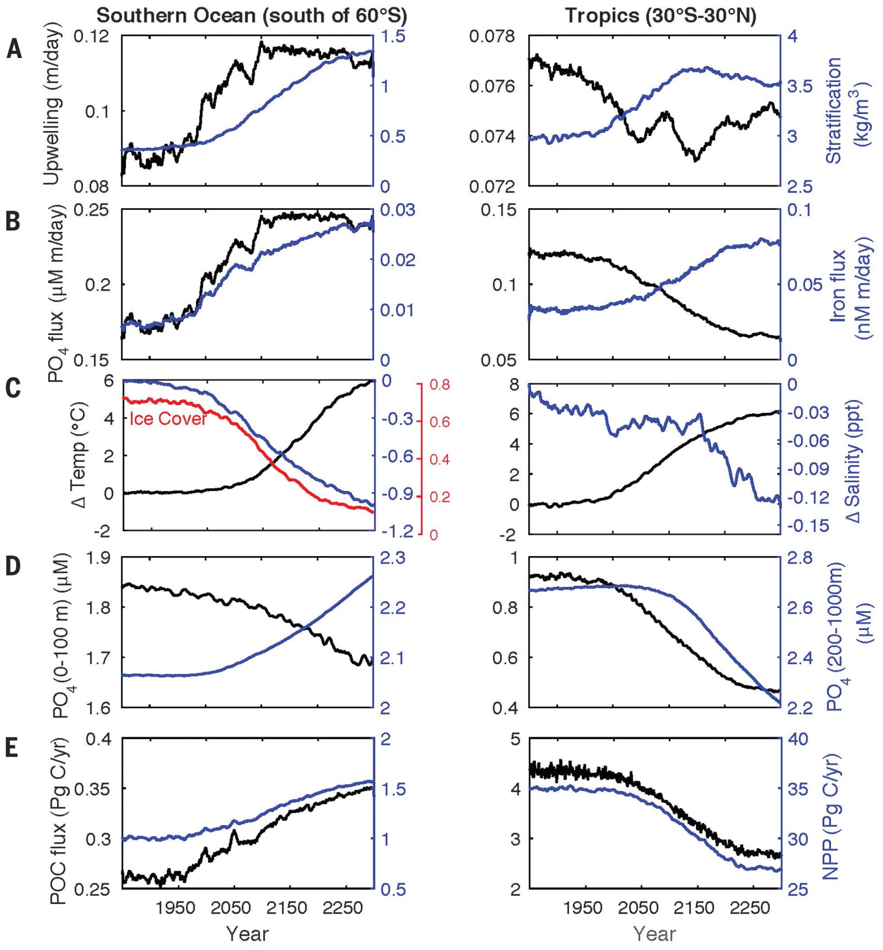

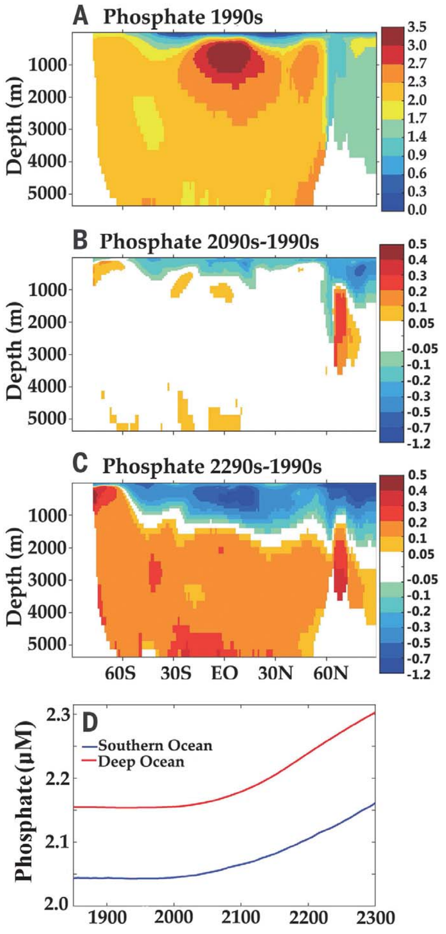

Fig. 3. Regional time series of ocean physical forcing and biogeochemical response. (**A**) Evolution of biogeochemical and physical variables over time (1850 to 2300) for the Southern Ocean and the tropics. The mean upwelling rate increases in the Southern Ocean but slows in the tropics, as surface stratification increases in both regions. (**B**) Upwelling rates for phosphate (expressed as the micromolar concentration per meter of upwelled water per day) and dissolved iron (expressed as the nanomolar concentration per meter of upwelled water per day), (**C**) changes in temperature and salinity [in parts per thousand (ppt)], (**D**) surface (0 to 100 m) and intermediate-depth (200 to 1000 m) phosphate concentrations, and (**E**) sinking POC flux and NPP [both in petagrams of carbon per year (Pg C/yr)]. The fractional sea ice cover is overlain in (C) (left column). Upwelling flux was averaged for 10°S to 10°N for the tropical time series, and stratification was estimated from the density difference between the surface and 200 m for both regions.

Fig. 4. Southern Ocean nutrient trapping transfers phosphate to the deep ocean. Zonal mean phosphate concentrations (micromolar) are shown for the 1990s (**A**), along with the differences in zonal phosphate concentrations in comparisons of the 1990s with the 2090s (**B**) and the 1990s with the 2290s (**C**). Phosphate concentrations increase over time in the high-latitude Southern Ocean (at all depths south of 60°S) and in the global deep ocean (below 2000 m and north of 60°S) (**D**).

Phytoplankton biomass and community composition do not change greatly, but growth rates increase and the growing season is longer, leading to a doubling of the annual biological surface phosphate drawdown by 2300 (table S2). Additional productivity increases are possible with additional iron input, because surface phosphate concentrations are far from depleted. One possible iron source (not included in our simulation) is from Antarctic glaciers (*25*). The strong climate warming would greatly increase glacial discharge (*26*), increasing iron inputs, allowing for even more efficient nutrient trapping, and modifying freshwater dynamic forcing of the oceans.

Marine food webs will shift with increasing nutrient stress outside the Southern Ocean. Relative changes in biological export are larger than those in NPP (table S1); because NPP can include substantial recycled production, changes in export more directly reflect the decreased flux of nutrients to surface waters (*8*) (tables S1 to S3 and supplementary materials). The smallest phytoplankton benefit most from increasing temperatures and nutrient depletion in surface waters (*27*), outcompeting larger phytoplankton and reducing the efficiency of biological export (*8*, *28*). Loss of the sea ice biome at both poles will considerably modify biological communities, with reduced competitiveness and, potentially, extinction of some polar-adapted, ice-dependent organisms, including the Antarctic krill central to Southern Ocean food webs (*29*) (supplementary materials).

Decreasing NPP and biological export north of 30°S more than offset productivity increases in the Southern Ocean, driving global-scale declines in NPP (−15%) and export (−30%) by 2300 (figs. S12 and S13 and table S1). The declines above 30°S are 24% for NPP and 41% for particulate organic carbon export (tables S1 to S3). The largest reductions occur in the North Atlantic, western Pacific, and southern Indian oceans, with zooplankton productivity closely tracking phytoplankton (figs. S12 and S13 and tables S1 to S4). Production at higher trophic levels (including potential fishery yield) is limited by lower–trophic-level production and trophic transfer efficiency (*30*–*32*). To estimate how changing zooplankton productivity influences higher trophic levels and maximum potential fishery yields, we used an empirical model with optimized transfer efficiencies, constrained by fishery data sets (*32*) (supplementary materials). We found that for higher trophic levels, production declines by more than

20% globally and by nearly 60% in the North Atlantic (fig. S14 and table S5). Spatial patterns are similar to zooplankton production shifts but are modified by decreasing transfer efficiency where the warm-water biome expands (*32*) (figs. S13 to S15).

The processes leading to the climate-driven transfer of nutrients to the deep ocean are scarcely apparent by 2100 but dominate ocean biogeochemistry by 2300. Little macronutrient accumulation occurs in the upper ocean around Antarctica by 2100 (Fig. 2 and figs. S3, S5, and S6). This trend is consistent with the finding of only a modest increase in biological carbon storage in the Southern Ocean across multiple CMIP5 models in 2100, driven by a slowdown of the deep circulation rather than by nutrient trapping (*4*). In 2300, tropical subsurface phosphate concentration is still declining and the deep ocean phosphate level is still increasing linearly (Figs. 3 and 4). Thus, the transfer of nutrients to the deep ocean will continue well past 2300, further depressing upper-ocean nutrient concentrations and global-scale productivity. ESM simulations must extend well past 2100 to capture key ocean physical and biogeochemical responses to multicentury climate warming.

Southern Ocean nutrient trapping appears to be a robust response to multicentury warming. All CMIP5 models project southward shift and intensification of the westerlies over the 21st century under the RCP8.5 scenario, despite considerable differences in the structure and performance of atmospheric models (*5*). Most CMIP5 models predict increasing Southern Ocean export by 2100, despite large differences in plankton and biogeochemical models (*4*, *6*–*8*, *24*, *28*). We found that the same climate-driven nutrient redistribution occurs in two other ESMs [the Hadley Centre Global Environmental Model, version 2 (HadGEM2) (*33*), and the Max-Planck-Institute Earth System Model (MPI-ESM) (*34*)] that conducted RCP8.5 simulations to the year 2300 (fig. S16). Both models show nutrient increases in the Southern Ocean and in the deep ocean, accompanied by nutrient reductions in the upper ocean. Thus, our results are not dependent on the model details of atmosphere-ocean circulation, plankton dynamics, or biogeochemistry, but rather seem to represent a robust Earth system response to multicentury climate warming.

Relatively modest increases in export are sufficient to induce nutrient trapping if they occur in the critical location above the Antarctic Divergence. Currently, heavy sea ice cover, cold temperatures, and iron limitation depress biological production in this region. Warming of surface waters and removal of sea ice greatly improve phytoplankton growth conditions, inducing strong regional nutrient trapping that further boosts productivity. If the climate warms enough to remove Southern Ocean sea ice, the nutrient redistribution and depression of global-scale productivity outlined here seem inevitable. Thus, the loss of Southern Ocean sea ice marks a critical biogeochemical tipping point in the Earth system. More research is needed on the physical forcings and the degree of warming necessary for removal of southern sea ice cover and the initiation of Southern Ocean nutrient trapping, including simulations with more moderate future trajectories of fossil fuel emissions. Rapid southern sea ice decline begins in about the year 2050 in our simulation, when mean surface air temperature has risen by ~2.5°C, with near-complete removal of sea ice by 2200 (Fig. 3 and fig. S9). This sea ice trend and the biogeochemical responses documented here support emission reduction targets that keep climate warming below 2°C (*26*).

The ongoing depletion of upper-ocean nutrients in 2300 will not reverse until the climate cools and sea ice returns to the Southern Ocean, depressing high-latitude productivity and enhancing northward lateral nutrient transfer. Southern Ocean dynamics will dominate this climate-cooling time scale, because the Southern Ocean will dominate ocean uptake of CO_2 by 2300 (figs. S17 and S18 and supplementary materials). The long time scales associated with ocean uptake and storage of anthropogenic CO_2 (*35*) and the subsequent time necessary for the circulation to return depleted nutrients to the upper ocean (*12*) ensure that NPP will be depressed for a thousand years or more. This puts the climate change impacts on marine biogeochemistry and productivity on the same time scale as continental ice sheets, with cumulative, catastrophic effects that will be increasingly difficult to avoid with delayed reductions in greenhouse gas emissions (*26*).

REFERENCES AND NOTES

1. J. L. Russell, K. W. Dixon, A. Gnanadesikan, R. J. Stouffer, J. R. Toggweiler, *J. Clim.* **19**, 6382–6390 (2006).
2. T. L. Frölicher *et al.*, *J. Clim.* **28**, 862–886 (2015).
3. T. Ito *et al.*, *Geophys. Res. Lett.* **42**, 4516–4522 (2015).
4. J. Hauck *et al.*, *Global Biogeochem. Cycles* **29**, 1451–1470 (2015).
5. T. J. Bracegirdle *et al.*, *J. Geophys. Res. Atmos.* **118**, 547–562 (2013).
6. L. Bopp *et al.*, *Biogeosciences* **10**, 6225–6245 (2013).
7. A. Cabré, I. Marinov, S. Leung, *Clim. Dyn.* **45**, 1253–1280 (2015).
8. W. W. Fu, J. T. Randerson, J. K. Moore, *Biogeosciences* **13**, 5151–5170 (2016).
9. J. L. Sarmiento, N. Gruber, M. A. Brzezinski, J. P. Dunne, *Nature* **427**, 56–60 (2004).
10. S. Dutkiewicz, M. Follows, P. Parekh, *Global Biogeochem. Cycles* **19**, (2005).
11. I. Marinov, A. Gnanadesikan, J. R. Toggweiler, J. L. Sarmiento, *Nature* **441**, 964–967 (2006).
12. I. Marinov *et al.*, *Global Biogeochem. Cycles* **22**, GB3007 (2008).
13. A. Oschlies, W. Koeve, W. Rickels, K. Rehdanz, *Biogeosciences* **7**, 4017–4035 (2010).
14. M. Holzer, F. W. Primeau, *J. Geophys. Res. Oceans* **118**, 1775–1796 (2013).
15. F. W. Primeau, M. Holzer, T. DeVries, *J. Geophys. Res. Oceans* **118**, 2547–2564 (2013).
16. B. Bronselaer, L. Zanna, D. R. Munday, J. Lowe, *Global Biogeochem. Cycles* **30**, 844–858 (2016).
17. D. P. van Vuuren *et al.*, *Clim. Change* **109**, 5–31 (2011).
18. Materials and methods are available as supplementary materials.
19. K. Lindsay *et al.*, *J. Clim.* **27**, 8981–9005 (2014).
20. M. C. Long, K. Lindsay, S. Peacock, J. K. Moore, S. C. Doney, *J. Clim.* **26**, 6775–6800 (2013).
21. J. K. Moore, K. Lindsay, S. C. Doney, M. C. Long, K. Misumi, *J. Clim.* **26**, 9291–9312 (2013).
22. J. T. Randerson *et al.*, *Global Biogeochem. Cycles* **29**, 744–759 (2015).
23. J. K. Moore, O. Braucher, *Biogeosciences* **5**, 631–656 (2008).
24. A. Tagliabue *et al.*, *Global Biogeochem. Cycles* **30**, 149–174 (2016).
25. L. J. A. Gerringa *et al.*, *Deep-Sea Res. II* **71**, 16–31 (2012).
26. J. Hansen *et al.*, *PLOS ONE* **8**, e81648 (2013).
27. P. Flombaum *et al.*, *Proc. Natl. Acad. Sci. U.S.A.* **110**, 9824–9829 (2013).
28. C. Laufkötter *et al.*, *Biogeosciences* **13**, 4023–4047 (2016).
29. A. J. Constable *et al.*, *Global Change Biol.* **20**, 3004–3025 (2014).
30. K. M. Brander, *Proc. Natl. Acad. Sci. U.S.A.* **104**, 19709–19714 (2007).
31. K. D. Friedland *et al.*, *PLOS ONE* **7**, e28945 (2012).
32. C. A. Stock *et al.*, *Proc. Natl. Acad. Sci. U.S.A.* **114**, E1441–E1449 (2017).
33. J. Caesar *et al.*, *J. Clim.* **26**, 3275–3284 (2013).
34. M. A. Giorgetta *et al.*, *J. Adv. Model. Earth Syst.* **5**, 572–597 (2013).
35. S. Solomon, G. K. Plattner, R. Knutti, P. Friedlingstein, *Proc. Natl. Acad. Sci. U.S.A.* **106**, 1704–1709 (2009).

ACKNOWLEDGMENTS

We received support from the Reducing Uncertainty in Biogeochemical Interactions through Synthesis and Computation (RUBISCO) Scientific Focus Area (SFA) in the Regional and Global Climate Modeling Program in the Climate and Environmental Sciences Division of the Biological and Environmental Research (BER) Division of the U.S. Department of Energy (DOE) Office of Science (as well as DOE BER Earth System Modeling Program grants ER65358 and DE-SC0016539 to J.K.M. and F.P.). Some authors received additional support from the NSF. The Coupled Model Intercomparison Project received support from the World Climate Research Programme and the DOE Program for Climate Model Diagnosis and Intercomparison. The National Center for Atmospheric Research (NCAR) provided computational and other support. NCAR is sponsored by the NSF.

SUPPLEMENTARY MATERIALS

www.sciencemag.org/content/359/6380/1139/suppl/DC1
Materials and Methods
Supplementary Text
Figs. S1 to S18
Tables S1 to S5
References (*36*–*47*)

10 August 2017; accepted 5 February 2018
10.1126/science.aao6379

NEUROSCIENCE

Local transformations of the hippocampal cognitive map

Julija Krupic,[1,2]* Marius Bauza,[2,3] Stephen Burton,[2,3] John O'Keefe[2,3]

Grid cells are neurons active in multiple fields arranged in a hexagonal lattice and are thought to represent the "universal metric for space." However, they become nonhomogeneously distorted in polarized enclosures, which challenges this view. We found that local changes to the configuration of the enclosure induce individual grid fields to shift in a manner inversely related to their distance from the reconfigured boundary. The grid remained primarily anchored to the unchanged stable walls and showed a nonuniform rescaling. Shifts in simultaneously recorded colocalized grid fields were strongly correlated, which suggests that the readout of the animal's position might still be intact. Similar field shifts were also observed in place and boundary cells—albeit of greater magnitude and more pronounced closer to the reconfigured boundary—which suggests that there is no simple one-to-one relationship between these three different cell types.

Place (*1*), head-direction (*2*), boundary (*3*–*5*), and grid cells (*6*) constitute the major units of the hippocampal cognitive map that forms the basis of our ability to navigate and form episodic memories (*7*). Based on the grid cell periodic firing pattern and presumed invariance, the predominant hypothesis of grid cell function states that they represent the spatial metric system of the brain (*8*). According to the major computational models, place and border cells act predominantly to stabilize the grid without determining its hexagonality (*9*–*12*). However, it has been recently shown that boundaries can profoundly reshape grid cell symmetry (*13*, *14*), but the nature of this influence, as well as its relation to other spatial cells, remains unknown.

To study the effect of boundaries on grid cell structure, we recorded from 347 spatially periodic cells (*15*) in the medial entorhinal cortex (seven rats) (fig. S1A). The firing pattern of the majority (63%) exhibited hexagonal symmetry in at least one of our four enclosures (grid cells), whereas that of other cells was more elliptical and irregular or had too few fields and did not pass the hexagonality criterion (fig. S2). Recordings were made while rats foraged for food in four familiar polygonal enclosures (presented in random order) that varied in shape from a left trapezoid (poly 129°) to a rectangle (poly 180°), with two intermediate shapes being irregular pentagons created by increasing the angle of the west-slanting wall of the trapezoid from 129° to either 145° or 160° (Fig. 1A).

We found that individual grid fields close to the slanting wall underwent average shifts as large as 41.6 cm (the largest in the rectangle to poly 145° transformation), whereas distant fields remained largely unchanged [the minimum (0.6 cm) and median (3.3 cm) field shifts in the same rectangle to poly 145° transformation], suggesting that the grid was influenced by the moving wall segment while remaining primarily anchored to the stable east (or north) wall (Fig. 1 and fig. S3). Fields as far as 78 cm in the x direction from the slanting wall (Fig. 1C, top) shifted more than expected by chance (as measured in repeated trials in the same enclosure, 5.7 cm) (see the supplementary materials). The amount of shift was inversely correlated with the distance to the slanting wall ($\rho_x = 0.93$, $P < 10^{-5}$; $\rho_y = 0.88$, $P = 0.004$, linear regression) (Fig. 1C), whereas the direction of shift was predominantly vertical, horizontal, or perpendicular to the slanting wall (Fig. 1D). Four head direction cells (three rats) recorded during such transformations showed little systematic change (fig. S4). The grid deformation was present for as long as we could record [>39 days in the rat (R2405) with the longest grid cell recordings] (fig. S5).

We next looked for the mechanism that could explain such grid deformations. First, we confirmed that the field movements did not result from changes in the animal's behavior in different geometric enclosures (figs. S6 and S7). Next, we ruled out the appealing hypothesis that the local shifts reflected purely short-range deformations resulting from individual "noninteracting" grid fields maintaining fixed distances of 30 (the typical border cell width), 50, or 70 cm to the walls (fig. S8). Finally, we investigated whether the field shifts could result from a global change in grid scale with the offset fixed only to the stationary east (or north) wall (fig. S9). The average grid rescaling was significantly different in contracting versus expanding enclosures (−2.0 ± 1.1%

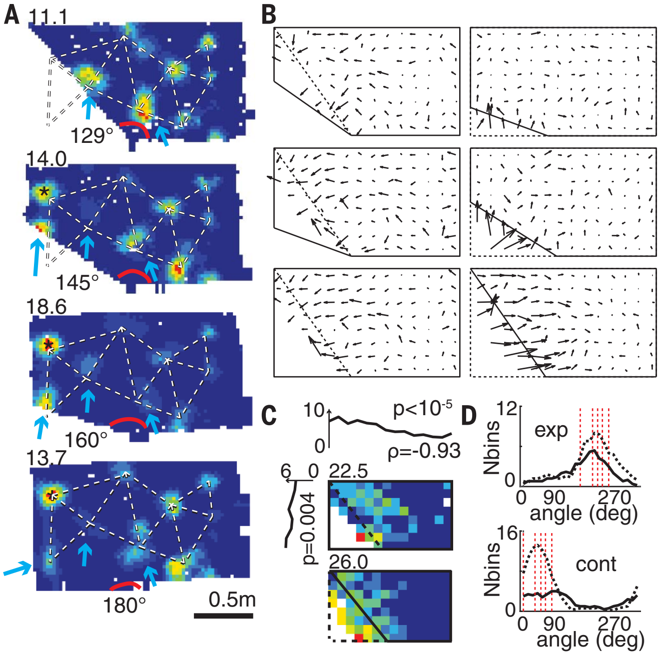

Fig. 1. Local grid deformations. (**A**) A representative grid cell (R2338) where a single field adjacent to the slanting wall shifts, with lesser displacements in some farther fields and none in distant fields. (Top left) Peak firing rates. Blue arrows indicate moving fields, * indicates a newly emerged field, and red arc, the slanting angle. Dashed line outlines grid structure in the rectangle. (**B**) Mean vector fields of all the recorded grid cells indicating average field shifts between pairs of successive (but not necessarily immediately following each other) geometrical enclosures; the vector tail specifies field position in the first enclosure. The first and the second enclosures are shown in dashed and solid lines, respectively. (**C**) (Top and left) Mean field shift across all transformations was inversely correlated with the distance to the slanting wall in x (top) and y (left) directions ($\rho_x = 0.93$, $P < 10^{-5}$; $\rho_y = 0.88$, $P = 0.004$); color-coded maps show the mean range of grid field shifts in poly 129° to rectangle (top) and rectangle to poly 129° transformations (bottom). (Top left) Peak shift in cm. (**D**) Directional changes of fields in expanding (exp) and contracting (cont) enclosures. (Top) Black solid and dashed lines represent transformations to poly 160° and rectangular enclosures, respectively. (Bottom) Black solid and dashed lines represent transformations to poly 129° and poly 145°, respectively. Dashed red lines show directions perpendicular to the slanting walls, as well as vertical and horizontal walls.

---

[1] Department of Physiology, Development and Neuroscience, University of Cambridge, Cambridge, CB2 3EG, UK. [2] Department of Cell and Developmental Biology, University College London, London WC1E 6BT, UK. [3] Sainsbury Wellcome Centre, University College London, London W1T 4JG, UK.
*Corresponding author. Email: jk727@cam.ac.uk

and 5.5 ± 1.2%, respectively; $P = 5.5 \times 10^{-6}$; $t_{554} = 4.59$; two-sample *t* test) (Fig. 2, A and B). In most transformations, rescaling was nonuniform across the enclosure (Fig. 2, C to E and supplementary materials). Importantly, the maximum field shift did not significantly correlate with grid scale and was comparable across all the recorded grid modules (Fig. 3, A to C) ($\rho = 0.19$, $P = 0.72$, linear regression; six grid cell modules with scales ranging from 29 to 86 cm in five rats), indicating that the ratio of scales between neighboring grid modules is not constant [also see (*16*)]. Furthermore, simultaneously recorded grid cells from different—as well as the same—grid modules showed a significant correlation between the magnitudes and directions of colocalized field shifts (Fig. 3, C to D). This indicates that the animal's position can be accurately decoded after a compensation for grid transformation; in contrast, uncoupled grid transformations could not be compensated and would result in reduced accuracy (Fig. 3E, fig. S10). The decoding error is also more pronounced close to the slanting wall for the nonlinear grid transformation compared to the linear, with the reversed tendency close to the stable wall (Fig. 3F).

What could underlie this nonhomogeneous grid rescaling? Previously, we suggested that competing place cells might constitute the basic building blocks of grid cells (*17*). In this model, a shift in one place-field position influences the positions of adjacent place fields, with the interaction force steeply decreasing as a function of the distance between fields. To test this idea, we recorded from 382 CA1 place cells (six rats) (fig. S1B) in the same enclosures. Like grids, place fields in close proximity to the slanting wall shifted with the wall, whereas the rest remained largely unaffected (Fig. 4). However, overall maximum place-field shift was significantly larger than that of the comparable colocalized grid fields (average difference across all transformations: 2.8 ± 0.24 cm, $P = 10^{-27}$, $t_{722} = 11.6$, two-sample *t* test). The shifts between simultaneously recorded colocalized grid cells (53) and place cells (101) (59 transformations, three rats) (fig. S11) were not significantly correlated (magnitudes and directions: 0.12 ± 0.07 and 0.08 ± 0.07, respectively, 11 transformations; $P = 0.25$, binomial test), although in some cases the correlation showed a trend toward significance (fig. S11). This could indicate that some place cells may be in register with grid cells and others not, possibly related to different spatial influences, such as those from border cells.

We found that individual grid fields shift by different amounts in response to local changes in enclosure geometry and that the magnitude of the shift is inversely correlated with the distance from the movable wall. Importantly, the grid remains primarily anchored to the stable wall of the enclosure, consistent with previous studies on other spatial cells and behavior, showing that the extent of cue control depends on its perceived stability (*18*–*20*). These results suggest that the local geometry of the enclosure plays a key role in constructing the grid as indicated by previous behavioral observations that rats relied on local geometry to find a reward location (*21*, *22*). We have also shown that colocalized grid fields remained in register across all grid cells, including ones from different grid modules, suggesting that in principle these distortions could be corrected by the readout system to estimate the metric (*23*). Perhaps more likely, the transformed grids could lead to a misperception of self-location in the room frame of reference.

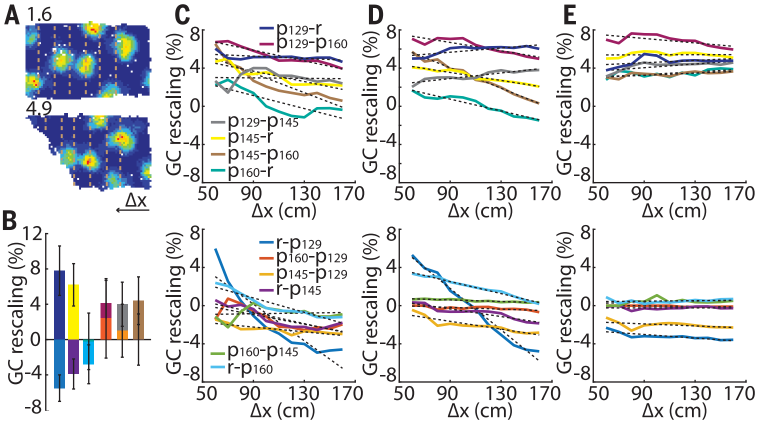

Fig. 2. Uniform versus nonuniform grid rescaling. (**A**) A typical grid cell with larger changes close to the slanting wall. Dashed lines indicate matched successive increments from right to left in exposed areas for homogeneity analysis. (**B**) Average grid rescaling in different transformations. Different colors represent different transformations specified in (C). (**C**) Average grid rescaling in *x* direction. (**D** and **E**) Simulated grid rescaling with nonuniform (D) and uniform (E) grid rescaling.

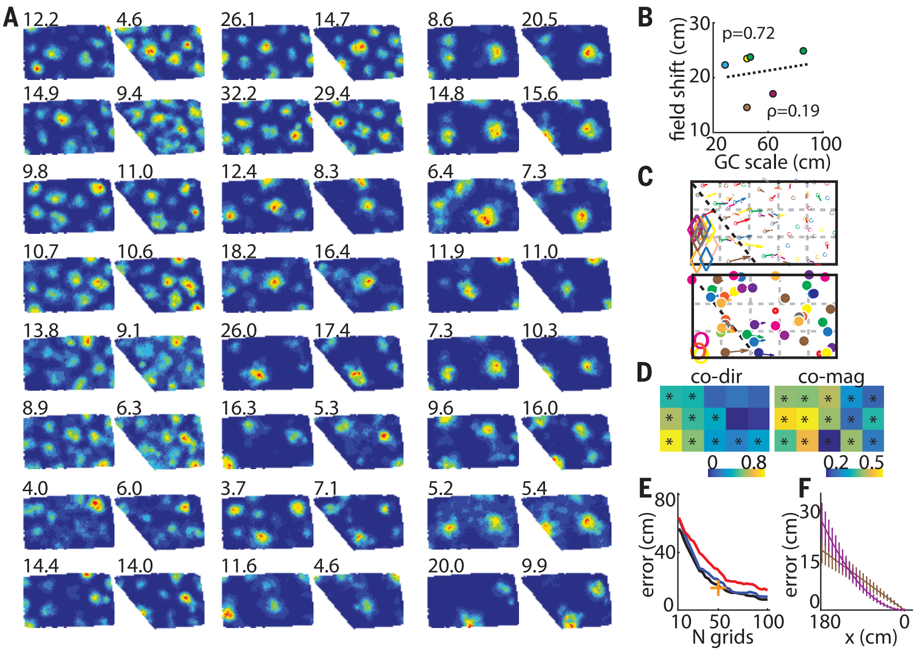

Fig. 3. Simultaneous changes in grid field positions. (**A**) Twenty-four corecorded grid cells (R2405) from two different modules (ratio ~1.6). (Top left) Peak firing rate. (**B**) Maximum average field shifts versus grid scale of six different grid modules (five rats). Individual animals are shown with different colors (green, R2405). (**C**) Vector fields of cells in (A). (Top and bottom) Smaller and larger modules, respectively. Different colors correspond to different cells. Diamonds and open circles indicate fields that disappeared in poly 129°. (**D**) Similarity matrices of field shift directions (left) and magnitudes (right) between corecorded grid cells from five rats combined (R2405, R2383, R2338, R2375, and R2298). All transformations from poly 129° to a rectangle (and vice versa) and poly 145° to a rectangle (and vice versa) were included. GC-GC direction and magnitude similarity thresholds: 0.20 and 0.16, respectively. (**E**) Position decoding error decreases with the number of cells and is smaller in grids nonuniformly transformed in register (blue) compared with uncoupled ones (red). Black indicates decoding in the absence of any transformation; + indicates decoding accuracy of our largest data set (50 simultaneously recorded grid cells). (**F**) Systematic position decoding error is larger in nonuniformly (violet) compared with uniformly (brown) transformed grid cells close to the slanting wall. The tendency reverses close to the stable east wall.

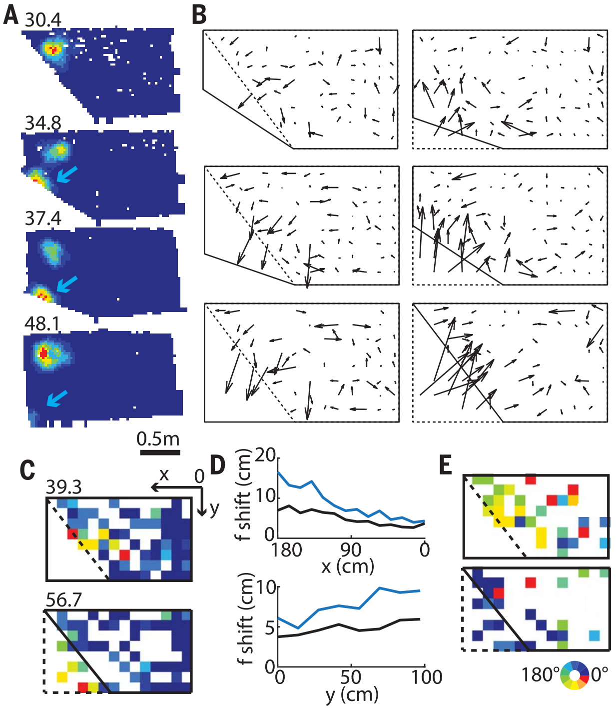

Fig. 4. Local changes in place fields. (**A**) Representative place cell with one of its fields shifting with the slanting wall while a second more distant field remains stable. (Top left) Peak firing rate. (**B**) Mean vector fields indicating the average place-field shifts between successive pairs of different geometrical enclosures. (**C**) Color-coded map showing the range of vector magnitudes. First and second enclosures are shown in dashed and solid lines, respectively. (Top left) Peak shift in cm. (**D**) Mean field shifts in all transformations (place cells, blue; grid cells, black) in *x* (top) and *y* (bottom) directions were more pronounced in place cells compared to grid cells, with the difference larger close to the slanting wall. (**E**) Color-coded map showing the range of vector directions.

Finally, we found that grid cells could undergo nonuniform transformations that might be implemented either by the Field-Boundary Interaction model (*17*) or by the Boundary Vector Cell model (*24*, *25*). Place cells show similar tendencies, albeit overall they shift by larger amounts. Previously it has been shown that place cells can be formed even in the absence of grid cells (*26*). Here, we demonstrate that they can undergo a different degree of transformation in response to the same geometric manipulation, suggesting that some place cells may be interacting with grid cells while others interact with border cells, as previously suggested (*27*), or alternatively their spatial properties may be formed by different underlying mechanisms.

REFERENCES AND NOTES

1. J. O'Keefe, J. Dostrovsky, *Brain Res.* **34**, 171–175 (1971).
2. J. S. Taube, R. U. Muller, J. B. Ranck Jr., *J. Neurosci.* **10**, 420–435 (1990).
3. T. Solstad, C. N. Boccara, E. Kropff, M.-B. Moser, E. I. Moser, *Science* **322**, 1865–1868 (2008).
4. C. Lever, S. Burton, A. Jeewajee, J. O'Keefe, N. Burgess, *J. Neurosci.* **29**, 9771–9777 (2009).
5. F. Savelli, D. Yoganarasimha, J. J. Knierim, *Hippocampus* **18**, 1270–1282 (2008).
6. T. Hafting, M. Fyhn, S. Molden, M.-B. Moser, E. I. Moser, *Nature* **436**, 801–806 (2005).
7. J. O'Keefe, L. Nadel, *The Hippocampus as a Cognitive Map* (Oxford Univ. Press, 1978).
8. E. I. Moser, M.-B. Moser, *Hippocampus* **18**, 1142–1156 (2008).
9. B. L. McNaughton, F. P. Battaglia, O. Jensen, E. I. Moser, M.-B. Moser, *Nat. Rev. Neurosci.* **7**, 663–678 (2006).
10. M. C. Fuhs, D. S. Touretzky, *J. Neurosci.* **26**, 4266–4276 (2006).
11. N. Burgess, C. Barry, J. O'Keefe, *Hippocampus* **17**, 801–812 (2007).
12. M. E. Hasselmo, *Hippocampus* **18**, 1213–1229 (2008).
13. J. Krupic, M. Bauza, S. Burton, C. Barry, J. O'Keefe, *Nature* **518**, 232–235 (2015).
14. T. Stensola, H. Stensola, M.-B. Moser, E. I. Moser, *Nature* **518**, 207–212 (2015).
15. J. Krupic, N. Burgess, J. O'Keefe, *Science* **337**, 853–857 (2012).
16. H. Stensola *et al.*, *Nature* **492**, 72–78 (2012).
17. J. Krupic, M. Bauza, S. Burton, C. Lever, J. O'Keefe, *Philos. Trans. R. Soc. Lond. B Biol. Sci.* **369**, 20130188 (2013).
18. J. J. Knierim, H. S. Kudrimoti, B. L. McNaughton, *J. Neurosci.* **15**, 1648–1659 (1995).
19. K. J. Jeffery, *Neuropharmacology* **37**, 677–687 (1998).
20. R. Biegler, R. G. Morris, *Q. J. Exp. Psychol. B* **49**, 307–345 (1996).
21. J. M. Pearce, M. A. Good, P. M. Jones, A. McGregor, *J. Exp. Psychol. Anim. Behav. Process.* **30**, 135–147 (2004).
22. P. M. Jones, J. M. Pearce, V. J. Davies, M. A. Good, A. McGregor, *Behav. Neurosci.* **121**, 1258–1271 (2007).
23. M. Stemmler, A. Mathis, A. V. M. Herz, *Sci. Adv.* **1**, e1500816 (2015).
24. C. Barry *et al.*, *Rev. Neurosci.* **17**, 71–97 (2006).
25. A. T. Keinath, R. A. Epstein, V. Balasubramanian, *bioRxiv* 174367 [Preprint]. 18 December 2017.
26. J. Koenig, A. N. Linder, J. K. Leutgeb, S. Leutgeb, *Science* **332**, 592–595 (2011).
27. M. P. Brandon, J. Koenig, J. K. Leutgeb, S. Leutgeb, *Neuron* **82**, 789–796 (2014).

ACKNOWLEDGMENTS

We thank E. Spokaite and D. Macikenas for helpful discussions and L. Kukovska for help with single-unit isolation. **Funding:** The research was supported by grants from the Wellcome Trust grants 090843/C/09/Z, 090843/D/09/Z, and 100154/Z/12/A and the Gatsby Charitable Foundation grants GAT3212 and GAT3531. J.K. is a Wellcome Trust/Royal Society Sir Henry Dale Fellow (grant 206682/Z/17/Z) and is supported by Kavli Foundation Dream Team project RG93383 and Isaac Newton Trust 17.37(t). J.O'K. is a Wellcome Trust Principal Research Fellow grant 203020/Z/16/Z. **Author contributions:** J.K., M.B., and J.O'K. designed and implemented the study and wrote the manuscript. S.B., M.B. and J.K. performed the experiments. J.K. planned the analysis. J.K. and M.B. analyzed the data. All authors discussed the results and contributed to the manuscript. **Competing interests:** The authors declare no competing financial interests. **Data and materials availability:** All data and code is available at www.krupiclab.com.

SUPPLEMENTARY MATERIALS

www.sciencemag.org/content/359/6380/1143/suppl/DC1
Materials and Methods
Figs. S1 to S11
References (*28*–*33*)

27 July 2017; accepted 12 January 2018
10.1126/science.aao4960

SOCIAL SCIENCE

The spread of true and false news online

Soroush Vosoughi,[1] Deb Roy,[1] Sinan Aral[2]*

We investigated the differential diffusion of all of the verified true and false news stories distributed on Twitter from 2006 to 2017. The data comprise ~126,000 stories tweeted by ~3 million people more than 4.5 million times. We classified news as true or false using information from six independent fact-checking organizations that exhibited 95 to 98% agreement on the classifications. Falsehood diffused significantly farther, faster, deeper, and more broadly than the truth in all categories of information, and the effects were more pronounced for false political news than for false news about terrorism, natural disasters, science, urban legends, or financial information. We found that false news was more novel than true news, which suggests that people were more likely to share novel information. Whereas false stories inspired fear, disgust, and surprise in replies, true stories inspired anticipation, sadness, joy, and trust. Contrary to conventional wisdom, robots accelerated the spread of true and false news at the same rate, implying that false news spreads more than the truth because humans, not robots, are more likely to spread it.

Foundational theories of decision-making (*1–3*), cooperation (*4*), communication (*5*), and markets (*6*) all view some conceptualization of truth or accuracy as central to the functioning of nearly every human endeavor. Yet, both true and false information spreads rapidly through online media. Defining what is true and false has become a common political strategy, replacing debates based on a mutually agreed on set of facts. Our economies are not immune to the spread of falsity either. False rumors have affected stock prices and the motivation for large-scale investments, for example, wiping out $130 billion in stock value after a false tweet claimed that Barack Obama was injured in an explosion (*7*). Indeed, our responses to everything from natural disasters (*8*, *9*) to terrorist attacks (*10*) have been disrupted by the spread of false news online.

New social technologies, which facilitate rapid information sharing and large-scale information cascades, can enable the spread of misinformation (i.e., information that is inaccurate or misleading). But although more and more of our access to information and news is guided by these new technologies (*11*), we know little about their contribution to the spread of falsity online. Though considerable attention has been paid to anecdotal analyses of the spread of false news by the media (*12*), there are few large-scale empirical investigations of the diffusion of misinformation or its social origins. Studies of the spread of misinformation are currently limited to analyses of small, ad hoc samples that ignore two of the most important scientific questions: How do truth and falsity diffuse differently, and what factors of human judgment explain these differences?

Current work analyzes the spread of single rumors, like the discovery of the Higgs boson (*13*) or the Haitian earthquake of 2010 (*14*), and multiple rumors from a single disaster event, like the Boston Marathon bombing of 2013 (*10*), or it develops theoretical models of rumor diffusion (*15*), methods for rumor detection (*16*), credibility evaluation (*17*, *18*), or interventions to curtail the spread of rumors (*19*). But almost no studies comprehensively evaluate differences in the spread of truth and falsity across topics or examine why false news may spread differently than the truth. For example, although Del Vicario *et al.* (*20*) and Bessi *et al.* (*21*) studied the spread of scientific and conspiracy-theory stories, they did not evaluate their veracity. Scientific and conspiracy-theory stories can both be either true or false, and they differ on stylistic dimensions that are important to their spread but orthogonal to their veracity. To understand the spread of false news, it is necessary to examine diffusion after differentiating true and false scientific stories and true and false conspiracy-theory stories and controlling for the topical and stylistic differences between the categories themselves. The only study to date that segments rumors by veracity is that of Friggeri *et al.* (*19*), who analyzed ~4000 rumors spreading on Facebook and focused more on how fact checking affects rumor propagation than on how falsity diffuses differently than the truth (*22*).

In our current political climate and in the academic literature, a fluid terminology has arisen around “fake news,” foreign interventions in U.S. politics through social media, and our understanding of what constitutes news, fake news, false news, rumors, rumor cascades, and other related terms. Although, at one time, it may have been appropriate to think of fake news as referring to the veracity of a news story, we now believe that this phrase has been irredeemably polarized in our current political and media climate. As politicians have implemented a political strategy of labeling news sources that do not support their positions as unreliable or fake news, whereas sources that support their positions are labeled reliable or not fake, the term has lost all connection to the actual veracity of the information presented, rendering it meaningless for use in academic classification. We have therefore explicitly avoided the term fake news throughout this paper and instead use the more objectively verifiable terms “true” or “false” news. Although the terms fake news and misinformation also imply a willful distortion of the truth, we do not make any claims about the intent of the purveyors of the information in our analyses. We instead focus our attention on veracity and stories that have been verified as true or false.

We also purposefully adopt a broad definition of the term news. Rather than defining what constitutes news on the basis of the institutional source of the assertions in a story, we refer to any asserted claim made on Twitter as news (we defend this decision in the supplementary materials section on “reliable sources,” section S1.2). We define news as any story or claim with an assertion in it and a rumor as the social phenomena of a news story or claim spreading or diffusing through the Twitter network. That is, rumors are inherently social and involve the sharing of claims between people. News, on the other hand, is an assertion with claims, whether it is shared or not.

A rumor cascade begins on Twitter when a user makes an assertion about a topic in a tweet, which could include written text, photos, or links to articles online. Others then propagate the rumor by retweeting it. A rumor’s diffusion process can be characterized as having one or more cascades, which we define as instances of a rumor-spreading pattern that exhibit an unbroken retweet chain with a common, singular origin. For example, an individual could start a rumor cascade by tweeting a story or claim with an assertion in it, and another individual could independently start a second cascade of the same rumor (pertaining to the same story or claim) that is completely independent of the first cascade, except that it pertains to the same story or claim. If they remain independent, they represent two cascades of the same rumor. Cascades can be as small as size one (meaning no one retweeted the original tweet). The number of cascades that make up a rumor is equal to the number of times the story or claim was independently tweeted by a user (not retweeted). So, if a rumor “A” is tweeted by 10 people separately, but not retweeted, it would have 10 cascades, each of size one. Conversely, if a second rumor “B” is independently tweeted by two people and each of those two tweets is retweeted 100 times, the rumor would consist of two cascades, each of size 100.

Here we investigate the differential diffusion of true, false, and mixed (partially true, partially false) news stories using a comprehensive data set of all of the fact-checked rumor cascades that spread on Twitter from its inception in 2006 to 2017. The data include ~126,000 rumor cascades spread by ~3 million people more than 4.5 million times. We sampled all rumor cascades investigated by six independent fact-checking organizations

---

[1] Massachusetts Institute of Technology (MIT), the Media Lab, E14-526, 75 Amherst Street, Cambridge, MA 02142, USA. [2] MIT, E62-364, 100 Main Street, Cambridge, MA 02142, USA.
*Corresponding author. Email: sinan@mit.edu

(snopes.com, politifact.com, factcheck.org, truthorfiction.com, hoax-slayer.com, and urbanlegends.about.com) by parsing the title, body, and verdict (true, false, or mixed) of each rumor investigation reported on their websites and automatically collecting the cascades corresponding to those rumors on Twitter. The result was a sample of rumor cascades whose veracity had been agreed on by these organizations between 95 and 98% of the time. We cataloged the diffusion of the rumor cascades by collecting all English-language replies to tweets that contained a link to any of the aforementioned websites from 2006 to 2017 and used optical character recognition to extract text from images where needed. For each reply tweet, we extracted the original tweet being replied to and all the retweets of the original tweet. Each retweet cascade represents a rumor propagating on Twitter that has been verified as true or false by the fact-checking organizations (see the supplementary materials for more details on cascade construction). We then quantified the cascades' depth (the number of retweet hops from the origin tweet over time, where a hop is a retweet by a new unique user), size (the number of users involved in the cascade over time), maximum breadth (the maximum number of users involved in the cascade at any depth), and structural virality (*23*) (a measure that interpolates between content spread through a single, large broadcast and that which spreads through multiple generations, with any one individual directly responsible for only a fraction of the total spread) (see the supplementary materials for more detail on the measurement of rumor diffusion).

As a rumor is retweeted, the depth, size, maximum breadth, and structural virality of the cascade increase (Fig. 1A). A greater fraction of false rumors experienced between 1 and 1000 cascades, whereas a greater fraction of true rumors experienced more than 1000 cascades (Fig. 1B); this was also true for rumors based on political news (Fig. 1D). The total number of false rumors peaked at the end of both 2013 and 2015 and again at the end of 2016, corresponding to the last U.S. presidential election (Fig. 1C). The data also show clear increases in the total number of false political rumors during the 2012 and 2016 U.S. presidential elections (Fig. 1E) and a spike in rumors that contained partially true and partially false information during the Russian annexation of Crimea in 2014 (Fig. 1E). Politics was the largest rumor category in our data, with ~45,000 cascades, followed by urban legends, business, terrorism, science, entertainment, and natural disasters (Fig. 1F).

When we analyzed the diffusion dynamics of true and false rumors, we found that falsehood diffused significantly farther, faster, deeper, and more broadly than the truth in all categories of information [Kolmogorov-Smirnov (K-S) tests are reported in tables S3 to S10]. A significantly greater fraction of false cascades than true cascades exceeded a depth of 10, and the top 0.01% of false cascades diffused eight hops deeper into the Twittersphere than the truth, diffusing to depths

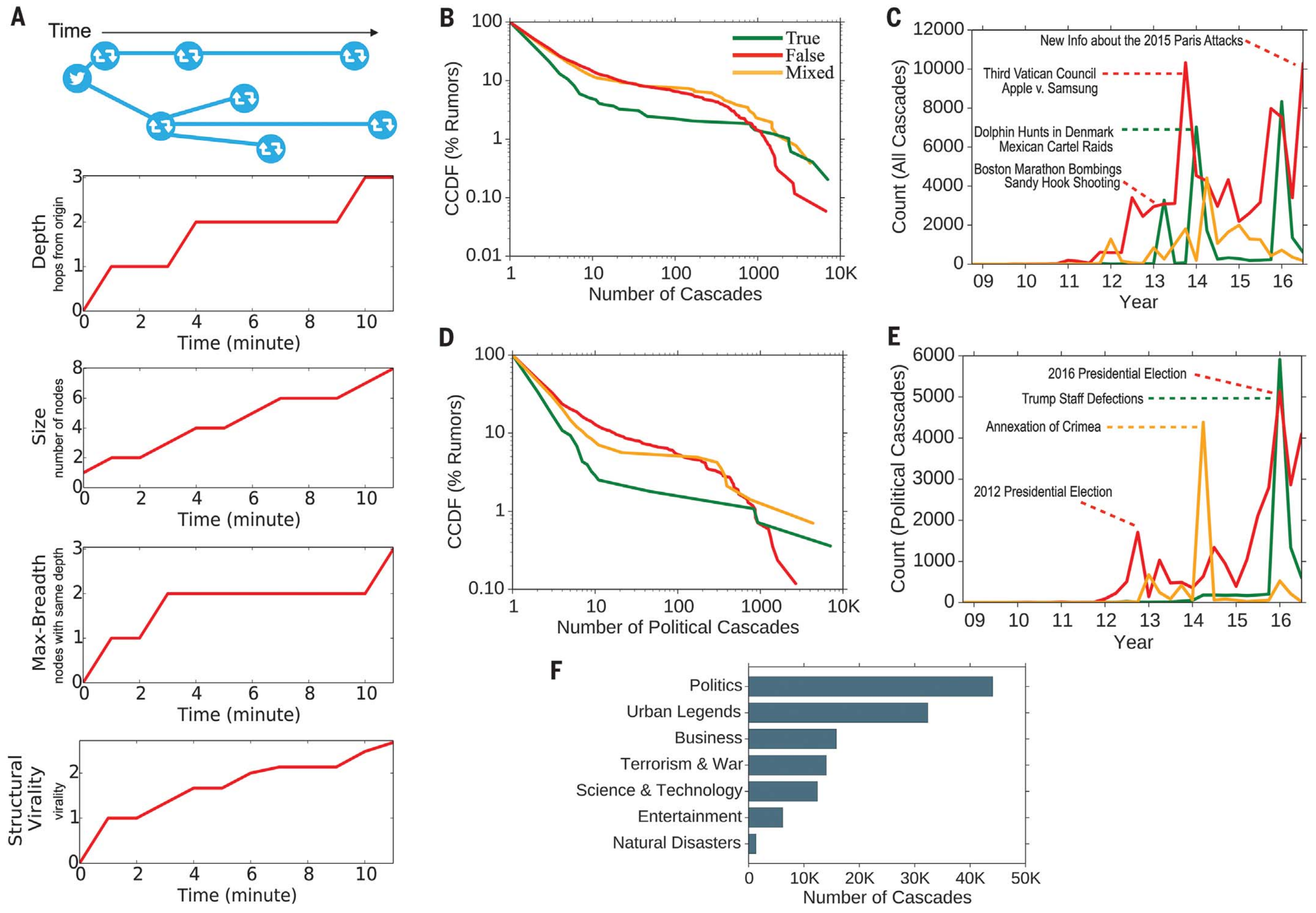

Fig. 1. Rumor cascades. (**A**) An example rumor cascade collected by our method as well as its depth, size, maximum breadth, and structural virality over time. "Nodes" are users. (**B**) The complementary cumulative distribution functions (CCDFs) of true, false, and mixed (partially true and partially false) cascades, measuring the fraction of rumors that exhibit a given number of cascades. (**C**) Quarterly counts of all true, false, and mixed rumor cascades that diffused on Twitter between 2006 and 2017, annotated with example rumors in each category. (**D**) The CCDFs of true, false, and mixed political cascades. (**E**) Quarterly counts of all true, false, and mixed political rumor cascades that diffused on Twitter between 2006 and 2017, annotated with example rumors in each category. (**F**) A histogram of the total number of rumor cascades in our data across the seven most frequent topical categories.

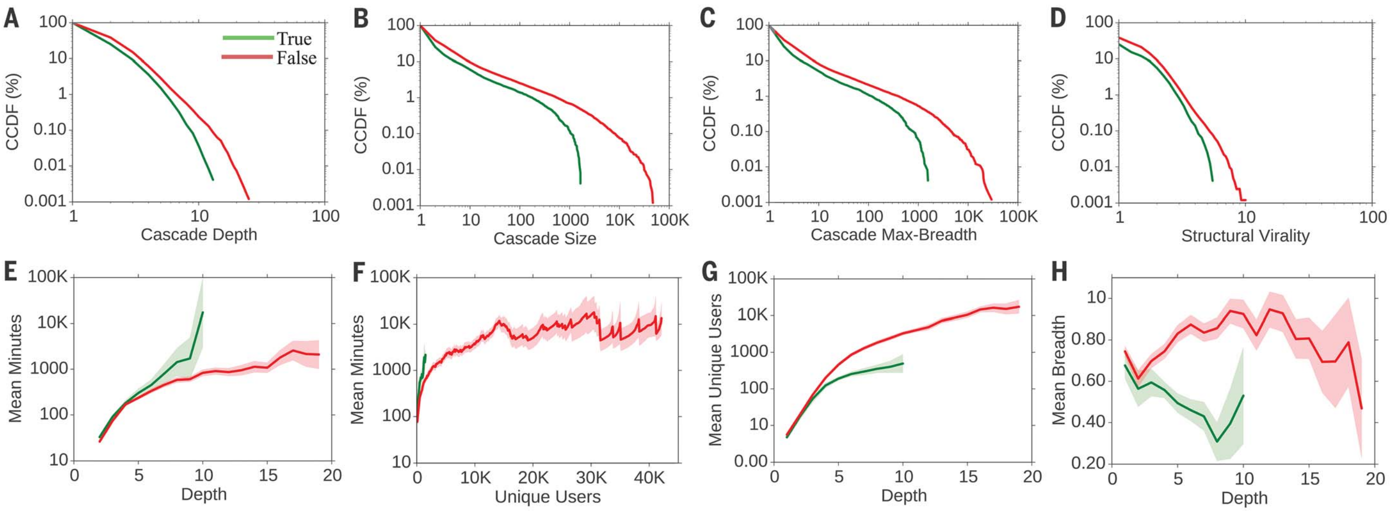

Fig. 2. Complementary cumulative distribution functions (CCDFs) of true and false rumor cascades. (**A**) Depth. (**B**) Size. (**C**) Maximum breadth. (**D**) Structural virality. (**E** and **F**) The number of minutes it takes for true and false rumor cascades to reach any (E) depth and (F) number of unique Twitter users. (**G**) The number of unique Twitter users reached at every depth and (**H**) the mean breadth of true and false rumor cascades at every depth. In (H), plot is lognormal. Standard errors were clustered at the rumor level (i.e., cascades belonging to the same rumor were clustered together; see supplementary materials for additional details).

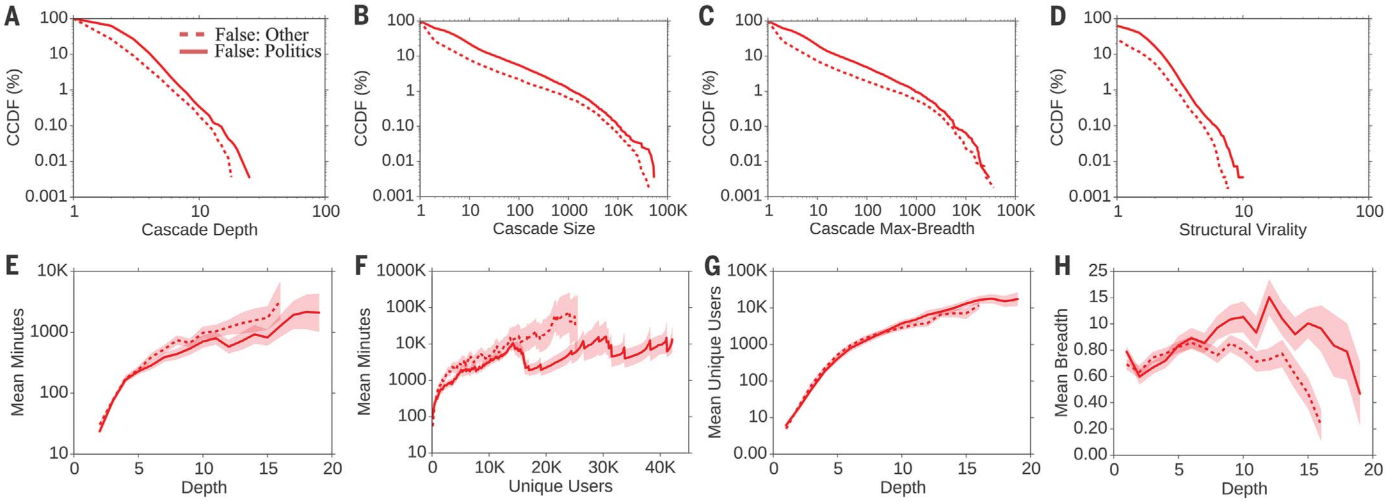

Fig. 3. Complementary cumulative distribution functions (CCDFs) of false political and other types of rumor cascades. (**A**) Depth. (**B**) Size. (**C**) Maximum breadth. (**D**) Structural virality. (**E** and **F**) The number of minutes it takes for false political and other false news cascades to reach any (E) depth and (F) number of unique Twitter users. (**G**) The number of unique Twitter users reached at every depth and (**H**) the mean breadth of these false rumor cascades at every depth. In (H), plot is lognormal. Standard errors were clustered at the rumor level.

greater than 19 hops from the origin tweet (Fig. 2A). Falsehood also reached far more people than the truth. Whereas the truth rarely diffused to more than 1000 people, the top 1% of false-news cascades routinely diffused to between 1000 and 100,000 people (Fig. 2B). Falsehood reached more people at every depth of a cascade than the truth, meaning that many more people retweeted falsehood than they did the truth (Fig. 2C). The spread of falsehood was aided by its virality, meaning that falsehood did not simply spread through broadcast dynamics but rather through peer-to-peer diffusion characterized by a viral branching process (Fig. 2D).

It took the truth about six times as long as falsehood to reach 1500 people (Fig. 2F) and 20 times as long as falsehood to reach a cascade depth of 10 (Fig. 2E). As the truth never diffused beyond a depth of 10, we saw that falsehood reached a depth of 19 nearly 10 times faster than the truth reached a depth of 10 (Fig. 2E). Falsehood also diffused significantly more broadly (Fig. 2H) and was retweeted by more unique users than the truth at every cascade depth (Fig. 2G).

False political news (Fig. 1D) traveled deeper (Fig. 3A) and more broadly (Fig. 3C), reached more people (Fig. 3B), and was more viral than any other category of false information (Fig. 3D). False political news also diffused deeper more quickly (Fig. 3E) and reached more than 20,000 people nearly three times faster than all other types of false news reached 10,000 people (Fig. 3F). Although the other categories of false news reached about the same number of unique users at depths between 1 and 10, false political news routinely reached the most unique users at depths greater than 10 (Fig. 3G). Although all other categories of false news traveled slightly more broadly at shallower depths, false political news traveled more broadly at greater depths, indicating that more-popular false political news items exhibited broader and more-accelerated diffusion dynamics

A

	median		mean		mean (log)		stdv (log)		ks-test
	false—true		false—true		false—true		false—true		
followers	410	466	2234	5240	2.62	2.68	0.69	0.88	D=0.104, p∼0.0
followees	383	509	1002	1707	2.59	2.72	0.85	0.96	D=0.136, p∼0.0
verified	0	0	0.002	0.006	nd	nd	nd	nd	D=0.005, p<0.001
engagement	9.52	9.54	19.70	24.65	0.91	0.90	0.65	0.76	D=0.054, p∼0.0
account age	982	1214	1072	1269	2.90	2.97	0.39	0.42	D=0.125, p∼0.0

B

	coef	odds ratio	std err	z	P>|z|	[95.0% Conf. Int.]	
account age	0.0002	1.000160	2.07e-05	7.759	0.000	0.000	0.000
engagement	0.0066	1.006648	0.000	18.019	0.000	0.006	0.007
falsehood	0.5350	1.707489	0.084	6.366	0.000	0.370	0.700
followees	-1.639e-05	0.999984	8.73e-06	-1.877	0.060	-3.35e-05	7.22e-07
followers	5.192e-05	1.000052	7.77e-06	6.682	0.000	3.67e-05	6.72e-05
intercept	-2.3941	0.091257	0.072	-33.437	0.000	-2.534	-2.254
verified	1.4261	4.162467	0.090	15.915	0.000	1.250	1.602

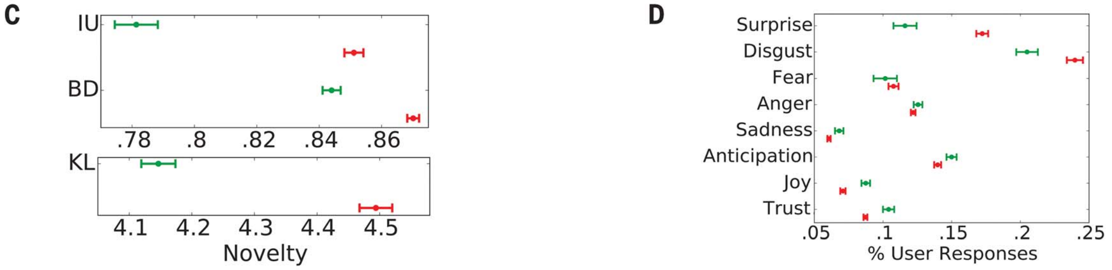

E

	mean		variance		ks-test
	false—true		false—true		
IU	0.85	0.78	0.0052	0.0072	D=0.457, p∼0.0
KL	4.49	4.15	0.1618	0.0948	D=0.433, p∼0.0
BD	0.87	0.84	0.0008	0.0008	D=0.415, p∼0.0

F

	mean		variance		ks-test
	false—true		false—true		
surprise	0.172	0.116	0.0167	0.0072	D=0.205, p∼0.0
disgust	0.240	0.205	0.0260	0.0227	D=0.102, p∼0.0
fear	0.108	0.102	0.0120	0.0095	D=0.021, p∼0.164
anger	0.122	0.126	0.0074	0.0111	D=0.023, p∼0.078
sadness	0.061	0.068	0.0038	0.0065	D=0.037, p∼0.0
anticipation	0.140	0.150	0.0093	0.0154	D=0.038, p∼0.0
joy	0.071	0.087	0.0054	0.0104	D=0.061, p∼0.0
trust	0.087	0.104	0.0058	0.0119	D=0.060, p∼0.0

Fig. 4. Models estimating correlates of news diffusion, the novelty of true and false news, and the emotional content of replies to news. (**A**) Descriptive statistics on users who participated in true and false rumor cascades as well as K-S tests of the differences in the distributions of these measures across true and false rumor cascades. (**B**) Results of a logistic regression model estimating users' likelihood of retweeting a rumor as a function of variables shown at the left. coeff, logit coefficient; *z*, *z* score. (**C**) Differences in the information uniqueness (IU), scaled Bhattacharyya distance (BD), and K-L divergence (KL) of true (green) and false (red) rumor tweets compared to the corpus of prior tweets the user was exposed to in the 60 days before retweeting the rumor tweet. (**D**) The emotional content of replies to true (green) and false (red) rumor tweets across seven dimensions categorized by the NRC. (**E**) Mean and variance of the IU, KL, and BD of true and false rumor tweets compared to the corpus of prior tweets the user has seen in the 60 days before seeing the rumor tweet as well as K-S tests of their differences across true and false rumors. (**F**) Mean and variance of the emotional content of replies to true and false rumor tweets across seven dimensions categorized by the NRC as well as K-S tests of their differences across true and false rumors. All standard errors are clustered at the rumor level, and all models are estimated with cluster-robust standard errors at the rumor level.

(Fig. 3H). Analysis of all news categories showed that news about politics, urban legends, and science spread to the most people, whereas news about politics and urban legends spread the fastest and were the most viral in terms of their structural virality (see fig. S11 for detailed comparisons across all topics).

One might suspect that structural elements of the network or individual characteristics of the users involved in the cascades explain why falsity travels with greater velocity than the truth. Perhaps those who spread falsity "followed" more people, had more followers, tweeted more often, were more often "verified" users, or had been on Twitter longer. But when we compared users involved in true and false rumor cascades, we found that the opposite was true in every case. Users who spread false news had significantly fewer followers (K-S test = 0.104, $P \sim 0.0$), followed significantly fewer people (K-S test = 0.136, $P \sim 0.0$), were significantly less active on Twitter (K-S test = 0.054, $P \sim 0.0$), were verified significantly less often (K-S test = 0.004, $P < 0.001$), and had been on Twitter for significantly less time (K-S test = 0.125, $P \sim 0.0$) (Fig. 4A). Falsehood diffused farther and faster than the truth despite these differences, not because of them.

When we estimated a model of the likelihood of retweeting, we found that falsehoods were 70% more likely to be retweeted than the truth (Wald chi-square test, $P \sim 0.0$), even when controlling for the account age, activity level, and number of followers and followees of the original tweeter, as well as whether the original tweeter was a verified user (Fig. 4B). Because user characteristics and network structure could not explain the differential diffusion of truth and falsity, we sought alternative explanations for the differences in their diffusion dynamics.

One alternative explanation emerges from information theory and Bayesian decision theory. Novelty attracts human attention (*24*), contributes to productive decision-making (*25*), and encourages information sharing (*26*) because novelty updates our understanding of the world. When information is novel, it is not only surprising, but also more valuable, both from an information theoretic perspective [in that it provides the greatest aid to decision-making (*25*)] and from a social perspective [in that it conveys social status on one that is "in the know" or has access to unique "inside" information (*26*)]. We therefore tested whether falsity was more novel than the truth and whether Twitter users were more likely to retweet information that was more novel.

To assess novelty, we randomly selected ~5000 users who propagated true and false rumors and extracted a random sample of ~25,000 tweets that they were exposed to in the 60 days prior to their decision to retweet a rumor. We then specified a latent Dirichlet Allocation Topic model (*27*), with 200 topics and trained on 10 million English-language tweets, to calculate the information distance between the rumor tweets and all the prior tweets that users were exposed to before retweeting the rumor tweets. This generated a probability distribution over the 200 topics for each tweet in our data set. We then measured how novel the information in the true and false rumors was by comparing the topic distributions of the rumor tweets with the topic distributions of the tweets to which users were exposed in the 60 days before their retweet. We found that false rumors were significantly more novel than the truth across all novelty metrics, displaying significantly higher information uniqueness (K-S test = 0.457, $P \sim 0.0$) (*28*), Kullback-Leibler (K-L) divergence (K-S test = 0.433, $P \sim 0.0$) (*29*), and Bhattacharyya distance (K-S test = 0.415, $P \sim 0.0$) (which is similar to the Hellinger distance) (*30*). The last two metrics measure differences between probability distributions representing the topical content of the incoming tweet and the corpus of previous tweets to which users were exposed.

Although false rumors were measurably more novel than true rumors, users may not have perceived them as such. We therefore assessed users' perceptions of the information contained in true and false rumors by comparing the emotional content of replies to true and false rumors. We categorized the emotion in the replies by using the leading lexicon curated by the National Research Council Canada (NRC), which provides a comprehensive list of ~140,000 English words and their associations with eight emotions based on Plutchik's (*31*) work on basic emotion—anger, fear, anticipation, trust, surprise, sadness, joy, and disgust (*32*)—and a list of ~32,000 Twitter hashtags and their weighted associations with the same emotions (*33*). We removed stop words and URLs from the reply tweets and calculated the fraction of words in the tweets that related to each of the eight emotions, creating a vector of emotion weights for each reply that summed to one across the emotions. We found that false rumors inspired replies expressing greater surprise (K-S test = 0.205, $P \sim 0.0$), corroborating the novelty hypothesis, and greater disgust (K-S test = 0.102, $P \sim 0.0$), whereas the truth inspired replies that expressed greater sadness (K-S test = 0.037, $P \sim 0.0$), anticipation (K-S test = 0.038, $P \sim 0.0$), joy (K-S test = 0.061, $P \sim 0.0$), and trust (K-S test = 0.060, $P \sim 0.0$) (Fig. 4, D and F). The emotions expressed in reply to falsehoods may illuminate additional factors, beyond novelty, that inspire people to share false news. Although we cannot claim that novelty causes retweets or that novelty is the only reason why false news is retweeted more often, we do find that false news is more novel and that novel information is more likely to be retweeted.

Numerous diagnostic statistics and manipulation checks validated our results and confirmed their robustness. First, as there were multiple cascades for every true and false rumor, the variance of and error terms associated with cascades corresponding to the same rumor will be correlated. We therefore specified cluster-robust standard errors and calculated all variance statistics clustered at the rumor level. We tested the robustness of our findings to this specification by comparing analyses with and without clustered errors and found that, although clustering reduced the precision of our estimates as expected, the directions, magnitudes, and significance of our results did not change, and chi-square ($P \sim 0.0$) and deviance (d) goodness-of-fit tests ($d = 3.4649 \times 10^{-6}$, $P \sim 1.0$) indicate that the models are well specified (see supplementary materials for more detail).

Second, a selection bias may arise from the restriction of our sample to tweets fact checked by the six organizations we relied on. Fact checking may select certain types of rumors or draw additional attention to them. To validate the robustness of our analysis to this selection and the generalizability of our results to all true and false rumor cascades, we independently verified a second sample of rumor cascades that were not verified by any fact-checking organization. These rumors were fact checked by three undergraduate students at Massachusetts Institute of Technology (MIT) and Wellesley College. We trained the students to detect and investigate rumors with our automated rumor-detection algorithm running on 3 million English-language tweets from 2016 (*34*). The undergraduate annotators investigated the veracity of the detected rumors using simple search queries on the web. We asked them to label the rumors as true, false, or mixed on the basis of their research and to discard all rumors previously investigated by one of the fact-checking organizations. The annotators, who worked independently and were not aware of one another, agreed on the veracity of 90% of the 13,240 rumor cascades that they investigated and achieved a Fleiss' kappa of 0.88. When we compared the diffusion dynamics of the true and false rumors that the annotators agreed on, we found results nearly identical to those estimated with our main data set (see fig. S17). False rumors in the robustness data set had greater depth (K-S test = 0.139, $P \sim 0.0$), size (K-S test = 0.131, $P \sim 0.0$), maximum breadth (K-S test = 0.139, $P \sim 0.0$), structural virality (K-S test = 0.066, $P \sim 0.0$), and speed (fig. S17) and a greater number of unique users at each depth (fig. S17). When we broadened the analysis to include majority-rule labeling, rather than unanimity, we again found the same results (see supplementary materials for results using majority-rule labeling).

Third, although the differential diffusion of truth and falsity is interesting with or without robot, or bot, activity, one may worry that our conclusions about human judgment may be biased by the presence of bots in our analysis. We therefore used a sophisticated bot-detection algorithm (*35*) to identify and remove all bots before running the analysis. When we added bot traffic back into the analysis, we found that none of our main conclusions changed—false news still spread farther, faster, deeper, and more broadly than the truth in all categories of information. The results remained the same when we removed all tweet cascades started by bots, including human retweets of original bot tweets (see supplementary materials, section S8.3) and when we used a second, independent bot-detection algorithm (see supplementary materials, section S8.3.5) and varied the algorithm's sensitivity threshold to verify the robustness of our analysis (see supplementary materials, section S8.3.4). Although the inclusion of bots, as measured by the two state-of-the-art bot-detection algorithms we used in our analysis, accelerated the spread of both true and false news, it affected their spread roughly equally. This suggests that false news spreads farther, faster, deeper, and more broadly than the truth because humans, not robots, are more likely to spread it.

Finally, more research on the behavioral explanations of differences in the diffusion of true and false news is clearly warranted. In particular, more robust identification of the factors of human judgment that drive the spread of true and false news online requires more direct interaction with users through interviews, surveys, lab experiments, and even neuroimaging. We encourage these and other approaches to the investigation of the factors of human judgment that drive the spread of true and false news in future work.

False news can drive the misallocation of resources during terror attacks and natural disasters, the misalignment of business investments, and misinformed elections. Unfortunately, although the amount of false news online is clearly increasing (Fig. 1, C and E), the scientific understanding of how and why false news spreads is currently based on ad hoc rather than large-scale systematic analyses. Our analysis of all the verified true and false rumors that spread on Twitter confirms that false news spreads more pervasively than the truth online. It also overturns conventional wisdom about how false news spreads. Though one might expect network structure and individual characteristics of spreaders to favor and promote false news, the opposite is true. The greater likelihood of people to retweet falsity more than the truth is what drives the spread of false news, despite network and individual factors that favor the truth. Furthermore, although recent testimony before congressional committees on misinformation in the United States has focused on the role of bots in spreading false news (*36*), we conclude that human behavior contributes more to the differential spread of falsity and truth than automated robots do. This implies that misinformation-containment policies should also emphasize behavioral interventions, like labeling and incentives to dissuade the spread of misinformation, rather than focusing exclusively on curtailing bots. Understanding how false news spreads is the first step toward containing it. We hope our work inspires more large-scale research into the causes and consequences of the spread of false news as well as its potential cures.

REFERENCES AND NOTES

1. L. J. Savage, *J. Am. Stat. Assoc.* **46**, 55–67 (1951).
2. H. A. Simon, *The New Science of Management Decision* (Harper & Brothers Publishers, New York, 1960).
3. R. Wedgwood, *Noûs* **36**, 267–297 (2002).
4. E. Fehr, U. Fischbacher, *Nature* **425**, 785–791 (2003).
5. C. E. Shannon, *Bell Syst. Tech. J.* **27**, 379–423 (1948).
6. S. Bikhchandani, D. Hirshleifer, I. Welch, *J. Polit. Econ.* **100**, 992–1026 (1992).
7. K. Rapoza, "Can 'fake news' impact the stock market?" *Forbes*, 26 February 2017; www.forbes.com/sites/kenrapoza/2017/02/26/can-fake-news-impact-the-stock-market/.
8. M. Mendoza, B. Poblete, C. Castillo, in *Proceedings of the First Workshop on Social Media Analytics* (Association for Computing Machinery, ACM, 2010), pp. 71–79.
9. A. Gupta, H. Lamba, P. Kumaraguru, A. Joshi, in *Proceedings of the 22nd International Conference on World Wide Web* (ACM, 2010), pp. 729–736.

10. K. Starbird, J. Maddock, M. Orand, P. Achterman, R. M. Mason, in *iConference 2014 Proceedings* (iSchools, 2014).
11. J. Gottfried, E. Shearer, "News use across social media platforms," Pew Research Center, 26 May 2016; www.journalism.org/2016/05/26/news-use-across-social-media-platforms-2016/.
12. C. Silverman, "This analysis shows how viral fake election news stories outperformed real news on Facebook," *BuzzFeed News*, 16 November 2016; www.buzzfeed.com/craigsilverman/viral-fake-election-news-outperformed-real-news-on-facebook/.
13. M. De Domenico, A. Lima, P. Mougel, M. Musolesi, *Sci. Rep.* **3**, 2980 (2013).
14. O. Oh, K. H. Kwon, H. R. Rao, in *Proceedings of the International Conference on Information Systems* (International Conference on Information Systems, ICIS, paper 231, 2010).
15. M. Tambuscio, G. Ruffo, A. Flammini, F. Menczer, in *Proceedings of the 24th International Conference on World Wide Web* (ACM, 2015), pp. 977–982.
16. Z. Zhao, P. Resnick, Q. Mei, in *Proceedings of the 24th International Conference on World Wide Web* (ACM, 2015), pp. 1395–1405.
17. M. Gupta, P. Zhao, J. Han, in *Proceedings of the 2012 Society for Industrial and Applied Mathematics International Conference on Data Mining* (Society for Industrial and Applied Mathematics, SIAM, 2012), pp. 153–164.
18. G. L. Ciampaglia *et al*., *PLOS ONE* **10**, e0128193 (2015).
19. A. Friggeri, L. A. Adamic, D. Eckles, J. Cheng, in *Proceedings of the International Conference on Weblogs and Social Media* (Association for the Advancement of Artificial Intelligence, AAAI, 2014)
20. M. Del Vicario *et al*., *Proc. Natl. Acad. Sci. U.S.A.* **113**, 554–559 (2016).
21. A. Bessi *et al*., *PLOS ONE* **10**, e0118093 (2015).
22. Friggeri *et al*. (*19*) do evaluate two metrics of diffusion: depth, which shows little difference between true and false rumors, and shares per rumor, which is higher for true rumors than it is for false rumors. Although these results are important, they are not definitive owing to the smaller sample size of the study; the early timing of the sample, which misses the rise of false news after 2013; and the fact that more shares per rumor do not necessarily equate to deeper, broader, or more rapid diffusion.
23. S. Goel, A. Anderson, J. Hofman, D. J. Watts, *Manage. Sci.* **62**, 180–196 (2015).
24. L. Itti, P. Baldi, *Vision Res.* **49**, 1295–1306 (2009).
25. S. Aral, M. Van Alstyne, *Am. J. Sociol.* **117**, 90–171 (2011).
26. J. Berger, K. L. Milkman, *J. Mark. Res.* **49**, 192–205 (2012).
27. D. M. Blei, A. Y. Ng, M. I. Jordan, *J. Mach. Learn. Res.* **3**, 993–1022 (2003).
28. S. Aral, P. Dhillon, "Unpacking novelty: The anatomy of vision advantages," Working paper, MIT–Sloan School of Management, Cambridge, MA, 22 June 2016; https://papers.ssrn.com/sol3/papers.cfm?abstract_id=2388254.
29. T. M. Cover, J. A. Thomas, *Elements of Information Theory* (Wiley, 2012).
30. T. Kailath, *IEEE Trans. Commun. Technol.* **15**, 52–60 (1967).
31. R. Plutchik, *Am. Sci.* **89**, 344–350 (2001).
32. S. M. Mohammad, P. D. Turney, *Comput. Intell.* **29**, 436–465 (2013).
33. S. M. Mohammad, S. Kiritchenko, *Comput. Intell.* **31**, 301–326 (2015).
34. S. Vosoughi, D. Roy, in *Proceedings of the 10th International AAAI Conference on Weblogs and Social Media* (AAAI, 2016), pp. 707–710.
35. C. A. Davis, O. Varol, E. Ferrara, A. Flammini, F. Menczer, in *Proceedings of the 25th International Conference Companion on World Wide Web* (ACM, 2016), pp. 273–274.
36. For example, this is an argument made in recent testimony by Clint Watts—Robert A. Fox Fellow at the Foreign Policy Research Institute and Senior Fellow at the Center for Cyber and Homeland Security at George Washington University—given during the U.S. Senate Select Committee on Intelligence hearing on "Disinformation: A Primer in Russian Active Measures and Influence Campaigns" on 30 March 2017; www.intelligence.senate.gov/sites/default/files/documents/os-cwatts-033017.pdf.

ACKNOWLEDGMENTS

We are indebted to Twitter for providing funding and access to the data. We are also grateful to members of the MIT research community for invaluable discussions. The research was approved by the MIT institutional review board. The analysis code is freely available at https://goo.gl/forms/AKIlZujpexhN7fY33. The entire data set is also available, from the same link, upon signing an access agreement stating that (i) you shall only use the data set for the purpose of validating the results of the MIT study and for no other purpose; (ii) you shall not attempt to identify, reidentify, or otherwise deanonymize the data set; and (iii) you shall not further share, distribute, publish, or otherwise disseminate the data set. Those who wish to use the data for any other purposes can contact and make a separate agreement with Twitter.

SUPPLEMENTARY MATERIALS

www.sciencemag.org/content/359/6380/1146/suppl/DC1
Materials and Methods
Figs. S1 to S20
Tables S1 to S39
References (*37*–*75*)

14 September 2017; accepted 19 January 2018
10.1126/science.aap9559

MICROBIOTA

Gut bacteria selectively promoted by dietary fibers alleviate type 2 diabetes

Liping Zhao,[1,2]*† Feng Zhang,[1]* Xiaoying Ding,[3]* Guojun Wu,[1]* Yan Y. Lam,[2]* Xuejiao Wang,[3] Huaqing Fu,[1] Xinhe Xue,[1] Chunhua Lu,[4] Jilin Ma,[4] Lihua Yu,[4] Chengmei Xu,[4] Zhongying Ren,[4] Ying Xu,[5] Songmei Xu,[5] Hongli Shen,[5] Xiuli Zhu,[5] Yu Shi,[6] Qingyun Shen,[6] Weiping Dong,[3] Rui Liu,[1] Yunxia Ling,[3] Yue Zeng,[7] Xingpeng Wang,[7] Qianpeng Zhang,[1] Jing Wang,[1] Linghua Wang,[1] Yanqiu Wu,[1] Benhua Zeng,[8] Hong Wei,[8] Menghui Zhang,[1] Yongde Peng,[3]† Chenhong Zhang[1]†

The gut microbiota benefits humans via short-chain fatty acid (SCFA) production from carbohydrate fermentation, and deficiency in SCFA production is associated with type 2 diabetes mellitus (T2DM). We conducted a randomized clinical study of specifically designed isoenergetic diets, together with fecal shotgun metagenomics, to show that a select group of SCFA-producing strains was promoted by dietary fibers and that most other potential producers were either diminished or unchanged in patients with T2DM. When the fiber-promoted SCFA producers were present in greater diversity and abundance, participants had better improvement in hemoglobin A1c levels, partly via increased glucagon-like peptide-1 production. Promotion of these positive responders diminished producers of metabolically detrimental compounds such as indole and hydrogen sulfide. Targeted restoration of these SCFA producers may present a novel ecological approach for managing T2DM.

The gut microbiota is a complex microbial ecosystem, and maintaining a mutualistic relationship with it is critical for human health (*1*). A notable example of such a relationship is the production of short-chain fatty acids (SCFAs) through bacterial fermentation of carbohydrates: The human host diet provides nondigestible carbohydrates to support bacterial growth, and in return, the bacteria generate SCFAs that provide an energy substrate to colonocytes, mitigate inflammation, and regulate satiety, etc. (*2*, *3*). Deficiency in SCFA production has been associated with diseases, including type 2 diabetes mellitus (T2DM) (*4*–*7*). In clinical trials, increased intake of nondigestible but fermentable carbohydrates (dietary fibers) alleviated the disease phenotypes of T2DM but was associated with vastly different treatment responses (*8*–*10*). Hundreds of gut bacterial species across many taxa share the genes for fermenting carbohydrates into SCFAs (*11*). Strains of the same SCFA-producing species also show different responses to increased availability of dietary fibers (*12*, *13*). To improve the clinical efficacy of dietary fiber interventions, it is critical to understand how members of the gut ecosystem respond as individual strains as well as how they interact with one another as functional groups when exposed to increased carbohydrates as a new environmental resource. In this study, we used exposure to a large amount of diverse fibers from dietary sources to perturb the gut ecosystem. We then applied a strain-level, microbiome-wide association approach to characterize the dynamics of the gut microbiota and its impact on glucose homeostasis in patients with T2DM. This strategy has led to the identification of a specific group of SCFA producers that alleviate T2DM by increasing SCFA production. This increased SCFA production restores a mutualistic relationship with the human host and diminishes producers of metabolically detrimental compounds.

We randomized patients with clinically diagnosed T2DM to receive either the usual care [patient education and dietary recommendations based on the 2013 Chinese Diabetes Society guidelines for T2DM (*14*)] as the control group (U group; n = 16 patients) or a high-fiber diet composed of whole grains, traditional Chinese medicinal foods, and prebiotics (the WTP diet; see materials and methods and table S1 in the supplementary materials) as the treatment group (W group; n = 27 patients) in an open-label, parallel-group study designated the GUT2D study (fig. S1). Both groups received acarbose (an amylase inhibitor) as the standardized medication. Acarbose transforms part of the starch in the diet into a "fiber" by reducing its digestion and making it more available as fermentable carbohydrate in the colon (*15*). By design, the W group had a significantly higher intake of dietary fibers with diverse structures than the U group, but the daily energy and macronutrient intakes were similar across groups (table S2). The level of hemoglobin A1c (HbA1c), our primary outcome measure, decreased significantly from baseline in a time-dependent manner in both groups; from day 28 onward, however, there was a greater reduction in the W group (Fig. 1A). The proportion of participants who achieved adequate glycemic control (HbA1c < 7%) at the end of the intervention was also significantly higher in the W group (89% versus 50% in the U group) (Fig. 1B). There was a temporal difference in fasting blood glucose levels—only the W group achieved a significant reduction by day 28, although at the end of the intervention there was no difference between groups (Fig. 1C)—and a similar trend was observed for postprandial glucose (Fig. 1D). The W group also showed greater reduction in body weight and better blood lipid profiles than the U group (table S3). Our clinical data indicate that increased availability of nondigestible but fermentable carbohydrates is sufficient to induce clinically relevant metabolic improvements in patients with T2DM, as demonstrated by the response to increasing undigested starch with acarbose in the U group. We observed more significant and faster improvement in clinical outcomes in the W group when more diverse carbohydrates were provided as added fibers in the diet.

To determine causality between the gut microbiota and fiber-induced improvement of host glycemic control, we transplanted the pre- and postintervention gut microbiota from the same participants into germ-free C57BL/6J mice. The mice that received pre- or postintervention microbiota showed more similarity in gut microbiota to their donors than to each other (fig. S2). Mice transplanted with the postintervention microbiota from either the W or U group showed better metabolic health parameters than those with the preintervention microbiota from the corresponding group. Mice that received postintervention microbiota from the W group had the lowest fasting and postprandial blood glucose levels among all gnotobiotic mice (Fig. 1E and fig. S3), a result that mirrored the better metabolic outcomes in participants of the W group than in those of the U group. The transferable effects of our treatments via microbial transplantation provide evidence for a causative contribution of the gut microbiota, modulated by dietary fibers, to improved glucose homeostasis in patients with T2DM.

Next we determined how the increased dietary fibers altered the global structure of the gut microbiota. Shotgun metagenomic sequencing was performed on 172 fecal samples collected at four time points (days 0, 28, 56, and 84) (table S4), which led to a catalog of 4,893,833 nonredundant microbial genes. Both groups had a notable reduction in gene richness (the number of genes identified per sample) from day 0 to day 28, along with significant clinical improvements, with no further changes afterward (Fig. 1F). Our

[1]State Key Laboratory of Microbial Metabolism and Ministry of Education Key Laboratory of Systems Biomedicine, School of Life Sciences and Biotechnology, Shanghai Jiao Tong University, Shanghai 200240, China. [2]Department of Biochemistry and Microbiology and New Jersey Institute for Food, Nutrition, and Health, School of Environmental and Biological Sciences, Rutgers University, NJ 08901, USA. [3]Department of Endocrinology and Metabolism, Shanghai General Hospital, Shanghai Jiao Tong University School of Medicine, Shanghai 200080, China. [4]Sijing Community Health Service Center of Songjiang District, Shanghai 201601, China. [5]Sijing Hospital of Songjiang District, Shanghai 201601, China. [6]Department of Endocrinology and Metabolism, Qidong People's Hospital, Jiangsu 226200, China. [7]Department of Gastroenterology, Shanghai General Hospital, Shanghai Jiao Tong University School of Medicine, Shanghai 200080, China. [8]Department of Laboratory Animal Science, College of Basic Medical Sciences, Army Medical University, Chongqing 400038, China.
*These authors contributed equally to this work.
†Corresponding author. Email: lpzhao@sjtu.edu.cn (L.Z.); pengyongde0908@126.com (Y.P.); zhangchenhong@sjtu.edu.cn (C.Z.)

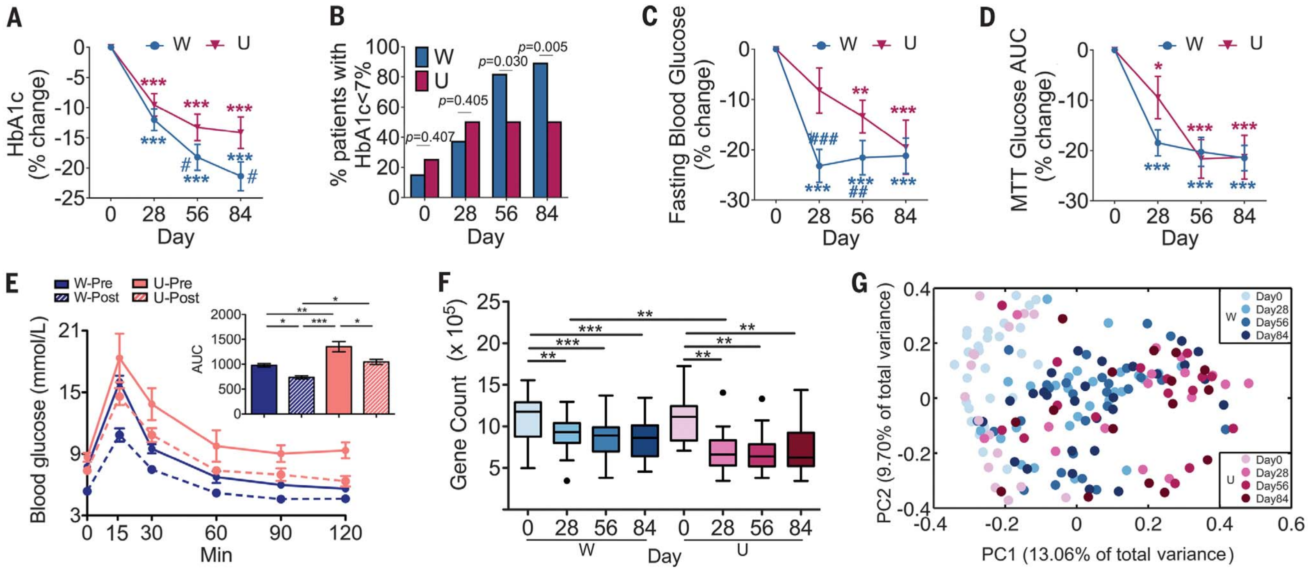

Fig. 1. A high-fiber diet alters the gut microbiota and improves glucose homeostasis in participants with T2DM. Changes in (**A**) HbA1c, (**B**) the percentage of participants with adequate glycemic control, (**C**) fasting blood glucose, and (**D**) the glucose area under the curve (AUC) in a meal tolerance test (MTT) for participants during the intervention are shown. Data are presented as percent changes from day 0 (± SE). A two-way repeated-measures analysis of variance (ANOVA) with Tukey's post hoc test was used for intra- and intergroup comparisons. $*P < 0.05$, $**P < 0.01$, and $***P < 0.001$ for comparison with the day 0 value for the same group; $\#P < 0.05$, $\#\#P < 0.01$, and $\#\#\#P < 0.001$ for comparison with the U group value at the same time point. $n = 27$ patients in the W group and 16 patients in the U group for all analyses except the MTT in (D), where $n = 15$ patients in the U group. (**E**) Oral glucose tolerance test (2 weeks after transplantation) of mice receiving transplanted pre- and postintervention human gut microbiota. The transplant material was derived from representative donors, one from the W group and one from the U group, both before (Pre; day 0) and after (Post; day 84) the intervention. $n = 5$ mice receiving transplanted material in each of the W-Pre, W-Post, and U-Pre groups, and $n = 4$ mice receiving transplanted material in the U-Post group. $*P < 0.05$, $**P < 0.01$, and $***P < 0.001$ by one-way ANOVA with Tukey's post hoc test for intra- and intergroup comparisons. (**F**) Gut microbiota diversity (gene richness). The change in gene counts was adjusted to 31 million mapped reads per sample. Boxes show the medians and the interquartile ranges (IQRs), the whiskers denote the lowest and highest values that were within 1.5 times the IQR from the first and third quartiles, and outliers are shown as individual points. Wilcoxon matched-pair signed-rank tests (two tailed) were used to analyze each pairwise comparison within each group. A Mann-Whitney test was used to analyze differences between the W and U groups at the same time point. $**P < 0.01$ and $***P < 0.001$ [adjusted by the Benjamini-Hochberg procedure (*35*)]. (**G**) Overall gut microbial structure. Principal coordinates analysis was performed on the basis of the Bray-Curtis distance for 422 bacterial genomes [co-abundance gene groups (CAGs)]. PC1, principal coordinate 1; PC2, principal coordinate 2.

data challenged the current notion that greater overall diversity implies better health (*16*). However, gene richness tended to be higher in the W group than in the U group after day 28, and this trend was associated with better clinical outcomes in the W group (Fig. 1F). Individual genes were binned into co-abundance gene groups (CAGs) with a canopy-based algorithm (*17*). A total of 422 CAGs containing >700 genes were inferred to represent the genomes of ecologically distinct bacterial populations (fig. S4). On the basis of Bray-Curtis distances from the 422 CAGs, the overall structure of the gut microbiota showed significant alteration from day 0 to day 28 in both groups, with no further changes afterward (Fig. 1G and fig. S5). At the end of the intervention (day 84), significant differences between the W and U groups reflected a distinct modulatory effect of the high-fiber intervention on the gut microbiota. A Procrustes analysis with all bioclinical variables combined and the 422 bacterial CAGs showed that compositional changes in the gut microbiota were associated with improvements in clinical outcomes (fig. S6).

We then conducted a gene-centric analysis of the metagenomic data sets to explore the functional changes in the gut microbiota that might contribute to improved host clinical outcomes (fig. S7). Both the WTP diet and acarbose increased the availability of fermentable carbohydrates, which led us to focus on genes for carbohydrate utilization (*18*). A total of 192,236 carbohydrate-active enzyme (CAZy)–encoding genes were identified and grouped into 315 CAZy gene families. The richness of CAZy genes followed a pattern similar to that of the total gene richness; that is, both decreased compared with the baseline but remained higher in the W group than in the U group after day 28 (fig. S8). We observed significant segregation between the pre- and all postintervention samples on the basis of the CAZy family profile (Fig. 2A and fig. S8). Among the CAZy genes for metabolizing different carbohydrate substrates, those contributing to starch and inulin degradation were significantly enriched, whereas those related to the use of pectin and mucin were depleted in both the W and U groups (fig. S8). There were intervention-specific effects on the capacity for carbohydrate metabolism (fig. S8); for instance, enrichment of genes encoding cohesin and dockerin as part of a multienzyme complex for plant cell wall degradation was observed only in the W group. Our data suggest that it is not global gene richness per se but the abundance distribution of specific functional genes such as those for CAZys that is more relevant for identifying health-related changes in the gut microbiota.

Pursuing our central hypothesis that SCFAs from increased intake of dietary fibers are one of the key mediators of the observed effects of the microbiota on host glucose homeostasis, we specifically examined the genes involved in the production of these metabolites. We used the abundance of genes that encode key enzymes to indicate the enrichment of production pathways—e.g., *fhs* for acetate and *but* for butyrate formation (*19*). In both W and U groups, the production pathways for acetic acid were significantly enriched (Fig. 2B). Four distinct pathways contribute to butyric acid production (*20*), and the most abundant of these (with *but* as the terminal gene) in the human gut increased significantly only in the W group after the intervention (Fig. 2C and fig. S9). Genes encoding other SCFA production pathways were unchanged or significantly reduced (fig. S9). The shifts in the abundance of genes encoding the SCFA production pathways

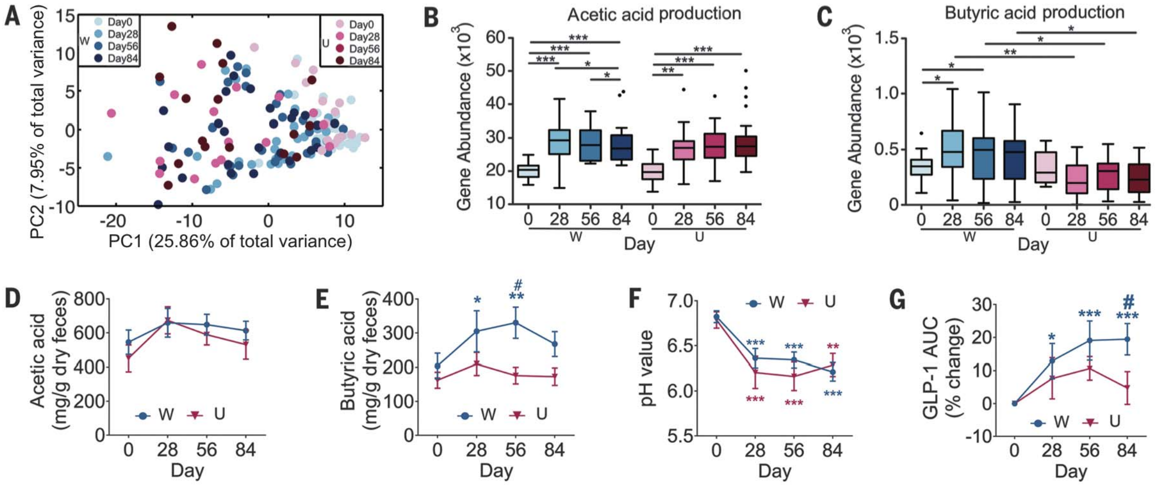

Fig. 2. A high-fiber diet alters gut bacterial fermentation of carbohydrates in participants with T2DM. (**A**) Changes in the abundance of carbohydrate-active enzyme (CAZy) family genes. Principal components analysis was conducted on the abundance (log transformed) of all 192,236 CAZy genes. PC1, principal component 1; PC2, principal component 2. (**B** and **C**) Changes in the abundance of genes that encode the key enzymes in (B) acetic acid production (formate-tetrahydrofolate ligase) and (C) butyric acid production [butyryl–coenzyme A (butyryl-CoA):acetate CoA transferase, represented by *but*]. Boxes, whiskers, and outliers denote values as described for Fig. 1F. Wilcoxon matched-pair signed-rank tests (two tailed) were used to analyze each pairwise comparison within each group. A Mann-Whitney test was used to analyze differences between the W and U groups at the same time point. *$P < 0.05$, **$P < 0.01$, and ***$P < 0.001$ [adjusted by the Benjamini-Hochberg procedure (*35*)]. (**D** and **E**) Changes in fecal concentrations of (D) acetic acid and (E) butyric acid. SCFAs were measured using gas chromatography, and amounts are expressed as milligrams per gram of dry feces (± SE). (**F** and **G**) Changes in (F) fecal water pH and (G) the glucagon-like peptide-1 (GLP-1) AUC in a meal tolerance test (± SE). For (D) to (G), two-way repeated-measures ANOVA with Tukey's post hoc test was used for intra- and intergroup comparisons. *$P < 0.05$, **$P < 0.01$, and ***$P < 0.001$ for comparison with day 0; #$P < 0.05$ for comparison with the U group at the same time point. $n = 27$ patients in the W group and 16 patients in the U group.

were largely consistent with the measured fecal SCFA content (Fig. 2, D and E, and fig. S10). Acetic acid concentrations were essentially similar in both groups throughout the study, increasing to day 28 and decreasing afterward to levels marginally higher than baseline (Fig. 2D), whereas butyric acid concentrations increased significantly only in the W group (Fig. 2E). Both groups had a significant reduction in fecal pH at day 28 (6.36 ± 0.11 versus 6.82 ± 0.07 at baseline for the W group and 6.21 ± 0.18 versus 6.79 ± 0.09 at baseline for the U group), and the pH remained at similar levels for the rest of the study (Fig. 2F). This pH change indicates increased SCFA production and an acidified gut lumen. Acetate and butyrate have been shown to improve glucose homeostasis by inducing gut production of glucagon-like peptide-1 (GLP-1) and peptide YY (PYY), which in turn stimulate insulin secretion (*21–24*). The trend of increased fecal acetate and butyrate concentrations in the W group coincided with a significantly greater postprandial GLP-1 area under the curve (AUC) (Fig. 2G) and a higher level of fasting PYY (fig. S10) for the W group than for the U group at the end of the intervention. This finding, together with the trend for the high-fiber intake to increase postprandial insulin (table S3), supports the notion of an SCFA-driven effect on the gut hormone-insulin secretion cascade that improves glucose regulation.

The different responses of SCFA-related functional genes to the high-fiber intervention prompted us to ask how individual bacteria that harbor the SCFA-producing genes respond to the increased availability of fermentable carbohydrates. From 180 bacterial CAGs that were shared by >20% of our samples, we assembled 154 high-quality draft genomes of prevalent bacteria (57% ± 11% total reads per sample were mapped) (table S5) that met at least five of the six reference genome criteria from the NIH Human Microbiome Project (www.hmpdacc.org/reference_genomes/finishing.php). These high-quality draft genomes of prevalent gut bacteria allowed us to examine compositional changes at the strain level, with functional annotation of each strain. We annotated 141 genomes as SCFA producers, as they harbored at least one of the key genes for SCFA production (table S6). Among those genomes, 79 belonged to bacterial strains that were nonresponders to the high-fiber intervention (i.e., they remained unchanged during the study); 47 belonged to negative responders (i.e., they were significantly reduced); and 15 belonged to positive responders (i.e., they were significantly promoted by the high-fiber diet) (table S6 and fig. S11). The enrichment of these 15 positive responders mostly peaked at day 28 (Fig. 3A) and remained stable afterward, consistent with the pattern we observed in the overall gut microbiota structure (Fig. 1F). These 15 strains are from three different phyla; some (e.g., Lachnospiraceae bacterium CAG0409 and Clostridiales bacterium CAG0023) are poorly characterized, whereas others are from well-known beneficial species. The response, however, was strain specific: only one of the six strains of *Faecalibacterium prausnitzii* was promoted (table S6). In the W group, all 15 positive responders harbored genes for acetate production, and 5 also possessed the capacity for butyrate production (Fig. 3B). In the U group, only 3 acetate producers among the 15 positive responders were promoted (Fig. 3C), which was likely a response to acarbose-induced starch delivery to the colon (*15*). These genome-level data were consistent with the enrichment of the acetic acid production pathways and a trend toward higher fecal acetate in both groups (Fig. 2, B and D). However, an effect of the high-fiber diet on promoting the butyrate production pathway and inducing butyrate production was observed only in the W group (Fig. 2, C and E). The 15 positive responders to the increased availability of diverse fermentable carbohydrates are the major active producers for SCFA production in the context of high-fiber intervention for T2DM. They are most likely the main drivers of the fiber-induced increase in SCFAs that contributes to improved host metabolic outcomes.

We then explored the relationships among these 15 positive responders and other members of the gut ecosystem. In the W group, correlation analysis revealed that each of the 15 positive responders had at least one significant inverse correlation with the negative responders (Fig. 3B and table S7). Similarly, the positive and negative responders in the U group were inversely correlated (Fig. 3C and table S7). Higher genetic capacity for using starch, inulin, and arabinoxylan (fig. S12); more efficient energy and SCFA production from the same amount of fermentable substrates; and greater tolerance to a low

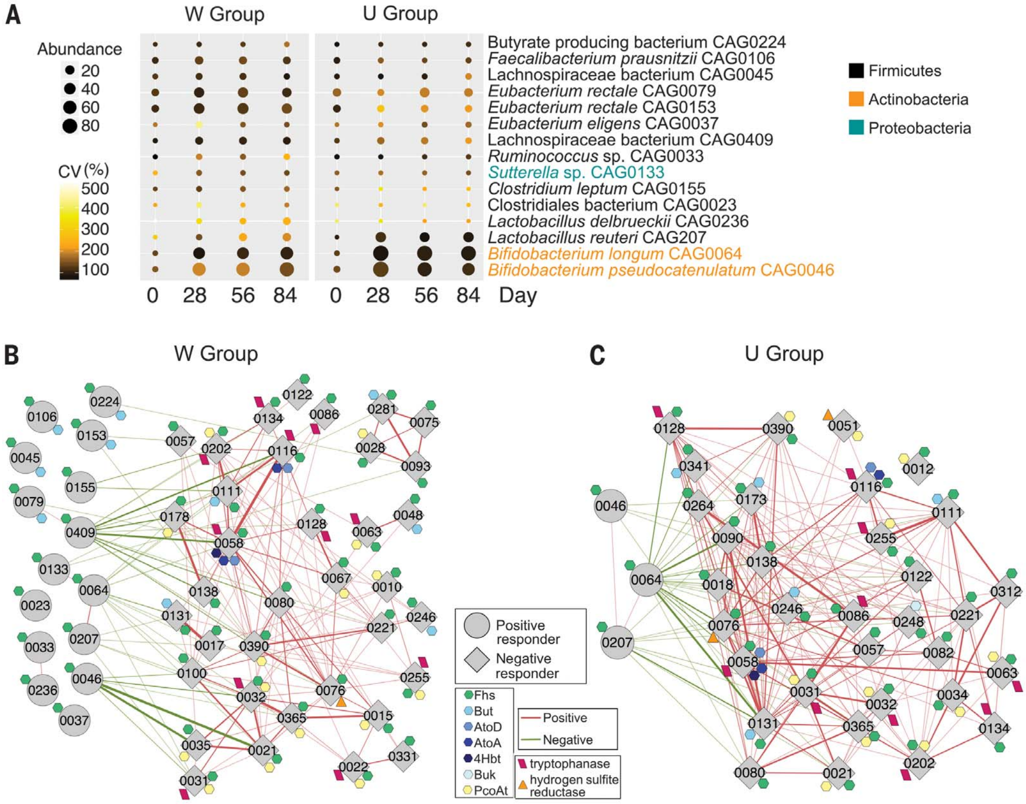

Fig. 3. A high-fiber diet selectively promotes a group of SCFA producers as the major active producers. (**A**) Time-course changes in the abundance of the active producers. The sizes and colors of the circles indicate the average abundance and the coefficient of variance (CV) of the abundance of the strains, respectively. Network plots highlight correlations between positive and negative responders at all time points in (**B**) the W group and (**C**) the U group. The correlation coefficients between CAGs were calculated using the method described by Bland and Altman (*36*). Lines between nodes represent correlations between the connected nodes, with linewidth indicating the correlation magnitude. For clarity, only lines corresponding to correlations with magnitudes of >0.4 were drawn. Fhs, formate-tetrahydrofolate ligase; But, butyryl-CoA:acetate CoA transferase; AtoA, acetoacetate CoA transferase alpha subunits; AtoD, acetoacetate CoA transferase beta subunits; 4Hbt, butyryl-CoA:4-hydroxybutyrate CoA transferase; Buk, butyrate kinase; PcoAt, propionate CoA-transferase/propionyl-CoA:succinate-CoA transferase.

gut luminal pH may explain why these 15 positive responders have a competitive edge over other potential SCFA producers (*25*, *26*). A well-known example is *Bifidobacterium* spp., which, via their "bifid shunt" pathway, are able to produce more adenosine triphosphate and acetate with a given amount of carbohydrates (*25*). For the negative responders, a preference for using animal carbohydrates and a lower tolerance for an acidified gut environment may partially explain why they were outcompeted in response to the high-fiber diet. For example, >20% of CAZy genes in *Bacteroides* spp. are associated with mucin metabolism (fig. S12), and many of these bacteria are known to be less tolerant to lower pH (*26*). Some negative responders also harbor genes that encode tryptophanase or hydrogen sulfite reductase, which are involved in producing metabolically detrimental indole and hydrogen sulfide, respectively (Fig. 3, B and C). The physiological relevance of the decline of these bacteria is supported by reduced gene abundance in the indole and hydrogen sulfide production pathways and reduced fecal amounts of these metabolites (fig. S13). Such changes may contribute to improved host glucose homeostasis, given the known inhibitory effects of these metabolites on GLP-1 and/or PYY production (*27*–*29*). Our data thus support a possible role for these positive responders in structuring a healthier gut ecosystem via production of SCFAs, which modify the gut environment to inhibit the detrimental bacteria, from carbohydrate fermentation. When these SCFA producers are maintained at a certain population level, their metabolic activities create environmental conditions—e.g., lower gut luminal pH, higher concentration of butyrate, and a stronger "competitive exclusion" effect (*26*, *30*, *31*)—that inhibit pathogenic or detrimental gut bacteria and support optimal host health (*26*).

In regard to the relationship with host disease phenotypes, seven positive responders in the W group showed at least one significant correlation with clinical parameters (Fig. 4A). Lachnospiraceae bacterium CAG0409 showed negative correlations with 13 clinical parameters in the W group. However, this bacterium was a nonresponder to acarbose and showed no correlations with any clinical parameters in the U group. The acetate-producing *Bifidobacterium pseudocatenulatum* was one of the most significantly promoted SCFA producers in this study. Inoculation with *B. pseudocatenulatum* strain C95 significantly reduced weight gain, body fat, fasting glucose, and insulin resistance; improved the postprandial glycemic response; and increased the cecum acetate content in mice with high-fat diet–induced obesity (Fig. 4B and fig. S14). In a separate gnotobiotic mouse cohort that received the baseline gut microbiota from a participant in the W group, a similar effect of *B. pseudocatenulatum* C95 inoculation in lowering the fasting blood glucose level was observed (fig. S15). To further understand how the positive responders affect host metabolic health as a group, we derived an active SCFA producer (ASP) index based on the abundance and diversity [Heip evenness (*32*)] of the 15 high-fiber–promoted SCFA producers (fig. S16). The ASP index was higher for the W group throughout the study, mirroring better clinical outcomes, and followed similar temporal trajectories for the W and U groups (Fig. 4C); that is, it increased from baseline and plateaued from day 28 onward despite continued decrease in HbA1c over the course of the intervention (Fig. 1A). The ASP index was negatively correlated with HbA1c when the data points at baseline and the end of the intervention were analyzed together (Fig. 4D). This relationship between the ASP index and HbA1c was also observed in another independent trial (designated QIDONG) in which a T2DM cohort received a similar high-fiber intervention (table S8 and fig. S17). These findings confirm the physiological importance of this group of SCFA producers in T2DM, at least in the context of largely similar regimens of fermentable carbohydrate supplementation. The ASP index reached a plateau at day 28 and remained unchanged throughout the rest of the intervention. When plotting the ASP index at baseline and day 28 with HbA1c at baseline and day 84, we observed a significant negative correlation similar to that observed with day 84 as the end point for the ASP index, indicating that changes in this group of bacteria at an early time point (day 28) may be informative for later (day 84) treatment outcomes (Fig. 4E).

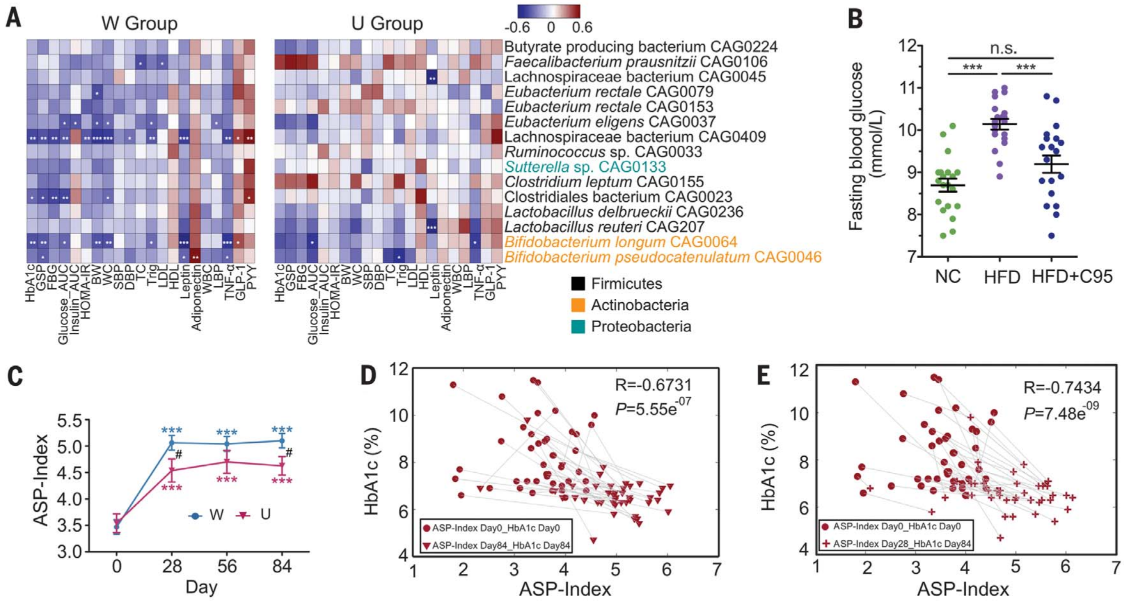

Fig. 4. The group of active producers for SCFA production correlates with metabolic outcomes in participants with T2DM. (**A**) In the heat map, asterisks denote correlations between the abundance of individual active SCFA producers and clinical outcomes. GSP, glycated serum protein; FBG, fasting blood glucose; HOMA-IR, (fasting glucose level × fasting insulin level)/22.5; BW, body weight; WC, waist circumference; SBP, systolic blood pressure; DBP, diastolic blood pressure; TC, total cholesterol; Trig, triglycerides; LDL, low-density lipoprotein; HDL, high-density lipoprotein; WBC, white blood cell count; LBP, lipopolysaccharide-binding protein; TNF-α, tumor necrosis factor–α. *$P < 0.05$; **$P < 0.01$; ***$P < 0.001$. (**B**) *B. pseudocatenulatum* C95 alleviates high-fat diet–induced dysregulation of glucose homeostasis in mice. Data are presented as the means ± SEM (n = 19 to 20 mice for each group). NC, normal chow diet; HFD, high-fat diet; HFD+C95, high-fat diet with *B. pseudocatenulatum* C95. Data were analyzed using one-way ANOVA followed by Tukey's post hoc test. ***$P < 0.001$; n.s., not significant. (**C**) Time-course changes in the ASP index $\left[\ln\left(\text{Heipevenness} \times 10^{10} \times \sum_{i=1}^{15} A_i\right)\right]$, where A_i is the abundance of active SCFA producer i. (**D**) Correlation between the ASP index (day 0 and day 84) and HbA1c (day 0 and day 84). n = 43 patients. R, correlation coefficient. (**E**) Correlation between the ASP index (day 0 and day 28) and HbA1c (day 0 and day 84). n = 43 patients. The correlation coefficients in (A), (D), and (E) were calculated using the method described by Bland and Altman (*36*).

The bloom of the positive responders preceded the physiologically relevant reduction in HbA1c. Such temporal difference, i.e., the gut microbiota quickly responding and reaching a plateau while the host metabolism "played catch-up" with new inputs from the gut ecosystem, not only implies a causative relationship between fiber-induced changes in gut microbiota and improvement of host metabolic health but also provides a critical time window early in the intervention that may inform the eventual effectiveness of microbiome-targeted dietary interventions.

In this study, we identified a group of acetate- and butyrate-producing bacterial strains that were selectively promoted by increased availability of diverse fermentable carbohydrates in the form of dietary fibers. These positive responders are likely the key players for maintaining the mutualistic relationship between the gut microbiota and the human host; promoting this active group of SCFA producers not only enhanced a beneficial function but also maintained a gut environment that keeps detrimental bacteria at bay.

Despite the increased availability of fermentable carbohydrates of diverse physicochemical structures, only a small number of bacteria with the genetic capacity for producing SCFAs were able to take advantage of this new resource and become the dominant positive responders. Such a group of species that "exploit the same class of environmental resources in a similar way" may be considered a "guild" in ecology (*33*). Members of a guild do not necessarily share taxonomic similarity, but they co-occur when adapting to the changing environment. In our case, the 15 positive responders are from three different phyla, but they act as a guild to augment deficient SCFA production from the gut ecosystem by responding to increased fermentable carbohydrate availability in similar ways. When they are considered as a functional group, the abundance and evenness of this guild of SCFA producers correlate with host clinical outcomes. Such guild-based analysis offers a more ecologically relevant way to reduce the dimensionality of microbiome data sets than the conventional taxon-based analysis and facilitates the identification of functionally important members of gut microbiota in human health and disease.

Our study suggests that chronic diseases such as T2DM may be a consequence of the loss of or deficiency in a beneficial function(s), such as SCFA production from carbohydrate fermentation, in the gut ecosystem. In ecological terms, the production of SCFAs from carbohydrate fermentation, which is needed to maintain human health, can be considered an "ecosystem service" provided by the gut microbiota to human hosts (*34*). Restoring or enhancing the lost or deficient function by reestablishing the functionally active ecological populations as ecosystem service providers (ESPs) is the key to a healthier microbiota, which can help alleviate disease phenotypes. Targeted promotion of the active SCFA producers as ESPs via personalized nutrition may present a novel ecological approach for manipulating the gut microbiota to manage T2DM and potentially other dysbiosis-related diseases.

REFERENCES AND NOTES

1. L. Zhao, *Nat. Rev. Microbiol.* **11**, 639–647 (2013).
2. A. Koh, F. De Vadder, P. Kovatcheva-Datchary, F. Bäckhed, *Cell* **165**, 1332–1345 (2016).
3. C. M. Sawicki *et al.*, *Nutrients* **9**, 125 (2017).
4. J. Qin *et al.*, *Nature* **490**, 55–60 (2012).
5. F. H. Karlsson *et al.*, *Nature* **498**, 99–103 (2013).
6. K. Forslund *et al.*, *Nature* **528**, 262–266 (2015).
7. N. Larsen *et al.*, *PLOS ONE* **5**, e9085 (2010).
8. A. Soare *et al.*, *Nutr. Metab. (London)* **11**, 39 (2014).
9. M. Chandalia *et al.*, *N. Engl. J. Med.* **342**, 1392–1398 (2000).
10. F. M. Silva, C. K. Kramer, D. Crispim, M. J. Azevedo, *J. Nutr.* **145**, 736–741 (2015).
11. H. J. Flint, S. H. Duncan, K. P. Scott, P. Louis, *Proc. Nutr. Soc.* **74**, 13–22 (2015).
12. G. Wu *et al.*, *mBio* **8**, e02348-16 (2017).
13. C. Zhang *et al.*, *EBioMedicine* **2**, 968–984 (2015).
14. Chinese Diabetes Society, *Chin. J. Diabetes Mellitus* **6**, 447–498 (2014).
15. M. Hiele, Y. Ghoos, P. Rutgeerts, G. Vantrappen, *Dig. Dis. Sci.* **37**, 1057–1064 (1992).
16. E. Le Chatelier *et al.*, *Nature* **500**, 541–546 (2013).
17. H. B. Nielsen *et al.*, *Nat. Biotechnol.* **32**, 822–828 (2014).
18. V. Lombard, H. Golaconda Ramulu, E. Drula, P. M. Coutinho, B. Henrissat, *Nucleic Acids Res.* **42**, D490–D495 (2014).
19. M. J. Claesson *et al.*, *Nature* **488**, 178–184 (2012).
20. M. Vital, A. C. Howe, J. M. Tiedje, *mBio* **5**, e00889-14 (2014).
21. L. B. Bindels, E. M. Dewulf, N. M. Delzenne, *Trends Pharmacol. Sci.* **34**, 226–232 (2013).
22. A. Everard, P. D. Cani, *Rev. Endocr. Metab. Disord.* **15**, 189–196 (2014).
23. P. D. Cani *et al.*, *Am. J. Clin. Nutr.* **90**, 1236–1243 (2009).
24. J. A. Parnell, R. A. Reimer, *Am. J. Clin. Nutr.* **89**, 1751–1759 (2009).
25. K. Pokusaeva, G. F. Fitzgerald, D. van Sinderen, *Genes Nutr.* **6**, 285–306 (2011).

26. S. H. Duncan, P. Louis, J. M. Thomson, H. J. Flint, *Environ. Microbiol.* **11**, 2112–2122 (2009).
27. M. T. Yokoyama, J. R. Carlson, *Am. J. Clin. Nutr.* **32**, 173–178 (1979).
28. C. Chimerel *et al*., *Cell Rep.* **9**, 1202–1208 (2014).
29. V. Bala *et al*., *Front. Physiol.* **5**, 420 (2014).
30. C. Q. Sun *et al*., *Chem. Biol. Interact.* **113**, 117–131 (1998).
31. J. Walter, R. Ley, *Annu. Rev. Microbiol.* **65**, 411–429 (2011).
32. C. Heip, *J. Mar. Biol. Assoc. U.K.* **54**, 555–557 (1974).
33. D. Simberloff, T. Dayan, *Annu. Rev. Ecol. Syst.* **22**, 115–143 (1991).
34. E. K. Costello, K. Stagaman, L. Dethlefsen, B. J. Bohannan, D. A. Relman, *Science* **336**, 1255–1262 (2012).
35. Y. Benjamini, Y. Hochberg, *J. R. Stat. Soc. Ser. B* **57**, 289–300 (1995).
36. J. M. Bland, D. G. Altman, *BMJ* **310**, 446 (1995).

ACKNOWLEDGMENTS

This work was supported by grants from the National Natural Science Foundation of China (31330005, 81401141, and 81370904), the Science and Technology Commission of Shanghai Municipality (14YF1402200), Key Projects of Shanghai Municipal Health Bureau Research Fund (201440033), Shanghai Jiao Tong University Research Funding on Medical and Engineering Interdisciplinary Projects (YG2015ZD08), Songjiang District Health Bureau of PANDENG Medical Program (0702N14003), and Shanghai Shen Kang Hospital Development Center funding for chronic disease prevention and control projects (SHDC12015304). L.Z. is a Canadian Institute for Advanced Research (CIFAR) fellow. We acknowledge a computing facility award for use of the Pi cluster at Shanghai Jiao Tong University. All data and code to understand and assess the conclusions of this research are available in the main text and supplementary materials and via the European Nucleotide Archive (ENA), where the raw pyrosequencing and Illumina read data for all samples have been deposited under accession numbers PRJEB1455 (GUT2D study) and PRJEB15179 (QIDONG study).

SUPPLEMENTARY MATERIALS

www.sciencemag.org/content/359/6380/1151/suppl/DC1
Materials and Methods
Supplementary Text
Figs. S1 to S17
Tables S1 to S8
References (*37–64*)

19 August 2017; accepted 19 January 2018
10.1126/science.aao5774

MICROBIOTA

Translocation of a gut pathobiont drives autoimmunity in mice and humans

S. Manfredo Vieira,[1] M. Hiltensperger,[1] V. Kumar,[2] D. Zegarra-Ruiz,[1] C. Dehner,[1] N. Khan,[1] F. R. C. Costa,[1*] E. Tiniakou,[1†] T. Greiling,[1‡] W. Ruff,[1] A. Barbieri,[3] C. Kriegel,[1] S. S. Mehta,[4] J. R. Knight,[4] D. Jain,[3] A. L. Goodman,[5] M. A. Kriegel[1,2§]

Despite multiple associations between the microbiota and immune diseases, their role in autoimmunity is poorly understood. We found that translocation of a gut pathobiont, *Enterococcus gallinarum*, to the liver and other systemic tissues triggers autoimmune responses in a genetic background predisposing to autoimmunity. Antibiotic treatment prevented mortality in this model, suppressed growth of *E. gallinarum* in tissues, and eliminated pathogenic autoantibodies and T cells. Hepatocyte–*E. gallinarum* cocultures induced autoimmune-promoting factors. Pathobiont translocation in monocolonized and autoimmune-prone mice induced autoantibodies and caused mortality, which could be prevented by an intramuscular vaccine targeting the pathobiont. *E. gallinarum*–specific DNA was recovered from liver biopsies of autoimmune patients, and cocultures with human hepatocytes replicated the murine findings; hence, similar processes apparently occur in susceptible humans. These discoveries show that a gut pathobiont can translocate and promote autoimmunity in genetically predisposed hosts.

The gut microbiota are implicated in the pathogenesis of multiple gut and systemic autoimmune diseases (*1*). The integrity of the gut barrier is essential to prevent the microbiota of a healthy individual from triggering adaptive immune responses (*2*–*7*). When intact commensals or pathogens escape the gut barrier, several defense mechanisms impede bacterial access to the systemic circulation. However, if these mechanisms fail, the mesenteric lymph nodes (MLNs) and liver represent further "firewalls" against commensal bacteria that escape the gut (*2*, *4*, *7*). Such mechanisms occur only during intestinal or vascular pathology, during chemotherapy, or in the absence of a functional innate immune system (*2*, *6*, *8*–*11*). Although recent studies show that gut commensals can reside within gastrointestinal-associated lymphoid tissues of unmanipulated, healthy hosts, it is unclear whether pathobiont translocation is involved in systemic autoimmunity (*12*).

In humans, systemic lupus erythematosus (SLE) is a multifactorial autoimmune disease that is associated with marked morbidity and mortality, especially in antiphospholipid antibody–positive patients. Besides the major histocompatibility complex locus, SLE is associated with several genetic risk loci for excessive signaling of RNA-sensing Toll-like receptor 7 (TLR7) and type I interferons (IFNs) (*13*). In normal animals, exogenous viral infections and retroviruses contribute to these immune responses and interact with the microbiota (*14*–*19*). In the specific pathogen-free (NZW × BXSB)F_1 hybrid mouse, responses to endogenous retrovirus glycoprotein 70 (ERV gp70) have been shown to drive lupus kidney disease via TLR7 (*20*, *21*). These mice eventually succumb to progressive autoimmune thrombi mediated by pathogenic antiphospholipid [β_2-glycoprotein I (β_2GPI)] antibodies. We asked whether, in animals predisposed to autoimmune responses, translocation of gut commensals drives IFN and anti–double-stranded DNA (dsDNA), anti–ERV gp70, and anti-β_2GPI responses. Consequently, we investigated whether pathological immune responses could be alleviated by therapeutic strategies such as antibiotic treatment or vaccination.

Mortality, lupus-related autoantibodies, and autoimmune manifestations were relieved in

---

[1] Department of Immunobiology, Yale School of Medicine, New Haven, CT, USA. [2] Department of Medicine, Yale School of Medicine, New Haven, CT, USA. [3] Department of Pathology, Yale School of Medicine, New Haven, CT, USA. [4] Yale Center for Genome Analysis, Yale School of Medicine, New Haven, CT, USA. [5] Department of Microbial Pathogenesis and Microbial Sciences Institute, Yale School of Medicine, New Haven, CT, USA.
*Present address: Department of Biochemistry and Immunology, Ribeirao Preto Medical School, Ribeirao Preto, SP, Brazil. †Present address: Department of Medicine, Johns Hopkins University School of Medicine, Baltimore, MD, USA. ‡Present address: Department of Dermatology, Oregon Health and Science University, Portland, OR, USA.
§Corresponding author. Email: martin.kriegel@yale.edu

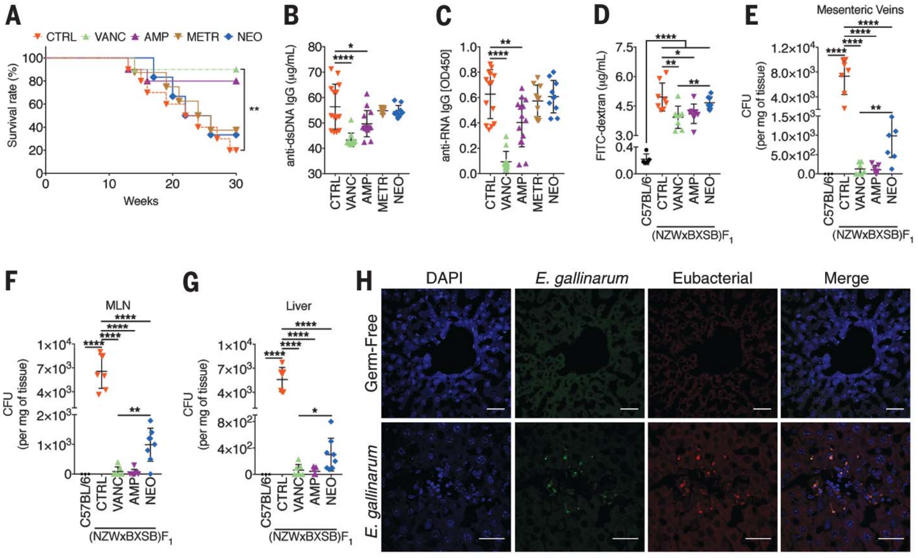

Fig. 1. Effect of antibiotics on autoimmunity and *E. gallinarum* translocation to the liver. (**A**) Vancomycin (VANC), ampicillin (AMP), metronidazole (METR), neomycin (NEO), or control water (CTRL) were provided in the drinking water of (NZW × BXSB)F_1 mice starting at 6 weeks of age (n = 15 each). Mice were followed for 30 weeks or until death from autoimmunity. (**B** and **C**) Serum anti-dsDNA (B) and anti-RNA (C) IgG at 16 weeks of age. (**D**) Serum levels of orally administered FITC-dextran as an indicator of gut barrier leakiness (n = 8 each). (**E** to **G**) Cultures of tissues from 16-week-old mice showed a selective growth of *E. gallinarum* in the mesenteric veins (E), MLN (F), and liver (G) (n = 7 each). (**H**) An *E. gallinarum*–specific FISH probe detects *E. gallinarum* in liver (scale bars, 30 µm) of *E. gallinarum*–monocolonized C57BL/6 mice 3 weeks after colonization in comparison to germ-free mice. One representative section from one mouse is shown from multiple sections with *E. gallinarum* signals within the tissues, representative of three mice in total. Data are presented as mean ± SD in (B) to (G); *$P < 0.05$, **$P < 0.01$, ***$P < 0.001$, ****$P < 0.0001$; log-rank test and Gehan-Breslow-Wilcoxon test in (A), analysis of variance (ANOVA) followed by Bonferroni multiple-comparisons test in (B) to (G).

(NZW × BXSB)F_1 hybrid mice after oral administration of vancomycin or ampicillin, implicating involvement of Gram-positive pathobionts in disease (Fig. 1, A to C, and fig. S1). In addition to anti-dsDNA and anti-RNA autoantibodies (Fig. 1, B and C), anti-β_2GPI immunoglobulin G (IgG), hepatic and serum ERV gp70, and anti–ERV gp70 immune complexes (ICs) were all suppressed by vancomycin treatment (fig. S2, A to L). Uptake of orally fed fluorescein isothiocyanate (FITC)–dextran into the systemic circulation of (NZW × BXSB)F_1 hybrid mice indicated grossly impaired gut barrier function relative to nonautoimmune C57BL/6 mice (Fig. 1D). At 16 weeks of age, we were able to detect marked bacterial growth in the mesenteric veins, MLNs, and liver, and 2 weeks later also in the spleen but not kidneys, which are affected by deposition of circulating immune complexes (Fig. 1, E to G, and fig. S2M). Translocation of microbiota was suppressed by vancomycin or ampicillin, both of which prevented mortality; neomycin was less effective at inhibiting translocation relative to vancomycin (Fig. 1, E to G).

Full-length 16*S* rDNA sequencing of single colonies from aerobic and anaerobic MLN, liver, and spleen cultures detected *Enterococcus gallinarum*, a Gram-positive gut commensal of animals and humans, in the mesenteric veins of 82% of (NZW × BXSB)F_1 hybrid mice. *E. gallinarum* was visualized in situ in MLNs and livers by fluorescence in situ hybridization (FISH) (Fig. 1H and fig. S2N). C57BL/6 control mice showed no systemic bacterial growth. Taxa identified by longitudinal fecal 16*S* rDNA sequencing revealed that *Enterococcus* spp. were enriched only in some fecal samples (fig. S3, A to C, and fig. S4). Species-specific polymerase chain reaction (PCR) did not detect *E. gallinarum* DNA in stool samples from human or murine autoimmune hosts (fig. S5, A to D); however, fecal or mucosal tissue culture followed by species-specific PCR consistently revealed *E. gallinarum* in the feces and small intestine, as well as in the liver, of (NZW × BXSB)F_1 mice (fig. S6, A to C). We also found *E. gallinarum* translocation to livers of (NZW × BXSB)F_1 mice in two other animal facilities at Yale after transfer of newly weaned animals equilibrated to different microbiomes (fig. S6, D and E).

To test whether *E. gallinarum* induces proinflammatory pathways and alters gut barrier–related molecules in small intestinal tissue during translocation into internal organs, we performed RNA expression profiling of *E. gallinarum*–monocolonized C57BL/6 mice and compared these data with those from *Enterococcus faecalis*– and *Bacteroides thetaiotaomicron*–monocolonized mice (Fig. 2, A to J, and figs. S7 and S8). The presence of *E. gallinarum* down-regulated ileal molecules related to barrier function (e.g., occludin, claudins, Plvap, Axin2), the mucus layer (e.g., Mucin-2), and antimicrobial defense (e.g., Reg3b, Defa2) and up-regulated those related to inflammation (e.g., Cxcr2, AhR/Cyp1a1, Enpp3). Enpp3 is known to increase numbers of plasmacytoid dendritic cells (pDCs) (*22*), which are key cells contributing to the IFN signature in human SLE (*13*)

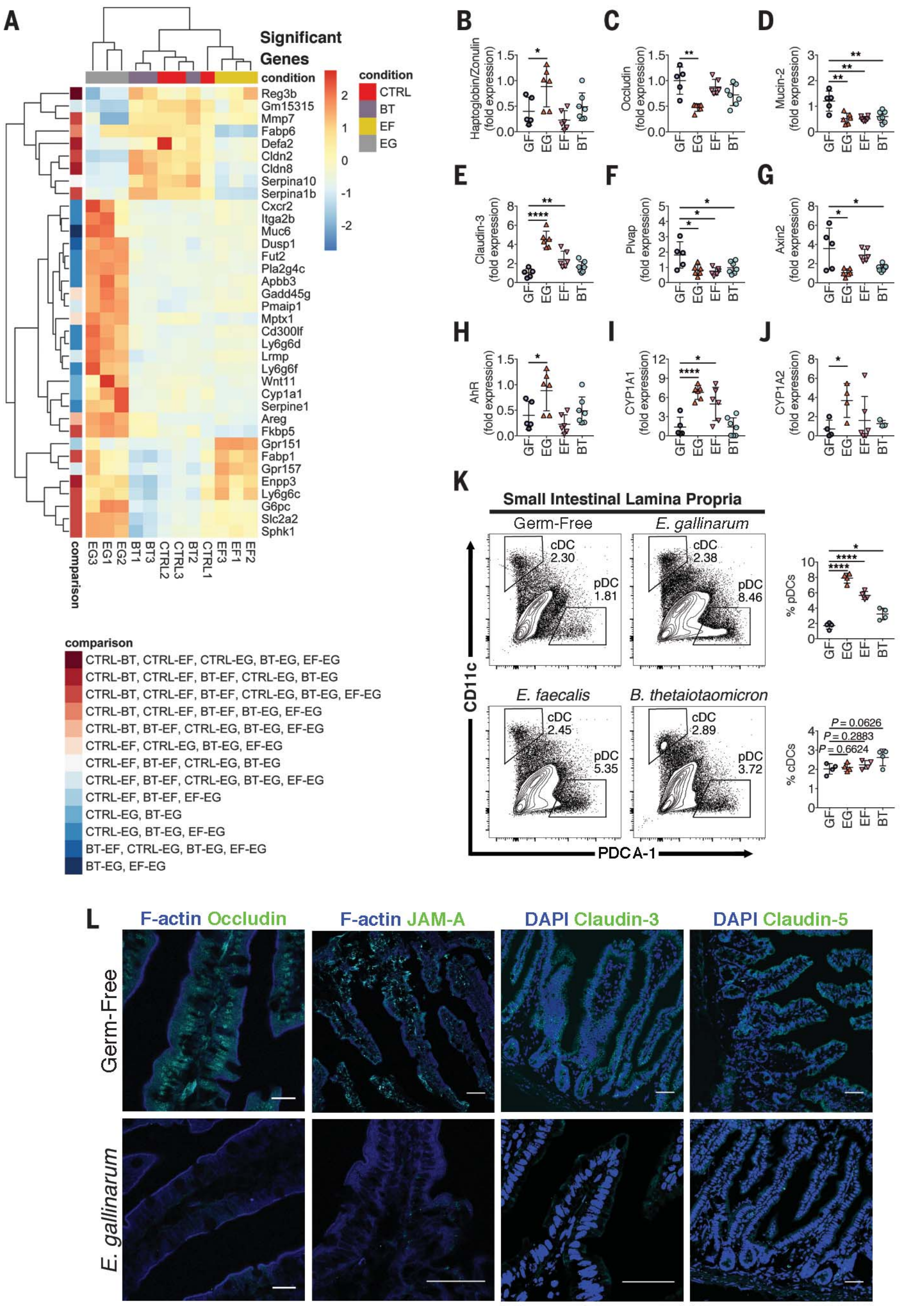

Fig. 2. RNA expression profiling and plasmacytoid dendritic cell frequencies in small intestine from germ-free mice monocolonized with *E. gallinarum*, *E. faecalis*, or *B. thetaiotaomicron*. Germ-free C57BL/6 mice were monocolonized with *E. gallinarum* (EG), *E. faecalis* (EF), or *B. thetaiotaomicron* (BT) for RNA-seq and fluorescence-activated cell sorting (FACS) analyses of the small intestine. (**A**) RNA-seq was performed with ileal tissue isolated from 14-week-old monocolonized mice (n = 3 each). Heat map shows transcripts differentially expressed in the ileum 8 hours after commensal delivery. (**B** to **J**) Reverse transcription quantitative PCR (RT-qPCR) analysis of ileum RNA (n = 6 each) as described in (A). (**K**) Plasmacytoid dendritic cell (pDC) and conventional dendritic cell (cDC) frequencies in the small intestinal lamina propria of 12-week-old germ-free mice (n = 4 each) were evaluated 3 weeks after monocolonization by FACS analysis. (**L**) Confocal imaging of gut tissues was performed as described in the supplementary materials. Localizations of TJ proteins are shown in green for occludin, JAM-A, claudin-3, and claudin-5. Images are representative of six different mice. DAPI, 4′,6-diamidino-2-phenylindole. Scale bars, 40 μm. Data are presented as mean ± SD in (B) to (K); $*P < 0.05$, $**P < 0.01$, $****P < 0.0001$; ANOVA followed by Bonferroni multiple-comparisons test in (B) to (K).

and which were induced by *E. gallinarum* monocolonization (Fig. 2K).

We used confocal microscopy to visualize the gut epithelial, vascular, and lymphatic barrier molecule changes we detected by RNA. Intestinal epithelial and endothelial cells have tight junctions formed by occludin, zonula occludens–1 (ZO-1), cingulin, and junctional adhesion molecule–A (JAM-A) (*23*). These cells also have adherent junctions formed by vascular endothelial cadherin (VE-cadherin) and β-catenin. A loss of expression of these junctional proteins was seen in gnotobiotic C57BL/6 mice monocolonized with *E. gallinarum*, except for ZO-1 and VE-cadherin (Fig. 2L and figs. S9 to S11). Claudin-2, -3, and -5 are expressed in lymphatic endothelial tight junctions, but in *E. gallinarum*–monocolonized mice they were weakly expressed relative to germ-free controls, except for pore-forming claudin-2 (Fig. 2L and fig. S12).

Liver-resident *E. gallinarum* possibly induces hepatic overexpression of ERV gp70 that fuels anti-ERV immune complex formation and systemic autoimmunity (fig. S2). We found that (NZW × BXSB)F_1–derived hepatocytes cocultured with *E. gallinarum* isolated from an (NZW × BXSB) F_1 liver induced multiple autoimmune-promoting factors, including the autoantigens ERV gp70 and β_2GPI, which were potently induced by *E. gallinarum* or *E. gallinarum* RNA (a potential TLR7/8 ligand) relative to *E. faecalis* (Fig. 3, A and B). In hepatocytes and dendritic cells, *E. gallinarum* RNA also induced expression of type I IFN and other proinflammatory cytokines (Fig. 3C and fig. S13).

Tryptophan-derived indoles are bacterial ligands for the aryl hydrocarbon receptor (AhR), which activates the AhR-CYP1A1 pathway, a known innate antimicrobial defense mechanism and inducer of T helper 17 (Th17) cells (*24*–*27*) that we also found to be up-regulated (Fig. 3, D to F). Furthermore, whole-genome sequencing revealed that *E. gallinarum* encodes the shikimate pathway, which generates AhR ligands (fig. S14 and table S1) (*26*). We tested whether *E. gallinarum*–immune interactions, possibly mediated by the AhR pathway, induced Th17 and T follicular helper (Tfh) cells in vivo that are crucial for systemic autoantibody production (*28*, *29*). Broad-spectrum antibiotic or vancomycin treatment in (NZW × BXSB)F_1 mice reduced levels of Th17 cells, Tfh cells, and their cytokine signatures (fig. S15, A to C). Vancomycin had no direct influence on immune cells in vitro (fig. S15D). The in vivo effects of vancomycin on T cells correlated with reduced *E. gallinarum* translocation, less immunopathology, and fewer autoantibodies in these mice, as well as suppression of serum and hepatic levels of the ERV gp70 autoantigen and anti–ERV gp70 immune complexes (Fig. 1 and

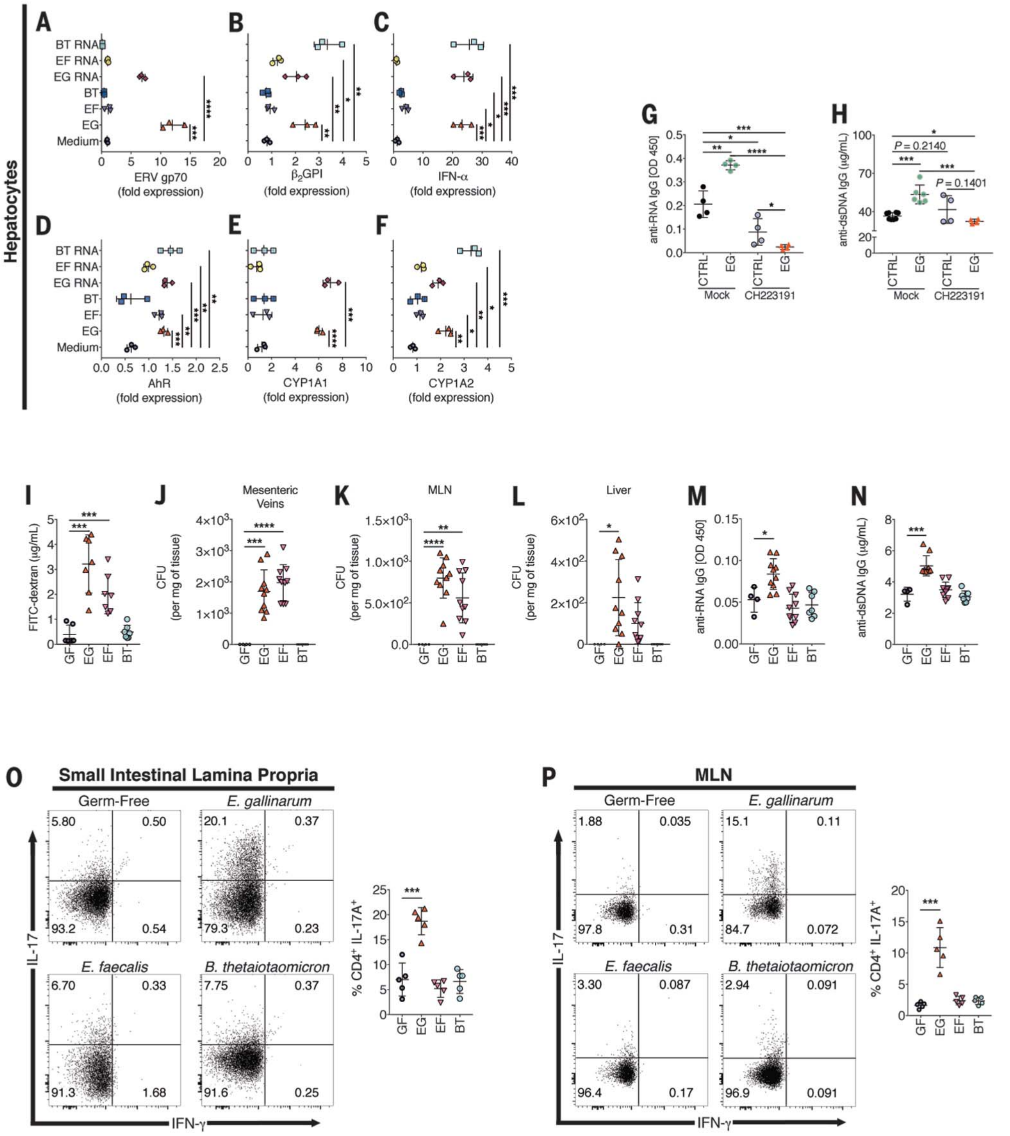

Fig. 3. Induction of hepatic AhR by *E. gallinarum*, AhR antagonism in (NZW × BXSB)F1 mice, and Th17 and autoantibody induction in *E. gallinarum*–monocolonized C57BL/6 mice. (**A** to **F**) *E. gallinarum*, *E. faecalis*, and *B. thetaiotaomicron* lysates or isolated RNA were cocultured with hepatocytes from 14-week-old (NZW × BXSB) F_1 mice (*n* = 3 each), and expression of ERV gp70, the autoantigen β_2GPI, IFN-α, and AhR was measured 6 hours later. (**G** and **H**) Serum anti-RNA (G) and anti-dsDNA (H) IgG of 16-week-old (NZWxBXSB)F_1 mice (*n* = 4 each) gavaged with vehicle or EG and treated with AhR antagonist CH223191 or mock, as described in the supplementary materials. (**I** to **L**) C57BL/6 germ-free (GF) mice were monocolonized with *E. gallinarum*, *E. faecalis*, and *B. thetaiotaomicron* at 12 weeks of age (*n* = 6 to 10 mice) and evaluated 3 weeks later for integrity of the gut barrier with FITC-dextran (I), and for translocation to the mesenteric veins (J), MLNs (K), and liver (L). (**M** and **N**) C57BL/6 germ-free mice (*n* = 4 to 10 mice) were monocolonized as in (I), and anti-RNA (M) and anti-dsDNA (N) IgG autoantibodies were measured 8 weeks later. (**O** and **P**) Th17 cells and Th1 cell frequencies were determined by intracellular FACS analysis of IL-17A and IFN-γ in small intestinal lamina propria (O) and MLN (P) $CD45^+$ $CD4^+$ $CD44^+$ T cells from germ-free and monocolonized mice (*n* = 5 each). Data are presented as mean ± SD in (A) to (P); **P* < 0.05, ***P* < 0.01, ****P* < 0.001, ****P < 0.0001; ANOVA followed by Bonferroni multiple-comparisons test.

fig. S2). Administration of an AhR-selective antagonist abrogated the Th17- and autoantibody-inducing effects of *E. gallinarum* in (NZW × BXSB)F_1 mice in vivo (Fig. 3, G and H, and fig. S16); this finding indicates that AhR signaling is involved in *E. gallinarum*–induced autoimmunity.

Because *E. gallinarum* has the potential for translocation in (NZW × BXSB)F_1 mice but not in C57BL/6 mice under specific pathogen-free conditions, we tested translocation in germ-free C57BL/6 mice monocolonized with *E. gallinarum*. In the absence of competing microbiota, *E. gallinarum* induced barrier leakage, autoantibodies, and translocation to mesenteric veins, MLNs, and livers of nonautoimmune C57BL/6 mice (Fig. 3, I to N). Autoantibody induction in C57BL/6 mice was not seen during monocolonization with other bacteria that either remain in the gut (*B. thetaiotaomicron*) or translocate to tissues (*E. faecalis*) (Fig. 3, I to N). Monocolonization with *E. gallinarum* induced Th17 cells in the small intestinal lamina propria and MLNs of C57BL/6 mice (Fig. 3, O and P), consistent with the finding that Th17 cells are abundant in (NZW × BXSB)F_1 mice and were depleted after vancomycin treatment (fig. S15). Experiments with antibiotic-pretreated (NZW × BXSB)F_1 hybrid mice gavaged with a translocating pathogen, *Salmonella typhimurium*, did not induce autoantibodies (fig. S17). By contrast, gavage of antibiotic-pretreated (NZW × BXSB)F_1 hybrid mice with *E. gallinarum* caused systemic autoimmune pathology (fig. S17D and fig. S18, control group).

To deplete the pathobiont selectively, we developed an intramuscular vaccination strategy using heat-killed *E. gallinarum* (fig. S18A). Vaccination against *E. gallinarum*, but not against *E. faecalis* nor *B. thetaiotaomicron*, reduced levels of serum autoantibodies and prolonged survival in (NZW × BXSB)F_1 mice (fig. S18, B to F). Vaccination also prevented translocation, as no growth of *E. gallinarum* was observed in internal organs (fig. S18G). Thus, pathobiont-specific treatment can abrogate host autoimmune processes without needing to suppress the immune system, which can lead to systemic adverse events in current clinical practice.

Longitudinal stool analyses from SLE patients revealed evidence for impaired gut barrier function with increased fecal albumin and calprotectin (Fig. 4, A and B). We thus tested for *E. gallinarum* translocation to human livers in patients with SLE and autoimmune hepatitis (AIH) who display serologic features of lupus, including antinuclear antibodies and anti-dsDNA IgG (table S2) (*30*). Liver biopsies from three SLE patients were positive for *E. gallinarum* (Fig. 4C); of six controls obtained from healthy liver transplant donors with normal liver histology, four were positive for the presence of other *Enterococcus* species but not *E. gallinarum*. Sterilely obtained human liver tissues from the same control patients, AIH patients, and cirrhosis patients [who are known to have grossly impaired gut barriers (*31*)] were subjected to 16*S* rDNA sequencing; the results show that *Enterococcus* spp. predominated in diseased tissues (Fig. 4D). Note that the majority

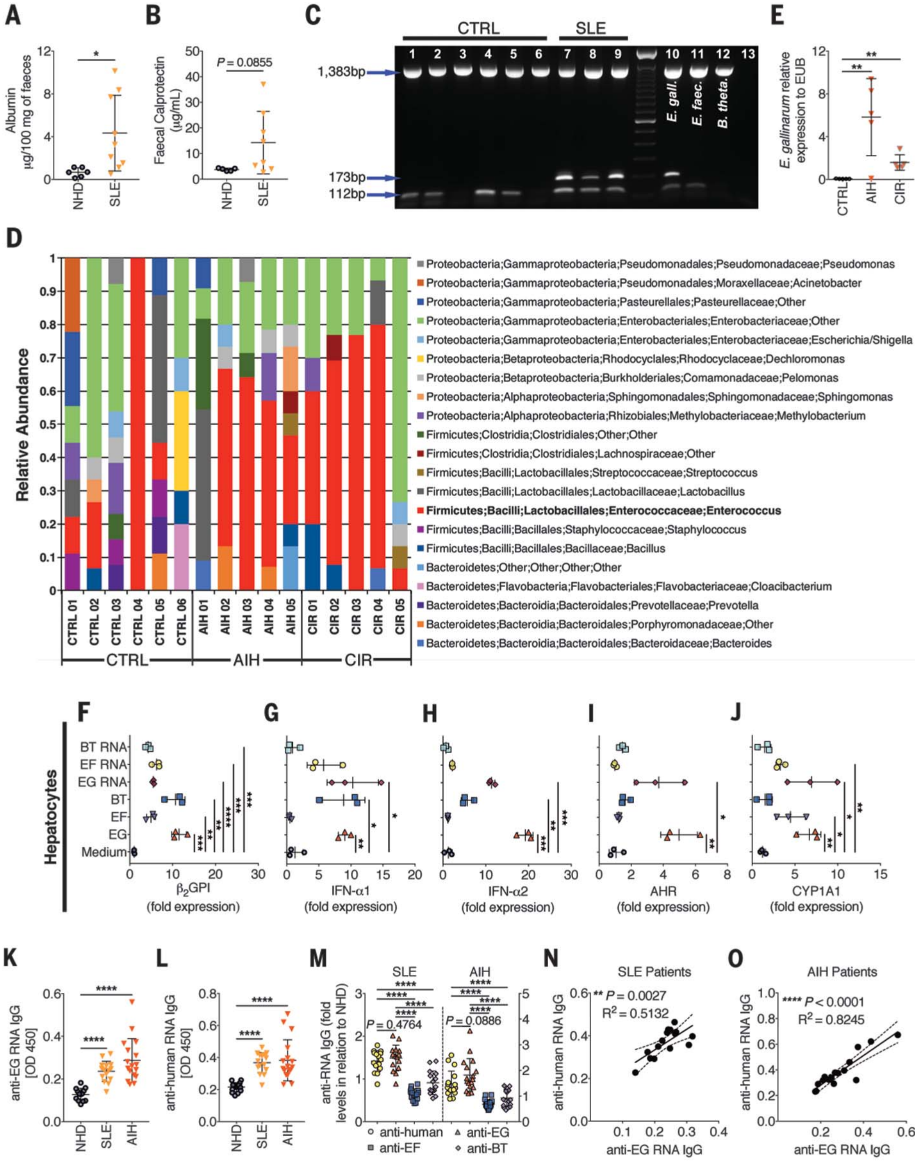

Fig. 4. Gut barrier function and *E. gallinarum* in liver biopsies of autoimmune patients with anti–*E. gallinarum* serum reactivities. (**A** and **B**) Feces from patients with SLE (n = 9) were screened for increased albumin (A) and calprotectin (B) as signs of an impaired gut barrier. NHD, normal healthy donors (n = 9). (**C**) Multiplex PCR for eubacterial [1383 base pairs (bp)], *Enterococcus* genus (112 bp), and *E. gallinarum* (173 bp) DNA on sterilely obtained and processed liver biopsies from cadaveric liver transplant donors (CTRL) or SLE patients. Lanes 10 to 12, bacterial strains as indicated; lane 13, water. (**D**) 16*S* rDNA sequencing of controls as in (C), autoimmune hepatitis (AIH) patients, and non-AIH cirrhosis (CIR) patients. (**E**) Liver biopsies from CTRL, AIH, and CIR patients (n = 5 to 6 each) were tested for *E. gallinarum* (EG) DNA by qPCR and normalized to any eubacterial (EUB) signal. (**F** to **J**) RT-qPCR of human primary hepatocytes (n = 3 each) stimulated with *E. gallinarum*, *E. faecalis*, or *B. thetaiotaomicron* as in Fig. 3. (**K** and **L**) SLE (n = 15) and AIH (n = 17) sera were screened for anti–*E. gallinarum* RNA IgG (K) and anti-human RNA IgG (L) by enzyme-linked immunosorbent assay (ELISA). (**M**) SLE and AIH serum IgG levels against human, *E. gallinarum*, *E. faecalis*, or *B. thetaiotaomicron* RNA normalized to NHD sera. (**N** and **O**) Correlation between anti–*E. gallinarum* RNA IgG and autoantibodies in SLE (N) and AIH (O) patients. Data are presented as mean ± SD; $^*P < 0.05$, $^{**}P < 0.01$, $^{***}P < 0.001$, $^{****}P < 0.0001$; Student t test in (A) and (B), ANOVA followed by Bonferroni multiple-comparisons test in (E) to (M), and Pearson correlation in (N) and (O).

of AIH liver biopsies, but not the healthy control livers, were positive for *E. gallinarum* (Fig. 4E).

Similar to the effects seen with murine hepatocytes (Fig. 3, A to F), primary human hepatocytes from healthy livers stimulated with *E. gallinarum* induced β_2GPI, type I interferon, and AHR/CYP1A1 (Fig. 4, F to J). Consistent with enhanced adaptive immune responses to *E. gallinarum*, the majority of SLE and AIH patients also showed increased serum antibody titers against *E. gallinarum* and particularly its RNA, which can act as a potential TLR7/8 stimulus and cross-reactive trigger (Fig. 4, K to O, and fig. S19). Comparison of anti–human RNA IgG autoantibody titers in SLE and AIH patients with anti–*E. gallinarum* RNA IgG showed that both were equally elevated, by contrast to anti–*E. faecalis* and anti–*B. thetaiotaomicron* RNA antibodies (Fig. 4, K to O).

Our findings show that the Gram-positive gut pathobiont *E. gallinarum* translocates, as a result of gut barrier breakdown, into systemic organs in autoimmune-prone hosts to drive autoimmune pathogenesis (fig. S20). Translocating bacteria may not only skew T helper cell differentiation but may also directly act on colonized tissues, such as the liver, to induce autoantigens, ERV proteins, cytokines, and other autoimmune-promoting factors. If the complexity of host tissue–microbiota interactions is considered in chronic autoimmunity, it may offer new therapeutic avenues for these debilitating and potentially lethal diseases.

REFERENCES AND NOTES

1. W. E. Ruff, M. A. Kriegel, *Trends Mol. Med.* **21**, 233–244 (2015).
2. M. L. Balmer *et al*., *Sci. Transl. Med.* **6**, 237ra66 (2014).
3. T. W. Hand *et al*., *Science* **337**, 1553–1556 (2012).
4. A. J. Macpherson, T. Uhr, *Science* **303**, 1662–1665 (2004).
5. N. G. Sandler, D. C. Douek, *Nat. Rev. Microbiol.* **10**, 655–666 (2012).
6. E. Slack *et al*., *Science* **325**, 617–620 (2009).
7. I. Spadoni *et al*., *Science* **350**, 830–834 (2015).
8. F. R. Costa *et al*., *J. Exp. Med.* **213**, 1223–1239 (2016).
9. G. F. Sonnenberg *et al*., *Science* **336**, 1321–1325 (2012).
10. D. Stanley *et al*., *Nat. Med.* **22**, 1277–1284 (2016).
11. S. Viaud *et al*., *Science* **342**, 971–976 (2013).
12. T. C. Fung *et al*., *Immunity* **44**, 634–646 (2016).
13. M. K. Crow, *J. Immunol.* **192**, 5459–5468 (2014).
14. M. C. Abt *et al*., *Immunity* **37**, 158–170 (2012).
15. T. Ichinohe *et al*., *Proc. Natl. Acad. Sci. U.S.A.* **108**, 5354–5359 (2011).
16. M. Kane *et al*., *Science* **334**, 245–249 (2011).
17. S. K. Kuss *et al*., *Science* **334**, 249–252 (2011).
18. S. M. Vieira, O. E. Pagovich, M. A. Kriegel, *Lupus* **23**, 518–526 (2014).
19. G. R. Young *et al*., *Nature* **491**, 774–778 (2012).
20. L. Baudino, K. Yoshinobu, N. Morito, M. L. Santiago-Raber, S. Izui, *Autoimmun. Rev.* **10**, 27–34 (2010).
21. N. Tabata *et al*., *J. Virol.* **74**, 4116–4126 (2000).
22. Y. Furuta *et al*., *PLOS ONE* **12**, e0172509 (2017).
23. A. C. Luissint, C. A. Parkos, A. Nusrat, *Gastroenterology* **151**, 616–632 (2016).
24. P. Moura-Alves *et al*., *Nature* **512**, 387–392 (2014).
25. C. Schiering *et al*., *Nature* **542**, 242–245 (2017).
26. B. Stockinger, P. Di Meglio, M. Gialitakis, J. H. Duarte, *Annu. Rev. Immunol.* **32**, 403–432 (2014).
27. M. Veldhoen *et al*., *Nature* **453**, 106–109 (2008).
28. L. Campisi *et al*., *Nat. Immunol.* **17**, 1084–1092 (2016).
29. J. E. Craft, *Nat. Rev. Rheumatol.* **8**, 337–347 (2012).
30. H. I. Fallatah, H. O. Akbar, *Autoimmune Dis.* **2012**, 312817 (2012).
31. I. Cirera *et al*., *J. Hepatol.* **34**, 32–37 (2001).

ACKNOWLEDGMENTS

We thank all patients enrolled under the IRB protocols 1408014402 and 1602017150 (ClinicalTrials.gov identifier NCT02394964) who have participated in this study, as well as K. DeFrancesco and I. Matos for patient recruitment at the Yale Center for Clinical Investigation, which is supported by CTSA grant UL1 RR024139 from the National Center for Research Resources, the National Center for Advancing Translational Science, and the NIH Roadmap for Medical Research. We also thank D. Assis, J. Boyer, and the Yale Liver Center for contributions of liver biopsy material; J. Galan for provision of *S. typhimurium*; J. Sterpka for technical assistance; O. Pagovich for initial antibiotics experiments; J. Weinstein for assistance with Tfh studies; N. Palm for use of an anaerobic chamber; M. Tokuyama and A. Iwasaki for contributing ERV anti-gp70 antibodies for ERV and ERV IC ELISAs; and E. Meffre, J. Craft, and G. Eberl for critically reading the manuscript. S.M.V. and M.A.K. are inventors on a patent application filed by Yale University related to the use of antibiotics and commensal vaccination to treat autoimmunity (U.S. Provisional Patent Application 62/448,510). Supported by NIH grants K08AI095318, R01AI118855, T32AI07019, and T32DK007017-39; Yale Rheumatic Diseases Research Core (NIH grant P30 AR053495); the Yale Liver Center (NIH grant P30 DK34989); Women's Health Research at Yale; the O'Brien Center at Yale (NIH grant P30DK079310); the Arthritis National Research Foundation; the Arthritis Foundation; and the Lupus Research Institute. Author contributions: S.M.V. designed, performed, and analyzed all murine, gnotobiotic, and human experiments; M.H., D.Z.R., N.K., F.R.C.C., E.T., T.G., and C.K. assisted in murine experiments including gnotobiotics; S.M.V., F.R.C.C., and D.Z.R. performed translocation and barrier function experiments; V.K., C.D., and T.G. were involved in consenting, recruiting, and sampling human study subjects; V.K., A.B., and D.J. obtained all liver biopsy samples; S.M.V. processed and analyzed data related to human material; S.M.V., V.K., C.D., A.B., and D.J. performed histopathologic studies and scoring; S.M.V. and C.D. performed FISH, immunofluorescence staining, and confocal microscopy; S.M.V., V.K., and W.R. performed 16*S* rDNA sequencing, data processing, and analysis; A.L.G. assisted in microbiologic studies and bioinformatics related to 16*S* rDNA sequencing; S.M.V. and S.S.M. processed and analyzed the RNA sequencing data; S.S.M. and J.R.K. assembled the bacterial genome; S.M.V. and S.S.M. analyzed the genome; S.M.V. produced the chemical structures drawing and biochemical pathway; S.M.V. and M.A.K. wrote the manuscript with input from all authors; M.A.K. conceived the study and supervised the project; and S.M.V. and M.A.K. participated in design and interpretation of all experiments. All data to understand and assess the conclusions of this research are available in the main text and supplementary materials, as well as via the following repositories: Whole-genome shotgun sequences have been deposited at DDBJ/ENA/GenBank under accession number PPHK00000000. The version described in this paper is version PPHK01000000. RNA-seq and 16*S* rRNA sequences have been deposited with the European Bioinformatics Institute under accession numbers PRJEB24586 and PRJEB24587, respectively.

SUPPLEMENTARY MATERIALS

www.sciencemag.org/content/359/6380/1156/suppl/DC1
Materials and Methods
Figs. S1 to S20
Tables S1 and S2
References (*32–50*)

11 December 2017; accepted 1 February 2018
10.1126/science.aar7201

COLITIS

C1orf106 is a colitis risk gene that regulates stability of epithelial adherens junctions

Vishnu Mohanan,[1,2] Toru Nakata,[1,2] A. Nicole Desch,[1,2] Chloé Lévesque,[3] Angela Boroughs,[2] Gaelen Guzman,[1] Zhifang Cao,[2] Elizabeth Creasey,[2] Junmei Yao,[2] Gabrielle Boucher,[3] Guy Charron,[3] Atul K. Bhan,[4,5] Monica Schenone,[1] Steven A. Carr,[1] Hans–Christian Reinecker,[5,6] Mark J. Daly,[1,5,7] John D. Rioux,[3,8] Kara G. Lassen,[1,2]* Ramnik J. Xavier[1,2,5,6,9]*

Polymorphisms in *C1orf106* are associated with increased risk of inflammatory bowel disease (IBD). However, the function of C1orf106 and the consequences of disease-associated polymorphisms are unknown. Here we demonstrate that C1orf106 regulates adherens junction stability by regulating the degradation of cytohesin-1, a guanine nucleotide exchange factor that controls activation of ARF6. By limiting cytohesin-1–dependent ARF6 activation, C1orf106 stabilizes adherens junctions. Consistent with this model, *C1orf106*$^{-/-}$ mice exhibit defects in the intestinal epithelial cell barrier, a phenotype observed in IBD patients that confers increased susceptibility to intestinal pathogens. Furthermore, the IBD risk variant increases C1orf106 ubiquitination and turnover with consequent functional impairments. These findings delineate a mechanism by which a genetic polymorphism fine-tunes intestinal epithelial barrier integrity and elucidate a fundamental mechanism of cellular junctional control.

Intestinal epithelial cells are required for gut homeostasis and are involved in numerous physiologic processes including nutrient absorption, protection against microbes, and intestinal restoration following insult (*1*). Abnormal intestinal permeability has been observed in patients with inflammatory bowel disease (IBD), a chronic inflammatory condition of the gastrointestinal tract (*2*). Healthy family members of some IBD patients have been reported to have changes to the intestinal barrier, suggesting that host genetics can underlie cell-intrinsic barrier defects, although the underlying mechanisms are as yet undefined (*3*). *C1orf106* was identified as an IBD susceptibility gene through genome-wide association studies, and follow-up exome sequencing revealed that a coding variant in *C1orf106* (*333F) increased risk of IBD (*4*–*6*). Here we elucidate the function of C1orf106 and find a role for it in epithelial homeostasis. We report a mechanism whereby the *C1orf106* IBD-associated risk variant decreases cellular junctional integrity, suggesting a means by which this variant increases susceptibility to IBD.

C1orf106 is highly expressed in the human intestine and intestinal epithelial cell lines but expressed at low levels in myeloid cells and mouse bone marrow–derived macrophages (fig. S1, A to C). In Caco-2 cells, a human colorectal cell line, C1orf106 protein expression increased as cells differentiated and formed a polarized epithelial monolayer, a characteristic feature of the intestinal epithelium (Fig. 1A). To decipher the function of C1orf106, we sought to identify C1orf106-interacting proteins by tandem mass spectrometry–based affinity proteomics, using epitope-tagged C1orf106 immunoprecipitated from human embryonic kidney (HEK) 293T cells. Cytohesin-1 and cytohesin-2 were two of the top interactors (Fig. 1B, fig. S1D, and table S1). Cytohesin-1 is one of the guanine exchange factors (GEFs) that control the activation of ARF6 guanosine triphosphatase (GTPase) (*7*). Depending on the GEF involved, ARF6 functions to control the recycling of proteins from the plasma membrane (*8*). Coimmunoprecipitation experiments confirmed the interaction between C1orf106 and cytohesin-1 and -2 by overexpression in HEK293T cells and with endogenous proteins in Caco-2 cells (Fig. 1, C and D, and fig. S1E). Domain-mapping experiments further indicated that the N-terminal domain of C1orf106 interacts specifically with the N-terminal domain of cytohesin-1 (Fig. 1, C and E).

To investigate the functional interaction between these proteins in a physiologically relevant model, we generated *C1orf106*$^{-/-}$ mice (fig. S2, A and B) and examined the steady-state levels of cytohesin-1 in this model system. We found that cytohesin-1 protein levels in colon and small intestine epithelial cells isolated from *C1orf106*$^{-/-}$ mice were consistently increased 1.5- to 2-fold compared with those in cells isolated from *C1orf106*$^{+/+}$ mice (Fig. 1F). Consistent with these findings, *C1orf106*$^{-/-}$ epithelial monolayers derived from colonic organoids also exhibited increased levels of cytohesin-1 protein in both membrane and cytosolic protein fractions (Fig. 1G), despite no difference in cytohesin-1 mRNA levels (fig. S3A). These data suggest that the increase in cytohesin-1 is posttranscriptionally regulated and is not due to differential localization of the protein in the membrane versus in the cytoplasmic compartments of the cells. Consistent with this hypothesis, increasing C1orf106 expression significantly decreased the levels of either overexpressed or endogenous cytohesin-1, indicating that C1orf106 expression is sufficient to regulate the steady-state levels of cytohesin-1 (Fig. 1H and fig. S3B). Similar results were observed with cytohesin-2 (fig. S3C). These data suggest that expression of C1orf106 limits the steady-state levels of cytohesins.

We next investigated whether cytohesin-1 levels were regulated by ubiquitination and proteasomal degradation. Treatment of cells with MG132, a proteasome inhibitor, increased the steady-state levels of cytohesin-1, suggesting that cytohesin-1 is degraded by the proteasome (fig. S4A). Overexpression of C1orf106 was sufficient to increase the levels of ubiquitinated cytohesin-1 (Fig. 2A). Analysis of colonic intestinal epithelial cells demonstrated that *C1orf106*$^{-/-}$ cells have reduced levels of ubiquitinated cytohesin-1 at steady state (Fig. 2B). These data suggest a model whereby C1orf106 expression limits cytohesin-1 levels through ubiquitin-mediated degradation.

C1orf106 has one putative domain of unknown function, DUF3338, which is predicted to be involved in protein-protein interactions but lacks enzymatic activity. Therefore, we hypothesized that C1orf106 acts as a cofactor for ubiquitin ligases to ubiquitinate cytohesins. To understand the mechanism of C1orf106-mediated control of cytohesin-1 protein levels, we identified C1orf106-binding proteins in our proteomics data that have the potential to mediate ubiquitination. Importantly, each subunit of the SKP1–CUL1–F-box (SCF) E3 ubiquitin ligase complex and two F-box substrate adaptors, BTRC1 and FBXW11, were identified as C1orf106 interactors (Fig. 1B, fig. S1D, and table S1). SCF ubiquitin ligase complexes play important roles in regulating the ubiquitination and subsequent degradation of specific substrate proteins (*9*, *10*). We performed coimmunoprecipitation experiments to determine which proteins from the SCF complex interact specifically with C1orf106 (Fig. 2, C and D, and fig. S4, B and C); we found that the substrate adapters BTRC1 and FBXW11 do so, suggesting that C1orf106 may serve as a substrate cofactor (Fig. 2, C and D).

To test the hypothesis that the SCF complex mediates the ubiquitination of cytohesin-1, we knocked down expression of *BTRC1* and *FBXW11* and evaluated cytohesin-1 expression levels. Cells treated with *FBXW11* small interfering RNA (siRNA) showed significantly increased levels of cytohesin-1 (Fig. 2E and fig. S5), suggesting

---

[1]The Broad Institute of MIT and Harvard, Cambridge, MA 02142, USA. [2]Center for Computational and Integrative Biology, Massachusetts General Hospital, Boston, MA 02114, USA. [3]Montreal Heart Institute Research Center, Montreal, Quebec H1T 1C8, Canada. [4]Pathology Department, Massachusetts General Hospital and Harvard Medical School, Boston, MA 02114, USA. [5]Center for the Study of Inflammatory Bowel Disease, Massachusetts General Hospital, Boston, MA 02114, USA. [6]Gastrointestinal Unit, Massachusetts General Hospital, Boston, MA 02114, USA. [7]Analytic and Translational Genetics Unit, Massachusetts General Hospital and Harvard Medical School, Boston, MA 02114, USA. [8]Department of Medicine, Université de Montréal, Montreal, Quebec H1T 1C8, Canada. [9]Center for Microbiome Informatics and Therapeutics, Massachusetts Institute of Technology, Cambridge, MA 02139, USA.
*Corresponding author. Email: klassen@broadinstitute.org (K.G.L.); xavier@molbio.mgh.harvard.edu (R.J.X.)

that the SCF complex containing FBXW11, but not BTRC1, regulates the stability of cytohesin-1. We next tested the effect of MLN4924, a small-molecule inhibitor of a NEDD8-activating enzyme that is required for neddylation and activation of cullin-RING ubiquitin E3 ligases, including the SCF complex. Treatment of human colon HT-29 cells with MLN4924 resulted in a dose-dependent increase in endogenous levels of cytohesin-1 (Fig. 2F) (*11*). Taken together, these results indicate that cytohesin-1 levels are dynamically regulated by ubiquitination by the SCF ubiquitin ligase complex and subsequent proteasomal degradation.

We next sought to understand how C1orf106-mediated degradation of cytohesin-1 alters epithelial cell function. Cytohesin-1 acts as a GEF to regulate the activity of ARF6, a GTPase that controls the rate of membrane receptor recycling and mediates signaling pathways that control actin remodeling (*12*). We therefore hypothesized that increased levels of cytohesin-1 protein in *C1orf106*$^{-/-}$ cells would increase levels of ARF6 activation. To test this hypothesis, we evaluated the levels of activated ARF6 (ARF6-GTP) in organoid-derived intestinal epithelial monolayers, finding that ARF6-GTP levels were 1.5 times as high in *C1orf106*$^{-/-}$ cells as in *C1orf106*$^{+/+}$ cells, despite comparable total levels of ARF6 (Fig. 3A). Given that activated ARF6-GTP localizes to the plasma membrane (*8*), we next analyzed ARF6 localization in these cells. Immunostaining confirmed increased levels of ARF6 at the plasma membrane in *C1orf106*$^{-/-}$ epithelial monolayers (Fig. 3B). Analysis of insoluble membrane fractions from *C1orf106*$^{+/+}$ and *C1orf106*$^{-/-}$ epithelial monolayers demonstrated increased levels of ARF6 in the membrane fraction in *C1orf106*$^{-/-}$ cells, further supporting the finding of increased levels of membrane-associated ARF6-GTP in these cells (fig. S6A).

ARF6 plays a key role in regulating surface levels of critical adherens junction proteins, and ARF6 activation in epithelial cells is known to increase internalization of E-cadherin (*8*, *13*). We therefore hypothesized that increased cytohesin-1 and

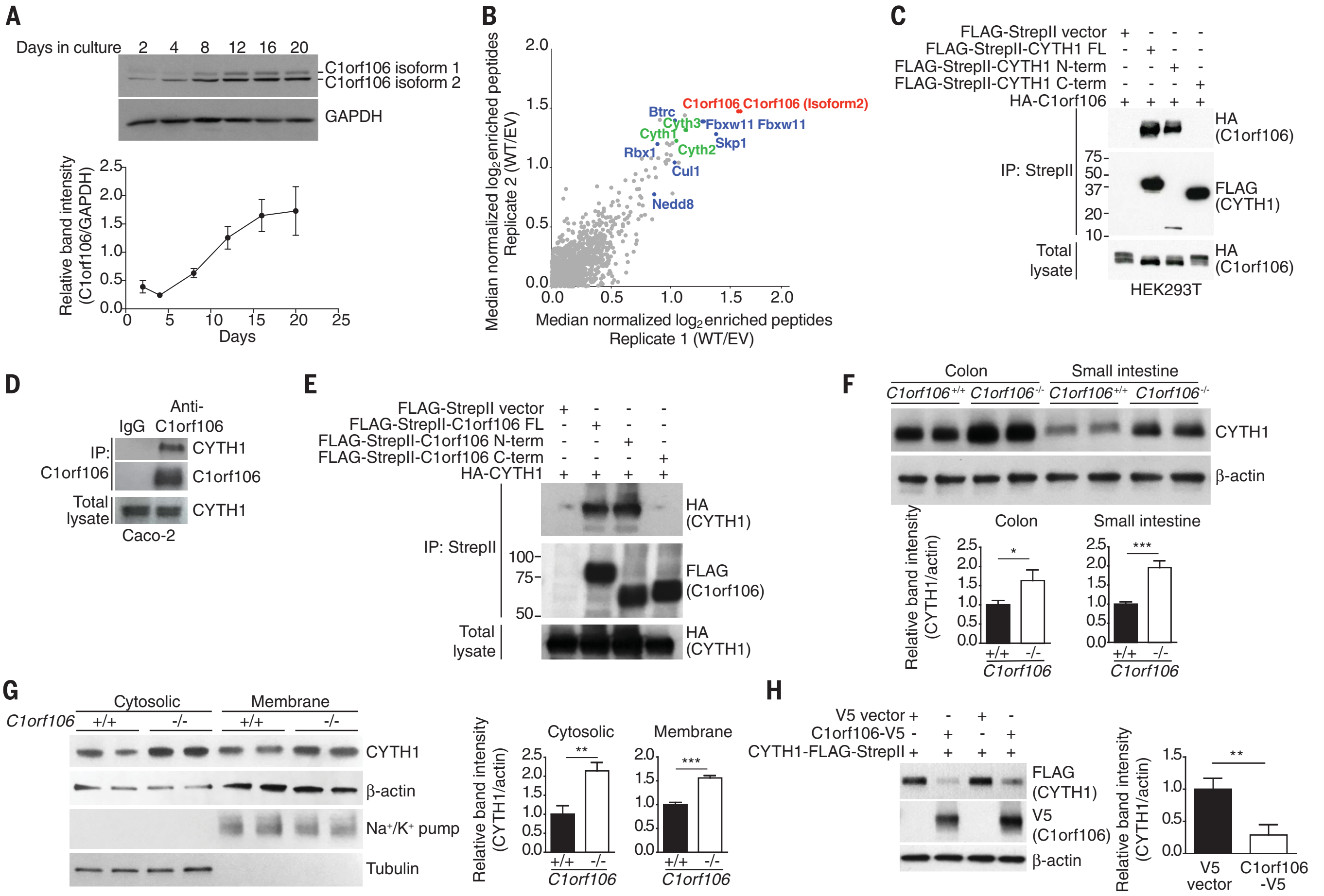

Fig. 1. C1orf106 modulates cytohesin-1 (CYTH1) levels. (**A**) C1orf106 protein levels were assessed during Caco-2 cell differentiation by immunoblot. Relative band intensity of C1orf106 isoform 1 at each time point was quantified and normalized to GAPDH (glyceraldehyde-3-phosphate dehydrogenase). Each value represents the mean of two independent experiments ± SEM. (**B**) $\log_2$ ratios of proteins enriched by FLAG antibody in HEK293T cells expressing FLAG-tagged C1orf106 (wild type, WT) to those enriched in cells transfected with an empty vector (EV); two replicates (one on each axis of the scatter plot) are shown. Each dot represents the $\log_2$ ratio for a protein. Red dots, bait; blue dots, members of the SCF complex; green dots, cytohesins. (**C**) HEK293T cells were transiently transfected with HA (hemagglutinin)–C1orf106 and either empty vector, full-length (FL) FLAG-StrepII-CYTH1, or the N- or C-terminal domains of CYTH1 (Strep, streptavidin). Samples were immunoprecipitated (IP) with anti-StrepII and probed for FLAG (CYTH1) and HA (C1orf106). (**D**) Caco-2 cell lysates were immunoprecipitated with anti-IgG or anti-C1orf106 and probed for CYTH1 and C1orf106. (**E**) HEK293T cells were transiently transfected with HA-CYTH1 and either empty vector, full-length FLAG-StrepII-C1orf106, or the N- or C-terminal domains of C1orf106. Samples were immunoprecipitated with anti-StrepII and probed for FLAG (C1orf106) and HA (CYTH1). (**F**) Immunoblot analysis of intestinal epithelial cells isolated from the colon or small intestine of *C1orf106*$^{+/+}$ and *C1orf106*$^{-/-}$ mice. Shown are samples from individual mice. (**G**) Immunoblot analysis of monolayers grown from colonic organoids from *C1orf106*$^{+/+}$ and *C1orf106*$^{-/-}$ mice. (**H**) Immunoblot analysis of HEK293T cells cotransfected with CYTH1-FLAG-StrepII and empty vector or C1orf106-V5. Two biologic replicates are shown. In (F) to (H), graphs show normalized CYTH1:actin ratios from three independent experiments, as quantified by densitometry. Error bars, SD. $^*P < 0.05$; $^{**}P < 0.01$; $^{***}P < 0.001$ (two-tailed Student's *t* test).

ARF6-GTP levels in *C1orf106*$^{-/-}$ intestinal epithelial cells would result in decreased surface levels of E-cadherin. As predicted, immunostaining for E-cadherin in *C1orf106*$^{-/-}$ intestinal epithelial monolayers revealed more than a threefold increase in the proportion of cells containing intracellular E-cadherin puncta compared with the proportion among *C1orf106*$^{+/+}$ cells (Fig. 3C). An increase in intracellular E-cadherin puncta was also observed in colonic tissue sections from *C1orf106*$^{-/-}$ mice (Fig. 3D). We detected no differences in the localization of epithelial tight junction proteins occludin, ZO-1, claudin1, or claudin2 and no differences in mRNA or protein levels (Fig. 3, B to D, and fig. S6, B to E). These data confirm that the effect was specific for E-cadherin. The staining pattern of E-cadherin in *C1orf106*$^{-/-}$ colonic organoids was disorganized along the junctions and revealed increased puncta formation in the cytosol (fig. S6F). Moreover, disorganized E-cadherin was also observed after knockdown of *C1orf106* in differentiated human Caco-2 cells (fig. S6G). Additionally, internalized E-cadherin colocalized with intracellular ARF6 puncta, consistent with a role for ARF6 in E-cadherin internalization (fig. S7A). ARF6 is known to regulate actin dynamics. We observed prominent vesicular staining for actin along the inner cell membrane in *C1orf106*$^{-/-}$ cells, which further supports a role for altered ARF6 dynamics in these cells (fig. S7B). To confirm decreased localization of E-cadherin along the cell surface, we performed biotinylation of extracellular membrane-bound proteins followed by immunoblot analysis of biotinylated E-cadherin in freshly isolated colonic intestinal epithelial cells and organoid-derived monolayers from *C1orf106*$^{+/+}$ and *C1orf106*$^{-/-}$ mice. Despite similar total expression of E-cadherin, we found more than a twofold decrease in surface E-cadherin in *C1orf106*$^{-/-}$ cells compared with *C1orf106*$^{+/+}$ cells (Fig. 3, E and F). These data suggest a critical role for C1orf106 in maintaining adherens junctions by limiting ARF6 activation through regulated cytohesin degradation.

Epithelial junction integrity is important in intestinal homeostasis, as well as tissue repair after damage (*14*). We next monitored epithelial barrier integrity by testing the ability of fluorescently labeled molecules to pass through the intestinal barrier. *C1orf106*$^{-/-}$ and *C1orf106*$^{+/+}$ mice exhibited similar permeability to FITC (fluorescein isothiocyanate)–dextran (4 KDa) (Fig. 3G). However, *C1orf106*$^{-/-}$ colon tissue showed significantly increased permeability to a smaller compound, Lucifer yellow (0.4 KDa) (Fig. 3H). Together, these data suggest that loss of C1orf106 confers increased permeability to smaller solutes (*15*). To further confirm this finding, we measured transepithelial electrical resistance (TEER) to assess barrier function in *C1orf106*$^{+/+}$ and *C1orf106*$^{-/-}$ monolayers derived from organoids and Caco-2 cells with stable knockdown of *C1orf106*. Maximal TEER was significantly reduced in *C1orf106*-deficient cells compared with control cells, indicating impaired epithelial barrier integrity (fig. S8, A and B).

To test whether changes in E-cadherin recycling altered the ability of *C1orf106*$^{-/-}$ cells to repair epithelial junctions after injury, we subjected organoid-derived monolayers to a calcium switch assay by treating cells with EGTA to disrupt extracellular E-cadherin interactions, followed by treatment with normal media; in this assay, we monitored E-cadherin staining to evaluate the reformation of junctions after 2 hours of recovery time (*16*). Whereas both *C1orf106*$^{+/+}$ and *C1orf106*$^{-/-}$ monolayers were similarly disrupted by EGTA treatment, *C1orf106*$^{-/-}$ monolayers displayed a lack of reorganization compared with *C1orf106*$^{+/+}$ monolayers after 2 hours of recovery (fig. S8C). TEER was also measured after calcium switch during the recovery phase. *C1orf106*$^{-/-}$ monolayers displayed decreased TEER compared with *C1orf106*$^{+/+}$ monolayers at baseline and during the recovery phase (fig. S8D). Selective knockdown of cytohesin-1 was sufficient to rescue

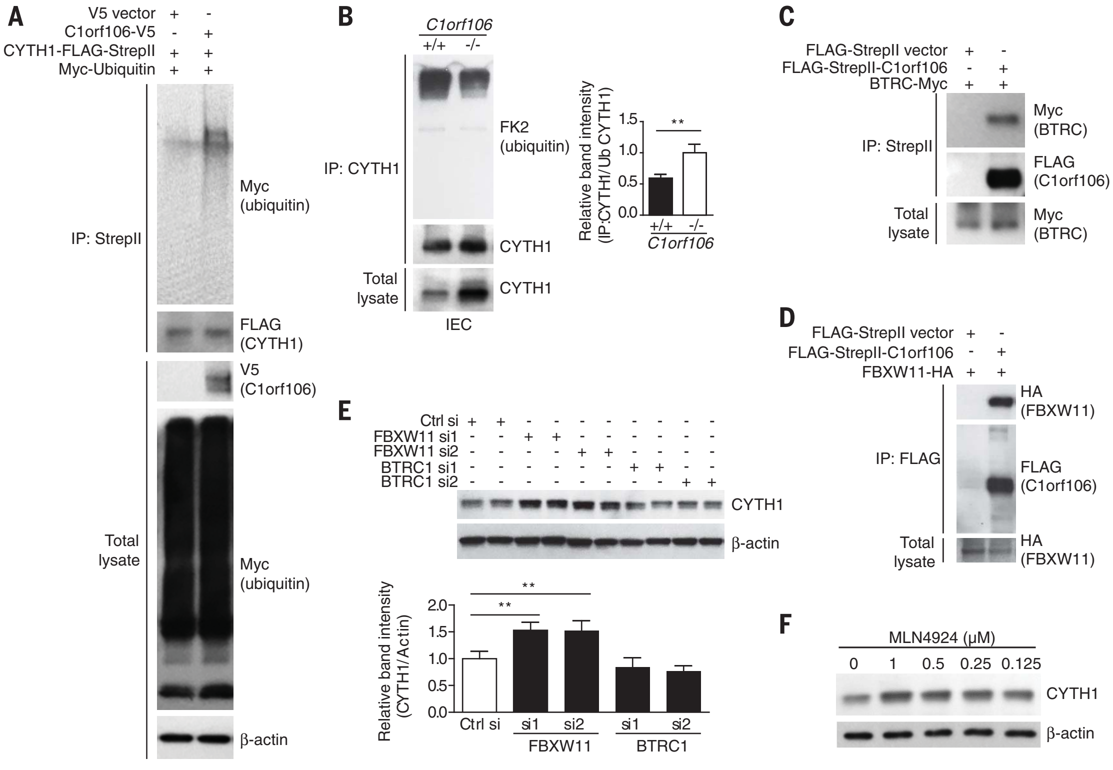

Fig. 2. C1orf106 regulates the ubiquitination of CYTH1 through the SCF ubiquitin ligase complex. (**A**) HEK293T cells were transfected with ubiquitin-Myc and CYTH1-FLAG-StrepII with or without C1orf106-V5. Samples were immunoprecipitated with anti-StrepII and probed for FLAG (CYTH1), V5 (C1orf106), and Myc (ubiquitin). (**B**) Endogenous CYTH1 was immunoprecipitated from *C1orf106*$^{+/+}$ and *C1orf106*$^{-/-}$ intestinal epithelial cell (IEC) monolayers and probed for CYTH1 and ubiquitin (FK2). The graph shows immunoprecipitated CYTH1:ubiquitinated CYTH1 ratios from three independent experiments, as quantified by densitometry. Error bars, SEM. $^{**}P < 0.01$ (two-tailed Student's *t* test). (**C**) HEK293T cells were transiently transfected with BTRC-Myc and either empty vector or full-length FLAG-StrepII-C1orf106. Samples were immunoprecipitated with anti-StrepII and probed for FLAG (C1orf106) and Myc (BTRC). (**D**) HEK293T cells were transfected with FLAG-StrepII-C1orf106 and FBXW11-HA and immunoprecipitated as in (C). (**E**) Immunoblot analysis of HEK293T cells transfected with siRNAs against BTRC or FBXW11 and probed for CYTH1. Samples from two biologic replicates are shown. The graph shows normalized CYTH1:actin ratios from three independent experiments, as quantified by densitometry. Error bars, SEM. $^{**}P < 0.01$ (two-tailed Student's *t* test). (**F**) Immunoblot analysis of HT-29 cells treated with DMSO (dimethyl sulfoxide) or MLN4924 and probed for CYTH1. Actin served as a loading control. Data are representative of three independent experiments.

baseline TEER in *C1orf106*$^{-/-}$ monolayers, demonstrating that cytohesin-1 is a key mediator of the observed barrier phenotype in *C1orf106*$^{-/-}$ cells (Fig. 3I and fig. S9, A and B).

In organoid-derived epithelial monolayers, *C1orf106*$^{-/-}$ cells had a significantly increased migratory rate at baseline and during hepatocyte growth factor–induced cell migration compared with *C1orf106*$^{+/+}$ cells (fig. S10). These findings suggest that loss of C1orf106 decreases junctional integrity, resulting in increased cellular migration at steady state, and that growth factor stimulation cannot compensate for this defect.

Increased susceptibility to microbial pathogens and dysbiosis is commonly associated with IBD (*17*). To determine whether *C1orf106*$^{-/-}$ mice have compromised epithelial barrier integrity resulting in increased bacterial dissemination, we challenged *C1orf106*$^{+/+}$ and *C1orf106*$^{-/-}$ mice with the extracellular intestinal murine pathogen *Citrobacter rodentium*, which induces colonic lesions, similarly to the clinical enteropathogenic *Escherichia coli* strains associated with Crohn's disease (*18*). Additionally, epithelial defenses are critical in limiting *C. rodentium* early after infection. *C1orf106*$^{-/-}$ mice exhibited significantly increased bacterial loads of *C. rodentium* at day 5 (Fig. 4A). Notably, translocation of *C. rodentium* to the mesenteric lymph nodes and spleen was also significantly increased in *C1orf106*$^{-/-}$ mice at day 5 (Fig. 4A). Although *C1orf106*$^{-/-}$ mice were able to control *C. rodentium* infection by day 12 postinfection, they exhibited significantly shortened colon length compared with *C1orf106*$^{+/+}$ mice and more severe histopathology, including crypt damage (Fig. 4, B to D, and fig. S11A). Cytokine response was not impaired in *C1orf106*$^{-/-}$ mice 12 days postinfection (fig. S11, B and C). Additionally, levels of immune cell types such as T and B lymphocytes, macrophages, dendritic cells, and innate lymphoid cells were unchanged at baseline (fig. S12A). Levels of interleukin-22, lipocalin-2, fecal immunoglobulin A (IgA), fecal albumin, and antimicrobial peptides were also unaltered at baseline, suggesting that these do

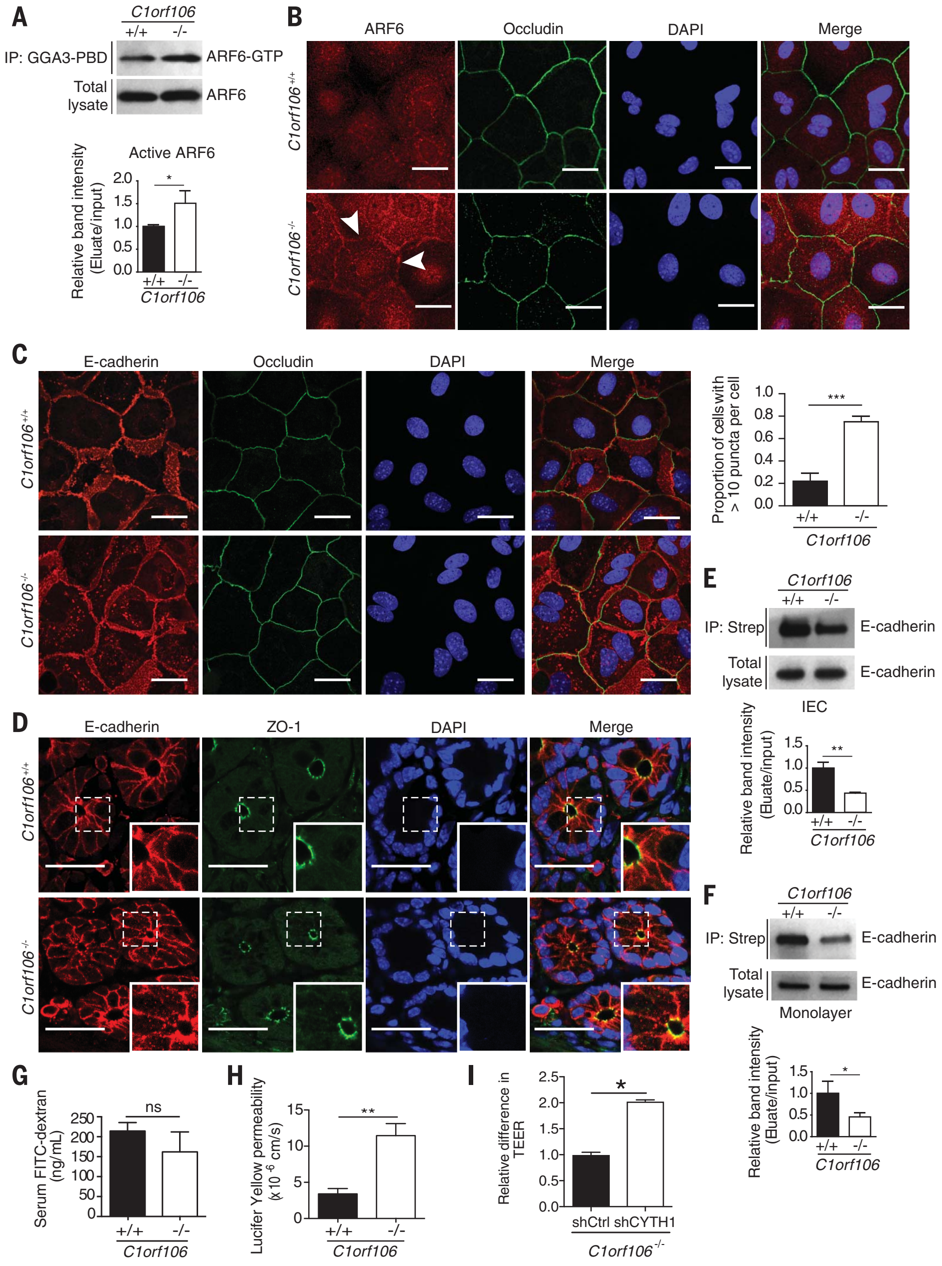

Fig. 3. C1orf106 controls surface E-cadherin levels through ARF6 activation. (**A**) IEC monolayers from *C1orf106*$^{+/+}$ and *C1orf106*$^{-/-}$ mice were immunoprecipitated with GGA3-PBD beads and probed with ARF6 antibody. Immunoblot is representative of three independent experiments. The graph shows total ARF6:ARF6-GTP ratios from three independent experiments, as quantified by densitometry. Error bars, SD. (**B**) Confocal images of colonic organoid–derived monolayers stained for ARF6, occludin, and nuclei (4′,6-diamidino-2-phenylindole, DAPI). Data are representative of three independent experiments. Arrowheads indicate ARF6 at the plasma membrane. Scale bars, 10 μm. (**C**) Confocal images of colonic organoid–derived monolayers stained for E-cadherin, occludin, and nuclei (DAPI). Scale bars, 30 μm. The graph shows quantification from three independent experiments of the percentage of cells that contained >10 intracellular E-cadherin puncta. Error bars, SEM. (**D**) Confocal immunofluorescence images of sections from *C1orf106*$^{+/+}$ and *C1orf106*$^{-/-}$ mouse colon stained for E-cadherin, ZO-1, and nuclei (DAPI). Scale bars, 30 μm. (**E** and **F**) Freshly isolated IECs (E) and organoid-derived monolayers (F) from *C1orf106*$^{+/+}$ and *C1orf106*$^{-/-}$ mice were biotinylated to label surface proteins and immunoprecipitated with streptavidin beads. Total lysate and immunoprecipitated lysate were probed for E-cadherin. Graphs show quantification from three independent experiments. Error bars, SD. (**G**) FITC-dextran levels in serum 3 hours postgavage in *C1orf106*$^{+/+}$ and *C1orf106*$^{-/-}$ mice. Error bars, SEM ($n = 3$ mice). Data are representative of three independent experiments. (**H**) Lucifer yellow permeability measurement from colon and small intestine epithelial tissues of *C1orf106*$^{+/+}$ and *C1orf106*$^{-/-}$ mice. Error bars, SEM from three independent experiments. (**I**) Relative difference in transepithelial electrical resistance (TEER) of colonic *C1orf106*$^{-/-}$ monolayers transduced with control vector (shCtrl) or shRNA against CYTH1 (shCYTH1) (sh, short hairpin). Data are representative of three independent experiments. Error bars, SEM. $^{*}P < 0.05$; $^{**}P < 0.01$; $^{***}P < 0.001$; ns, not significant [two-tailed Student's *t* test for (A), (C), and (E) to (I)].

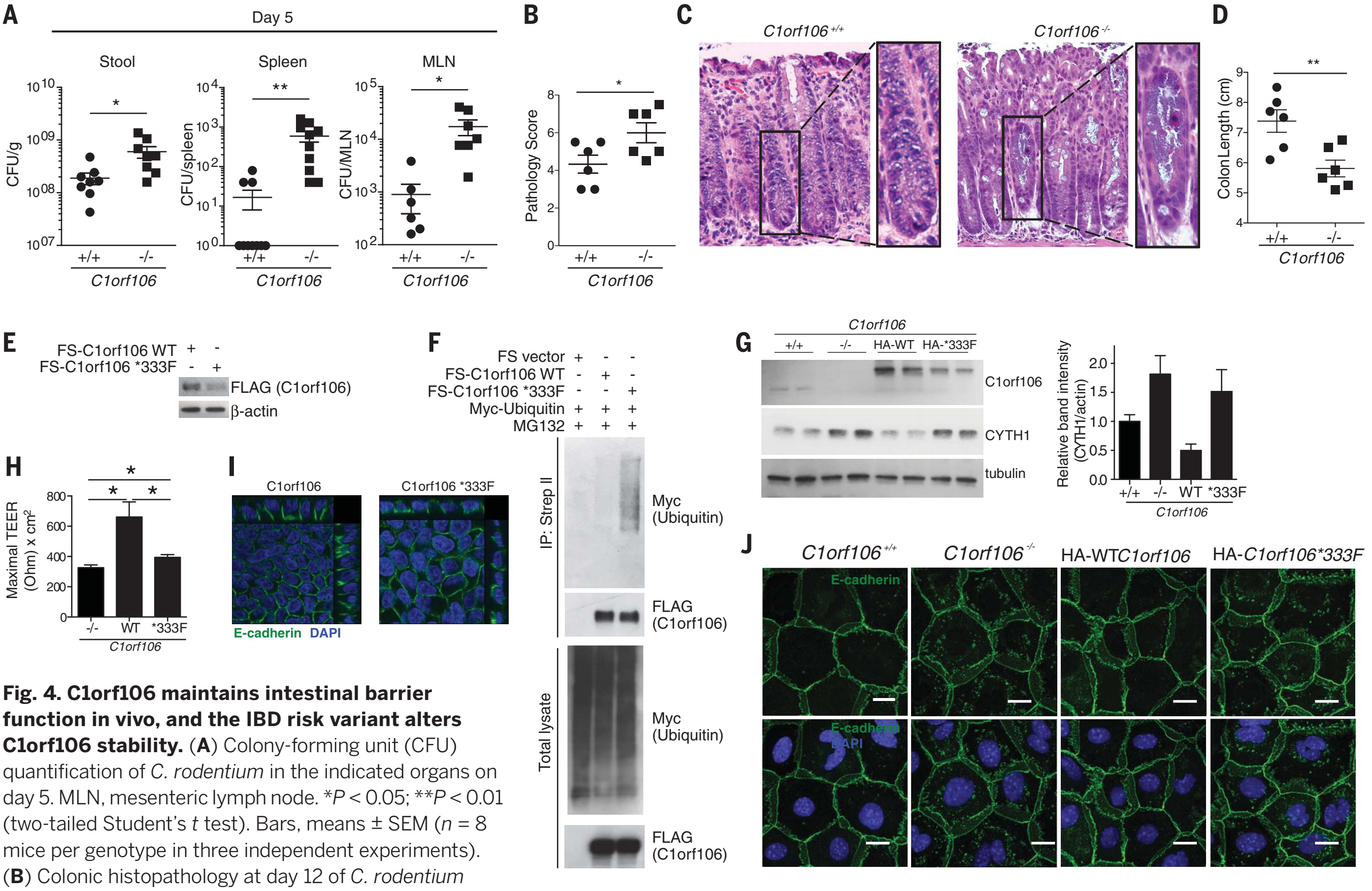

Fig. 4. C1orf106 maintains intestinal barrier function in vivo, and the IBD risk variant alters C1orf106 stability. (**A**) Colony-forming unit (CFU) quantification of *C. rodentium* in the indicated organs on day 5. MLN, mesenteric lymph node. $*P < 0.05$; $**P < 0.01$ (two-tailed Student's *t* test). Bars, means ± SEM ($n = 8$ mice per genotype in three independent experiments). (**B**) Colonic histopathology at day 12 of *C. rodentium* infection. $*P < 0.05$. Bars, means ± SEM ($n = 6$ mice per genotype in two independent experiments). (**C**) Representative hematoxylin and eosin–stained sections of colon from *C1orf106*$^{+/+}$ and *C1orf106*$^{-/-}$ mice infected for 5 days with *C. rodentium*. (**D**) Colon length from *C1orf106*$^{+/+}$ and *C1orf106*$^{-/-}$ mice at day 12 of *C. rodentium* infection. $**P < 0.01$ (Student's *t* test). Bars, means ± SEM ($n = 6$ mice per genotype in two independent experiments). (**E**) Immunoblot analysis of HEK293T cells transfected with FLAG–StrepII–C1orf106 WT or FLAG–StrepII–C1orf106 *333F (FS, FLAG-StrepII). (**F**) HEK293T cells were transfected with Myc-ubiquitin and either empty vector, FLAG–StrepII–C1orf106 WT, or FLAG–StrepII–C1orf106 *333F. Lysates from cells treated with 10 μM MG132 were immunoprecipitated with StrepII and probed for FLAG (C1orf106) and Myc (ubiquitin). (**G**) Immuboblot analysis of colonic *C1orf106*$^{+/+}$, *C1orf106*$^{-/-}$, HA–C1orf106 WT, and HA–C1orf106 *333F organoid-derived monolayers probed for C1orf106 or CYTH1. β-actin and tubulin served as loading controls. Error bars, SD. Data representative of three independent experiments. (**H**) Maximal TEER of monolayers from *C1orf106*$^{-/-}$, HA–C1orf106 WT, and HA–C1orf106 *333F organoids. $*P < 0.05$ (Student's *t* test). Error bars, SEM. Data are representative of at least three independent experiments. (**I**) Confocal immunofluorescence images (*XZ* and *YZ* planes) of LS174T cells stably overexpressing the indicated C1orf106 allele. Cells were stained for E-cadherin and nuclei (DAPI). (**J**) Confocal images of colonic organoid–derived monolayers from *C1orf106*$^{+/+}$, *C1orf106*$^{-/-}$, HA–C1orf106 WT, and HA–C1orf106 *333F, stained for E-cadherin and nuclei (DAPI). Scale bars, 10 μm.

not contribute to the early impairment in bacterial defense (fig. S12, B to F). *C1orf106*$^{-/-}$ mice also exhibited impaired recovery from dextran sodium sulfate–induced colitis, as evidenced by greater body weight loss, reduced colon length, and more severe histopathology, consistent with an impaired ability to recover from intestinal insults (fig. S13, A to D).

Deep exon sequencing has identified a coding variant in *C1orf106*, *333F, which is associated with increased risk of IBD. Expression of C1orf106 *333F was reproducibly decreased during transient transfection compared with that of wild-type C1orf106 (C1orf106 WT), despite comparable levels of mRNA, suggesting that the risk variant is poorly expressed or unstable (Fig. 4E and fig. S14A). To test whether the decreased levels of C1orf106 *333F protein were due to ubiquitination and degradation by the proteasome, we treated cells with MG132; treatment with this proteasome inhibitor restored C1orf106 *333F protein to WT levels (Fig. 4F). We also observed increased ubiquitination of C1orf106 *333F compared with WT, suggesting that the IBD risk polymorphism increases protein turnover of C1orf106, resulting in decreased expression of functional protein (Fig. 4F). Consistent with these results, we found that C1orf106 *333F had a half-life of 10.2 hours, compared with the C1orf106 WT half-life of almost 17 hours, using a cyclohexamide assay in LS174T cells (fig. S14B). To study the phenotypic effects of the decreased half-life of C1orf106 *333F, *C1orf106*$^{-/-}$ organoids were transduced with either C1orf106 WT or C1orf106 *333F. Expression of C1orf106 *333F was not sufficient to restore WT levels of C1orf106, mediate degradation of cytohesin-1, or increase the TEER in *C1orf106*$^{-/-}$ monolayers (Fig. 4, G and H). Expression of C1orf106 *333F disrupted E-cadherin and actin organization and staining in monolayer-derived intestinal epithelial cells and human intestinal cells (Fig. 4, I and J, and fig. S15). Taken together, these data suggest a mechanism by which the *333F polymorphism decreases C1orf106 protein stability and thus confers increased susceptibility to IBD by compromising gut epithelial integrity through impaired turnover and degradation of cytohesin-1.

Our findings define a critical function for C1orf106 in IBD by regulating the integrity of intestinal epithelial cells. We have shown that C1orf106 functions as a molecular rheostat to limit cytohesin levels through SCF complex–dependent degradation and thereby modulates barrier integrity. The finding that C1orf106 regulates the surface levels of E-cadherin is notable given that polymorphisms in both *C1orf106* and *CDH1* (E-cadherin) are associated with increased risk of ulcerative colitis, a form of IBD (*19*). Increasing the stability of C1orf106 may be a potential therapeutic strategy to increase the integrity of the epithelial barrier for the treatment of IBD.

REFERENCES AND NOTES

1. B. Khor, A. Gardet, R. J. Xavier, *Nature* **474**, 307–317 (2011).
2. J. Mankertz, J. D. Schulzke, *Curr. Opin. Gastroenterol.* **23**, 379–383 (2007).
3. D. Hollander *et al*., *Ann. Intern. Med.* **105**, 883–885 (1986).
4. C. A. Anderson *et al*., *Nat. Genet.* **43**, 246–252 (2011).
5. M. A. Rivas *et al*., *Nat. Genet.* **43**, 1066–1073 (2011).
6. Y. Liu *et al*., *PLOS Genet.* **7**, e1001338 (2011).
7. J. E. Casanova, *Traffic* **8**, 1476–1485 (2007).
8. J. G. Donaldson, C. L. Jackson, *Nat. Rev. Mol. Cell Biol.* **12**, 362–375 (2011).
9. D. Frescas, M. Pagano, *Nat. Rev. Cancer* **8**, 438–449 (2008).
10. J. R. Skaar, J. K. Pagan, M. Pagano, *Nat. Rev. Mol. Cell Biol.* **14**, 369–381 (2013).
11. T. A. Soucy *et al*., *Nature* **458**, 732–736 (2009).
12. W. Kolanus, *Immunol. Rev.* **218**, 102–113 (2007).
13. F. Palacios, L. Price, J. Schweitzer, J. G. Collard, C. D'Souza-Schorey, *EMBO J.* **20**, 4973–4986 (2001).
14. T. J. Harris, U. Tepass, *Nat. Rev. Mol. Cell Biol.* **11**, 502–514 (2010).
15. L. Shen, C. R. Weber, D. R. Raleigh, D. Yu, J. R. Turner, *Annu. Rev. Physiol.* **73**, 283–309 (2011).
16. G. Swaminathan, C. A. Cartwright, *Oncogene* **31**, 376–389 (2012).
17. D. Knights, K. G. Lassen, R. J. Xavier, *Gut* **62**, 1505–1510 (2013).
18. S. Nell, S. Suerbaum, C. Josenhans, *Nat. Rev. Microbiol.* **8**, 564–577 (2010).
19. UK IBD Genetics Consortium, Wellcome Trust Case Control Consortium 2, *Nat. Genet.* **41**, 1330–1334 (2009).

ACKNOWLEDGMENTS

We thank the members of the Xavier laboratory for helpful discussions, N. Nedelsky and T. Reimels for editorial and graphics assistance, and J. Rush for comments. We thank the Center for Celiac Research and Treatment for their assistance with the intestinal permeability experiment. **Funding:** This work was supported by funding from the Crohn's & Colitis Foundation, funded by a generous anonymous donor; the Helmsley Charitable Trust; and National Institutes of Health (NIH) grants DK043351, AI109725, and DK062432 to R.J.X. H.–C.R. was supported by NIH grants AI113333, DK068181, DK091247, and DK043351. J.D.R. holds a Canada Research Chair, and this work was supported by NIH grant DK064869 to J.D.R. This project also benefited from infrastructure supported by the Canada Foundation for Innovation (grants 202695, 218944, and 20415; J.D.R.). **Author contributions:** V.M., G.G., A.B., A.N.D., C.L., G.B., G.C., T.N., E.C., J.Y., and Z.C. performed experiments. V.M., M.S., G.G., A.B., A.N.D., C.L., G.B., G.C., T.N., and A.K.B. analyzed data. V.M., M.S., M.D., A.N.D., C.L., G.B., G.C., H–C.R., T.N., J.D.R., K.G.L., and R.J.X. designed the research. V.M., M.S., S.A.C., M.J.D., H–C.R., J.D.R., K.G.L., and R.J.X. provided intellectual contributions throughout the project. V.M., R.J.X., and K.G.L. wrote the paper. **Competing interests**: The authors declare no competing financial interests. **Data and materials availability:** Data in this paper are tabulated in the main text and supplementary materials. The original mass spectra can be downloaded from MassIVE (Mass Spectrometry Interactive Virtual Environment; http://massive.ucsd.edu) using the identifier MSV000081941. The data are directly accessible at ftp://massive.ucsd.edu/MSV000081941.

SUPPLEMENTARY MATERIALS

www.sciencemag.org/content/359/6380/1161/suppl/DC1
Materials and Methods
Figs. S1 to S15
Table S1
References (*20–28*)

1 March 2017; resubmitted 1 October 2017
Accepted 21 January 2018
Published online 1 February 2018
10.1126/science.aan0814

MOLECULAR BIOLOGY

Nascent DNA methylome mapping reveals inheritance of hemimethylation at CTCF/cohesin sites

Chenhuan Xu and Victor G. Corces*

The faithful inheritance of the epigenome is critical for cells to maintain gene expression programs and cellular identity across cell divisions. We mapped strand-specific DNA methylation after replication forks and show maintenance of the vast majority of the DNA methylome within 20 minutes of replication and inheritance of some hemimethylated CpG dinucleotides (hemiCpGs). Mapping the nascent DNA methylome targeted by each of the three DNA methyltransferases (DNMTs) reveals interactions between DNMTs and substrate daughter cytosines en route to maintenance methylation or hemimethylation. Finally, we show the inheritance of hemiCpGs at short regions flanking CCCTC-binding factor (CTCF)/cohesin binding sites in pluripotent cells. Elimination of hemimethylation causes reduced frequency of chromatin interactions emanating from these sites, suggesting a role for hemimethylation as a stable epigenetic mark regulating CTCF-mediated chromatin interactions.

Cytosine DNA methylation in mammals is maintained mainly by the canonical DNA maintenance methyltransferase DNMT1 during each cell cycle (*1*, *2*). By interacting with proliferating cell nuclear antigen (PCNA) and ubiquitin-like–containing PHD and RING finger domains 1 (UHRF1) during DNA replication, DNMT1 is recruited to replication foci and loaded onto hemiCpGs to methylate the nascent cytosines (Cs) (*3*–*5*). Although the onset of this process is closely coupled with the entry into S phase, the kinetics of maintenance methylation and the content of the nascent DNA methylome have never been studied quantitatively on a genome-wide scale (*6*). Furthermore, although various biochemical (*7*, *8*) and genetic perturbation experiments (*6*, *9*–*12*) have strongly suggested the involvement of the de novo methyltransferase DNMT3A/3B in maintenance methylation, direct evidence of in vivo interaction between DNMTs and hemiCpGs is missing.

To gain insights into these key aspects of maintenance methylation, we used nascent DNA bisulfite sequencing (nasBS-seq) to measure cytosine methylation frequency strand-specifically on nascent chromatin across the genome (fig. S1, A and B, and supplementary materials). We first labeled H9 human embryonic stem cells (H9-hESCs) with the nucleotide analog ethynyl-deoxyuridine (EdU) for 20 min as a pulse condition. Libraries for a chase condition were also made by labeling the cells with EdU for 20 min and growing them for another 8 hours in the absence of EdU to monitor the maintenance methylation at a later time point within the cell cycle. We obtained 357 to 544 million uniquely mapped and deduplicated alignments from libraries for each strand, covering 5.6 to 9.8 billion Cs (fig. S2, A and B), converging to 24 million parent-daughter CpG dyads (pdCpGs) from either pulse or chase (fig. S2C). The methylation frequency was highly reproducible between replicates for each library (fig. S2D). Methylation frequency between parental Cs (pC) and daughter Cs (dC) in the same pdCpGs (Fig. 1A and fig. S3A), and between the same Cs in pulse and chase (fig. S3B), were highly correlated. Although Cs in the context of CH are not symmetrically methylated in mammals (*13*), their methylation was also maintained on the dCs in the other nascent DNA duplex (fig. S3C). The methylation frequency of dCs was globally maintained in both pulse and chase irrespective of the nature of the genomic features investigated (fig. S3D). These results suggest that the vast majority of the DNA methylome is maintained within 20 min after passage of replication forks and thereafter.

Despite the high correlation of methylation frequency between pC and dC, the two Cs in many CpGs showed differential methylation frequency (Fig. 1B and fig. S4A), suggesting the existence of hemiCpGs with a spectrum of frequencies (fig. S4B). The strand-specific nascent DNA methylome enables the resolution of different types of hemiCpGs with respect to the parent-daughter axis. Using a highly stringent cutoff for differences in 5-methylcytosine (mC) [$\Delta mC \leq -75\%$, or $\geq 75\%$, $\Delta mC = m(pC - dC)$], we obtained a list of 23,305 CpGs with at least one dyad showing hemimethylation either in pulse or chase (Fig. 1C). The vast majority (96%) of them were hemimethylated in only one dyad and failed to reproduce the methylation pattern in the other condition (fig. S4, C to F), suggesting that they may represent the rapid DNA methylation turnover events abundant in pluripotent cells (*14*). In contrast, the methylation pattern of the remaining 4% CpGs hemimethylated in both dyads in a concordant way (Cs on either two Watson or two Crick strands are methylated) was highly consistent between pulse and chase (Fig. 1D), suggesting that concordant hemiCpGs were stably inherited through S phase. By concatenating the data from pulse and chase (see supplementary materials), we expanded the category of concordant hemiCpGs to include 2467

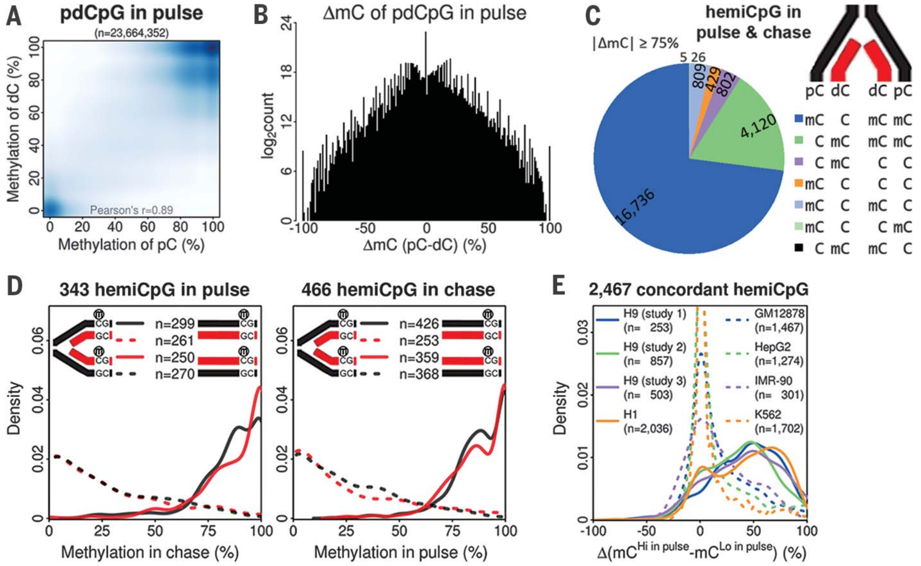

Fig. 1. The vast majority of the DNA methylome is maintained 20 min after replication. (**A**) Correlation of methylation frequency between pCs and dCs within the same pdCpGs in pulse. (**B**) Count of pdCpGs in pulse with differential ΔmC values. (**C**) Different types of hemiCpGs with all four Cs mapped at least four times. (**D**) For concordant hemiCpGs in pulse, the distribution of methylation frequency of four Cs in chase is shown (left), and vice versa (right). (**E**) All concordant hemiCpGs were intersected with WGBS data sets from other human cells. The distribution of ΔmC values is shown for each data set.

Department of Biology, Emory University, 1510 Clifton Road NE, Atlanta, GA 30322, USA.
*Corresponding author. Email: vcorces@emory.edu

CpGs and confirmed their stable inheritance across up to six passages (>12 cell divisions) (fig. S4, G and H). The ΔmC values of these CpGs were compared with several whole-genome BS-seq (WGBS) data sets in various human cells. Unexpectedly, the majority of them are conserved in other pluripotent cells but are absent in nonpluripotent cells (Fig. 1E), suggesting that hemimethylation could be cell type–specific and well conserved across related cell lineages.

WGBS only reports the independent methylation frequency of two Cs in the same CpGs. To obtain methylation status of CpGs per se, we developed a computational method called in silico strand annealing (iSA) to resolve the nasBS-seq data and identify pairs of alignments sharing exactly the same two ends between strands of parent^{Watson} and daughter^{Crick} and between daughter^{Watson} and parent^{Crick} (Fig. 2A and supplementary materials). We employed a "moving-ends" statistical test to justify that most of these pairs (26- to 111-fold enrichment over random pairing) represent distinct nascent double-stranded DNA (dsDNA) fragments (fig. S5A). iSA enabled us to call intramolecule CpGs (intraCpGs) from single dsDNA fragments and to determine their methylation state to be one of four types: methylation (intraCpG^{me}), unmethylation (intraCpG^{unme}) or pC- or dC- hemimethylation (intraCpG$^{hemi\text{-}pC}$ or intraCpG$^{hemi\text{-}dC}$). About 4.5 and 2.1 million intraCpGs were called from all replicates in pulse and chase, respectively (Fig. 2B). The two conditions showed nearly identical fractions for all four types, including a surprisingly high and consistent 14% combined fraction of intraCpG^{hemi}. Next, we used iSA to resolve published WGBS data sets in mouse early embryonic stages (*15*) and showed that hemiCpGs account for 4 to 18% of the DNA methylome (Fig. 2C) and is relatively depleted at transcription start sites (TSSs) (Fig. 2D). Murine intracisternal A-particle (IAP) retrotransposons are resistant to demethylation during early embryogenesis (*15*). Indeed, in inner cell mass (ICM) cells, intraCpG^{me} accounts for 47% of the DNA methylome in IAPs versus 14% genome-wide, whereas intraCpG^{hemi} accounts for 17 versus 16% genome-wide. Notably, ICM cells have the highest frequency of hemiCpGs on gene bodies, where it correlates slightly with transcription level, although it anticorrelates with transcription at promoters (fig. S5B), suggesting a pleiotropic role of hemiCpGs on gene expression. iSA was also used to resolve WGBS and Tet-assisted bisulfite sequencing (TAB-seq) data sets in H1-hESCs (fig. S5C) (*16*) and showed that although 5-hydroxymethylcytosine (5hmC) preferentially exists in hemimethylated form (fig. S5D), the vast majority of hemiCpGs discovered by nasBS-seq/WGBS is contributed by mC (fig. S5E). The ΔmC values from WGBS highly correlate with the frequency of hemiCpGs resolved by iSA (fig. S5F), suggesting that ΔmC values from WGBS can serve as a proxy for the frequency of hemimethylation.

The use of 20-min EdU labeling achieved a synchronization of genomic fragments by their replicative "age" of 10 min on average (0 to 20 min after passage of the local replication fork). The same frequency of hemiCpGs in pulse and chase suggests that the maintenance methylation reaction happens in a subminute scale (a 1-min-long methylation reaction would result in the pulse sample having 5% more hemiCpGs than chase), preventing nasBS-seq from revealing the rich plethora of pC-methylated hemiCpGs en route to maintenance methylation. We thus postulated that an enrichment of binding events between DNMTs and nascent chromatin would achieve both spatial and temporal enrichment of such transient interactions and would help identify cognate substrate CpGs maintained by a certain DNMT. Hence, we used chromatin immunoprecipitation on nascent chromatin followed by bisulfite sequencing (nasChIP-BS-seq) to specifically map the nascent DNA methylome targeted by DNMT1, DNMT3A, or DNMT3B in both pulse and chase (fig. S6, A and B). Unexpectedly, in pulse but not in chase, all three DNMT-targeted methylomes of the two daughter strands showed incomplete methylation, which was most apparent at centers of alignments, indicative of the precise location of DNMTs (fig. S6C). Analysis of the data using iSA revealed that ~42, 46, and 44% of all DNMT1-, DNMT3A- and DNMT3B-targeted CpGs in pulse were intraCpG$^{hemi\text{-}pC}$, respectively, whereas the same category only contributed 7, 6, and 5% in chase, respectively (Fig. 3A and fig. S6D).

Furthermore, binding sites for all three DNMTs showed an enrichment of CpGs over flanking sequences in pulse (fig. S6E). In chase, the enrichment diminished for DNMT1 and DNMT3B, whereas DNMT3A showed an enrichment of methylated CpGs (fig. S6E), suggesting that DNMTs may have differential occupancy preferences on nascent and mature chromatin (*17*, *18*). When viewed through the pulse nasBS-seq, the vast majority of DNMT-targeted intraCpG$^{hemi\text{-}pC}$ were fully methylated (Fig. 3B), suggesting that they were methylated shortly after the binding events. In DNMT1 knockout (KO) cells (*12*), both DNMT1-targeted intraCpG$^{hemi\text{-}pC}$ and intraCpG^{me} showed higher than average reduction of methylation, suggesting that their methylation state is maintained by DNMT1 (Fig. 3C). Under DNMT3A/3B double KO (*12*), both DNMT3A- and 3B-targeted intraCpG$^{hemi\text{-}pC}$ showed significantly higher reduction of methylation than the targeted intraCpG^{me}

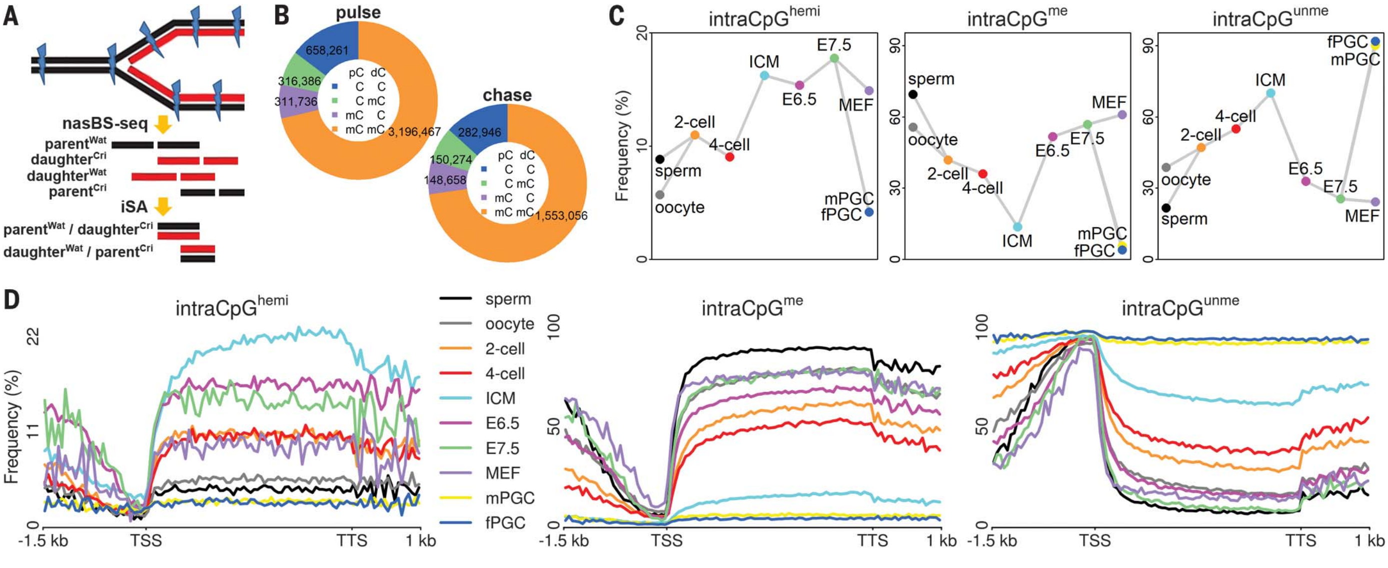

Fig. 2. HemiCpG is an important component of the DNA methylome. (**A**) Schematic representation of the principles underlying the iSA method. (**B**) The fraction of all four types of intraCpGs in pulse and chase. (**C**) The frequency of three types of intraCpGs (with two types of intraCpGs^{hemi} combined) at different mouse embryonic stages. ICM, inner cell mass; MEF, mouse embryonic fibroblast; mPGC/fPGC, male/female primordial germ cell. (**D**) The frequency of three types of intraCpGs at genic regions at different mouse embryonic stages.

(Fig. 3C), suggesting that these intraCpG$^{hemi\text{-}pC}$ are better candidates for DNMT3-maintained CpG than the targeted intraCpG^{me}. Indeed, these two types of CpGs showed mutually exclusive distribution, suggesting that they are subject to different regulation (fig. S6F). We next asked if nasChIP-BS-seq can also capture the substrate state of dCs en route to de novo methylation by examining the methylation state of targeted dCs in either inherited hemiCpGs or maintained CH methylation. In both cases, the yet-to-be-methylated dCs showed extensive hypomethylation in DNMT3A/3B nasChIP-BS-seq but not in nasBS-seq (Fig. 3D and fig. S6G). These results suggest that nasChIP-BS-seq can visualize the transient interactions

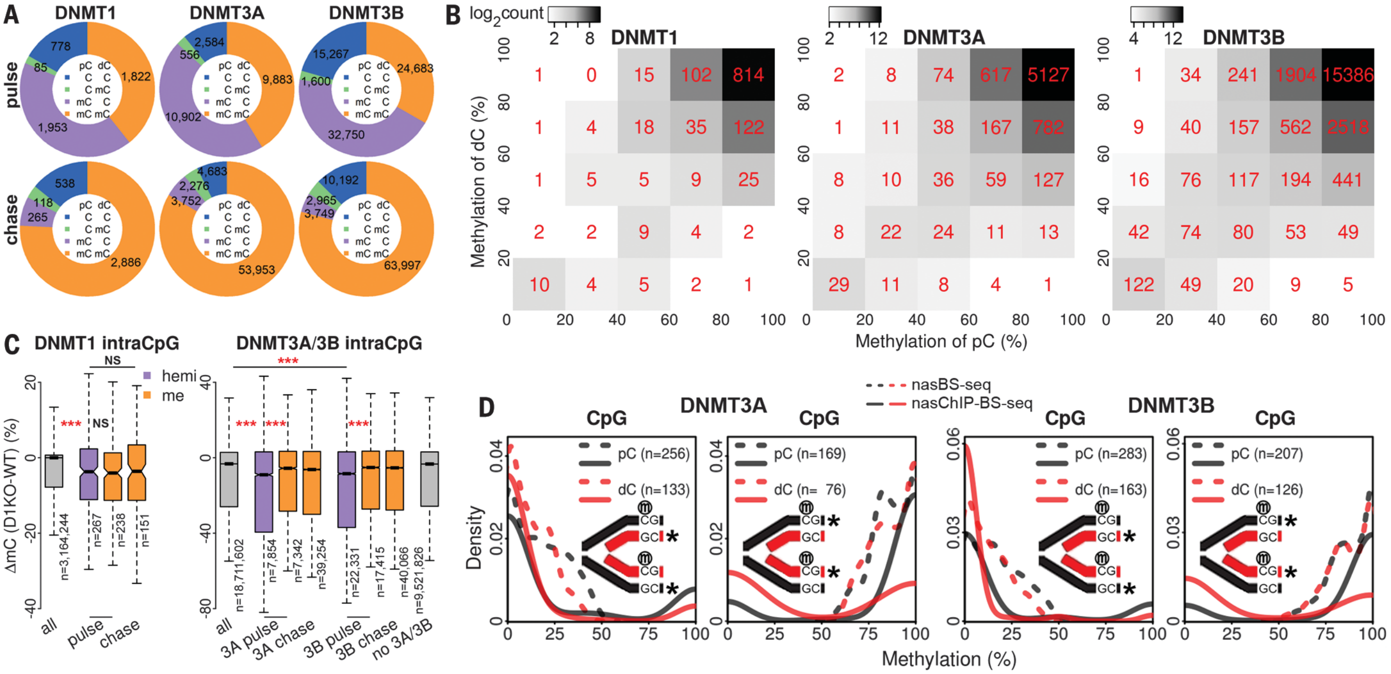

Fig. 3. Transient interactions between DNMTs and substrate dCs in both maintenance and de novo methylation. (**A**) The fraction of all four types of DNMT-targeted intraCpGs in pulse and chase. (**B**) Counts of all DNMT-targeted intraCpGs$^{hemi\text{-}pC}$ in pulse allocated to the appropriate cells according to their methylation frequency in pulse nasBS-seq. (**C**) Reduction of methylation under DNMT1 KO (24 hours) or DNMT3A/3B double KO (late) is shown for all CpGs, DNMT-targeted intraCpGs$^{hemi\text{-}pC}$, and intraCpGs^{me} in pulse and chase and unmapped CpGs. $***P < 0.001$. NS, not significant. (**D**) Distribution of methylation frequency of the four Cs in concordant hemiCpGs viewed through nasBS-seq and DNMT3A/3B nasChIP-BS-seq. The asterisks mark the two Cs inspected in each panel.

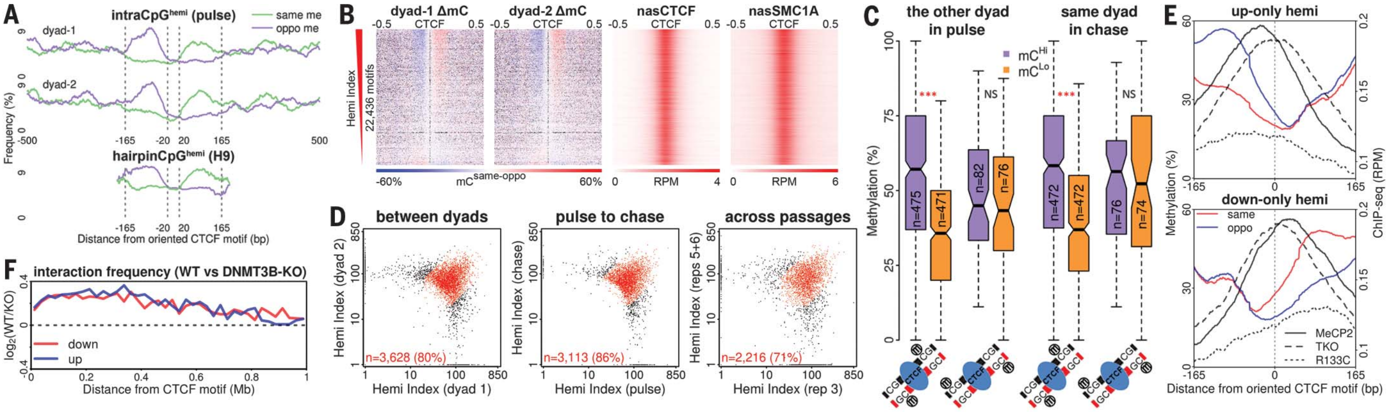

Fig. 4. Inherited hemiCpGs flanking CTCF/cohesin sites may regulate chromatin interactions. (**A**) Frequency of motif or opposite strand-methylated (same me or oppo me) intraCpGs^{hemi} around oriented CTCF motifs co-occupied by CTCF/SMC1A from the two nascent DNA duplexes. Frequency of hairpinCpG^{hemi} from CTCF ChIP-hairpinBS-seq is also shown. (**B**) All CTCF motifs co-occupied by CTCF/SMC1A in pulse were ranked by their hemi-index. ΔmC of CpGs from the two nascent DNA duplexes and reads per million (RPM) for CTCF and SMC1A nasChIP-seq within a 1-kb window surrounding the motifs are shown. Black in the ΔmC heat maps represents missing data points. (**C**) All hemiCpGs (ΔmC ≥ 67% or ≤ −67%) from two flanking regions in (B) were retrieved. Methylation frequency of the two Cs in the other dyad in pulse (left) or the same dyad in chase (right) are shown. $***P < 0.001$. NS, not significant. (**D**) The hemi-index of CTCF motifs showing HI > 50 in the pooled data were compared between two dyads, from pulse to chase, and across five passages. (**E**) Occupancy of WT and R133C mutant MeCP2 in WT mESC, and MeCP2 in DNMT1/3A/3B triple KO (TKO) mESCs was profiled around CTCF motifs showing upstream- or downstream-only hemimethylation in mESCs. (**F**) The ratio between interaction contacts from Hi-ChIP in WT and DNMT3B-KO HUES64 hESCs emanating from occupied CTCF motifs and extending up to ±1-Mb window is shown.

between a certain DNMT and substrate dCs in both maintenance and de novo methylation (fig. S6H).

To identify chromatin features associated with hemiCpGs, we examined the frequency of different types of intraCpG at different genomic features in H1-hESC. CTCF binding sites showed a very high ratio of intraCpG^{hemi} over intraCpG^{me} (fig. S7A). CTCF/cohesin binding sites orchestrate three-dimensional chromatin interactions across the mammalian genome (*19*). We then developed nasChIP-seq to map the binding landscape of CTCF and SMC1A (a cohesin subunit) on nascent chromatin in H9-hESC (fig. S7, B to E). By examining the average methylation profiles of the strands harboring the CTCF motif and the opposite strands around oriented CTCF motifs, we found two short regions flanking occupied CTCF motifs exhibiting an apparent spectrum of ΔmC with opposing orientation on the two sides (fig. S8A). The same pattern exists in H1-hESC, naïve H9-hESC, mouse ESC (mESC) (fig. S8A), and mouse embryos as early as the eight-cell stage (fig. S8B). Two independent methods, iSA and ChIP-hairpinBS-seq, confirmed at the single-molecule level that this spectrum of ΔmC indeed reflects an enrichment of hemiCpGs (Fig. 4A and fig. S8, C and D). The flanking hemiCpGs adopt a conformation of rotational symmetry with respect to CTCF motifs (fig. S8E), enabling us to search for the same pattern by screening the published ChIP-seq data sets of 60 chromatin-binding proteins in H1-hESC (*20*). This pattern is only exhibited by sites co-occupied by CTCF and RAD21 (a cohesin subunit) (fig. S8F). We also determined that this pattern is contributed by 5mC more than by 5hmC (fig. S8G) (*16*). Next, we built a hemi-index (HI) to quantitatively rank all CTCF motifs by the degree to which they associate with this pattern (see supplementary materials). The CTCF motifs from the two nascent DNA duplexes are highly concordant in HI (Fig. 4B), suggesting that these hemiCpGs were inherited during DNA replication. To confirm this, the methylation frequency was compared between the two dyads in pulse and between the same dyads in pulse and chase. The inheritance of ΔmC was observed in both cases, only from the enriched type of hemiCpGs (Fig. 4C). We also confirmed the inheritance at the level of CTCF motifs by comparing their HI between (i) two dyads, (ii) pulse and chase, and (iii) two cell populations with >10 cell divisions apart (Fig. 4D).

Methyl-CpG-binding domain (MBD) proteins can bind to both mCpG and mCA (*21*, *22*), suggesting that their binding to mC is not selective for the methylation state of the other strand. To investigate their putative association with hemiCpGs, we analyzed published WGBS and MBD ChIP-seq in mESC (*23*). To overcome the insufficient resolution of ChIP-seq, we profiled the occupancy of MBD proteins at CTCF motifs showing inherited hemimethylation either upstream-only or downstream-only. Indeed, MeCP2, Mbd1a, Mbd1b, Mbd2a, and Mbd2t all showed orientation-specific colocalization with hemimethylation (Fig. 4E and fig. S9). An MeCP2 mutant in the MBD domain (R133C) prominent in Rett syndrome showed significantly reduced colocalization with hemimethylation (Fig. 4E). Interestingly, in the absence of DNA methylation, MeCP2 loses the orientation-specific occupancy with no changes in occupancy level (Fig. 4E), whereas all other MBD proteins show reduced occupancy (fig. S9), suggesting that binding of MeCP2 shifts from a hemiCpG-dependent mode to a methylation-independent mode in the absence of DNA methylation. MeCP2 physically interacts with cohesin and regulates chromatin looping (*24*–*26*), compelling us to investigate the relationship between hemimethylation and CTCF-mediated chromatin interactions. We first determined that hemimethylation is not significantly altered under an acute and near-complete loss of CTCF protein (fig. S10, A and B) (*27*), suggesting that the inheritance of hemimethylation is CTCF-independent. In hESC, DNMT3B-KO alone is sufficient to eliminate most of the inherited hemimethylation at CTCF motifs with minimal impact on surrounding DNA methylation (fig. S10C) (*12*). ChIP-seq revealed that DNMT3B-KO led to no changes in RAD21 occupancy and a mild increase (~1.3-fold) in CTCF occupancy at CTCF motifs (fig. S10, D and E). We then performed RAD21 HiChIP (protein-centric chromatin conformation capture) in both wild-type (WT) and DNMT3B-KO hESC and found that loss of DNMT3B causes reduced interactions emanating from these CTCF motifs, extending up to 1 Mb apart (Fig. 4F), with no changes in interaction directionality bias (fig. S10D). This suggests that loss of hemimethylation renders the CTCF/cohesin complex to a less productive state, possibly through an altered mechanism of physical interaction with MeCP2.

Our results provide temporal and strand resolution of the nascent DNA methylome, identifying hemiCpGs with distinct methylation kinetics during DNA replication. Several studies have observed hemiCpGs in cells under heterogeneous cell cycle conditions using a hairpin adaptor-based strategy (*11*, *28*, *29*). Our study adds the resolution of the parent-daughter axis and the dimension of replication timing, and integrates a single-molecule perspective to the understanding of hemimethylation. The efficient reoccupancy by CTCF/cohesin and inheritance of flanking hemimethylation during DNA replication, and the colocalization with MBD proteins, support a model suggesting that CTCF sites actively engaged in chromatin interactions are marked by hemiCpGs shortly after passage of the local replication forks, which may facilitate timely assembly of the interaction complex, possibly with the involvement of MBD proteins, to ensure the proper inheritance of chromatin interactome and gene expression programs.

REFERENCES AND NOTES

1. R. Holliday, J. E. Pugh, *Science* **187**, 226–232 (1975).
2. J. A. Law, S. E. Jacobsen, *Nat. Rev. Genet.* **11**, 204–220 (2010).
3. L. S. Chuang *et al.*, *Science* **277**, 1996–2000 (1997).
4. M. Bostick *et al.*, *Science* **317**, 1760–1764 (2007).
5. J. Sharif *et al.*, *Nature* **450**, 908–912 (2007).
6. G. Liang *et al.*, *Mol. Cell. Biol.* **22**, 480–491 (2002).
7. H. Gowher, A. Jeltsch, *J. Mol. Biol.* **309**, 1201–1208 (2001).
8. A. Aoki *et al.*, *Nucleic Acids Res.* **29**, 3506–3512 (2001).
9. T. Chen, Y. Ueda, J. E. Dodge, Z. Wang, E. Li, *Mol. Cell. Biol.* **23**, 5594–5605 (2003).
10. A. Tsumura *et al.*, *Genes Cells* **11**, 805–814 (2006).
11. J. Arand *et al.*, *PLOS Genet.* **8**, e1002750 (2012).
12. J. Liao *et al.*, *Nat. Genet.* **47**, 469–478 (2015).
13. Y. He, J. R. Ecker, *Annu. Rev. Genomics Hum. Genet.* **16**, 55–77 (2015).
14. Z. Shipony *et al.*, *Nature* **513**, 115–119 (2014).
15. L. Wang *et al.*, *Cell* **157**, 979–991 (2014).
16. M. Yu *et al.*, *Cell* **149**, 1368–1380 (2012).
17. S. Jeong *et al.*, *Mol. Cell. Biol.* **29**, 5366–5376 (2009).
18. S. Sharma, D. D. De Carvalho, S. Jeong, P. A. Jones, G. Liang, *PLOS Genet.* **7**, e1001286 (2011).
19. C. T. Ong, V. G. Corces, *Nat. Rev. Genet.* **15**, 234–246 (2014).
20. ENCODE Project Consortium, *Nature* **489**, 57–74 (2012).
21. R. R. Meehan, J. D. Lewis, S. McKay, E. L. Kleiner, A. P. Bird, *Cell* **58**, 499–507 (1989).
22. H. W. Gabel *et al.*, *Nature* **522**, 89–93 (2015).
23. T. Baubec, R. Ivánek, F. Lienert, D. Schübeler, *Cell* **153**, 480–492 (2013).
24. K. D. Kernohan *et al.*, *Dev. Cell* **18**, 191–202 (2010).
25. K. D. Kernohan, D. Vernimmen, G. B. Gloor, N. G. Bérubé, *Nucleic Acids Res.* **42**, 8356–8368 (2014).
26. S. Horike, S. Cai, M. Miyano, J. F. Cheng, T. Kohwi-Shigematsu, *Nat. Genet.* **37**, 31–40 (2005).
27. E. P. Nora *et al.*, *Cell* **169**, 930–944.e22 (2017).
28. C. D. Laird *et al.*, *Proc. Natl. Acad. Sci. U.S.A.* **101**, 204–209 (2004).
29. L. Zhao *et al.*, *Genome Res.* **24**, 1296–1307 (2014).

ACKNOWLEDGMENTS

We thank members of the Corces laboratory for critical feedback and discussion, A. Meissner for providing the WT and DNMT3B-KO hESC, and E. P. Nora for providing the CTCF-AID mESC. We also thank A. Jones and the Genomic Services Laboratory at the HudsonAlpha Institute for Biotechnology for their help in performing Illumina sequencing of samples. **Funding:** This work was supported by U.S. Public Health Service Award 5P01 GM085354. The content is solely the responsibility of the authors and does not necessarily represent the official views of the National Institutes of Health. **Author contributions:** C.X. and V.G.C. conceived the project; C.X. designed and performed the experiments and analyzed the data; C.X. and V.G.C. wrote the manuscript. **Competing interests:** No competing interests. **Data and materials availability:** All sequence data have been deposited in the Gene Expression Omnibus under accession number GSE97394.

SUPPLEMENTARY MATERIALS

www.sciencemag.org/content/359/6380/1166/suppl/DC1
Materials and Methods
Figs. S1 to S10
References (*30*–*42*)

28 April 2017; resubmitted 15 December 2017
Accepted 16 January 2018
10.1126/science.aan5480

PROTEIN FOLDING

Thermal proximity coaggregation for system-wide profiling of protein complex dynamics in cells

Chris Soon Heng Tan,[1,2]* Ka Diam Go,[3] Xavier Bisteau,[1] Lingyun Dai,[3] Chern Han Yong,[4,5] Nayana Prabhu,[3] Mert Burak Ozturk,[1,6] Yan Ting Lim,[3] Lekshmy Sreekumar,[3] Johan Lengqvist,[7] Vinay Tergaonkar,[1,6,8] Philipp Kaldis,[1,6] Radoslaw M. Sobota,[1,2] Pär Nordlund[3,1,7]*

Proteins differentially interact with each other across cellular states and conditions, but an efficient proteome-wide strategy to monitor them is lacking. We report the application of thermal proximity coaggregation (TPCA) for high-throughput intracellular monitoring of protein complex dynamics. Significant TPCA signatures observed among well-validated protein-protein interactions correlate positively with interaction stoichiometry and are statistically observable in more than 350 annotated human protein complexes. Using TPCA, we identified many complexes without detectable differential protein expression, including chromatin-associated complexes, modulated in S phase of the cell cycle. Comparison of six cell lines by TPCA revealed cell-specific interactions even in fundamental cellular processes. TPCA constitutes an approach for system-wide studies of protein complexes in nonengineered cells and tissues and might be used to identify protein complexes that are modulated in diseases.

A living cell arises from a myriad of biomolecule interactions occurring in time and space among proteins, nucleic acids, metabolites, and lipids. Central to this intricate biological network are protein complexes that mediate the biochemical processes and the structural organization of the cell. They assemble and dissociate dynamically according to cellular needs and are implicated in many different diseases (*1*, *2*).

Large-scale studies using specific cell lines (*3*–*9*), complemented by focused efforts, have contributed to a large protein-protein interaction network depicting the plausible cellular wiring and functional organization of the human proteome. However, the conservation of the assembled protein network and identified protein complexes across cell types, physiological states, and diseased conditions is unclear. Methods that permit efficient, system-wide, and hypothesis-free identification of differentiated protein complexes in nonengineered and diseased cells will expedite biological studies.

Here, we explored the cellular thermal shift assay (CETSA) for the study of protein complex dynamics (*10*). By using protein mass spectrometry (MS) with multiplexed quantification for CETSA (MS-CETSA or thermal proteome profiling), melting curves are generated for thousands of proteins (*11*–*13*). In this work, we analyzed MS-CETSA data generated from samples without exogenous ligands. We validated thermal proximity coaggregation (TPCA) as an approach for system-wide intracellular monitoring of protein complex dynamics.

TPCA is based on the hypothesis that interacting proteins coaggregate upon heat denaturation, leading to similar solubility across different temperatures (Fig. 1A). We first investigated TPCA with the well-characterized Cdk2–cyclin E1 complex, deriving the melting curves using immunoblots for both proteins overexpressed in human embryonic kidney (HEK) 293T cells (fig. S1, A and B). Individually expressed cyclin E1–V5 and Cdk2-HA (hemagglutinin) display distinct melting curves, but they interact and are stabilized with similar melting curves when coexpressed (Fig. 1B and fig. S1A), consistent with the TPCA hypothesis.

To evaluate the generality of TPCA, we obtained the melting curves for 7693 human proteins (table S1) collated from eight MS-CETSA experiments of the same K562 lysate (Fig. 1C). We assembled 111,776 protein-protein interactions annotated in BioGRID (*14*), InAct (*15*), and MINT (*16*) databases occurring among the 7693 proteins (table S2). Using Euclidean distance as an inverse measure of curve similarity, we observed that interacting protein pairs generally have higher curve similarity than all protein pairs ($P < 2.2 \times 10^{-16}$, one-tailed Mann-Whitney test, Fig. 1D). This similarity is more pronounced for interactions reported by multiple publications (Fig. 1D and fig. S2). We also observed high curve similarity for interactions from two recent large-scale studies (*5*, *6*) using yeast two-hybrid (Y2H) and affinity purification (AP)–MS/MS, and for subunit pairs of complexes in the CORUM database (Fig. 1E) (*17*). Thus, it is unlikely that the observed TPCA signatures arose from ascertainment bias and the experimental methods used.

We computed the average curve similarity among all subunit pairs of each protein complex and assessed TPCA signatures at the protein complex level. For the 558 nonredundant human complexes having at least three subunits with melting curves, 160 exhibited nonrandom TPCA signatures among subunits collectively ($P < 0.05$, table S3, Fig. 1F, and fig. S3). Next, we obtained MS-CETSA data from the K562 cell lysate that was depleted of low–molecular weight (LMW) ligands by desalting (table S4). We observed decreased average curve similarity for most protein complexes (~88%, fig. S4A and table S5), suggesting that LMW ligand depletion caused increased complex dissociation. However, we observed multiple protein complexes with negligible changes in TPCA but with melting curves of all subunits shifted similarly, such as the PA700 proteasome subcomplex that could be due to adenosine 5´-triphosphate (ATP) depletion (Fig. 2A and fig. S5). Thus, whole-protein complexes can remain intact yet thermally destabilized by LMW ligand depletion. In comparison, MS-CETSA data from a new batch of K562 lysate shared good reproducibility with the previous lysate (Pearson's R = 0.88, fig. S3B). We observed a higher reproducibility (fig. S4C) for proteins with at least three quantified peptides in each data set, and thus combined existing and new data sets for subsequent analysis (table S6).

Six MS-CETSA experiments were performed on intact K562 cells (table S7). We observed melting curves of all protein pairs to be statistically more similar in the lysate data (Fig. 2B), whereas those for interacting protein pairs are statistically more similar in intact cell data (Fig. 2B). We also observed that protein complexes have better average curve similarity among subunits in intact cell data than in lysate data (figs. S6, A to D, and S7). Overall, intact cell data reveal more protein complexes with nonrandom TPCA signatures than the lysate data (Fig. 2C; fig. S6, E and F; and table S8).

TPCA-significant protein complexes in stress response, cell cycle, and DNA processing pathways are statistically enriched in intact cell data over lysate data (fig. S6G). Many DNA-chromatin–associated complexes and membrane-associated complexes—as exemplified by the Nup 107-160 nuclear pore subcomplex and the origin recognition complex, respectively (Fig. 2D)—exhibit significant TPCA signatures only in intact cells, presumably due to disruption of DNA-chromatin and native membranes in cell lysate. Our analysis suggests that the replication factor complex C (RFC) remains assembled in both intact cell and

---

[1]Institute of Molecular and Cell Biology (IMCB), A*STAR (Agency for Science, Technology and Research), Singapore. [2]Institute of Medical Biology (IMB), A*STAR (Agency for Science, Technology and Research), Singapore. [3]School of Biological Sciences, Nanyang Technological University, Singapore. [4]Program in Cancer and Stem Cell Biology, Duke–National University of Singapore (NUS) Medical School, Singapore. [5]Centre for Computational Biology, Duke–NUS Medical School, Singapore. [6]Department of Biochemistry, Yong Loo Lin School of Medicine, National University of Singapore, Singapore. [7]Department of Oncology-Pathology, Cancer Center Karolinska, Karolinska Institutet, Stockholm, Sweden. [8]Centre for Cancer Biology (University of South Australia and SA Pathology), Adelaide, Australia.
***Corresponding author. Email: cshtan@imcb.a-star.edu.sg (C.S.H.T.); pnordlund@ntu.edu.sg (P.N.)**

lysate (Fig. 2E, top) but that the whole complex is thermally destabilized in lysate (Fig. 2E, top left), presumably due to the absence of DNA-chromatin.

We observed many instances in which subcomplexes exhibit distinct TPCA signatures between intact cell and lysate data sets. For example, the 40*S* and 60*S* ribosomal subcomplexes each have subunits with similar curves that shifted closer to the other subcomplex in intact cell data (Fig. 2F), presumably because more fully assembled ribosomes are translating

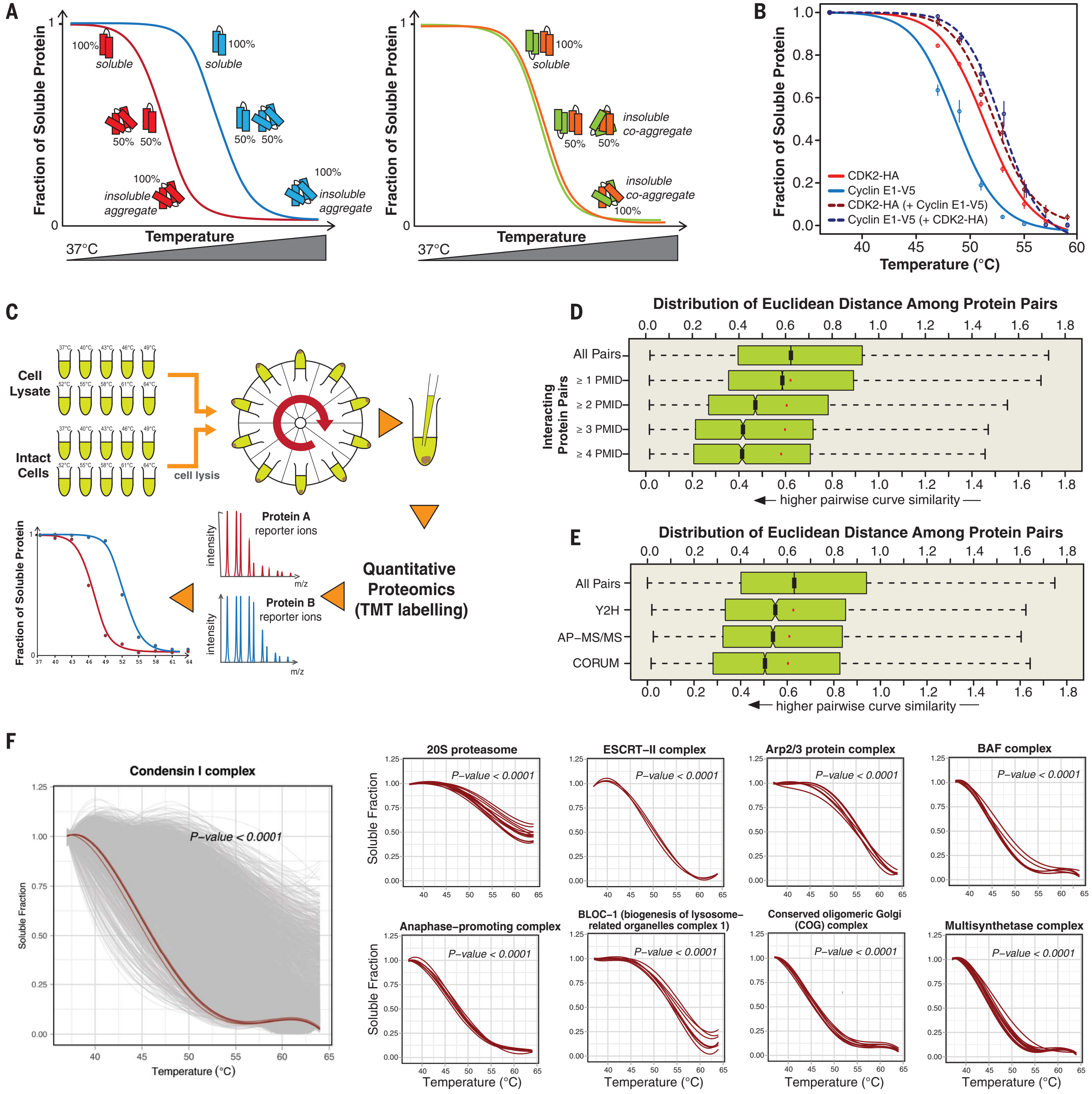

Fig. 1. Interacting protein pairs exhibit strong TPCA signature. (**A**) Principle of TPCA for monitoring protein-protein interactions: Coaggregation and precipitation among interacting proteins result in similar protein solubility across different denaturing temperatures. (**B**) Cointeracting cyclin E1 and Cdk2 exhibit similar melting curves: HEK 293T cells were transfected with plasmids encoding V5-tagged cyclin E1 and/or HA-tagged Cdk2, followed by the intact cell CETSA experiment. Data are from immunoblots of three biological replicates (mean ± SD) and are fitted with a three-parameter log-logistic function. Representative immunoblots are shown in fig. S1B. (**C**) Schematic overview of MS-CETSA experiment. m/z, mass/charge ratio; TMT, tandem mass tags. (**D**) Distribution of melting curve similarities between known interacting protein pairs according to number of reporting publications: PMID, PubMed identifier. Red dots indicate the median of all protein pairs of each respective protein subset. (**E**) Distribution of melting curve similarities of known interacting protein pairs reported in Rolland *et al*. (*6*), Huttlin *et al*. (*5*), and CORUM. (**F**) Protein melting curves of selected protein complexes: red lines, complex subunits. For the leftmost plot, the solubility curves of ~4000 other proteins are plotted in gray.

mRNA in cells than in lysate. Another example is the NDC80 kinetochore complex with two distinct subunit groups based on melting curves that are more similar to each other in intact cell data than in lysate data (Fig. 2E, bottom). The two distinct subunit groups correspond to the two stable heterodimers that are associated with each other through a short tetramerization protein region (Fig. 2G) (*18*, *19*). TPCA analysis suggests that the two subcomplexes had dissociated in lysate. These observations suggest that TPCA can reveal fundamental differences in protein complex organization and their functional states.

The stoichiometry of interaction and abundance between subunits in a complex can potentially

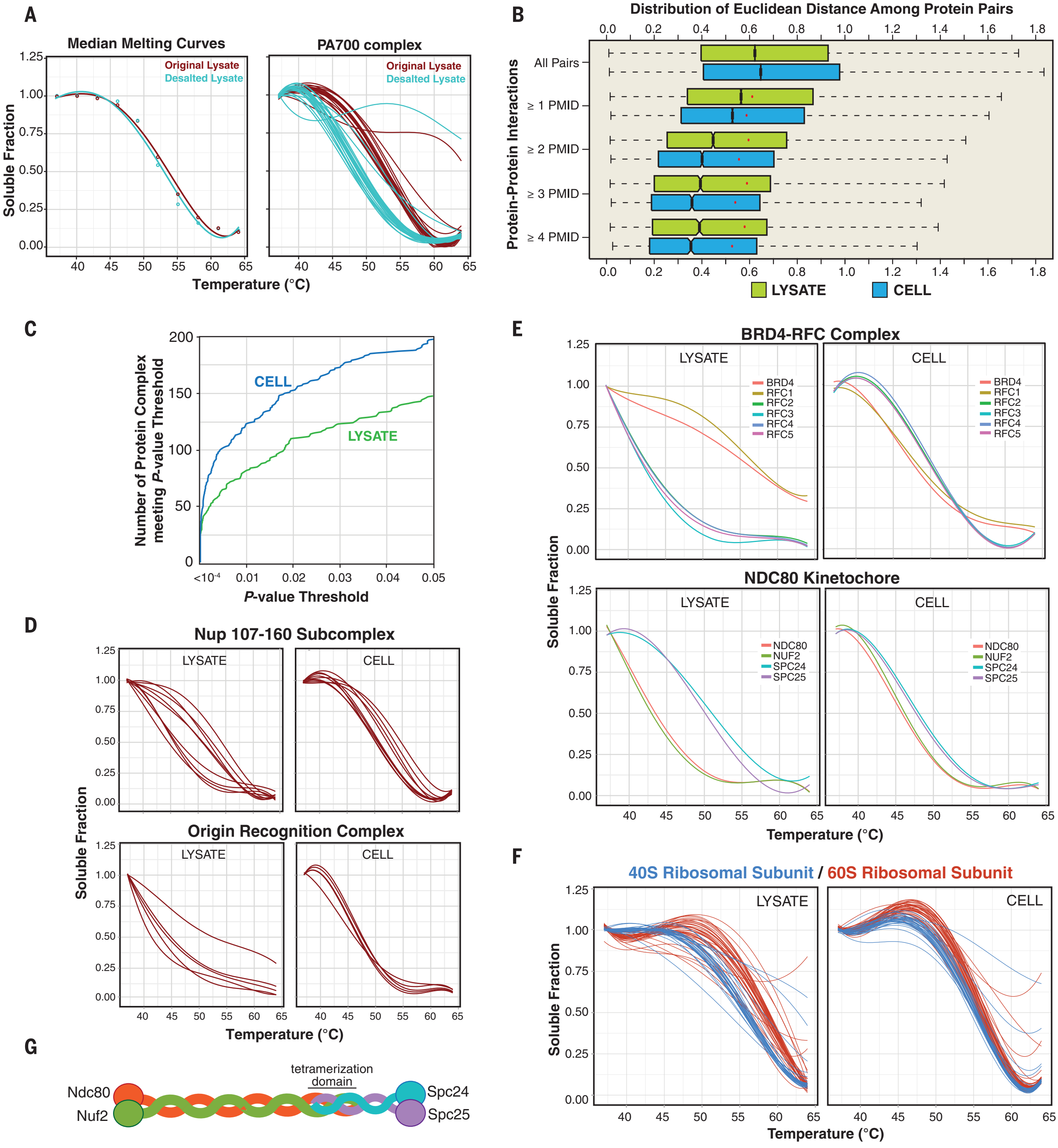

Fig. 2. TPCA signature is stronger in data from intact cells. (**A**) Effect of desalting cell lysate on subunit melting curves of PA700 proteasome subcomplex. (**B**) Distribution of melting curve similarities among known interacting protein pairs computed from cell lysate and intact cell data, respectively. Red dots indicate the median of all protein pairs of each respective protein subset. (**C**) Number of CORUM protein complexes with nonrandom TPCA behavior at different statistical thresholds. (**D**) Example of DNA-chromatin– and membrane-associated complexes. (**E** and **F**) Examples of subcomplexes that differ in cell and in lysate. (**G**) Schematics of structure for NDC80 kinetochore.

influence its TPCA signature. We analyzed such data for the interacting protein pairs reported with highest confidence in Hein *et al.* (*9*) and observed positive correlation of the TPCA signature with interaction stoichiometry (Spearman's $R = -0.22$, $P < 0.001$, Fig. 3A and fig. S8A) and abundance stoichiometry (Spearman's $R = -0.21$, $P < 0.001$, Fig. 3B and fig. S8B). The protein pairs with both interaction stoichiometry and abundance stoichiometry greater than 80% exhibit much stronger TPCA signatures than those meeting the two criteria separately (Fig. 3C). In comparison, proteins paired solely by similar abundance do not exhibit strong TPCA signatures [fig. S9, A to C, and table S9 (*20*)]. Accordingly, multiplying interaction stoichiometry with abundance stoichiometry results in values that correlate better with TPCA signature (Spearman's $R = -0.27$, $P < 0.001$, Fig. 3D and fig. S8C). Thus, interaction and abundance stoichiometry between interacting proteins are intrinsically captured by TPCA, albeit semiquantitatively.

Under the core-attachment model, subsets of proteins form the stable core of protein complexes that are differentially or temporally bound by other proteins (*21*, *22*). We investigated this model with TPCA, comparing melting curves of protein pairs from the complex core to curves for pairs between the core and the attachment subunits (Fig. 3E). We identified the core-core pairs in each complex as those found in two or more other CORUM complexes and core-attachment pairs as those found in that complex only. For most of the complexes, the TPCA signature of core-core pairs is either similar to or much stronger than that of the core-attachment pairs (Fig. 3F). This is in accordance with the core-attachment model in which core-attachment interactions generally occur at lower stoichiometry. Thus, TPCA signature potentially encapsulates the temporal and core-attachment organization of many complexes.

Next, we explored TPCA for system-wide monitoring of protein complex dynamics between cell states. We obtained intact cell MS-CETSA data from K562 cells arrested in the S phase of the cell cycle using methotrexate (fig. S10) and from dimethyl sulfoxide (DMSO)–treated unsynchronized cells (tables S10 and S11). We assessed statistical significance for enhanced TPCA (i.e., higher average curve similarity) observed for any CORUM complex (see materials and methods). We identified 18 protein complexes, some containing overlapping subunits, that have statistically enhanced TPCA signature across both biological replicates in S phase–synchronized cells (tables S12 to S14).

All but three identified modulated protein complexes had previously been implicated in the S phase. They include the CAF-1 complex (Fig. 3G), which forms and localizes to the replication fork during S phase (*23*); the TREX-THO complex (Fig. 3G, bottom right) required for replication fork progression (*24*, *25*); and the TRAP complex required for S phase progression (*26*). We also identified many chromatin-nucleosome remodeling and associated complexes such as BAF (Fig. 3G, top right), LARC, and BRG1-SIN3A (*27*), consistent with the expected remodeling of chromatin during the S phase. Histone mRNAs were up-regulated prior to S phase but were rapidly degraded with halted DNA replication (*28*). We identified three modulated protein complexes—the mRNA decay complex, the exosome, and the integrator complex—that are involved in histone mRNA degradation. Deletion of RRP6, a subunit of exosome, was reported to increase histone mRNA HTB1 during S phase (*29*), thus highlighting the role of this complex during S phase. Integrator complex was implicated in the processing of replication-dependent histone mRNAs (*30*).

Two of the three identified complexes not known to be implicated in S phase are the MDC1-MRN-ATM-FANCD2 and the DNA ligase III–XRCC–PNK–polymerase III complexes. However, they are involved in the DNA damage response in accordance with the known DNA-damaging effect of methotrexate (*31*). The third complex not implicated in S phase is the tumor necrosis factor–α (TNF-α)–nuclear factor κB (NF-κB) signaling complex (Fig. 3G). We validated that methotrexate increases the assembly of the associated IκBα-p65-p50 protein complex by suppressing activation of the NF-κB signaling pathway, in both the presence and absence of TNF, through inhibiting phosphorylation of the IκB kinase α/β (IKKα/β) complex, IκBα, and p65 in K562 cells (Fig. 3, H and I). We subsequently combined data from both replicates—the better data coverage and precision (table S15) allowed us to uncover more complexes that are differentially modulated between S phase and unsynchronized cells (table S16 and fig. S11).

The enhanced TPCA signature of identified complexes largely arose from curve convergence of most subunits (Fig. 4A). Nevertheless, this could arise from synchronized changes in protein expression. Thus, we quantified relative protein abundance between the DMSO- and methotrexate-treated cells using MS. We observed high reproducibility in relative abundance (Pearson's $R = 0.87$, fig. S12 and table S17) across biological replicates and identified only five subunits ($P < 0.05$, or nine at $P < 0.1$) with differential protein expression (Fig. 4A and table S18) that are mostly parts of the mediator and integrator megacomplexes. Thus, most subunits exhibit enhanced TPCA signature with each other without differential protein expression (Fig. 4A).

Next, we analyzed TPCA signature across multiple cell lines. We generated MS-CETSA data from HEK 293T, A375, HCT116, MCF7, and HL60 intact cells. Combining data from two biological replicates, each with two technical MS runs (average Pearson's $R = 0.92$ between biological replicates, fig. S13), we obtained melting curves for ~7600 proteins on average for each cell line (fig. S14A and tables S19 to S23). On average, 33.8% of the qualified CORUM complexes exhibit a nonrandom TPCA signature ($P < 0.05$) in each cell line (figs. S14B and S15 to S20), with ~70% overlap between cell lines. We also obtained data from mouse liver and observed ~37.7% of qualified protein complexes (three or more subunits with melting curves) with nonrandom TPCA signatures (tables S24 to S26 and figs. S21 and S22). Thus, TPCA is observable across multiple cell lines and from tissue samples. Many protein complexes exhibit strong TPCA behavior across the six cell lines (fig. S23), but we also found many complexes with high quality but distinct curves across cell lines (figs. S24 and S25). This suggests plausible variation in protein complex stoichiometry and composition among cell lines, even for fundamental and abundant protein complexes, that could arise from changes in interaction stoichiometry and/or protein abundance.

Subsequently, we generated weighted networks of reported interactions among proteins identified in all the six cell lines with TPCA-derived *z*-scores (table S26). A basal network averaging the *z*-scores, after removing the highest and the lowest *z*-scores for each interaction, is also constructed. Comparing the basal network with cell-specific TPCA-weighted networks facilitates identifying potentially differentiated interactions, pathways, and functional modules (table S27). Focusing on HCT116, we found that the RAS-RAF-MEK-ERK pathway contains many interactions with highly differentiated TPCA signatures (Fig. 4B). Retrospectively, we observed marked similarity in melting curves of BRAF and RAF1 proteins in HCT116 cells compared to other cell lines (Fig. 4C), consistent with expected dimerization of BRAF and RAF1 driven by active $\mathrm{KRAS}^{\mathrm{G13D}}$ in HCT116. TPCA analysis also suggests that BRAF-CRAF interaction with MEK is up-regulated in HCT116 cells but is down-regulated in A375 cells, which express $\mathrm{BRAF}^{\mathrm{V600E}}$ (Fig. 4B). This is in line with the recent finding that the interaction is up-regulated in cells expressing mutant KRAS and wild-type BRAF but suppressed in cells with mutant BRAF (*32*). Thus, TPCA could potentially capture cell-specific interactions and pathways.

Lastly, we validated that known and potentially previously unknown protein complexes can be identified from the existing human interactome map using graph or network clustering algorithms (*22*, *33*–*36*) with TPCA-based scoring of interactions (Fig. 4D, figs. S26 and S27, and supplementary text). The best performance was obtained with the COACH algorithm, which incorporates the core-attachment model of protein complexes (*22*). Using this algorithm and TPCA-based scoring of interactions gives a performance comparable to that of published interaction reliability scores that incorporate publication count and functional similarity (*37*). We also observed that TPCA profiling in its current format carries predictive power for protein-protein interactions, with the area under the curve ranging from 0.62 to 0.79 depending on the interaction data sets (Fig. 4, E and F), which collectively suggests that TPCA profiles could also serve to discover new interactions and protein complexes in combination with other approaches.

TPCA enables the intracellular study of the dynamics of multiple protein complexes simultaneously in intact nonengineered cells and tissues. About one-third of the qualified CORUM complexes in each cell line exhibit nonrandom TPCA

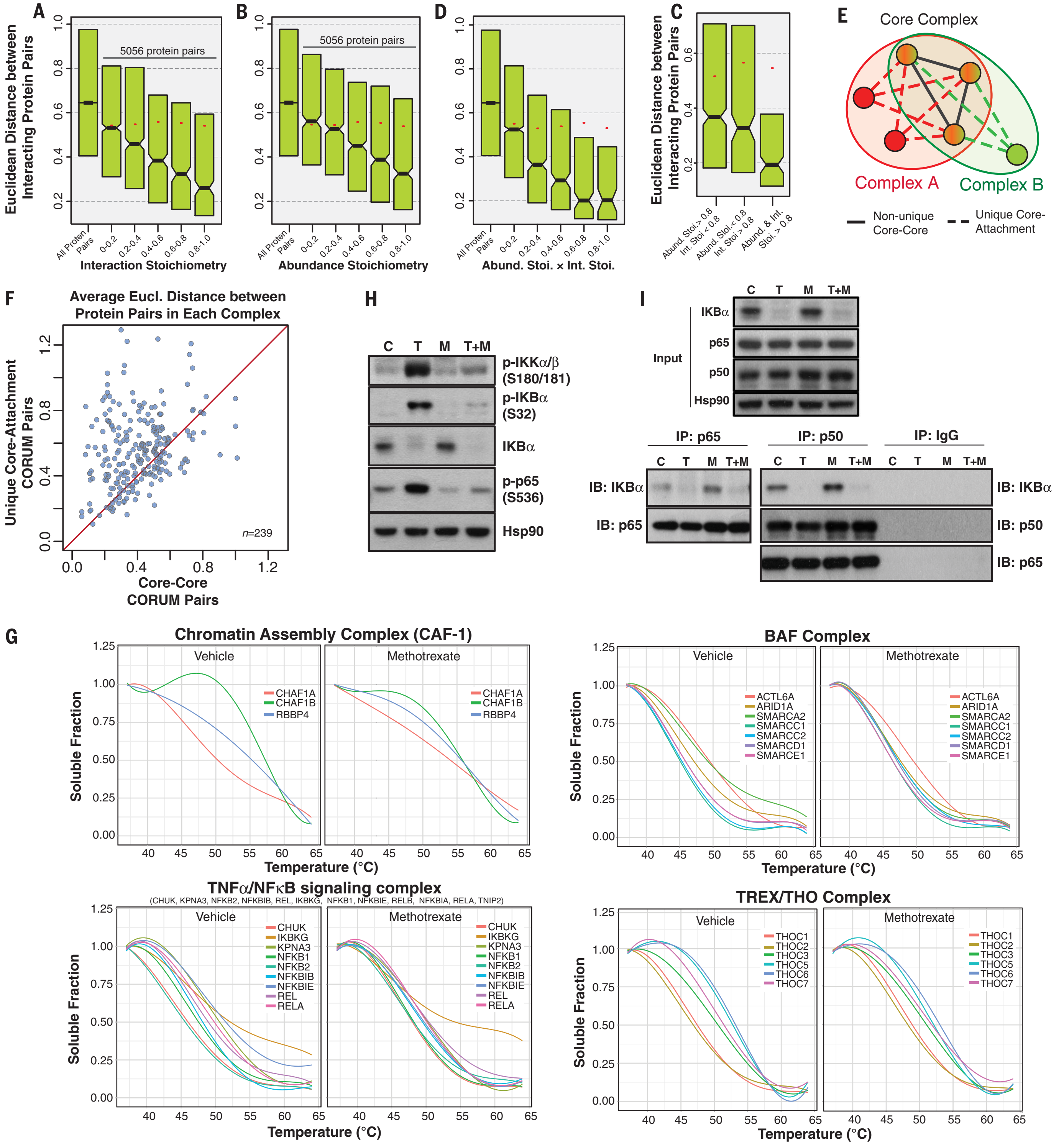

Fig. 3. TPCA signature interaction stoichiometry and abundance stoichiometry between interacting proteins. Correlation of TPCA signature (intact cell MS-CETSA data) with (**A**) protein interaction stoichiometry and (**B**) protein abundance stoichiometry of interacting protein pairs reported in Hein *et al*. (*9*). (**C**) Protein pairs with high stoichiometry in both parameters exhibiting the highest TPCA signature. (**D**) Multiplication of interaction and abundance stoichiometry correlates better with TPCA signature. (**E**) Core-attachment model for functional organization of protein complexes. (**F**) Core-attachment protein pairs of a complex generally exhibit weaker TPCA signature than core-core protein pairs. Each dot represents a protein complex. (**G**) Melting curves for subunits of the chromatin assembly complex 1 (CAF-1), the chromatin-remodeling BAF complex, the NF-κB complex, and the THO complex from methotrexate-treated and vehicle-treated K562 cells. (**H**) Assessment of the NF-κB signaling pathway upon methotrexate treatment in K562 cells. Western blotting analysis of canonical NF-κB signaling pathway members in whole-cell lysate. (**I**) Immunoprecipitation of NF-κB p65 and p50 showing increased interaction with IκBα upon methotrexate treatment. C, control (DMSO); T, TNF-α; M, methotrexate; T+M, TNF-α+methotrexate. IP, immunoprecipitation; IB, immunoblotting; IgG, immunoglobulin G. Hsp90 served as a loading control.

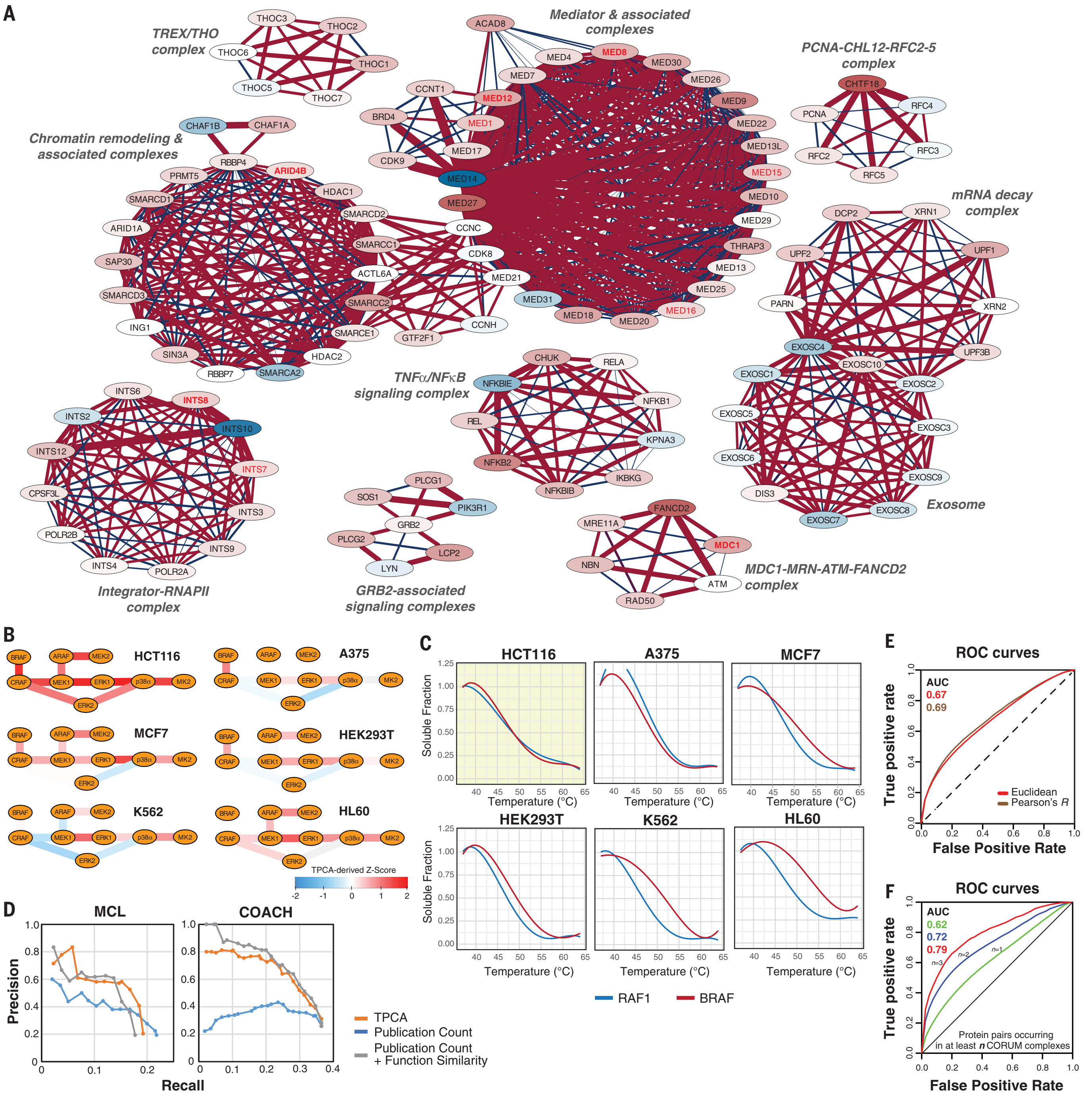

Fig. 4. TPCA signature reveals cell-specific interactions and is predictive of protein complexes. (**A**) Network view of protein complexes with nonrandom increase in TPCA behavior in methotrexate-treated K562 cells. Subunits of protein complexes are visualized as nodes with the edge connecting every pair of subunits within a complex. A red node indicates that the protein has greater stability in methotrexate-treated cells than in vehicle-treated cells, whereas a blue node indicates the reverse. Color intensity correlates linearly with difference in stability. A red line or edge between two nodes indicates that melting curves of the two proteins are more similar in methotrexate-treated cells, and a blue line or edge indicates the reverse. Line or edge width correlates linearly with difference in melting curve similarity. Differentially expressed proteins are indicated in red ($P < 0.10$) and bold type ($P < 0.05$). (**B**) TPCA analysis reports differentiated interactions in RAF-MEK-ERK pathway in HCT116. TPCA-derived *z*-scores are used to facilitate comparison of TPCA signatures across cell lines. A higher *z*-score implies increased interactions. (**C**) Melting curves of BRAF and RAF1 across the six cell lines. (**D**) Prediction of CORUM protein complexes using graph or network clustering algorithms on protein interaction network weighted with publication count, reliability score (publication count + function similarity) (*33*), and TPCA-based scoring. Precision and recall were evaluated against CORUM reference complexes (of size >3) with Jaccard similarity ≥ 0.5 considered as match. (**E**) Predictability of interacting protein pairs (table S2) reported by two or more publications using TPCA. (**F**) Predictability of co-complex pairs using TPCA. Melting curve data of intact K562 cells (table S7) are used. Euclidean distance between all protein pairs with melting curve is computed and ranked by ascending order (lower Euclidean distance first). All protein pairs are considered as negative data except those known to interact (table S2) or annotated as part of CORUM complexes.

signatures, with 58% of the complexes exhibiting nonrandom TPCA signatures in at least one of the cell lines profiled. Membrane-embedded complexes are included in CORUM but are likely not amenable to the protocol adopted in this work (*13*). Nonsignificant TPCA signatures could arise for protein complexes with very low interaction stoichiometry—increased assembly can be monitored by changes in TPCA signature. TPCA profiling suggests that many complexes can remain intact yet thermally destabilized in the absence of interaction with DNA and LMW ligands such as ATP (Fig. 2, A and E). We observed many mitochondrial proteins that seem more temperature-resistant in intact cells, as observed previously (*11*). It is unclear whether TPCA is intrinsic and captured by the recent limited proteolysis and MS methodology (*38*).

We observed many more complexes with significant TPCA signature in cells than in lysates, suggesting that TPCA could potentially aid the intracellular studies of weak or transient protein-protein interactions that are not preserved in lysate, including protein complexes that depend on the integrity of chromatin-DNA, membrane, and associated structures for stability. TPCA could be used to validate complexes identified by other proteome-wide methodologies and help in their functional characterization across different cell states and conditions. TPCA also permits studying chemical modulators of protein complexes and interactions directly in nonengineered cells and tissues. Analogous to quantifying expression of genes and proteins from a reference genome and reference proteome, respectively, we envisage TPCA-based profiling with reference interactomes as a system-wide discovery strategy for modulated cellular processes. The method therefore can facilitate the discovery of protein complexes involved in diseases, some as potential therapeutic targets or, by TPCA profiles in patient tissue samples, for prognosis of disease progression or optimization of therapy.

REFERENCES AND NOTES

1. T. Ideker, R. Sharan, *Genome Res.* **18**, 644–652 (2008).
2. X. Wang *et al*., *Nat. Biotechnol.* **30**, 159–164 (2012).
3. A. Malovannaya *et al*., *Cell* **145**, 787–799 (2011).
4. P. C. Havugimana *et al*., *Cell* **150**, 1068–1081 (2012).
5. E. L. Huttlin *et al*., *Cell* **162**, 425–440 (2015).
6. T. Rolland *et al*., *Cell* **159**, 1212–1226 (2014).
7. R. M. Ewing *et al*., *Mol. Syst. Biol.* **3**, 89 (2007).
8. U. Stelzl *et al*., *Cell* **122**, 957–968 (2005).
9. M. Y. Hein *et al*., *Cell* **163**, 712–723 (2015).
10. D. Martinez Molina, P. Nordlund, *Annu. Rev. Pharmacol. Toxicol.* **56**, 141–161 (2016).
11. M. M. Savitski *et al*., *Science* **346**, 1255784 (2014).
12. K. V. Huber *et al*., *Nat. Methods* **12**, 1055–1057 (2015).
13. F. B. Reinhard *et al*., *Nat. Methods* **12**, 1129–1131 (2015).
14. A. Chatr-Aryamontri *et al*., *Nucleic Acids Res.* **43**, D470–D478 (2015).
15. H. Hermjakob *et al*., *Nucleic Acids Res.* **32**, D452–D455 (2004).
16. L. Licata *et al*., *Nucleic Acids Res.* **40**, D857–D861 (2012).
17. A. Ruepp *et al*., *Nucleic Acids Res.* **38** (suppl. 1), D497–D501 (2010).
18. C. Ciferri *et al*., *Cell* **133**, 427–439 (2008).
19. H. W. Wang *et al*., *J. Mol. Biol.* **383**, 894–903 (2008).
20. J. R. Wiśniewski, M. Y. Hein, J. Cox, M. Mann, *Mol. Cell. Proteomics* **13**, 3497–3506 (2014).
21. Z. Dezso, Z. N. Oltvai, A. L. Barabási, *Genome Res.* **13**, 2450–2454 (2003).
22. M. Wu, X. Li, C. K. Kwoh, S. K. Ng, *BMC Bioinformatics* **10**, 169 (2009).
23. M. Hoek, B. Stillman, *Proc. Natl. Acad. Sci. U.S.A.* **100**, 12183–12188 (2003).
24. B. Gómez-González, I. Felipe-Abrio, A. Aguilera, *Mol. Cell. Biol.* **29**, 5203–5213 (2009).
25. R. E. Wellinger, F. Prado, A. Aguilera, *Mol. Cell. Biol.* **26**, 3327–3334 (2006).
26. M. Ito, C. X. Yuan, H. J. Okano, R. B. Darnell, R. G. Roeder, *Mol. Cell* **5**, 683–693 (2000).
27. H. Cho *et al*., *Mol. Cell. Biol.* **18**, 5355–5363 (1998).
28. W. F. Marzluff, E. J. Wagner, R. J. Duronio, *Nat. Rev. Genet.* **9**, 843–854 (2008).
29. R. Canavan, U. Bond, *Nucleic Acids Res.* **35**, 6268–6279 (2007).
30. J. R. Skaar *et al*., *Cell Res.* **25**, 288–305 (2015).
31. S. A. Martin *et al*., *EMBO Mol. Med.* **1**, 323–337 (2009).
32. J. R. Haling *et al*., *Cancer Cell* **26**, 402–413 (2014).
33. G. Liu, L. Wong, H. N. Chua, *Bioinformatics* **25**, 1891–1897 (2009).
34. T. Nepusz, H. Yu, A. Paccanaro, *Nat. Methods* **9**, 471–472 (2012).
35. S. Pu, J. Vlasblom, A. Emili, J. Greenblatt, S. J. Wodak, *Proteomics* **7**, 944–960 (2007).
36. M. Li, J. E. Chen, J. X. Wang, B. Hu, G. Chen, *BMC Bioinformatics* **9**, 398 (2008).
37. H. N. Chua, W. K. Sung, L. Wong, *Bioinformatics* **22**, 1623–1630 (2006).
38. P. Leuenberger *et al*., *Science* **355**, eaai7825 (2017).

ACKNOWLEDGMENTS

We thank H. Y. Chang for support and A. Larsson for suggestions. **Funding:** This research was funded directly by Young Investigator Grant (1610151038) awarded to C.S.H.T. by the Biomedical Research Council of the Agency for Science, Technology and Research (A*STAR). Support for this research was provided by a startup grant from Nanyang Technological University and grants from the Swedish Research Council, the Swedish Cancer Society, and the Knut and Alice Wallenberg foundation awarded to P.N., and by National Medical Research Council (NMRC) grant MOHIAFCAT2/004/2015 to P.N. and R.M.S. Research in the lab of V.T. is supported by grant NRF2016NRF-CRP001-024 from the National Research Foundation Singapore. P.K. and X.B. are supported by the Biomedical Research Council, A*STAR, and NMRC-CBRG14nov086 grants. **Authors contributions:** P.N. initiated the study; C.S.H.T. conceptualized TPCA and designed and implemented associated algorithms; C.S.H.T, X.B., P.K., V.T., R.M.S., and P.N. designed and supervised experiments; C.S.H.T. and C.H.Y. performed computational analysis; K.D.G., C.S.H.T., X.B., M.B.O., L.D., N.P., Y.T.L., and L.S. performed experiments; R.M.S. and J.L. supervised MS analysis; C.S.H.T. wrote the original manuscript; and C.S.H.T. and P.N. reviewed and edited the manuscript. **Competing interests:** P.N. is the inventor of a patent controlled by Pelago Biosciences AB and Evitra Proteoma AB covering the basic CETSA method. J.L. is a paid consultant of Pelago Biosciences AB for MS analysis. All other coauthors declare no competing interests. **Data and materials availability:** All data are available in the supplementary materials.

SUPPLEMENTARY MATERIALS

www.sciencemag.org/content/359/6380/1170/suppl/DC1
Materials and Methods
Supplementary Text
Figs. S1 to S27
Tables S1 to S27

22 February 2017; resubmitted 28 September 2017
Accepted 27 January 2018
Published online 8 February 2018
10.1126/science.aan0346

HEART DEVELOPMENT

Defining the earliest step of cardiovascular lineage segregation by single-cell RNA-seq

Fabienne Lescroart,[1]* Xiaonan Wang,[2,3]* Xionghui Lin,[1]* Benjamin Swedlund,[1] Souhir Gargouri,[1] Adriana Sànchez-Dànes,[1] Victoria Moignard,[2,3] Christine Dubois,[1] Catherine Paulissen,[1] Sarah Kinston,[2,3] Berthold Göttgens,[2,3]†‡ Cédric Blanpain[1,4]†‡

Mouse heart development arises from *Mesp1*-expressing cardiovascular progenitors (CPs) that are specified during gastrulation. The molecular processes that control early regional and lineage segregation of CPs have been unclear. We performed single-cell RNA sequencing of wild-type and *Mesp1*-null CPs in mice. We showed that populations of *Mesp1* CPs are molecularly distinct and span the continuum between epiblast and later mesodermal cells, including hematopoietic progenitors. Single-cell transcriptome analysis of *Mesp1*-deficient CPs showed that Mesp1 is required for the exit from the pluripotent state and the induction of the cardiovascular gene expression program. We identified distinct populations of *Mesp1* CPs that correspond to progenitors committed to different cell lineages and regions of the heart, identifying the molecular features associated with early lineage restriction and regional segregation of the heart at the early stage of mouse gastrulation.

The mammalian heart is composed of different regions (ventricles, atria, and great vessels) and cell types, including cardiomyocytes (CMs), endocardial cells (ECs), smooth muscle cells (SMCs), and epicardial cells (EPs) (*1*). Heart development begins at gastrulation, during which CPs leave the primitive streak (PS) and migrate toward the anterolateral pole of the embryo (*2*). From embryonic day 6.25 (E6.25) to E7.25, *Mesp1* marks the early CPs within the PS, whereas a day later, *Mesp1* is expressed in the somites (*2*, *3*). *Mesp1*$^+$ cells give rise to all heart cells, ECs of the aorta and brain, some muscles of the head and neck, as well as to few somitic derivatives and liver cells from its later expression (*2*, *4*–*6*). Temporally inducible *Mesp1* lineage tracing shows that at E6.5, *Mesp1*$^+$ cells mark left ventricle (LV) progenitors, whereas the right ventricle, atria, outflow, and inflow tracts and head muscles arise from *Mesp1*$^+$ cells at E7.25, which correspond respectively to the first and second heart fields (FHF and SHF, respectively). No somitic or liver derivatives were labeled at these early time points (*4*, *5*, *7*). In addition, most of the *Mesp1* CPs differentiate into either CMs or ECs, suggesting that lineage segregation occurs early during gastrulation (*4*, *5*). It remains unknown whether molecular heterogeneity between E6.5 and E7.25 *Mesp1*$^+$ CPs reflects stochasticity in gene expression, transcriptional priming, or early lineage and regional segregation.

To investigate the molecular and cellular basis of the earliest stages of CP specification and diversification, we performed single-cell RNA sequencing (scRNA-seq) of *Mesp1* CPs at E6.75 and E7.25. To this end, *Mesp1-rtTA/tetO-H2B–GFP* (green fluorescent protein) mice were treated with doxycycline at different time points after fertilization in order to label only early *Mesp1*-expressing cells and no somitic derivatives (Fig. 1A), embryos were dissociated into single cells, and H2B-GFP–positive CPs were isolated by means of fluorescence-activated cell sorting (FACS) (fig. S1). A total of 172 and 341 *Mesp1* CPs at E6.75 and E7.25, respectively, were sequenced and analyzed further after passing through a stringent quality control pipeline (supplementary materials, materials and methods). We recently reported single-cell transcriptomes for E6.5 epiblast cells, as well as E7.25/7.5 Flk1-expressing progenitors (*8*). Visualization by use of dimensionality reduction techniques allowed us to order the cells along developmental progression and assign a time stamp to each cell, demonstrating that the *Mesp1*$^+$ CPs at E6.75 and E7.25 likely represent a continuum of differentiation (Fig. 1, B and C, and fig. S2) (*8*).

To determine the role of Mesp1 in regulating the cardiovascular differentiation program and the heterogeneity of early CPs, we performed scRNA-seq of FACS-isolated *Mesp1*-expressing cells in *Mesp1* knockout (KO) context (fig. S3) (*2*). We sequenced transcriptomes of 85 single *Mesp1*-null cells isolated at E6.75, before the appearance of the developmental defect associated with *Mesp1* deficiency (Fig. 2A). Pseudotime analysis revealed that *Mesp1* KO cells presented a developmental block, being stuck in the gene expression program of epiblast cells (Fig. 2B). Principal components analysis showed that principal component 2 captured expression differences between wild-type (WT) and *Mesp1* KO cells (fig. S4), with 206 down-regulated and 136 up-regulated genes (table S1). We found a highly significant overlap for genes differentially expressed between WT and *Mesp1* KO cells in vivo and genes that are down- or up-regulated after

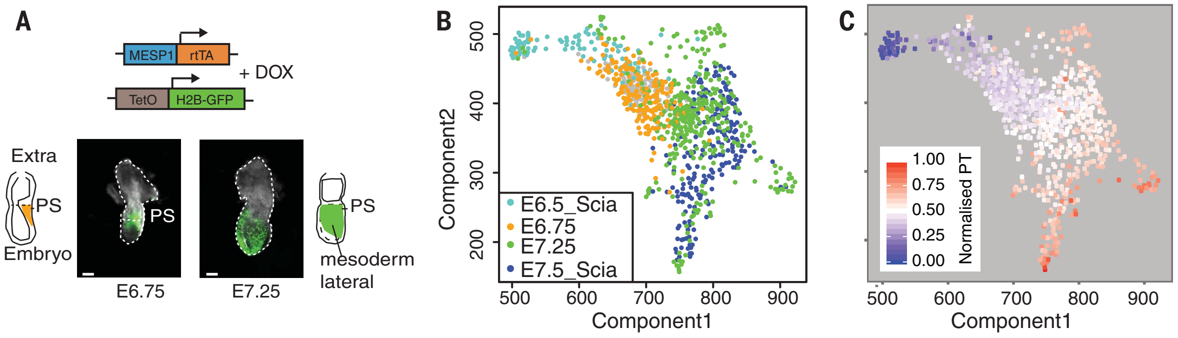

Fig. 1. scRNA-seq of *Mesp1*$^+$ CPs fills the gap between E6.5 epiblast cells and E7.5 mesodermal cells. (**A**) Scheme of the experimental strategy used for isolating *Mesp1*-expressing CPs in vivo. Scale bar, 200 μm. (**B**) SPRING plot of 892 cells showing *Mesp1* CPs at E6.75 and E7.25 and the published epiblast cells (E6.5_Scia) and E7.5 Flk1$^+$ progenitors (E7.5_Scia) with read count of Mesp1 > 0. (**C**) SPRING plot colored by the inferred pseudotime time for all 892 cells.

---

[1] Université Libre de Bruxelles, Laboratory of Stem Cells and Cancer, Brussels B-1070, Belgium. [2] Department of Haematology, Cambridge Institute for Medical Research, University of Cambridge, Cambridge CB2 0XY, UK. [3] Wellcome and Medical Research Council Cambridge Stem Cell Institute, University of Cambridge, Cambridge, UK. [4] WELBIO, Université Libre de Bruxelles, Brussels B-1070, Belgium.
*These authors contributed equally to this work. †These authors contributed equally to this work. **‡Corresponding author. Email: bg200@cam.ac.uk (B.G.); cedric.blanpain@ulb.ac.be (C.B.)**

Mesp1-induced gain of function in embryonic stem cells (ESCs) in vitro (*9*), many of which are direct Mesp1 target genes (Fig. 2C, fig. S5, and table S1). Several well-known regulators of pluripotency—including *Nanog*, *Eras*, *Pou5f1/Oct4* (*10*), and markers of the epiblast, including *E-Cadherin/Cdh1*, *Epcam*, *Cldn6*, and *Cldn7*—were up-regulated in single *Mesp1* KO cells (Fig. 2, D to F, and table S1), which is consistent with the defect of exiting the pluripotent epiblast stage. By contrast, the genes down-regulated in *Mesp1* KO cells were greatly enriched for Mesp1 target genes controlling epithelial-mesenchymal transition (EMT) (*Snai1* and *Zeb2*), migration (*Rasgrp3*), and cardiovascular commitment (*Etv2*, *Hand1*, *Myl7*, *Gata4*, *Flk1*, and *Pdgfra*) (Fig. 2, F and G, and fig. S5) (*9*, *11*). Pdgfra/Flk1–expressing cells that mark *Mesp1* CPs in human and mouse ESC differentiation in vitro and during mouse gastrulation in vivo (*5*, *12*, *13*) were much reduced in *Mesp1* KO cells, supporting the absence of CP specification (fig. S6).

SPRING analysis, which allows visualizing high-dimensional single-cell expression data (*14*), of WT *Mesp1*-expressing cells at E6.75 and E7.25 identified five distinct destination cell types (DCTs) protruding from a core of intermingled cells (Fig. 3, A and B). All cells present within the DCTs came from E7.25 embryos, which is consistent with cell fate diversification of *Mesp1*-derived lineages during the late stages of gastrulation. To further define the nature of the five DCTs, we identified genes with specifically elevated expression in each of the five groups (Fig. 3, B and C; fig. S7; and table S2). This analysis identified both known and previously unrecognized genes associated with cardiovascular development. DCT1 was enriched among others in *Sox7*, *Etv2*, and *Tal1* transcripts, which are markers of the endothelial or endocardial lineage (*15*, *16*). DCT2 was marked by the expression of *Hand1*, *Bmp4*, *Tnnc1*, *Tbx3*, *Hand2*, *Tbx20*, *Gata4*, *Myl4*, and *Mef2c*, which are well-known CM markers (Fig. 3C, fig. S7, and table S2) (*7*, *17*). Bmp4 promotes CM differentiation (*18*). Moreover, Hand1 lineage tracing showed that *Hand1*-expressing cells contribute to the LV and to the myocardial and epicardial lineages, with no contribution to the endocardium (*17*). These data suggest that DCT2 corresponds to CPs committed to the CM lineage. In situ hybridization of *Sox7* (EC

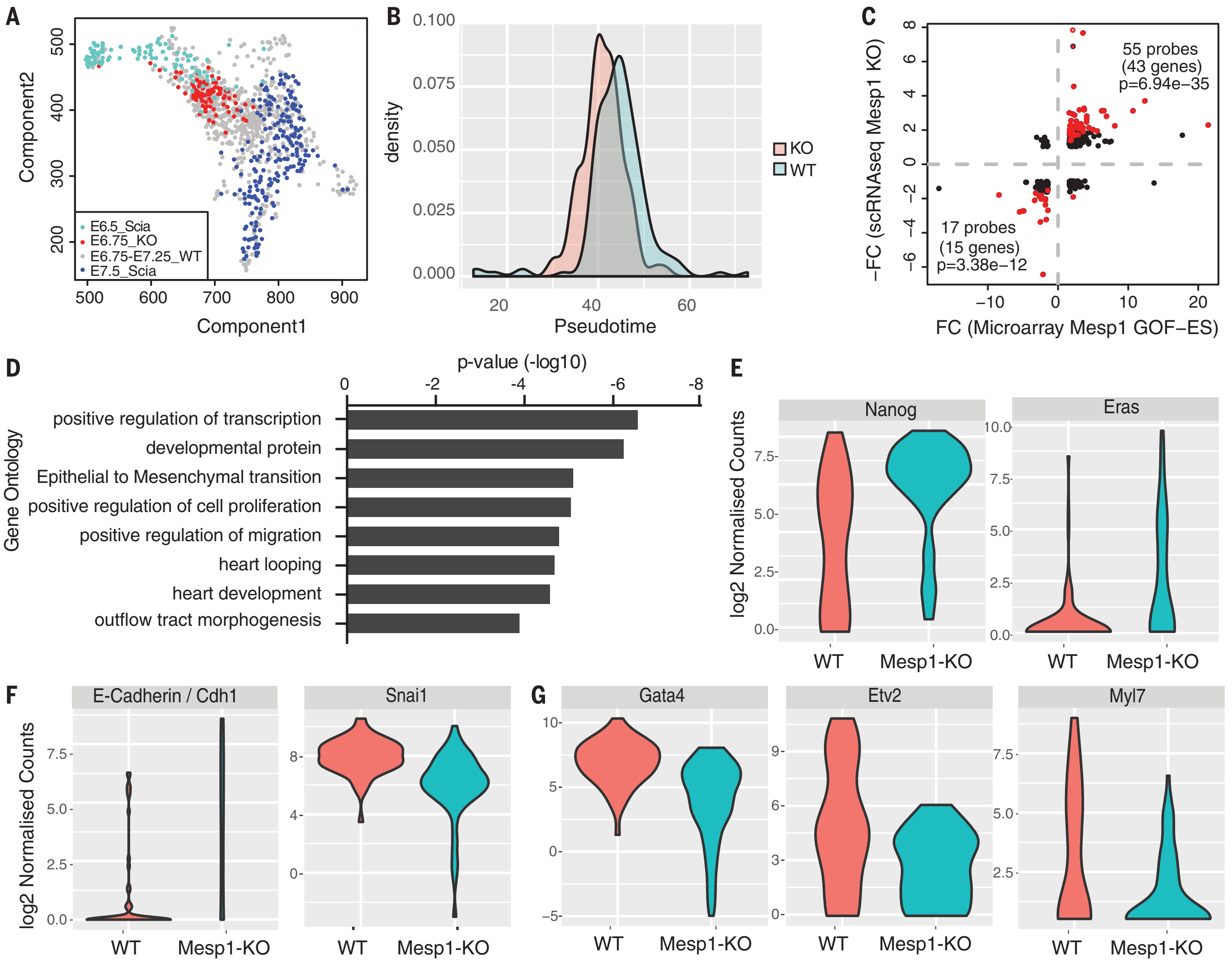

Fig. 2. Mesp1 controls the exit from pluripotency, EMT, and cardiovascular specification. (**A**) SPRING plot of all 892 cells, including *Mesp1* KO cells colored by cell types. (**B**) Pseudotime time distribution for WT and *Mesp1* KO cells at E6.75. (**C**) Comparison of the genes differentially expressed in scRNA-seq experiments between control and *Mesp1* KO cells and the genes regulated by Mesp1 gain of function (GOF) in ESCs. The 58 genes in agreement with the scRNA-seq experiment with false discovery rates of <0.1 were highlighted in red. The significance of the overlap was calculated by means of hypergeometric test using the phyper function in R. (**D**) Gene ontology enrichment for genes down-regulated in *Mesp1* KO cells. (**E** to **G**) Violin plots showing the mean and variance difference between WT and *Mesp1* KO cells of (E) genes regulating pluripotency (*Nanog* and *Eras*), (F) EMT (*Cdh1* and *Snai1*), and (G) cardiovascular fate (*Gata4*, *Etv2*, and *Myl7*).

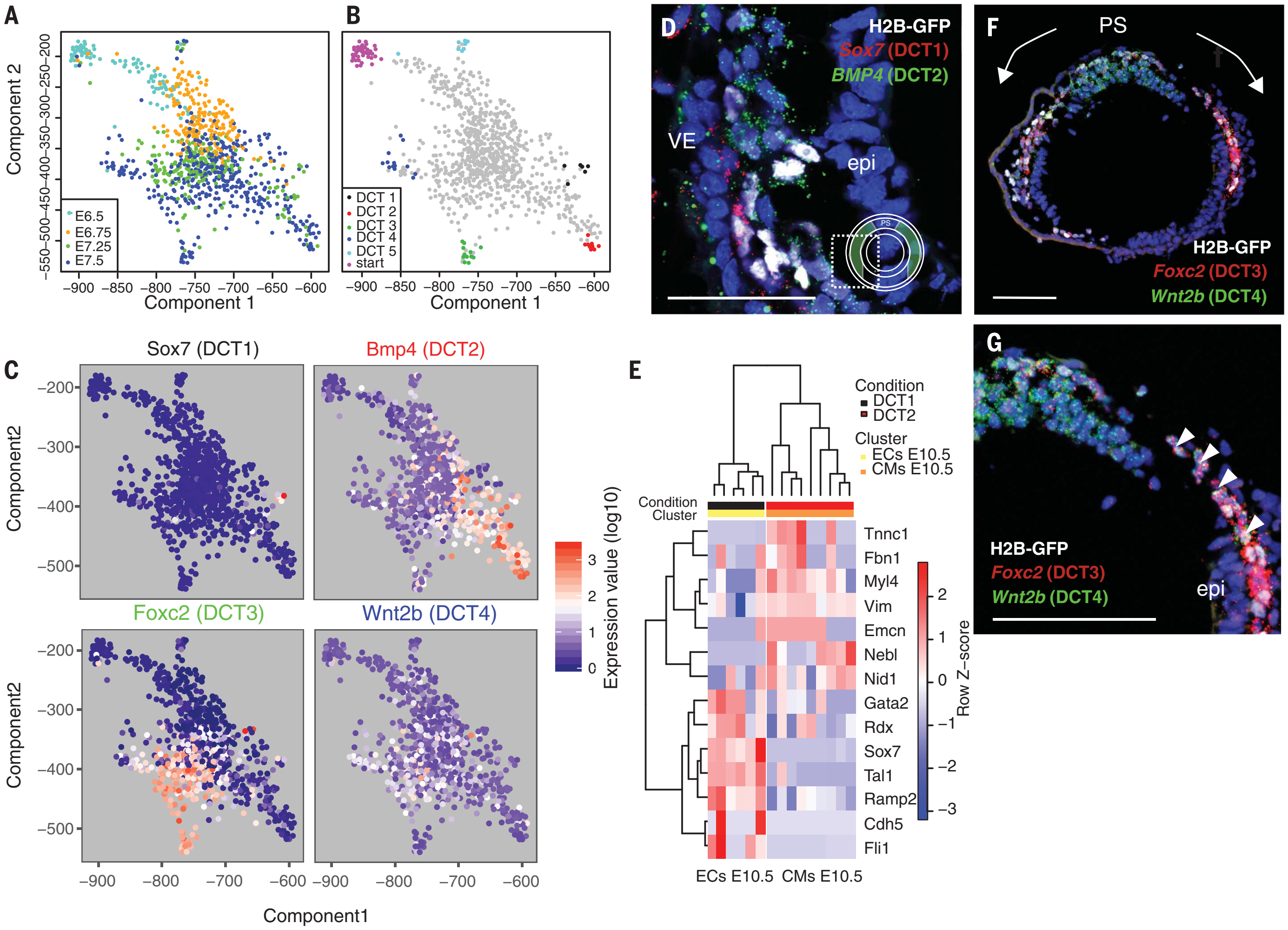

Fig. 3. *Mesp1* single-cell analysis identifies different progenitors committed to different fates and heart regions. (**A**) SPRING analysis of the 807 WT Mesp1-H2B-GFP^{+} cells at E6.75 and E7.25 and *Mesp1*$^{+}$ Scia cells. (**B**) The five end points revealed by means of SPRING analysis were considered as five distinct cell types (DCT1-5). (**C**) Expression of key genes specific for DCT1-4. (**D**) RNA-FISH of *Sox7* and *Bmp4* on sections of *Mesp1-rtTA/tetO-H2B-GFP* embryos at E7.25. (**E**) Heatmap of DCT1 and DCT2 end point cells based on unsupervised clustering of the expression of CM and EC marker genes identified at E10.5 (*24*) combined with newly identified genes enriched in DCT1 or DCT2. (**F** and **G**). RNA-FISH of *Foxc2* and *Wnt2b* on sections of *Mesp1-rtTA/tetO-H2B-GFP* embryos at E7.25. Higher magnification is found in (G). Scale bar, 50 μm.

marker) and *Bmp4* (CM marker) on *Mesp1-rtTA/tetO-H2B-GFP* embryos showed that these two markers did not colocalize in Mesp1-H2B-GFP–expressing cells at E7.25, which is consistent with the notion that DCT1 and DCT2 mark two distinct *Mesp1* populations committed to EC and CM differentiation (Fig. 3D). Unsupervised hierarchical clustering of DCT1 and DCT2 markers with CM and EC markers identified by means of scRNA-seq of more mature mouse hearts at E10.5 (*19*) further showed that DCT1 and DCT2 cells clustered respectively with EC and CM lineage (Fig. 3E).

DCT3 and DCT4 are enriched in genes expressed and regulating SHF development (*Tbx1*, *Foxc2*, *Hoxb1*, and *Hoxa1*) (Fig. 3C, fig. S7, and table S2) (*20*–*22*). Lineage tracing experiments have previously shown that *Tbx1* (DCT3) marks anterior SHF progenitors, whereas *Hoxb1* and *Hoxa1* (DCT4) mark posterior SHF (*20*, *22*), suggesting that DCT3 and DCT4 correspond to *Mesp1* CPs committed to the anterior and posterior SHFs. RNA–fluorescence in situ hybridization (FISH) experiments further showed that *Foxc2* (DCT3) and *Wnt2b* (DCT4) were largely nonoverlapping, with *Wnt2b* localized closer to the PS, whereas *Foxc2*-expressing cells were found more anterolaterally at E7.25 (Fig. 3, F and G). A subset of SHF progenitors, called cranio-pharyngeal progenitors, express *Tcf21* and contribute to the formation of some head muscles (*23*). RNA-FISH showed that *Tcf21* is preferentially expressed in a subset of DCT3 *Mesp1* H2B-GFP expressing *Foxc2*, whereas little overlap was observed between DCT4 progenitors expressing *Wnt2b* and *Tcf21* (fig. S8). Consistent with the notion that DCT3 marks cranio-pharyngeal progenitors, the "pharyngeal" cluster found in our previous Flk1^{+} scRNA-seq (*8*) are closest to DCT3 (fig. S7). DCT5 expressed endoderm markers such as *Sox17* and *Foxa2* and may have no relation with cardiac development (fig. S7 and table S2).

On the basis of the cumulative evidence that suggested our scRNA-seq captures the developmental progression from epiblast to early cardiovascular lineage segregation, we next investigated the expression of genes with known biological function, which revealed specific expression of cardiovascular, mesodermal, and other genes regulating signaling pathways across the various DCT populations (fig. S9). Analysis of genes dynamically expressed during the trajectory toward DCT1 and DCT2 revealed the existence of gene clusters peaking in expression at sequential points along the pseudotemporal ordering. These gene clusters showed enrichment for gene ontology categories associated with developmental progression in which the predicted trajectory provided consistency between the pseudotime and the real developmental time (fig. S10 and table S3). Moreover, cells coexpressing genes enriched in both DCT3 and DCT4 presented early pseudotime values than either DCT3 or DCT4 cells,

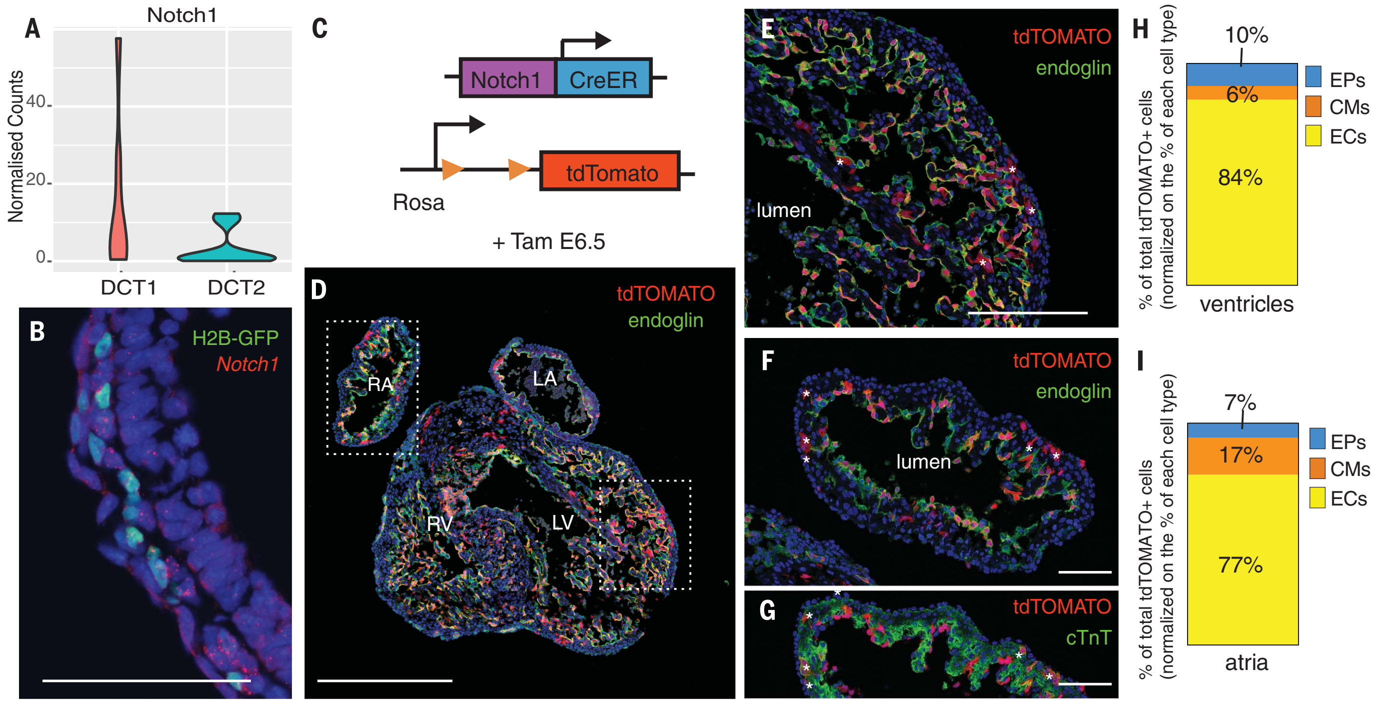

Fig. 4. Notch1 marks *Mesp1* progenitors committed to the endocardial fate. (**A**) Violin plot of *Notch1* expression in DCT1 and DCT2 cells. (**B**) *Notch1* RNA-FISH on a section of an E7.25 *Mesp1-rtTA/tetO-H2B-GFP* embryo. Scale bar, 50 μm. (**C**) Experimental strategy used for tracing *Notch1*-expressing cells at E6.5. (**D** to **G**) Confocal analysis of immunostaining for [(D) to (F)] endoglin (EC marker) and (G) cTNT (CM marker) of *Notch1-CreERT2/Rosa-tdTomato* heart sections at E12.5. (D) Lower magnification. Scale bar, 500 μm. Higher magnifications of the (E) LV and (G) RA showed that most tdTomato$^+$ cells are ECs, although rare CMs are also marked (asterisks). Scale bars, 200 μm. (**H** and **I**) Percentage of tdTomato$^+$ cells in ECs, CMs, and EPs in (H) the ventricles (7804 cells counted; *n* = 6 embryos from three different litters) and (I) the atria (4819 cells counted; *n* = 7 embryos from three different litters).

which is consistent with the presence of immature progenitors that undergo multilineage priming before making cell fate decision into either DCT3 or DCT4 lineages (fig. S11).

To more clearly differentiate between the putative differentiation paths to the DCT1/EC and DCT2/CM progenitors, we determined the genes involved in embryonic development that are specifically up- or down-regulated in a given DCT (fig. S12). Of particular interest, DCT2 cells showed reduced *Notch1* expression (Fig. 4A). Different studies have shown the importance of Notch1 in the latter stages of cardiovascular development, in regulating endocardium, valve formation, trabeculation, and myocardium compaction (*24*). However, a role for Notch in the early steps of cardiovascular lineage commitment during gastrulation has not been previously described. RNA-FISH and immunostaining showed that *Notch1* was indeed expressed and active in a subset of Mesp1-H2B-GFP$^+$ cells (Fig. 4B and fig. S13). To determine whether *Notch1* expression in DCT1 cluster marks *Mesp1*$^+$ CPs committed to the EC fate, we induced lineage tracing by administrating tamoxifen to *Notch1-CreERT2/Rosa-tdTomato* mice at E6.5 (*25*) and assessed the fate of marked cells at E12.5 (Fig. 4, C to G). tdTomato$^+$ cells in the ventricles were almost exclusively found in the EC (83.9 ± 3.0%), with minor contribution to the CM (6.0 ± 1.4%) and to the EPs (10.2 ± 2.1%) (Fig. 4H), which is consistent with the notion that DCT1 marks early *Mesp1/Notch1* double-positive CPs committed to the EC fate. In the atria, *Notch1-CreERT2* marked preferentially the ECs (76.9% ± 2.9), although a smaller contribution to the CM lineage was also observed (16.6% ± 2.7) (Fig. 4I), which is consistent with a lower expression of *Notch1* in DCT2 cluster. In addition to marking ECs of the heart, *Notch1-CreERT2*, similar to *Mesp1-Cre*, also marked, at the early stage of gastrulation, ECs of the aorta, intersomitic, and brain vessels (fig. S14).

Altogether, our single-cell profiling of early CPs shows that *Mesp1* CPs segregate rapidly from the epiblast into distinct cardiovascular lineages. The analysis of *Mesp1* KO cells showed that Mesp1 is required to exit the pluripotent state of the epiblast and promotes EMT, migration, and cardiovascular specification in vivo. Consistent with the early regional and lineage segregation found with clonal analysis (*4*, *5*), our scRNA-seq demonstrates that *Mesp1* CPs are also molecularly heterogeneous, as previously suggested by scRNA-seq during in vitro ESC differentiation (*26*), and identifies temporally and spatially distinct *Mesp1* subpopulations that likely correspond to CPs committed to the different cardiovascular lineages and regions of the heart at the early stages of gastrulation (fig. S15). Future studies will be required to determine whether the early cardiovascular lineage segregation uncovered here is also occurring for the other mesodermal and endodermal cells and whether defects in the early commitment steps are associated with congenital diseases and heart malformations. Last, our results will be important to design new strategies to direct the differentiation of ESC into a specific cardiovascular lineage.

REFERENCES AND NOTES

1. S. Martin-Puig, Z. Wang, K. R. Chien, *Cell Stem Cell* **2**, 320–331 (2008).
2. Y. Saga *et al.*, *Development* **126**, 3437–3447 (1999).
3. A. Bondue, C. Blanpain, *Circ. Res.* **107**, 1414–1427 (2010).
4. W. P. Devine, J. D. Wythe, M. George, K. Koshiba-Takeuchi, B. G. Bruneau, *eLife* **3**, e03848 (2014).
5. F. Lescroart *et al.*, *Nat. Cell Biol.* **16**, 829–840 (2014).
6. I. Harel *et al.*, *Dev. Cell* **16**, 822–832 (2009).
7. M. Buckingham, S. Meilhac, S. Zaffran, *Nat. Rev. Genet.* **6**, 826–835 (2005).
8. A. Scialdone *et al.*, *Nature* **535**, 289–293 (2016).
9. A. Bondue *et al.*, *Cell Stem Cell* **3**, 69–84 (2008).
10. G. Martello, A. Smith, *Annu. Rev. Cell Dev. Biol.* **30**, 647–675 (2014).
11. R. C. Lindsley *et al.*, *Cell Stem Cell* **3**, 55–68 (2008).
12. A. Bondue *et al.*, *J. Cell Biol.* **192**, 751–765 (2011).
13. S. J. Kattman *et al.*, *Cell Stem Cell* **8**, 228–240 (2011).
14. C. Weinreb, S. Wolock, A. Klein, *Bioinformatics* 10.1093/bioinformatics/btx792 (2017).
15. T. Behrens *et al.*, *BMC Cancer* **16**, 395 (2016).
16. S. Palencia-Desai *et al.*, *Development* **138**, 4721–4732 (2011).
17. R. M. Barnes, B. A. Firulli, S. J. Conway, J. W. Vincentz, A. B. Firulli, *Dev. Dyn.* **239**, 3086–3097 (2010).
18. T. M. Schultheiss, J. B. Burch, A. B. Lassar, *Genes Dev.* **11**, 451–462 (1997).
19. D. M. DeLaughter *et al.*, *Dev. Cell* **39**, 480–490 (2016).
20. T. Huynh, L. Chen, P. Terrell, A. Baldini, *Genesis* **45**, 470–475 (2007).
21. T. Kume, H. Jiang, J. M. Topczewska, B. L. Hogan, *Genes Dev.* **15**, 2470–2482 (2001).
22. N. Bertrand *et al.*, *Dev. Biol.* **353**, 266–274 (2011).
23. I. Harel *et al.*, *Proc. Natl. Acad. Sci. U.S.A.* **109**, 18839–18844 (2012).

24. D. MacGrogan, M. Nus, J. L. de la Pompa, *Curr. Top. Dev. Biol.* **92**, 333–365 (2010).
25. S. Fre *et al.*, *PLOS ONE* **6**, e25785 (2011).
26. S. S. Chan, H. H. W. Chan, M. Kyba, *Biochem. Biophys. Res. Commun.* **474**, 469–475 (2016).

ACKNOWLEDGMENTS

We thank the Light Microscopy Facility for help with confocal imaging and F. Hamey for help with SPRING analysis. F.L. has been supported by the Fonds de la Recherche Scientifique (FNRS), the European Molecular Biology Organization long-term fellowship, and the Leducq Fondation. Work in the Gottgens laboratory is supported by grants from the Wellcome, Bloodwise, Cancer Research UK, National Institute of Diabetes and Digestive and Kidney Diseases, and core support grants by the Wellcome to the Wellcome–Medical Research Council Cambridge Stem Cell Institute. C.B. is an investigator of WELBIO. Work in C.B.'s laboratory was supported by the FNRS, the Université Libre de Bruxelles Foundation, the European Research Council, the Bettencourt Schueller Foundation (C.B. and F.L.), and the Leducq Fondation as part of the network "22q11.2 deletion syndrome: Novel approaches to understand cardiopharyngeal pathogenesis."

SUPPLEMENTARY MATERIALS

www.sciencemag.org/content/359/6380/1177/suppl/DC1
Materials and Methods
Figs. S1 to S15
Tables S1 to S4
References (*27*–*50*)

18 July 2017; accepted 11 January 2018
Published online 25 January 2018
10.1126/science.aao4174

TECHNICAL COMMENT

PALEOANTHROPOLOGY

Comment on "The growth pattern of Neandertals, reconstructed from a juvenile skeleton from El Sidrón (Spain)"

Jeremy M. DeSilva

Rosas *et al*. (Reports, 22 September 2017, p. 1282) calculate El Sidrón J1 to have reached only 87.5% of its adult brain size. This finding is based on an overestimation of Neandertal brain size. Pairwise comparisons with a larger sample of Neandertal fossils reveal that it is unlikely that the brain of El Sidrón would have grown appreciably larger.

Rosas *et al.* (*1*) are to be congratulated for their discovery and whole-body analysis of El Sidrón J1—an important addition to our understanding of Neandertal paleobiology, growth, and development. Although Rosas *et al.* present a rich, whole-body treatment of El Sidrón J1, an emphasis was made in the paper—and widely reported by the science media (*2*)—that at 7.7 years of age, this individual had only achieved 87.5% of its total brain volume and was therefore still growing its brain. This finding would be quite extraordinary, given that 95% of brain growth is achieved in modern human children by the age of 6 to 7 years (*3*, *4*).

The cranial capacity estimated for El Sidrón J1 is 1330 cc (*1*). Careful and clever analysis of bone surface remodeling on the J1 occipital demonstrates that this region of the skull was still osteogenic, consistent with the juvenile status of the individual. The relationship between occipital remodeling and the magnitude of remaining brain growth is unknown, however. Future work examining whether evidence for occipital remodeling is present in juvenile modern humans or Neandertals who are >8 years old (e.g., Teshik-Tash, Le Moustier 1) and have reached adult brain volume will be informative. The authors propose that only 87.5% of full brain capacity had been reached in El Sidrón J1 on the basis of a Neandertal adult brain volume of 1520 cc (*1*). This adult value is an overestimate.

The use of 1520 cc for adult Neandertal brain size is explained as an average of five different studies [table S32 of (*1*)]. The largest adult cranial capacity average used to create this consensus value (*5*) is an average of only six adult Neandertal crania (Amud, Shanidar 5, La Ferrassie, La Chapelle, Spy 2, Tabun C1), which also happen to possess some of the largest brain sizes of the known Neandertals (Table 1). The lowest of the average Neandertal cranial capacities (1494 cc) used to create the consensus average derives from a source that restricts its analysis to nine Würm Neandertals (*6*). However, there is a math error in that paper, and the average of the listed cranial capacities should have been 1468.7 cc, not 1494 cc. Additionally, using values from Holloway *et al.* (*7*) for those Neandertals would result in an average cranial capacity of 1438.3 cc. A third value of 1498 cc, based on Holloway *et al.*, is used to generate the consensus average (*1*). In Holloway *et al.*, an average for *Homo sapiens neanderthalensis* is reported as 1487.5 ml in appendix I and 1427.2 ml in appendix II. The 1427.2-ml value is almost identical (1428 ml) to the average of reported adult values in the text of Holloway *et al.* However, Holloway *et al.* also attribute fossils typically assigned to *Homo sapiens* [Jebel Ihroud ($n = 2$) and Skhul ($n = 4$)] to Neandertals. When these are removed, the average Neandertal adult cranial capacity in Holloway *et al.* is 1414.8 ml. Given these problems with the values used to generate the consensus average of cranial capacity in adult Neandertals, it is necessary to recalculate the likely percentage of adult brain size achieved by the El Sidrón juvenile.

When all adult crania assigned to Neandertals ($n = 26$) are used (Table 1), the average adult brain size is 1388 cc, and the El Sidrón juvenile had reached 97.4 ± 12.6% of its full growth. When those crania listed specifically in table S32 of (*1*) are used, the average adult Neandertal brain is 1438 cc and the El Sidrón juvenile had reached 94 ± 12.6% of its adult cranial capacity. To account for temporal changes in Neandertal cranial capacity (Fig. 1), it is reasonable to only use crania from the later (<115,000 years ago) Würm Neandertals, which average 1459 cc. Using this value, the El Sidrón juvenile had achieved 92.5 ± 12.0% of its full growth. However, because the dimensions of Krapina 1 are used to help reconstruct the El Sidrón J1 cranium (*1*), it would make sense to include the Krapina fossils as well, in which case the average Neandertal adult brain was 1437 cc and El Sidrón J1 had reached 93.9 ± 11.8% of its brain growth.

Note that in every case, El Sidrón J1 is within the 95% confidence interval of the mean for 100%

Department of Anthropology, Dartmouth College, Hanover, NH, USA. **Email: jeremy.m.desilva@dartmouth.edu**

Fig. 1. Neandertal brain size evolution. Adult cranial capacity is known for 26 Neandertals (blue circles). Notice that there is a slight but statistically significant ($r = 0.49$, $P = 0.006$) increase in brain size over the course of Neandertal evolution. El Sidrón J1 (red ×) falls comfortably within the range of adult cranial capacities in late Würm Neandertals.

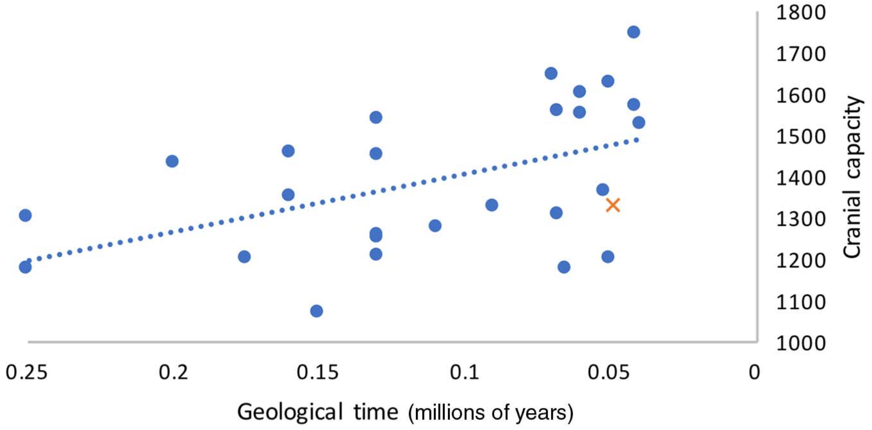

brain growth (Fig. 2). The only statistically supported way in which the El Sidrón juvenile could be used as evidence for continued brain growth in a 7.7-year-old Neandertal is if his cranial capacity (1330 cc) is compared exclusively with the largest half of the Würm Neandertals. Accurately identifying the sex of Neandertal crania is fraught with challenges, and using just the largest-brained Neandertals as a comparative male sample biases the results and borders on circular reasoning. Given both spatial and temporal variation in Neandertal brain size, I would recommend caution in inferring Neandertal brain ontogeny from El Sidrón J1 until the average adult brain size in this specific population of Neandertals at El Sidrón is better understood.

There is inherent error in using isolated specimens and cross-sectional data to infer longitudinal patterns. Therefore, attempts to reconstruct the pattern of Neandertal brain growth should incorporate all of the available data. Consider, for instance, that the ~3-year-olds (*8*) Roc de Marsal (1325 cc) and Engis 2 (1362 cc) have brain sizes similar to, or slightly larger than, El Sidrón J1. The 4.6-year-old Devil's Tower child (*8*) has a cranial capacity of 1400 cc, exceeding that found in the developmentally older El Sidrón J1. These specimens should not be used to argue for early cessation of Neandertal brain growth any more than El Sidrón J1 can be used for extended brain growth. Instead, when all of the currently available data are plotted (Fig. 3), Neandertals and modern humans present very similar brain growth curves. Neandertals therefore probably did experience human-like extended brain ontogeny [(*9*), but see (*10*)]. On the basis of the evidence currently available, it is quite likely that El Sidrón J1 had very nearly reached his full brain volume.

Table 1. Neandertal cranial capacities. Würm Neandertals (living <115,000 years ago) are in italics. Cranial capacities are from (*1*, *7*, *11*–*13*).

Specimen	Cranial capacity	Developmental age	Percent of El Sidrón juvenile cranial capacity
Saccopastore 1	1174	Adult	113.3
Saccopastore 2	1300	Adult	102.3
Reilingen	1430	Adult	93.0
Biache	1200	Adult	110.8
Apidima 2	1454	Adult	91.5
Fontechevade II	1350	Adult	98.5
La Chaise	1065	Adult	124.9
Lazaret	1250	Subadult	106.4
Krapina 1	1293	6 to 8 years	—
Krapina 2	1450	Subadult	91.7
Krapina 3	1255	Adult	106.0
Krapina 5	1535	Adult	86.6
Krapina 6	1205	Adult	110.4
Tabun C1	1271	Adult	104.6
Subalyuk	1187	3.2 years	—
Ganovce	1320	Adult	100.8
Teshik-Tash	1525	~9 years	—
Roc de Marsal	1325	3 years	—
La Ferrassie	1640	Adult	81.1
Spy I	1305	Adult	101.9
Spy II	1553	Adult	85.6
La Quina 5	1172	Adult	113.5
La Quina 18	1200	6 to 8 years	—
Mezmaiskaya	429	Infant	—
Engis 2	1362	3.2 years	—
Shanidar 1	1600	Adult	83.1
Shanidar 5	1550	Adult	85.8
Monte Circeo	1360	Adult	97.8
Gibraltar–Devil's Tower	1400	4.6 years	—
Gibraltar–Forbes Quarry	1200	Adult	110.8
La Chapelle	1625	Adult	81.9
El Sidrón J1	1330	7.7 years	—
Dederiyeh 1	1096	1.55 years	—
Dederiyeh 2	1089	2.0 years	—
Pech de l'Aze	1135	2.5 years	—
Amud	1740	Adult	76.4
Le Moustier 1	1565	Subadult	85.0
Le Moustier 2	418	Infant	—
Feldhofer	1525	Adult	87.2

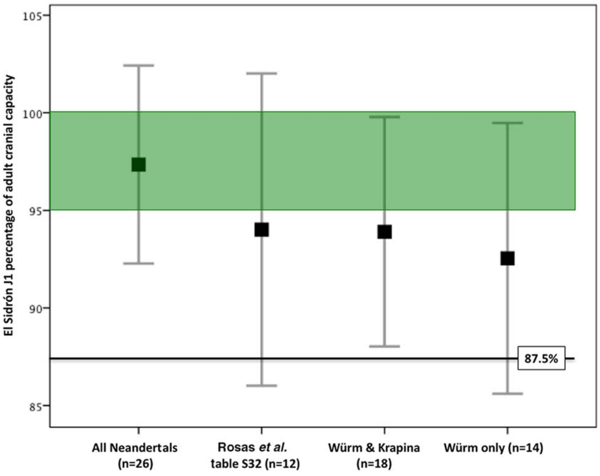

Fig. 2. El Sidrón J1 relative brain size. The cranial capacity of El Sidrón (1330 cc) was divided by all adult Neandertal cranial capacities to calculate a percentage of adult brain size achieved by the age of the individual's death (7.7 years). The mean value (black square) is plotted along with the 95% confidence interval of the mean (gray bars). Note that the percentage of brain size achieved at death in a similarly aged modern human (95 to 100%; green highlighted range) either encompasses the mean (for all Neandertals) or very nearly does. These data suggest that El Sidrón J1 had achieved significantly more of its adult cranial capacity than the 87.5% reported by Rosas *et al*. (*1*), and likely had little remaining brain growth.

REFERENCES

1. A. Rosas *et al*., *Science* **357**, 1282–1287 (2017).
2. N. St. Fleur, "For Neanderthals, growing big brains took more time." *New York Times* (21 September 2017).
3. A. S. Dekaban, D. Sadowsky, *Ann. Neurol.* **4**, 345–356 (1978).
4. R. K. Lenroot, J. N. Giedd, *Neurosci. Biobehav. Rev.* **30**, 718–729 (2006).
5. J. L. Arsuaga *et al*., *Proc. Natl. Acad. Sci. U.S.A.* **112**, 11524–11529 (2015).
6. J. D. Hawks, M. H. Wolpoff, *Evolution* **55**, 1474–1485 (2001).

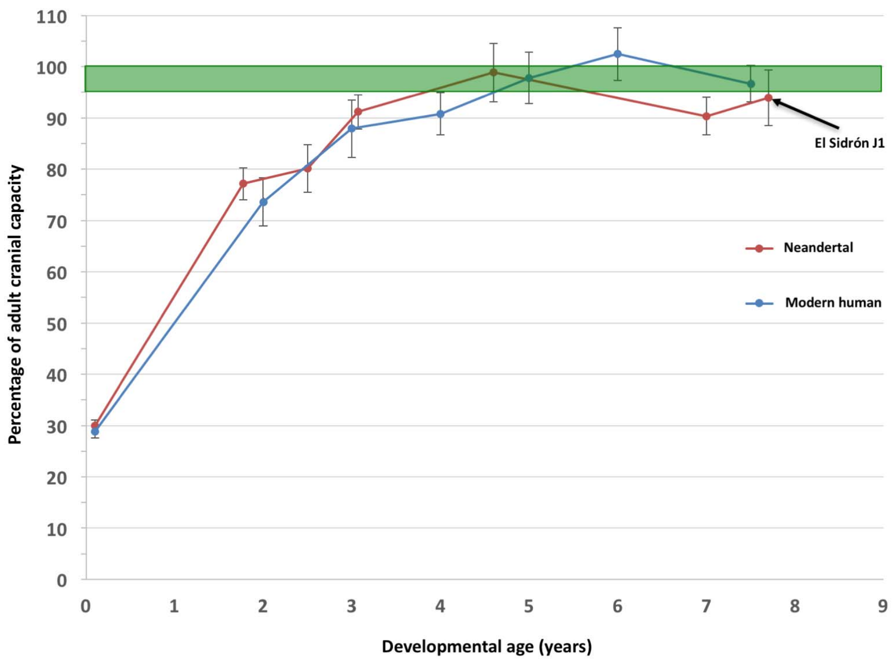

Fig. 3. Neandertal brain ontogeny. El Sidrón J1 is one of 13 known juvenile Neandertal crania (Table 1). Developmental ages of these individuals were based on data in (*1*, *8*, *13*, *14*). These juvenile cranial capacities were each divided by the 18 Würm + Krapina adult cranial capacities to calculate a Neandertal brain growth curve. Error bars indicate 95% confidence interval of the mean of the percentage of brain growth achieved by that chronological age in Neandertals and modern humans. Human data were drawn from (*15*). Notice the similarities between human and Neandertal brain development [see also (*9*)]. Although El Sidrón J1 is slightly smaller than expected, in this broader context it appears best interpreted as normal variation in Neandertals. Accepting the premise that El Sidrón J1 (at age 7.7 years) is evidence for extended brain growth in the Neandertals would also necessitate accepting that Neandertals essentially ceased brain growth between the ages of 3 and 7.7 years, only to resume again.

7. R. L. Holloway, D. C. Broadfield, M. S. Yuan, *The Human Fossil Record, Volume 3: Brain Endocasts—The Paleoneurological Evidence* (Wiley, 2004).
8. H. Coqueugniot, J. J. Hublin, *Period. Biol.* **109**, 379–385 (2007).
9. M. S. Ponce de León, T. Bienvenu, T. Akazawa, C. P. E. Zollikofer, *Curr. Biol.* **26**, R665–R666 (2016).
10. P. Gunz, S. Neubauer, B. Maureille, J.-J. Hublin, *Curr. Biol.* **20**, R921–R922 (2010).
11. K. Harvati, C. Stringer, P. Karkanas, *J. Hum. Evol.* **60**, 246–250 (2011).
12. R. Caspari, J. Radovcić, *Am. J. Phys. Anthropol.* **130**, 294–307 (2006).
13. M. S. Ponce de León *et al.*, *Proc. Natl. Acad. Sci. U.S.A.* **105**, 13764–13768 (2008).
14. T. M. Smith *et al.*, *Proc. Natl. Acad. Sci. U.S.A.* **107**, 20923–20928 (2010).
15. F. Marchand, *Über das Hirngewicht des Menschen* (Teubner, Leipzig, 1902).

30 October 2017; accepted 17 January 2018
10.1126/science.aar3611

TECHNICAL RESPONSE

PALEOANTHROPOLOGY

Response to Comment on "The growth pattern of Neandertals, reconstructed from a juvenile skeleton from El Sidrón (Spain)"

Antonio Rosas,[1]*† Luis Ríos,[1,2]† Almudena Estalrrich,[1,3] Helen Liversidge,[4] Antonio García-Tabernero,[1] Rosa Huguet,[5] Hugo Cardoso,[6] Markus Bastir,[1] Carles Lalueza-Fox,[7] Marco de la Rasilla,[8] Christopher Dean[9]

The comment by DeSilva challenges our suggestion that brain growth of the El Sidrón J1 Neandertal was still incomplete at 7.7 years of age. Evidence suggests that endocranial volume is likely to represent less than 90% adult size at El Sidrón as well as Neandertal male plus Krapina samples, in line with further evidence from endocranial surface histology and dural sinus groove size.

DeSilva (*1*) challenges one of several conclusions we drew from the analysis of the El Sidrón J1 skeleton (*2*)—namely, the suggestion that the brain of this juvenile Neandertal was still growing at the time of his death (7.7 years old). The main objective of our research on the El Sidrón J1 skeleton was to present a study of growth and maturation of a Neandertal juvenile from an organismic perspective, rather than focusing on one specific region or system such as the dentition or cranium. DeSilva (*1*) seems to agree that we presented a "rich, whole-body treatment of El Sidrón J1," although he then writes that "an emphasis was made in the paper—and widely reported by the science media (*2*)—that at 7.7 years of age, this individual had only achieved 87.5% of its total brain volume, and was therefore still growing its brain."

We would prefer to limit our response to the findings and interpretations that we presented in the report, without reference to the remarks expressed and emphasized in the media. Basically, we do not agree that undue emphasis was made in the paper regarding an extended period of brain growth in Neandertals based on the estimation of the endocranial volume (EV), which is the variable studied by DeSilva. We studied the pattern of growth and maturation of the teeth, postcranium, spine, body, and cranium. For the latter, we considered three types of information: surface histology, the size of the dural sinus grooves, and the EV. What we really emphasized were the following points: (i) The growth and maturation of the dentition and postcranium fell well within the modern human range, and thus we did not observe a fundamental difference in the overall pace of growth in comparison with modern humans. (ii) One divergent aspect of ontogeny is the timing of maturation of the spine. (iii) On the basis of the three types of aforementioned observations, the brain of El Sidrón J1 could still be growing. (iv) The maturation of the spine, together with ongoing brain growth, could point to an extended period of growth and maturation of the neuraxis.

The review of EV estimations in Neandertals by DeSilva contributes to the ongoing debate about the rate and duration of EV growth in Neandertal ontogeny (*3*, *4*). Variation in sample size, accuracy, and comparability of different measurement techniques of EV remains an issue in all comparative studies of Neandertals. For the sake of clarity, we address the questions raised by DeSilva using only the values of EV provided by him (*1*). DeSilva presents successive different combinations of specimens in order to provide Neandertal averages. It is interesting to note that as we restrict the initial Neandertal sample accordingly to fit the characteristics of the El Sidrón sample, the percentage of adult EV attained by El Sidrón J1 decreases, as shown in Table 1. When the five male Würm Neandertal specimens are considered, the percentage of adult EV attained by El Sidrón J1 would be 81.79%. According to DeSilva, to restrict the comparison to adult male Neandertals is questionable because of problems with sex estimation, and although we agree with this general concern in paleoanthropology, we offer this comparison in order to present the whole range of possible estimations. We also agree with DeSilva that the Krapina fossils could be included in the reference sample for methodological reasons, and in this case (Würm males and Krapina adults), the percentage of adult EV attained by El Sidrón J1 would be 87.7%. If we consider all the comparisons included in Table 1, the average of percentage adult size attained by El Sidrón J1 is 90.67%.

In addition to this debate focused on direct estimations of EV, in our report we also included a second method for estimating the EV derived from the isolated occipital bone, which we briefly summarize here. A significant lineal relationship was found between the size of the occipital bone (geometric morphometric centroid size) and the endocranial volume in modern humans ($n = 20$; $y = 104.8581x - 243.6349$; $P = 0.0016$; $r = 0.6736$; $r^2 = 0.4537$). The fitted lineal function in seven mostly male Würm Neandertals ($y = 153.56x - 953.5652$; $P = 0.0598$; $r = 0.7350$; $r^2 = 0.5403$; table S33 in our report) yields a Neandertal adult mean ± 2SD of 1499 ± 270 cm^3. The predicted value of 1253.2 cm^3 for El Sidrón J1 (specimen SD-2300) lies at the lower end of this interval (1228.6 to 1769.4 cm^3), whereas the value of 1448 cm^3 for El Sidrón adult occipital SD-1219 is close to the mean. The EV of El Sidrón J1 estimated by this method represents 86.5% of the adult occipital from El Sidrón (SD-1219). With

Table 1. Neandertal endocranial volumes and percentage of adult size attained by El Sidrón J1. All values come from DeSilva (*1*).

Sample	EV (cm^3)	Percentage of El Sidrón J1
DeSilva table 1	1388	97.4
Rosas *et al*. table S32 with DeSilva values	1438	94
Würm	1459	92.5
Würm and Krapina	1437	93.9
Male Würm	1626	81.79
Male Würm and Krapina	1515	87.7

---

[1] Paleoanthropology Group, Department of Paleobiology, Museo Nacional de Ciencias Naturales–CSIC, 28006 Madrid, Spain. [2] Department of Physical Anthropology, Aranzadi Society of Sciences, 20014 Donostia–San Sebastián, Gipuzkoa, Spain. [3] Department of Paleoanthropology, Senckenberg Research Institute and Natural History Museum Frankfurt, 60325 Frankfurt, Germany. [4] Institute of Dentistry, Queen Mary University of London, London E1 2AD, UK. [5] Institut Català de Paleoecologia Humana i Evolució Social (IPHES)–Unidad Asociada al CSIC, Campus Sescelades (Edifici W3), Universitat Rovira i Virgili, 43007 Tarragona, Spain. [6] Department of Archaeology, Simon Fraser University, Burnaby, British Columbia V5A 1S6, Canada. [7] Institute of Evolutionary Biology (CSIC-UPF), 08003 Barcelona, Spain. [8] Área de Prehistoria Departamento de Historia, Universidad de Oviedo, 33011 Oviedo, Spain. [9] Department of Cell and Developmental Biology, University College London, London WC1E 6BT, UK.
***Corresponding author. Email: arosas@mncn.csic.es**
†These authors contributed equally to this work.

the data used, the predicted value for J1 would be unlikely for an adult Neandertal male, although it is clear that predictions derived from this method must be considered as relative estimations of EV.

As mentioned, beyond the discussion on EV, we supported our suggestion of ongoing brain growth with other observations. The presence in El Sidrón J1 of inner occipital resorption areas, the smallest widths of the dural sinuses in a large hominin sample, and extremely fresh neural relieves are not conclusive by themselves, but they support our interpretation of potential continued brain growth. When considered together with the observations on spine maturation, we suggested that Neandertal neural growth and maturation might be extended in comparison with modern humans.

We agree that using isolated specimens and cross-sectional data is not the best methodology to infer growth and maturation—a problem that pervades paleoanthropology. Our study surely is a first step toward a more comprehensive understanding of the absence or presence of ontogenetic differences between two *Homo* species that successfully interbred. Detecting any potential differences with certainty will probably require the complete analysis of many Neandertal subadult skeletons, both known and yet to be discovered.

REFERENCES

1. J. DeSilva, *Science* **359**, eaar3611 (2018).
2. A. Rosas *et al.*, *Science* **357**, 1282–1287 (2017).
3. M. S. Ponce de León, T. Bienvenu, T. Akazawa, C. P. E. Zollikofer, *Curr. Biol.* **26**, R665–R666 (2016).
4. P. Gunz, S. Neubauer, B. Maureille, J.-J. Hublin, *Curr. Biol.* **20**, R921–R922 (2010).

15 November 2017; accepted 17 January 2018
10.1126/science.aar3820

The International Cosmos Prize

The Harmonious Coexistence between Nature and Mankind

To carry on and further develop the philosophy of "The Harmonious Coexistence between Nature and Mankind" presented at the International Garden and Greenery Exposition, Osaka, Japan, 1990 (Expo'90), the International Cosmos Prize recognizes outstanding research activities and achievements both in Japan and abroad that are in line with this philosophy.

The award ceremony is held every autumn in Osaka, Japan. The prizewinner is awarded a monetary prize of 40 million yen.

2017 Prizewinner

Dr. Jane Goodall **Founder, Jane Goodall Institute**

Dr. Goodall has been studying wild chimpanzees since 1960 so as to paint a fuller picture of chimpanzees. She has conducted afforestation programs to provide habitats for chimpanzees, and an environmental educational project. She began Roots & Shoots, environmental learning program by young people. More than 150,000 groups are actively working in 99 countries under this program.

Prizewinner 2012~2016

2012

Dr. Edward Osborne Wilson
Nationality : U.S.A.

2013

Dr. Robert Treat Paine
Nationality : U.S.A.

2014

Dr. Philippe Descola
Nationality : France

2015

Dr. Johan Rockström
Nationality : Sweden

2016

Dr. Kunio Iwatsuki
Nationality : Japan

WHO WILL BE THE NEXT PRIZEWINNER?
We are now calling for recommendations for the 2018 International Cosmos Prize!

If you have a candidate whom you would like to recommend, please e-mail us at the address below.
We will send you a recommendation form (in Microsoft Word). The deadline for recommendations is April 15.
EXPO '90 FOUNDATION **E-mail: rec-cosmos@expo-cosmos.or.jp**

WASEDA
University

Waseda University pushes forward with global academic network

Innovative programs and prioritized funding have propelled Waseda University to record highs in world university rankings, underscoring the university's reputation for openness, dynamism, and diversity.

Borderless education and research for energy solutions

—Energy and Nanomaterials

In order to nurture students who will play leading roles in addressing major issues related to energy—its production, storage, and sustainable use—**Hiroyuki Nishide, head of Energy and Nanomaterials Unit,** has initiated major changes to internationalize administrative, education, and research policies at Waseda University.

"Energy problems cannot be resolved by any one country or individual institute," says Nishide. "The Top Global University (TGU) Project offers the perfect opportunity to launch borderless education and research programs at Waseda University to educate the energy experts of the future."

The Joint Supervision Program (JSP), the first to be established at Waseda, and Joint Appointment (JA), a new personnel system, lie at the heart of the new global education and research programs initiated by Nishide.

Students in JSP receive guidance from advisors at both Waseda and one of its partner universities: Monash University, Korea University, or the University of Bonn. A certificate from both universities is awarded upon completion of the program. "The first three graduates from this program have found excellent jobs at blue chip companies with good salaries," Nishide says. Waseda is now expanding this framework to universities in Sweden and the United States.


Hiroyuki Nishide

"Importantly, our new personnel hiring policies have enabled 'joint appointments' of researchers from countries such as Italy, Sweden, and the United States, who teach at Waseda and conduct research with our students," adds Nishide. This approach has resulted in joint research and publications, as well as a joint appointment faculty member who obtained a tenured position.

Such an open approach underscores Waseda University's commitment to maintaining global standards of education and research. These initiatives have also led to more joint publications and higher citations—important factors in assessing international competitiveness.

Recent research in the unit includes the development of innovative nanomaterials for storing hydrogen using so-called ketone polymers.[1] "These findings enable the safe and robust transport of hydrogen," says Nishide. "You can carry hydrogen in your pocket!"

[1] R. Kato *et al., Nat. Comm.* **7**, 13032 (2016), doi: 10.1038/ncomms13032.

Energy and Nanomaterials Unit
www.waseda.jp/inst/sgu/en/unit/new-horizon-materials-for-life-and-energy-devices

Japanese culture from a global perspective

—Global Japanese Studies


Hirokazu Toeda

Waseda University has built on its tradition of disseminating research on Japanese arts and culture, as demonstrated by alumnus Ryusaku Tsunoda (1877–1964), who played a major role in introducing Japanese culture to the world during his tenure at Columbia University.

"Inspired by such figures, our unit reexamines Japanese culture from a genuinely global perspective by developing institutional hubs," says **Hirokazu Toeda, head of the Global Japanese Studies Unit.** Currently, we are working with Columbia University and the University of California, Los Angeles (UCLA) to establish the World Academia Alliance in Japanese Studies (WAAJS), which will enable the smooth exchange of knowledge and people between institutes. Ultimately, we want to create an international model for Japanese Studies."

Other recent activities by the unit include creating bilingual publications, such as *Censorship, Media and Literary Culture in Japan: From Edo to Postwar*, running a double-degree program with Columbia University's Department of East Asian Languages and Cultures, and launching English-based undergraduate and graduate programs: the Global Studies in Japanese Cultures Program (JCulP), and Global Japanese Literary and Cultural Studies (Global-J).

Additionally, a partnership between Waseda, UCLA, and the Tadashi Yanai Initiative for Globalizing Japanese Humanities used innovative technology to develop an application for teaching nonstandard Japanese *hentaigana* characters. The application is expected to have lasting impact, both domestically and abroad, on scholars of Japanese literature.

"We have also recently organized a series of events at UCLA, celebrating the traditional Japanese performing art of *kyogen*," Toeda says. "We hope to continue contributing to cultural diversity in the world by sharing what Japanese arts and culture has to offer."

Global Japanese Studies Unit
www.waseda.jp/inst/sgu/en/unit/gjs

Look out for more news from Waseda University in the March 16 and 23 issues of *Science*. www.sciencemag.org/advertorials

eppendorf
& Science
PRIZE FOR
NEURO
BIOLOGY

2017 Winner
Flavio Donato, Ph.D.
Kavli Institute
Norwegian University of
Science and Technology

For research on how neural networks mature during development to represent space in the brain

Application Deadline
June 15, 2018

Call for Entries

Eppendorf & Science Prize for Neurobiology
The annual Eppendorf & Science Prize for Neurobiology is an international award which honors young scientists for their outstanding contributions to neurobiological research based on methods of molecular and cell biology. The winner and finalists are selected by a committee of independent scientists, chaired by *Science's* Senior Editor, Dr. Peter Stern. To be eligible, you must be 35 years of age or younger.

As the Grand Prize Winner, you could be next to receive
> Prize money of US$25,000
> Publication of your work in *Science*
> Full support to attend the Prize Ceremony held in conjunction with the Annual Meeting of the Society for Neuroscience in the USA
> 10-year AAAS membership and online subscription to *Science*
> Complimentary products worth US$1,000 from Eppendorf
> An invitation to visit Eppendorf in Hamburg, Germany

It's easy to apply! Learn more at:

www.eppendorf.com/prize

eppendorf Science AAAS

AAAS® and Science® are registered trademarks of the American Association for the Advancement of Science, USA. Eppendorf® and the Eppendorf Brand Design are registered trademarks of Eppendorf AG, Germany. All rights reserved, including graphics and images. Copyright © 2018 by Eppendorf AG. Kurstin Roe Photography.

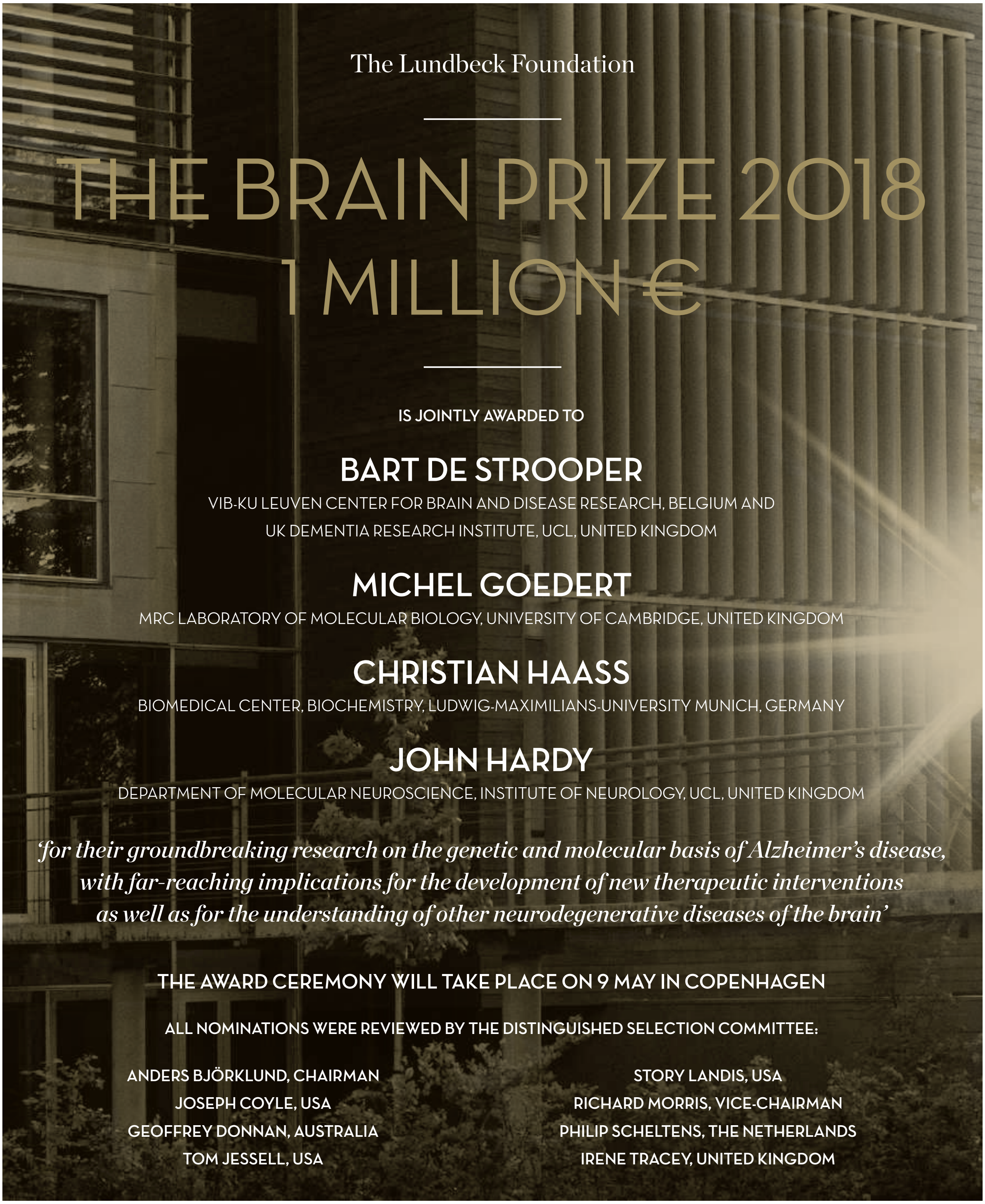

The Lundbeck Foundation

THE BRAIN PRIZE 2018
1 MILLION €

IS JOINTLY AWARDED TO

BART DE STROOPER

VIB-KU LEUVEN CENTER FOR BRAIN AND DISEASE RESEARCH, BELGIUM AND
UK DEMENTIA RESEARCH INSTITUTE, UCL, UNITED KINGDOM

MICHEL GOEDERT

MRC LABORATORY OF MOLECULAR BIOLOGY, UNIVERSITY OF CAMBRIDGE, UNITED KINGDOM

CHRISTIAN HAASS

BIOMEDICAL CENTER, BIOCHEMISTRY, LUDWIG-MAXIMILIANS-UNIVERSITY MUNICH, GERMANY

JOHN HARDY

DEPARTMENT OF MOLECULAR NEUROSCIENCE, INSTITUTE OF NEUROLOGY, UCL, UNITED KINGDOM

'for their groundbreaking research on the genetic and molecular basis of Alzheimer's disease, with far-reaching implications for the development of new therapeutic interventions as well as for the understanding of other neurodegenerative diseases of the brain'

THE AWARD CEREMONY WILL TAKE PLACE ON 9 MAY IN COPENHAGEN

ALL NOMINATIONS WERE REVIEWED BY THE DISTINGUISHED SELECTION COMMITTEE:

ANDERS BJÖRKLUND, CHAIRMAN
JOSEPH COYLE, USA
GEOFFREY DONNAN, AUSTRALIA
TOM JESSELL, USA

STORY LANDIS, USA
RICHARD MORRIS, VICE-CHAIRMAN
PHILIP SCHELTENS, THE NETHERLANDS
IRENE TRACEY, UNITED KINGDOM

THE BRAIN PRIZE

Born European and awarded in Denmark, The Brain Prize recognizes and rewards outstanding contributions to neuroscience, from basic to clinical

new products: DNA/RNA analysis

Automated Single-Cell Transfection
The NanoFountain Probe Electroporation system (NFP-E) performs automated, precise, and efficient delivery of molecules inside cells. A high-resolution, 3-axis robotic arm with feedback control, which is integrated to an inverted optical microscope, brings a sterile glass probe into contact with individual adherent cells cultured on standard dishes or multiwell plates. The NFP-E uses localized low-voltage electric fields to open transient pores on the cell membrane and transport proteins and/or nucleic acids inside the cell. Through image acquisition and proprietary hardware/software, the system exhibits point-click-transfect capabilities, which means that cells can be selected with the click of a mouse and the system will transfect all targeted cells automatically at a rate of 15 cells/min. The NFP-E is an ideal solution for cell-specific gene editing, clonal cell line generation, hard-to-transfect cells, pathway analysis, and drug screening.
Infinitesimal LLC
For info: 224-251-8192
www.infinitesimal-llc.com

CRISPR Libraries
DESKGEN Series CRISPR Libraries support gene editing efforts in academic and biopharma settings. The series consists of six new CRISPR library products, each of which can be tailored to an investigator's list of genomic targets using any delivery method. Disrupt Libraries can be used to functionally knock out genes to reveal novel druggable targets and essential pathways. Tile Libraries saturate coding and noncoding regions to reveal genotype–phenotype relationships. SNP-In Libraries allow high-throughput insertion and deletion knockins across the genome. Interfere Libraries silence target gene expression with CRISPR interference (CRISPRi). Activate Libraries allow overexpression of target genes with CRISPR activation (CRISPRa). Predict Libraries provide a unique scoring algorithm optimized for teams working on specific model cell lines or organisms, enabling other libraries to be designed more effectively.
Desktop Genetics
For info: +44-(0)-207-078-7291
www.deskgen.com/landing

Custom mRNAs
AMS Biotechnology (AMSBIO) provides custom-designed, highly modified mRNAs prepared by an advantageous in vitro transcription methodology. Traditional approaches for engineering changes in cellular expression profiles have employed mostly DNA- or RNA-based viral and nonviral vectors. Unfortunately, these methods carry high risks due to genomic integration with permanent genetic alteration of cells, and safety and ethical concerns relating to the use of DNA-based vectors in human clinical therapy. Until recently, concerns about RNA degradation problems have halted widespread use. The AMSBIO custom synthetic mRNA service uses Ψ-containing mRNA, which is translated more efficiently than its unmodified counterpart, and results in higher protein expression while reducing the innate antiviral response. This service includes synthesis of synthetic DNA; plasmid cloning; purification; full DNA sequencing documentation; PCR amplification of insert; and subsequent RNA synthesis by in vitro transcription, purification, and characterization. AMSBIO synthetic mRNA is made to research grade for development applications and to Good Manufacturing Practice grade for cell therapy.
AMS Biotechnology
For info: 617-945-5033
www.amsbio.com/highly-modified-mrna.aspx

DNA Library Prep Kit
Do you need a faster, more reliable solution for DNA fragmentation and library construction? The NEBNext Ultra II FS DNA Library Prep Kit meets the dual challenge of generating superior NGS libraries from ever-decreasing input amounts and providing simple scalability. Enzymatic shearing increases library yields by reducing DNA damage and sample loss. Our new fragmentation reagent is also combined with end repair and deoxyadenosine (dA)-tailing reagents, and a single protocol is used for the full range of input amounts (100 pg–500 ng) and guanine–cytosine content. You'll be thrilled to pieces with the result—a reliable, flexible, high-quality library prep that is fast and scalable.
New England BioLabs
For info: 800-632-5227
www.neb.com

DNA Centrifugal Sample Concentrator
Genevac's miVac DNA centrifugal sample concentrator is designed to efficiently remove water and organic solvents from biological samples containing nucleic acids. The compact benchtop system includes a built-in high-performance vacuum pump, concentration chamber with electromagnetic drive for quiet, maintenance-free operation, and a fixed aluminum rotor for microcentrifuge tubes. To use the system, simply position it on your lab bench, connect the power lead and exhaust tube, and start benefiting from fast, trouble-free nucleic acid concentration. A clear acrylic lid allows you to monitor progress and is specially treated with a novel coating to resist the most aggressive chemicals and solvents. Experimental parameters including concentration time and temperature can be easily selected and set using the intuitive dial and display system. To improve performance and productivity, Genevac has developed built-in special operating modes for removing water and alcohols—the most common solvents encountered when concentrating nucleic acid samples.
SP Scientific
For info: 845-255-5000
www.spscientific.com

Agarose Tablets
Midori Green Advance Agarose Tablets are a fast, clean solution for preparing agarose gels without any additional time-consuming steps, such as weighing or adding different components. Just add the tablet to pure cold water, heat, and pour. Once the gel hardens, it's ready for loading. Each tablet contains the perfect amount of Midori Green Advance DNA Stain, TBE (Tris-Borate-EDTA) powder, and 0.5 g of the highest-purity agarose—you don't need anything else but water. If you're tired of prepping agarose gels for your lab, this is the quickest, easiest solution to reduce effort and improve the quality of your gels. Midori Green Advance Nucleic Acid Stain is a new, safe alternative to traditional ethidium bromide (EtBr) stain for detecting double-stranded DNA, single-stranded DNA, and RNA in agarose gels. Most importantly, Midori Green is not considered hazardous waste, and can be disposed of according to standard laboratory procedures.
Bulldog Bio
For info: 603-570-4248
www.bulldog-bio.com/midori_green_agarose_tablets.html

Electronically submit your new product description or product literature information! Go to www.sciencemag.org/about/new-products-section for more information.

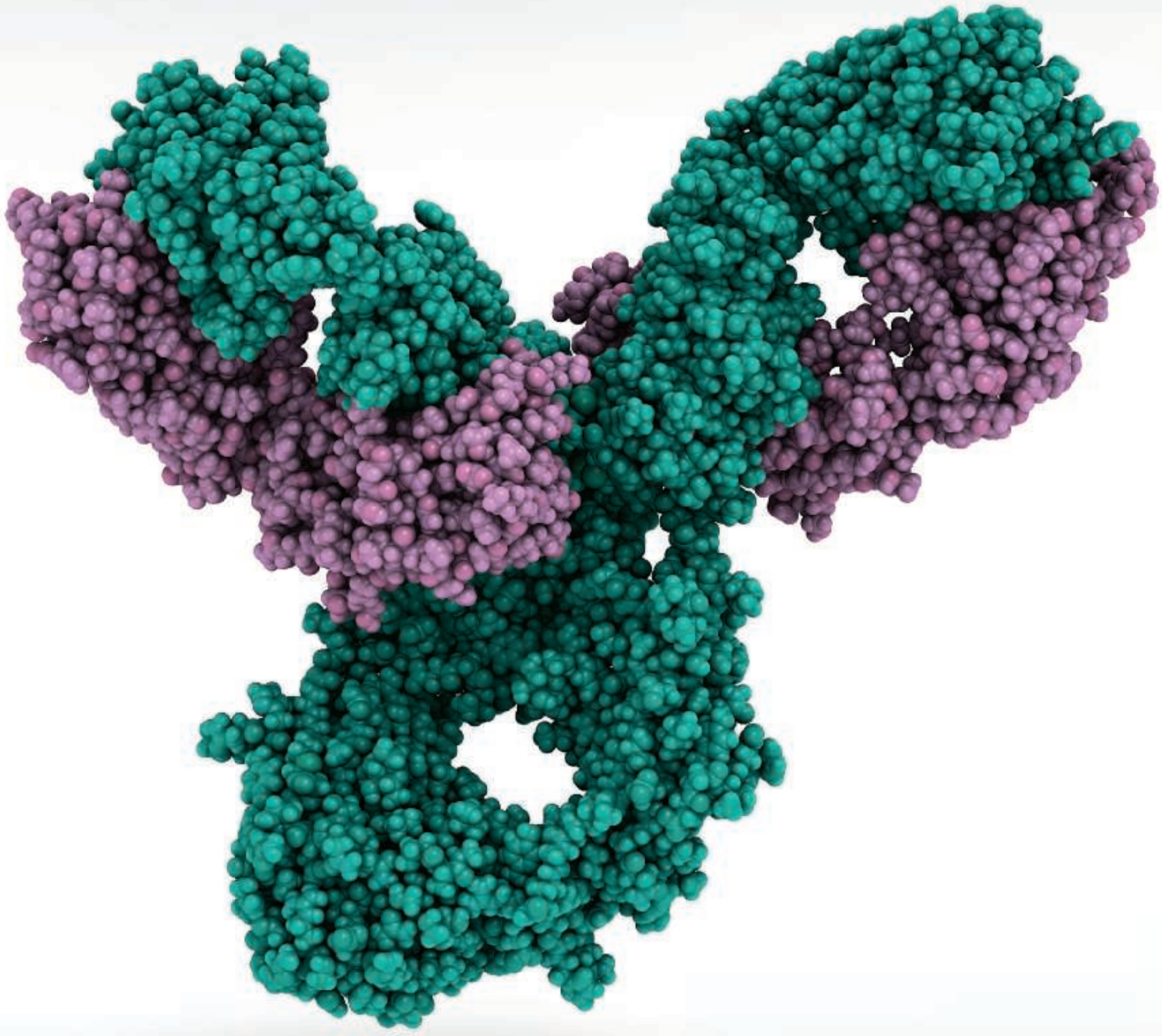

AXION RESEARCH

E-mail : info@axion-research.com
www.axionr.com/eng/

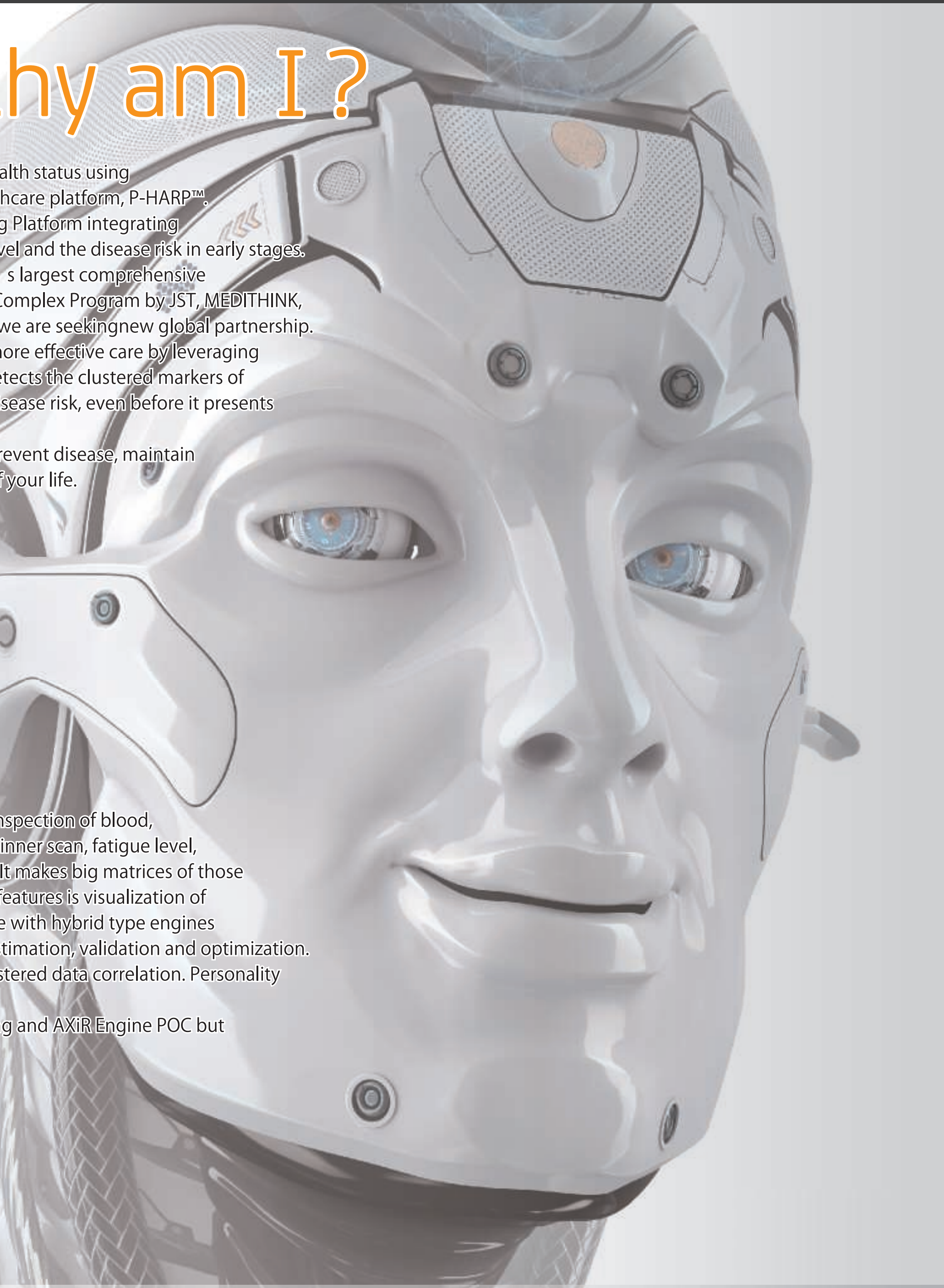

How healthy am I ?

Axion Research can exactly inform you on your health status using digital health data. We' re introducing new healthcare platform, P-HARP™. It stands for Precision Health Analysis Researching Platform integrating AXiR Engine® to estimate the individual health level and the disease risk in early stages. We have strategic partnership with RIKEN: Japan' s largest comprehensive research institution in natural science, Research Complex Program by JST, MEDITHINK, NIS plus, Fatigue Lab., SAXA and the others, and we are seekingnew global partnership. The healthcare providers will be able to deliver more effective care by leveraging the results of our robust predictive model that detects the clustered markers of disease earlier or very small indication offuture disease risk, even before it presents itself or is clearly identified.

P-HARP will be able to make recommendations to prevent disease, maintain your health condition, and improve the quality of your life.

AXiR Engine

P-HARP
PRECISION HEALTH ANALYSIS RESEARCH PLATFORM

AXiR Engine®

AXiR Engine is designed for multiple inputs like inspection of blood, urine, breathing gas, skin gas, body composition inner scan, fatigue level, Exosomes, microRNA, ncRNA, HLA, DNA and etc. It makes big matrices of those and estimation using some of those. One of the features is visualization of future risk and the self-learning can be advantage with hybrid type engines with AI Engines and the three type engines for estimation, validation and optimization. Replica Generator works well to support it by clustered data correlation. Personality Emotion Enginegrasps peoples' mind deeply.

We' ve just started those challenge with PAT filing and AXiR Engine POC but it shows highly potential.

Business Model

AXiON Research provides AXiR Engine and P-HARP customized services for the customers and partners. Healthcare Services are built in various application. We' re interested in strategic alliance partners to accelerate the market adoption.

Global Partnership

AXiON Research is building global partnership with AR/VR and robotics companies targeting healthcare industry. We' re also looking for worldwide business partners.

Fund Raising

We' re closing Angel Round in March and April 2018 in Japan. We' re also seeking it globally out of Japan in April, May and June 2018. Please contact us http://axionr.com

AXION RESEARCH INC.

Science Careers

SCIENCE CAREERS ADVERTISING

For full advertising details, go to ScienceCareers.org and click For Employers, or call one of our representatives.

AMERICAS

+1 202 326-6577
+1 202 326-6578
advertise@sciencecareers.org

EUROPE, INDIA, AUSTRALIA, NEW ZEALAND, REST OF WORLD

+44 (0) 1223 326527
advertise@sciencecareers.org

CHINA, KOREA, SINGAPORE, TAIWAN, THAILAND

+86 131 4114 0012
advertise@sciencecareers.org

JAPAN

+81 3-6459-4174
advertise@sciencecareers.org

CUSTOMER SERVICE

AMERICAS

+1 202 326-6577

REST OF WORLD

+44 (0) 1223 326528

advertise@sciencecareers.org

Science Careers
FROM THE JOURNAL SCIENCE AAAS

ScienceCareers.org

Advance your career with expert advice from *Science* Careers.

Download Free Career Advice Booklets!

ScienceCareers.org/booklets

Featured Topics:

- Networking
- Industry or Academia
- Job Searching
- Non-Bench Careers
- And More

Science Careers
FROM THE JOURNAL SCIENCE AAAS

POSITIONS OPEN

LUX ET VERITAS

ION CHANNEL PHARMACOLOGY/PHYSIOLOGY AND experienced pain researcher, YALE MEDICAL SCHOOL: Two positions available for Postdoctoral Research Associate or Associate Research Scientists at the Center for Neuroscience and Regeneration Research, Yale Medical School. One position requires experience in molecular biology and cell biology, transgenic mouse technology, small animal surgery and animal behavior with an emphasis on pain. The second position is for an electrophysiologist with experience in patch-clamp and pharmacological analysis of ion channels. They will join a multidisciplinary research team investigating role of Na channels in hyperexcitability disorders including neuropathic pain (see Dib-Hajj et al, *Nature Reviews Neurosci.* **14: 49-62**; 2013; Dib-Hajj et al. *Pain* 158 Suppl **1: S97-S107, 2017**; Yang et al, *Trends Pharmacol Sci*, **2018**) M.D., Ph.D., or M.D./Ph.D. degree and publications in ion channel electrophysiology/pharmacology or animal behavior are essential. Experience with voltage- and current-clamp analysis of DRG, or immunohistochemistry and viral platforms for gene transfer are desirable. Superb opportunity to work collaboratively within a highly productive, interactive team setting. Send statement of interest, Curriculum Vitae and three letters of reference to: **Stephen G. Waxman, MD, PhD (stephen.waxman@yale.edu) or Sulayman D. Dib-Hajj, PhD (sulayman.dib-hajj@yale.edu).**

Science Careers
FROM THE JOURNAL SCIENCE AAAS

Follow us for jobs, career advice and more!

🐦 @ScienceCareers

f /ScienceCareers

in Science Careers

ScienceCareers.org

Special Job Focus:

Biology

Issue date: March 30
Book ad by March 15

Ads accepted until March 23 if space allows

129,562 subscribers in print every week	**70,202** unique active job seekers searching for biology positions in 2017	**57,556** applications submitted for biology position in 2017

What makes *Science* the best choice for recruiting?

- Read and respected by 400,000 readers around the globe
- 80% of readers read *Science* more often than any other journal
- Your ad dollars support AAAS and its programs, which strengthens the global scientific community.

Why choose this issue for your advertisement?

- Relevant ads lead off the career section with a special biology banner
- Bonus distribution to Experimental Biology: April 21–25, San Diego, CA.

Expand your exposure.
Post your print ad online to benefit from:

- Link on the job board homepage directly to a landing page for biology jobs
- Additional marketing driving relevant job seekers to the job board.

To book your ad:
advertise@sciencecareers.org

The Americas
+ 202 326 6577

Europe
+44 (0) 1223 326527

Japan
+81 3 6459 4174

China/Korea/Singapore/Taiwan
+86 131 4114 0012

Produced by the *Science*/AAAS Custom Publishing Office.

SCIENCECAREERS.ORG

ScienceCareers
FROM THE JOURNAL SCIENCE AAAS

FOR RECRUITMENT IN SCIENCE, THERE'S ONLY ONE *SCIENCE*.

Cleveland Clinic
Lerner Research Institute

Postdoctoral Fellowships Available

The Lerner Research Institute is home to all basic, translational and clinical research at Cleveland Clinic, the No. 2 ranked U.S. hospital by *U.S. News and World Report*. With over $140M in federal grants and an annual research budget of $260M, the Lerner is consistently ranked among the top research institutes in the nation. Postdoctoral fellows routinely obtain grant funding and first-author publications in top-tier journals.

Postdoctoral Job Opportunities:
http://www.lerner.ccf.org/jobs/postdoctoral/
For further information email: RETC@ccf.org

The Lerner Experience

- Opportunity to train among world-class scientists and physician-scientists in a top-ranked healthcare institution
- Multidisciplinary, disease-focused research programs
- 175 principal investigators in 12 departments with over 700,000 square feet of research space
- Competitive salary and benefits package
- Active Postdoctoral Association and 250+ postdocs
- Career development opportunities and support through the Research Education and Training Center

City of Cleveland

Cleveland is a multicultural city with nationally acclaimed museums, sports, restaurants, and music and arts programs. Situated on Lake Erie, the area offers stunning views, beaches, and water sports. Low cost of living, with below average traffic and commute times for major cities.

AWARDS

HFSP

THE INTERNATIONAL HUMAN FRONTIER SCIENCE PROGRAM ORGANIZATION (HFSPO)

CALL FOR NOMINATIONS FOR THE 2019 HFSP NAKASONE AWARD

The HFSP Nakasone Award is awarded to scientists in recognition of pioneering work that has moved the frontier of the life sciences. This may encompass conceptual, experimental or technological breakthroughs. The award recognizes the vision of former Prime Minister Nakasone of Japan in the creation of HFSPO.

The competition is open; it is not limited to HFSP awardees and there is no age limit for candidates. In selecting the awardee the HFSPO Council of Scientists will pay particular attention to recent breakthroughs by younger scientists. The awardee will receive an unrestricted research grant of 10,000 USD, a commemorative medal and an invitation to deliver the HFSP Nakasone lecture at the 2019 HFSP Awardees Meeting.

The 2018 Nakasone Awardee is Svante Pääbo of the Max Planck Institute for Evolutionary Anthropology in Leipzig, Germany, for his discovery of the extent to which hybridization with Neanderthals and Denisovans has shaped the evolution of modern humans, and his development of techniques for sequencing DNA from fossils.

Nominations must be received before **27 April 2018** and include the HFSPO nomination form and the nominee's CV (see **http://www.hfsp.org/awardees/hfsp-nakasone-award** for more information).

WORKING LIFE

By **Maria Ter-Mikaelian**

Why our ways parted

My father has been a scientist for almost 40 years. I hadn't planned to follow in his footsteps, but to my surprise, I found myself drawn to research as an undergraduate. I went on to earn a Ph.D. in neuroscience, but I grew disillusioned and ultimately changed careers to become a science writer. Recently, I sat down with my father, who is currently a senior scientist at the Ontario Forest Research Institute in Canada, to reflect on what influenced his decision to stay in academia and mine to leave it. Our conversation has been translated from Russian and edited for brevity and clarity.

Michael Ter-Mikaelian: When I started doing research, it captivated me. While I was working on my first mathematical problem, I would ponder it for hours while walking with you in the stroller—and suddenly, I solved it! I was so excited that I couldn't sleep that night. Having once experienced that, you want to keep doing it. I've never felt the same elation again, but there is definitely still enjoyment. To a large extent that's what drives what I do.

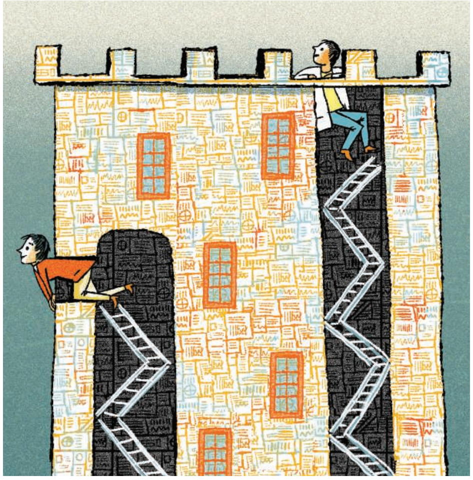

"What influenced his decision to stay in academia and mine to leave it?"

Maria Ter-Mikaelian: When I started doing research, I had the feeling that the people around me were such idealists. They just wanted to know the truth about how the world works, and they would have done it for free. One of the things that disillusioned me later, during my Ph.D., was the impression that to stay afloat in academic research, you have to constantly think about what will be "sexy" and what your brand is.

Michael: I know what you mean. A certain pragmatism is definitely necessary. But still, the people I know don't choose their research direction based on what is sexy. That was my downfall, in a way. I got interested in something; I did one project on it. All my life, I jumped from one topic to another. Mostly, I do it for my own enjoyment and for the respect of the small circle of people whose opinions matter to me. They certainly aren't pragmatists. They do what they think is interesting. If my goal had been international recognition of my brand, then I would have been constantly disappointed.

Maria: When I was finishing my Ph.D., I had the feeling that I was just mucking around. The problems I was working on were so narrow and esoteric, and they were using up so many resources—if not money, then my time and effort, and the effort of other people who were reading my work.

Michael: Quite a while ago, I came to the conclusion that that's how science works. There are lots of people, each doing their own little thing, like ants laying little bricks. There is not much use or progress from any of it. Then, someone comes along who synthesizes it all and makes a leap. Even then, some of the bricks will turn out to be completely useless. That's how it has to be. I accepted the fact that I probably won't be that synthesizer, and that's OK. I still believe that the work of those little bricklayers is important. It's necessary.

Maria: Maybe you stayed in science because you believe in that more than I do—that our petty little activities are necessary in the grand scheme of things. I just felt that I was going to be the bricklayer who was doing something silly off to the side that wasn't even going to be part of the building.

Michael: It's not that I believe it more than you do. It might be that it's enough for me, but not enough for you.

Maria: Particularly when I was finishing my Ph.D., there weren't many people who I could talk to and see that big picture. The grad students and postdocs I was friends with all had the view that academia is hopeless, and they were all very disillusioned in research as a career.

Michael: What you were exposed to, that's what you based your conclusions on. Life is not always a result of a conscious decision. You look back and think, "It could have turned out completely differently." ■

Maria Ter-Mikaelian is a science writer based in New York City. Send your story to SciCareerEditor@aaas.org.

ILLUSTRATION: ROBERT NEUBECKER